Modelling the oxidation of polycristalline austenitic stainless steels using a phase field approach coupled with mechanics

Victor de Rancourt

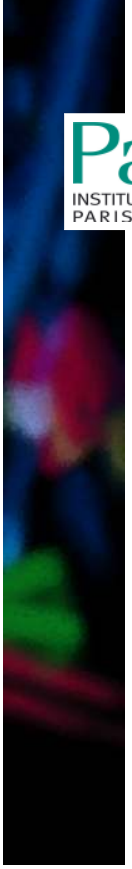

ParisTech
INSTITUT DES SCIENCES ET TECHNOLOGIES
PARIS INSTITUTE OF TECHNOLOGY

MINES ParisTech

École doctorale 432: Sciences des métiers de l'ingénieur

Doctorat ParisTech

THÈSE

pour obtenir le grade de docteur délivré par

L'École Nationale Supérieure des Mines de Paris

Spécialité: "Sciences et Génie des matériaux"

Présentée et soutenue publiquement par :

Victor de Rancourt

le 12 juin 2015

Modélisation de l'oxydation des aciers inoxydables polycristallins par une approche en champs de phases couplée avec la mécanique

~~~

Modelling the oxidation of polycristalline austenitic stainless steels using a phase field approach coupled with mechanics

Directeurs de thèse: **Samuel FOREST**
Esteban P. BUSSO

Co-encadrement de thèse: **Benoît APPOLAIRE**

Jury :

M. Krzysztof WOLSKI, Directeur de recherche, centre SMS-EMSE, Saint-Étienne	Président
M. Jérôme FAVERGEON, Professeur des Universités, Laboratoire Robertval, Compiègne	Rapporteur
M. Alexandre LEGRIS, Directeur de recherche, Laboratoire UMT, Lille	Rapporteur
M. Benoît APPOLAIRE, Maître de recherche, ONERA, Châtillon	Examinateur
M. Samuel FOREST, Directeur de recherche CNRS, Mines ParisTech, Paris	Examinateur
M. Robert SPATSCHEK, Group leader, Max-Planck Institute für Eisenforschung, Düsseldorf,	Examinateur
M. Esteban BUSSO, Directeur scientifique, ONERA, Palaiseau	Invité
M. Thierry COUVANT, Ingénieur de recherche, EDF R&D, Moret-sur-Loing	Invité

THÈSE

Mines ParisTech
Centre des Matériaux
10 rue Henri-Auguste Desbruères, 91000, Evry, France
~~~

“Là où il y a une volonté; il y a un chemin.”

Gaston Rébuffat

Acknowledgements

Ce travail est le fruit d'une collaboration fructueuse en idées et en développements entre le **Centre des Matériaux (CDM)**, **EDF R&D** et le **Laboratoire d'Étude des Microstructures (LEM-ONERA)**. Dans chacun de ces laboratoires, j'y ai reçu le meilleur accueil possible et y ai trouvé un environnement de travail idéal. Trois ans se sont ainsi écoulés à la vitesse de l'éclair. Il y eut des moments difficiles (il en faut !), des jubilations devant des théories prometteuses, mais aussi le quotidien que j'ai simplement adoré partager avec chacun d'entre vous. Je ne me suis pas ennuyé, et c'est peu dire !

Je ne saurai jamais assez remercier **Samuel Forest** pour m'avoir épaulé durant tout ce temps. J'espère avoir pu, de mon côté, satisfaire suffisament de ses attentes (qui s'avèrent être infinies !). L'enthousiasme débordant de Samuel a été une grande source de motivation tout au long de ce travail pour la modeste personne que je suis. Je remercie également **Esteban Busso** pour ses conseils avisés notamment pour la communication scientifique dans la langue de Shakespeare qui m'ont été plus qu'utiles à bien des reprises. Mes remerciements s'adressent particulièrement à **Benoît Appolaire** (mais aussi à l'ensemble du LEM à l'ONERA dont Yann Le Bouar, Alphonse Finel, Mathieu Fèvre, Benoît Devincre, Pierre-Louis Valdenaire, Maeva Cottura, Pierre-Antoine Geslin et Anaïs Gaubert) pour leur soutien lors des développements et analyses dans les moindres détails du modèle de champ de phases (dont les fameuses "intrusions" d'oxyde). Je remercie **Thierry Couvant** ainsi que **Sylvain Leclercq** pour m'avoir fait partager leur expérience de la métallurgie des aciers ainsi que pour m'avoir accordé leur confiance dans la direction de ce travail. Pour finir, je remercie **Kais Ammar** pour m'avoir assisté lors de mon décollage dans l'univers des champs de phases et de la programmation dans Zébulon en m'épargnant de nombreuses turbulences. Vous avez tous contribué à ce travail par vos conseils bienveillants qui ont aiguisé ma manière de penser. J'espère que vous aurez du plaisir à retrouver un peu de vous au travers de la lecture du manuscrit.

Je tiens à remercier Messieurs **Jérôme Favergeon** et **Alexandre Legris** pour avoir accepté la dure tâche de rapporteurs. J'espère que le travail est à la hauteur de vos espérances ! Je remercie également Messieurs **Robert Spatschek** et **Krzysztof Wolski** pour avoir accepté les rôles d'examinateur et président respectivement. *Ich bedanke mich bei Herrn Spatschek auch für die Vorlesung über Cuda während der Phase-Field Summer Schule in Peyresq !*

Je tiens également à remercier l'équipe VAL composée de Kais Ammar, Djamel Missoum-Benziane et Nikolaï Osipov pour leur disponibilité et leurs compétences en matière de logiciel et surtout de débogages. Et également les scientifiques et personnels du CDM dont André Pineau, George Cailletaud, Christophe Colin, Jacques Besson, Yves Bienvenu, Anne-Françoise Gourgues-Lorenzon, Jérôme Crépin, Cécilie Duhamel, David Ryckelynck, Vladislav Yastrebov, Vladimir Esin, Mathieu Mazière, Henry Proudhon, Lucien Laiarinandrasana, Odile Adam, Véronique Matos, Véronique Diamantino, Konaly Sar, Jean-Yves Herry, Françoise Di Rienzo, Grégory Saint-Luce, Gérard Brabant, Olivier Delhomme, Catherine Rouil et Zak.

La thèse n'aurait pas eu la même saveur sans mes collègues de bureau et particulièrement Aurélien pour nos réunions déjantées avec Samuel le soir, Harry et Mouhcine pour leurs connaissances

expérimentales (et en Gimp !), Justin, Damien et Hayat pour leur convivialité. Au delà du bureau, je ne saurai oublier mes camarades doctorants et étudiants en master pour, notamment, nos parties de foot endiablées. Mesdames et messieurs Goeffrey, Franck, Hicham, Romain, Georges, Aberrahim, Mohamed, Régis, Raphaël, Samuel, Arina, Jia, Erembert, Nicolas, David, Victor le grand et Victor du sud (incroyable 3 Victor d'un coup !), Rim, Adrien, Josiane, Judith, Emmanuelle, Emma, Bogdan, Raphaël, Mickael, Vincent, Jacqueline, Mériem, Nada, Mona, Guillaume, Georges, *re*-David, Clément, Pierre-Alexis, François-Xavier, Francesco, Guillaume, Davide, Florent, Armel Brice et Dimitri entre autres, sachez que je vous remercie pour ces tous petits moments de détente bien agréables.

Et pour finir, je souhaite remercier mes professeurs des classes préparatoires **Jean-Yves Poirier** pour la physique et **Karim Abdeljelil** pour les mathématiques ainsi que mon professeur de programmation scientifique et science des matériaux **Daniel Weygand** pour tous leurs encouragements qui m'ont conduit aussi loin ! Je remercie également tous les contributeurs de logiciels libres qui m'ont été bien utiles au cours de mes études dont l'incroyable **Richard Stallman** pour le bonheur qu'Emacs me procure au quotidien !

Et maintenant, place à la lecture... Ah oui, je remercie aussi ma famille toujours au top, les camarades du lycée, des Arts, les parapotes et les versaillais street hockeyeurs avec lesquels il est impossible de s'ennuyer !

Abstract

Austenitic stainless steels and nickel based alloys are widely used for their mechanical properties at high temperatures. Their durability can be increased by the addition of chromium resulting in the formation of a protective oxide layer such as chromia (Cr_2O_3). Nevertheless, it is established from vacuum mechanical tests that oxidation significantly decreases their fatigue life. In fact, oxide growth can be followed with the injection of defects such as vacancies, deleterious chemical elements and residual stresses, *etc.*, into the metal. The resulting cracking micromechanisms are therefore governed by complex interactions between the environment and the metal surface, implying the chemical composition and the microstructure of the metal.

To date, materials life prediction is a necessity for the nuclear industry due to safety and economic issues. The enhancement of the model dimensionality allows to explicitly account for multi-physics interactions between oxide and metallic phases under mechanical loads. The thesis is in line with it and relies on the development of a phase field model coupled with mechanics that heavily relies on the principles of continuum thermodynamics. The effective behaviour of the interface is obtained by homogenisation methods allowing the mixture of separate behaviours, as it is the case on a ductile metallic substrate and its fragile oxide. Oxide growth residual stresses and mechanical load induced stresses can be relaxed by viscoplasticity, which is isotropic and anisotropic respectively for the oxide and the substrate. Full field finite element simulations are performed to study both generalised and intergranular oxidation under mechanical loads. The simulations highlight the possibility of triggering breakaway oxidation by the generation of tensile stresses in the fragile oxide, which can be localised along oxide intrusions at grain boundaries.

Keywords: oxidation, mechanics, polycrystal, modeling, phase field, finite element

Résumé

Les aciers austénitiques et alliages à base de nickel sont des matériaux de choix pour leurs propriétés mécaniques à haute température. L'enrichissement en chrome améliore leur durabilité de par la formation d'une couche d'oxyde protectrice à l'exemple de la chromine (Cr_2O_3). Il est néanmoins établi, par des essais mécaniques sous vide, que l'oxydation réduit de manière notable leur durée de vie en fatigue. En effet, la croissance d'oxyde peut être accompagnée d'une introduction de défauts tels que l'injection de lacunes, d'éléments délétères comme l'hydrogène mais également de contraintes résiduelles, *etc.*, dans le métal. Les micromécanismes de fissuration sont ainsi régis par des interactions complexes entre l'environnement et la surface du métal, faisant intervenir composition chimique et microstructure.

Aujourd'hui, les enjeux de sécurité et de compétitivité font de la prévision de la durée de vie de ces alliages une nécessité pour l'industrie nucléaire. L'augmentation de la dimension des modèles permet de prendre en compte de manière explicite les interactions multiphysiques du couple oxyde/métal sous l'action d'un chargement mécanique. La thèse s'inscrit dans cette démarche et propose une formulation d'un modèle de champs de phases couplé avec la mécanique et fondé sur les principes de la thermodynamique des milieux continus. Le comportement effectif de l'interface est présentement obtenu *via* des méthodes d'homogénéisation permettant de combiner des comportements mécaniques dissemblables, à l'image d'un substrat ductile et de son oxyde fragile. Les contraintes induites par la formation d'oxyde et également par le chargement mécanique peuvent être relaxées viscoplastiquement, de manière isotrope et anisotrope, respectivement dans l'oxyde et dans le substrat. Des simulations par éléments finis de l'oxydation généralisée ainsi que de l'oxydation intergranulaire sous chargement mécanique sont effectuées. Ces dernières mettent en évidence la possibilité d'un phénomène d'oxydation catastrophique par la génération de contraintes de tensions dans l'oxyde fragile, lesquelles peuvent être localisées le long des intrusions d'oxyde dans les joints de grains.

Mots clés : oxydation, mécanique, polycristal, modélisation, champs de phases, éléments finis

Contents

Notations

Tensors	
λ	scalar
$\underline{\boldsymbol{u}}$, u_k	vector
$\underset{\sim}{\boldsymbol{\varepsilon}}$, ε_{ij}	second order tensor
$\underset{\approx}{\boldsymbol{\Lambda}}$, Λ_{ijkl}	fourth order tensor
$\{\underline{\boldsymbol{x}}, \underline{\boldsymbol{y}}, \underline{\boldsymbol{z}}\}$	orthonormal set

Operators	
$\cdot$	scalar product
:	double contraction
$\nabla\cdot$	divergence
∇	gradient
Δ	laplacian

Formulas	
$\iiint \nabla \cdot \underline{\boldsymbol{J}}\, dV = \oiint \underline{\boldsymbol{J}} \cdot \underline{\boldsymbol{n}}\, dS$	divergence theorem
$\dfrac{\delta F}{\delta \rho} = \dfrac{\partial f}{\partial \rho} - \nabla \cdot \dfrac{\partial f}{\partial \nabla \rho}$	functionnal derivative where $F = \displaystyle\int_V f(\rho, \nabla\rho) dV$

Acronyms

AUSS	Austenitic stainless steel
BCC	Body-centred cubic
BCT	Body-centred tetragonal
CEFM	Coupled environment fracture model
CERT	Constant extension rate tensile testing
CF	Creep fatigue
CGP	Crack growth path
CGR	Crack growth rate
CPK	Corey, Pauling and Koltun
EDX	Energy dispersive X-ray
FCC	Face-centred cubic
HCP	Hexagonal close-packed
IBVP	Initial and boundary value problem
IGSCC	Intergranular stress corrosion cracking
KMC	Kinetic Monte-Carlo
MD	Molecular dynamics
MMAE	Method of matched asymptotic expansions
MPC	Multi-point constraint
ODE	Ordinary differential equation
OECD	Organisation for Economic Co-operation and Development
PBR	Pilling-Bedworth ratio
PWR	Pressurized water reactor
SCC	Stress corrosion cracking
SEM	Scanning electron microscopy
SIMS	Secondary ion mass spectrometry
SSRT	Slow strain rate testing
TEM	Transmission electron microscopy
TGSCC	Transgranular stress corrosion cracking

CHAPTER

1 Introduction

Contents

La corrosion est un phénomène de vieillissement qui peut mener à la rupture des composants. Lorsque celle-ci est couplée avec un chargement mécanique, cette rupture peut être très largement prématurée. On parle ainsi de corrosion sous contraintes. Des ruptures par corrosion sous contraintes peuvent être observées dans les circuits de refroidissement des réacteurs à eau pressurisée entre autres. Aujourd'hui, la prévision du phénomène de corrosion sous contraintes demeure une question ouverte. En effet, les mécanismes responsables de la rupture du couple métal oxyde ne sont toujours pas complètement identifiés. De ce fait, de nombreuses hypothèses ont été formulées et nécessitent des validations expérimentales approfondies. Or, la corrosion sous contraintes est un phénomène à la fois local et complexe ce qui rend l'analyse des résultats expérimentaux extrêmement délicate (problème de représentativité statistique, d'identification des mécanismes prépondérants, ...). Parmi ces hypothèses, on retrouve principalement les phénomènes de fragilisation par ségrégation dont les chefs de file sont l'hydrogène, l'oxygène, le phosphore, *etc.* La rupture est ensuite amorcée dans ces sites segrégés par ces éléments délétères car les propriétés mécaniques y sont localement diminuées. Une autre hypothèse consiste simplement en la rupture de la couche d'oxyde protectrice par l'action de contraintes mécaniques locales, qu'elles soient de nature résiduelles ou bien appliquées par un chargement mécanique. À ce titre, la modélisation des champs de concentrations et des contraintes à l'échelle du grain s'avère être nécessaire pour pouvoir comprendre ces mécanismes. Néanmoins, la plupart des modèles précédemment développés couplant mécanique et diffusion ne prennent pas en compte la phase d'oxyde en tant que telle. Des études de l'oxydation à haute température montrent que la couche d'oxyde génère des contraintes dans le substrat qui peuvent être relaxées de manière viscoplastique. Lorsque l'interface métal-oxyde est non planaire (ce qui est le cas pour la quasi-totalité des observations), cela engendre des contraintes hétérogènes dans la couche d'oxyde mais aussi dans le substrat. Il est aujourd'hui admis que la propagation de fissures de corrosion sous contraintes est intimement liée à la rupture de cette couche d'oxyde. L'étude porte ainsi sur la croissance d'oxyde sur un substrat polycristallin. Les interactions de l'oxyde avec des défauts cristallins comme les joints de grains et bandes de localisation plastique accroissent la probabilité de rupture par corrosion sous contraintes de part la déstabilisation de la morphologie de l'interface métal-oxyde. La cause de cette déstabilisation étant que ces défauts se comportent comme des court-circuits de diffusion, et ce aussi bien pour l'oxygène que pour les éléments d'alliage. Du fait d'un lien incontestable entre défauts cristallins et zones de rupture, une attention particulière doit être donnée aux contraintes mécaniques locales lors de la croissance d'oxyde. Pour cela, la thèse repose sur l'application de la méthode des champs de phases à la croissance d'oxyde et incorpore différents phénomènes de relaxation plastique.

1.1 Context

As mentioned in [IAEA, 2011], the safety standards of atomic energy must ensure the peaceful use of such a power source, which can only be guaranteed by the development of a cutting-edge expertise for the whole process. Stress corrosion cracking is often mentioned amongst all issues encountered in nuclear reactors. It is an ageing degradation phenomenon that can lead to the premature failure of a variety of nuclear reactor components. This is why R&D programs have been established for its mitigation and prevention. Theoretical research was done in the field of chemistry and materials sciences, to respectively identify all involved chemical processes along with materials behaviour. The two main areas of research are presently the field of passivation of metals, to optimise nuclear reactor coolants along with corrosion resistant alloys [Marcus, 1998], and the field of failure of materials, for the formulation of damage laws, *e.g.* creep damage, fatigue damage, irradiation damage, *etc.*, necessary for the life prediction of nuclear reactors. To date, it resulted in the formulation of crack propagation laws that account for coupled stress-oxidation mechanisms, for instance, the EAC[1] model of [Shoji et al., 2010] amongst other. Stress corrosion cracks are frequently emerging along grain boundaries for which deeper oxidation levels can be reported. The typical stress corrosion crack pattern is

[1] Environmentally assisted cracking

illustrated in Fig. 1.1.

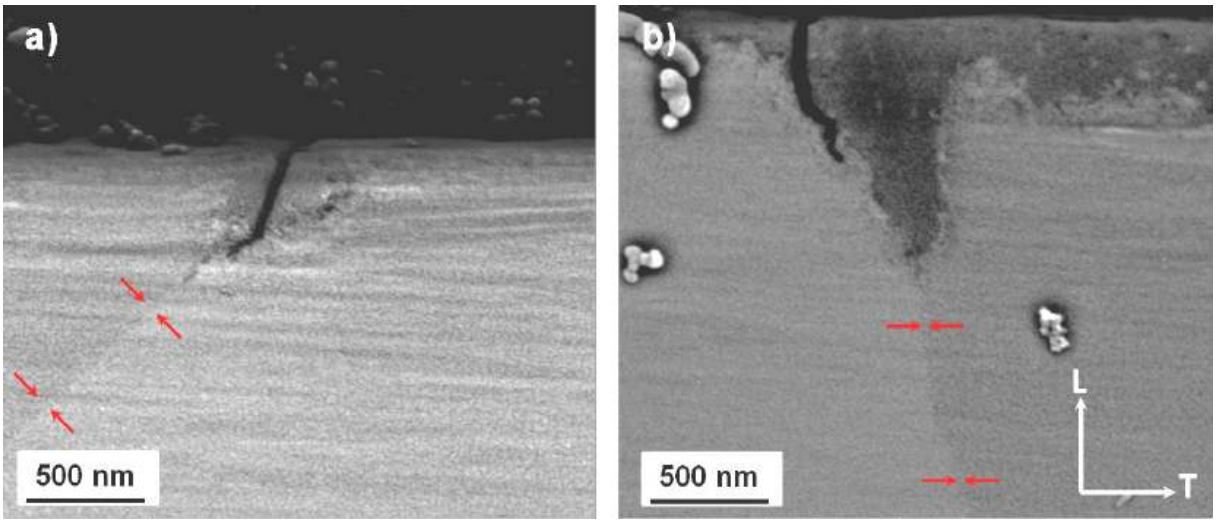

[Wehbi, 2014]

Figure 1.1: SEM micrograph of an emerging stress corrosion crack within a nickel based alloy that has been put under a tensile mechanical load. The crack is localised along the grain boundary in (a) and sideways of the oxide intrusion in (b).

The figure shows the formation of an isolated oxide intrusion along a grain boundary, that acts as a privileged spot for cracking. Cracks are shown to be propagated either along the grain boundary or along the metal-oxide interface sideways of the oxide intrusion. Moreover, the grain boundary behaviour is also reported to be complex at the crack tip as it can be deflected in some cases, *e.g.* [Bruemmer and Thomas, 2005].

Despite a large amount of experimental data available at elevated temperatures in PWRs, the thesis has been mainly focused on high temperature oxidation for simplicity. It is well-known that creep and creep fatigue micro-cracks can be generated within the bulk alloy around precipitates or at the free surface of the metal along localised slip bands, grain boundaries and triple junctions, *etc.*, see [Pineau and Antolovich, 2009, Antolovich and Armstrong, 2014], that act as stress concentrators. The crystal plasticity framework [Méric et al., 1991a, Méric et al., 1991b, Busso and McClintock, 1996, Kocks and Mecking, 2003, Busso and Cailletaud, 2005] that accounts for grain boundaries and crystal orientations in the transmission of mechanical stresses within polycrystals is essential to evaluate stress extrema provided that the mechanical behaviour of the single crystal is well known. The complexity of materials behaviour can be extended to account for a variety of additional phenomena, like damage, precipitation, diffusion-creep, dislocation pile-ups, grain boundary sliding, *etc.*, to improve the evaluation of such local stress fields. Calculations at the scale of the grain can then be bridged to upper scales to improve the accuracy of the life prediction of structural parts.

It is well known that strong interactions between the material and the environment can drastically decrease its creep fatigue life. The Fig. 1.2 from [Weiss and Pineau, 1993] shows a SEM micrograph of an austenitic stainless steel that experienced a corrosion fatigue test. It evidences the clear interplay between crystal defects – like localised slip bands or grain boundaries – with oxide growth. The formation of such an oxide intrusion has been explained from the passivity loss – or higher reactivity – of the oxide growing within two-dimensional crystal defects, see also [Herbert et al., 2012]. Nevertheless, the mechanisms for such a passivity loss are still not resolved to date but may be related to pipe diffusion or to the formation of another – more porous – oxide. It is well established that grain boundaries generally act as diffusion short circuits. Here, the figure suggests that slip bands can be considered as diffusion short circuits as well. Such intrusions are the tip of the iceberg of the metal-oxide behaviour, the invisible part being the penetration and segregation of chemical elements or eventually the injection of vacancies from the free surface into the metal. Hydrogen embrittlement is one well-known degradation phenomenon leading to EAC, see [Gutierrez-Solana et al., 1993, Barnoush, 2011]

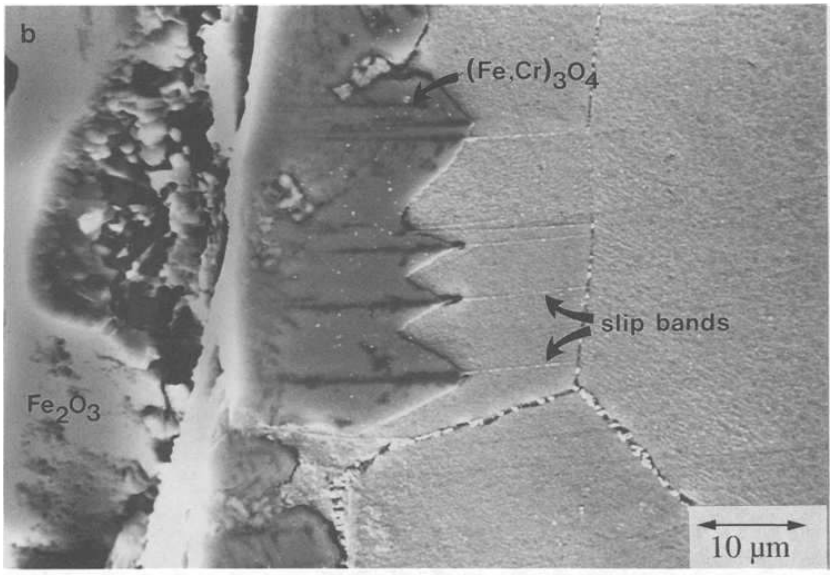

[Weiss and Pineau, 1993]

Figure 1.2: SEM micrograph of a torsion creep fatigue specimen (316L) after 60 min of oxidation under air at 600°C.

amongst others. The decrease of the creep fatigue life of materials undergoing oxidation has been qualitatively explained by the bypassing of the classical fatigue crack initiation stage here promoted by the brittle failure of the oxide layer, [Weiss and Pineau, 1993]. The crack tip growth kinetics is then often assumed to be driven by a repeated depassivation/repassivation mechanism. The depassivation stage can be found in the literature with varying nature, *e.g.* mechanical failure, dissolution, *etc.*, see [Stellwag, 1998].

Finally, the establishment of initial localised plasticity prior to cycling – with or without oxidation – has also been evidenced to reduce the fatigue life of austenitic stainless steels, *i.e.* [Couvant et al., 2005, Couvant et al., 2007, Kamaya and Haruna, 2007, le Pêcheur, 2008, Couvant et al., 2009, Huguenin et al., 2010, Guilhem, 2011, Huguenin, 2012, Lozano-Perez et al., 2012]. This effect has been attributed to the generation of an extra hardening in the metal, that can result in the formation of additional emerging triple junctions and localised slip bands hence leading to a more heterogeneously distributed stress. Alternatively, it can also be attributed to the generation of several more crack initiation sites, localised at the free surface.

It is worth noting that the study performed by [Weiss and Pineau, 1993] was dedicated to the assessment of the creep fatigue life of austenitic stainless steels. Those alloys were intended to be used for the nuclear reactor SuperPhénix, which was a sodium-cooled fast reactor. Currently, nuclear power installations are mostly pressurised water reactors, for which the service conditions are different. For instance, the operating temperature is lower, which suggests *a priori* for less critical conditions but the supercritical water is known to be corrosive *a contrario* to liquid sodium. Nevertheless, liquid metal environments are known to be able to induce significant intergranular damage due to the wetting phenomenon, see [Legris et al., 2005]. In air, wetting patterns can also be found between the solid-solid oxide metal interface as shown along grain boundaries in Fig. 1.3. Therefore, the stress-corrosion behaviour of metal parts used in pressurised water reactors needs to be characterised by taking into account such phenomena.

In practice, the stress corrosion resistance is mainly evaluated from U-bend or creep tests in simulated primary water [Baboian, 2004]. The provided data allows to determine a range of conditions for which the material is not damaged. But experimental campaigns are time costly – creep tests can go up to decades. Moreover, due to the availability of testing machines and the variety of alloy grades to be tested, those experimental campaigns do not necessarily eliminate all data spread. This data spread has to be circumvented by using large safety coefficients in mechanical dimensioning

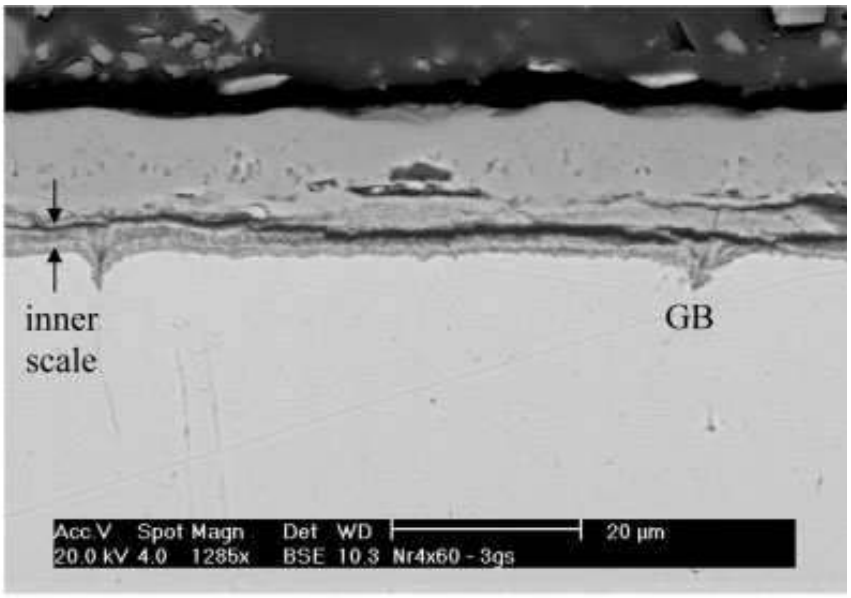

[Krupp et al., 2006]

Figure 1.3: SEM micrograph of a low-alloyed Fe-Cr steel (X60) after 72 hours of oxidation under air at 550°C.

and in maintenance schedules. Nevertheless, experimental campaigns allow to highlight different interactions between materials, loadings and environments, like the effect of the temperature, hydrogen content, *etc.* on the stress corrosion crack growth rate for instance, see [Huguenin, 2012] for more details. An important result is that stress corrosion cracking resulted to be thermally activated hence suggesting that it can be diffusion controlled. The characterisation of the mechanisms leading to stress corrosion cracking in pressurised reactors has been performed since the 60s over several countries. Despite this, no model is yet general enough to predict the behaviour of a given grade undergoing the combined action of stresses and environment. The main difficulty lies in the fact that stress corrosion cracking – in the conditions of primary water – can have an initiation time of several decades, [IAEA, 2011]. One can then easily see the difficulty to characterise a nebula of grades – steels or nickel based alloys – and formulate accurate ageing laws accounting for numerous interactions between the metal, the environment and the loads over such a period. This is why, as for many ageing phenomena, stress corrosion cracking is still difficult to predict. The improvement of the current life expectancy laws must therefore be performed by combining strongly targeted experiments with complex numerical models.

The actual inaccuracy of life expectancy models reveals gaps in the description of the cracking micromechanisms within the coupled stresses-environment operating conditions of pressurised water reactors. Nevertheless, it resulted in an abundant literature, containing many stress corrosion cracking models, which are reviewed in [Laghoutaris, 2009] for instance. Amongst them, different mechanisms leading to the weakening up to the breaking of the metallic phase can be found. They are namely the oxygen ingress within grain boundaries, the rapid diffusion and segregation of hydrogen into grain boundaries and localised slip bands and underlying embrittlement, the depletion of metallic component from cationic oxide growth and underlying infiltration of vacancies in the metal, carbides precipitation within grain boundaries and underlying chromium depletion, and so on. At this point, it is certain that the various concentration fields of both components and vacancies are highly heterogeneous in the vicinity of the metal-oxide interface – or the interdiffusion area – hence coming along with a large spectrum of material properties within the sample. The present remarks suggest therefore for the development of a field theory that embraces diffusion and stresses, like the ones developed in [Musienko and Cailletaud, 2009, Plessier, 2010] for instance. Nowadays, multiphysics simulations are possible thanks to the always increasing computational power. Amongst the models available in the literature, the problem of oxide growth stresses has

been widely discussed by experiments and simulations, *e.g.* [Barnes et al., 1989, Huntz et al., 1998, Krishnamurthy and Srolovitz, 2003, Krishnamurthy and Srolovitz, 2004, Zhou et al., 2010b] amongst others. Such growth stresses can play a crucial role in intergranular stress corrosion cracking, see [Evans, 1983]. Unfortunately, the question of growth stresses is still debated. Most of the authors select an effective misfit strain as a fitting parameters to generate the growth stresses [Clarke, 2002], which is also the case in the present work. To date, oxidation offers a wide field of study as many of their secrets are still to be discovered. Amongst them, one can mention the topics of growth stress, scale fracture, oxide spallation, buckling (see [Goedjen et al., 1994]), *etc.*, and stress corrosion cracking. Strangely, growth stresses are often neglected in the literature of stress corrosion cracking within PWRs, whereas it is widely discussed in the literature devoted to the high temperature oxidation of superalloys.

1.2 Motivations

Phase field modelling is appealing due to its ability to solve, with a relative ease, complex moving interface problems, *i.e.* dendritic solidification [Karma, 2001, Gránásy et al., 2006, Steinbach, 2009], as illustrated in Fig. 1.4. The micrographs shown in Fig. 1.2 and 1.3 emphasise the moving bound-

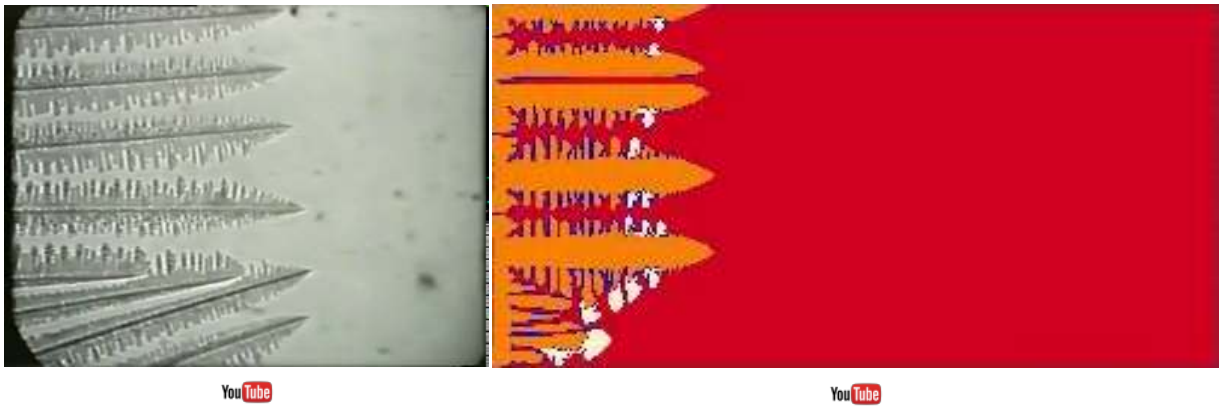

(a) (b)

Figure 1.4: (a) shows a snapshot of an experimental movie of dendritic solidification found in https://www.youtube.com/watch?v=S07fPo45BvM but unfortunately comes without any information, most likely a transparent model material [Huang and Wang, 2012]. (b) is a phase field simulation of the solidification of a stainless steel from Dr. J. Vitek relayed by H. K. D. H. Bhadeshia found in https://www.youtube.com/watch?v=XbhLrktoBnU; other interesting movies can be found in his YouTube account **bhadeshia123**.

ary context of growing oxide intrusions. This is why phase field methods appear to be well-suited for simulating oxide growth as complex-shaped interfaces are often involved. The aforementioned figures evidence a sawtooth shaped metal-oxide interface for the case of the slip band at high temperature, and a curved oxide intrusion in the case of the grain boundary. Due to such a variety of interface morphologies, simulation of the growth of oxide intrusions is a numerical challenge and hence the need for the well-known flexibility of the phase field method. Phase field methods are basically the approximation of a sharp interface problem done by performing the smoothing of all interface gradients over a prescribed finite thickness, which is termed the interface thickness in return. Phase field models can be easily coupled with other phenomena, *e.g.* heat, diffusion, elasticity, plasticity, *etc.* – see [Steinbach, 2009]. To that, the microstructure can also be accounted for and coupled with the metal-oxide phase field by the use of additional phase fields, *e.g.* a grain boundary field [Abrivard, 2009, Abrivard et al., 2012b, Abrivard et al., 2012a]. To date, the developments made by the phase field community are now sufficiently advanced to undertake the simulation of the grain boundary and slip band oxidation problems.

1.3 Objectives

Currently, stress corrosion cracking models have been developed at EDF R&D. Those models are based on the simulation of the ingress of external deleterious components such as oxygen of hydrogen, *i.e.* [Musienko and Cailletaud, 2009, Zhou, 2010]. Such models are nevertheless not accounting for multicomponent diffusion and neglect the growth stresses that are generated by the misfitting oxide layer. The starting point of the thesis was was to investigate the suitability of a finite element based phase field method for the modelling of oxide growth. To that end, the problem was decomposed into the following series of objectives:

- To identify the main causes of environment assisted cracking of polycristalline alloys in PWRs
- To develop a generic phase field stress multicomponent diffusion coupled framework that strongly relies on continuum thermodynamics
- To formulate coupling relationships linking oxidation and diffusion short circuits
- To apply the model to austenitic stainless steels at high temperatures
- To study the failure behaviour of the oxide layer and the poycristalline alloy

The model must account for the growth of the oxide intrusions found along grain boundaries and localised slip bands. The growth of the oxide will be driven by the multicomponent diffusion of oxygen and alloying elements. Growth stresses will be here accounted for by means of an eigenstrain intrinsic to the oxide phase, [Huntz et al., 2002, Clarke, 2002]. The crystal plasticity framework will be implemented regarding the size of the simulation domain and the effect of external loads during oxidation will be studied. Further, this study can be useful to understand the mechanism of stress corrosion cracks initiation, by performing analyses of local stress fields and reviewing the assumption usually done in the field of stress corrosion cracking. It is worth noting that during the thesis, EDF R&D initiated the creation of the MAI-SN[2], which objective is to better coordinate the field experience of the MAI with academic researchers for efficient R&D achievements in the field of environmentally assisted cracking. In fact, there is a strong need for the better characterisation of materials' life expectancy for improved safety coefficients in the nuclear energy domain. The thesis should then provide a framework for the investigation of numerous damage mechanisms in a near future, such as irradiation damage for instance.

1.4 Outline

The work is divided into four chapters.

The first one is devoted to a bibliographic review of the problem of oxide growth in stainless steels. It begins with a general introduction on stainless steels and related oxides. The chapter also focuses on the observation of composition heterogeneities in the interdiffusion area and on the mechanical behaviour of the metal and oxide phases. Moreover, some fundamental aspects of oxide growth are reviewed by describing some theoretical approaches used in the modelling of oxide growth. The properties of the metal-oxide interface and the diffusion short-circuit behaviour of crystal defects like grain boundaries and slip bands is also discussed.

The second chapter represents the core of the present work. It introduces the formulation of a phase field model that heavily relies on the principles of thermodynamics. The model is formulated within the framework of homogenisation based phase field approaches. The homogenisation approach allows to mix separate materials behaviour, as for the nano-grained oxide and the substrate, for which different viscoplasticity mechanisms can occur. Homogenisation assumptions are shown to naturally originate from the thermodynamic potential used in the description of the system's total energy. The differences between the well-known Voigt/Taylor and Reuss/Sachs homogenisation

[2]Material Ageing Institute Scientific Network

schemes are then discussed. The chapter ends with numerical simulations of growing precipitates, while considering isotropic up to anisotropic viscoplasticity. The simulations emphasise the role of viscoplasticity on the morphological evolution of precipitates.

The third chapter is devoted to the study of oxide growth limited to the case of a planar interface. It extends the work of [Huntz et al., 2002], as it explicitly accounts for mass transports during oxide growth. The ternary and quaternary systems – (Fe-Cr-O) and (Fe-Cr-Ni-O) – are studied and the model is shown to reproduce the chromium depletion and the nickel enrichment discussed in the first chapter. The chapter ends with an analysis of mechanical stress fields resulting from a variety of applied mechanical loads during oxidation. The chapter highlights the harmful effect of the plastic deformation of the substrate and the oxide on the oxide integrity as tensile stresses are shown to arise in almost all cases.

The fourth chapter is devoted to the study of oxide intrusions as illustrated in the present introduction. To this aim, a grain boundary model is implemented and is coupled with diffusion and the total free energy to model diffusion short circuits and wetting effects. Preliminary simulations of growing precipitates are performed to analyse the interactions between wetting and diffusion short circuits with respect to the thermodynamic data provided in the work. Finally, the growth of a single oxide intrusion is simulated and stress and concentration fields are analysed. Stress concentrations are found in the substrate at the tip of the oxide intrusion, which is expected, but also at the free surface within the fragile oxide. Due to viscoplastic relaxation effects, the grain boundary opening stresses are shown to become positive in those two areas. Such preliminary results shed a new light on the crack initiation micromechanisms involved in high temperature oxidation embrittlement of superalloys.

References

[Abrivard, 2009] Abrivard, G. (2009). *A coupled crystal plasticity - phase field formulation to describe microstructural evolution in polycrystalline aggregates during recrystallisation.* PhD thesis, Mines ParisTech.

[Abrivard et al., 2012a] Abrivard, G., Busso, E., Forest, S., and Appolaire, B. (2012a). Phase field modelling of grain boundary motion driven by curvature and stored energy gradients. Part I: Theory and numerical implementation. *Philosophical Magazine*, 92(28-30):3618–3642.

[Abrivard et al., 2012b] Abrivard, G., Busso, E., Forest, S., and Appolaire, B. (2012b). Phase field modelling of grain boundary motion driven by curvature and stored energy gradients. Part II: Application to recrystallisation. *Philosophical Magazine*, 92(28-30):3643–3664.

[Antolovich and Armstrong, 2014] Antolovich, S. D. and Armstrong, R. W. (2014). Plastic strain localization in metals: origins and consequences. *Progress in Materials Science*, 59(0):1–160.

[Baboian, 2004] Baboian, R. (2004). *Corrosion tests and standards : application and interpretation.* West Conshohocken, PA : ASTM International, 2nd ed edition. ASTM Stock Number: MNL20–2nd.

[Barnes et al., 1989] Barnes, J., Goedjen, J., and Shores, D. (1989). A model for stress generation and relief in oxide Metal systems during a temperature change. *Oxidation of Metals*, 32(5-6):449–469.

[Barnoush, 2011] Barnoush, A. (2011). Hydrogen embrittlement.

[Bruemmer and Thomas, 2005] Bruemmer, S. M. and Thomas, L. (2005). High-resolution characterizations of stress-corrosion cracks in austenitic stainless steel from crack growth tests in BWR-simulated environments. In TMS (The Minerals, M. . M. S., editor, *Proceedings of the 12th International Conference on Environmental Degradation of Materials in Nuclear Power System Water Reactors* .

[Busso and Cailletaud, 2005] Busso, E. and Cailletaud, G. (2005). On the selection of active slip systems in crystal plasticity. *International Journal of Plasticity*, 21(11):2212 – 2231.

[Busso and McClintock, 1996] Busso, E. and McClintock, F. (1996). A dislocation mechanics-based crystallographic model of a B2-type intermetallic alloy. *International Journal of Plasticity*, 12(1):1 – 28.

[Clarke, 2002] Clarke, D. (2002). Stress generation during high-temperature oxidation of metallic alloys. *Current Opinion in Solid State and Materials Science*, 6(3):237–244.

[Couvant et al., 2009] Couvant, T., Legras, L., Herbelin, A., Musienko, A., Ilevbrev, G., Delafosse, D., Cailletaud, G., and Hickling, J. (2009). Development of understanding of the interaction between localized deformation and SCC of austenitic stainless steel exposed to primary PWR environment. In *Proceedings of the Fourteenth International Conference on Environmental Degradation of Materials in Nuclear Power Systems Water Reactors*, pages 182–194. American Nuclear Society (ANS).

[Couvant et al., 2007] Couvant, T., Legras, L., Pokor, C., Vaillant, F., Brechet, Y., Boursier, J., and Moulart, P. (2007). Investigations on the mechanisms of PWSCC of strain hardened austenitic stainless steels. In *13th Env Degradation Conf, Whistler, Canada, 19-23 août 2007*.

[Couvant et al., 2005] Couvant, T., Legras, L., Vaillant, F., Boursier, J., and Rouillon, Y. (2005). Effect of strain-hardening on stress corrosion cracking of AISI 304L stainless steel in PWR environment at 360°C. In *Proceedings of the 12th International Conference on Environmental Degradation of Materials in Nuclear Power System*.

[Evans, 1983] Evans, H. (1983). The role of oxide grain boundaries in the development of growth stresses during oxidation. *Corrosion Science*, 23(5):495 – 506.

[Goedjen et al., 1994] Goedjen, J., Stout, J., Guob, Q., and Shores, D. (1994). Evaluation of stresses in Ni-NiO and Cr-Cr_2O_3 during high temperature oxidation by in situ X-ray diffraction. *Materials Science and Engineering: A*, 177(12):115 – 124.

[Gránásy et al., 2006] Gránásy, L., Pusztai, T., Börzsönyi, T., Tóth, G., Tegze, G., Warren, J., and Douglas, J. (2006). Polycrystalline patterns in far-from-equilibrium freezing: a phase field study. *Philosophical Magazine*, 86(24):3757–3778.

[Guilhem, 2011] Guilhem, Y. (2011). *Numerical investigation of the local mechanical fields in 316L steel polycrystalline aggregates under fatigue loading*. PhD thesis, Mines ParisTech.

[Gutierrez-Solana et al., 1993] Gutierrez-Solana, F., Gonzalez, J., Varona, J., and Biezma, M. (1993). Modelling the stress corrosion cracking of low alloy steels. *Corrosion Science*, 35(14):499 – 505.

[Herbert et al., 2012] Herbert, F., Van Vliet, K., and Yildiz, B. (2012). Plasticity-induced oxidation reactivity on Ni(100) studied by scanning tunneling spectroscopy. *MRS Communications*, 2:23–27.

[Huang and Wang, 2012] Huang, W. and Wang, L. (2012). Solidification researches using transparent model materials - 1 A review. *Science China Technological Sciences*, 55(2):377–386.

[Huguenin, 2012] Huguenin, P. (2012). *Amorçage des fissures de corrosion sous contrainte dans les aciers inoxydables austénitiques pré-déformés et exposés au milieu primaire des réacteurs à eau sous pression*. PhD thesis, Mines ParisTech.

[Huguenin et al., 2010] Huguenin, P., Herms, E., Vaillant, F., Crépin, J., Duhamel, C., and Proudhon, H. (2010). Approche expérimentale de l'amorçage de la CSC des aciers inoxydables austénitiques pré-déformés en mileu primaire de REP. In *MATERIAUX 2010*.

[Huntz et al., 2002] Huntz, A., Calvarin Amiri, G., Evans, H., and Cailletaud, G. (2002). Comparison of oxidation-growth stresses in NiO film measured by deflection and calculated using creep analysis or finite-element modeling. *Oxidation of Metals*, 57(5-6):499–521.

[Huntz et al., 1998] Huntz, A., Piant, A., Lebrun, J., and Daghigh, S. (1998). Evidence of stress relaxation in thermally grown oxide layers – experiments and modelling. *Materials Science and Engineering: A*, 248(12):44 – 55.

[IAEA, 2011] IAEA (2011). *Stress corrosion cracking in light water reactors: good practices and lessons learned*. IAEA Nuclear Energy Series.

[Kamaya and Haruna, 2007] Kamaya, M. and Haruna, T. (2007). Influence of local stress on initiation behavior of stress corrosion cracking for sensitized 304 stainless steel. *Corrosion Science*, 49(8):3303 – 3324.

[Karma, 2001] Karma, A. (2001). Phase-field formulation for quantitative modeling of alloy solidification. *Phys. Rev. Lett.*, 87:115701.

[Kocks and Mecking, 2003] Kocks, U. and Mecking, H. (2003). Physics and phenomenology of strain hardening: the {FCC} case. *Progress in Materials Science*, 48(3):171 – 273.

[Krishnamurthy and Srolovitz, 2003] Krishnamurthy, R. and Srolovitz, D. (2003). Stress distributions in growing oxide films. *Acta Materialia*, 51(8):2171 – 2190.

[Krishnamurthy and Srolovitz, 2004] Krishnamurthy, R. and Srolovitz, D. (2004). Stress distributions in growing polycrystalline oxide films. *Acta Materialia*, 52(13):3761 – 3780.

[Krupp et al., 2006] Krupp, U., Trindade, V., Schmidt, P., Christ, H.-J., Buschmann, U., and Wiechert, W. (2006). Oxidation mechanisms of Cr-containing steels and Ni-base alloys at high temperatures Part II: Computer-based simulation. *Materials and Corrosion*, 57(3):263–268.

[Laghoutaris, 2009] Laghoutaris, P. (2009). *Corrosion sous contrainte de l'alliage 600 en milieu primainre des réacteurs à eau sous pression : apport à la compréhension des mécanismes*. PhD thesis, Mines ParisTech.

[le Pêcheur, 2008] le Pêcheur, A. (2008). *Fatigue thermique d'un acier inoxydable austénitique : influence de l'état de surface par une approche multi-échelles*. PhD thesis, École Centrale Paris.

[Legris et al., 2005] Legris, A., Vogt, J.-B., Verleene, A., and Serre, I. (2005). Wetting and mechanical properties, a case study: Liquid metal embrittlement of a martensitic steel by liquid lead and other liquid metals. *Journal of Materials Science*, 40(9-10):2459–2463.

[Lozano-Perez et al., 2012] Lozano-Perez, S., Kruska, K., Iyengar, I., Terachi, T., and Yamada, T. (2012). The role of cold work and applied stress on surface oxidation of 304 stainless steel. *Corrosion Science*, 56(0):78 – 85.

[Marcus, 1998] Marcus, P. (1998). Surface science approach of corrosion phenomena. *Electrochimica Acta*, 43(12):109 – 118.

[Méric et al., 1991a] Méric, L., Poubanne, P., and Cailletaud, G. (1991a). Single crystal modeling for structural calculations: Part 1, model presentation. *Journal of engineering materials and technology*, 113:162–170.

[Méric et al., 1991b] Méric, L., Poubanne, P., and Cailletaud, G. (1991b). Single crystal modeling for structural calculations: Part 2, finite element implementation. *Journal of engineering materials and technology*, 113:162–170.

[Musienko and Cailletaud, 2009] Musienko, A. and Cailletaud, G. (2009). Simulation of inter- and transgranular crack propagation in polycrystalline aggregates due to stress corrosion cracking. *Acta Materialia*, 57(13):3840 – 3855.

[Pineau and Antolovich, 2009] Pineau, A. and Antolovich, S. (2009). High temperature fatigue of nickel-base superalloys – a review with special emphasis on deformation modes and oxidation. *Engineering Failure Analysis*, 16(8):2668–2697. Special issue honouring Professor Manuel Elices on the occasion of his 70th birthday.

[Plessier, 2010] Plessier, F. (2010). *Simulation par éléments finis du comportement mécanique de polycristaux chargés en hydrogène*. PhD thesis, Université de Bordeaux 1.

[Shoji et al., 2010] Shoji, T., Lu, Z., and Murakami, H. (2010). Formulating stress corrosion cracking growth rates by combination of crack tip mechanics and crack tip oxidation kinetics. *Corrosion Science*, 52(3):769 – 779.

[Steinbach, 2009] Steinbach, I. (2009). Phase-field models in materials science. *Modelling and Simulation in Materials Science and Engineering*, 17(7):073001.

[Stellwag, 1998] Stellwag, B. (1998). The mechanism of oxide film formation on austenitic stainless steels in high temperature water. *Corrosion Science*, 40(23):337 – 370.

[Wehbi, 2014] Wehbi, M. (2014). *Modélisation de l'amorçage de la Corrosion Sous Contrainte dans les alliages base nickel 182 et 82 en milieu primaire des Réacteurs à Eau sous Pression*. PhD thesis, Mines ParisTech.

[Weiss and Pineau, 1993] Weiss, J. and Pineau, A. (1993). Fatigue and creep-fatigue damage of austenitic stainless steels under multiaxial loading. *Metallurgical and Materials Transactions A*, 24:2247–2261.

[Zhou, 2010] Zhou, H. (2010). *Stress-diffusion interaction during oxide-scale growth on metallic alloys*. PhD thesis, Georgia Institute of Technology.

[Zhou et al., 2010] Zhou, H., Qu, J., and Cherkaoui, M. (2010). Stress-oxidation interaction in selective oxidation of Cr–Fe alloys. *Mechanics of Materials*, 42(1):63 – 71.

CHAPTER

2 Bibliography

Contents

Cette partie est consacrée à la présentation des aciers austénitiques utilisés dans les réacteurs à eau pressurisée. De nombreuses études ont été consacrées à la compréhension de leur comportement de passivation ainsi que de tenue mécanique, et ce pour une vaste gamme de températures, d'environnements ainsi que de chargements mécaniques. Dans ce travail, l'approche proposée consiste à l'élaboration d'un modèle de matériau composé comme un assemblage de briques élémentaires, lesquelles sont constituées des phases d'un matériau dont le comportement physique (ou bien multiphysique) est obtenu par la superposition des comportements chimique et mécanique faisant intervenir des relations de couplage. Ainsi, il semble nécessaire de détailler chacun de ces comportements.

Toutefois, cette approche reste actuellement modeste vis-à-vis de la complexité inhérente aux mécanismes d'amorçage et de propagation de fissures de corrosion sous contrainte. Elle ne s'attache donc pas à donner une explication détaillée des nombreux mécanismes de croissance d'oxyde et de corrosion sous contrainte présents dans la littérature. Ces mécanismes sont en grande partie décrits dans les études menées par le CEA et EDF R&D et détaillés, entre autre dans [Machet et al., 2004, Soulas, 2006, Laghoutaris, 2009].

Néanmoins, elle apporte au lecteur une base jugée suffisante afin de permettre la compréhension des principaux phénomènes chimiques et mécaniques à l'échelle micrométrique intervenants dans le milieu primaire. De plus, elle apporte des notions théoriques fondamentales pour la compréhension des cinétiques de croissance introduites dans le modèle de champs de phases ainsi que des mécanismes d'élasto-viscoplasticité adjoints.

2.1 Chromium-rich steels and their oxides

2.1.1 Composition

From discovery up to the generalised use of γ-Fe stainless steels

Rapid technological advances in the domain of metallurgy driven by the awakening of modern sciences were carried out at the beginning of the 18^{th} century. The discovery of nickel by Axel Frederick Cronsted in 1751, molybdenum by Karl Wilhelm Scheele in 1778 and chromium by Nicolas-Louis Vauquelin in 1797 heralded the beginning of stainless steels. In 1821, the mineralogist and geologist Pierre Berthier and physicist and chemist Michael Faraday independently highlighted the beneficial effect of chromium for the reduction of the surface degradation induced by an acid attack of an iron based alloy. Later, in 1904, Leon Guillet and Albert Portevin independently developed processes for the elaboration of martensitic and ferritic stainless steels, whereas the elaboration of austenitic stainless steels first took place in 1909. Therefore, those years marked the early days of stainless grades [Lai et al., 2012]. Rapidly after, in the 1910s, an industrial process for the elaboration of martensitic stainless steels was developed in Great Britain by Harry Brearly, and then for austenitic stainless steels by Benno Strauss and Edward Muller at Krupp AG, and finally for ferritic stainless steels by Frederick Becket and Christian Dantsizen, [Cunat, 2002].

Half a century was then needed to create modern factories and improve the mining and the extraction of the main alloying elements, *i.e.* Cr, Ni, Mo, Mn, to make stainless steels profitable and reliable enough for a widespread use. Today, stainless steels are a resounding success as numerous common objects up to specific industrial equipment are made out of a broad family of stainless steels. Steel grades have been thus developed for costs optimisation purposes given a specific need or in response to a lack of available resources, *i.e.* molybdenum instead of nickel. Moreover, it must also be said that, the access to natural resources, is a current key point for the economical stability of developed countries. Unfortunately, some mineral resources can be acquired in conflict areas such as in Africa, which are in return termed as conflict minerals. Some well defined conflict minerals are, cobalt, tungsten and tantalum, which are used in steels [Baker, 2013]. Nevertheless, a response has been undertaken from a close collaboration between the OECD and the main developed countries for a responsible control of the supply chains of minerals, [OECD, 2013]. Finally, a European stan-

dard has been published for stainless steels, which imposes a minimal chromium mass content of at least 10.5%, *e.g.* EN10088-1:2005.

Steel grades systems

Steels are thus broadly used and several terminology standards have been developed to make industries along with research facilities work in unison. In this work, we follow the grade terminology of the AISI[1], which is inspired from the SAE[2] steel grades system and denotes the composition range of the alloy. Among those austenitic stainless steels, alloy AISI 304/SAE 30304, which represents 80% of the global volume of AUSS and alloy AISI 316/SAE 30316, used for good corrosion resistance, can be found in PWRs along with several other grades as given in Fig. 2.1, [SSIC, 2014]. The present work

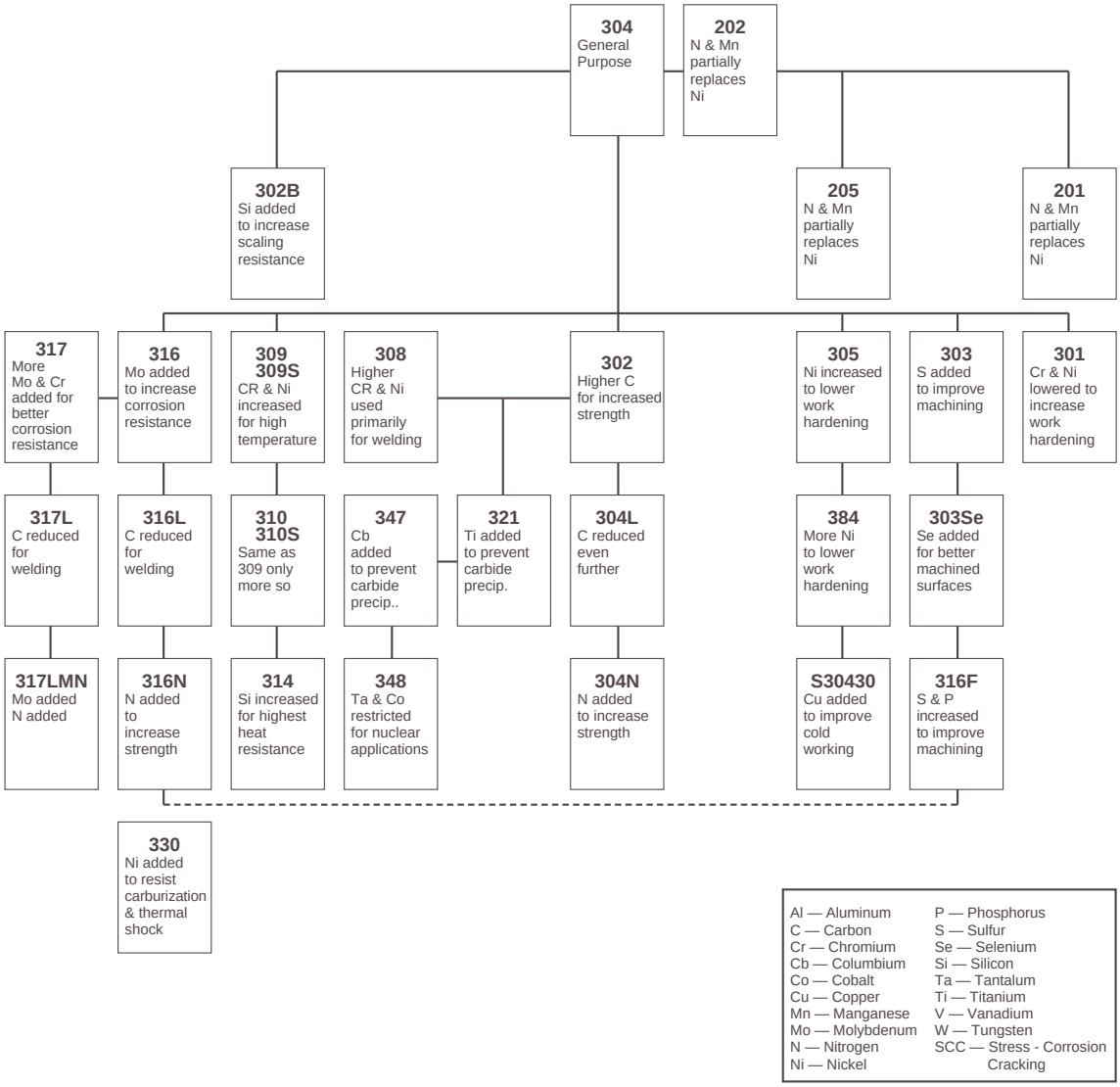

[SSIC, 2014]

Figure 2.1: Chart showing several austenitic steels AISI grades with their respective main applications.

focuses mainly on the grades, which are used in french PWRs for canopy seals (308L), pressurizer heaters (316L), baffle former bolts (316L), *etc.*, for their corrosion resistance capabilities, along with high temperature mechanical properties. The 316 grade is molybdenum enriched and therefore has a better resistance to pitting and crevice corrosion in chloride environments than the 304 grade, and

[1] American Iron and Steel Institute
[2] Society of Automotive Engineers

is also the second most frequently found grade within stainless steels. The "L" script, *e.g.* 316L and 304L, means a low carbon content, resulting in an immunity to sensitization, which is caused by the chromium depletion that results from the precipitation of chromium carbides at grain boundaries. That is why they are recommended for welded components. We note also that amongst chromium-nickel austenitic stainless steels, 316L offers very good creep resistance, stress to rupture and tensile strength at elevated temperatures (290-360°C). A detailed composition of 316, 316L, 304 and 304L is found in Table 2.1 (in weight percent). The present work is not intended to the study of a very spe-

	C	Mn	Si	P	S	Cr	Mo	Ni	N
316	0.08	2	0.75	0. - 0.045	0.03	16-18	2-3	10-14	0.1
316L	0.03	2	0.75	0.045	0.03	16-18	2-3	10-14	0.1
304	0.08	2	0.75	0.045	0.03	18-20	-	8-12	0.1
304L	0.03	2	0.75	0.045	0.03	18-20	-	8-10.5	0.1

[Cunat, 2002]

Table 2.1: Composition ranges of common 3xx grades in weight percent.

cific grade. Therefore, the material of the study should be considered as an idealised stainless steel that undergoes the combined action of mechanical loadings and extreme environmental conditions. Moreover, we choose to further work with atomic compositions instead of mass compositions, although they do not significantly differ, as illustrated in Table 2.2.

	C	Mn	Si	P	S	Cr	Mo	Ni	N
316 (% wt.)	0.08	2	0.75	0	0.03	16	2	10	0.1
316 (% at.)	0.367	2	1.47	0	0.005	16.97	1.15	9.39	0.39

Table 2.2: Example of atomic and mass compositions equivalence for a specific 316L steel.

2.1.2 Phases

Austenitic stainless steels can embed several phases depending on their composition along with a possible thermo-mechanical treatment. Moreover, they equally react with oxygen to build oxides or hydroxides, which will be considered in this work as additional phases. As shown in Fig. 2.2 from [Weiss and Pineau, 1993], the oxide formation can be quite complex. For this case, the grown scale is composed of two oxide layers. In the aforementioned figure, the growth of the outer oxide layer, which is coloured in orange, is controlled by a chemical reaction at the free surface. In contrast, the growth of the inner oxide layer, which is coloured in blue, is controlled by a chemical reaction that occurs at the metal-oxide interface. The present oxide structure is hence termed a double layer [Stellwag, 1998]. Moreover, the picture shows different contrasts for the oxides localised in grains and those localised at grain boundaries, suggesting that different oxides could be formed in the vicinity of the grain boundaries of γ-Fe. Finally, it clearly appears that the promoted oxidation of slip bands, that could be twin bands in the figure, leaves a shaded path in the oxide. The nature of this shaded areas is still unresolved, but nevertheless, suggests an inheritance-like process of the microstructure of the former γ-Fe phase during growth. Finally, Cr_2O_3 forms in the inner oxide layer since the chromium

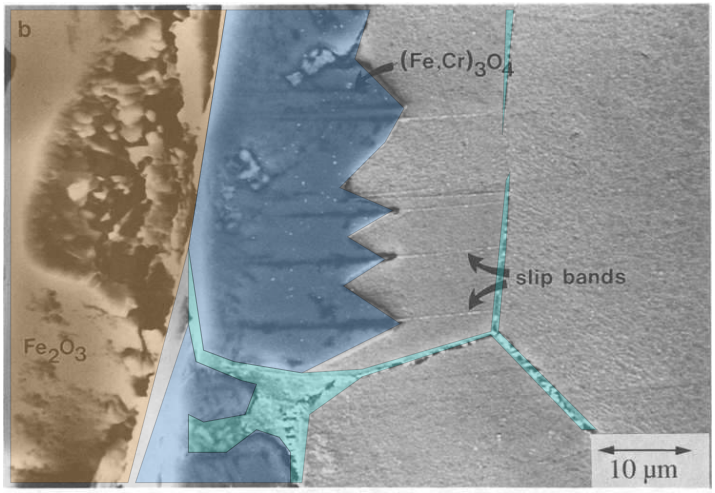

[Weiss and Pineau, 1993]

Figure 2.2: SEM micrograph from Fig. 1.2 on which a schematic illustration of the double layer is superimposed. The inner oxide layer (in blue) grows inside the substrate (in grey). The outer oxide layer (in orange) grows on the substrate along with its inner oxide.

embedded in the alloy has a higher reactivity than the other alloying elements. This Cr_2O_3 oxide is known to be a passivation layer, which protects the base metal against corrosion. The nature of the oxide phases is different to that of the metallic phases, as atomic bonds are strongly modified, *i.e.* ionic bonds versus metallic bonds. Therefore, a clear distinction between metallic and oxides phases needs to be made. A brief overview of the commonly observed phases is given next.

Traces of ferrite α

Ferrite is the stable form of iron carbon alloys at low temperatures. The combination of specific alloying and thermomecanical treatment can result in the complete removal of ferrite. But it appears that residual traces of ferrite can be found in γ-Fe, *i.e.* [Huguenin, 2012], which is known to be stabilised by chromium. Nevertheless, the nickel concentration should be sufficiently high to lower the phase fraction of ferrite to a few percent. Ferrite has a body-centred cubic lattice of atoms as illustrated in Fig. 2.5.

Austenite γ as the main phase

Austenite is clearly the dominant phase of the alloy and is stabilised by nickel. Austenitic stainless steels used in PWRs are characterised by a polycrystalline microstructure with mean grain diameters ranging from *i.e.* 27 µm for 316L and 90 µm for 304L [Couvant et al., 2009], that varies with the thermomechanical processing. Austenite is one of the most famous cubic-face-centred iron based crystal lattices as illustrated in Fig. 2.5. Moreover, nickel local enrichment up to 30 at.% have been reported in the substrate close to the metal oxide interface, as shown in Fig. 2.3, along with chromium depleted areas.

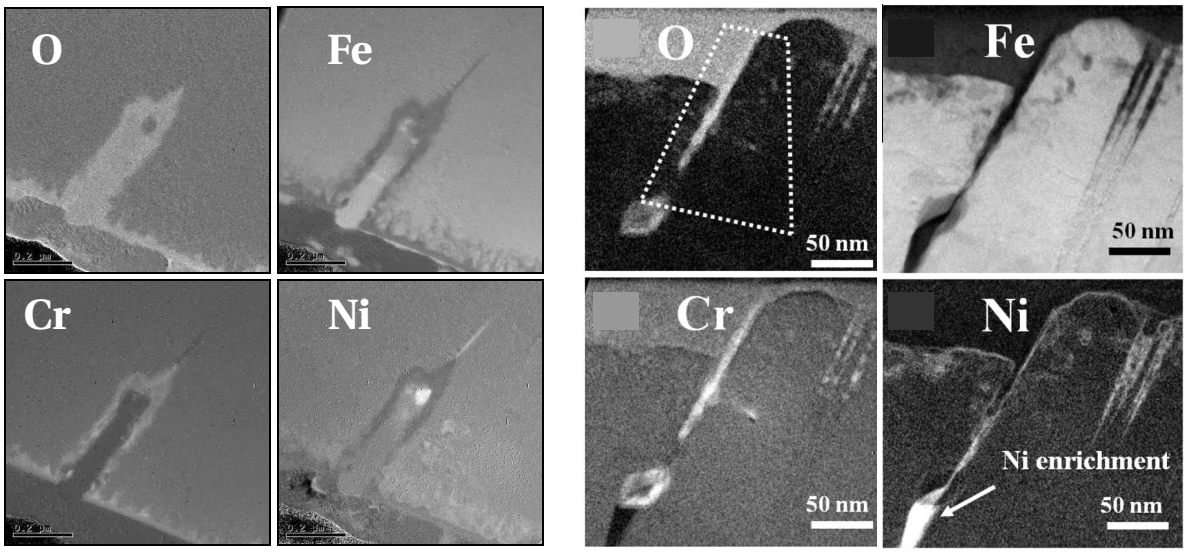

[Couvant et al., 2009] (a)

[Kruska et al., 2012] (b)

Figure 2.3: EFTEM elemental maps (a) in the vicinity of an intergranular crack for a 316L stainless steels and (b) in the vicinity of a grain boundary and localised slip bands for a 304 stainless steel, after exposition to simulated primary water.

Presence of precipitates

In γ-Fe, carbides precipitates can be reported. The chemical composition of carbides is $M_{23}C_6$, where M is found to be chromium, but can be titanium or niobium as well. It can be observed that grain boundaries are possible germination sites for carbides as shown in Fig. 2.4, [IAEA, 2011]. Moreover, the formation of such precipitates can lead to a chromium depletion of about 2 at.% within the adjacent grain boundaries, which is suspected to cause the so-called sensitisation of the alloy[3]. In order to avoid such a sensitisation, austenitic steels can be impoverished in carbon until no carbides can form, *i.e.* the "L" grades 304L and 316L.

On-going martensite formation

As stated in [IAEA, 2011], non-sensitised stainless steels are nevertheless subject to IGSCC, which is assumed to be caused by cold working. The causes of the underlying cracking micromechanisms are not yet fully understood, although the interaction between deformation induced martensite, high residual stresses and localised deformation can be possible explanations. 304L stainless steel is subjected to the deformation induced martensitic transformation, [Couvant et al., 2009]. The martensitic

[3] sensitisation is the term employed when a thermal treatment or a welding step make stress corrosion cracking to be prematurely activated, *e.g.* due to the precipitation of carbides during welding

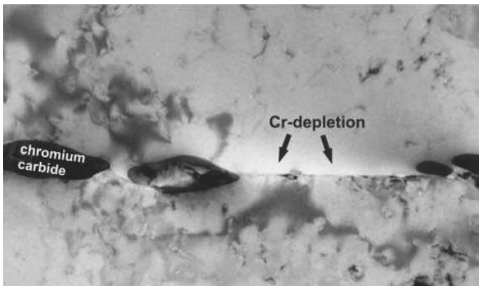

[IAEA, 2011]

Figure 2.4: TEM micrograph showing the precipitation of lens-shaped chromium carbides along grain boundaries. Precipitation mostly induces here a harmful localised chromium depletion in γ-Fe and therefore has to be avoided as much as possible. The scale of the image is not mentioned in the micrograph, but the size of carbides can be estimated to be about a few hundred nanometers.

phase transformation is amongst the most well-known diffusionless phase transformation induced by rather large amounts of cooperative lattice rotations as illustrated in Fig. 2.5. The martensitic phase transformation is also termed as a military transformation in contrast with civilian transformations, *i.e.* diffusive phase transformations. Finally, martensite can be found under several forms, showing different crystal lattices, and is therefore beyond the scope of the work.

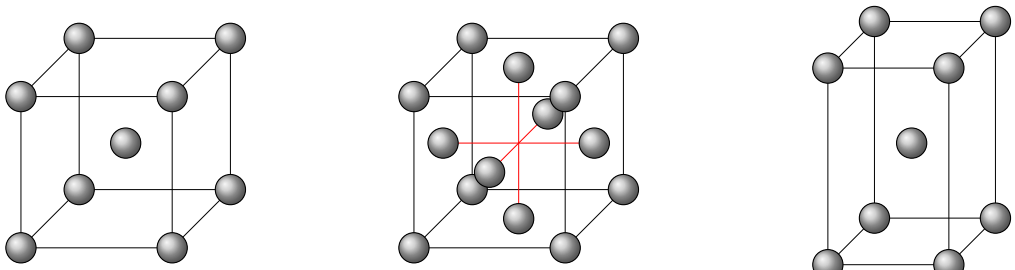

Figure 2.5: Crystal structures for (a) ferrite as BCC (b) austenite as FCC and (c) martensite as BCT. Colours follows CPK colouring where grey spheres denote the metal atoms.

Oxide phases

Several oxide phases can form on austenitic stainless steels, the formation of which is dependent of the ratio of oxygen anions with metallic cations. During the early stage of oxidation, FeO is preferentially formed. It is then followed by Fe_3O_4 and finally Fe_2O_3, [Machet et al., 2004, Cheng et al., 2011], as the (anions:cations) ratio increases, *i.e.* from 1:1 by 4:3 to 3:2. It can be noted that the combination of FeO and Fe_2O_3 results in the stoichiometry of Fe_3O_4. Such "mixed" phase is termed a spinel phase. Moreover, all aforementioned oxide phases can be classified as rust. In order to prevent the metal from building such rust, the embedded chromium happens to build a well-known passive layer of chromia Cr_2O_3 inside the inner oxide layer.

Low (anions:cations) ratio oxides : Wüstite (FeO) and Bunsenite (NiO)

The crystal structures of wüstite (FeO) and bunsenite (NiO) are found to be the same as halite (NaCl). The structure of halite is a cubic-face-centred lattice of oxygen anions where metal cations are located inside the octahedral sites.

Medium (anions:cations) ratio oxides : Spinel ($Fe_xCr_yNi_{(1-x-y)}O_4$)

The spinel structure consists of a close-packing of oxygen atoms where metal cations occupy either octahedral or tetrahedral sites. Divalent cations are found in one eighth of the tetrahedral sites whereas trivalent cations occupy one half of the octahedral sites. The spinel structure can incorporate a wide range of compositions, so that several oxides can be built. First, magnetite has the composition $FeFe_2O_4$, where Fe_2 can be exchanged with Cr_2 to form chromite $FeCr_2O_4$. Moreover, the spinel phase is mentioned to be able to incorporate a high concentration of vacancies so that the maghemite γ-Fe_2O_3 has the spinel structure, whereas its stoichiometry suggests a corundum crystal lattice. Therefore, spinels are mostly depicted by indices x, y and z in their formula ($Fe_xCr_yNi_{1-x-y}O_4$).

High (anions:cations) ratio oxides : Hematite and Chromia (Fe_2O_3 and Cr_2O_3)

The structure of chromia Cr_2O_3 is another well-known corundum structure. Hematite, has the same anions:cation ratio and is frequently found as α-Fe_2O_3, which has a rhombohedral corundum structure as well. It is made of an hexagonal close-packing of oxygen anions with metal atoms occupying two thirds of the octahedral sites.

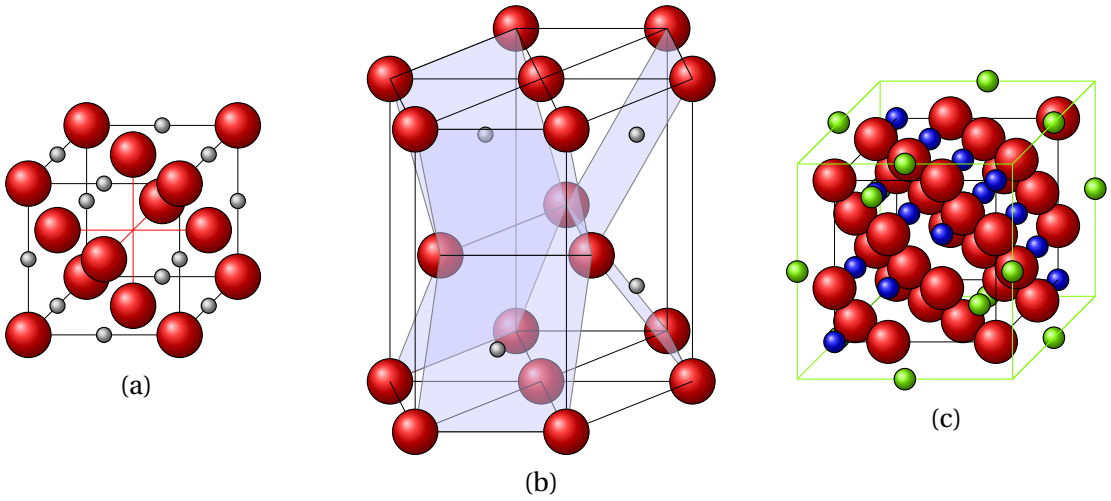

Figure 2.6: Crystal structure of rust and the passive layer (a) halite for FeO (b) corundum for Fe_2O_3 and Cr_2O_3 (c) and spinel for Fe_3O_4. In terms of CPK colouring, oxygen is red and metal atoms are grey, apple green for divalent cations and blue for trivalent cations in the case of the spinel structure.

2.1.3 Phase equilibrium

A digression on scaling

Thermodynamic potentials are core elements of continuum based modelling approaches as they allow to ensure that the first and second principles of thermodynamics are enforced. Constitutive approaches are based on the formulation of an energy functional along with a dissipation potential from which the state and constitutive laws are obtained [Germain et al., 1983]. However, the scale of the model has to be clearly defined prior to the formulation of a thermodynamic potential. The material point at which the thermodynamic potentials are evaluated embeds the chosen characteristic length of the problem. For example, the micrographs shown in Fig. 1.2 and 1.3 do suggest different characteristic lengths. These two characteristic lengths are here dependent on the conditions of oxidation, *i.e.* temperature, environment, *etc.* The characteristic length must be small enough to capture the main physical phenomena leading to oxide growth. At this point, the characteristic length can be downscaled while being enhanced with more detailed physics, by the increase of

the model dimensionality. Or it can be upscaled as well by reducing the RVE into a single material point. This procedure is necessary to enhance the constitutive laws of "macroscopic" internal variables. The multilevel finite element method – or FE^2 – is a typical example of such scale transition as the "macroscopic" constitutive laws are obtained directly by computations on a "microscopical" RVE instead of being defined by averaged internal variables, [Feyel, 2003]. Nevertheless, approaches based on internal variables remain the preferred choice in terms of modelling for the finer description of the "macroscopic" behaviours, *i.e.* life-prediction models of large structures. Therefore, there is a strong effort to understand all microscopical phenomena in materials science by the development of enhanced multiphysics modelling frameworks. It then requires more accurate observation techniques to validate the models, *i.e.* APT, TEM, *etc.* Finally, it should be emphasised that the characteristic length and the characteristic time are not independent from each other. Therefore, downscaling naturally implies the decrease of the characteristic time as illustrated in Fig. 2.7. Thermodynamic potentials are therefore defined at a given scale, where the upward transition should

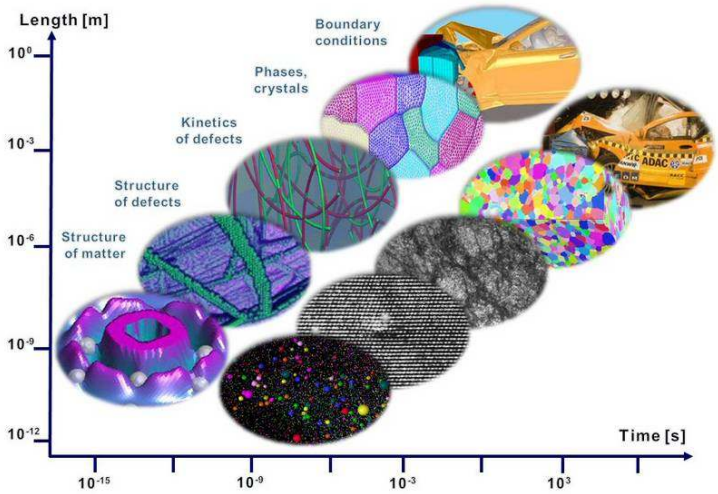

[from the websites of Dierk Raabe and Max-Planck Institute für Eisenforschung]
[http://www.dierk-raabe.com/]

Figure 2.7: Schematic illustration of downscaling in computational materials science for a crash test experimental set-up. The macroscopic behaviour is the result of an accumulation of microscopical effects.

naturally be done from volume and time averaging, while enforcing the principles of thermodynamics. The downward transition is possible only from the addition of new degrees of freedom, used for the explicit modelling of micro-mechanisms, *i.e.* creep damage, dislocation pile-ups, Coble-creep, dislocation creep, *etc.*, where the corresponding models belong to generalised continua. In the field of stress corrosion cracking, the smallest scale modelled is that of the atom from *ab-initio* methods, *i.e.* molecular dynamics. Nevertheless, the available time and space scales covered by such methods are too small to move towards upper scales. However, it allowed to highlight non negligible stress-diffusion interactions and to reproduce the local nickel enrichment at the metal-oxide interface, *e.g.* [Das et al., 2008, Das et al., 2009]. Continuum approaches up to crystal plasticity were also developed, *e.g.* coupled with the diffusion and segregation of hydrogen along grain boundaries in stainless steels by [Miresmaeili et al., 2010] and coupled with grain boundary diffusion along with cohesive zones to study inter- and transgranular stress corrosion crack propagation mechanisms [Musienko and Cailletaud, 2009]. Finally, most of the works done in the field of SCC were focused on the evaluation of averaged crack growth rate relationships without accounting for a continuum description, *i.e.* [Shoji et al., 2010].

Thermodynamic potentials

Thermodynamic potentials are the fundamental quantities used in continuum modelling. They express the state of matter through its averaged energy. The internal energy U is one of the primary thermodynamic potentials and varies with the extensive variables, *i.e.* entropy S in [J.K^{-1}], the volume V [m^3] and n_i which is the molar quantity of component i in [mol]. Moreover, the dual quantities to such extensive variables can be expressed and are respectively the intensive variables, *i.e.* temperature T [K], pressure P [J.m^{-3}] and the chemical potential μ_i [J.mol^{-1}]. On the basis of such a set of thermodynamic variables, several other thermodynamic potentials can be obtained from the internal energy by the use of Legendre transformations, as illustrated in Fig. 2.8. The evolution of the studied

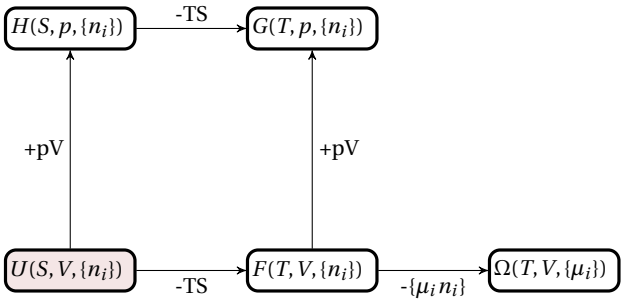

Figure 2.8: Common thermodynamic potentials are obtained from the internal energy U on the basis of Legendre transformations. H is the enthalpy, G the Gibbs free energy or free enthalpy, F is the Helmholtz free energy or free energy and Ω is the Landau potential or grand potential.

system is motivated by the minimisation of the total internal energy, which can be controlled by any of the above thermodynamic potentials. Choosing a reference thermodynamic potential is then arbitrary, [Houlsby and Puzrin, 2000]. However, it is preferable that the state variables can be controlled during the evolution of the studied system. We note that the free energy F, is a good candidate for solid materials. This is mainly due to the fact that solid materials are frequently assumed to be closed systems, tested under controlled temperature for which a displacement field is imposed.

Chemical equilibrium

Chemical equilibrium can be prescribed at the interface to control the growth of a phase within another one. The reader is referred to the work of [Perevoshchikova, 2012] for a more comprehensive description of the chemical equilibrium in multicomponent systems. Isobaric-isothermal-isochoric chemical equilibrium of a multicomponent system containing l chemical elements and composed of two phases $\pi = \alpha, \beta$ is considered here. The present system is illustrated in Fig. 2.9, for which the motion of the interface is allowed and is caused by the transfer of chemical components between the phases. If stresses are neglected, the Gibbs and Helmholtz potentials depend only on the molar

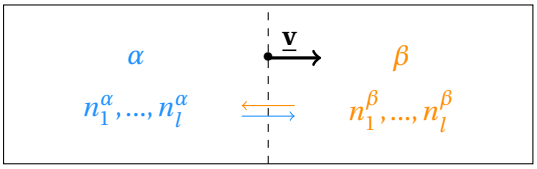

Figure 2.9: Illustration of a two phase system α-β containing l components separated by a moving planar interface with velocity $\underline{\boldsymbol{v}}$. The motion of the planar interface is caused by the transfer of chemical elements from one phase to another enforced by chemical equilibrium.

quantities n_i and can be shown to be equal. Therefore, they will be denoted by a single functional,

which is here noted $\tilde{f}$, for the sake of generality. The variation of the total energy reads:

$$d\tilde{f} = d\tilde{f}^{\alpha} + d\tilde{f}^{\beta} = \sum_{i=1}^{l} \left(\frac{\partial \tilde{f}^{\alpha}}{\partial n_i^{\alpha}} \bigg|_{\substack{n_k^{\alpha} \\ k \neq i}} dn_i^{\alpha} + \frac{\partial \tilde{f}^{\beta}}{\partial n_i^{\beta}} \bigg|_{\substack{n_k^{\beta} \\ k \neq i}} dn_i^{\beta} \right), \tag{2.1}$$

where:

$$\bar{\mu}_i^{\pi} = \frac{\partial \tilde{f}^{\pi}}{\partial n_i} \bigg|_{\substack{n_k^{\pi} \\ k \neq i}}, \tag{2.2}$$

is the chemical potential of the component i in the phase π. Moreover, mass conservation imposes:

$$n_{i \in [\![1,l]\!]} = n_i^{\alpha} + n_i^{\beta} = \text{cste}, \tag{2.3}$$

which allows to rewrite (2.1) into:

$$d\tilde{f} = d\tilde{f}^{\alpha} + d\tilde{f}^{\beta} = \sum_{i=1}^{l} \left(\bar{\mu}_i^{\alpha} - \bar{\mu}_i^{\beta} \right) dn_i^{\alpha}. \tag{2.4}$$

Equilibrium is a state where the total energy is constant, hence $df = 0$ and the equality of chemical potentials at the interface [Emmerich, 2003]:

$$\forall i \in [\![1,l]\!], \bar{\mu}_i^{\alpha} = \bar{\mu}_i^{\beta}. \tag{2.5}$$

Chemical equilibrium expressed as a concentration jump

In practice, the measurement of chemical potentials is not direct, and concentration fields are measured instead. In the this section, it will be shown that the chemical equilibrium is equivalent to an interface concentration jump. Such a concentration jump can be also obtained graphically, which is known as the common tangent rule.

The concentrations are defined as follows:

$$c_i^{\pi} = \left(\sum_{j=1}^{l} n_j^{\pi} \right)^{-1} n_i^{\pi} = \frac{n_i^{\pi}}{N^{\pi}}, \tag{2.6}$$

where it is recalled that $\pi \in [\![\alpha, \beta]\!]$.

Assuming that the energy $\tilde{f}^{\pi}$ can be rewritten into a molar energy $\tilde{f}_m^{\pi}$ as follows [Cottrell, 2000]:

$$\tilde{f}^{\pi}(n_{i \in [\![1,l]\!]}^{\pi}) = N^{\pi} \tilde{f}_m^{\pi}(c_{i \in [\![1,l]\!]}^{\pi}), \tag{2.7}$$

Moreover, one concentration can be discarded given the constrain:

$$\sum_{i=1}^{l} c_i^{\pi} = 1, \tag{2.8}$$

hence:

$$\tilde{f}_m^{\pi}(c_{i \in [\![1,l]\!]}^{\pi}) = f_m^{\pi}(c_{i \in [\![1,l-1]\!]}^{\pi}), \tag{2.9}$$

where f_m is the potential on which the phase field model developed in chapter 3 will rely. The chemical potential now reads:

$$\bar{\mu}_{i \in [\![1,l]\!]}^{\pi} = \frac{\partial \tilde{f}^{\pi}}{\partial n_i^{\pi}} \bigg|_{\substack{n_k^{\pi} \\ k \neq i}} = \frac{\partial N^{\pi} f_m^{\pi}}{\partial n_i^{\pi}} \bigg|_{\substack{n_k^{\pi} \\ k \neq i}} = f_m^{\pi} + N^{\pi} \frac{\partial f_m^{\pi}}{\partial n_j^{\pi}} \bigg|_{\substack{n_k^{\pi} \\ k \neq i}}. \tag{2.10}$$

If $i \neq l$ then the chemical potential reads:

$$\begin{aligned} \bar{\mu}_i^\pi &= f_m^\pi + N^\pi \left(\left. \frac{\partial f_m^\pi}{\partial c_i^\pi} \right|_{\substack{c_k^\pi \\ k\neq i}} \left. \frac{\partial c_i^\pi}{\partial n_i^\pi} \right|_{\substack{n_k^\pi \\ k\neq i}} + \sum_{\substack{j=1 \\ j\neq i}}^{l-1} \left. \frac{\partial f_m^\pi}{\partial c_j^\pi} \right|_{\substack{c_k^\pi \\ k\neq j}} \left. \frac{\partial c_j^\pi}{\partial n_i^\pi} \right|_{\substack{n_k^\pi \\ k\neq j}} \right) \\ &= f_m^\pi + (1 - c_i^\pi) \left. \frac{\partial f_m^\pi}{\partial c_i^\pi} \right|_{\substack{c_k^\pi \\ k\neq i}} - \sum_{\substack{j=1 \\ j\neq i}}^{l-1} c_j^\pi \left. \frac{\partial f_m^\pi}{\partial c_j^\pi} \right|_{\substack{c_k^\pi \\ k\neq j}} . \end{aligned} \tag{2.11}$$

Otherwise, if $i = l$, then the chemical potential of the remaining component is given by:

$$\bar{\mu}_l^\pi = f_m^\pi + N^\pi \sum_{j=1}^{l-1} \left. \frac{\partial f_m^\pi}{\partial c_j^\pi} \right|_{\substack{c_k^\pi \\ k\neq j}} \left. \frac{\partial c_j^\pi}{\partial n_i^\pi} \right|_{\substack{n_k^\pi \\ k\neq j}} = f_m^\pi - \sum_{j=1}^{l-1} c_j^\pi \left. \frac{\partial f_m^\pi}{\partial c_j^\pi} \right|_{\substack{c_k^\pi \\ k\neq j}} . \tag{2.12}$$

Equations (2.11) and (2.12) result then in a system of l equations. Using Gibbs' phase rule, the number of degrees of freedom d of the system is obtained for isothermal and isobaric conditions:

$$d = l - p , \tag{2.13}$$

where p is the number of phases, which is equal to two in the present example. Finally, the chemical equilibrium can be solved only by the introduction of d additional equations, *i.e.* mass conservation, fixed concentrations, *etc.*

Chemical equilibrium in a binary alloy (A-B) with two phases

The constituents are here written (A-B) to denote the binary system. For a binary alloy (A-B), where $c = c_A$ and $c_B = 1 - c$, the chemical equilibrium is defined as:

$$\begin{aligned} \bar{\mu}_A^\alpha &= \bar{\mu}_A^\beta \\ \bar{\mu}_B^\alpha &= \bar{\mu}_B^\beta \end{aligned} , \tag{2.14}$$

which can be rewritten using (2.11) and (2.12) into:

$$\begin{aligned} f_m^\alpha + (1 - c^\alpha) \frac{\partial f_m^\alpha}{\partial c^\alpha} &= f_m^\beta + \left(1 - c^\beta\right) \frac{\partial f_m^\beta}{\partial c^\beta} , \\ f_m^\alpha - c^\alpha \frac{\partial f_m^\alpha}{\partial c^\alpha} &= f_m^\beta - c^\beta \frac{\partial f_m^\beta}{\partial c^\beta} . \end{aligned} \tag{2.15}$$

For this case, $d = 0$ and the system (2.15) itself allows to calculate all equilibrium concentrations. Moreover, it comes out that the pseudo-equilibrium condition can be obtained from the system (2.15):

$$\frac{\partial f_m^\alpha}{\partial c^\alpha} = \frac{\partial f_m^\beta}{\partial c^\beta} , \tag{2.16}$$

The pseudo-equilibrium condition can be generalised to multicomponent systems from (2.11) and (2.12). It is then a necessary but not sufficient condition of the chemical equilibrium. Finally, the equation (2.15) allows to calculate c^α and c^β, which is nothing less than the interface concentration jump.

The chemical potentials of a given component in each phase can be interpreted graphically from (2.11) and (2.12) by plotting the free energies f_m^π against c^π. They are nothing less than the tangential projection of the free energies f_m^π on the axis of the corresponding pure components as seen in Fig. 2.10. This is why the chemical equilibrium induces the so-called common tangent rule, as illustrated in Fig. 2.10 (c). The line with circle markers (in green) in Fig. 2.10 (c) represents the interface concentration jump, also called the tie-line. It is illustrated on a concentration-distance plot in Fig. 2.11.

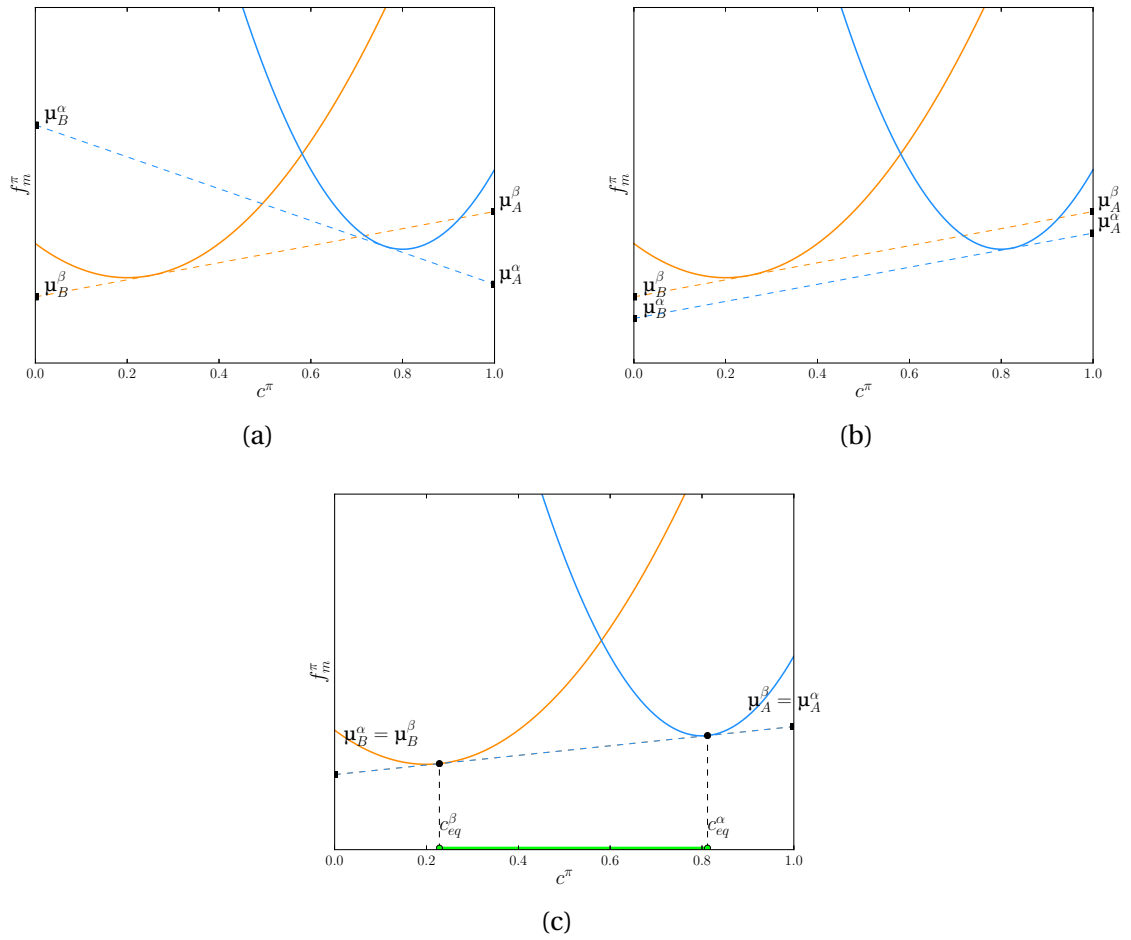

Figure 2.10: Graphical interpretation of the chemical potentials (a) out-of-equilibrium (b) for the pseudo-equilibrium and (c) for the chemical equilibrium. The tie-line, which is the concentration jump enforced by the chemical equilibrium and is illustrated in the subfigure (c) on the concentration axis by the line with circle markers (in green).

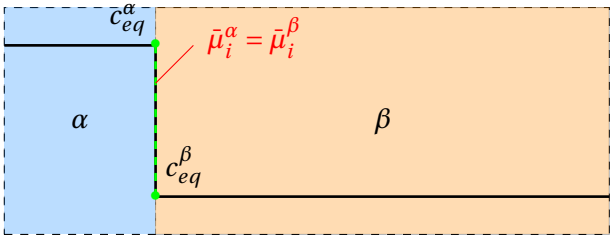

Figure 2.11: Equilibrium concentration-distance profile for an infinite slab. The line with circle markers (in green, dashed) represents the concentration jump enforced by the chemical equilibrium.

Chemical equilibrium in a ternary alloy (A-B-C) with two phases

The constituents are here written (A-B-C) to denote the ternary system. Ternary alloys reduce to a system containing two concentration fields. Here we chose those concentrations to be c_A, c_B where the remaining one is $c_C = 1 - c_A - c_B$. The concentration set $\{c_A, c_B\}$ is then naturally enclosed within a triangular shaped domain., which is illustrated in Fig. 2.12. The ternary chemical equilibrium is

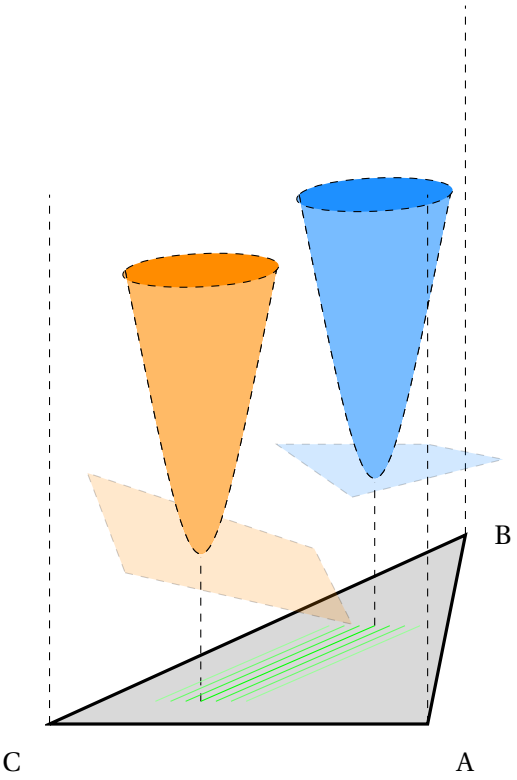

Figure 2.12: The physical domain of concentrations in ternary systems is represented by a grey triangular shaped domain. Energies – the two elliptic paraboloids – are defined within the perimeter of the triangle ABC. A beam of tie-lines is obtained by making the free energies' tangent planes (in translucent orange and blue) to coincide.

determined by (2.11) and (2.12):

$$\begin{aligned} \bar{\mu}_A^\alpha &= \bar{\mu}_A^\beta \\ \bar{\mu}_B^\alpha &= \bar{\mu}_B^\beta \\ \bar{\mu}_C^\alpha &= \bar{\mu}_C^\beta \end{aligned} , \tag{2.17}$$

which can be rewritten as:

$$\begin{aligned} f_m^\alpha + \left(1 - c_A^\alpha\right) \left.\frac{\partial f_m^\alpha}{\partial c_A^\alpha}\right|_{c_B} - c_B^\alpha \left.\frac{\partial f_m^\alpha}{\partial c_B^\alpha}\right|_{c_A} &= f_m^\beta + \left(1 - c_A^\beta\right) \left.\frac{\partial f_m^\beta}{\partial c_A^\beta}\right|_{c_B} - c_B^\alpha \left.\frac{\partial f_m^\alpha}{\partial c_B^\alpha}\right|_{c_A} \\ f_m^\alpha - c_A^\alpha \left.\frac{\partial f_m^\alpha}{\partial c_A^\alpha}\right|_{c_B} + \left(1 - c_B^\alpha\right) \left.\frac{\partial f_m^\alpha}{\partial c_B^\alpha}\right|_{c_A} &= f_m^\beta - c_A^\beta \left.\frac{\partial f_m^\beta}{\partial c_A^\beta}\right|_{c_B} + \left(1 - c_B^\alpha\right) \left.\frac{\partial f_m^\alpha}{\partial c_B^\alpha}\right|_{c_A} \\ f_m^\alpha - c_A^\alpha \left.\frac{\partial f_m^\alpha}{\partial c_A^\alpha}\right|_{c_B} - c_B^\alpha \left.\frac{\partial f_m^\alpha}{\partial c_B^\alpha}\right|_{c_A} &= f_m^\beta - c_A^\beta \left.\frac{\partial f_m^\beta}{\partial c_A^\beta}\right|_{c_B} - c_B^\alpha \left.\frac{\partial f_m^\alpha}{\partial c_B^\alpha}\right|_{c_A} \end{aligned} . \tag{2.18}$$

Here $d = 1$, this is why an additional equation is needed to isolate a single tie-line. The system of equations (2.18) implies that the tangent planes of the energy potentials are coincident. It appears that infinite possibilities of common tangent planes can be found. Using the solute balance – or fixing one interface concentration – results then in the calculation of a single tie-line. This tie-line can be plotted inside the concentrations' domain represented by the triangle ABC in Fig. 2.12. Finally, a planar beam of tie-lines can be obtained by using an interval of initial conditions.

Phase diagram of the ternary system (Fe-Cr-O)

Phases diagrams are essential tools in metallurgy and different techniques can be used to obtain them. First, one can formulate the Gibbs' potentials of the phases from thermodynamic databases within a given multicomponent system and solve all chemical equilibria, see [Kjellqvist et al., 2008, Pujilaksono et al., 2011] for the (Fe-Cr-O) system. Experimental works are also useful, such as diffusion couple techniques, see [Kodentsov et al., 2001]. The diffusion couple technique has been applied for the ternary (Fe-Cr-O) system in [Laheij et al., 1980] as shown in Fig. 2.13. This figure highlights, on the basis of diffusion' paths that, a layer of Cr_2O_3 has to be formed between γ-Fe and the free surface, and that the diffusion's path from γ-Fe by Cr_2O_3 to rust phases should be Z-shaped. Nevertheless, for

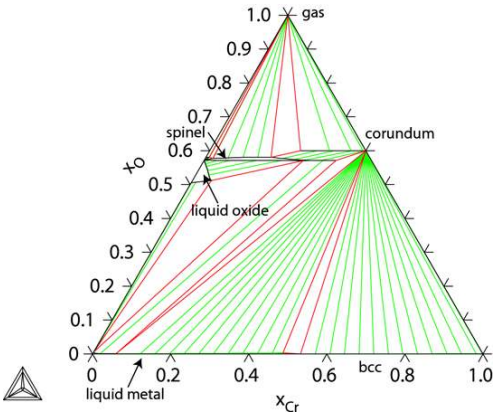

[Kjellqvist et al., 2008]
(a)

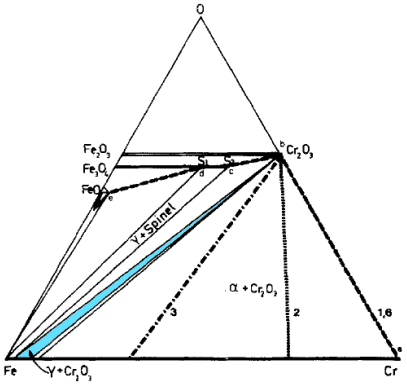

[Laheij et al., 1980]
(b)

Figure 2.13: Isothermal sections of the (Fe-Cr-O) phase diagram (a) at 1600°C (b) at 1200°C.

temperatures lower than 500°C, the characterisation of isothermal sections of phase diagrams remain challenging as the characteristic diffusion time shows a rapid increase.

2.1.4 Chemical and electrochemical reactions

The chemical potential is used as the driving force of a chemical reaction. It is also important to recall some fundamental notions of chemistry, which are frequently used in the field of corrosion modelling.

Chemical reactions For example, the following chemical reaction, for which the quantities A, B, C and D can depict either components or molecules:

$$A + B \rightleftharpoons C + D\,, \tag{2.19}$$

happens to be governed by the following chemical equilibrium:

$$\bar{\mu}_A + \bar{\mu}_B = \bar{\mu}_C + \bar{\mu}_D\,. \tag{2.20}$$

The present chemical equilibrium can be obtained by taking the derivative of the total Gibbs free energy with respect to the extent of reaction [Richet, 2001]. In an ideal solid solution, the activity a_i of a component i is introduced:

$$a_i = \exp\left(\frac{\bar{\mu}_i - \bar{\mu}_i^0}{RT}\right), \tag{2.21}$$

where R [J.K^{-1}.mol^{-1}] is the gas constant, T [K] the temperature and $\bar{\mu}_i^0$ is the standard chemical potential of the pure phase at T=0K. The chemical potential then can be rewritten as,

$$\bar{\mu}_i = \bar{\mu}_i^0 + RT\log(a_i)\,, \tag{2.22}$$

and the rate of the reaction K is given by the ratio of activities of the products with the reactants:

$$K = \frac{a_C a_D}{a_A a_B}\,. \tag{2.23}$$

It should be noted that in the field of corrosion, the activity of oxygen is often reported under the form of its partial pressure.

Electrochemical reactions

The field of electrochemistry is devoted to the study of chemical reactions for which a charge transfer must be accounted for. Electrons can then be identified as additional components, for which a "chemical potential" exists and is referred to as Fermi level, [Kofstad, 1972]. For metals, the principle of electroneutrality is often mentionned and enforces the flux of charges to be zero anywhere. From this assumption, the diffusive ionic transport will be counterbalanced by a gradient of electric potential. The gradient of electric potential will, in return, affect the ionic transport, which is referred as electrophoretic migration, see [Liapis and Grimes, 2005]. It appears that the presence of charges close to an interface can build an electric double layer, which incorporates an additional characteristic length, known as the Debye length. The formation of such a double layer leads then to a loss of charge neutrality in the vicinity of the interface. The phenomena of adsorption into the metallic substrate can be related as a consequence of the double layer, see [Bernard, 2001].

For dry oxidation, the metal atoms are ionised:

$$M \rightleftharpoons M^{n+} + ne^-\,, \tag{2.24}$$

and oxygen atoms are ionised:

$$\frac{1}{2}O_2(g) + 2e^- \rightleftharpoons O^{2-}\,, \tag{2.25}$$

and together resulting in the following redox reaction,

$$2M + n\frac{1}{2}O_2(g) \rightleftharpoons M_2O_n\,, \tag{2.26}$$

In aqueous environments or for wet oxidation, the reactive component is provided by the self ionisation of water:

$$H_2O \rightleftharpoons H^+ + OH^- \qquad \text{or} \qquad H_2O + H^+ \rightleftharpoons H_3O^+\,, \tag{2.27}$$

where OH^- reacts with the metallic cations and forms hydrated oxides, see [Couvant et al., 2007]. The products of water self-ionisation, and OH^-, are likely to react with the metal to form hydroxides. Hydroxydes can spontaneously transform into anhydrous oxydes, [Jolivet and Henry, 2012], which are found as crystalline structures. It then results in a complex oxide layer composed of a layer of hydroxydes that embeds anhydrous oxide grains, [Marcus, 1998].

$$M^{n+} + nOH^- \rightleftharpoons M(OH)_n\,. \tag{2.28}$$

It should be noted that when hydrated oxides are involved, the domains of phase stability are given from Pourbaix diagrams as the formed oxide strongly depends on pH, [Beverskog and Puigdomenech, 1996]. The formed hydroxide can react with the metal cations M^{n+}

at the metal-oxide interface to form the anhydrous oxide phase. Finally, the remaining protons can recombine with the surplus electrons to form dihydrogen. The transport of dihydrogen into the metal and segregation into areas of high hydrostatic stress or within crystal defects is known to lead to brittle failure. This is why the aforementioned phenomena is called hydrogen embrittlement, [Barnoush, 2011].

$$\begin{aligned} &M \rightleftharpoons M^{n+} + ne^- \\ &M(OH)_n + M^{n+} \rightleftharpoons M_2O_n + nH^+ \\ &2H^+ + 2e^- \rightleftharpoons H_2 \end{aligned} \quad . \tag{2.29}$$

Finally, proofs for the diffusion of OH^- in nickel-based alloys can be found in [Jambon et al., 2011].

2.1.5 Local concentration fields of stainless steels and related oxides

The chemical behaviour of the (Fe-Cr-Ni-O-*etc.*) system results in general in heterogeneously distributed concentrations. Observations and measurements of such heterogeneities are mainly based on EFTEM, EDX, SIMS and APT techniques, see [Montemor et al., 2000, Couvant et al., 2009, Sun et al., 2009, Lozano-Perez et al., 2010, Kruska et al., 2012]. The present section is devoted to a brief summary of theses reference works. However, it should be noted that the behaviour of stainless steels undergoing oxidation can also be obtained from theoretical calculations. The free energies provided in [Kjellqvist et al., 2008, Kjellqvist and Selleby, 2009] are a good starting point for the description of the chemical behaviour but they lack the kinetics. Fortunately, transport parameters, *e.g* diffusivities, mobilities, *etc*, can be evaluated from KMC or MD simulations, *e.g.* [Diawara et al., 2004, Diawara et al., 2010, Van Der Geest et al., 2013], but these techniques are computer-intensive. This is why experimental measurements are preferentially used, *i.e.* [Adda and Philibert, 1966, Gale and Totemeier, 2003], which are mostly based on tracer methods. It should be noted that mass transports, in the case of multicomponents systems, is a rather complex field of study. Here, the authors reported strong concentration heterogeneities, which are presently encountered in stainless steels as shown in Fig. 2.3. Such strong concentration heterogeneities must result in a complex interdependence of mass fluxes, see [Larché and Cahn, 1983]. But due to the lack of available data in the literature, such an interdependence is often neglected.

A closer look at the elemental maps of an (Fe-Cr) alloy with minor nickel at 800°C under CH_4-H_2O as shown in Fig.2.14 highlights strong interactions between the formed oxides and the grain boundary network of the base metal, [Horita et al., 2004]. They reported the presence of Cr_2O_3, which embeds concentrations gradients of Si, Fe and Mn that coincide with the former grain boundary network. This result suggests that the Cr_2O_3 layer can embed another oxides that could play the role of diffusion short circuits. At 360°C under hydrogenated pressurised water, the chemical behaviour is shown to be quite different. A depletion of Fe along with an enrichment in Ni in the vicinity of the metal-oxide interface is reported within the base metal. It follows that depletion in Cr is equally reported in grain boundaries, or in localised slip bands, of the base metal. Finally, the concentration profiles throughout the oxide up to the bulk alloy are shown in Fig. 2.15 from [Couvant et al., 2009], which were further corroborated by the measurements of [Lozano-Perez et al., 2010, Kruska et al., 2012]. Moreover a segregation of lithium, which is provided by the pressurised water, in the oxidised grain boundary is shown in Fig. 2.16. This has been assumed by [Kruska et al., 2012] to be a possible explanation of the promoted oxidation within grain boundaries. However such an assumption is still not proved and could eventually be rejected, as noted by the concerned authors. Similar behaviour has been reported under air, see Fig. 1.2, for which the lithium supply is absent. Such a segregation behaviour of the oxidised grain boundary shows that it cannot be confused in any way with the “bulk” oxide. This is why the key role played by oxidised crystal defects is still under investigation, for a better characterisation of the available spectrum and distribution of oxides.

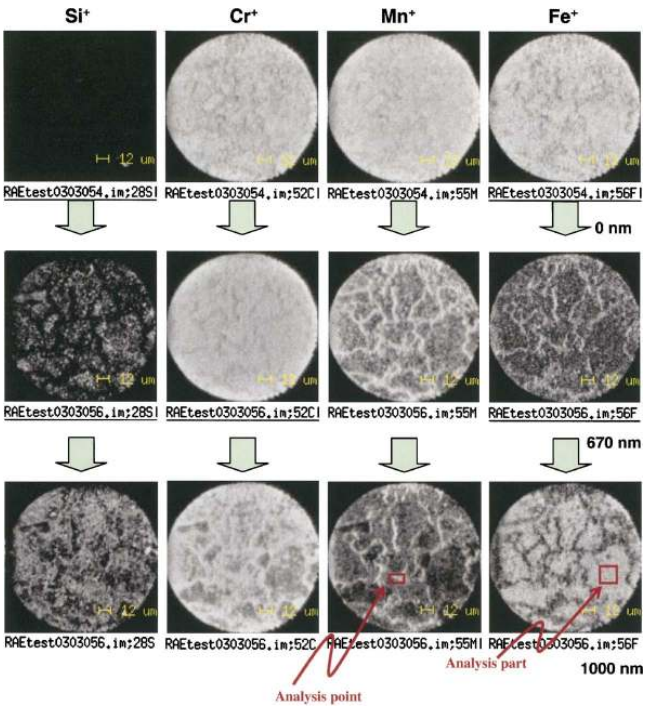

[Horita et al., 2004]

Figure 2.14: SIMS micrograph of an oxidised (Fe-Cr) alloy at 800°C at different depths. The 0 nm position corresponds to the free surface of the oxide scale; 670 nm is located into the oxide scale close to the metal oxide interface and 1000 nm corresponds to the bulk alloy close to the metal oxide interface.

2.1.6 Mechanical behaviour

Inner oxide layer

Characterisation methods of thin oxide layers

In the present work, the mechanical behaviour of the inner oxide is limited to that of Cr_2O_3. The

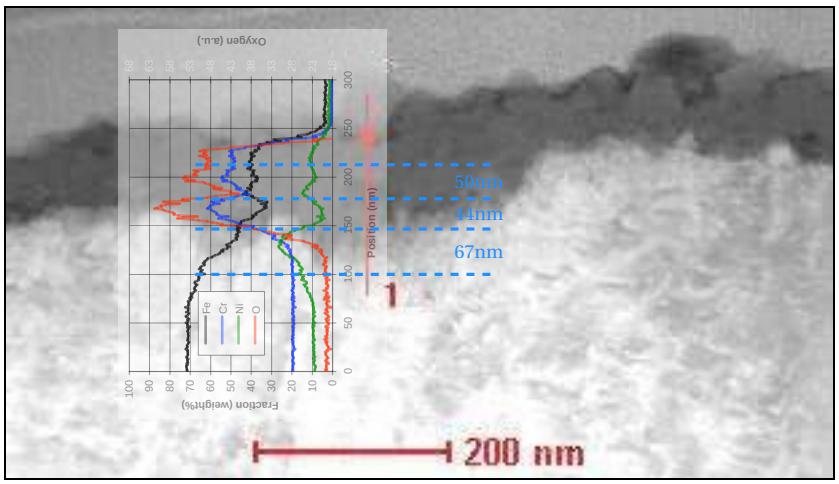

[Couvant et al., 2009]

Figure 2.15: EDX profiles throughout the metal oxide layer in the presence of localised slip bands for a 304L after 270 hours under tension in a primary hydrogenated environment at 360°C.

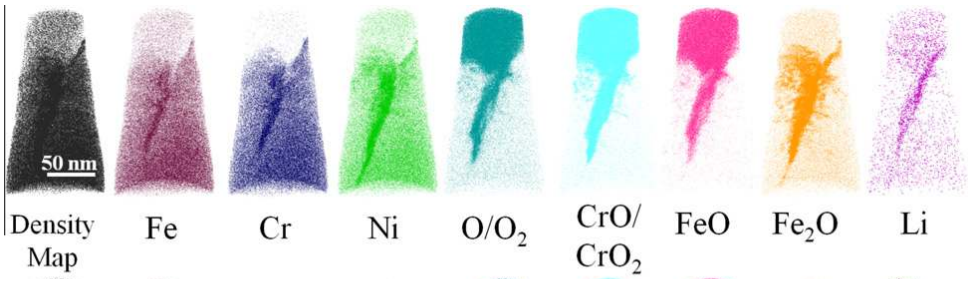

[Kruska et al., 2012]

Figure 2.16: Elemental maps from APT of a 304 stainless steel showing an oxidised grain boundary in simulated primary water.

mechanical behaviour of oxide layers cannot be obtained from classical methods such as as tensile testing due to their narrow thickness along with brittleness. Nevertheless, stress measurements can be done from Raman spectrometry and X-ray diffraction techniques, as done in [Mougin et al., 2001, Huntz et al., 1998] also through the resolution of inverse problems, see [Taylor et al., 2006]. Nanoindentation tests are also useful to characterise the elastic properties of oxides films, which has been done in [Mougin, 2001] for Cr_2O_3. The oxide film has shown a stiffness in the range of 270-300 GPa, which is in agreement with the nanoindentation tests done for deposited Cr_2O_3 layers, [Ji et al., 2004, Pang et al., 2007].

Elastic behaviour of oxides

Nanoindentation testing of Cr_2O_3 layers formed in air at different temperatures resulted in the following values of Young's modulus, [Huntz et al., 1998]:

$$E^{Cr_2O_3}(T) = 349.6 - 0.12\,T \qquad [\text{GPa}]\,, \tag{2.30}$$

where the temperature T is expressed in K, giving thus at 0°C $E^{Cr_2O_3}(273.15) \simeq 317$ GPa and for 900°C $E^{Cr_2O_3}(1173.15) \simeq 209$ GPa. However, for deposited Cr_2O_3 films, [Pang et al., 2007] showed that the Young modulus can drop below 200 GPa at room temperature depending on the conditions of deposition.

Viscoplastic behaviour or creep of oxides

The classical deformation-mechanism maps of [Frost and Ashby, 1982], which are shown in Fig. 2.17, give an overview[4] of the different mechanisms of plasticity and creep for Cr_2O_3. Those maps indicate that the domain of power-law creep is barely reached at 800°C. This is why the viscoplastic relaxation has to be considered only at high temperatures or for very long times.

On the basis of the aforementioned deformation-mechanism maps, creep can be suspected to play a crucial role in the relaxation of oxide growth stresses at high temperatures – above 700°C – as suggested by [Huntz et al., 1998, Mougin, 2001], see Fig. 2.18: Previous works reported that the viscoplastic relaxation occurs only due to the creep of the substrate, as suggested by [Barnes et al., 1989].

In the following, the high temperature creep of Cr_2O_3 will be accounted for on the basis of the assessment of a power-law creep performed by [Mougin, 2001]:

$$\dot{\varepsilon}_p = A\sigma^n = \left(\frac{\sigma}{K}\right)^n \tag{2.31}$$

where $\dot{\varepsilon}_p$ is the inelastic strain rate, A, n, and K are the viscosity parameters of the material, and are temperature dependent. The parameters for the above power-law creep used by [Mougin, 2001]

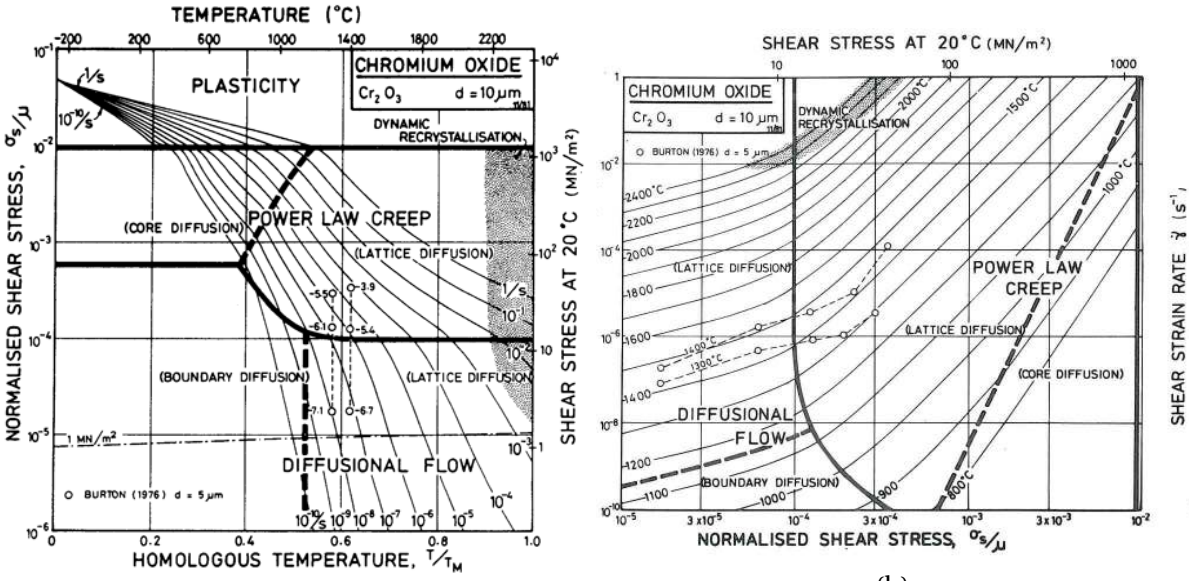

(a) (b)

[Frost and Ashby, 1982]

Figure 2.17: Deformation-mechanism maps showing (a) isovalues of strain rates plotted against temperature and shear stress and (b) strain rate against shear stress for isothermal tests for Cr_2O_3 with mean grain diameter of 10 µm. T_M is the melting temperature of Cr_2O_3 and is equal to 2710K.

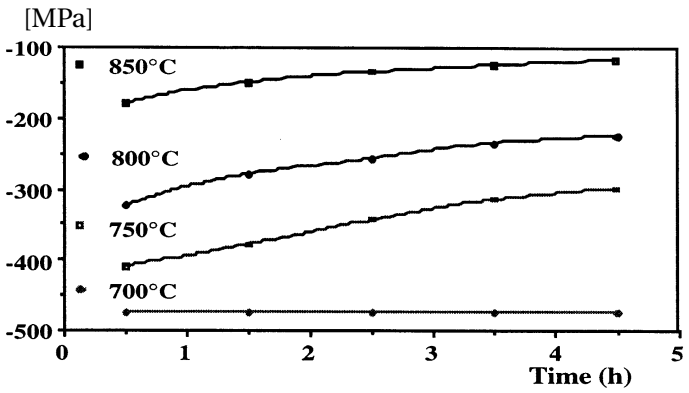

[Huntz et al., 1998]

Figure 2.18: Relaxation of growth and thermal stresses of an oxide formed at 900°C cooled and maintained at lower temperatures.

and [Huntz et al., 1998] are reported in Table 2.3. To the author's knowledge, neither plasticity nor viscoplasticity of Cr_2O_3 in PWRs are mentioned in the literature. It appears that the mechanical behaviour of grown oxides in PWRs can be significantly different from the oxides grown in air. Nevertheless, they share some common points, *e.g.* a texture gradient that goes from small equiaxed grains in the vicinity of the metal-oxide interface up to larger columnar grains.

Failure behaviour of oxides

The oxide Cr_2O_3 is reported to be brittle below 750°C, *e.g.* [Mougin, 2001, Couvant et al., 2007]. Moreover, the brittle failure of the oxide layer is generally avoided due to the fact that compressive

[4] A warning is made to the user of the deformation-mechanism maps for a careful use due to the potential lack of input data

Temperature [°C]	600	700	750	800	850	900
n	5.86	5.9	5.82	5.2	5.01	4.95
K [MPa.s$^{1/n}$]	13330	12500	10320	10635	9641	7738

Table 2.3: Assessment of the power-law creep for Cr_2O_3 at elevated temperatures.

stresses are more likely to be found within the oxide.

Nevertheless, in the case of thermal or mechanical cycling at high temperatures, the viscoplastic relaxation of Cr_2O_3 has been shown to develop tensile stresses within the oxide layer under these conditions, [Huntz et al., 1998]. To date, it appears that the mechanisms leading to the failure of the oxide layer are poorly documented. Finally, it should be noted that the failure of Cr_2O_3 – or evaporation as well – is likely to be followed by a phenomena of breakaway oxidation, *e.g.* [Busso et al., 2010, Pujilaksono et al., 2011], which can be observed from thermogravimetric measurements.

Metallic substrate

Usual characterisation methods

Unlike oxide films, the mechanical properties of γ-Fe can be obtained from standardised mechanical tests. This is why the mechanical behaviour of γ-Fe has been studied extensively in the literature. Elasticity, hardening along with the creep and creep-fatigue behaviour up to the monocrystalline behaviour of austenitic stainless steels can be mentioned as deformation mechanisms of interest for the present work. It should be noted that numerous publications on the mechanical behaviour of austenitic stainless steels can be found in the literature such that the present section is not intended to be exhaustive.

Microstructure of austenitic stainless steels

Austenitic stainless steels are typically composed of equiaxed grains that can embed a high fraction of twin bands, as shown in Fig. 2.19. Those twin bands can be generated during solidification and act as obstacles for dislocations which plays a crucial role in the hardening behaviour.

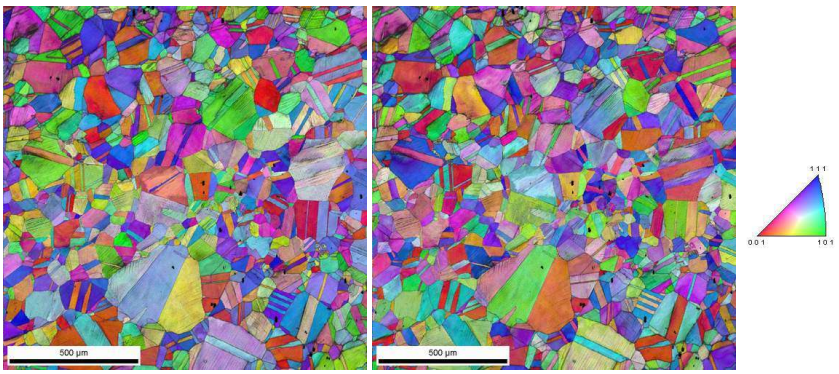

(a) (b)

[Couvant et al., 2009]

Figure 2.19: Inverse pole figure of a 316L stainless steel showing a high fraction of twin boundaries (30-50%). The normal axis is set in the rolling direction in (a) and in the transverse direction in (b).

Elastic behavior of stainless steels

The temperature dependent elastic modulus is provided in [Davis and Committee, 1994] :

$$E^{\gamma\text{-Fe}}(T) = 200 - 0.08T \qquad \text{[GPa]}\,, \tag{2.32}$$

where T is expressed in K, giving thus for 0°C $E^{Cr_2O_3}(273.15) = 200$ GPa and for 900°C $E^{Cr_2O_3}(1173.15) = 128$ GPa, which is quite in agreement with other published results [Couvant et al., 2009].

Plastic behavior

As mentioned by [Blandin and Friedel, 1966, Huguenin, 2012, Galindo-Nava et al., 2012], the stacking fault energy γ_{SFE} is a key element in the determination of the plastic behaviour of FCC phases, such as austenite. The plasticity of low stacking fault energy metals can be the result of a phase transformation, *e.g.* the martensitic phase transformation. Nevertheless, materials with medium stacking fault energies, such as γ-Fe, are likely to relax by dislocation planar glide inside dense planes. Finally, non planar glide up to dislocation climb can be activated for high stacking fault energy FCC lattices. Moreover, it appears that the stacking fault energy can be assessed for γ-Fe as a functional that depends on the concentration in alloying elements. The stacking fault energy also depends on the temperature or on the thermal treatment, see [Yonezawa et al., 2013] amongst others. An example of estimate for the stacking fault energy is given in [Huguenin, 2012]:

$$\gamma_{SFE} = 25.7 + 2(\%Ni) + 410(\%C) - 0.9(\%Cr) - 77(\%N) - 13(\%Si) - 1.2(\%Mn)\ [\text{mJ.m}^{-2}]\,. \tag{2.33}$$

The stacking fault energy also plays a crucial role in the evolution of the spatial arrangement of dislocations during fatigue loadings as mentioned by [Lukáš and Klesnil, 1973, Guilhem, 2011]. Such dislocation patterns can result in the formation of diffusion short circuits in return. Lastly, the stacking fault energy can be calculated within a coupled multicomponent diffusion framework and can be used to estimate the possibility of triggering a martensitic phase transformation.

Again, the deformation-mechanism maps of [Frost and Ashby, 1982] for γ-Fe, given in Fig. 2.20, indicate that creep becomes significant from 600°C. At high temperatures, about 900°C, a brief comparison between the power-law creep behaviour of γ-Fe and Cr_2O_3 can then be done. The comparison of Figs. 2.20 (b) and 2.17 (b) highlights higher creep rates of several orders of magnitude for γ-Fe under equivalent loading conditions. Creep and creep-fatigue of austenitic stainless steels has been extensively studied at temperatures above 500°C. The study of the high temperature behaviour of austenitic stainless steels has been motivated by the development of future Gen. IV nuclear power plants and the former SuperPhénix reactor, [Weiss and Pineau, 1993, Rieth et al., 2004, Holmström et al., 2013]. Nevertheless, under the service conditions of PWRs, *i.e.* below 350°C, creep becomes negligible. The deformation mechanism becomes then dominated by plasticity. This is why the hardening of γ-Fe increases while the temperature decreases as illustrated in Fig. 2.21 from [Pommier et al., 2015]. Stainless steels have been shown to feature a complex hardening behaviour. Therefore, it has been studied extensively over a wide range of loadings, *i.e.* monotonic tensile and tensile-compressive tests, cycling, bi-axial loads up to complex strain paths or non-proportional loadings [Cailletaud, 1988, Taleb et al., 2014]. The present work will then focus on specific behaviours available in the literature, and is not intended to be a comprehensive study of the mechanical behaviour of austenitic stainless steels, which complexity goes far beyond the scope of the thesis.

Amongst the properties of interest, it is important to note that experimental works evidenced the effect of additional or extra hardening, which has been suspected to enhance the SCC susceptibility of AUSS. A possible explanation for that relies on the combination of high levels of hardening with the decrease of the fracture toughness of grain boundaries or localised slip bands caused by the environment. It has been shown by [Cailletaud, 1988, Couvant et al., 2009] that such an additional hardening can be evidenced by the crystal plasticity framework. This is why the assessment of a monocristalline law has been done in [Cailletaud, 1988, Couvant et al., 2009, Miresmaeili et al., 2010, Guilhem, 2011,

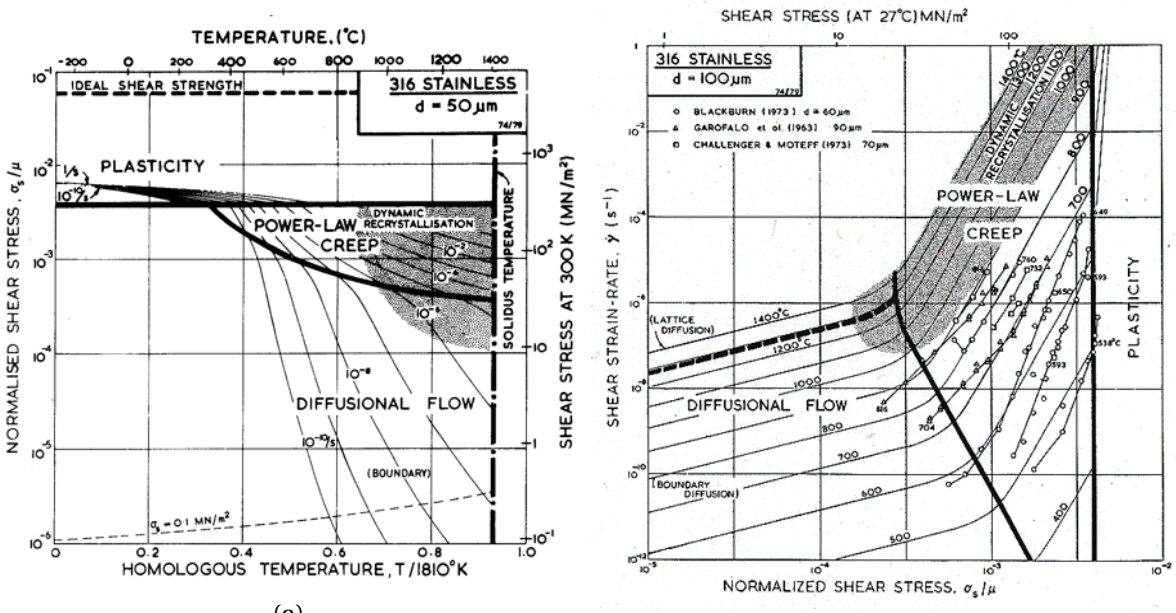

(a) (b)

[Frost and Ashby, 1982]

Figure 2.20: Deformation-mechanism maps of a 316 stainless steel in (a-b). Here, d represents the mean grain diameter.

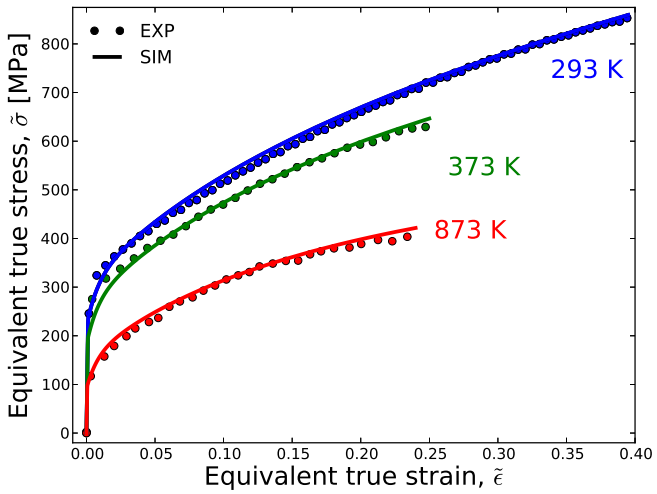

[Pommier et al., 2015]

Figure 2.21: Monotonic tensile test, with imposed strain rate of 10^{-2} s^{-1}, performed at different temperatures for a 316L stainless steel.

Guilhem et al., 2013] from room temperature up to 360°C. Hardening parameters were then calibrated against monotonic and cyclic loadings and are given in Table 2.4 for the Cailletaud-Méric monocrystalline behaviour. In the approach of Cailletaud-Méric, the flow rule of a given slip system is analogous to the classical macroscopic flow rule [Cailletaud, 1988, Busso and Cailletaud, 2005]:

$$\dot{\gamma}_s = \left\langle \frac{|\tau_s - B_s| - S_s}{K} \right\rangle^n \text{sign}\left(\tau_s - B_s\right), \tag{2.34}$$

where $\langle . \rangle$ are the Macaulay brackets, τ_s is the resolved shear stress obtained from the projection of the tensorial stress on the running slip system, B_s is the back-stress or kinematic hardening and is related to the interaction between dislocation and obstacles, *i.e.* impurities, precipitates, *etc.*, whereas

the isotropic hardening S_s is related to the increase of dislocation density. Finally, K and n are the viscosity parameters. The plastic strain rate of a material point is then obtained from the summation over all slip systems of the product between the slip rate and the orientation tensor $\underset{\sim}{\boldsymbol{M}}_s$ – or Schmid tensor – of the considered slip system s:

$$\underset{\sim}{\dot{\boldsymbol{\epsilon}}}_p = \sum_s \dot{\gamma}_s \underset{\sim}{\boldsymbol{M}}_s, \tag{2.35}$$

The non-linear kinematic hardening is defined as follows:

$$B_s = C\alpha_s \qquad \text{and} \qquad \dot{\alpha}_s = \dot{\gamma}_s - d\alpha_s|\dot{\gamma}_s|, \tag{2.36}$$

where α_s is the internal variable associated with a dimensionless hardening, C and d are fitting parameters that account for the linear response and the saturation of α_s. The non-linear isotropic hardening is defined by:

$$S_s = S_0 + \Delta S \sum_r h_{rs} \left(1 - \exp\left(-b\gamma_s^{\text{acc}}\right)\right), \tag{2.37}$$

where S_0 is the initial shear resistance or the resolved shear stress, ΔS is the maximum shear resistance increase of the slip plane, h_{rs} accounts for the interaction rules between the slip systems and is also known as the interaction or hardening matrix, b accounts for the relative increase of dislocation density with respect to the accumulated plastic slip $\gamma_s^{\text{acc}} = \int |\dot{\gamma}_s| dt$. Nevertheless, crystal

	[Cailletaud, 1988]	[Couvant et al., 2009]	[Guilhem et al., 2013]
Temp. [°C]	ambient	ambient / 360	150
E [GPa]	-	200 / 185	C_{1111} = 197, C_{1122} = 125, C_{1212} = 122
ν [-]	-	0.3	0.3
K [MPa.s$^{1:n}$]	50	65 / 10	12
n [-]	25	7 / 4	11
S_0 [MPa]	50	65 / 50	40
ΔS [MPa]	50	45 / 45	10
b [-]	500	3 / 3	3
C [MPa]	1000	600 / 600	40000
d [-]	20	20 / 20	1500
h_{rs} [-]	1	1	[Queyreau et al., 2009, Gérard et al., 2009]

Table 2.4: Assessment of the crystal plasticity behaviour of γ-Fe at low temperatures.

plasticity laws based on physical parameters equally exist. Physically based crystal plasticity laws require the deep understanding of the microstructural state of the studied material. Such models are mainly found to be based on balance equations for dislocations, *e.g.* [Busso and McClintock, 1996, Kocks and Mecking, 2003, Cheong and Busso, 2004].

Finally, in the assessment performed by [Couvant et al., 2009], the viscosity parameters, K and n, along with the critical shear stress S_0 are the only parameters that have been modified to make the transition between 20°C and 360°C. For high temperatures, such parameters must be modified as well and can be calibrated against creep measurements provided in the literature, *e.g.* [le Pêcheur, 2008, Nagesha et al., 2009, Rieth et al., 2004, Holmström et al., 2013, Taleb et al., 2014].

2.2 Oxide growth mechanisms

2.2.1 Oxide metal interface

Epitaxy relationships between the oxide and the metal

Before introducing the concept of epitaxial growth, it is worth noting that the firstly formed oxide layer is more probably composed of amorphous hydrated oxides. Such hydrated oxide condensates can be seen as an accumulation of oxygen tetrahedra, each of them embedding an inner metallic cation. With time, the oxide tends to crystallise, which is probably caused by its dehydration. Once the oxide is crystallised, it then locally adjusts its lattice to the one of the underlying base metal. Such an adjustment generates a misfit between the two adjoining lattices and results in epitaxy stresses. However, epitaxy stresses can be relaxed by the production of dislocation arrays, [Soulas, 2006]. Moreover, the epitaxy relationships between the oxide and the base metal lattices is mentioned to be gradually lost throughout the oxide. This is why the thickness of an epitaxial layer must range between 50 to 100 nm. Beyond such thicknesses, the epitaxial layer tends to become polycrystalline and its texture can show preferential orientations. [Maurice et al., 1998] has reported epitaxy relationships of Cr_2O_3 growing on a (100)Fe-18Cr-13Ni substrate as shown in Fig. 2.22. It resulted then that the principal axis of the HCP lattice of Cr_2O_3 is perpendicular to the (100) plane of the substrate. Finally, the directions $[21\bar{3}0]$ of the oxide and [011] of the base metal were shown to be aligned. It is worth noting

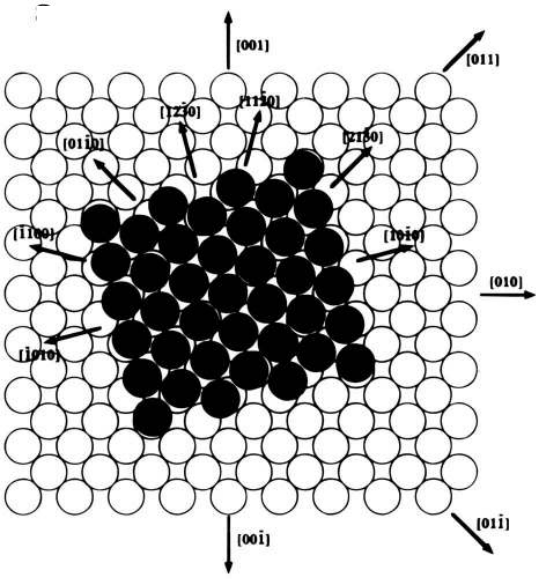

[Maurice et al., 1998]

Figure 2.22: Illustration of the epitaxy relationship between Cr_2O_3 (black lattice) and γ-Fe (white lattice).

that Bollmann's method can be used to estimate the epitaxial stresses, see [Kurpaska et al., 2011] for instance.

Surface properties

The metal-oxide interface embeds a local excess of energy, which is also termed interface energy. Such an interface energy characterises the adhesion energy of the oxide on the metallic substrate and can be quantified from first principle calculations. It has been found that the interface energy of Cr_2O_3 on γ-Fe is approximately 1 $J.m^{-2}$, [Punkkinen et al., 2013]. It is also important to recall that grain boundaries equally embed such an excess energy, which depends on the orientation mismatch

between the grains [Balluffi, 1992]. The intersection of an interface, such as the metal-oxide interface, with a grain boundary is known as a triple junction. The morphology of such a triple junction is governed by the Young-Laplace formula:

$$\gamma_{GB} = 2\gamma_{\phi}\cos(\theta)\,, \tag{2.38}$$

where γs is the interface excess energy and θ the dihedral angle formed at the triple junction. This equilibrium is known as wetting and is often observed at grain boundaries in the case of precipitation or else as a technique to measure grain boundary energies, *e.g.* [Haber et al., 1985, Aral, 2003, Nestler et al., 2003, López et al., 2004, Abrivard, 2009, Kaplan et al., 2013]. This is illustrated in Fig. 2.23.

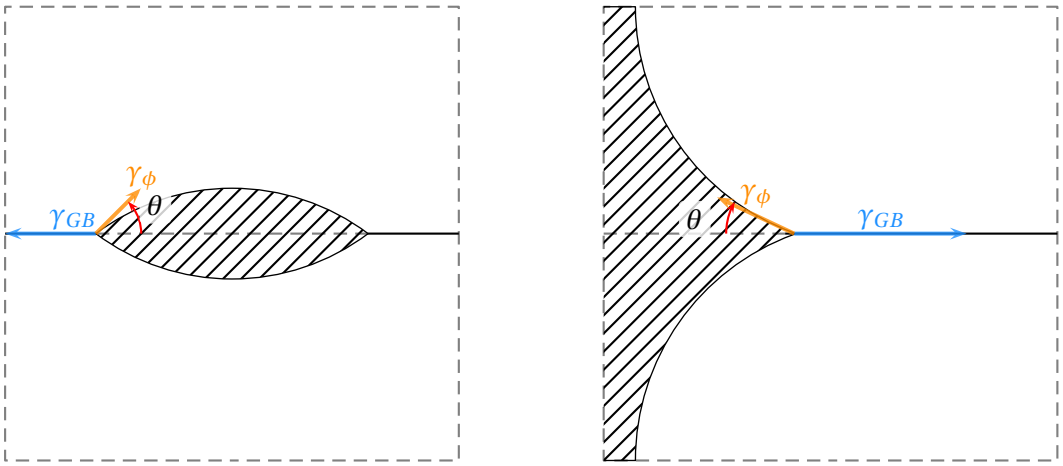

(a) (b)

Figure 2.23: (a) Classical lens-shape of a precipitate formed at a grain boundary and (b) classical triple junction of a phase with a grain boundary.

2.2.2 Mass transport and interface motion

A brief history of oxide growth

Oxidation is generally taken as an harmful phenomenon. Nevertheless, specific oxide layers have protective properties because they can be followed by the decrease of the oxidation rate, which is known as passivation. To date, passivation refers to a whole scientific and engineering domain dedicated to the optimisation of metallic parts within hostile environments. The following history of passivation, is based on [Stringer and Wright, 2003]. Faraday was a pioneer to link chemical reactions with the generation of electric currents. It is known as Faraday's laws of electrolysis, and is of fundamental importance in the field of passivation as the measured current can be linked with the oxide growth kinetics. The conditions for which such a current becomes negligible delimits the domain of passivity.

The study of the passivation of metals began most likely in 1919 with Tamman, who was the first to highlights the parabolic oxide growth in what was called the tarnishing of metals. He was followed by Pilling and Bedworth, [Pilling and Bedworth, 1923] who outlined that such a rate of oxide growth is governed by the intrinsic properties of the oxide. They developed the first model based on the inner diffusion of oxygen inside the metal and introduced the so-called Pilling-Bedworth ratio. The Pilling-Bedworth ratio gives a first idea of the passivation properties of oxides. Then, it is worth adding the contribution of Dunn who first introduced an Arrhenius law dependency- instead of a power law within the oxide growth rate constant. Moreover, following [Stringer and Wright, 2003], Pfeil outlined that the initial position of the free surface remains unchanged during oxidation of iron and separates the outer layer from the inner layer, which suggests a counter-diffusion mechanism of metal and oxygen atoms. Further, following [Stringer and Wright, 2003], Frenkel gave a more detailed description of

the transport mechanism by introducing the concepts of crystalline defects in the field of passivation, in 1926. The first model of oxidation that incorporated this concept has been formulated by Wagner [Wagner, 1933]. The work of Wagner was based on the Nernst and Debye theory of ionic diffusion and is still used nowadays.

The mobilities of atoms or ions can be related to the concentration of crystal defects [Kofstad, 1972], *e.g.* point defects, line defects and surface defects. Interstitials, vacancies or foreign atoms are common point defects, dislocations are well-known line defects and grain boundaries, stacking faults or cracks are surface defects. In addition to that, electronic defects, such as electron holes and free electrons, migrate within the ionic crystal. They can play a role on mass transport by generating an electric field, which in return adds a supplementary external force acting on the transport of charged species.

The field of passivation is very active due to its practical importance. Since then, the number of published papers dealing with oxidation almost doubles every decade. To date, countless models based on point defects along with thermodynamic data are available, *e.g.* [Andresen and Ford, 1996, Tsai et al., 1996, Bertrand et al., 2004, Danielewski et al., 2005, Danielewski and Wierzba, 2008, Macdonald, 2012]. Finally, due to the improvement of observation and characterisation techniques [Olsson and Landolt, 2003], the scanning resolution of passive films has been improved down to the nanoscale. Further developments are focused on the effects of localised oxide intrusions as well as the heterogeneity of concentration fields in the vicinity of structural defects and the effects of stresses.

Nucleation process of the oxide film

The main steps for the nucleation of an oxide film are the following [Atkinson, 1985]:

- Nucleation of oxides nodules at the free surface by adsorption of oxygen bearing molecules followed by the ionisation of oxygen atoms
- Surface growth and coalescence of the oxide nuclei by surface diffusion of oxygen atoms and impingement up to full coverage of the free surface
- Thickening of the oxide film by inner and outer growth

Growth Mechanisms

The system to be studied in this thesis consists of a metallic substrate on which the oxide layer – also termed scale – grows. The oxide layer can embed several oxides and is often reported to be duplex.

The oxide layer can grow either internally or externally. External growth occurs when atoms diffuse from the substrate throughout the scale to react at the free surface. Moreover, the resulting oxide can be dissolved, which has been modelled in [Seyeux et al., 2013]. Such growth is referred as cationic because cationic diffusion is the dominant mass transport. On the contrary, internal growth occurs when oxygen atoms – or other atoms coming from the environment – diffuse throughout the oxide layer to react with metal atoms at the metal-oxide interface, which is also referred as anionic growth. The scale can present a duplex structure when both external and internal growth occur simultaneously, as illustrated in Fig. 2.24. In passivation, the growth kinetics is often reduced to a rate law in the form of a power law with exponent n. This rate law gives the oxide thickness L as a function of time and temperature:

$$L(t) = (K_n.t)^{1/n},\ n \geq 1\,, \tag{2.39}$$

where K_n can have different values depending on the type of growth:

- linear K_l, for porous materials or cracked oxide layers

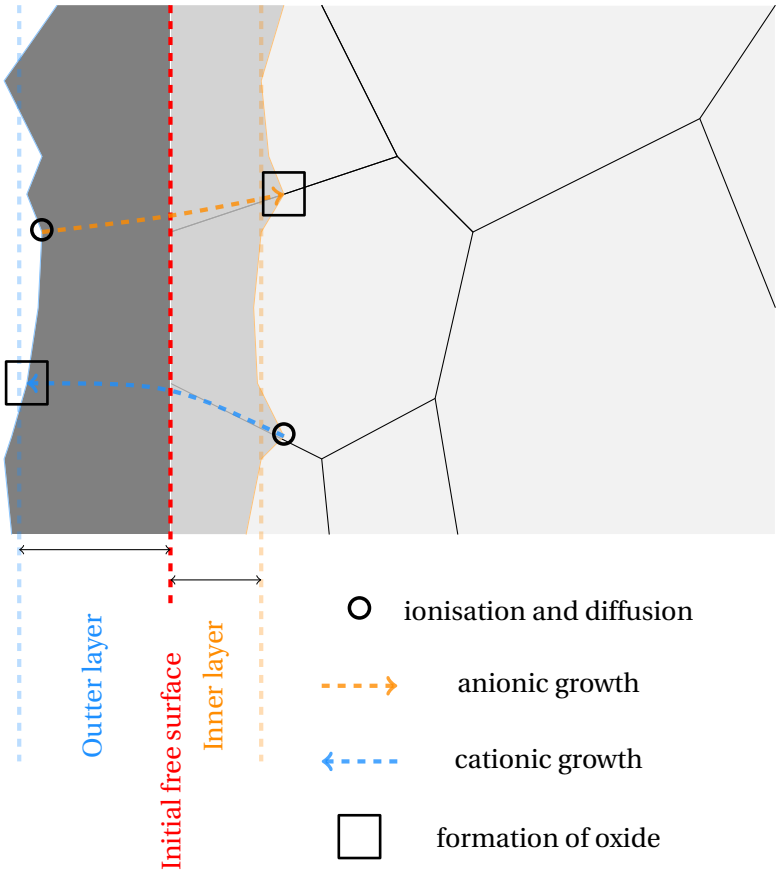

Figure 2.24: Illustration of the growth of a duplex oxide on a polycrystalline substrate.

- parabolic K_p, for passive layers
- cubic K_c,
- logarithmic K_e where $L(t) = K_e \log(a.t + 1)$ with a a constant, often reported for thin films

The rate constants K_n can be dependent on numerous parameters, *e.g.* temperature, partial pressures gradients, the oxide microstructure, *etc.* The rate law parameters K_n and n are useful, in the sense that they depict the rate limiting step. For example, a linear rate constant suggests that diffusion inside the oxide is not the rate limiting step unlike for a parabolic rate constant.

The undertanding of the growth rate allows to create new composite materials, composed of metallic bounds and ionic bounds. This property contrast is used for material design purposes and enters the fields of surface treatments or coatings. Examples of surface treatments by oxidation are found in thermal barrier coatings [Frachon, 2009, Seiler et al., 2010] for the protection against thermal fatigue, in the thermal oxidation of silicon to create a localised non-conductive patterned surface and naturally in passivation, allowing metals to be protected against corrosion, *etc.*

Three cases are reviewed in Appendix A. All of them correspond to a parabolic growth. The two first ones are limited to the inner oxide growth and are respectively limited to the supply of oxygen throughout the oxide and limited to the supply of chromium from the substrate:

$$K_p = 2 D_O^{\text{ox.}} \frac{c_O^{\text{ox.}} - c_O^{\text{ox. / met.}}}{c_O^{\text{ox. / met.}} - c_O^{\text{met. / ox.}}}, \tag{2.40}$$

where $D_O^{\text{ox.}}$ is the oxygen diffusivity inside the oxide and $c_O^{\text{ox.}}$, $c_O^{\text{ox. / met.}} - c_O^{\text{met. / ox.}}$ respectively the concentration of oxygen at the free surface and the concentration jump at the interface from the oxide to

the metal. The growth rate for the second case reads:

$$K_p = 4D_M^{met.} F^{-1}\left(\frac{c_M^{\text{met.}} - c_M^{\text{met. / ox.}}}{c_M^{\text{ox. / met.}} - c_M^{\text{met. / ox.}}}\right)^2, \tag{2.41}$$

where $D_M^{met.}$ is the diffusivity of the alloying element inside the metal, $c_M^{\text{met.}}$ the concentration of the alloying element in the metal far away from the interface, $c_M^{\text{ox. / met.}} - c_M^{\text{met. / ox.}}$ the concentration jump from the oxide to the metal and finally F the transcendental function defined in the aforementioned appendix. The remaining rate constant corresponds to the model of Wagner and simultaneously embodies inner and outer growth. Such a rate constant is obtained by assuming electroneutrality and oxide stoichiometry and is frequently used in the field of high temperature oxidation. The rate constant for oxide growth with a stoichiometry M_2O_3 controlled by the ionic supply reads:

$$K_p = \frac{1}{2} c_{an}\left(D_{an} + \frac{2}{3} D_{ca}\right) \log \frac{\mathscr{P}_{O_2}^{ox.}}{\mathscr{P}_{O_2}^{ox./met.}}, \tag{2.42}$$

where c_{an} is the anions concentration, D_{ca} and D_{an} are cations and anions diffusivities within the oxide and $\mathscr{P}_{O_2}^{ox.}$ and $\mathscr{P}_{O_2}^{ox./met.}$ the partial pressure of oxygen at the free surface and at the metal oxide interface in the oxide.

2.2.3 Growth stresses

Pilling-Bedworth ratio

Growth stresses are frequently mentioned to be generated by the so-called Pilling-Bedworth ratio (PBR), *e.g.* [Pilling and Bedworth, 1923, Evans, 1983, Huntz et al., 1993, Yang et al., 2012]. Nevertheless, the use of the PBR can be justified only in the case of anionic growth without any loss of base metal or alloying elements. In this case, the new oxide will grow inside the substrate, for which growth stresses are generated by the molar volume difference between the oxide and the metal.

The PBR is also described as the ratio between the volume of the elementary oxide cell with the elementary base metal cells necessary for the formation of the unit cell of oxide:

$$R_{\text{PB}} = \frac{V_{\text{oxide}}}{V_{\text{metal}}}. \tag{2.43}$$

If the volume occupied by the new oxide is greater than the volume needed for its formation, then the PBR becomes greater than one. The oxide will be then in a state of compression, making porosity along with the effective mobility of atoms to decrease. In the metal, tensile stresses can be transmitted during the formation of such oxides if the thickness of the oxide layer is not negligible to that of the substrate and also in the case of a non planar metal oxide interface. In Tab. 2.5, some PBRs are given for indicative purpose: Such PBRs were given for pure base metals. Chromium is the alloying

Cr_2O_3 / Cr	FeO / Fe	NiO / Ni
2.07	1.7	1.7

[Revie, 2008]

Table 2.5: Pilling-Bedworth ratios for different oxides and their pure base metals.

element responsible for the growth of $Cr_2O_3$and occupies 16% of the lattice sites of γ-Fe. Given the stoichiometric HCP lattice of Cr_2O_3, four chromium atoms are needed for the formation of a unit cell of Cr_2O_3. A unit cell of γ-Fe possesses four nodes, it then contains in average $4 \times 0.16 = 0.64$ atoms of chromium, such that $\frac{4}{0.64} = 6.25$ unit cells of γ-Fe are needed to form an unit cell of Cr_2O_3.

The PBR – while considering experimentally measured lattice parameters of γ-Fe and Cr_2O_3– and its corresponding average growth strain $\langle \varepsilon_\star \rangle$ read then:

$$R_{PB} = \frac{3 \times 4.9607^2 \times 13.599 \times \frac{\sqrt{3}}{2}}{6.25 \times 3.62^3} = 2.93 \qquad \text{and} \qquad \sqrt[3]{R_{PB}} = 1 + \langle \varepsilon_\star \rangle = \sqrt[3]{2.93} = 1.43\,. \tag{2.44}$$

The resulting mean eigenstrain is 43%.

Anisotropic Growth stresses

The present work is based on the statements of [Clarke, 2002], that lateral growth strain levels, which are sustained during the oxide growth, are about 0.5-1%. But growth strains normal to the metal oxide interface can be larger than the aforementioned lateral growth strains. Therefore, the Pilling-Bedworth ratio can, to some extend, be enforced by the use of anisotropic eigenstrains, *i.e.* [Huntz et al., 2002]:

$$R_{PB} = (1 + \varepsilon_{nn})\,(1 + \varepsilon_{tt})^2\,, \tag{2.45}$$

where $\underline{\boldsymbol{t}}$ are the in plane directions and $\underline{\boldsymbol{n}}$ the normal direction of the metal-oxide interface. It is also possible to relate in plane growth strains with epitaxy relationships between the metal and its oxide, as presented in the section devoted to interfaces. Nevertheless, it has been observed that such lateral strains can be relaxed by the presence of arrays of interface dislocations, inducing thus a loss of coherency, *i.e.* [Maurice et al., 1998].

Growth stresses of other nature

Further, secondary causes for the generation of growth stresses can be explained by deviation from stoichiometry. The deviation from the initial composition of the crystal lattice is known to locally modify the crystal lattice parameters, *e.g.* [Larché and Cahn, 1985, Favergeon et al., 2005, Ammar, 2010, Villani et al., 2014], which in return generate stresses. For instance, growth stresses have been chosen to be induced by chromium heterogeneities in the work of *e.g.* [Zhou, 2010, Zhou et al., 2010, Zhou et al., 2010b]. Moreover, Rhines and Wolves explained the average 1% of lateral growth strains to be induced by nonstoichiometry inside grain boundaries within the oxide layer, *e.g.* [Krishnamurthy and Srolovitz, 2003, Krishnamurthy and Srolovitz, 2004]. Lastly, the difference of thermal expansion coefficients between the oxide and the substrate along with nonisothermal conditions leads to the generation of thermal stresses, *e.g.* [Mougin, 2001]. Thermal stresses are here neglected as the study is limited to the case of isothermal oxide growth.

Viscoplastic relaxation of the growth stresses

Finally, the viscoplastic relaxation of growth strains can be evidenced at high temperature. Viscoplasticity was first accounted for in [Barnes et al., 1989], for which the oxide layer was purely elastic whereas the substrate was able to deform viscoplastically. He was later followed by [Huntz et al., 1998], who evidenced the viscoplastic relaxation of Cr_2O_3 for temperatures above 750°C. They also found that growth stresses increased in the oxide layer along with the oxide thickness, whereas the elastic analysis resulted in a decrease. Such phenomenon has been explained from the increase of the oxide grain size leading to lesser viscoplastic relaxation levels within the oxide. Low growth stresses levels were then reported in the oxide layer due to their rapid viscoplastic relaxation as seen in Fig. 2.25. The figure shows successive measurements of the mean in plane stress within the oxide layer for a grown oxide at 900°C that is first cooled to ambient temperature and then reheated to 900°C. It shows that growth stresses are close to zero at 900°C, suggesting thus that growth stresses must be rapidly relaxed at such temperature.

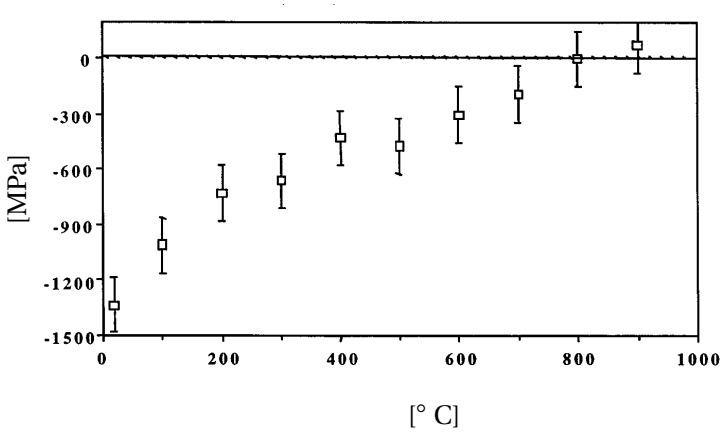

[Huntz et al., 1998]

Figure 2.25: Measurements of combined growth and thermal stresses for Cr_2O_3 formed at 900°C suggesting for negligible growth stresses at the temperature of growth.

2.2.4 Grain boundary oxidation

Short Paths of Diffusion

Tracer experiments are conducted to assess the diffusivities of chemical elements in solids. Nevertheless, the presence of crystal defects, which are here grain boundaries, leads to the heterogeneous penetration of oxides – or oxide intrusions Deepest oxide penetration levels are obtained along grain boundaries, which are known to act as diffusion short circuits, in the same way as slip bands. It appears then, due to the presence of crystal defects, that concentration-distance plots of tracer elements deflect at a given depth. The first part of the aforementioned curve is known to be mainly account for bulk diffusion, for which the diffusivity can be assessed using the classical error function erf. The second part, the deepest one, highlights a specific grain boundary diffusion regime. Data about the effective grain boundary diffusion can be extracted from comparison of the experimental penetration curves on the basis of the analytic solution provided by Whipple. Given the values of the grain boundary phase fraction, and assuming it to be invariant along the depth axis, one can evaluate the mean grain boundary diffusivity coefficient, for example using the data provided in Fig. 2.26. Such a sys-

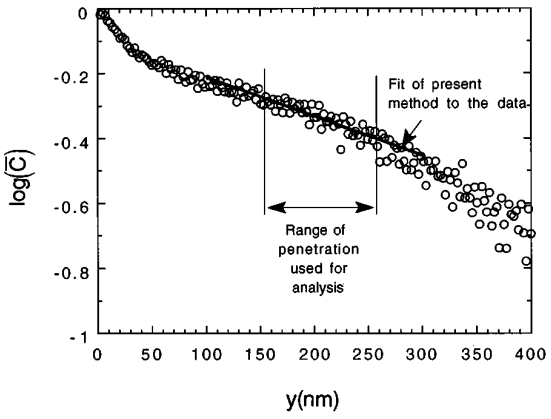

[Chung and Wuensch, 1996]

Figure 2.26: Concentration profile of ^{18}O tracer of a MgO bicrystal where the interval for the calculation of the grain boundary diffusivity starts after 50 nm.

tematic study of grain boundary diffusion has been pioneered by Fisher, [Fisher, 1951]. He proposed to model the diffusion short circuit behaviour of grain boundaries from a unit pulse description of

diffusivities, which is at its highest over a rather small area of finite thickness – the grain boundary thickness. The simplicity and the usefulness of such a model made its success, which is why it is still used today. An illustration of Fisher's grain boundary model is given in Fig. 2.27 as it appears in the original paper of 1951, where the problem was first solved on the basis of a finite difference approach. Shortly after, he was followed by Le Claire [Le Claire, 1951] and Whipple [Whipple, 1954] who found

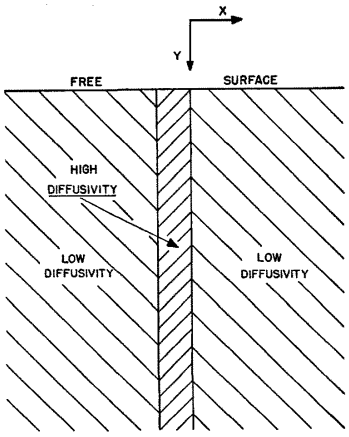

[Fisher, 1951]

Figure 2.27: Fisher's grain boundary model, where the grain boundary is nothing but a thin region of enhanced diffusivity.

an integral solution of Fisher's problem. Later, diffusion anisotropy has been accounted for, first in the normal direction of the grain boundary plane and then inside the grain boundary plane itself, along with segregation [Young and Funderlic, 1973, Mishin and Yurovitskii, 1991]. The grain boundary, as a surface defect embeds an excess of energy. In 1964, Borisov, Golikov and Scherbedinsky formulated a relationship to link grain- and grain boundary diffusivities to the grain boundary energy, which has been confirmed in the case of pure metals where self-diffusion occurs, see [Guiraldenq, 1975].

The grain boundary energy is crucial in the study of grain boundary segregation up to intergranular precipitation. In general, impurities make the grain boundary energy to decrease, which is more likely to be followed by the decrease of the grain boundary diffusivity – at least for the base metal. It follows that preferential segregation of alloying elements is driven by the decrease of the grain boundary energy, see [Divinski et al., 2010, Prokoshkina et al., 2013]. By comparison, low angle grain boundaries can be seen as a superposition of static dislocations whose spacing governs the misfit angle between the grains. The evidences brought by [Trindade et al., 2005] that low-angle grain boundaries are weaker diffusion short circuits than high-angle grain boundaries due to their lower excess energy clearly illustrate the previous statements. Therefore, non segregated high-angle grain boundaries must play a crucial role for the generation of oxide intrusions. Finally, the reader is referred to [Raabe et al., 2014] for a more comprehensive description of the properties and issues encountered in the field of grain boundary engineering.

Enhanced oxidation driving force

In the field of oxidation, grain boundary diffusion plays a major role in the formation of oxide intrusions as shown in Fig. 2.28, [Lozano-Perez et al., 2012]. Moreover, such oxide intrusions have been suspected to inject tensile stresses in the polycrystalline substrate caused by a Pilling-Bedworth ratio greater than one as mentioned in [Evans, 1983]. Therefore, they are suspected to be responsible for the preferential nucleation of cracks. The investigation of the failure strength of oxidised grain boundaries is to date of primary concern. Some studies devoted to the characterisation of such a strength were performed and the topic is still investigated to obtain statistically reliable data, see [Dugdale et al., 2013] for nickel based alloys. They mentioned that, grain boundary failure occurred around 350 MPa in operating conditions, whereas the oxidised grain boundary, in their study,

has failed at 1.35 GPa in a vacuum environment. The reasons for such a decrease have been attributed mainly to the supply of hydrogen from the environment. For prior cold-worked stainless steels, [Lozano-Perez et al., 2011] observed both inter- and transgranular crack initiation at the vicinity of the oxidised grain boundary. Finally, the influence of strain heterogeneities across grain boundaries along with the neighbouring effects induced by the promoted slip of favourably oriented grains with respect to the Schmid factor, has been considered in the failure analysis of grain boundaries, [Couvant et al., 2009]. The questions raised in the last study are still investigated to clearly identify the possible role played by strain gradients along with plasticity on oxidation.

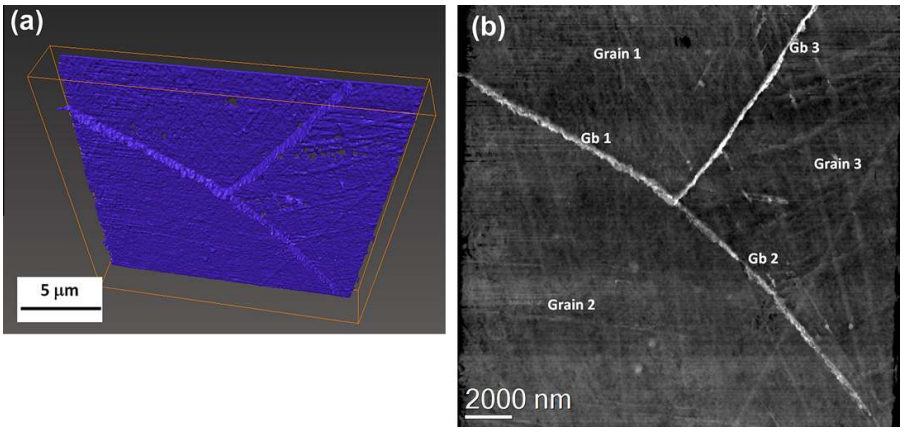

[Lozano-Perez et al., 2012]

Figure 2.28: Grain boundary oxidation of a 304 steels oxidised in simulated primary water showing (a) the 3d map of the chromium-based oxide layer and (b) the 2d topological map where the brighter regions reveal the promoted intrusion of the oxide along the grain boundaries.

2.2.5 Plasticity promoted oxidation

In the same way as for grain boundaries, a dislocation core contains a free volume which is known to lower the activation energy for diffusion. Such an enhanced diffusion has been evidenced by MD simulations, *e.g.* [Purja Pun and Mishin, 2009], where different behaviours between screw and edge dislocations were reported. The effective diffusivity of chemical elements within plastically deformed metallic matrices is therefore likely to be enhanced as proposed by [Hart, 1957]. The series of papers of Le Claire [Le Claire and Rabinovitch, 1981, Le Claire and Rabinovitch, 1982, Le Claire and Rabinovitch, 1983, Le Claire and Rabinovitch, 1984] deals with the problem of diffusion throughout an array of dislocations. The reader is also referred to [Kaur et al., 1989] for an exhaustive review of analytic diffusion problems. For a simple case of a periodic arrangement of parallel dislocations, as illustrated in Fig. 2.29, the effective diffusivity in the direction of the dislocation line has been found to depend on the dislocation density ρ in the similar fashion as for the Hart formula:

$$D_{\text{eff}} = D_{\text{bulk}} \left(1 + \pi r^2 \rho \left(\Delta - 1\right)\right), \tag{2.46}$$

where r is the dislocation core radius and Δ the ratio of diffusivities between the dislocation core and the bulk.

At lower temperature, an effect of "clogging" of the dislocation is nevertheless mentioned. Such a "clogging" effect occurs if the interspacing between dislocations is too high with respect to the characteristic bulk diffusion time, see [Ruoff and Balluffi, 1963]. Nevertheless, the situation is changed when dislocations become mobile – or else if the plastic strain rate is non zero – because dislocations can drag the alloying elements along their way.

It is know that dislocations can gather and build several types of substructures. Localised slip bands are among such structural defects and have been shown to promote oxidation in a similar way

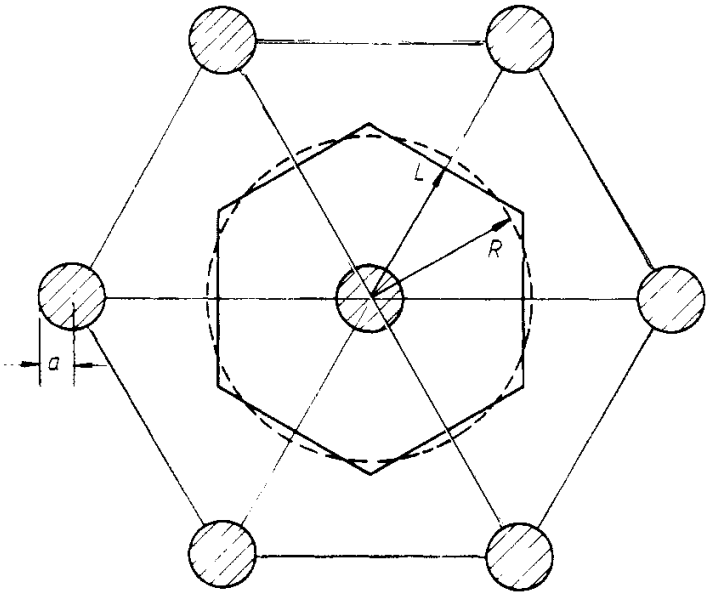

[Le Claire and Rabinovitch, 1983]

Figure 2.29: Illustration of the periodic array of dislocations where the circles represent the dislocation cores of radius a. The hexagonal cell represents the periodic cell.

to grain boundaries, [Weiss and Pineau, 1993, Budiman et al., 2007]. As for grain boundaries, the induced localised slip bands of AUSS feature the preferential oxide intrusion. Such oxide intrusions have been supposed to act as preferential sites for intragranular cracking, [Couvant et al., 2009]. Several authors [Lozano-Perez et al., 2009, Lozano-Perez et al., 2012], also evidenced the promoted oxidation in deformation bands in simulated primary water as shown in Fig. 2.30.

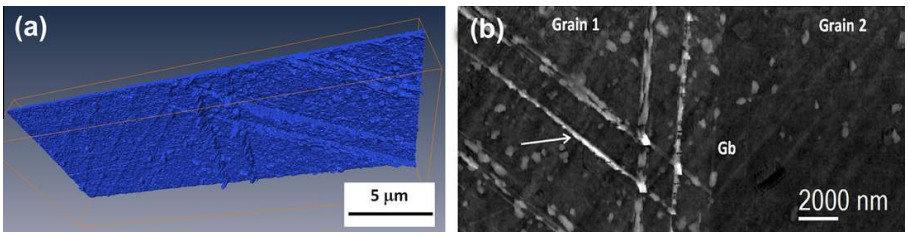

[Lozano-Perez et al., 2012]

Figure 2.30: AUSS oxidised under stress showing oxide intrusions inside deformation bands (a) 3d reconstruction of the oxide penetration depth and (b) 2d topological map of oxide penetration where high depths are localised by bright areas.

References

[Abrivard, 2009] Abrivard, G. (2009). *A coupled crystal plasticity - phase field formulation to describe microstructural evolution in polycrystalline aggregates during recrystallisation*. PhD thesis, Mines ParisTech.

[Adda and Philibert, 1966] Adda, Y. and Philibert, J. (1966). *La diffusion dans les solides*. Number vol. 1 in Bibliothèque des sciences et techniques nucléaires. Institut National des Sciences et Techniques Nucléaires.

[Ammar, 2010] Ammar, K. (2010). *Modelling and simulation of phase transformation-mechanics coupling using a phase field method*. PhD thesis, Mines ParisTech.

[Andresen and Ford, 1996] Andresen, P. and Ford, F. (1996). Response to On the modeling of stress corrosion cracking of iron and nickel base alloys in high temperature aqueous environments. *Corrosion Science*, 38(6):1011 – 1016.

[Aral, 2003] Aral, G. (2003). *Parallel molecular dynamics simulations of dynamics of oxidation and reactive wetting in metal/ceramic systems*. PhD thesis, Louisiana State University.

[Atkinson, 1985] Atkinson, A. (1985). Transport processes during the growth of oxide films at elevated temperature. *Rev. Mod. Phys.*, 57:437–470.

[Baker, 2013] Baker, S. (2013). Conflict minerals: Potential impact on AIIS members. E-newsletter for AIIS Members and the Steel Community.

[Balluffi, 1992] Balluffi, R. (1992). Grain boundary diffusion mechanisms in metals. *Journal of Electronic Materials*, 21(1):527–553.

[Barnes et al., 1989] Barnes, J., Goedjen, J., and Shores, D. (1989). A model for stress generation and relief in oxide Metal systems during a temperature change. *Oxidation of Metals*, 32(5-6):449–469.

[Barnoush, 2011] Barnoush, A. (2011). Hydrogen embrittlement.

[Bernard, 2001] Bernard, M. (2001). *Croissance électrochimique : un modèle de gaz sur réseau en champ moyen*. PhD thesis, École Polytechnique.

[Bertrand et al., 2004] Bertrand, N., Desgranges, C., Gauvain, D., Monceau, D., and Poquillon, D. (2004). Low temperature oxidation of pure iron: Growth kinetics and scale morphologies. In *Materials Science Forum*.

[Beverskog and Puigdomenech, 1996] Beverskog, B. and Puigdomenech, I. (1996). Revised Pourbaix diagrams for iron at 25300°c. *Corrosion Science*, 38(12):2121 – 2135.

[Blandin and Friedel, 1966] Blandin, A. and Friedel, J. (1966). Les énergies de fautes d'empilement et de mâcles dans les métaux normaux. In *Journal de Physique, Colloque C3*.

[Budiman et al., 2007] Budiman, A., Hau-Riege, C., Besser, P., Marathe, A., Joo, Y.-C., Tamura, N., Patel, J. R., and Nix, W. (2007). Plasticity-amplified diffusivity: Dislocation cores as fast diffusion paths in Cu interconnects. In *Reliability physics symposium, 2007. proceedings. 45th annual. ieee international*, pages 122–127.

[Busso and Cailletaud, 2005] Busso, E. and Cailletaud, G. (2005). On the selection of active slip systems in crystal plasticity. *International Journal of Plasticity*, 21(11):2212 – 2231.

[Busso et al., 2010] Busso, E., Evans, H., Qian, Z., and Taylor, M. (2010). Effects of breakaway oxidation on local stresses in thermal barrier coatings. *Acta Materialia*, 58(4):1242–1251.

[Busso and McClintock, 1996] Busso, E. and McClintock, F. (1996). A dislocation mechanics-based crystallographic model of a B2-type intermetallic alloy. *International Journal of Plasticity*, 12(1):1 – 28.

[Cailletaud, 1988] Cailletaud, G. (1988). Une approche micromécanique du comportement des polycristaux. *Revue de Physique Appliquée*, 23(4):353–365.

[Cheng et al., 2011] Cheng, X., Feng, Z., Li, C., Dong, C., and Li, X. (2011). Investigation of oxide film formation on 316L stainless steel in high-temperature aqueous environments. *Electrochimica Acta*, 56(17):5860 – 5865.

[Cheong and Busso, 2004] Cheong, K. and Busso, E. (2004). Discrete dislocation density modelling of single phase FCC polycrystal aggregates. *Acta Materialia*, 52(19):5665 – 5675.

[Chung and Wuensch, 1996] Chung, Y.-C. and Wuensch, B. (1996). An improved method, based on Whipple's exact solution, for obtaining accurate grain-boundary diffusion coefficients from shallow solute concentration gradients. *Journal of Applied Physics*, 79:8323–8329.

[Clarke, 2002] Clarke, D. (2002). Stress generation during high-temperature oxidation of metallic alloys. *Current Opinion in Solid State and Materials Science*, 6(3):237–244.

[Cottrell, 2000] Cottrell, A. (2000). *An introduction to metallurgy*. Materials science. Universities Press (India) Pvt. Limited.

[Couvant et al., 2009] Couvant, T., Legras, L., Herbelin, A., Musienko, A., Ilevbrev, G., Delafosse, D., Cailletaud, G., and Hickling, J. (2009). Development of understanding of the interaction between localized deformation and SCC of austenitic stainless steel exposed to primary PWR environment. In *Proceedings of the Fourteenth International Conference on Environmental Degradation of Materials in Nuclear Power Systems Water Reactors*, pages 182–194. American Nuclear Society (ANS).

[Couvant et al., 2007] Couvant, T., Legras, L., Pokor, C., Vaillant, F., Brechet, Y., Boursier, J., and Moulart, P. (2007). Investigations on the mechanisms of PWSCC of strain hardened austenitic stainless steels. In *13th Env Degradation Conf, Whistler, Canada, 19-23 août 2007*.

[Cunat, 2002] Cunat, P. (2002). *The euro inox handbook of stainless steel*. Materials and applications series, Volume 1. Euro Inox.

[Danielewski et al., 2005] Danielewski, M., Filipek, R., Pawełkiewicz, M., Klassek, D., and Kurzydłowski, K. (2005). Modelling of oxidation of Fe-Ni-Cr alloys. In *Defect and Diffusion Forum Vols. 237-240 (2005) pp 958-964*.

[Danielewski and Wierzba, 2008] Danielewski, M. and Wierzba, B. (2008). Diffusion processes determining the oxidation rate of multicomponent alloys. *Corrosion Science*, 50(4):1161 – 1168.

[Das et al., 2009] Das, N., Suzuki, K., Ogawa, K., and Shoji, T. (2009). Early stage {SCC} initiation analysis of fcc Fe–Cr–Ni ternary alloy at 288°C: A quantum chemical molecular dynamics approach. *Corrosion Science*, 51(4):908 – 913.

[Das et al., 2008] Das, N., Suzuki, K., Takeda, Y., Ogawa, K., and Shoji, T. (2008). Quantum chemical molecular dynamics study of stress corrosion cracking behavior for fcc Fe and FeCr surfaces. *Corrosion Science*, 50(6):1701 – 1706.

[Davis and Committee, 1994] Davis, J. and Committee, A. (1994). *Stainless Steels*. ASM specialty handbook. ASM International.

[Diawara et al., 2010] Diawara, B., Beh, Y.-A., and Marcus, P. (2010). Nucleation and growth of oxide layers on stainless steels (Fe-Cr) using a virtual oxide layer model. *The Journal of Physical Chemistry C*, 114(45):19299–19307.

[Diawara et al., 2004] Diawara, B., Legrand, M., Legendre, J., and Marcus, P. (2004). Use of Quantum Chemistry Results in 3D Modeling of Corrosion of Iron-Chromium Alloys. *Journal of The Electrochemical Society*, 151(3):B172–B178. 7 pages.

[Divinski et al., 2010] Divinski, S., Reglitz, G., and Wilde, G. (2010). Grain boundary self-diffusion in polycrystalline nickel of different purity levels. *Acta Materialia*, 58(2):386 – 395.

[Dugdale et al., 2013] Dugdale, H., Armstrong, D., Tarleton, E., Roberts, S., and Lozano-Perez, S. (2013). How oxidized grain boundaries fail. *Acta Materialia*, 61(13):4707 – 4713.

[Emmerich, 2003] Emmerich, H. (2003). *The Diffuse Interface Approach in Material Science: Thermodynamic Concepts and Applications of Phase-Field Models*. Springer.

[Evans, 1983] Evans, H. (1983). The role of oxide grain boundaries in the development of growth stresses during oxidation. *Corrosion Science*, 23(5):495 – 506.

[Favergeon et al., 2005] Favergeon, J., Montesin, T., and Bertrand, G. (2005). Mechano-chemical aspects of high temperature oxidation: A mesoscopic model applied to zirconium alloys. *Oxidation of Metals*, 64(3-4):253–279.

[Feyel, 2003] Feyel, F. (2003). A multilevel finite element method (FE2) to describe the response of highly non-linear structures using generalized continua. *Computer Methods in Applied Mechanics and Engineering*, 192(2830):3233 – 3244. Multiscale Computational Mechanics for Materials and Structures.

[Fisher, 1951] Fisher, J. C. (1951). Calculation of diffusion penetration curves for surface and grain boundary diffusion. *Journal of Applied Physics*, 22(1):74–77.

[Frachon, 2009] Frachon, J. (2009). *Multiscale approach to predict the lifetime of EB-PVD thermal barrier coating*. PhD thesis, Mines de Paris.

[Frost and Ashby, 1982] Frost, H. and Ashby, F. (1982). *Deformation-mechanism maps: the plasticity and creep of metals and ceramics*. Pergamon Press.

[Gale and Totemeier, 2003] Gale, W. and Totemeier, T. (2003). *Smithells metals reference book*. Elsevier Science.

[Galindo-Nava et al., 2012] Galindo-Nava, E., Sietsma, J., and Rivera-Díaz-del Castillo, P. (2012). Dislocation annihilation in plastic deformation: II. Kocks–Mecking analysis. *Acta Materialia*, 60(67):2615 – 2624.

[Gérard et al., 2009] Gérard, C., NGuyen, F., Osipov, N., Cailletaud, G., Bornert, M., and Caldemaison, D. (2009). Comparison of experimental results and finite element simulation of strain localization scheme under cyclic loading. *Computational Materials Science*, 46(3):755 – 760. Proceedings of the 18th International Workshop on Computational Mechanics of Materials IWCMM-18.

[Germain et al., 1983] Germain, P., Nguyen, Q., and Suquet, P. (1983). Continuum thermodynamics. *J. of Applied Mechanics*, 50:1010–1020.

[Guilhem, 2011] Guilhem, Y. (2011). *Numerical investigation of the local mechanical fields in 316L steel polycrystalline aggregates under fatigue loading*. PhD thesis, Mines ParisTech.

[Guilhem et al., 2013] Guilhem, Y., Basseville, S., Curtit, F., Stéphan, J., and Cailletaud, G. (2013). Numerical investigations of the free surface effect in three-dimensional polycrystalline aggregates. *Computational Materials Science*, 70(0):150–162.

[Guiraldenq, 1975] Guiraldenq, P. (1975). Diffusion intergranulaire et énergie des joints de grains. *Journal de Physique Colloques*, 36(C4):C4–201–C4–211.

[Haber et al., 1985] Haber, J., Machej, T., and Czeppe, T. (1985). The phenomenon of wetting at solid/solid interface. *Surface Science*, 151(1):301 – 310.

[Hart, 1957] Hart, E. (1957). On the role of dislocations in bulk diffusion. *Acta Metallurgica*, 5(10):597–.

[Holmström et al., 2013] Holmström, S., Pohja, R., Nurmela, A., Moilanen, P., and Auerkari, P. (2013). Creep and creep-fatigue behaviour of 316 stainless steel. *Procedia Engineering*, 55(0):160–164. 6th International Conference on Creep, Fatigue and Creep-Fatigue Interaction.

[Horita et al., 2004] Horita, T., Xiong, Y., Yamaji, K., Kishimoto, H., Sakai, N., Brito, M., and Yokokawa, H. (2004). Imaging of mass transports around the oxide scale/FeCr alloy interfaces. *Solid State Ionics*, 174(14):41 – 48.

[Houlsby and Puzrin, 2000] Houlsby, G. and Puzrin, A. (2000). A thermomechanical framework for constitutive models for rate-independent dissipative materials. *International Journal of Plasticity*, 16(9):1017 – 1047.

[Huguenin, 2012] Huguenin, P. (2012). *Amorçage des fissures de corrosion sous contrainte dans les aciers inoxydables austénitiques pré-déformés et exposés au milieu primaire des réacteurs à eau sous pression*. PhD thesis, Mines ParisTech.

[Huntz et al., 2002] Huntz, A., Calvarin Amiri, G., Evans, H., and Cailletaud, G. (2002). Comparison of oxidation-growth stresses in NiO film measured by deflection and calculated using creep analysis or finite-element modeling. *Oxidation of Metals*, 57(5-6):499–521.

[Huntz et al., 1993] Huntz, A., Liu, C., Kornmeier, M., and Lebrun, J. (1993). The determination of stresses during oxidation of Ni: in situ measurements by XRD at high temperature. *Corrosion Science*, 35(58):989 – 997.

[Huntz et al., 1998] Huntz, A., Piant, A., Lebrun, J., and Daghigh, S. (1998). Evidence of stress relaxation in thermally grown oxide layers – experiments and modelling. *Materials Science and Engineering: A*, 248(12):44 – 55.

[IAEA, 2011] IAEA (2011). *Stress corrosion cracking in light water reactors: good practices and lessons learned*. IAEA Nuclear Energy Series.

[Jambon et al., 2011] Jambon, F., Marchetti, L., Jomard, F., and Chêne, J. (2011). Mechanism of hydrogen absorption during the exposure of alloy 600-like single-crystals to PWR primary simulated media. *Journal of Nuclear Materials*, 414(3):386–392.

[Ji et al., 2004] Ji, A., Wang, W., Song, G., Wang, Q., Sun, C., and Wen, L. (2004). Microstructures and mechanical properties of chromium oxide films by arc ion plating. *Materials Letters*, 58(14):1993–1998.

[Jolivet and Henry, 2012] Jolivet, J. and Henry, M. (2012). *De la solution à l'oxyde - Condensation des cations en solution aqueuse. Chimie de surface des oxyde*. Savoirs Actuels. EDP Sciences.

[Kaplan et al., 2013] Kaplan, W., Chatain, D., Wynblatt, P., and Carter, W. (2013). A review of wetting versus adsorption, complexions, and related phenomena: the rosetta stone of wetting. *Journal of Materials Science*, 48(17):5681–5717.

[Kaur et al., 1989] Kaur, I., Gust, W., and für Metallforschung, M.-P.-I. (1989). *Fundamentals of Grain and Interphase Boundary Diffusion*. Ziegler Press.

[Kjellqvist and Selleby, 2009] Kjellqvist, L. and Selleby, M. (2009). Adding C to the thermodynamic description of the Cr-Fe-Ni-O system. *Calphad*, 33(2):393–397. Tools for Computational Thermodynamics.

[Kjellqvist et al., 2008] Kjellqvist, L., Selleby, M., and Sundman, B. (2008). Thermodynamic modelling of the Cr-Fe-Ni-O system. *Calphad*, 32(3):577 – 592.

[Kocks and Mecking, 2003] Kocks, U. and Mecking, H. (2003). Physics and phenomenology of strain hardening: the {FCC} case. *Progress in Materials Science*, 48(3):171 – 273.

[Kodentsov et al., 2001] Kodentsov, A., Bastin, G., and van Loo, F. (2001). The diffusion couple technique in phase diagram determination. *Journal of Alloys and Compounds*, 320(2):207–217. Materials Constitution and Thermochemistry. Examples of Methods, Measurements and Applications. In Memoriam Alan Prince.

[Kofstad, 1972] Kofstad, P. (1972). *Nonstoichiometry, Diffusion, and Electrical Conductivity in Binary Metal Oxides*. Wiley - Interscience.

[Krishnamurthy and Srolovitz, 2003] Krishnamurthy, R. and Srolovitz, D. (2003). Stress distributions in growing oxide films. *Acta Materialia*, 51(8):2171 – 2190.

[Krishnamurthy and Srolovitz, 2004] Krishnamurthy, R. and Srolovitz, D. (2004). Stress distributions in growing polycrystalline oxide films. *Acta Materialia*, 52(13):3761 – 3780.

[Kruska et al., 2012] Kruska, K., Lozano-Perez, S., Saxey, D., Terachi, T., Yamada, T., and Smith, G. (2012). Nanoscale characterisation of grain boundary oxidation in cold-worked stainless steels. *Corrosion Science*, 63(0):225–233.

[Kurpaska et al., 2011] Kurpaska, L., Favergeon, J., Lahoche, L., Moulin, G., and Roelandt, J.-M. (2011). Determination of the epitaxial strains of a thermally grown oxide on a metallic substrate. In Publications, T. T., editor, *Materials Science Forum*, volume 696, pages 176–182.

[Laghoutaris, 2009] Laghoutaris, P. (2009). *Corrosion sous contrainte de l'alliage 600 en milieu primainre des réacteurs à eau sous pression : apport à la compréhension des mécanismes*. PhD thesis, Mines ParisTech.

[Laheij et al., 1980] Laheij, M., Loo, F., and Metselaar, R. (1980). Phase relations in the Fe-Cr-O system at 1200°C investigated by means of a diffusion couple technique. *Oxidation of Metals*, 14(3):207–215.

[Lai et al., 2012] Lai, J., Lo, J., Shek, C., and Lo, K. (2012). *Stainless Steels: An Introduction and Their Recent Developments*. Bentham Science Publishers.

[Larché and Cahn, 1983] Larché, F. and Cahn, J. (1983). An invariant formulation of multicomponent diffusion in crystals. *Scripta metallurgica*, 17(7)(3):927–932.

[Larché and Cahn, 1985] Larché, F. and Cahn, J. (1985). Overview no. 41 the interactions of composition and stress in crystalline solids. *Acta Metallurgica*, 33(3):331 – 357.

[Le Claire, 1951] Le Claire, A. (1951). Grain boundary diffusion in metals. *Philosophical Magazine Series 7*, 42(328):468–474.

[Le Claire and Rabinovitch, 1981] Le Claire, A. and Rabinovitch, A. (1981). A mathematical analysis of diffusion in dislocations. I. Application to concentration 'tails'. *Journal of Physics C: Solid State Physics*, 14(27):3863.

[Le Claire and Rabinovitch, 1982] Le Claire, A. and Rabinovitch, A. (1982). A mathematical analysis of diffusion in dislocations. II. Influence at low densities on measured diffusion coefficients. *Journal of Physics C: Solid State Physics*, 15(16):3455.

[Le Claire and Rabinovitch, 1983] Le Claire, A. and Rabinovitch, A. (1983). A mathematical analysis of diffusion in dislocations. III. Diffusion in a dislocation array with diffusion zone overlap. *Journal of Physics C: Solid State Physics*, 16(11):2087.

[Le Claire and Rabinovitch, 1984] Le Claire, A. and Rabinovitch, A. (1984). A mathematical analysis of diffusion in dislocations. IV. Diffusion-controlled absorption or desorption for a solid containing dislocations. *Journal of Physics C: Solid State Physics*, 17(6):991.

[le Pêcheur, 2008] le Pêcheur, A. (2008). *Fatigue thermique d'un acier inoxydable austénitique : influence de l'état de surface par une approche multi-échelles*. PhD thesis, École Centrale Paris.

[Liapis and Grimes, 2005] Liapis, A. and Grimes, B. (2005). The coupling of the electrostatic potential with the transport and adsorption mechanisms in ion-exchange chromatography systems: Theory and experiments. *Journal of Separation Science*, 28(15):1909–1926.

[López et al., 2004] López, G., Mittemeijer, E., and Straumal, B. (2004). Grain boundary wetting by a solid phase, microstructural development in a Zn-5 wt% Al alloy. *Acta Materialia*, 52(15):4537 – 4545.

[Lozano-Perez et al., 2012] Lozano-Perez, S., Kruska, K., Iyengar, I., Terachi, T., and Yamada, T. (2012). The role of cold work and applied stress on surface oxidation of 304 stainless steel. *Corrosion Science*, 56(0):78 – 85.

[Lozano-Perez et al., 2011] Lozano-Perez, S., Rodrigo, P., and Gontard, L. (2011). Three-dimensional characterization of stress corrosion cracks. *Journal of Nuclear Materials*, 408(3):289–295.

[Lozano-Perez et al., 2010] Lozano-Perez, S., Saxey, D., Yamada, T., and Terachi, T. (2010). Atom-probe tomography characterization of the oxidation of stainless steel. *Scripta Materialia*, 62(11):855–858.

[Lozano-Perez et al., 2009] Lozano-Perez, S., Yamada, T., Terachi, T., Schröder, M., English, C., Smith, G., Grovenor, C., and Eyre, B. (2009). Multi-scale characterization of stress corrosion cracking of cold-worked stainless steels and the influence of Cr content. *Acta Materialia*, 57(18):5361–5381.

[Lukáš and Klesnil, 1973] Lukáš, P. and Klesnil, M. (1973). Cyclic stress-strain response and fatigue life of metals in low amplitude region. *Materials Science and Engineering*, 11(6):345 – 356.

[Macdonald, 2012] Macdonald, D. (2012). The passive state in our reactive metals-based civilization. *Arabian Journal for Science and Engineering*, 37(5):1143–1185.

[Machet et al., 2004] Machet, A., Galtayries, A., Zanna, S., Klein, L., Maurice, V., Jolivet, P., Foucault, M., Combrade, P., Scott, P., and Marcus, P. (2004). XPS and STM study of the growth and structure of passive films in high temperature water on a nickel-base alloy. *Electrochimica Acta*, 49(2223):3957 – 3964.

[Marcus, 1998] Marcus, P. (1998). Surface science approach of corrosion phenomena. *Electrochimica Acta*, 43(12):109 – 118.

[Maurice et al., 1998] Maurice, V., Yang, W., and Marcus, P. (1998). X-ray photoelectron spectroscopy and scanning tunneling microscopy study of passive films formed on (100) Fe-18Cr-13Ni single-crystal surfaces. *Journal of the electrochemical society*, 145:909–919.

[Miresmaeili et al., 2010] Miresmaeili, R., Saintier, N., Notsu, H., Olive, J.-M., and Kanayama, H. (2010). One-Way Coupled Crystal Plasticity-Hydrogen Diffusion Simulation on Artificial Microstructure. *Journal of Computational Science and Technology*, 4:105–120.

[Mishin and Yurovitskii, 1991] Mishin, Y. and Yurovitskii, I. (1991). A generalized model of grain boundary diffusion. *Philosophical Magazine A*, 64(6):1239–1249.

[Montemor et al., 2000] Montemor, M., Ferreira, M., Hakiki, N., and Da Cunha Beo, M. (2000). Chemical composition and electronic structure of the oxide films formed on 316L stainless steel and nickel based alloys in high temperature aqueous environments. *Corrosion science*, 42:1635–1650.

[Mougin, 2001] Mougin, J. (2001). *Tenue mécanique de couches d'oxyde thermique générées sur le chrome et sur quelques aciers inoxydables ferritiques étude des contraintes et de l'adhérence*. PhD thesis, Institut National Polytechnique de Grenoble.

[Mougin et al., 2001] Mougin, J., Rosman, N., Lucazeau, G., and Galerie, A. (2001). In situ Raman monitoring of chromium oxide scale growth for stress determination. *Journal of Raman Spectroscopy*, 32:739–744.

[Musienko and Cailletaud, 2009] Musienko, A. and Cailletaud, G. (2009). Simulation of inter- and transgranular crack propagation in polycrystalline aggregates due to stress corrosion cracking. *Acta Materialia*, 57(13):3840 – 3855.

[Nagesha et al., 2009] Nagesha, A., Valsan, M., Kannan, R., Bhanu, K. S. R., Bauer, V., Christ, H.-J., and Singh, V. (2009). Thermomechanical fatigue evaluation and life prediction of 316L(N) stainless steel. *International Journal of Fatigue*, 31(4):636 – 643.

[Nestler et al., 2003] Nestler, B., Wheeler, A., and Garcke, H. (2003). Modelling of microstructure formation and interface dynamics. *Computational Materials Science*, 26(0):111 – 119.

[OECD, 2013] OECD (2013). OECD Due Diligence Guidance for Responsible Supply Chains of Minerals from Conflict-Affected and High-Risk Areas: Second Edition. OECD Publishing.

[Olsson and Landolt, 2003] Olsson, C.-O. and Landolt, D. (2003). Passive films on stainless steels-chemistry, structure and growth. *Electrochimica Acta*, 48(9):1093 – 1104.

[Pang et al., 2007] Pang, X., Gao, K., and Volinsky, A. (2007). Microstructure and mechanical properties of chromium oxide coatings. *Journal of Materials Research*, 22:3531–3537.

[Perevoshchikova, 2012] Perevoshchikova, N. (2012). *Modeling of austenite to ferrite transformation in steels*. PhD thesis, Université de Lorraine.

[Pilling and Bedworth, 1923] Pilling, N. and Bedworth, R. (1923). The oxidation of metals at high temperatures. *Journal of the Institute of Metals*, 29:529–582.

[Pommier et al., 2015] Pommier, H., Busso, E., and Morgeneyer, T. (2015). A viscoplastic constitutive model based on evolving microstructural length scales: Application to AISI 316L austenitic stainless steel. *In Preparation*.

[Prokoshkina et al., 2013] Prokoshkina, D., Esin, V., Wilde, G., and Divinski, S. (2013). Grain boundary width, energy and self-diffusion in nickel: Effect of material purity. *Acta Materialia*, 61(14):5188 – 5197.

[Pujilaksono et al., 2011] Pujilaksono, B., Jonsson, T., Heidari, H., Halvarsson, M., Svensson, J.-E., and Johansson, L.-G. (2011). Oxidation of binary FeCr alloys (Fe-2.25Cr, Fe-10Cr, Fe18Cr and Fe25Cr) in O_2 and in O_2+H_2O environment at 600°C. *Oxidation of Metals*, 75(3-4):183–207.

[Punkkinen et al., 2013] Punkkinen, M., Kokko, K., Levämäki, H., Ropo, M., Lu, S., Delczeg, L., Zhang, H., Delczeg-Czirjak, E., Johansson, B., and Vitos, L. (2013). Adhesion of the iron-chromium oxide interface from first-principles theory. *Journal of Physics: Condensed Matter*, 25(49):495501.

[Purja Pun and Mishin, 2009] Purja Pun, G. and Mishin, Y. (2009). A molecular dynamics study of self-diffusion in the cores of screw and edge dislocations in aluminum. *Acta Materialia*, 57(18):5531–5542.

[Queyreau et al., 2009] Queyreau, S., Monnet, G., and Devincre, B. (2009). Slip systems interactions in α-iron determined by dislocation dynamics simulations. *International Journal of Plasticity*, 25(2):361 – 377.

[Raabe et al., 2014] Raabe, D., Herbig, M., Sandlöbes, S., Li, Y., Tytko, D., Kuzmina, M., Ponge, D., and Choi, P.-P. (2014). Grain boundary segregation engineering in metallic alloys: A pathway to the design of interfaces. *Current Opinion in Solid State and Materials Science*, 18(4):253–261. Slip Localization and Transfer in Deformation and Fatigue of Polycrystals.

[Revie, 2008] Revie, R. (2008). *Corrosion and Corrosion Control*. Wiley.

[Richet, 2001] Richet, P. (2001). *The Physical Basis of Thermodynamics: With Applications to Chemistry*. Springer US.

[Rieth et al., 2004] Rieth, M., Falkenstein, A., Graf, P., Heger, S., Jäntsh, U., Klimiankou, M., Materna-Morris, E., and Zimmerman, H. (2004). Creep of the austenitic steel AISI 316L(N). Wissenschaftliche Berichte.

[Ruoff and Balluffi, 1963] Ruoff, A. and Balluffi, R. (1963). Strain enhanced diffusion in metals. II. Dislocation and grain boundary short circuiting models. *Journal of Applied Physics*, 34(7):1848–1853.

[Seiler et al., 2010] Seiler, P., Bäker, M., and Rösier, J. (2010). FEM simulation of oxidation induced stresses with a coupled crack propagation in a TBC model system. *IOP Conference Series: Materials Science and Engineering*, 10(1):012056.

[Seyeux et al., 2013] Seyeux, A., Maurice, V., and Marcus, P. (2013). Oxide film growth kinetics on metals and alloys: I. Physical model. *Journal of The Electrochemical Society*, 160(6):C189–C196.

[Shoji et al., 2010] Shoji, T., Lu, Z., and Murakami, H. (2010). Formulating stress corrosion cracking growth rates by combination of crack tip mechanics and crack tip oxidation kinetics. *Corrosion Science*, 52(3):769 – 779.

[Soulas, 2006] Soulas, R. (2006). *Effet de la cristallographie sur les premiers stades de l'oxydation des aciers austénitiques 316L*. PhD thesis, Grenoble.

[SSIC, 2014] SSIC (2014). *Design guidelines for the selection and use of stainless steels*. Speciality steel industry of north america.

[Stellwag, 1998] Stellwag, B. (1998). The mechanism of oxide film formation on austenitic stainless steels in high temperature water. *Corrosion Science*, 40(23):337 – 370.

[Stringer and Wright, 2003] Stringer, J. and Wright, I. (2003). Future directions for high temperature oxidation and corrosion research society. In *High Temperature Oxidation and Materials Chemistry*, pages 1–16.

[Sun et al., 2009] Sun, M., Wu, X., Zhang, Z., and Han, E.-H. (2009). Oxidation of 316 stainless steel in supercritical water. *Corrosion Science*, 51(5):1069 – 1072.

[Taleb et al., 2014] Taleb, L., Cailletaud, G., and Saï, K. (2014). Experimental and numerical analysis about the cyclic behavior of the 304L and 316L stainless steels at 350°C. *International Journal of Plasticity*, 61(0):32 – 48.

[Taylor et al., 2006] Taylor, M., Evans, H., Busso, E., and Qian, Z. (2006). Creep properties of a Ptaluminide coating. *Acta Materialia*, 54(12):3241 – 3252.

[Trindade et al., 2005] Trindade, V., Krupp, U., Wagenhuber, P.-G., and Christ, H.-J. (2005). Oxidation mechanisms of Cr-containing steels and Ni-base alloys at high-temperatures. Part I: The different role of alloy grain boundaries. *Materials and Corrosion*, 56(11):785–790.

[Tsai et al., 1996] Tsai, S., Huntz, A., and Dolin, C. (1996). Growth mechanism of Cr_2O_3 scales: oxygen and chromium diffusion, oxidation kinetics and effect of yttrium. *Materials Science and Engineering: A*, 212(1):6 – 13.

[Van Der Geest et al., 2013] Van Der Geest, A., Islam, M., Couvant, T., and Diawara, B. (2013). Energy ordering of grain boundaries in Cr_2O_3: insights from theory. *Journal of Physics: Condensed Matter*, 25(48):485005.

[Villani et al., 2014] Villani, A., Busso, E., Ammar, K., Forest, S., and Geers, M. (2014). A fully coupled diffusional-mechanical formulation: numerical implementation, analytical validation, and effects of plasticity on equilibrium. *Archive of Applied Mechanics*, 84(9-11):1647–1664.

[Wagner, 1933] Wagner, C. (1933). On the study of scaling reactions. *Z. Phys. Chem. B*, 21:42.

[Weiss and Pineau, 1993] Weiss, J. and Pineau, A. (1993). Fatigue and creep-fatigue damage of austenitic stainless steels under multiaxial loading. *Metallurgical and Materials Transactions A*, 24:2247–2261.

[Whipple, 1954] Whipple, R. (1954). Concentration contours in grain boundary diffusion. *Philosophical Magazine Series 7*, 45(371):1225–1236.

[Yang et al., 2012] Yang, F., Fang, D., and Liu, B. (2012). A theoretical model and phase field simulation on the evolution of interface roughness in the oxidation process. *Modelling and Simulation in Materials Science and Engineering*, 20(1):015001.

[Yonezawa et al., 2013] Yonezawa, T., Suzuki, K., Ooki, S., and Hashimoto, A. (2013). The effect of chemical composition and heat treatment conditions on stacking fault energy for Fe-Cr-Ni austenitic stainless steel. *Metallurgical and Materials Transactions A*, 44(13):5884–5896.

[Young and Funderlic, 1973] Young, G. and Funderlic, R. (1973). On the grain boundary diffusion theory of Fisher and Whipple. *Journal of Applied Physics*, 44(11):5151–5154.

[Zhou, 2010] Zhou, H. (2010). *Stress-diffusion interaction during oxide-scale growth on metallic alloys*. PhD thesis, Georgia Institute of Technology.

[Zhou et al., 2010a] Zhou, H., Qu, J., and Cherkaoui, M. (2010a). Finite element analysis of oxidation induced metal depletion at oxide-metal interface. *Computational Materials Science*, 48(4):842 – 847.

[Zhou et al., 2010b] Zhou, H., Qu, J., and Cherkaoui, M. (2010b). Stress-oxidation interaction in selective oxidation of Cr–Fe alloys. *Mechanics of Materials*, 42(1):63 – 71.

CHAPTER

3 A generic phase field approach to model phase transformation coupled with plasticity and multicomponent diffusion

Contents

L'approche par la méthode des champs de phase s'est révélée être un outil remarquable pour modéliser des problèmes d'interfaces mobiles. Elle consiste à modéliser une interface par un champ scalaire, lui-même régi par une équation aux dérivées partielles de type équation de transport non conservative, *c.f.* (3.8). Le champ scalaire, également appelé le paramètre d'ordre présente une rapide variation au travers de l'interface – un "saut" continu. Cette variation rapide est imposée par l'introduction d'une densité d'énergie additionelle liée à l'interface qui consiste en deux termes qui sont mis en compétition. Un de ces termes favorise la formation de phase – appelé le double puit pour le cas biphasé – et l'autre pénalise la formation d'une interface d'épaisseur nulle – le terme de gradient. L'interface générée par la solution à l'équilibre de cette équation de transport est appelée interface diffuse et la propagation de ce champ se fait de façon à respecter la condition d'équilibre chimique.

Dans cette zone diffuse, des propriétés effectives sont obtenues par le biais d'interpolations des propriétés des phases en contact. Il convient alors d'assurer la convergence du modèle diffus vers le modèle discontinu associé lorsque l'épaisseur de l'interface est réduite à une épaisseur nulle. Pour cela, il est nécessaire de pouvoir quantifier l'erreur générée par l'élargissement de l'interface intrinsèque à la méthode des champs de phases. Cette étude de convergence peut être menée par le biais d'une analyse asymptotique ou par une analyse numérique. Il apparaît que les différentes méthodes d'interpolation possibles, des variables, des comportements, *etc.*, vont conduire à différent taux de convergence vers la solution du problème discontinu. Cela peut servir de base pour justifier certains choix d'interpolation. Parmi ces méthodes d'interpolations, les méthodes d'homogénéisation ont révélé leur potentiel pour découpler les comportements mécaniques des phases par exemple. Ainsi, des lois de comportements peuvent être attribuées de manière découplée pour chaque phase. Cela est utile pour modéliser des transformations de phases dans des matériaux dont la nature des phases est très contrastée, à l'instar des oxydes et métaux.

Dans ce chapitre, deux modèles de champs de phases sont formulés dans le cadre rigoureux de la thermodynamique des milieux continus. Nous montrons que les hypothèses de Voigt/Taylor et Reuss/Sachs utilisées pour l'homogénéisation des comportements mécaniques sont directement liées à la formulation de l'énergie totale du système. La convergence relative des deux modèles est étudiée. L'ensemble du travail est par la suite basé sur l'hypothèse de Voigt/Taylor. Des cas de croissance d'un précipité dans une matrice supersaturée sont étudiés en considérant la déformation viscoplastique d'une des deux phases. Il est montré que la viscosité impacte la convergence du modèle vers la solution du problème de l'interface discrète.

The chapter is devoted to the formulation of a rigorous thermodynamic framework for multicomponent systems undergoing phase transformations while stresses are accounted for. The phase transformation is embedded in a single phase field variable ϕ as the system is here limited to two phases. A free energy density is assigned to the phase field and is composed of a double-well potential and a gradient energy term, as typically done in phase field modelling. Multicomponent diffusion is accounted for on the basis of the phase diagram data, which is provided by chemical free energies. Stresses are accounted for as well, including complex material behaviours by making use of internal variables, *e.g.* to describe the viscoplastic flow, hardening laws, *etc.* The model is intended to simulate the growth of an oxide M_nO. The growth is driven by the supply of oxygen O_2 from the environment and the supply of a metallic element M from the substrate, here chromium. The chemical and mechanical free energies are coupled with the phase field variable by means of a non linear interpolation. The dissipation potential is also formulated to account for energy losses. For instance, the motion of the interface – or formation of new phases – is motivated by the decrease of the total energy, plastic strains yield the elastic energy, *etc.* Such a dissipation potential is coupled with the phase field variable analogously to the chemical and elastic bulk free energies. Finally, homogenisation like assumptions have to be defined to determine an effective behaviour inside the interface. The homogenisation framework allows separate phase behaviours to be considered, which is of importance here due to the large property contrasts between oxides and metals, *e.g.* creep/plasticity, brittle/ductile, *etc.* It is shown that the homogenisation assumptions of Voigt/Taylor and Reuss/Sachs for stresses and strains can

be obtained by deriving the state laws from either the Helmholz free energy or the Gibbs free energy – also respectively mentioned as the free energy and the free enthalpy. By doing so, the classical state laws and constitutive laws of the phases are retrieved and are uncoupled from the phase field variable. Nevertheless, different driving forces are obtained with respect to the phase field transport equation, see [Spatschek and Eidel, 2013, Mosler et al., 2014] for instance. It appears that excess quantities can be generated inside the interface depending on the homogenisation procedure. In this chapter, we will study the elastic excess energy that is found in the Voigt/Taylor approach. The vanishing of such excess energy at the sharp interface limit is evidenced and the convergence rate between both homogenisation schemes is studied numerically.

Finally, the effect of viscosity is studied considering the Voigt/Taylor approach. The influence of viscosity on the convergence rate towards the sharp interface limit is shown. An range of viscosities, for which acceptable convergence rates occur, is identified. Such preliminary results are of great importance for the forthcoming simulations of oxidation as viscoplasticity can be triggered in both the oxide and metal phases.

3.1 Introduction

The phase field approach has become a ubiquitous tool to simulate microstructure evolution in solid materials undergoing phase transformation [Steinbach, 2009, Finel et al., 2010, Steinbach and Shchyglo, 2011]. Phases are treated as continuous fields where each one is endowed with a transport equation, or phase field equation. Such fields vary rapidly inside the phase boundaries over a given width, which constitutes the interface thickness. The interface is then said to be diffused. Such diffused interfaces can have a physical justification when their thicknesses come close to a few inter-atomic distances. The transport equations associated to the phase fields allow to predict the evolving morphology of new phases, and accounts for the phase transformation kinetics. For many diffusion-controlled phase transformations, stresses can play a significant role in both the transformation kinetics and the morphology evolution of the growing phases. The transport equations for phase fields were firstly coupled to Cauchy's first law of motion restricted to the elastic behaviour of the phases in [Wang et al., 1993, Wang and Khachaturyan, 1995, Dreyer and Müller, 2000, Hu and Chen, 2001]. More recently, the attention was focused on the extension to plasticity and viscoplasticity, as done by [Ubachs et al., 2004, Guo et al., 2005, Ubachs et al., 2005, T. Uehara et al., 2007, Guo et al., 2008, Gaubert et al., 2008, Ammar et al., 2009, Gaubert et al., 2010, Kundin et al., 2011].

Two main approaches have been proposed to determine the effective behaviour of the diffuse interface. They are namely the interpolation and homogenisation approaches according to the terminology used by [Ammar et al., 2009c, Ammar et al., 2011, Ammar et al., 2014]. These methods are closely related to the "coarse–graining" and the "two–phase" approaches mentioned in [Plapp, 2011], respectively. In the latter reference, and in the "two-phase" approach, the diffuse interface is "*seen as a mixture of two phases that each retain their macroscopic properties*", and for which standard homogenisation methods coming for instance from the mechanics of heterogeneous materials [Sanchez-Palencia and Zaoui, 1987, Zaoui, 2002, Qu and Cherkaoui, 2006, François et al., 2012], can be used to derive the effective response. In this work, the "two-phase" approach is also referred to as the homogenisation approach. In this case, the phase field parameter then plays a role akin to the volume fraction of one phase within the diffuse interface. In contrast, a single constitutive behaviour is used for both phases in the interpolation approach for which the corresponding material parameters are interpolated between the bounding values reached in each phase.

The choice of the interpolation method for the effective interface behaviour originated from the work of [Tiaden et al., 1998], who introduced solute partitioning on the basis of the mixture theory. Such a solute partitioning was then reinterpreted shortly later on by [Kim et al., 1999], who used a Reuss-like assumption for the diffusion behaviour throughout the interface, which they called the pseudo-equilibrium. After that, [Steinbach and Apel, 2006] used the Reuss assumption, by analogy to the work of [Kim et al., 1999], to account for the elastic behaviour of the phases.

[Ammar et al., 2009c, Ammar et al., 2011, Ammar et al., 2014] also applied the Voigt homogenisation scheme that relies on identical strain values for both phases at each material point. Mixed schemes as they arise in laminate microstructures were then employed by [Durga et al., 2013, Mosler et al., 2014] in order to reduce spurious stress concentration effects within the interface. Nevertheless, the popularity of the interpolation method – known as Khatchaturyan's approach – was such that the first attempts to introduce nonlinear material behaviour of phases relied on it, see for instance [Guo et al., 2005, Guo et al., 2008, Gaubert et al., 2008, Gaubert et al., 2010, Cottura et al., 2012], except in [Ammar et al., 2009].

The choice of a suitable homogenisation scheme generally depends on the morphology of the mixture of phases within the diffuse interface. As such, a mixture very often does not correspond to a physical reality and various schemes have been applied without reference to the real structure of the interface. But the homogenisation and interpolation schemes can be of practical importance with respect to the convergence of the diffuse interface problem to the sharp interface problem. It is now admitted that the Reuss-like assumption done in [Kim et al., 1999] improves such a convergence. Finally, [Ammar et al., 2014] highlighted the paradigm of inheritance in the frameworks of the interpolation and homogenisation methods. The interpolation method embeds inheritance of the internal variables during the phase transformation. In contrast, the homogenisation method makes the internal variables of each phase to be independent from each other. Nevertheless, inheritance can be added or discarded by the use of suitable evolutionary laws for the internal variables.

In work by [Durga et al., 2013, Mosler et al., 2014] the combination of homogenisation and phase field methods to the elastic behaviour of phases was successfully applied. We extend here these frameworks to the consideration of elastoviscoplastic deformation modes of the individual phases. We emphasise the role of thermodynamics, and especially the second law or entropy principle, in selecting suitable homogenisation schemes in the phase field models. The constitutive setting is presented based on an original thermodynamic framework extending that used in nonlinear mechanics of materials to the phase field approach [Germain et al., 1983, Maugin, 1992, Maugin, 1999]. It relies heavily on the exploitation of the second principle of thermodynamics in order to formulate constitutive assumptions, systematically ensuring the positivity of the dissipation rate at each time and at each material point. This represents an alternative to the use of variational derivatives of the free energy function as done classically in phase field approaches since the pioneering work by [Cahn and Hilliard, 1958]. It has the advantage that the theory can be readily applied to finite bodies with specific and unambiguous boundary conditions, in contrast to usual periodic or infinite microstructures and corresponding vanishing boundary conditions used in the latter reference, [Durga et al., 2013, Mosler et al., 2014]. The space of state variables is extended to include internal variables accounting for material work-hardening. Mechanical dissipation then results from the competition of energy storage due to the multiplication of dislocations and to dissipation induced by dislocation motion. The theory is suitable for the material evolution at a mesoscale where individual dislocations are not resolved but rather represented by suitable densities. It typically applies at the grain scale in a polycrystal where the continuum crystal plasticity has been shown in many cases to be able to provide a reliable description of slip processes. The introduction of crystal plasticity into phase field models goes back to works by [Zhou et al., 2008, Gaubert et al., 2008, Gaubert et al., 2010, Kundin et al., 2011, Cottura et al., 2012, Abrivard et al., 2012b, Abrivard et al., 2012a] coupled with grain boundary migration for the latter.

The framework also encompasses the consideration of continuum damage mechanics because the additional internal variables can account for material weakening by cavity growth or microcracking [Lemaitre and Chaboche, 1994, Lemaitre and Desmorat, 2004, Besson, 2004, Besson et al., 2010]. In this field, phase field approaches meet gradient damage mechanical models as recognised recently in the literature [Forest, 2009, Miehe et al., 2010b, Miehe et al., 2010a, Aslan and Forest, 2011, Forest et al., 2011, Forest et al., 2014]. A common thermodynamic framework exists that reconciles gradient damage and phase field approaches as used in recent works by [Hofacker and Miehe, 2012, Borden et al., 2012, Hofacker and Miehe, 2013, Voyiadjis and Mozaffari, 2013, Vignollet et al., 2014] for isotropic materials and [Aslan and Forest, 2009, Aslan et al., 2011a, Aslan et al., 2011] in combination with crystal plasticity. However, the discussion in the present work is limited to viscoplasticity,

leaving open the possibility of applying the proposed framework to damage applications.

The novel aspects of the present work are the proposed thermodynamic framework incorporating nonlinear material behaviour into phase field approaches, the thermodynamic background justifying the use of two specific homogenisation schemes in the theory, and, finally, the possibility of using crystal plasticity constitutive equations for distinct phases with different crystallographic structures. They are illustrated by preliminary finite element simulations based on the implementation of [Ammar et al., 2009, Stiemer et al., 2010] of phase growth involving eigenstrains responsible for the activation of plasticity during transformation. Both the precipitate shape and growth kinetics are shown to depend on the specific constitutive behaviour of the individual phases. For the sake of simplicity, the theory is fomulated within the small perturbation framework although extensions to finite deformation models is possible and necessary for many applications, see [Borukhovich et al., 2014].

3.2 Homogenisation based phase field modelling

3.2.1 Description of a two-phase multi-component material

The present phase field framework is based on the introduction of a phase field parameter ϕ accounting for a two-phase system, α-β, with constant values $\phi = 1$ and $\phi = 0$, respectively in α and β. The phase field varies rapidly and continuously from 0 to 1 in the diffuse interface zone over a thickness δ as defined in [Kim et al., 1999]. The physical degrees of freedom attributed to each material point in the continuum are the concentration c_i of a given chemical element i, and the displacement $\underline{\boldsymbol{u}}$ with the corresponding strain tensor $\underset{\sim}{\boldsymbol{\varepsilon}}$ defined as the symmetric part of the displacement field gradient.

Prior to homogenisation, all of the chosen energy potentials along with their respective state variables, fluxes and conjugates are first interpolated:

$$\Xi_\mathrm{i} = h(\phi)\Xi_\mathrm{i}^{\alpha} + \bar{h}(\phi)\Xi_\mathrm{i}^{\beta}\,, \tag{3.1}$$

where Ξ can be regarded for instance as the free energy density f or the Gibbs free energy density g together with the concentration c_i of component i with the conjugate diffusion potential μ_i along with mass flux $\underline{\boldsymbol{J}}_i$, and also the strain tensor $\underset{\sim}{\boldsymbol{\varepsilon}}$ and stress tensor $\underset{\sim}{\boldsymbol{\sigma}}$. Accordingly, the quantities Ξ^{α} and Ξ^{β}: c_i^{α}, c_i^{β}, $\underset{\sim}{\boldsymbol{\varepsilon}}^{\alpha}$, *etc.*, can be regarded as fictitious or auxiliary variables, see [Kim et al., 1999, Ammar et al., 2009c]. The weighting function h, analogous to a phase fraction, fulfils the following requirements:

$$h(1) = 1, \quad h(0) = 0, \qquad h'(\phi) = \begin{cases} 0, & \text{if } \phi = 1 \text{ or } \phi = 0, \\ > 0, & \text{if } 0 < \phi < 1\,. \end{cases} \tag{3.2}$$

The complementing function $\bar{h}$ is defined as $\bar{h}(\phi) = 1 - h(\phi)$. The conditions on the derivative of h discard the linear function $h(\phi) = \phi$ classically required by volume averaging in homogenisation theory. In phase field models, interpolation aims at localising the mixture of phases within a narrow diffuse interface zone. A standard choice for h is the following third order polynomial function [Steinbach, 2009]:

$$h(\phi) = \phi^2\left(3 - 2\phi\right). \tag{3.3}$$

Finally, the total strain tensor attributed to each phase at each material point is split into three distinct mechanical contributions:

$$\underset{\sim}{\boldsymbol{\varepsilon}}^{\alpha,\beta} = \underset{\sim}{\boldsymbol{\varepsilon}}_e^{\alpha,\beta} + \underset{\sim}{\boldsymbol{\varepsilon}}_p^{\alpha,\beta} + \underset{\sim}{\boldsymbol{\varepsilon}}_\star^{\alpha,\beta}\,, \tag{3.4}$$

where the subscripts e stands for elasticity, p for (visco)plasticity and $\star$ for a constant and uniform eigenstrain. The latter is to be independent of concentration and temperature for simplicity.

3.2.2 Balance equations

The total concentrations are subjected to the local form of the mass balance:

$$\dot{c}_\mathrm{i} + \nabla \cdot \underline{\boldsymbol{J}}_\mathrm{i} = 0\,, \tag{3.5}$$

for each component i, in the absence of source terms. The mass balance equation is associated with Dirichlet or Neumann conditions at the boundary of the body where the concentration or the normal flux $j = \underline{\boldsymbol{J}} \cdot \underline{\boldsymbol{n}}$ are prescribed, $\underline{\boldsymbol{n}}$ denoting the normal surface vector.

The stress tensor fulfils the static balance of momentum equation:

$$\nabla \cdot \underset{\sim}{\boldsymbol{\sigma}} = \underline{\mathbf{0}}\,, \tag{3.6}$$

in the absence of body forces. The Cauchy balance equation is complemented by the displacement or traction vector, $\underline{\boldsymbol{t}} = \underset{\sim}{\boldsymbol{\sigma}} \cdot \underline{\boldsymbol{n}}$, controlled boundary conditions.

The internal energy enters the local balance of energy equations

$$\dot{e} = \underset{\sim}{\boldsymbol{\sigma}} : \underset{\sim}{\dot{\boldsymbol{\varepsilon}}} - \pi\dot{\phi} + \underline{\boldsymbol{\xi}} \cdot \nabla\dot{\phi}\,, \tag{3.7}$$

where generalised stresses $\underline{\boldsymbol{\xi}}$ and π are introduced as work conjugates to the change in phase field parameter ϕ and its gradient, following [Gurtin, 1996, Ammar et al., 2009]. The first term in the right-hand side is the classical mechanical power of internal forces whereas the second and third terms account for the additional internal energy change associated with boundary motion.

The generalised stresses are postulated to fulfil an additional balance equation, which is the phase field transport equation, in the form:

$$\pi + \nabla \cdot \underline{\boldsymbol{\xi}} = 0\,. \tag{3.8}$$

The balance of generalised stresses is associated with Dirichlet or Neumann boundary conditions where the phase field parameter or the generalised stress vector, $\underline{\boldsymbol{\xi}} \cdot \underline{\boldsymbol{n}}$, are prescribed at the boundary. In the spirit of homogenisation theory, the partial quantities $c_\mathrm{i}^{\alpha,\beta}, \underset{\sim}{\boldsymbol{\sigma}}^{\alpha,\beta}$ are *not* subjected to similar balance equations. This is in contrast to mixture theories as discussed by [Müller, 2001].

The variational formulation of balance equations (3.6) and (3.8) constitute the generalised principle of virtual power, for all subdomain V of the body, with boundary ∂V are:

$$\int_V \left(\underset{\sim}{\boldsymbol{\sigma}} : \nabla \underline{\boldsymbol{u}}^* + \pi\phi^* - \underline{\boldsymbol{\xi}} \cdot \nabla\phi^* \right) dV = \int_{\partial V} \left(\underset{\sim}{\boldsymbol{\sigma}} \cdot \underline{\boldsymbol{n}} \cdot \underline{\boldsymbol{u}}^* - \underline{\boldsymbol{\xi}} \cdot \underline{\boldsymbol{n}}\phi^* \right) dS\,, \tag{3.9}$$

using the virtual velocity fields $\{\underline{\boldsymbol{u}}^*, \phi^*\}$, as discussed in [Ammar et al., 2009].

The generalised principle of virtual power is complemented by the variational formulation of the mass balance (3.5):

$$\int_V \left(\dot{c}_\mathrm{i} c^* - \underline{\boldsymbol{J}}_\mathrm{i} \cdot \nabla c^* \right) dV = -\int_{\partial V} \left(\underline{\boldsymbol{J}}_\mathrm{i} \cdot \underline{\boldsymbol{n}} \right) c^*\, dS\,, \tag{3.10}$$

for the field of virtual concentration c^*.

The previous variational formulations are directly applicable to the finite element method. The discretisation of these equations first presented in [Ammar et al., 2009] is recalled and extended in Appendix B.

3.3 Constitutive framework based on the Helmholtz free energy potential or free energy

Thermodynamic principles relies on an appropriate choice of state and internal variables. The internal energy, e, and Helmholtz free energy or free energy, f, functions differ by one argument, namely

the entropy variable, s, entering the internal energy function and the temperature variable, T, arising in the free energy. They are related by the corresponding Legendre transformation:

$$f = e - sT\,. \tag{3.11}$$

These functions are defined per unit volume.

The approach is devoted to the case of a two-phase multi-component system made of solid crystalline materials, as defined in the previous section. As an illustrative example, the phase β is a single crystal phase undergoing plastic slip according to crystal plasticity theory, see [Busso and McClintock, 1996, Asaro and Lubarda, 2006, Besson et al., 2010], whereas the phase α exhibits an isotropic elastoviscoplastic behaviour.

3.3.1 State and internal variables

The considered space of state and internal variables for the two-phase α-β system is chosen as:

$$\text{STATE} = \{\phi, \nabla\phi, c_{\text{i}}^{\alpha}, \underset{\sim}{\boldsymbol{\varepsilon}}_e^{\alpha}, c_{\text{i}}^{\beta}, \underset{\sim}{\boldsymbol{\varepsilon}}_e^{\beta}, \rho_s^{\beta}, x_s^{\beta}\}\,, \tag{3.12}$$

where ϕ is a smooth phase indicator field, c_{i} are site fractions occupied by the chemical species i in the crystalline solid, $\underset{\sim}{\boldsymbol{\varepsilon}}_e^{\alpha,\beta}$ is the elastic strain tensor attributed to each phase at each material point. The model internal variables are represented by the hardening variables, ρ_s^{β} and x_s^{β}, where the subscript s indicates the slip system number according to the crystal plasticity model. The variable ρ_s^{β} is akin to a dislocation density measure directly related, [Busso and Cailletaud, 2005] to the critical resolved shear stress for the activation of slip system s according to Schmid's law, whereas x_s accounts for kinematic hardening needed for cyclic plasticity [Méric et al., 1991a, Méric et al., 1991b]. Let N denote the total number of slip systems characterising the crystalline phase β, typically $N = 12$ in FCC crystals. For brevity, no hardening variable is introduced in the phase α, without restriction to the generality of the constitutive formulation that allows for distinct behaviour laws for both phases. Under general anisothermal conditions, the previous set should be complemented by the temperature variable.

The dual set is composed of the thermodynamic forces associated to the state and internal variables following the framework of continuum thermodynamics:

$$\text{FORCES} = \{-\pi, \underline{\boldsymbol{\xi}}, \mu_{\text{i}}^{\alpha}, \underset{\sim}{\boldsymbol{\sigma}}^{\alpha}, \mu_{\text{i}}^{\beta}, \underset{\sim}{\boldsymbol{\sigma}}^{\beta}, R_s^{\beta}, X_s^{\beta}\}\,, \tag{3.13}$$

where π and $\underline{\boldsymbol{\xi}}$ are the generalised stresses introduced by [Gurtin, 1996, Ammar et al., 2009], $\mu_i^{\alpha,\beta}$ are the diffusion potentials, $\underset{\sim}{\boldsymbol{\sigma}}^{\alpha,\beta}$ are stress tensors, R_s^{β} is the slip resistance and X_s^{β} the back-stress as described in [Busso and Cailletaud, 2005, Besson et al., 2010] for each slip system s.

3.3.2 Partition of the free energy density function

The volumetric free energy density f of the two-phase material is decomposed at each material point into diffuse interface, chemical and mechanical parts, respectively called f_ϕ, f_c, f_ε:

$$f = f_\phi + \sum_i f_{c_i} + f_\varepsilon\,, \tag{3.14}$$

where i denotes the chemical component number and the interface contribution of the free energy density is defined as [Kim et al., 1999]:

$$f_\phi(\phi, \nabla\phi) = 3\gamma\left(\frac{1}{\lambda}W(\phi) + \lambda \parallel \nabla\phi \parallel^2\right), \tag{3.15}$$

with γ the interface energy, $\lambda = \frac{1}{2}\frac{\delta}{z}$ with δ the diffuse interface thickness, z a parameter defined as $z = \log(0.95/0.05)$ and W the double well function defined as:

$$W(\phi) = \phi^2 \left(1-\phi\right)^2 . \tag{3.16}$$

Bulk free energies are coupled by means of the phase field variable using the same averaging relations as in Section 3.2 for the state variables, thermodynamic forces and fluxes (3.1):

$$\begin{aligned} f_{c_i}(\phi, c_{\mathrm{i}}^{\alpha}, c_{\mathrm{i}}^{\beta}) &= h(\phi) f_{c_i}^{\alpha}(c_{\mathrm{i}}^{\alpha}) + \bar{h}(\phi) f_{c_i}^{\beta}(c_{\mathrm{i}}^{\beta}) , \\ f_{\varepsilon}(\phi, \underset{\sim}{\boldsymbol{\varepsilon}}_e^{\alpha}, \underset{\sim}{\boldsymbol{\varepsilon}}_e^{\beta}, \rho_s^{\beta}, x_s^{\beta}) &= h(\phi) f_{\varepsilon}^{\alpha}(\underset{\sim}{\boldsymbol{\varepsilon}}_e^{\alpha}) + \bar{h}(\phi) f_{\varepsilon}^{\beta}(\underset{\sim}{\boldsymbol{\varepsilon}}_e^{\beta}, \rho_s^{\beta}, x_s^{\beta}) . \end{aligned} \tag{3.17}$$

A possible dependence of f_ε on concentrations can be added in Eq. (3.17) but is not considered here for simplicity. to the proposed general framework. As a result of the coupling with the phase field variable ϕ shown in Eq. (3.17), the minimisation of the free energy may lead to two phases in equilibrium and, thus, to the construction of diagrams corresponding to chemical equilibrium under mechanical stress, as studied extensively in [Cahn and Larché, 1984, Johnson, 1987, Frolov and Mishin, 2012].

3.3.3 State laws relating thermodynamic variables and their associated forces

The local form of the second principle of thermodynamics is written as:

$$\dot{s} \geq \nabla \cdot \underline{\boldsymbol{\Phi}} , \tag{3.18}$$

where s is the volumetric entropy density and $\underline{\boldsymbol{\Phi}}$ the entropy density flux. The time derivative of (3.11) for the isothermal case allows us to rewrite (3.18) into:

$$\dot{e} - \dot{f} \geq T \nabla \cdot \underline{\boldsymbol{\Phi}} . \tag{3.19}$$

The free energy density is a function of the state variables (3.12). Its time derivative can be expanded according to the chain rule:

$$\dot{f} = \frac{\partial f}{\partial \phi}\dot{\phi} + \frac{\partial f}{\partial \nabla \phi}\cdot\nabla\dot{\phi} + \sum_i \frac{\partial f}{\partial c_{\mathrm{i}}^{\alpha}}\dot{c}_{\mathrm{i}}^{\alpha} + \sum_i \frac{\partial f}{\partial c_{\mathrm{i}}^{\beta}}\dot{c}_{\mathrm{i}}^{\beta} + \frac{\partial f}{\partial \underset{\sim}{\boldsymbol{\varepsilon}}_e^{\alpha}} : \dot{\underset{\sim}{\boldsymbol{\varepsilon}}}_e^{\alpha} + \frac{\partial f}{\partial \underset{\sim}{\boldsymbol{\varepsilon}}_e^{\beta}} : \dot{\underset{\sim}{\boldsymbol{\varepsilon}}}_e^{\beta} + \sum_s \frac{\partial f}{\partial \rho_s^{\beta}}\dot{\rho}_s^{\beta} + \sum_s \frac{\partial f}{\partial x_s^{\beta}}\dot{x}_s^{\beta} . \tag{3.20}$$

The entropy flux is related to the mass entropy flux and the diffusion potential, following [de Groot and Mazur, 1962, Coleman and Noll, 1963, Ammar et al., 2009, Villani et al., 2014]:

$$\underline{\boldsymbol{\Phi}} = \frac{1}{T}\sum_i \mu_{\mathrm{i}} \underline{\boldsymbol{J}}_{\mathrm{i}} . \tag{3.21}$$

Expanding Eqs. (3.19) to (3.21) and using the mass and energy balance equations (3.5) and (3.7) combined with the averaging relations (3.17) lead to the Clausius-Duhem inequality:

$$\begin{aligned} &-\left(\pi + \frac{\partial f}{\partial \phi}\right)\dot{\phi} + \left(\underline{\boldsymbol{\xi}} - \frac{\partial f}{\partial \nabla \phi}\right)\cdot\nabla\dot{\phi} + \sum_i \mu_{\mathrm{i}}\dot{c}_{\mathrm{i}} - h\frac{\partial f^{\alpha}}{\partial c_{\mathrm{i}}^{\alpha}}\dot{c}_{\mathrm{i}}^{\alpha} - \bar{h}\frac{\partial f^{\beta}}{\partial c_{\mathrm{i}}^{\beta}}\dot{c}_{\mathrm{i}}^{\beta} - \sum_i \underline{\boldsymbol{J}}_{\mathrm{i}}\cdot\nabla\mu_{\mathrm{i}} \\ &+\underset{\sim}{\boldsymbol{\sigma}} : \dot{\underset{\sim}{\boldsymbol{\varepsilon}}} - h\frac{\partial f^{\alpha}}{\partial \underset{\sim}{\boldsymbol{\varepsilon}}_e^{\alpha}} : \dot{\underset{\sim}{\boldsymbol{\varepsilon}}}_e^{\alpha} - \bar{h}\frac{\partial f^{\beta}}{\partial \underset{\sim}{\boldsymbol{\varepsilon}}_e^{\beta}} : \dot{\underset{\sim}{\boldsymbol{\varepsilon}}}_e^{\beta} - \sum_s \bar{h}\frac{\partial f^{\beta}}{\partial \rho_s^{\beta}}\dot{\rho}_s^{\beta} - \sum_s \bar{h}\frac{\partial f^{\beta}}{\partial x_s^{\beta}}\dot{x}_s^{\beta} \geq 0 . \end{aligned} \tag{3.22}$$

The previous inequality is first exploited for the individual phases. The particular case $\phi = 1$ corresponds to the pure phase α:

$$\sum_i \left(\mu_{\mathrm{i}}^{\alpha} - \frac{\partial f^{\alpha}}{\partial c_{\mathrm{i}}^{\alpha}}\right)\dot{c}_{\mathrm{i}}^{\alpha} - \sum_i \underline{\boldsymbol{J}}_{\mathrm{i}}^{\alpha}\cdot\nabla\mu_{\mathrm{i}}^{\alpha} + \left(\underset{\sim}{\boldsymbol{\sigma}}^{\alpha} - \frac{\partial f^{\alpha}}{\partial \underset{\sim}{\boldsymbol{\varepsilon}}_e^{\alpha}}\right) : \dot{\underset{\sim}{\boldsymbol{\varepsilon}}}_e^{\alpha} + \underset{\sim}{\boldsymbol{\sigma}}^{\alpha} : \dot{\underset{\sim}{\boldsymbol{\varepsilon}}}_p^{\alpha} \geq 0 , \tag{3.23}$$

whereas the particular case for the phase β, $\phi = 0$, reads:

$$\sum_i \left(\mu_{\mathrm{i}}^{\beta} - \frac{\partial f^{\beta}}{\partial c_{\mathrm{i}}^{\beta}}\right) \dot{c}_{\mathrm{i}}^{\beta} - \sum_i \underline{\boldsymbol{J}}_{\mathrm{i}}^{\beta} \cdot \nabla \mu_{\mathrm{i}}^{\beta} + \left(\underset{\sim}{\boldsymbol{\sigma}}^{\beta} - \frac{\partial f^{\beta}}{\partial \underset{\sim}{\boldsymbol{\varepsilon}}_e^{\beta}}\right) : \dot{\underset{\sim}{\boldsymbol{\varepsilon}}}_e^{\beta} + \underset{\sim}{\boldsymbol{\sigma}}^{\beta} : \dot{\underset{\sim}{\boldsymbol{\varepsilon}}}_p^{\beta} - \sum_s \frac{\partial f^{\beta}}{\partial \rho_s^{\beta}} \dot{\rho}_s^{\beta} - \sum_s \frac{\partial f^{\beta}}{\partial x_s^{\beta}} \dot{x}_s^{\beta} \geq 0 . \tag{3.24}$$

Assuming that the diffusion potentials and the stress tensors do not depend explicitly on $\dot{c}_{\mathrm{i}}^{\alpha}$, $\dot{c}_{\mathrm{i}}^{\beta}$, $\dot{\underset{\sim}{\boldsymbol{\varepsilon}}}_e^{\alpha}$ and $\dot{\underset{\sim}{\boldsymbol{\varepsilon}}}_e^{\beta}$, the left-hand sides of the two previous inequalities are linear forms with respect to the concentration and elastic strain increments. Following [Coleman and Noll, 1963], their positivity requires that the cofactors must vanish so that:

$$\mu_{\mathrm{i}}^{\alpha} = \frac{\partial f^{\alpha}}{\partial c_{\mathrm{i}}^{\alpha}}, \qquad \mu_{\mathrm{i}}^{\beta} = \frac{\partial f^{\beta}}{\partial c_{\mathrm{i}}^{\beta}}, \qquad \underset{\sim}{\boldsymbol{\sigma}}^{\alpha} = \frac{\partial f^{\alpha}}{\partial \underset{\sim}{\boldsymbol{\varepsilon}}_e^{\alpha}}, \qquad \underset{\sim}{\boldsymbol{\sigma}}^{\beta} = \frac{\partial f^{\beta}}{\partial \underset{\sim}{\boldsymbol{\varepsilon}}_e^{\beta}} . \tag{3.25}$$

The thermodynamic forces associated with the hardening variables are then defined as:

$$R_s^{\beta} = \frac{\partial f^{\beta}}{\partial \rho_s^{\beta}}, \qquad X_s^{\beta} = \frac{\partial f^{\beta}}{\partial x_s^{\beta}} . \tag{3.26}$$

The residual dissipation rate inequality is obtained after combining (3.22) with (3.25), (3.26) and (3.1):

$$\begin{aligned} &-\pi^{\sharp}\dot{\phi} + \left(\underline{\boldsymbol{\xi}} - \frac{\partial f}{\partial \nabla\phi}\right) \cdot \nabla\dot{\phi} + \sum_i h\left(\mu_{\mathrm{i}} - \mu_{\mathrm{i}}^{\alpha}\right) \dot{c}_{\mathrm{i}}^{\alpha} + \sum_i \bar{h}\left(\mu_{\mathrm{i}} - \mu_{\mathrm{i}}^{\beta}\right) \dot{c}_{\mathrm{i}}^{\beta} - \underline{\boldsymbol{J}}_{\mathrm{i}} \cdot \nabla\mu_{\mathrm{i}} \\ &+ h\left(\underset{\sim}{\boldsymbol{\sigma}} - \underset{\sim}{\boldsymbol{\sigma}}^{\alpha}\right) : \dot{\underset{\sim}{\boldsymbol{\varepsilon}}}_e^{\alpha} + \bar{h}\left(\underset{\sim}{\boldsymbol{\sigma}} - \underset{\sim}{\boldsymbol{\sigma}}^{\beta}\right) : \dot{\underset{\sim}{\boldsymbol{\varepsilon}}}_e^{\beta} + h\underset{\sim}{\boldsymbol{\sigma}} : \dot{\underset{\sim}{\boldsymbol{\varepsilon}}}_p^{\alpha} + \bar{h}\underset{\sim}{\boldsymbol{\sigma}} : \dot{\underset{\sim}{\boldsymbol{\varepsilon}}}_p^{\beta} - \bar{h}\sum_s R_s^{\beta}\dot{\rho}_s^{\beta} - \bar{h}\sum_s X_s^{\beta}\dot{x}_s^{\beta} \geq 0 , \end{aligned} \tag{3.27}$$

where $\pi^{\sharp}$ is defined as

$$\pi^{\sharp} = \pi + \frac{\partial f}{\partial \phi} - h'(\phi)\left(\sum_i \mu_{\mathrm{i}}\left(c_{\mathrm{i}}^{\alpha} - c_{\mathrm{i}}^{\beta}\right) + \underset{\sim}{\boldsymbol{\sigma}} : \left(\underset{\sim}{\boldsymbol{\varepsilon}}^{\alpha} - \underset{\sim}{\boldsymbol{\varepsilon}}^{\beta}\right)\right) . \tag{3.28}$$

The quantity $\pi^{\sharp}$ is similar to the dissipative microforce introduced by [Gurtin, 1996].
At this point, it is still assumed that the diffusion potential and stress tensor functions do not explicitly depend on the rates $\dot{c}_{\mathrm{i}}^{\alpha}$, $\dot{c}_{\mathrm{i}}^{\beta}$ and $\dot{\underset{\sim}{\boldsymbol{\varepsilon}}}_e^{\alpha}$ and $\dot{\underset{\sim}{\boldsymbol{\varepsilon}}}_e^{\beta}$. It follows that the following conditions must hold to ensure positivity of the previous dissipation rate:

$$\mu_{\mathrm{i}} = \mu_{\mathrm{i}}^{\beta} = \mu_{\mathrm{i}}^{\alpha}, \qquad \underset{\sim}{\boldsymbol{\sigma}} = \underset{\sim}{\boldsymbol{\sigma}}^{\alpha} = \underset{\sim}{\boldsymbol{\sigma}}^{\beta} . \tag{3.29}$$

The first condition of equal partial diffusion potentials was adopted as a starting point by [Kim et al., 1999]. The equality of partial stresses associated with each phase at a material point corresponds to the well-known Reuss/Sachs approximation in the mechanical homogenisation theory and was first applied by [Steinbach and Apel, 2006] and discussed in [Ammar et al., 2009c, Durga et al., 2013, Mosler et al., 2014].

Finally, following [Gurtin, 1996], the generalised stress vector $\underline{\boldsymbol{\xi}}$ is assumed to be independent of $\nabla\dot{\phi}$, which provides the last state law:

$$\underline{\boldsymbol{\xi}} = \frac{\partial f}{\partial \nabla\phi}, \tag{3.30}$$

As a result, the residual dissipation inequality reads:

$$-\pi^{\sharp}\dot{\phi} - \underline{\boldsymbol{J}}_{\mathrm{i}} \cdot \nabla\mu_{\mathrm{i}} + h\underset{\sim}{\boldsymbol{\sigma}} : \dot{\underset{\sim}{\boldsymbol{\varepsilon}}}_p^{\alpha} + \bar{h}\left(\underset{\sim}{\boldsymbol{\sigma}} : \dot{\underset{\sim}{\boldsymbol{\varepsilon}}}_p^{\beta} - \sum_s R_s^{\beta}\dot{\rho}_s^{\beta} - \sum_s X_s^{\beta}\dot{x}_s^{\beta}\right) \geq 0 . \tag{3.31}$$

The mechanical contributions in the previous inequality contain the plastic power and the possible energy storage by means of an increase of internal variables.

At this stage, specific choices for the bulk volumetric free energy densities can be introduced in the form of quadratic potentials for the purpose of illustration. The chemical contributions

$$f_{c_i}^{\alpha,\beta}(c_{\mathrm{i}}^{\alpha,\beta}) = \frac{1}{2}\, k_i^{\alpha,\beta}\left(c_{\mathrm{i}}^{\alpha,\beta} - \hat{c}_{\mathrm{i}}^{\alpha,\beta}\right)^2, \tag{3.32}$$

correspond to elliptic paraboloids with minimum at $\hat{c}_i^{\alpha,\beta}$ and curvature given by $k_i^{\alpha,\beta}$. The elasticity contribution for the α phase

$$f_{\varepsilon}^{\alpha}(\underset{\sim}{\boldsymbol{\varepsilon}}_e^{\alpha}) = \frac{1}{2}\, \underset{\sim}{\boldsymbol{\varepsilon}}_e^{\alpha} : \underset{\approx}{\boldsymbol{\Lambda}}^{\alpha} : \underset{\sim}{\boldsymbol{\varepsilon}}_e^{\alpha}, \tag{3.33}$$

involves the fourth order tensor of elastic moduli of the bulk phase, $\underset{\approx}{\boldsymbol{\Lambda}}^{\alpha}$. The energy stored by elasticity and hardening for the phase β is taken from [Busso and Cailletaud, 2005, Besson et al., 2010]:

$$f_{\varepsilon}^{\beta}(\underset{\sim}{\boldsymbol{\varepsilon}}_e^{\beta}) = \frac{1}{2}\, \underset{\sim}{\boldsymbol{\varepsilon}}_e^{\beta} : \underset{\approx}{\boldsymbol{\Lambda}}^{\beta} : \underset{\sim}{\boldsymbol{\varepsilon}}_e^{\beta} + \frac{1}{2}\, b^{\beta} Q^{\beta} \sum_{s,r} H^{sr} \rho_s^{\beta} \rho_r^{\beta} + \frac{1}{2}\, C^{\beta} \sum_{s} x_s^{\beta 2}, \tag{3.34}$$

Here, the hardening parameters are Q^{β}, b^{β} and C^{β}. The interaction matrix H^{sr} accounts for self and latent hardening induced by dislocation interactions.

Based on the previous quadratic potentials, the state laws (3.25), (3.26) and (3.30) combined with (3.29) provide:

$$\mu_i^{\alpha,\beta} = k_i^{\alpha,\beta}\left(c_i^{\alpha,\beta} - \hat{c}_i^{\alpha,\beta}\right) = \mu_i, \tag{3.35}$$

along with

$$\underset{\sim}{\boldsymbol{\sigma}}^{\alpha,\beta} = \underset{\approx}{\boldsymbol{\Lambda}}^{\alpha,\beta} : \underset{\sim}{\boldsymbol{\varepsilon}}_e^{\alpha,\beta} = \underset{\sim}{\boldsymbol{\sigma}}, \tag{3.36}$$

$$R_s^{\beta} = b^{\beta} Q^{\beta} \sum_{r} H^{s,r} \rho_r^{\beta}, \qquad X_s^{\beta} = C^{\beta} x_s^{\beta}. \tag{3.37}$$

The generalised stress vector is proportional to the gradient of the phase field variable, following (3.15) and (3.30):

$$\underline{\boldsymbol{\xi}} = 6\gamma\lambda\nabla\phi. \tag{3.38}$$

3.3.4 Constitutive laws from the dissipation potential

The positivity of the dissipation rate in (3.31) can be identically fulfilled by introducing a convex dissipation potential depending on the generalised stresses, conjugate to the flow of phase field, concentration, plastic strain and hardening variables:

$$\Omega = \Omega(\pi^{\sharp}, \nabla\mu_{\mathrm{i}}^{\alpha}, \nabla\mu_{\mathrm{i}}^{\beta}, \underset{\sim}{\boldsymbol{\sigma}}^{\alpha}, \underset{\sim}{\boldsymbol{\sigma}}^{\beta}, R_s^{\beta}, X_s^{\beta}; \phi), \tag{3.39}$$

The dissipation potential Ω is a function of thermodynamic forces and may also depend on the thermodynamic variables that have to be considered as parameters, according to [Germain et al., 1983]. Here ϕ is used in the decomposition of the dissipation potential in weighted contributions of the individual phases, as done for the free energy density function:

$$\Omega = \Omega_{\pi}(\pi^{\sharp}) + h(\phi)\Omega^{\alpha}(\nabla\mu_{\mathrm{i}}^{\alpha}, \underset{\sim}{\boldsymbol{\sigma}}^{\alpha}) + \bar{h}(\phi)\Omega^{\beta}(\nabla\mu_{\mathrm{i}}^{\beta}, \underset{\sim}{\boldsymbol{\sigma}}^{\beta}, R_s^{\beta}, X_s^{\beta}). \tag{3.40}$$

Looking at (3.23), (3.24), (3.25) and (3.26), quadratic or power law dissipation potentials can be chosen in the form:

$$\begin{aligned}
\Omega_\pi(\pi^\sharp) &= M_\phi \pi^{\sharp 2}, \\
\Omega^\alpha(\nabla\mu_{\mathrm{i}}^\alpha, \underset{\sim}{\boldsymbol{\sigma}}^\alpha) &= \tfrac{1}{2}\underset{\sim}{\boldsymbol{L}}_{\mathrm{i}}^\alpha : (\nabla\mu_{\mathrm{i}}^\alpha \otimes \nabla\mu_{\mathrm{i}}^\alpha) + \frac{K^\alpha}{n^\alpha+1}\left\langle \frac{\sqrt{\frac{3}{2}\underset{\sim}{\boldsymbol{\sigma}}_{\mathrm{dev}}^\alpha : \underset{\sim}{\boldsymbol{\sigma}}_{\mathrm{dev}}^\alpha} - R_0^\alpha}{K^\alpha}\right\rangle^{n^\alpha+1}, \\
\Omega^\beta(\nabla\mu_i^\beta, \underset{\sim}{\boldsymbol{\sigma}}^\beta, R_s^\beta, X_s^\beta) &= \tfrac{1}{2}\underset{\sim}{\boldsymbol{L}}_i^\beta : (\nabla\mu_{\mathrm{i}}^\beta \otimes \nabla\mu_{\mathrm{i}}^\beta) + \frac{K^\beta}{n^\beta+1}\sum_s \left\langle \frac{|\underset{\sim}{\boldsymbol{\sigma}}^\beta : \underset{\sim}{\boldsymbol{m}}_s^\beta - X_s^\beta| - R_0^\beta - R_s^\beta}{K^\beta}\right\rangle^{n^\beta+1}.
\end{aligned} \tag{3.41}$$

M_ϕ and $\underset{\sim}{\boldsymbol{L}}_i^{\alpha,\beta}$ are the mobility parameters respectively for the phase-field and diffusion. The Macaulay brackets $\langle . \rangle$ deliver the positive part of the concerned quantity. A Mises yield criterion with constant threshold R_0^α is chosen for the α phase whereas the Schmid law is adopted in the β phase, R_0^β being the initial critical resolved shear stress and R_s^β the hardening for each slip system. The deviatoric stress tensors are called $\underset{\sim}{\boldsymbol{\sigma}}_{\mathrm{dev}}^{\alpha,\beta}$. The crystallographic orientation tensor $\underset{\sim}{\boldsymbol{m}}_s^\beta$ is the symmetrised tensor product of the slip direction and normal to the slip plane for each slip system s, see [Asaro and Lubarda, 2006]. The material parameters $K^{\alpha,\beta}$ and $n^{\alpha,\beta}$ account for the generally nonlinear viscous properties of both phases.

The dissipation potential is used to derive the flow rules for diffusion and viscoplasticity. The mass flux vectors present in the Clausius-Duhem inequalities obtained in (3.23) and (3.24) are derived from the dissipation potential for $\phi = 1$ and $\phi = 0$ as follows:

$$\underset{\sim}{\boldsymbol{J}}_{\mathrm{i}}^\alpha = -\frac{\partial\Omega^\alpha}{\partial\nabla\mu_{\mathrm{i}}^\alpha} = -\underset{\sim}{\boldsymbol{L}}_{\mathrm{i}}^\alpha \cdot \nabla\mu_{\mathrm{i}}^\alpha \qquad \text{and} \qquad \underset{\sim}{\boldsymbol{J}}_{\mathrm{i}}^\beta = -\frac{\partial\Omega^\beta}{\partial\nabla\mu_{\mathrm{i}}^\beta} = -\underset{\sim}{\boldsymbol{L}}_{\mathrm{i}}^\beta \cdot \nabla\mu_{\mathrm{i}}^\beta, \tag{3.42}$$

where diffusion mobilities $\underset{\sim}{\boldsymbol{L}}_{\mathrm{i}}^{\alpha,\beta}$ can be related to the diffusivities $\underset{\sim}{\boldsymbol{D}}_{\mathrm{i}}^{\alpha,\beta}$ and hence retrieve the generalised Fick law of diffusion:

$$\mathbf{L}_{\mathrm{i}}^{\alpha,\beta} = \left(\frac{\partial^2 f^{\alpha,\beta}}{\partial c_{\mathrm{i}}^{\alpha,\beta 2}}\right)^{-1} \mathbf{D}_{\mathrm{i}}^{\alpha,\beta}. \tag{3.43}$$

Using then the flux averaging relations (3.1) and (3.29), one obtains:

$$\underset{\sim}{\boldsymbol{J}}_{\mathrm{i}} = -\left(h(\phi)\mathbf{L}_{\mathrm{i}}^\alpha + \bar{h}(\phi)\mathbf{L}_{\mathrm{i}}^\beta\right)\nabla\mu_{\mathrm{i}}, \tag{3.44}$$

so that effective mobilities can be defined as the average of the bulk diffusivities of the phases:

$$\mathbf{L}_{\mathrm{i}}(\phi) = h(\phi)\mathbf{L}_{\mathrm{i}}^\alpha + \bar{h}(\phi)\mathbf{L}_{\mathrm{i}}^\beta. \tag{3.45}$$

The plastic flow and hardening rules can also be derived from the dissipation potential following the theory of standard generalised materials [Besson et al., 2010]:

$$\dot{\underset{\sim}{\boldsymbol{\varepsilon}}}_p^\alpha = \frac{\partial\Omega_p^\alpha}{\partial\underset{\sim}{\boldsymbol{\sigma}}^\alpha} = \left\langle \frac{\sqrt{\frac{3}{2}\underset{\sim}{\boldsymbol{\sigma}}_{\mathrm{dev}}^\alpha : \underset{\sim}{\boldsymbol{\sigma}}_{\mathrm{dev}}^\alpha} - R_0^\alpha}{K^\alpha}\right\rangle^{n^\alpha} \sqrt{\frac{3}{2}} \frac{\underset{\sim}{\boldsymbol{\sigma}}_{\mathrm{dev}}^\alpha}{\sqrt{\underset{\sim}{\boldsymbol{\sigma}}_{\mathrm{dev}}^\alpha : \underset{\sim}{\boldsymbol{\sigma}}_{\mathrm{dev}}^\alpha}}. \tag{3.46}$$

This corresponds to standard von Mises power-law viscoplasticity with threshold R_0^α. As for the phase β:

$$\dot{\underset{\sim}{\boldsymbol{\varepsilon}}}_p^\beta = \frac{\partial\Omega_p^\beta}{\partial\underset{\sim}{\boldsymbol{\sigma}}^\beta} = \sum_s \left\langle \frac{|\tau_s^\beta - X_s^\beta| - R_s^\beta}{K}\right\rangle^{n^\beta} \underset{\sim}{\boldsymbol{m}}_s^\beta \,\mathrm{sign}\left(\underset{\sim}{\boldsymbol{\sigma}}^\beta : \underset{\sim}{\boldsymbol{m}}_s^\beta - X_s^\beta\right) = \sum_s \dot{\gamma}_s \underset{\sim}{\boldsymbol{m}}_s, \tag{3.47}$$

where $\dot{\gamma}_s$ is the slip rate for the slip system number s. $\tau_s^\beta = \underset{\sim}{\sigma}^\beta : \underset{\sim}{m}_s^\beta$ is called the resolved shear stress of the slip system s. It is the driving force for slip activation, which is here corrected by a back–stress X_s^β.

The evolutionary laws for nonlinear hardening are defined following [Busso and Cailletaud, 2005, Besson et al., 2010]:

$$\dot{\rho}_s^\beta = (1 - b^\beta \rho_s^\beta)|\dot{\gamma}_s|, \qquad \dot{x}_s^\beta = \left(\text{sign}(\underset{\sim}{\sigma}^\beta : \underset{\sim}{m}_s^\beta - X_s^\beta) - d^\beta x_s^\beta\right)|\dot{\gamma}_s|. \tag{3.48}$$

More sophisticated evolution laws like the Kocks-Busso equations for the dislocation densities can be used in the model, instead of $(3.48)_1$, [Busso and Cailletaud, 2005].

Finally, the evolution of the phase field parameter is derived from the quadratic part of the dissipation potential depending on $\pi^\sharp$ as follows:

$$\dot{\phi} = -\frac{\partial \Omega}{\partial \pi^\sharp} = -M_\phi \pi^\sharp. \tag{3.49}$$

The latter equation can be reformulated into the well–known Allen-Cahn relation by introducing the generalised stress balance equation (3.8) and the state law (3.30) combined with (3.28):

$$\dot{\phi} = M_\phi \left(6\gamma\lambda\Delta\phi - \frac{\partial f}{\partial \phi} + h'(\phi)\left(\sum_i \mu_i\left(c_i^\alpha - c_i^\beta\right) + \underset{\sim}{\sigma} : \left(\underset{\sim}{\varepsilon}^\alpha - \underset{\sim}{\varepsilon}^\beta\right)\right)\right). \tag{3.50}$$

It is convenient to rewrite the enhanced Allen-Cahn equation (3.50) after separating the phase transformation driving force F_ϕ^R as follows:

$$\dot{\phi} = M_\phi \left(3\gamma\left(2\lambda\Delta\phi - \frac{1}{\lambda}W'(\phi)\right) - h'(\phi)F_\phi^R\right), \tag{3.51}$$

where

$$F_\phi^R = f^\alpha - f^\beta - \sum_i \mu_i\left(c_i^\alpha - c_i^\beta\right) - \underset{\sim}{\sigma} : \left(\underset{\sim}{\varepsilon}^\alpha - \underset{\sim}{\varepsilon}^\beta\right). \tag{3.52}$$

It can be noted that the source term F_ϕ^R is often referred as the phase field driving force. It is defined as the difference of a particular thermodynamic potential at the interface, which is here the same one as for [Frolov and Mishin, 2012, Eq. 29] for the phase transformation's driving force in the case of a sharp interface model considering coherent interfaces.

The above constitutive laws are then consistent with a positive dissipation rate at each material point and at each time.

3.4 Constitutive framework based on the Gibbs free energy potential or free enthalpy

It has been shown in Section 3.3 that the restrictions implied by the entropy principle on the form of the constitutive and state laws based on the homogenisation approach from the volumetric free energy density have lead us to select the Reuss homogenisation scheme regarding stresses and diffusion potentials attached to each phase at each material point. Following a similar reasoning as in [Plapp, 2011], an alternative formulation is put forward in this section, based on the use of the Gibbs free energy or free enthalpy that will prompt us to introduce an alternative homogenisation scheme for the mechanical part of the model. The volumetric free enthalpy density function g is defined as the Legendre transformation of the volumetric internal energy density e:

$$g = e - sT - \underset{\sim}{\sigma} : \underset{\sim}{\varepsilon}. \tag{3.53}$$

3.4.1 State and internal variables

Whereas entropy and strain are the canonical variables of the internal energy density function, temperature and stress are the arguments of the free enthalpy. Accordingly, the state space (3.12) designed for the Helmholtz free energy must be modified into:

$$\text{STATE} = \{\phi, \nabla\phi, c_{\text{i}}^{\alpha}, \underset{\sim}{\boldsymbol{\sigma}}^{\alpha}, \underset{\sim}{\boldsymbol{\varepsilon}}_p^{\alpha}, c_{\text{i}}^{\beta}, \underset{\sim}{\boldsymbol{\sigma}}^{\beta}, \underset{\sim}{\boldsymbol{\varepsilon}}_p^{\beta}, \rho_s^{\beta}, x_s^{\beta}\}, \tag{3.54}$$

where the plastic strain tensors $\underset{\sim}{\boldsymbol{\varepsilon}}_p^{\alpha,\beta}$ enter as internal variables, together with the hardening variables already introduced in (3.12).

3.4.2 Partition of the free enthalpy density function

The volumetric free enthalpy density g is decomposed into interface, chemical and mechanical parts, respectively g_ϕ, g_c and g_σ as follows:

$$g = g_\phi(\phi, \nabla\phi) + g_c(\phi, c_{\text{i}}^{\alpha}, c_{\text{i}}^{\beta}) + g_\sigma(\phi, \underset{\sim}{\boldsymbol{\sigma}}^{\alpha}, \underset{\sim}{\boldsymbol{\varepsilon}}_p^{\alpha}, \underset{\sim}{\boldsymbol{\sigma}}^{\beta}, \underset{\sim}{\boldsymbol{\varepsilon}}_p^{\beta}, \rho_s^{\beta}, x_s^{\beta}), \tag{3.55}$$

where the diffuse interface excess enthalpy g_ϕ is identical to (3.15).

Bulk free energies are coupled by means of the phase field variable using the same averaging rules as for the state variables, thermodynamic forces and fluxes (3.1):

$$\begin{aligned} g_c(\phi, c_{\text{i}}^{\alpha}, c_{\text{i}}^{\beta}) &= h(\phi) g_c^{\alpha}(c_{\text{i}}^{\alpha}) + \overline{h}(\phi) g_c^{\beta}(c_{\text{i}}^{\beta}), \\ g_\sigma(\phi, \underset{\sim}{\boldsymbol{\sigma}}^{\alpha}, \underset{\sim}{\boldsymbol{\sigma}}^{\beta}, \underset{\sim}{\boldsymbol{\varepsilon}}_p^{\beta}, \rho_s^{\beta}, x_\alpha^{\beta}) &= h(\phi) g_\sigma^{\alpha}(\underset{\sim}{\boldsymbol{\sigma}}^{\alpha}, \underset{\sim}{\boldsymbol{\varepsilon}}_p^{\alpha}) + \overline{h}(\phi) g_\sigma^{\beta}(\underset{\sim}{\boldsymbol{\sigma}}^{\beta}, \underset{\sim}{\boldsymbol{\varepsilon}}_p^{\beta}, \rho_s^{\beta}, x_\alpha^{\beta}). \end{aligned} \tag{3.56}$$

3.4.3 State laws relating thermodynamic variables and their associated forces

The time derivative of (3.53), under isothermal conditions, is used next to rewrite the second law of thermodynamics (3.18) as:

$$\dot{e} - \dot{g} - \underset{\sim}{\boldsymbol{\sigma}} : \dot{\underset{\sim}{\boldsymbol{\varepsilon}}} - \underset{\sim}{\boldsymbol{\varepsilon}} : \dot{\underset{\sim}{\boldsymbol{\sigma}}} \geq T \nabla \cdot \underline{\boldsymbol{\Phi}}. \tag{3.57}$$

Taking the local energy balance equation (3.7) into account leads to the following expression:

$$-\underset{\sim}{\boldsymbol{\varepsilon}} : \dot{\underset{\sim}{\boldsymbol{\sigma}}} - \pi\dot{\phi} + \underline{\boldsymbol{\xi}} \cdot \nabla\dot{\phi} - \dot{g} \geq T \nabla \cdot \underline{\boldsymbol{\Phi}}, \tag{3.58}$$

where the stress rate tensor $\dot{\underset{\sim}{\boldsymbol{\sigma}}}$ can be expanded into:

$$\dot{\underset{\sim}{\boldsymbol{\sigma}}} = h(\phi)\dot{\underset{\sim}{\boldsymbol{\sigma}}}^{\alpha} + \bar{h}(\phi)\dot{\underset{\sim}{\boldsymbol{\sigma}}}^{\beta} + h'(\phi)\dot{\phi}\left(\underset{\sim}{\boldsymbol{\sigma}}^{\alpha} - \underset{\sim}{\boldsymbol{\sigma}}^{\beta}\right). \tag{3.59}$$

Using the expression (3.21) for the entropy flux and the chain rule for g, the inequality (3.58) becomes:

$$\begin{aligned} &-\pi^*\dot{\phi} + \left(\underline{\boldsymbol{\xi}} - \frac{\partial g}{\partial \nabla\phi}\right) \cdot \nabla\dot{\phi} + h \sum_i \left(\mu_{\text{i}} - \frac{\partial g^{\alpha}}{\partial c_{\text{i}}^{\alpha}}\right) \dot{c}_{\text{i}}^{\alpha} + \bar{h} \sum_i \left(\mu_{\text{i}} - \frac{\partial g^{\beta}}{\partial c_{\text{i}}^{\beta}}\right) \dot{c}_{\text{i}}^{\beta} - \sum_i \underline{\boldsymbol{J}}_{\text{i}} \cdot \nabla\mu_{\text{i}} \\ &-h\left(\left(\underset{\sim}{\boldsymbol{\varepsilon}} + \frac{\partial g^{\alpha}}{\partial \underset{\sim}{\boldsymbol{\sigma}}^{\alpha}}\right) : \dot{\underset{\sim}{\boldsymbol{\sigma}}}^{\alpha} + \frac{\partial g^{\alpha}}{\partial \underset{\sim}{\boldsymbol{\varepsilon}}_p^{\alpha}} : \dot{\underset{\sim}{\boldsymbol{\varepsilon}}}_p^{\alpha}\right) - \bar{h}\left(\left(\underset{\sim}{\boldsymbol{\varepsilon}} + \frac{\partial g^{\beta}}{\partial \underset{\sim}{\boldsymbol{\sigma}}^{\beta}}\right) : \dot{\underset{\sim}{\boldsymbol{\sigma}}}^{\beta} + \frac{\partial g^{\beta}}{\partial \underset{\sim}{\boldsymbol{\varepsilon}}_p^{\beta}} : \dot{\underset{\sim}{\boldsymbol{\varepsilon}}}_p^{\beta} + \sum_s \frac{\partial g^{\beta}}{\partial \rho_s^{\beta}} \dot{\rho}_s^{\beta} + \sum_s \frac{\partial g^{\beta}}{\partial x_s^{\beta}} \dot{x}_s^{\beta}\right) \geq 0, \end{aligned} \tag{3.60}$$

where

$$\pi^* = \pi + \frac{\partial g}{\partial \phi} - h'(\phi)\left(\sum_i \mu_{\text{i}}\left(c_{\text{i}}^{\alpha} - c_{\text{i}}^{\beta}\right) - \underset{\sim}{\boldsymbol{\varepsilon}} : \left(\underset{\sim}{\boldsymbol{\sigma}}^{\alpha} - \underset{\sim}{\boldsymbol{\sigma}}^{\beta}\right)\right). \tag{3.61}$$

The particular case $\phi = 1$ corresponding to the pure phase α yields:

$$\sum_i \left(\mu_{\mathrm{i}}^{\alpha} - \frac{\partial g^{\alpha}}{\partial c_{\mathrm{i}}^{\alpha}}\right)\dot{c}_{\mathrm{i}}^{\alpha} - \sum_i \underline{\boldsymbol{J}}_{\mathrm{i}}^{\alpha}\cdot\nabla\mu_{\mathrm{i}}^{\alpha} - \left(\underset{\sim}{\boldsymbol{\varepsilon}}^{\alpha} + \frac{\partial g^{\alpha}}{\partial \underset{\sim}{\boldsymbol{\sigma}}^{\alpha}}\right) : \dot{\underset{\sim}{\boldsymbol{\sigma}}}^{\alpha} - \frac{\partial g^{\alpha}}{\partial \underset{\sim}{\boldsymbol{\varepsilon}}_p^{\alpha}} : \dot{\underset{\sim}{\boldsymbol{\varepsilon}}}_p^{\alpha} \geq 0. \tag{3.62}$$

The particular case $\phi = 0$ corresponding to the pure phase β yields:

$$\sum_i \left(\mu_{\mathrm{i}}^{\beta} - \frac{\partial g^{\beta}}{\partial c_{\mathrm{i}}^{\beta}}\right)\dot{c}_{\mathrm{i}}^{\beta} - \sum_i \underline{\boldsymbol{J}}_{\mathrm{i}}^{\beta}\cdot\nabla\mu_{\mathrm{i}}^{\beta} - \left(\underset{\sim}{\boldsymbol{\varepsilon}}^{\beta} + \frac{\partial g^{\beta}}{\partial \underset{\sim}{\boldsymbol{\sigma}}^{\beta}}\right) : \dot{\underset{\sim}{\boldsymbol{\sigma}}}^{\beta} - \frac{\partial g^{\beta}}{\partial \underset{\sim}{\boldsymbol{\varepsilon}}_p^{\beta}} : \dot{\underset{\sim}{\boldsymbol{\varepsilon}}}_p^{\beta} - \sum_s \frac{\partial g^{\beta}}{\partial \rho_s^{\beta}}\dot{\rho}_s^{\beta} - \sum_s \frac{\partial g^{\beta}}{\partial x_s^{\beta}}\dot{x}_s^{\beta} \geq 0. \tag{3.63}$$

The resulting dissipation rate is a linear form with respect to $\dot{c}_{\mathrm{i}}^{\alpha}$, $\dot{c}_{\mathrm{i}}^{\beta}$ and $\dot{\underset{\sim}{\boldsymbol{\sigma}}}^{\alpha}$ and $\dot{\underset{\sim}{\boldsymbol{\sigma}}}^{\beta}$. The positivity of dissipation rate then requires that the conjugate quantities vanish in both cases (3.62) and (3.63):

$$\mu_{\mathrm{i}}^{\alpha} = \frac{\partial g^{\alpha}}{\partial c_{\mathrm{i}}^{\alpha}}, \qquad \mu_{\mathrm{i}}^{\beta} = \frac{\partial g^{\beta}}{\partial c_{\mathrm{i}}^{\beta}}, \qquad \underset{\sim}{\boldsymbol{\varepsilon}}^{\alpha} = -\frac{\partial g^{\alpha}}{\partial \underset{\sim}{\boldsymbol{\sigma}}^{\alpha}}, \qquad \underset{\sim}{\boldsymbol{\varepsilon}}^{\beta} = -\frac{\partial g^{\beta}}{\partial \underset{\sim}{\boldsymbol{\sigma}}^{\beta}}, \tag{3.64}$$

and by definition:

$$R_s^{\beta} = -\frac{\partial g^{\beta}}{\partial \rho_s^{\beta}}, \qquad X_s^{\beta} = -\frac{\partial g^{\beta}}{\partial x_s^{\beta}}, \qquad \underset{\sim}{\boldsymbol{\sigma}}^{\alpha} = -\frac{\partial g^{\alpha}}{\partial \underset{\sim}{\boldsymbol{\varepsilon}}_p^{\alpha}}, \qquad \underset{\sim}{\boldsymbol{\sigma}}^{\beta} = -\frac{\partial g^{\beta}}{\partial \underset{\sim}{\boldsymbol{\varepsilon}}_p^{\beta}}, \tag{3.65}$$

The two last conditions are required for the plastic power to appear in the dissipation rate.
Returning to the general case given by (3.60) and using the mixture rules (3.1) and the state laws, (3.64) to (3.65), the dissipation rate inequality becomes:

$$\begin{aligned} &-\pi^*\dot{\phi} + \left(\underline{\boldsymbol{\xi}} - \frac{\partial g}{\partial \nabla\phi}\right)\cdot\nabla\dot{\phi} + h\sum_i\left(\mu_{\mathrm{i}} - \mu_{\mathrm{i}}^{\alpha}\right)\dot{c}_{\mathrm{i}}^{\alpha} + \bar{h}\sum_i\left(\mu_{\mathrm{i}} - \mu_{\mathrm{i}}^{\beta}\right)\dot{c}_{\mathrm{i}}^{\beta} - \sum_i \underline{\boldsymbol{J}}_{\mathrm{i}}\cdot\nabla\mu_{\mathrm{i}} \\ &-h\left(\left(\underset{\sim}{\boldsymbol{\varepsilon}} - \underset{\sim}{\boldsymbol{\varepsilon}}^{\alpha}\right) : \dot{\underset{\sim}{\boldsymbol{\sigma}}}^{\alpha} - \underset{\sim}{\boldsymbol{\sigma}}^{\alpha} : \dot{\underset{\sim}{\boldsymbol{\varepsilon}}}_p^{\alpha}\right) - \bar{h}\left(\left(\underset{\sim}{\boldsymbol{\varepsilon}} - \underset{\sim}{\boldsymbol{\varepsilon}}^{\beta}\right) : \dot{\underset{\sim}{\boldsymbol{\sigma}}}^{\beta} - \underset{\sim}{\boldsymbol{\sigma}}^{\beta} : \dot{\underset{\sim}{\boldsymbol{\varepsilon}}}_p^{\beta} + \sum_s R_s^{\beta}\dot{\rho}_s^{\beta} + \sum_s X_s^{\beta}\dot{x}_s^{\beta}\right) \geq 0. \end{aligned} \tag{3.66}$$

Additional conditions result from the fact that the previous dissipation rate is assumed to be a positive linear form with respect to $\dot{c}_{\mathrm{i}}^{\alpha}$, $\dot{c}_{\mathrm{i}}^{\beta}$ and $\dot{\underset{\sim}{\boldsymbol{\sigma}}}^{\alpha}$ and $\dot{\underset{\sim}{\boldsymbol{\sigma}}}^{\beta}$:

$$\mu_{\mathrm{i}} = \mu_{\mathrm{i}}^{\beta} = \mu_{\mathrm{i}}^{\alpha}, \qquad \underset{\sim}{\boldsymbol{\varepsilon}} = \underset{\sim}{\boldsymbol{\varepsilon}}^{\alpha} = \underset{\sim}{\boldsymbol{\varepsilon}}^{\beta}. \tag{3.67}$$

The latter strain relations correspond to the Voigt approximation in homogenisation theory. Taking these relations into account and keeping the state law (3.49) for the gradient of the phase field, the following residual dissipation is obtained from (3.66):

$$-\pi^*\dot{\phi} - \sum_i \underline{\boldsymbol{J}}_{\mathrm{i}}\cdot\nabla\mu_{\mathrm{i}} + h\left(\underset{\sim}{\boldsymbol{\sigma}}^{\alpha} : \dot{\underset{\sim}{\boldsymbol{\varepsilon}}}_p^{\alpha}\right) + \bar{h}\left(\underset{\sim}{\boldsymbol{\sigma}}^{\beta} : \dot{\underset{\sim}{\boldsymbol{\varepsilon}}}_p^{\beta} - \sum_s R_s^{\beta}\dot{\rho}_s^{\beta} - \sum_s X_s^{\beta}\dot{x}_s^{\beta}\right) \geq 0. \tag{3.68}$$

At this stage, specific choices for the free enthalpy potentials are presented as an illustration of possible constitutive equations within the proposed framework. The following quadratic potentials are retained:

$$g_c^{\alpha,\beta}(c_{\mathrm{i}}^{\alpha,\beta}) = \frac{1}{2}k_{\mathrm{i}}^{\alpha,\beta}\left(c_{\mathrm{i}}^{\alpha,\beta} - \widehat{c}_{\mathrm{i}}^{\alpha,\beta}\right)^2, \tag{3.69}$$

$$g_{\sigma}^{\alpha}(\underset{\sim}{\boldsymbol{\sigma}}^{\alpha,\beta}) = -\frac{1}{2}\underset{\sim}{\boldsymbol{\sigma}}^{\alpha} : \underset{\approx}{\boldsymbol{S}}^{\alpha} : \underset{\sim}{\boldsymbol{\sigma}}^{\alpha} - \underset{\sim}{\boldsymbol{\sigma}}^{\alpha} : \underset{\sim}{\boldsymbol{\varepsilon}}_{\star}^{\alpha} - \underset{\sim}{\boldsymbol{\sigma}}^{\alpha} : \underset{\sim}{\boldsymbol{\varepsilon}}_p^{\alpha}, \tag{3.70}$$

$$g_{\sigma}^{\beta}(\underset{\sim}{\boldsymbol{\sigma}}^{\beta}, \underset{\sim}{\boldsymbol{\varepsilon}}_p^{\beta}, s_{\alpha}^{\beta}, b_{\alpha}^{\beta}) = -\frac{1}{2}\underset{\sim}{\boldsymbol{\sigma}}^{\beta} : \underset{\approx}{\boldsymbol{S}}^{\beta} : \underset{\sim}{\boldsymbol{\sigma}}^{\beta} - \underset{\sim}{\boldsymbol{\sigma}}^{\beta} : \underset{\sim}{\boldsymbol{\varepsilon}}_{\star}^{\beta} - \underset{\sim}{\boldsymbol{\sigma}}^{\beta} : \underset{\sim}{\boldsymbol{\varepsilon}}_p^{\beta} - \frac{1}{2}b^{\beta}Q^{\beta}\sum_{sr}H^{sr}\rho_s^{\beta}\rho_r^{\beta} - \frac{1}{2}C^{\beta}\sum_s x_s^{\beta 2}. \tag{3.71}$$

The chemical potentials are still given by the relations (3.35), whereas (3.36) is changed into:

$$\underset{\sim}{\boldsymbol{\varepsilon}}^{\alpha,\beta} = -\frac{\partial g_{\sigma}^{\alpha,\beta}}{\partial \underset{\sim}{\boldsymbol{\sigma}}^{\alpha,\beta}} = \underset{\approx}{\boldsymbol{S}}^{\alpha,\beta} : \underset{\sim}{\boldsymbol{\sigma}}^{\alpha,\beta} + \underset{\sim}{\boldsymbol{\varepsilon}}_{p}^{\alpha,\beta} + \underset{\sim}{\boldsymbol{\varepsilon}}_{\star}^{\alpha,\beta} = \underset{\sim}{\boldsymbol{\varepsilon}}, \tag{3.72}$$

where $\underset{\approx}{\boldsymbol{S}}^{\alpha/\beta}$ are the fourth order tensors of elastic complicance. The plastic stored energies expressed in Eq. (3.37) remain unchanged here.

3.4.4 Constitutive laws from the dissipation potential

Positivity of the residual dissipation rate can be ensured by choosing a convex dissipation potential Ω^* depending on the generalised forces associated with the flow of phase field, mass and plastic strain:

$$\Omega^* = \Omega^*(\pi^*, \nabla\mu_{\mathrm{i}}^{\alpha}, \nabla\mu_{\mathrm{i}}^{\beta}, \dot{\underset{\sim}{\boldsymbol{\varepsilon}}}_{p}^{\alpha}, \dot{\underset{\sim}{\boldsymbol{\varepsilon}}}_{p}^{\beta}, R_s^{\beta}, X_s^{\beta}; \phi)\,. \tag{3.73}$$

The chosen dissipation potential contains contributions from the diffuse interface and from the individual phases dissipative behaviour:

$$\Omega^* = \Omega_{\phi}^*(\pi^*) + h(\phi)\Omega^{*\alpha}(\nabla\mu_{\mathrm{i}}^{\alpha}, \dot{\underset{\sim}{\boldsymbol{\varepsilon}}}_{p}^{\alpha}) + \bar{h}(\phi)\Omega^{*\beta}(\nabla\mu_{\mathrm{i}}^{\beta}, \dot{\underset{\sim}{\boldsymbol{\varepsilon}}}_{p}^{\beta}, R_s^{\beta}, X_s^{\beta})\,. \tag{3.74}$$

Quadratic individual dissipations are chosen for as many physical mechanisms as possible including diffuse interface mobility and bulk diffusion:

$$\begin{cases} \Omega_{\pi}^*(\pi^*) & = & M_{\phi}\pi^{*2}\,, \\ \Omega^{*\alpha}(\nabla\mu_{\mathrm{i}}^{\alpha}, \dot{\underset{\sim}{\boldsymbol{\varepsilon}}}_{p}^{\alpha}) & = & \frac{1}{2}\underset{\sim}{\boldsymbol{L}}_{\mathrm{i}}^{\alpha} : \nabla\mu_{\mathrm{i}}^{\alpha} \otimes \nabla\mu_{\mathrm{i}}^{\alpha} + \Omega^{*\alpha}{}_{p}(\dot{\underset{\sim}{\boldsymbol{\varepsilon}}}_{p}^{\alpha})\,, \\ \Omega^{*\beta}(\nabla\mu_{\mathrm{i}}^{\beta}, \dot{\underset{\sim}{\boldsymbol{\varepsilon}}}_{p}^{\beta}, R_s^{\beta}, X_s^{\beta}) & = & \frac{1}{2}\underset{\sim}{\boldsymbol{L}}_{\mathrm{i}}{}^{\beta} : \nabla\mu_{\mathrm{i}}^{\beta} \otimes \nabla\mu_{\mathrm{i}}^{\beta} + \Omega^{*\beta}{}_{p}(\dot{\underset{\sim}{\boldsymbol{\varepsilon}}}_{p}^{\beta}, R_s^{\beta}, X_s^{\beta})\,. \end{cases} \tag{3.75}$$

The constitutive laws for diffusion are the same as in section 3.3.4.

The non–quadratic viscoplastic potential $\Omega^{*\alpha,\beta}_{p}$ is the dual potential to (3.41). It is obtained by a Legendre transformation according to [Halphen and Nguyen, 1975, eq. 20] and expresses the stress as the derivative with respect to plastic strain rate:

$$\underset{\sim}{\boldsymbol{\sigma}}^{\alpha} = \frac{\partial \Omega_{p}^{*\alpha}}{\partial \dot{\underset{\sim}{\boldsymbol{\varepsilon}}}_{p}^{\alpha}}, \qquad \underset{\sim}{\boldsymbol{\sigma}}^{\beta} = \frac{\partial \Omega_{p}^{*\beta}}{\partial \dot{\underset{\sim}{\boldsymbol{\varepsilon}}}_{p}^{\beta}}. \tag{3.76}$$

Note that the hardening laws (3.48) are still in use in the present context.

Regarding phase transformation, the evolution law for the phase field parameter reads:

$$\dot{\phi} = -\frac{\partial \Omega^*}{\partial \pi^*} = -M_{\phi}\pi^*\,, \tag{3.77}$$

where M_{ϕ} is the phase field mobility. The new form of the enhanced Allen-Cahn equation is obtained after substituting (3.5) and (3.30) in the latter evolution equation. Then,

$$\dot{\phi} = M_{\phi}\left(3\gamma\frac{\delta}{z}\Delta\phi - \frac{\partial g}{\partial\phi} + h'(\phi)\left(\mu_{\mathrm{i}}\left(\sum_i c_{\mathrm{i}}^{\alpha} - c_{\mathrm{i}}^{\beta}\right) - \underset{\sim}{\boldsymbol{\varepsilon}} : \left(\underset{\sim}{\boldsymbol{\sigma}}^{\alpha} - \underset{\sim}{\boldsymbol{\sigma}}^{\beta}\right)\right)\right). \tag{3.78}$$

The generalised Allen-Cahn equation (3.78) can also be rewritten by introducing the phase field driving force F_{ϕ}^{V} as done in (3.51). The phase field driving force now has the following form:

$$F_{\phi}^{V} = g^{\alpha} - g^{\beta} - \mu_{\mathrm{i}}\left(c_{\mathrm{i}}^{\alpha} - c_{\mathrm{i}}^{\beta}\right) + \underset{\sim}{\boldsymbol{\varepsilon}} : \left(\underset{\sim}{\boldsymbol{\sigma}}^{\alpha} - \underset{\sim}{\boldsymbol{\sigma}}^{\beta}\right). \tag{3.79}$$

which can be rewritten in terms of the Helmholtz free energy as follows :

$$F_\phi^V = f^\alpha - f^\beta - \mu_\mathrm{i}\left(c_\mathrm{i}^\alpha - c_\mathrm{i}^\beta\right). \tag{3.80}$$

The above driving force is then the Legendre transformation of the driving force obtained on the basis of the Helmholz free energy shown in Eq. (3.52), see [Spatschek and Eidel, 2013].

3.5 Excess of elastic energy in the interface

The free energy of both models – Voigt/Taylor and Reuss/Sachs – can be compared. It appears that the Voigt/Taylor approach enhance the total free energy with an excess elastic energy, that needs to be clearly defined. It must be noted that, prior to homogenisation, the free energy defined in the Helmholz approach is not equivalent to the free energy obtained in the Gibbs approach, which is briefly discussed below.

If we introduce the Legendre transformation from the Helmholtz to the Gibbs free energy densities for any two phased system :

$$g = f - \underset{\sim}{\boldsymbol{\sigma}} : \underset{\sim}{\boldsymbol{\varepsilon}}. \tag{3.81}$$

The phase field framework implies:

$$g = f - \left(h\left(\phi\right)\underset{\sim}{\boldsymbol{\sigma}}^\alpha + \bar{h}\left(\phi\right)\underset{\sim}{\boldsymbol{\sigma}}^\beta\right) : \left(h\left(\phi\right)\underset{\sim}{\boldsymbol{\varepsilon}}^\alpha + \bar{h}\left(\phi\right)\underset{\sim}{\boldsymbol{\varepsilon}}^\beta\right). \tag{3.82}$$

Besides, for any phase α or β, the bulk free enthalpy can also be expressed:

$$g^{\alpha,\beta} = f^{\alpha,\beta} - \underset{\sim}{\boldsymbol{\sigma}}^{\alpha,\beta} : \underset{\sim}{\boldsymbol{\varepsilon}}^{\alpha,\beta}. \tag{3.83}$$

If we apply (3.83) into the phase field model, the one that is based on the interpolation of the bulk free enthalpies g, it becomes,

$$\begin{aligned} g &= h(\phi)g^\alpha + \bar{h}(\phi)g^\beta, \\ &= h(\phi)f^\alpha + \bar{h}(\phi)f^\beta - \left(h(\phi)\underset{\sim}{\boldsymbol{\sigma}}^\alpha : \underset{\sim}{\boldsymbol{\varepsilon}}^\alpha + \bar{h}(\phi)\underset{\sim}{\boldsymbol{\sigma}}^\beta : \underset{\sim}{\boldsymbol{\varepsilon}}^\beta\right), \\ &= f - \left(h(\phi)\underset{\sim}{\boldsymbol{\sigma}}^\alpha : \underset{\sim}{\boldsymbol{\varepsilon}}^\alpha + \bar{h}(\phi)\underset{\sim}{\boldsymbol{\sigma}}^\beta : \underset{\sim}{\boldsymbol{\varepsilon}}^\beta\right), \end{aligned} \tag{3.84}$$

which is *a priori* not equivalent to (3.82).

Both homogenisation schemes will then enforce the equivalence between (3.84) and (3.82). While writing $\langle x\rangle$ the average value, or here the interpolated value, of x, the equivalence of (3.82) and (3.84) can be also reformulated as follows,

$$\langle\underset{\sim}{\boldsymbol{\sigma}}\rangle : \langle\underset{\sim}{\boldsymbol{\varepsilon}}\rangle = \langle\underset{\sim}{\boldsymbol{\sigma}} : \underset{\sim}{\boldsymbol{\varepsilon}}\rangle, \tag{3.85}$$

which is known as the Hill-Mandel principle of *Macro*-homogeneity, see [Besson et al., 2010].

In the end, the macroscopic free energies f^V and f^R can be compared depending on the chosen homogenisation scheme, respectively Voigt/Taylor and Reuss/Sachs. For the Reuss/Sachs homogenisation scheme, it can be shown that:

$$\begin{aligned} f_e^R &= h(\phi)f_e^\alpha(\underset{\sim}{\boldsymbol{\varepsilon}}_e^\alpha) + \bar{h}(\phi)f_e^\beta(\underset{\sim}{\boldsymbol{\varepsilon}}_e^\beta), \\ &= \frac{1}{2}h(\phi)\underset{\sim}{\boldsymbol{\sigma}}^\alpha : \underset{\sim}{\boldsymbol{\varepsilon}}_e^\alpha + \frac{1}{2}\bar{h}(\phi)\underset{\sim}{\boldsymbol{\sigma}}^\beta : \underset{\sim}{\boldsymbol{\varepsilon}}_e^\beta, \\ &= \frac{1}{2}h(\phi)\underset{\sim}{\boldsymbol{\sigma}} : \underset{\approx}{\boldsymbol{S}}^\alpha : \underset{\sim}{\boldsymbol{\sigma}} + \frac{1}{2}\bar{h}(\phi)\underset{\sim}{\boldsymbol{\sigma}} : \underset{\approx}{\boldsymbol{S}}^\beta : \underset{\sim}{\boldsymbol{\sigma}}, \\ &= \frac{1}{2}\underset{\sim}{\boldsymbol{\sigma}} : \left(h(\phi)\underset{\approx}{\boldsymbol{S}}^\alpha + \bar{h}(\phi)\underset{\approx}{\boldsymbol{S}}^\beta\right) : \underset{\sim}{\boldsymbol{\sigma}}, \\ &= \frac{1}{2}\underset{\sim}{\boldsymbol{\sigma}} : \underset{\sim}{\boldsymbol{\varepsilon}}_e, \end{aligned} \tag{3.86}$$

and for the Voigt/Taylor scheme:

$$\begin{aligned}
f_e^V &= g(\phi) + \langle \underset{\sim}{\boldsymbol{\sigma}} \rangle : \underset{\sim}{\boldsymbol{\varepsilon}}, \\
&= \frac{1}{2} h(\phi) \underset{\sim}{\boldsymbol{\sigma}}^\alpha : \underset{\sim}{\boldsymbol{\varepsilon}}_e^\alpha + \frac{1}{2} \bar{h}(\phi) \underset{\sim}{\boldsymbol{\sigma}}^\beta : \underset{\sim}{\boldsymbol{\varepsilon}}_e^\beta, \\
&= \frac{1}{2} \left(\underset{\sim}{\boldsymbol{\sigma}} : \underset{\sim}{\boldsymbol{\varepsilon}} - h(\phi) \underset{\sim}{\boldsymbol{\sigma}}^\alpha : (\underset{\sim}{\boldsymbol{\varepsilon}}_\star^\alpha + \underset{\sim}{\boldsymbol{\varepsilon}}_p^\alpha) - \bar{h}(\phi) \underset{\sim}{\boldsymbol{\sigma}}^\beta : (\underset{\sim}{\boldsymbol{\varepsilon}}_\star^\beta + \underset{\sim}{\boldsymbol{\varepsilon}}_p^\beta) \right), \\
&= \frac{1}{2} \underset{\sim}{\boldsymbol{\sigma}} : \underset{\sim}{\boldsymbol{\varepsilon}}_e + \frac{1}{2} \left(\underset{\sim}{\boldsymbol{\sigma}} : \left(\underset{\sim}{\boldsymbol{\varepsilon}}_\star + \underset{\sim}{\boldsymbol{\varepsilon}}_p \right) - h(\phi) \underset{\sim}{\boldsymbol{\sigma}}^\alpha : (\underset{\sim}{\boldsymbol{\varepsilon}}_\star^\alpha + \underset{\sim}{\boldsymbol{\varepsilon}}_p^\alpha) - \bar{h}(\phi) \underset{\sim}{\boldsymbol{\sigma}}^\beta : (\underset{\sim}{\boldsymbol{\varepsilon}}_\star^\beta + \underset{\sim}{\boldsymbol{\varepsilon}}_p^\beta) \right), \\
&= \frac{1}{2} \underset{\sim}{\boldsymbol{\sigma}} : \underset{\sim}{\boldsymbol{\varepsilon}}_e + \frac{1}{2} h(\phi) \sigma^\alpha : \left(\underset{\approx}{\boldsymbol{\Lambda}}_{\text{eff}}^{-1} : \left(h(\phi) \underset{\approx}{\boldsymbol{\Lambda}}^\alpha : \left(\underset{\sim}{\boldsymbol{\varepsilon}}_\star^\alpha + \underset{\sim}{\boldsymbol{\varepsilon}}_p^\alpha \right) + \bar{h}(\phi) \underset{\approx}{\boldsymbol{\Lambda}}^\beta : \left(\underset{\sim}{\boldsymbol{\varepsilon}}_\star^\beta + \underset{\sim}{\boldsymbol{\varepsilon}}_p^\beta \right) \right) - \underset{\sim}{\boldsymbol{\varepsilon}}_\star^\alpha - \underset{\sim}{\boldsymbol{\varepsilon}}_p^\alpha \right) \\
&\quad + \frac{1}{2} \bar{h}(\phi) \sigma^\beta : \left(\underset{\approx}{\boldsymbol{\Lambda}}_{\text{eff}}^{-1} : \left(h(\phi) \underset{\approx}{\boldsymbol{\Lambda}}^\alpha \left(\underset{\sim}{\boldsymbol{\varepsilon}}_\star^\alpha + \underset{\sim}{\boldsymbol{\varepsilon}}_p^\alpha \right) + \bar{h}(\phi) \underset{\approx}{\boldsymbol{\Lambda}}^\beta \left(\underset{\sim}{\boldsymbol{\varepsilon}}_\star^\beta + \underset{\sim}{\boldsymbol{\varepsilon}}_p^\beta \right) \right) - \underset{\sim}{\boldsymbol{\varepsilon}}_\star^\beta - \underset{\sim}{\boldsymbol{\varepsilon}}_p^\beta \right).
\end{aligned} \tag{3.87}$$

The above equation can be simplified through the expression of an inelastic strain jump:

$$\Delta \underset{\sim}{\boldsymbol{\varepsilon}}_\dagger = \left(\underset{\sim}{\boldsymbol{\varepsilon}}_\star^\alpha + \underset{\sim}{\boldsymbol{\varepsilon}}_p^\alpha \right) - \left(\underset{\sim}{\boldsymbol{\varepsilon}}_\star^\beta + \underset{\sim}{\boldsymbol{\varepsilon}}_p^\beta \right), \tag{3.88}$$

so that the Voigt/Taylor's energy can be rewritten as,

$$f_e^V = \frac{1}{2} \underset{\sim}{\boldsymbol{\sigma}} : \underset{\sim}{\boldsymbol{\varepsilon}}_e + \frac{1}{2} h(\phi) \bar{h}(\phi) \underset{\approx}{\boldsymbol{\Lambda}}_{\text{eff}}^{-1} : \left(\underset{\sim}{\boldsymbol{\sigma}}^\beta : \underset{\approx}{\boldsymbol{\Lambda}}^\alpha - \underset{\sim}{\boldsymbol{\sigma}}^\alpha : \underset{\approx}{\boldsymbol{\Lambda}}^\beta \right) : \Delta \underset{\sim}{\boldsymbol{\varepsilon}}_\dagger, \tag{3.89}$$

which contains an excess quantity compared to Eq. (3.86). The elastic excess energy, embedded in Voigt/Taylor's scheme is plotted for the unidimensional case of a laminate precipitate embedded in a matrix, for the case of homogeneous elasticity, see Fig. 3.1. The mechanical problem consists here of two semi-infinite phases α/β that are respectively defined for the intervals $x \in]-\infty, 0[$ and $x \in]0, +\infty[$, the point $x = 0$ being the interface. The phase alpha embeds a non-zero eigenstrain in the y direction, which, along with the stress-free top surface will result in the generation of stresses in both phases, see Appendix D for details along with a phase fraction set to 50%. The obtained elastic excess energy is similar to what has been reported by [Mosler et al., 2014, Fig. 1].

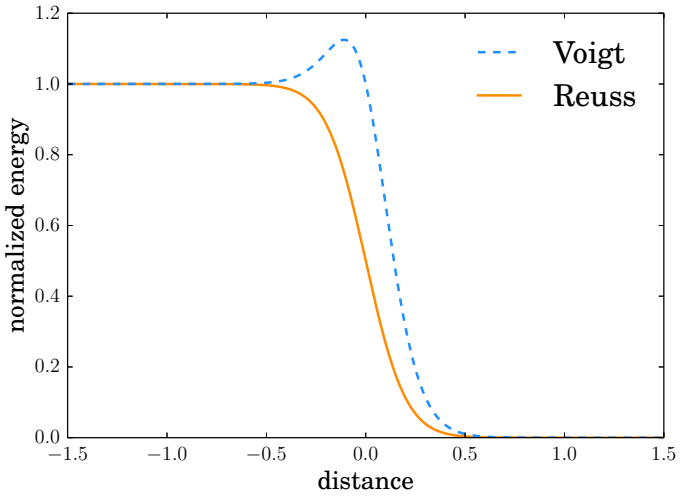

Figure 3.1: Illustrative example of Voigt/Taylor's excess elastic energy for the case of a laminate precipitate embedded in a matrix with misfit strain considering homogeneous elasticity. The shape of the interface free energy excess is given by the function $h(\phi)\bar{h}(\phi)$.

3.6 Preliminary thoughts on the sharp interface limit

The present section is devoted to the question of the convergence between Voigt and Reuss approaches limited to the unidimensional case for an infinite body.

First of all, the function of interest is here:

$$H(x \in]-\infty,+\infty[) = h \circ \phi(x)\ \bar{h} \circ \phi(x) \in]0,1[\,, \tag{3.90}$$

which is an even function when the interface is chosen at $x = 0$. In the following, we assume that the excess energy remains bounded for any values of interface thickness δ. It is also assumed the H function can be integrated over the whole body with respect to the construction of the phase field model.

The excess free energy can be calculated as an additional interface energy term by integration of Eq. (3.89) over the body:

$$\gamma_{\text{excess}} = \int_{-\infty}^{+\infty} \left(\frac{1}{2} H(x) \underset{\approx}{\mathbf{\Lambda}}_{\text{eff}}^{-1} : \left(\underset{\sim}{\boldsymbol{\sigma}}^{\beta} : \underset{\approx}{\mathbf{\Lambda}}^{\alpha} - \underset{\sim}{\boldsymbol{\sigma}}^{\alpha} : \underset{\approx}{\mathbf{\Lambda}}^{\beta} \right) : \Delta \underset{\sim}{\boldsymbol{\varepsilon}}_{\dagger} \right) \mathrm{dx}. \tag{3.91}$$

The absolute value of the excess interface energy is assumed to be bounded by the positive real value B[1]:

$$|\gamma_{\text{excess}}| \leq B \int_{-\infty}^{+\infty} H(x) \mathrm{dx}, \tag{3.92}$$

which can be rewritten as follows as H is even:

$$|\gamma_{\text{excess}}| \leq B \left(\int_{-\delta/2}^{+\delta/2} H(x) \mathrm{dx} + 2 \int_{+\delta/2}^{+\infty} H(x) \mathrm{dx} \right). \tag{3.93}$$

Then, a change of variable can be performed:

$$X = \frac{x}{\delta}, \tag{3.94}$$

where δ is the interface thickness. Eq. (3.92) can be bounded:

$$|\gamma_{\text{excess}}| \leq B\delta \left(\int_{-1/2}^{1/2} H(X) \mathrm{dX} + 2 \int_{1/2}^{+\infty} H(X) \mathrm{dX} \right). \tag{3.95}$$

Eq. (3.95) can be bounded using B' a bound for $\int_{1/2}^{+\infty} H(X) \mathrm{dX}$:

$$|\gamma_{\text{excess}}| \leq B\delta \left(1 + 2B'\right). \tag{3.96}$$

At the sharp interface limit, the excess vanishes:

$$\lim_{\delta \to 0} \gamma_{\text{excess}} = 0, \tag{3.97}$$

which means that the excess energy embedded into the Voigt/Taylor scheme vanishes in the sharp interface limit. It can be intuited that the Voigt/Taylor and Reuss/Sachs driving forces converge between each other because the excess free energy vanishes in the sharp interface limit. The difference of driving force between the Voigt/Taylor and Reuss/Sachs approaches is here ΔF:

$$\Delta F = \int_{-\infty}^{+\infty} \left(\frac{\partial f_e^V}{\partial \phi} - \frac{\partial f_e^R}{\partial \phi} \right) \mathrm{dx}, \tag{3.98}$$

[1] $B = \max_{(x,\delta)} \frac{1}{2} \left(\left| \underset{\approx}{\mathbf{\Lambda}}_{\text{eff}}^{-1} : \left(\underset{\sim}{\boldsymbol{\sigma}}^{\beta} : \underset{\approx}{\mathbf{\Lambda}}^{\alpha} - \underset{\sim}{\boldsymbol{\sigma}}^{\alpha} : \underset{\approx}{\mathbf{\Lambda}}^{\beta} \right) : \Delta \underset{\sim}{\boldsymbol{\varepsilon}}_{\dagger} \right| \right)$

which can be rewritten given Eqs. (3.86) and (3.89):

$$\Delta F = \int_{-\infty}^{+\infty} \frac{1}{2} \left(\frac{\partial H}{\partial \phi}(x) \underset{\approx}{\Lambda}_{\text{eff}}^{-1} + H(x) \frac{\partial \underset{\approx}{\Lambda}_{\text{eff}}^{-1}}{\partial \phi} \right) : \left(\underset{\sim}{\sigma}^{\beta} : \underset{\approx}{\Lambda}^{\alpha} - \underset{\sim}{\sigma}^{\alpha} : \underset{\approx}{\Lambda}^{\beta} \right) : \Delta \underset{\sim}{\varepsilon}_{\dagger} \mathrm{d}x. \tag{3.99}$$

The integrand can be separated in two parts:

$$\begin{aligned} \Delta F \quad = \quad & \int_{-\infty}^{+\infty} \frac{1}{2} \frac{\partial H}{\partial \phi}(x) \underset{\approx}{\Lambda}_{\text{eff}}^{-1} : \left(\underset{\sim}{\sigma}^{\beta} : \underset{\approx}{\Lambda}^{\alpha} - \underset{\sim}{\sigma}^{\alpha} : \underset{\approx}{\Lambda}^{\beta} \right) : \Delta \underset{\sim}{\varepsilon}_{\dagger} \mathrm{d}x \\ & + \int_{-\infty}^{+\infty} \frac{1}{2} H(x) \frac{\partial \underset{\approx}{\Lambda}_{\text{eff}}^{-1}}{\partial \phi} : \left(\underset{\sim}{\sigma}^{\beta} : \underset{\approx}{\Lambda}^{\alpha} - \underset{\sim}{\sigma}^{\alpha} : \underset{\approx}{\Lambda}^{\beta} \right) : \Delta \underset{\sim}{\varepsilon}_{\dagger} \mathrm{d}x. \end{aligned} \tag{3.100}$$

Using the triangle inequality, the above equation can be rewritten:

$$\begin{aligned} |\Delta F| \quad \leq \quad & \left| \int_{-\infty}^{+\infty} \frac{1}{2} \frac{\partial H}{\partial \phi}(x) \underset{\approx}{\Lambda}_{\text{eff}}^{-1} : \left(\underset{\sim}{\sigma}^{\beta} : \underset{\approx}{\Lambda}^{\alpha} - \underset{\sim}{\sigma}^{\alpha} : \underset{\approx}{\Lambda}^{\beta} \right) : \Delta \underset{\sim}{\varepsilon}_{\dagger} \mathrm{d}x \right| \\ & + \left| \int_{-\infty}^{+\infty} \frac{1}{2} H(x) \frac{\partial \underset{\approx}{\Lambda}_{\text{eff}}^{-1}}{\partial \phi} : \left(\underset{\sim}{\sigma}^{\beta} : \underset{\approx}{\Lambda}^{\alpha} - \underset{\sim}{\sigma}^{\alpha} : \underset{\approx}{\Lambda}^{\beta} \right) : \Delta \underset{\sim}{\varepsilon}_{\dagger} \mathrm{d}x \right|, \end{aligned} \tag{3.101}$$

which can be further written:

$$\begin{aligned} |\Delta F| \quad \leq \quad & \left| \int_{-\infty}^{+\infty} \frac{1}{2} \frac{\partial H}{\partial \phi}(x) \underset{\approx}{\Lambda}_{\text{eff}}^{-1} : \left(\underset{\sim}{\sigma}^{\beta} : \underset{\approx}{\Lambda}^{\alpha} - \underset{\sim}{\sigma}^{\alpha} : \underset{\approx}{\Lambda}^{\beta} \right) : \Delta \underset{\sim}{\varepsilon}_{\dagger} \mathrm{d}x \right| \\ & + \int_{-\infty}^{+\infty} \frac{1}{2} H(x) \left| \frac{\partial \underset{\approx}{\Lambda}_{\text{eff}}^{-1}}{\partial \phi} : \left(\underset{\sim}{\sigma}^{\beta} : \underset{\approx}{\Lambda}^{\alpha} - \underset{\sim}{\sigma}^{\alpha} : \underset{\approx}{\Lambda}^{\beta} \right) : \Delta \underset{\sim}{\varepsilon}_{\dagger} \right| \mathrm{d}x. \end{aligned} \tag{3.102}$$

The second term can be rewritten by using the positive real value B''[2] and by using the same change of variable as in Eq. (3.94)

$$|\Delta F| \leq \left| \int_{-\infty}^{+\infty} \frac{1}{2} \frac{\partial H}{\partial \phi}(x) \underset{\approx}{\Lambda}_{\text{eff}}^{-1} : \left(\underset{\sim}{\sigma}^{\beta} : \underset{\approx}{\Lambda}^{\alpha} - \underset{\sim}{\sigma}^{\alpha} : \underset{\approx}{\Lambda}^{\beta} \right) : \Delta \underset{\sim}{\varepsilon}_{\dagger} \mathrm{d}x \right| + B'' \delta (1 + 2B'), \tag{3.103}$$

which can be further written:

$$|\Delta F| \leq B \int_{-\infty}^{+\infty} \left| \frac{\partial H}{\partial \phi}(x) \right| \mathrm{d}x + B'' \delta (1 + 2B'). \tag{3.104}$$

Then,

$$|\Delta F| \leq B \left(\int_{-\delta/2}^{+\delta/2} \left| \frac{\partial H}{\partial \phi}(x) \right| + 2 \int_{\delta/2}^{+\infty} \left| \frac{\partial H}{\partial \phi}(x) \right| \mathrm{d}x \right) + B'' \delta (1 + 2B'). \tag{3.105}$$

The former change of variable, see Eq. (3.94), can be performed:

$$|\Delta F| \leq B \delta \left(\int_{-1/2}^{+1/2} \left| \frac{\partial H}{\partial \phi}(x) \right| + 2 \int_{1/2}^{+\infty} \left| \frac{\partial H}{\partial \phi}(x) \right| \mathrm{d}x \right) + B'' \delta (1 + 2B'), \tag{3.106}$$

For which the terms in parentheses can be bounded by construction of the phase field model:

$$|\Delta F| \leq B B''' \delta + B'' \delta (1 + 2B'). \tag{3.107}$$

[2] $B'' = \max\limits_{(x,\delta)} \frac{1}{2} \left(\left| \frac{\partial \underset{\approx}{\Lambda}_{\text{eff}}^{-1}}{\partial \phi} : \left(\underset{\sim}{\sigma}^{\beta} : \underset{\approx}{\Lambda}^{\alpha} - \underset{\sim}{\sigma}^{\alpha} : \underset{\approx}{\Lambda}^{\beta} \right) : \Delta \underset{\sim}{\varepsilon}_{\dagger} \right| \right)$

This is why, Voigt/Taylor ans Reuss/Sachs driving forces converge towards each other at the sharp interface limit:

$$\lim_{\delta \to 0} \Delta F = 0 \,. \tag{3.108}$$

However, the assumptions performed in this analysis must be investigated in more details with respect to the construction of the phase field model – choice of interpolation functions, of double well potential for instance.

3.7 Finite element implementation

The numerical resolution of the present initial and boundary value problem – or IBVP – is made by means of a space discretisation based on the finite element method and a time discretisation based on first order finite differences. We use a unique element, which embeds several degrees of freedom for the multiphysics problem. The evolution of the degrees of freedom is computed with respect to the constitutive laws for the Voigt/Taylor and Reuss/Sachs approaches. The integration of internal variables is made *via* an explicit fourth order Runge-Kutta method. The equilibrium defined by the monolithic system of balance equations – for mass, phase field and momentum – is enforced at each time step from an implicit Newton algorithm.

The natural choice of degrees of freedom is:

$$\text{DOF} = \{\phi, c_i, \underline{\boldsymbol{u}}\} \,. \tag{3.109}$$

Such a set is not appropriate in the homogenisation – or "two-phase" – framework because it does not allow to evaluate c_i^α and c_i^β easily. As (3.35) connects c_i^α and c_i^β together, it results that c_i^α alone is sufficient to evaluate c_i, see (3.1). A more appropriate set of degrees of freedom is then:

$$\text{DOF} = \{\phi, c_i^\alpha, \underline{\boldsymbol{u}}\} \,. \tag{3.110}$$

3.7.1 Monolithic global resolution of the coupled problem

The time evolution of the multiphysics set of nodal variables is obtained by solving the weak form of the balance equations (3.9) – for the phase field equation and the Cauchy static equilibrium – and (3.10) – for mass balance. The system of equations is solved on the basis of a residual quantity R, which is defined as the difference between the internal and external forces – where internal forces are the volume integral of the weak form of the balance equations and external forces the remaining surface integral. The Newton algorithm adapted to the present multiphysics approach is illustrated in Fig. 3.2. Moreover, an adaptive time stepping procedure is used in the simulations, see [Besson et al., 2010].

3.7.2 Local integration of the constitutive equations according to Voigt homogenisation scheme

First of all, we recall that:

$$\underset{\sim}{\boldsymbol{\varepsilon}} = \underset{\sim}{\boldsymbol{\varepsilon}}^\alpha = \underset{\sim}{\boldsymbol{\varepsilon}}^\beta \,. \tag{3.111}$$

The algorithm for the behaviour in the case of the Voigt/Taylor approach is illustrated in Fig. 3.3. The elastic strains of each phase – $\underset{\sim}{\boldsymbol{\varepsilon}}_e^\alpha$ and $\underset{\sim}{\boldsymbol{\varepsilon}}_e^\beta$ – are integrated along with other internal variables presented in the flow chart. During the Runge-Kutta step, the stress tensors of each phase – $\underset{\sim}{\boldsymbol{\sigma}}^\alpha$ and $\underset{\sim}{\boldsymbol{\sigma}}^\beta$ – are first updated. The activation of plasticity in each phase is then calculated on the basis of the respective current stress. The increment of the internal variables is calculated. After that, the plastic strain

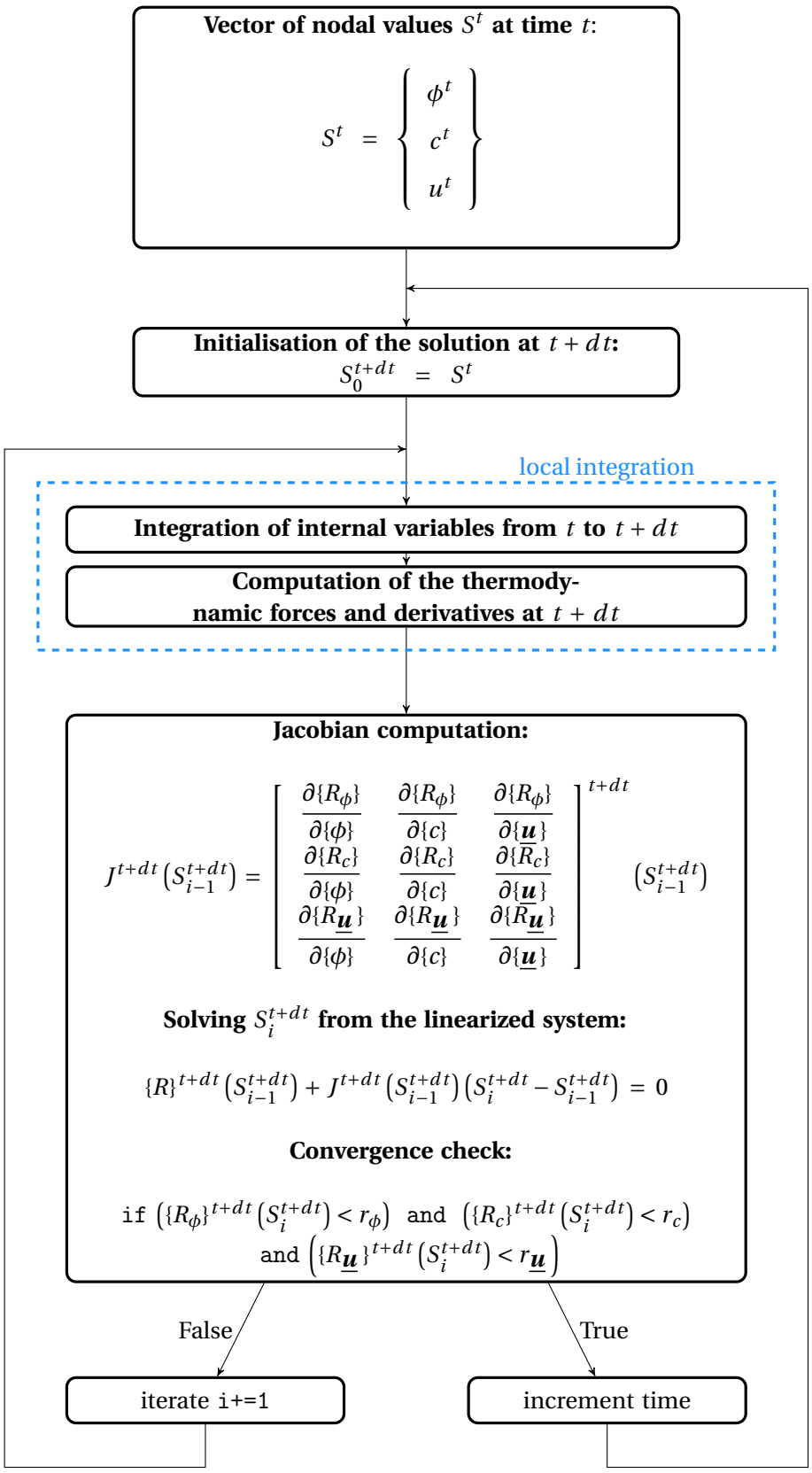

Figure 3.2: The Newton algorithm is illustrated in the form of a flow chart for the case of a multiphysics problem containing a phase field ϕ, one or several concentrations c and displacements $\underline{\boldsymbol{u}}$. The algorithm steps inside the dashed blue box are related to the material behaviour, wherein the internal variables are integrated and the thermodynamic forces along with their derivatives are evaluated at $t+dt$.

increment are calculated of each phase and so is the increment of elastic strains for each phase. Finally, averaged quantities are evaluated at each time step for visualisation purpose – termed auxiliary variables. For instance for the total stress is calculated according to,

$$\underset{\sim}{\boldsymbol{\sigma}} = h(\phi)\underset{\sim}{\boldsymbol{\sigma}}^{\alpha} + \bar{h}(\phi)\underset{\sim}{\boldsymbol{\sigma}}^{\beta}. \tag{3.112}$$

The effective elasticity tensor:

$$\underset{\approx}{\boldsymbol{\Lambda}}_{\text{eff}} = h(\phi)\underset{\approx}{\boldsymbol{\Lambda}}^{\alpha} + \bar{h}(\phi)\underset{\approx}{\boldsymbol{\Lambda}}^{\beta}, \tag{3.113}$$

followed by the total plastic, eigen- and elastic strains:

$$\begin{aligned}
\underset{\sim}{\boldsymbol{\varepsilon}}_{p} &= \underset{\approx}{\boldsymbol{\Lambda}}_{\text{eff}}^{-1} : \left(h(\phi)\underset{\approx}{\boldsymbol{\Lambda}}^{\alpha} : \underset{\sim}{\boldsymbol{\varepsilon}}_{p}^{\alpha} + \bar{h}(\phi)\underset{\approx}{\boldsymbol{\Lambda}}^{\beta} : \underset{\sim}{\boldsymbol{\varepsilon}}_{p}^{\beta} \right), \\
\underset{\sim}{\boldsymbol{\varepsilon}}_{\star} &= \underset{\approx}{\boldsymbol{\Lambda}}_{\text{eff}}^{-1} : \left(h(\phi)\underset{\approx}{\boldsymbol{\Lambda}}^{\alpha} : \underset{\sim}{\boldsymbol{\varepsilon}}_{\star}^{\alpha} + \bar{h}(\phi)\underset{\approx}{\boldsymbol{\Lambda}}^{\beta} : \underset{\sim}{\boldsymbol{\varepsilon}}_{\star}^{\beta} \right), \\
\underset{\sim}{\boldsymbol{\varepsilon}}_{e} &= \underset{\approx}{\boldsymbol{\Lambda}}_{\text{eff}}^{-1} : \left(h(\phi)\underset{\approx}{\boldsymbol{\Lambda}}^{\alpha} : \underset{\sim}{\boldsymbol{\varepsilon}}_{e}^{\alpha} + \bar{h}(\phi)\underset{\approx}{\boldsymbol{\Lambda}}^{\beta} : \underset{\sim}{\boldsymbol{\varepsilon}}_{e}^{\beta} \right).
\end{aligned} \tag{3.114}$$

3.7.3 Local integration of the constitutive equations according to Reuss homogenisation scheme

Here, we choose to integrate the effective elastic strain along with the plastic strains of each phase as they appear in the time derivative of the effective elastic strain as seen in Fig. 3.4. Analogously to the Voigt/Taylor approach, the internal variables for plasticity are also integrated after updating the stress for the underlying time steps of the Runge-Kutta algorithm. It is worth noting here that the integration of the effective elastic strain involves the phase field ϕ, which is known to drastically decrease the efficiency of the Runge-Kutta integration. Examples of Runge-Kutta integration making use of external fields are found in thermo-mechanical calculations involving viscoplasticity, when the Young modulus and so the stress are temperature dependent. The aforementioned problem is *not* encountered in the Voigt/Taylor approach, which is why its convergence is significantly faster than for the Reuss/Sachs approach. Finally, auxiliary variables can be calculated, for instance, the elastic strain of each phase:

$$\underset{\sim}{\boldsymbol{\varepsilon}}_{e}^{\alpha} = \underset{\approx}{\boldsymbol{S}}^{\alpha} : \underset{\sim}{\boldsymbol{\sigma}} \qquad \text{and} \qquad \underset{\sim}{\boldsymbol{\varepsilon}}_{e}^{\beta} = \underset{\approx}{\boldsymbol{S}}^{\beta} : \underset{\sim}{\boldsymbol{\sigma}}, \tag{3.115}$$

and the effective plastic and elastic strains:

$$\begin{aligned}
\underset{\sim}{\boldsymbol{\varepsilon}}_{p} &= h(\phi)\underset{\sim}{\boldsymbol{\varepsilon}}_{p}^{\alpha} + \bar{h}(\phi)\underset{\sim}{\boldsymbol{\varepsilon}}_{p}^{\beta}, \\
\underset{\sim}{\boldsymbol{\varepsilon}}_{\star} &= h(\phi)\underset{\sim}{\boldsymbol{\varepsilon}}_{\star}^{\alpha} + \bar{h}(\phi)\underset{\sim}{\boldsymbol{\varepsilon}}_{\star}^{\beta}.
\end{aligned} \tag{3.116}$$

3.8 Case study

3.8.1 Definition of the problem

Plane strain finite element analyses of a growing misfitting precipitate embedded in a supersaturated matrix – where the phases are respectively noted α and β – are performed to compare the Voigt/Taylor and Reuss/Sachs schemes. The misfit is here simplified by choosing a zero out-of-plane component:

$$\varepsilon_{\star}^{\alpha} = \begin{pmatrix} 0.01 & & \\ & 0.01 & \\ & & 0 \end{pmatrix}. \tag{3.117}$$

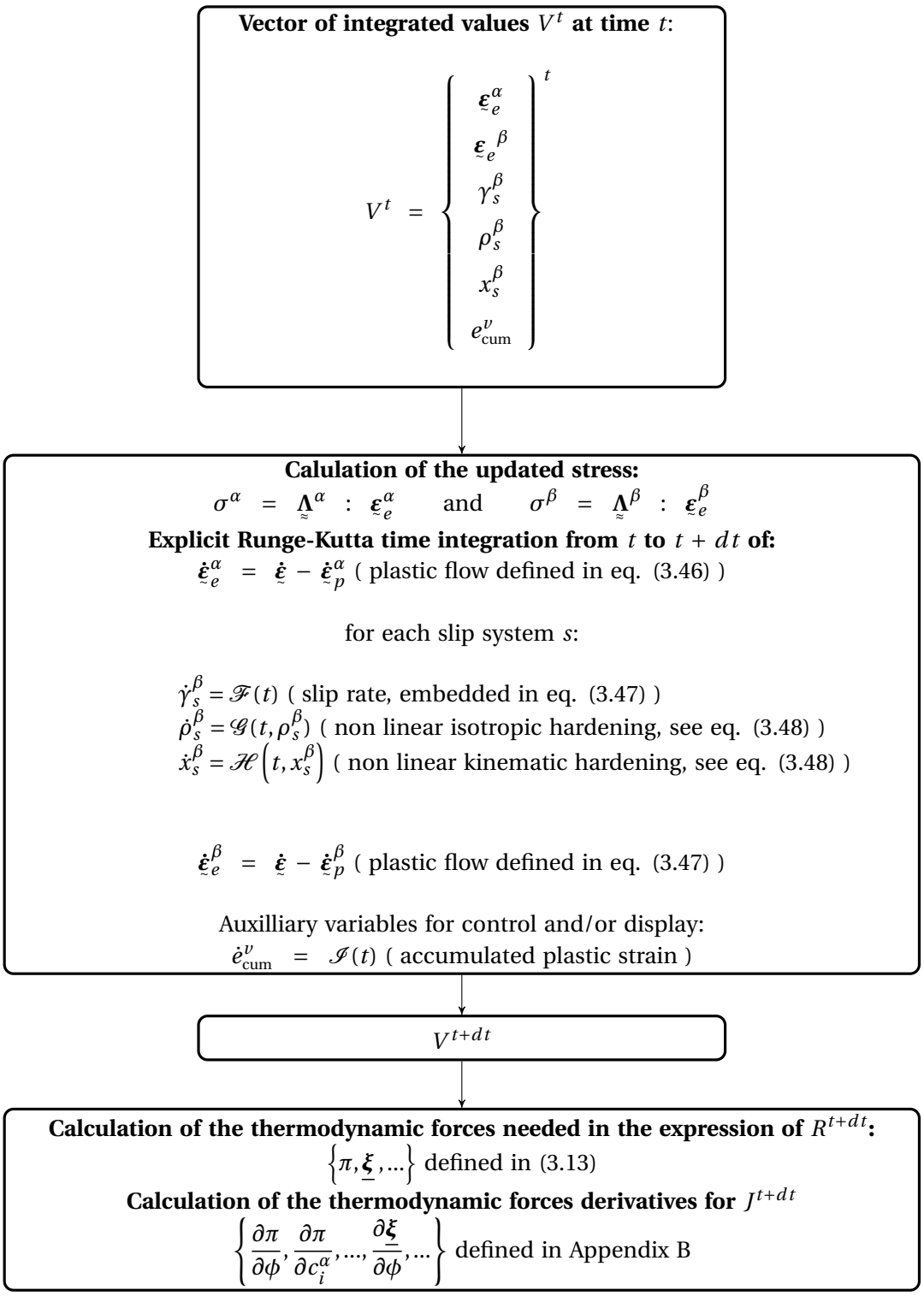

Figure 3.3: Algorithm steps for the integration of the internal variables, the calculation of the thermodynamic forces and corresponding derivatives for the Voigt/Taylor's approach.

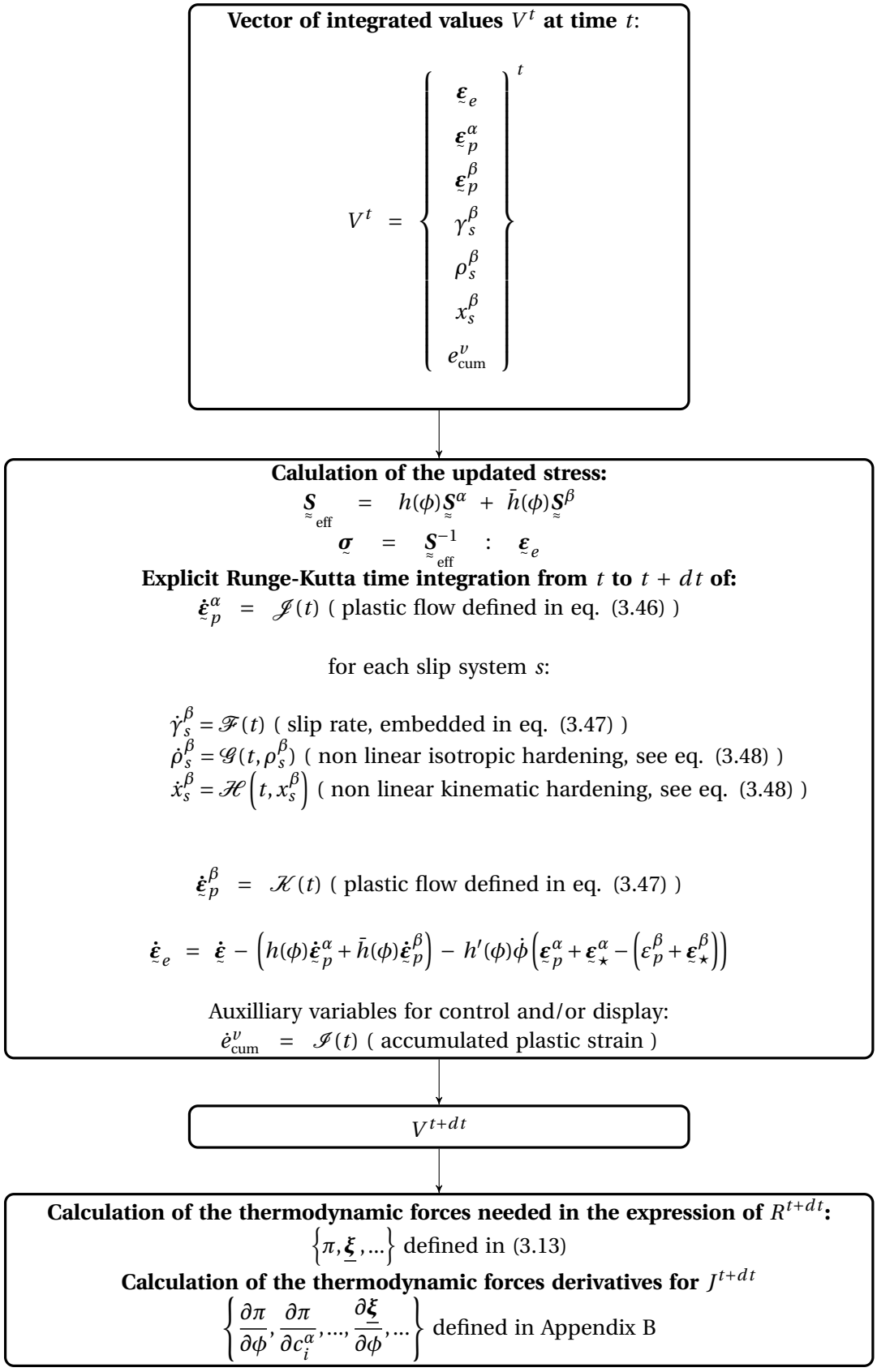

Figure 3.4: Algorithm steps for the integration of the internal variables, the calculation of the thermodynamic forces and corresponding derivatives for the Reuss/Sachs's approach.

The growth is here driven by a single concentration field hence the binary system. The growing precipitate is stoichiometric, whereas large deviations from the stoichiometry in the matrix can be found. Therefore, the growth stresses significantly impact the chemical equilibrium and so the growth kinetics. An analytic approximation of the shift of concentration induced by stresses is provided by [Johnson, 1987]. The numerical comparison of the Voigt/Taylor and Reuss/Sachs approaches will be done for two cases:

- planar interface (Case I)
- curved interface (Case II)

The analysis of a planar interface is often made in phase field analyses to be compared with the respective analytic solutions obtained in the sharp interface limit. The analysis of a curved interface is complex in the framework of sharp interfaces. This is why, diffuse interface models – or phase field models – are often used to circumvent such a difficulty. The present study shows that the curvature modifies the convergence rate of the diffuse interface model towards its underlying sharp interface limit.

Material parameters

For all simulations, identical parameters are used for the material behaviour, which are all given in Table 3.1. We choose parameters close to the physical properties used in the forthcoming phase field simulations of oxidation. Here, homogeneous elasticity is considered. We treat the chromium concentration field, for which the stoichiometry is set to 0 and 0.33, respectively in the matrix and in the precipitate. The precipitate can be considered as a growing oxide nodule for which the oxygen supply is *not* the rate limiting step. The eigenstrain is chosen following [Clarke, 2002] and set to 1%. In addition to that, the interface thickness is chosen as 5 nm and the interface energy is equal to 100 $mJ.m^{-2}$. The interface mobility is chosen high enough to simulate a diffusion-controlled growth, see [Kim et al., 1999, Eq (67)]. The mesh density is set to ten linear elements within the interface, which is more than what is usually done. Here, the mesh resolution is 5 Å. Nevertheless, the simulations parameters are dimensionless so that the problem can be extrapolated for larger mesh resolutions and other sets of material parameters, *e.g.* diffusivities, interface energy, *etc.* More details are found in Appendix E about the mesh sensitivity, time step sensitivity, *etc.*

	E [GPa]	ν	D [$m^2.s^{-1}$]	k [$GJ.m^{-3}$]	a
precipitate	210	0.3	$4.7e^{-19}$	100	0.33
matrix	210	0.3	$5.6e^{-17}$	1	0

Table 3.1: Material parameters used for the 1D/2D simulations.

Scaling of the initial and boundary values problem

Simulations cannot be performed if the physical units are not appropriate. To circumvent such a problem, the nondimentionalisation is systematically performed in the following. Nondimensionalisation of material parameters, simulation time and sample size relies on a characteristic length L, a characteristic time τ followed by a characteristic energy density E. The dimensionless quantities used in the simulations are given in Table 3.2. The resulting dimensionless values are denoted with a tilde symbol, for instance, $\tilde{t}$ stands for the dimensionless time.

The nondimensionalisation of all physical quantities is explained in more details in Appendix F. It is worth noting that the time is normalised against the characteristic diffusion time throughout the total length of the sample. A normalised time equal to one, $\tilde{\tau} = 1$, corresponds then to asymptotic response of the diffusion problem.

L [nm]	τ [s]	E [GJ.m^{-3}]
200	$L^2/\max(D) = 714$	1

Table 3.2: Characteristic physical parameters used for the nondimensionalisation.

Geometry and boundary conditions

The unidimensional sample – Case I – has a length of 200 nm and the two dimensional sample – Case II – consists of a finely meshed 200×200 nm^2 domain embedded in a coarse mesh, see Fig. 3.5 and 3.6. No-flux boundary conditions are prescribed on the sample with respect to the single concentration field. The mechanical boundary conditions are – for both cases I and II – defined as follows. The bottom surface is fixed along the direction y, the right surface is fixed along the direction x. A multi-point constraint (MPC) is applied to the top and left surfaces to enforce them to remain flat anytime. They can be summarised as follows,

$$\begin{aligned}
&\forall t, \quad \forall x, \quad u_y(x,0,t) = 0, \\
&\forall t, \quad \forall y, \quad u_x(L,y,t) = 0, \\
&\forall t, \quad \forall x, \quad u_y(x,h,t) = u_y(t), \\
&\forall t, \quad \forall y, \quad u_x(0,y,t) = u_x(t),
\end{aligned} \tag{3.118}$$

where L is the width for the Case I and the half-width for the Case II. The parameter h is the height of the sample.

Initial concentration fields

To fulfil the description of the initial and boundary value problems, one needs to express the initial concentration fields. For both cases, they are homogeneous in each phase. The initial concentration field of the Case I is illustrated in Fig. 3.7. The concentration in the precipitate – or the α phase – is set equal to the well of the chemical free energy defined in Table 3.1 ($c_0 = a^p = 0.33$), whereas the concentration in the matrix – or the β phase – is supersaturated to an arbitrary value – here 5.5% as illustrated in Fig. 3.7 – to make the precipitate grow. During the simulations, the interface concentrations are rapidly selected by the operative tie-line, so that a typical depletion profile is found in the matrix in the vicinity of the interface.

For the Case II, the initial concentration field is illustrated in Fig. 3.8, where small differences appear with respect to Fig. 3.7 to correct the deviation induced by the curvature – or Gibbs-Thomson effect. The overstoichiometry found in the matrix is lower than the supersaturation for the Case I. The overstoichiometry can be calculated *a priori* to enclose the growing precipitate into the finely meshed domain.

3.9 Results

3.9.1 Influence of the homogenisation scheme in the case of elasticity

Unidimensional growth with elasticity

The growth of a laminate precipitate is first studied (Case I) using both Voigt/Taylor and Reuss/Sachs schemes. It is known that elastic stresses modify the chemical equilibrium and so the growth kinetics. From the analytic solution of the equilibrium concentrations with stresses provided by [Johnson, 1987], one can evaluate the asymptotic phase fraction of the precipitate when stresses

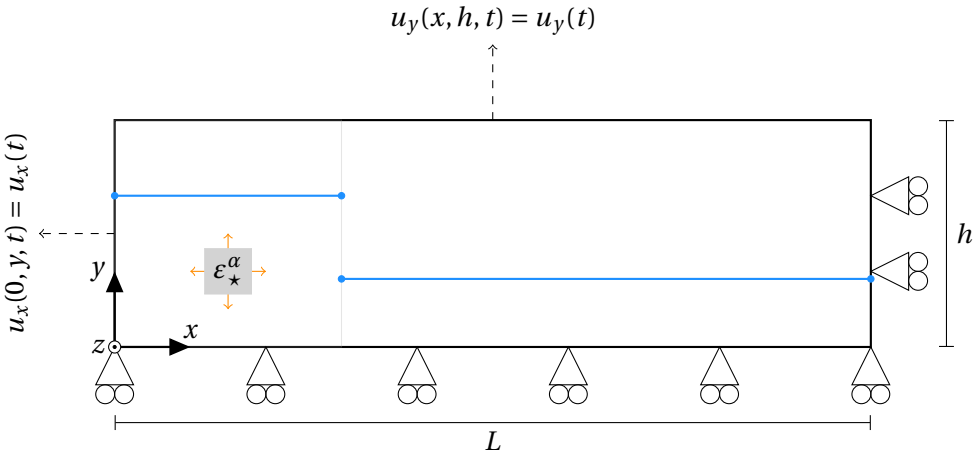

Figure 3.5: Mechanical boundary conditions for the Case I. The initial concentration field is also represented but will be given next in more details.

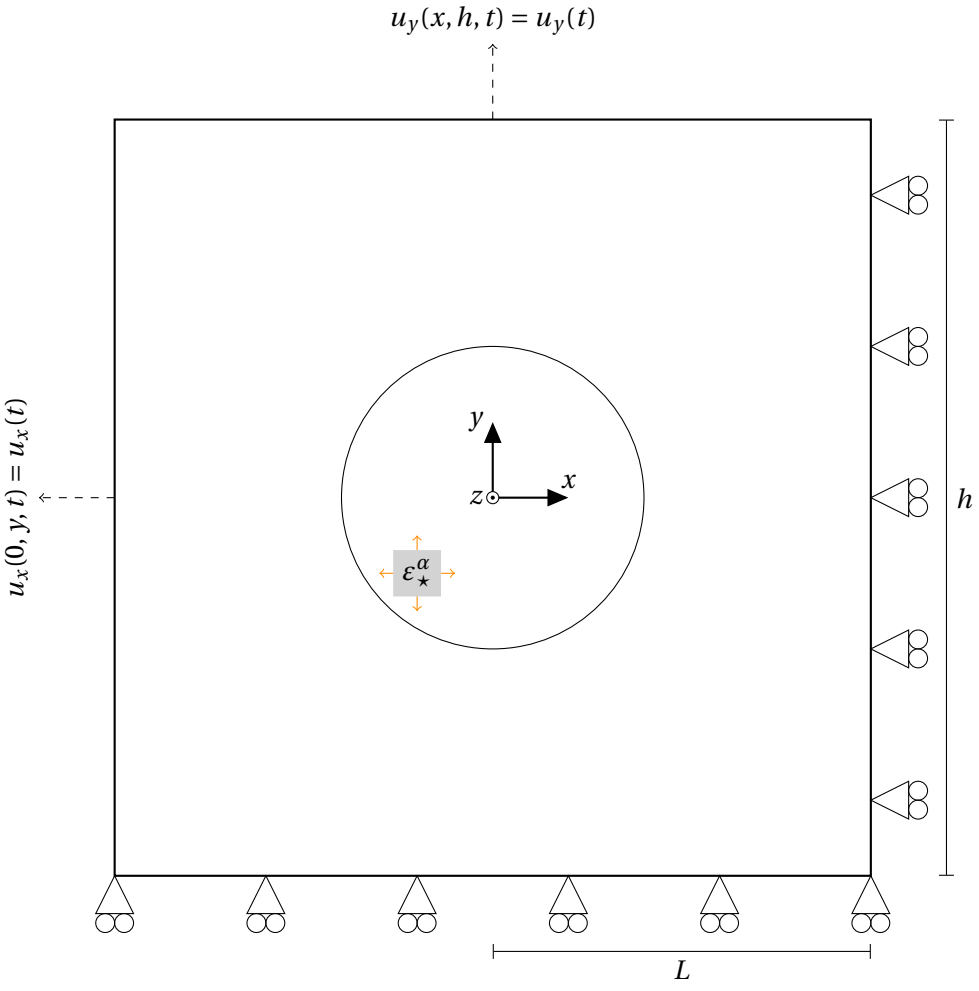

Figure 3.6: Mechanical boundary conditions for the Case II.

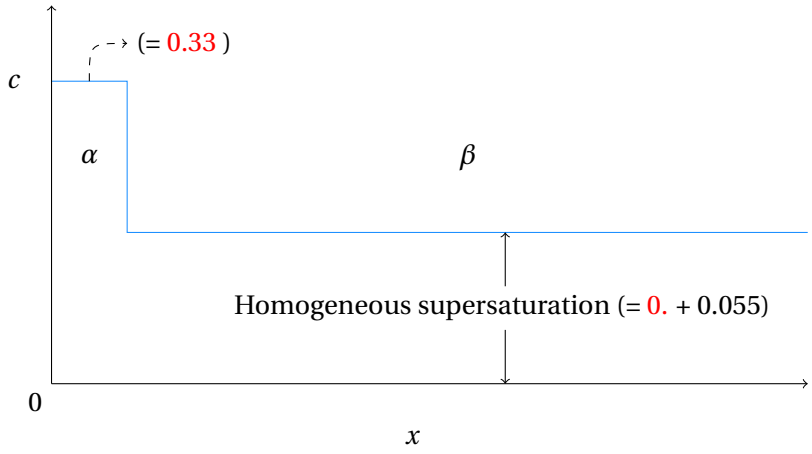

Figure 3.7: Initial concentration field for the Case I.

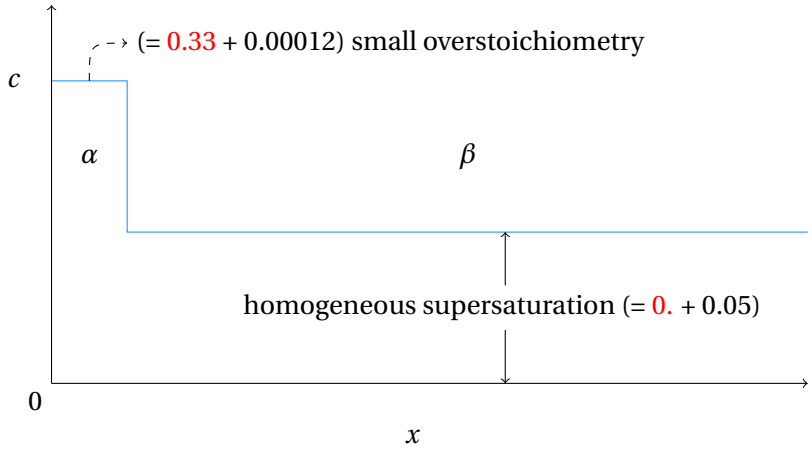

Figure 3.8: Initial concentration field for Case II.

are accounted for. The asymptotic phase fraction in the case for which stresses are neglected – when restricted to diffusion – can be calculated as well. The two aforementioned asymptotic phase fractions are shown in Fig. 3.9 by the horizontal dashed lines. The figure represents the growth curves in the case of elasticity and restricted to diffusion through the evolving phase fraction f. The growth kinetic curves are shown to tend towards the predicted asymptotic values. It is also shown that elasticity significantly modifies the final phase fraction. Finally, the growth curves of the elastic grown precipitates shown in the case of the Voigt/Taylor and Reuss/Sachs approaches emphasise the negligible role of the homogenisation methods in the present case. Such a growth is driven by the concentration gradient in the matrix, which is prescribed by the interface equilibrium concentrations – or the operative tie-line. The evolution of interface concentrations is given in Fig. 3.10. The evolution of which is obtained by an extrapolation procedure of the continuous field to the interface – the sharp interface limit. This procedure is illustrated in the figure within the encapsulated picture and is given in Appendix H.4 in the form of a Python script. We see that the interface concentration on the precipitate side is kept quasi-constant during the growth, see Fig. 3.10. This is enforced by the high curvature of the chemical free energy of the precipitate, k=100GJ.m^{-3}, see Table 3.1. On the matrix side, and when elastic stresses are accounted for, the concentration evolves with respect to the growth kinetics shown in Fig. 3.9. This is due to the fact that the operative tie-line is here dependent of the phase fraction. In parallel, the evolution of the matrix sided concentration for the case of pure diffusion is more rapid. The small differences between Voigt/Taylor and Reuss/Sachs schemes can be attributed to the extrapolation procedure of the diffuse concentration field. Moreover, interface concentrations for the case limited to diffusion are also illustrated and contrast with the case with elasticity for the matrix sided concentration. This emphasises the role played by stresses on the operative tie-line.

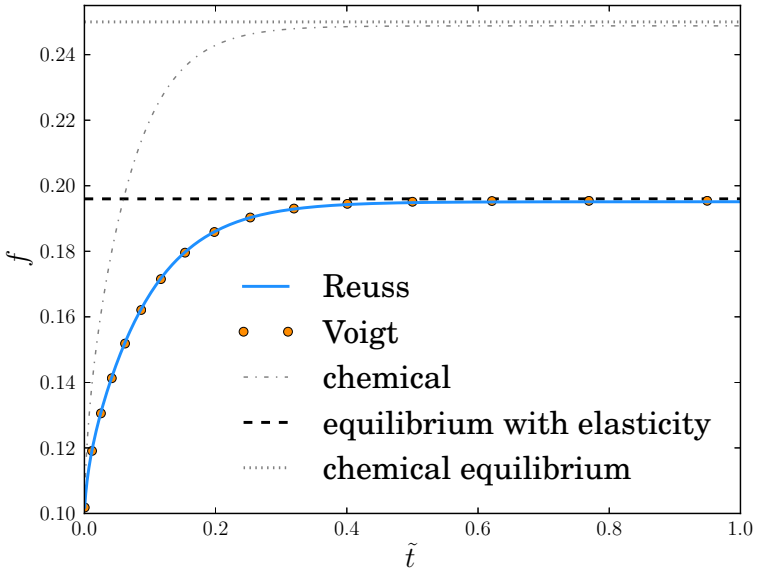

Figure 3.9: Parabolic evolution curves of a laminate precipitate growing in a supersaturated matrix for Voigt/Taylor and Reuss/Sachs approaches.

We have previously shown that the driving force for the phase field evolution is different for Voigt/Taylor and Reuss/Sachs approaches. Such driving forces were previously noted $F_\phi^{V,R}$, see Eqs. (3.52) and (3.79). In fact, it is more accurate to say that the coupled source terms of the phase field equation depend on the homogenisation approach. Therefore, the common terminology needs to be reformulated as it collides with the definition of the true phase transformation driving force, here $F^{V,R}$. The true driving force is given by the averaging of the quantity $F_\phi^{V,R}$ multiplied by the derivative

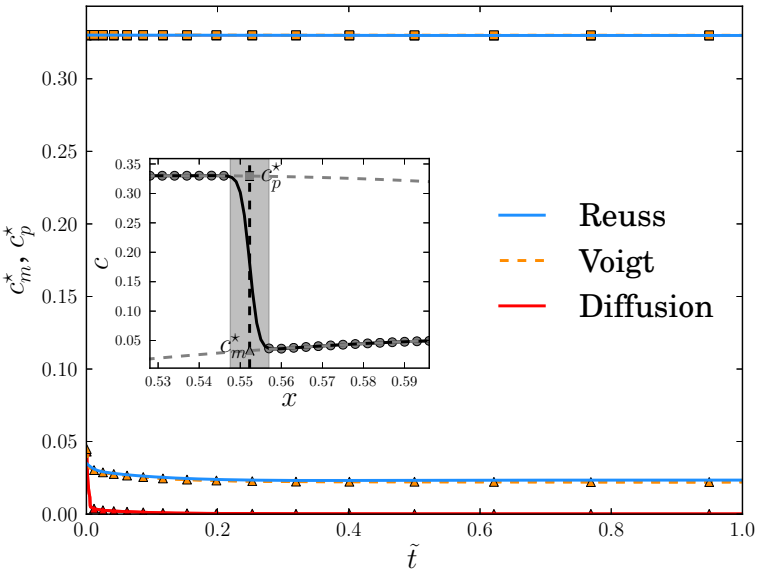

Figure 3.10: Evolution of the interface concentrations during the growth of a laminate precipitate in a supersaturated matrix. The interface concentrations – c_m^* and c_p^*, respectively matrix sided and precipitate sided – are extrapolated at the sharp interface limit following the procedure shown in the encapsulated picture. The concentrations above the encapsulated frame are the one of the precipitate, whereas the concentrations below correspond to the matrix sided ones.

of the interpolation function h' over the whole body:

$$F^{V,R} = \int_{-\infty}^{+\infty} h'(\phi) F_{\phi}^{V,R} dx. \tag{3.119}$$

This quantity is illustrated in Fig. 3.11. In this figure, it is shown that the phase transformation driving forces for both Voigt/Taylor and Reuss/Sachs schemes are close to each other[3] whereas the quantities $F_{\phi}^{V,R}$ are clearly different.

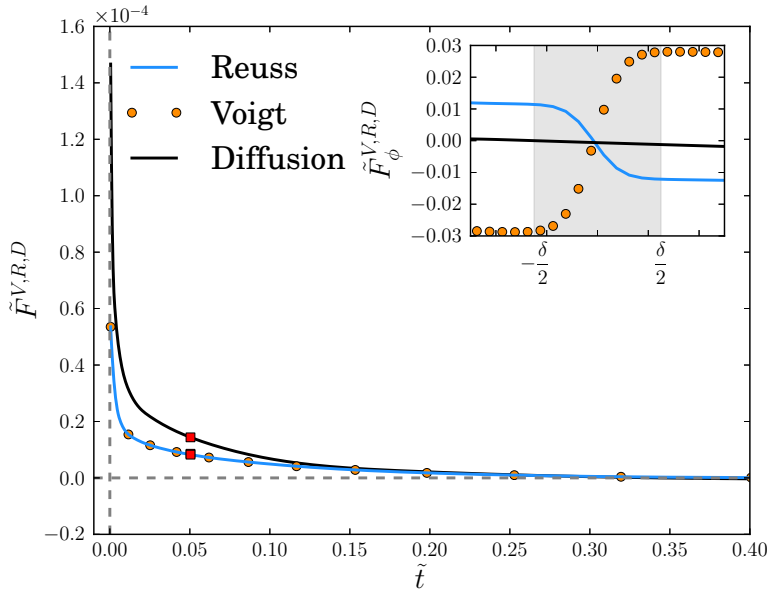

Figure 3.11: Evolution of the true driving force during the relaxation of the precipitate. The local driving forces for Voigt/Taylor and Reuss/Sachs approaches are superimposed for the times indicated by the red squares.

2D growth with elasticity

In the following, we show that the curvature of the interface influences the convergence rate towards the sharp interface limit. Here, Voigt/Taylor and Reuss/Sachs approaches are shown to converge at the first order in interface thickness δ. To this aim, the growth of a cylindrical misfitting precipitate embedded in a supersaturated matrix is considered (Case II). While the sample size is kept constant, the interface thickness is varied. In order to compare the evolution of the phase fractions for Voigt/Taylor and Reuss/Sachs approaches, we define an accumulated relative error:

$$\text{Err} = \frac{1}{\tilde{t}_{\max}} \int_0^{\tilde{t}_{\max}} \frac{|f^V(t) - f^R(t)|}{f^V(t)} dt, \tag{3.120}$$

Several interface thicknesses are treated and we give here their dimensionless values that are 3.5%, 4.5%, 5.5%, 6.5% and 7% of 200 nm, which is the length of the finely meshed domain. While the interface thickness is decreased, one has to refine the mesh accordingly, which make computations below the quantity 3.5% barely tractable – the number of DoFs is proportional to $(1/\delta)^2$, where δ is the interface thickness. Moreover, the figure shows the extrapolation of the simulation results towards the sharp interface limit, on the basis of a linear regression. The present results emphasise the first order convergence towards the sharp interface limit.

[3] note that equal interface thicknesses has been considered here, see "Homogenisation of viscoplastic constitutive laws within phase field approaches" from Rancourt *et al* for more details

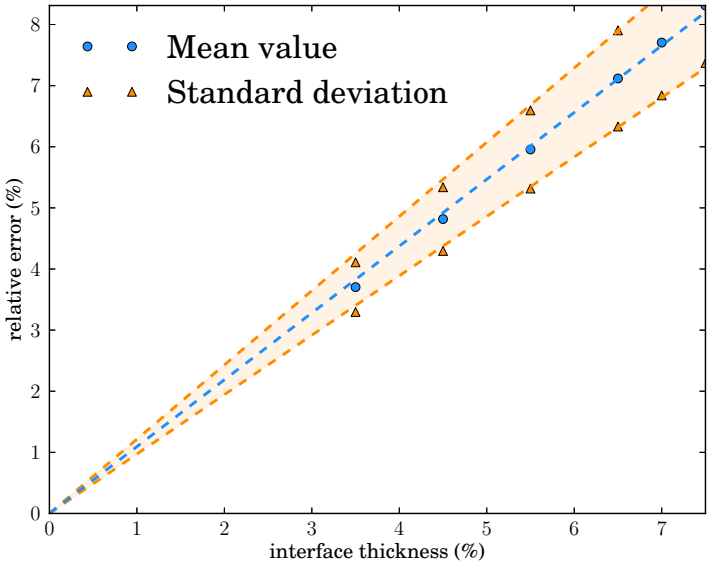

Figure 3.12: Influence of the interface thickness on the relative convergence of Reuss/Sachs and Voigt/Taylor schemes. Evaluation of the relative error between Voigt/Taylor and Reuss/Sachs approaches with respect to the interface thickness, and extrapolation of the corresponding rate of convergence through linear regression methods.

Preliminary analysis of plasticity

With a view to perform computations including the effects of viscoplasticity, the von Mises stress fields resulting from the elastic Case I are analysed. Possible differences between Voigt/Taylor and Reuss/Sachs approaches can arise when plasticity is considered due to different von Mises stresses. In the cases of the Voigt/Taylor approach, the activation of plasticity is here performed from the von Mises stress of the respective phases – that are $\sigma^{\alpha}_{\mathrm{VM}}$ and $\sigma^{\beta}_{\mathrm{VM}}$ – accordingly to the constitutive laws and the present dissipation potential. Nevertheless, the von Mises stress of the effective stress field could be used instead from the formulation of a new dissipation potential. In the case of a two phased system α-β, all von Mises stress fields are illustrated in Fig. 3.13. Such a preliminary result shows some deviations between the different von Mises stresses inside the interface. Differences of the growth rate curves have occurred depending on the choice of the von Mises stress field in the case of viscoplasticity in preliminary simulations. The activation of plasticity will then need to be investigated in more details in a future work. In the following study, plastic activation has been chosen to be done by the von Mises stresses of the phases accordingly to the theory developed in the present chapter. It will be verified that the simulations, in the case of viscoplasticity are well converged in terms of mesh resolution, time stepping and interface thickness. The question of the choice of yield stress inside the interface is left open, for simplicity.

3.9.2 Isotropic viscoplastic phase in contact with an elastic phase

Cases I and II are now enhanced with a viscoplastic behaviour based on a power-law creep restricted to one phase only, see Eq. (3.46). The study is here restricted to the Voigt/Taylor approach. Viscoplasticity will be assumed to be activated either within the precipitate or within the matrix. The effect of the viscosity parameter K in the range [10-100000] MPa.s$^{1/n}$ is investigated, while the parameter n remains always equal to 5.

We also included the cases of pure diffusion and diffusion along with elasticity as reference cases throughout the present study – here referred as the diffusion and elastic reference cases. We show that viscosity makes the growth curves to shift from the elastic reference case to the diffusion refer-

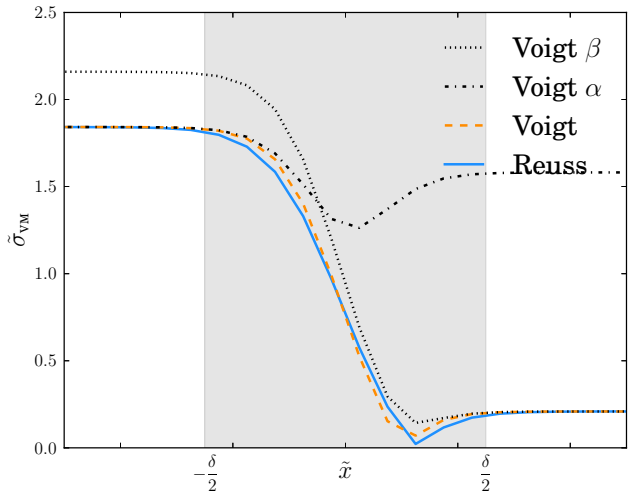

Figure 3.13: Plot of the von Mises stress for Reuss/Sachs and Voigt/Taylor schemes throughout the interface. In the Voigt/Taylor approach, three stress fields are available for the separate phases along with the averaged one. The phase α is located on the left hand side of the interface.

ence case, see Fig. 3.14. The growth kinetics curves for the elastic and diffusion reference cases are illustrated in the figure using solid lines marked with triangles and squares respectively.

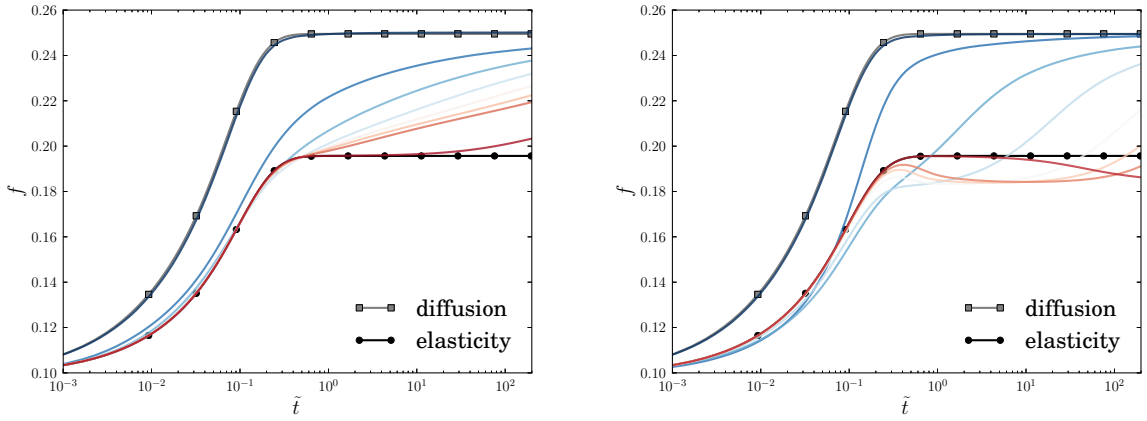

(a) (b)

Figure 3.14: Evolution of the phase fraction with respect to a logarithmic dimensionless time with varying viscosities in (a) the precipitate (b) the matrix. Colours gradients illustrate the viscosity, the material becomes more and more viscous – or rate dependent – from the blue to the red curves.

The present simulations have been performed for an interface thickness of 5 nm, which represents 2.5% of the total sample length. The curves emphasise the competition between the transient regime for diffusion and the one for stress relaxation. The higher the viscosity, the higher the characteristic time for the stress relaxation. Characteristic times for diffusion τ_d and for viscosity τ_v can be defined as follows,

$$\tau_d = \frac{L^2}{D} \qquad \text{and} \qquad \tau_v = \left(\frac{K}{E}\right)^n \tag{3.121}$$

where L is a characteristic length in the problem, D the diffusivity, K and n the viscosity parameters and E the Young modulus.

The Fig. 3.14 (a) illustrates the influence of the relaxation time on the growth kinetics. It results in a beam of curves lying inbetween the elastic and chemical cases. The result is expected and can be

interpreted as the gradual lost of stresses effects due to their relaxation.

The second case, see Fig. 3.14 (b), shows a different behaviour. For high viscosities – when $\tau_d \ll \tau_v$ –, the phase fraction can first go below the one for the elastic case, see Fig. 3.14 (b). Moreover, for higher viscosities, the phase fraction can significantly decrease to a plateau value. This indicates a backward motion of the growing phase and then a further growth of it.

The plateau value is due a spurious effect within the interface. In fact, viscoplasticity is rapidly activated within the interface in the precipitate's side due to a higher von Mises stress. The resulting stress relaxation skews the driving force and routs the interface. With time, sufficient viscoplastic relaxation levels in the matrix side are able to reroute the interface. Such a spurious phenomenon becomes negligible when the characteristic time for viscoplasticity is small regarding the interface motion and if the von Mises stress is higher within the viscoplastic phase as seen in case of a viscoplastic precipitate.

Mesh and time stepping sensitivity analyses have been performed to validate the present results. In the following, the influence of the interface thickness is studied for the worst case that is the viscoplastic matrix for several viscosities. The viscosities are K= [9000, 2000] MPa.s$^{1/5}$ and the results are illustrated in Fig. 3.15. The figure shows the convergence of the simulations with the decrease of the interface thickness. The rate of convergence to the sharp interface limit has been verified and a small

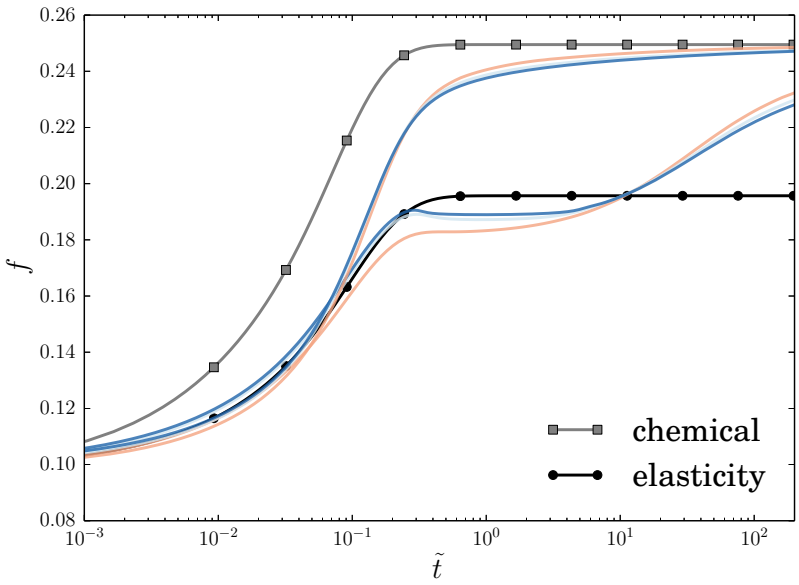

Figure 3.15: Interface thickness sensitivity analysis for different viscosities K= 9000, 2000 MPa.s$^{1/n}$. The red curves are for large interfaces and the blue ones for small interfaces. The dimensionless interfaces are set to 0.5%, 1% and 2.5% of 200 nm. A logarithmic time scale is here used.

dependency on viscosity has been found. As a matter of facts, the smaller the viscosity, the better the convergence to the sharp interface limit. It has been found that the range [100-2000] MPa.s$^{1/5}$ showed a good rate of convergence towards the sharp interface limit. Such a range of viscosities is shown to ensure quantitative computations.

In the following computations, viscosities are restricted to the viscosity interval [100-2000] MPa.s$^{1/n}$ with n = 5. We consider the growth for the Case II including viscosity in one phase only, for simplicity. In addition to that, a yield stress R_0 = 200 MPa is introduced into the power-law creep constitutive law. The two dimensional viscoplastic growth kinetics is illustrated in Fig. 3.16, where the cases of the viscoplastic precipitate and of the viscoplastic matrix have been studied.

Fig. 3.16 (a) shows the growth kinetics for the viscoplastic matrix, whereas Fig. 3.16 (b) shows the growth kinetics for the viscoplastic precipitate, each featuring the elastic and diffusion reference behaviours and the viscoplastic regimes. The study is here limited to the transient regime. The asymptotic behaviour can be inferred from the previous unidimensional simulations, but remains to be

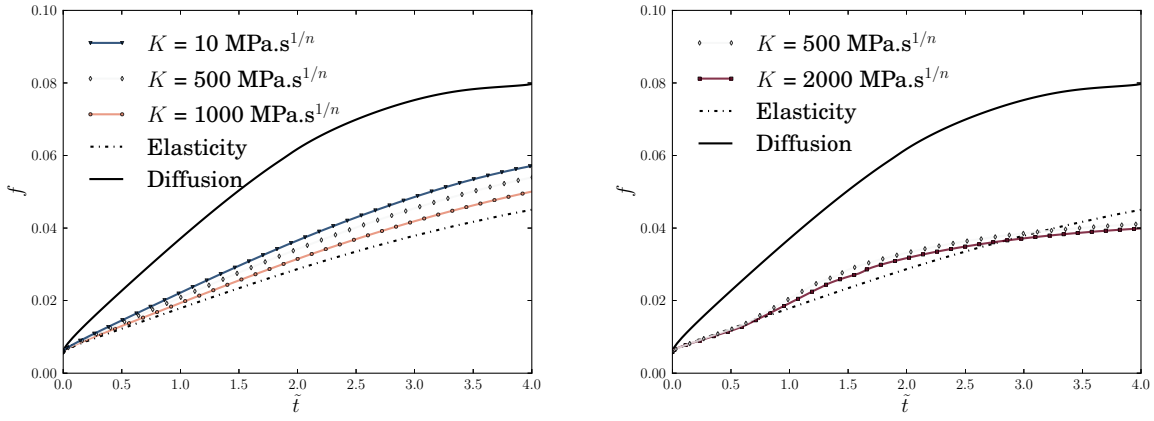

(a) (b)

Figure 3.16: Evolution of the phase fraction with varying viscosities for (a) the matrix (b) the precipitate.

studied in more detail. On the left figure, the viscoplastic regimes are shown to be localised in between the elastic and diffusion reference cases, which is expected. Moreover, the growth kinetics is parabolic. The shape evolution along with the evolution of the fields for the case of the viscoplastic matrix is illustrated in Fig. 3.17 and 3.18. On the right hand side, the case of the viscoplastic precipitate is shown to first follow the elastic regime and then shifts to another growth regime, which goes below the elastic regime. This is due to the fact that a morphological shape instability has been triggered. The morphological – or shape – instability of the viscoplastic precipitate is shown in Fig. 3.19 and 3.20. Such a shape instability is dependent of the mesh anisotropy – here a squared grid. Another mesh geometry has been studied leaving the shape instability to be triggered with an angle of 45° with respect the reference frame, but is not shown in this work. Finally, it has been checked that the instability is delayed by the addition of hardening within the viscoplastic precipitate, see Fig. 3.21 and 3.22. This instability is assumed to be of the type of a Mullins-Sekerka shape instability [Mullins and Sekerka, 1963] – or an Asaro-Tiller-Grinfeld instability, but has not been investigated in more detail as it is considered to be out of the scope of the work.

3.9.3 Anisotropic viscoplasticity of the matrix phase with embedded growing elastic precipitate

We have previously shown that isotropic viscoplasticity can lead to the destabilisation of the precipitate's morphology. A preliminary study of the effect of anisotropic viscoplasticity of the matrix phase is now performed. The macroscopic Norton behaviour is then replaced by the crystal plasticity framework. As commonly done in plane strain crystal plasticity, effective slip systems are here defined. In the case of a FCC lattice, we choose [101] and [010] respectively as abscissa and ordinate of the simulated domain. Three effective slip systems are then chosen. They are defined as follows, the $(\bar{1}1\bar{1})$ plane with the [110] & [011] directions for the slip system C, the (111) plane with the $[\bar{1}10]$ & $[01\bar{1}]$ directions for the slip system B and finally, the $(\bar{1}11)$ & $(11\bar{1})$ planes along with the [101] direction for the slip system A. Such slip systems are based on two effective slip systems to describe the effective octahedral slip (C and B) and one effective slip system to describe an effective slip along C and B (A). They are readily used in the literature, see [Flouriot et al., 2003, Shishvan et al., 2011] and illustrated in Fig. 3.23.

Material parameters for the crystal plasticity behaviour are given in Table 3.3.

Case with slip on A, B and C

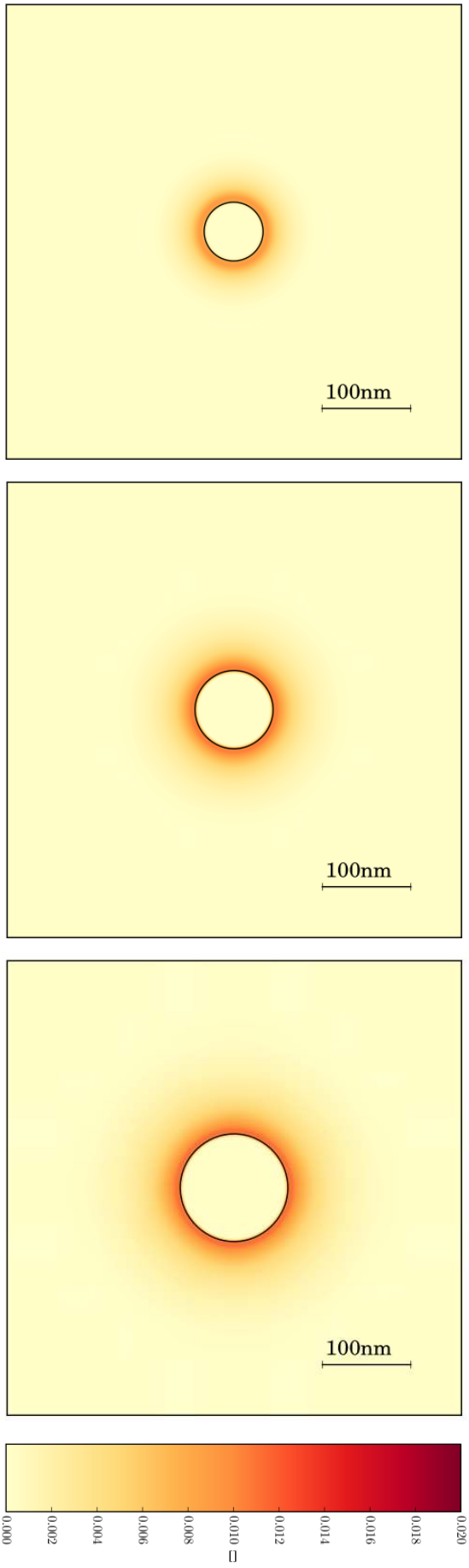

Figure 3.17: Evolution of accumulated viscoplastic slip $\gamma_{acc} = \sum \gamma_s$ for the viscoplastic matrix. The black line corresponds to the interface position $\phi = 0.5$.

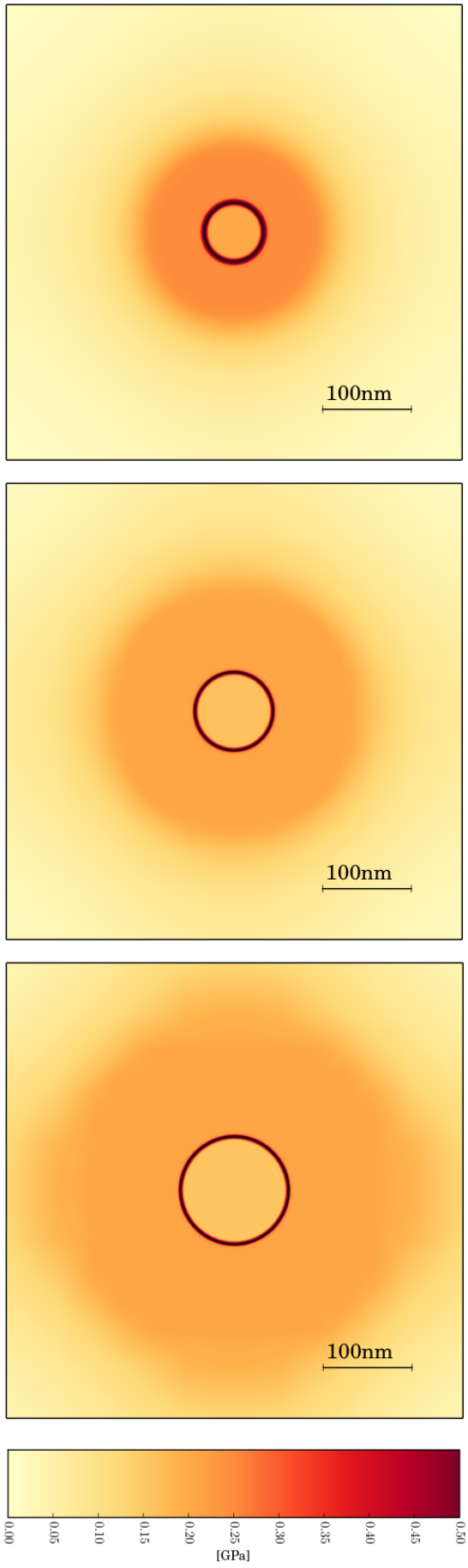

Figure 3.18: Evolution of von Mises stress for the viscoplastic matrix. The black line corresponds to the interface position $\phi = 0.5$.

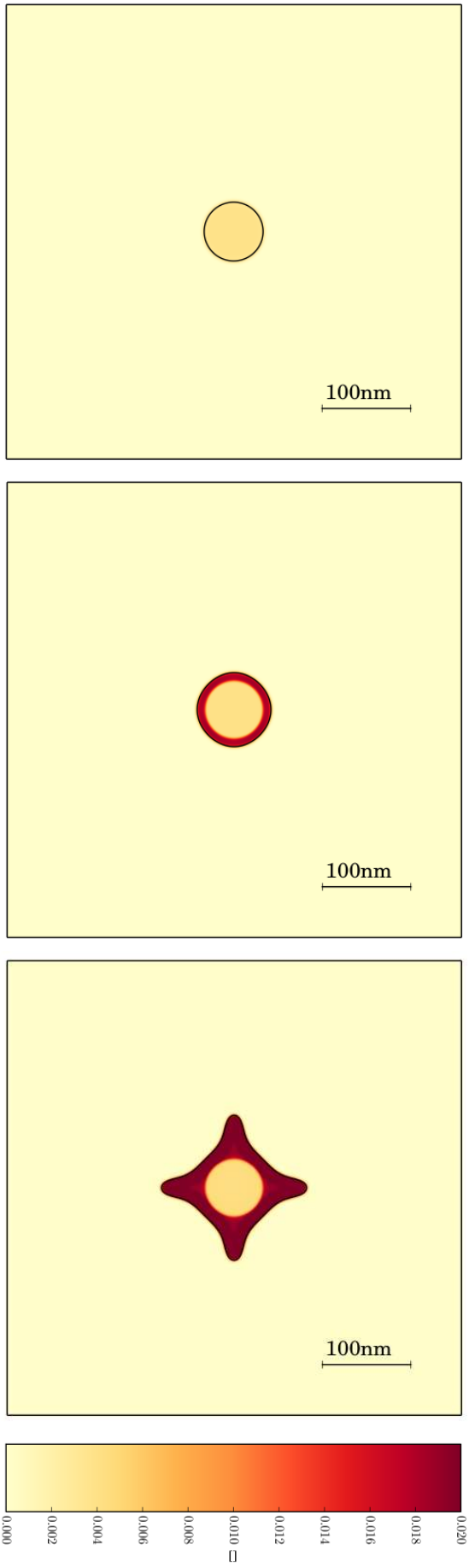

Figure 3.19: Evolution of accumulated viscoplastic slip for the viscoplastic precipitate. The black line corresponds to the interface position $\phi = 0.5$.

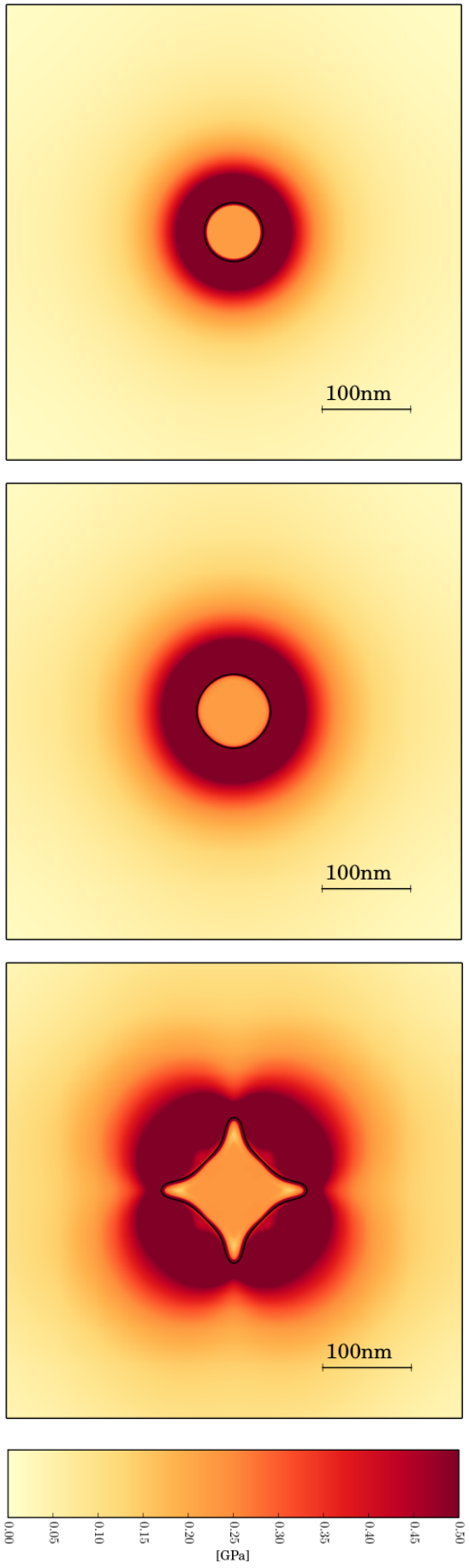

Figure 3.20: Evolution of the von Mises stress for the viscoplastic precipitate. The black line corresponds to the interface position $\phi = 0.5$.

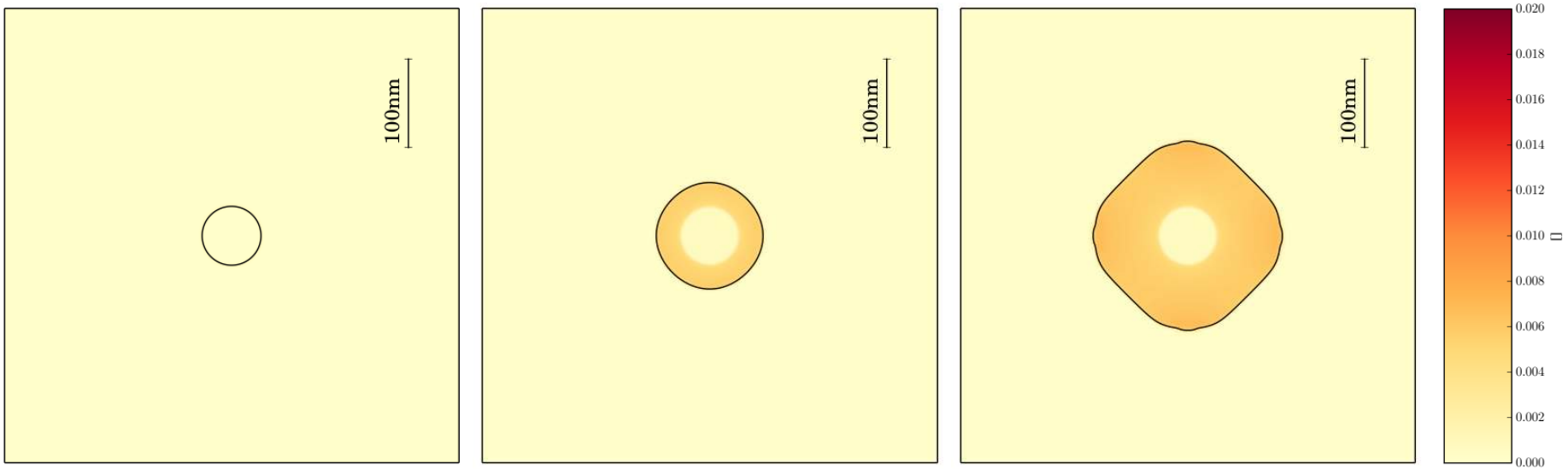

Figure 3.21: Delay of the morphological instability due to hardening within the viscoplastic precipitate. Evolution of accumulated viscoplastic slip for the viscoplastic precipitate using isotropic hardening with modulus $H = 150$ GPa. The black line corresponds to the interface position $\phi = 0.5$.

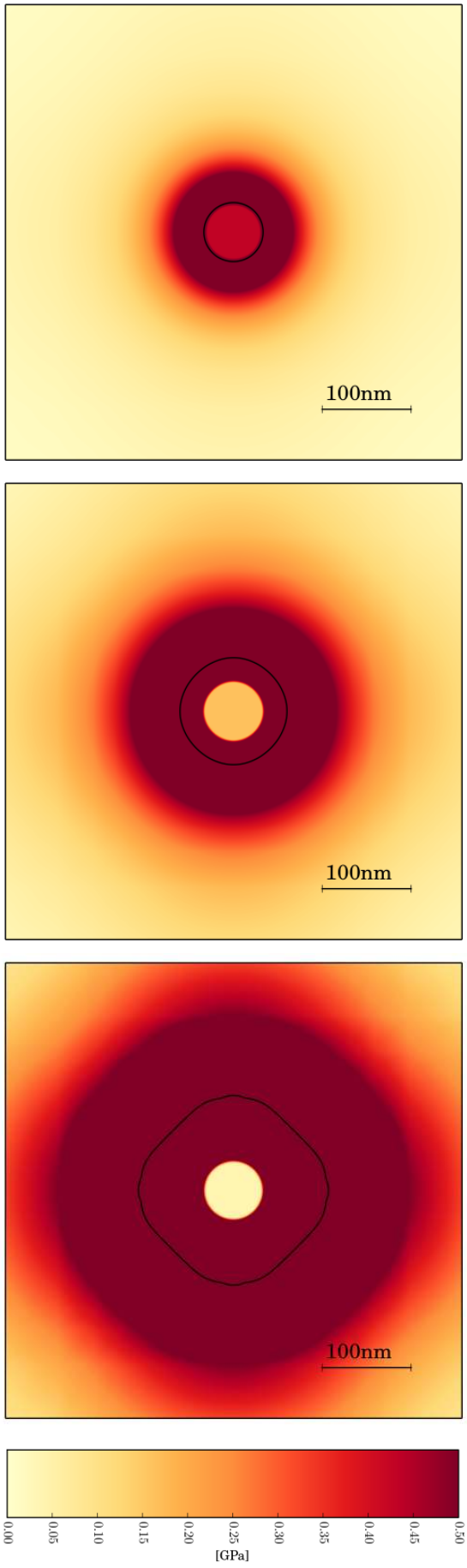

Figure 3.22: Delay of the morphological instability due to hardening within the viscoplastic precipitate. Evolution of the von Mises stress for the viscoplastic precipitate using isotropic hardening with modulus $H = 150$ GPa. The black line corresponds to the interface position $\phi = 0.5$.

K [MPa.s$^{1/n}$]	n [-]	S_0 [MPa]	Q [MPa]	b [-]	c [MPa]	d [-]	h_{rs} [-]
100	5	65	45	3	600	20	1

Table 3.3: Crystal plasticity parameters.

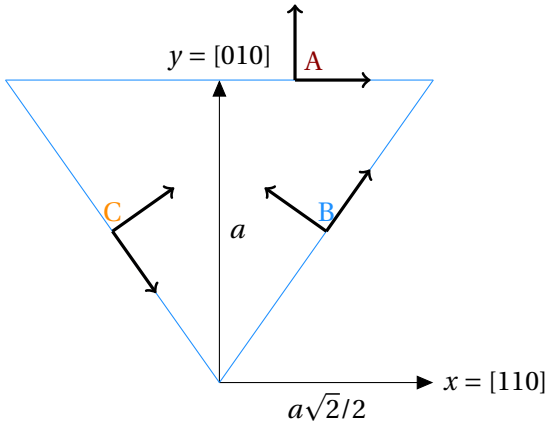

Figure 3.23: Illustration of the effective slip systems where a is the lattice parameter and the effective slip systems A, B and C are coplanar. The blue triangle represents an octahedral plane of the FCC lattice. The simulation plane is defined by the vectors x and y.

Figs. 3.24 and 3.25 illustrate the role of crystal plasticity. The slip is shown to be heterogeneous around the precipitate. A light faceting of the precipitate can be shown in the regions of highest slip. In fact, heterogeneous slip induces heterogeneous hardening of the matrix, which, in return impacts the operative tie-line and the growth locally. It is sufficient to explain the morphological change of the precipitate.

Case with slip on A only

Figs. 3.26 and 3.27 illustrate the role of crystal plasticity when a unique slip system is activated, here A. A slip band is generated given the direction of the slip system A and a kink band is also activated perpendicularly to the slip direction defined by A. This is due to the use of a symmetrised Schmid tensor in the driving force for slip. Such a behaviour is modified in the framework of finite strain for instance. Then, the same conclusions as for the case with three slip systems can be drawn. The slip induces an heterogeneous hardening which slows down the growth kinetics in return by the selection of another operative tie-line. Finally, the faceting of the precipitate occurs and the shape of the precipitate tends to be rectangular. It is worth noting that such a faceting can be followed by the decohesion of the precipitate.

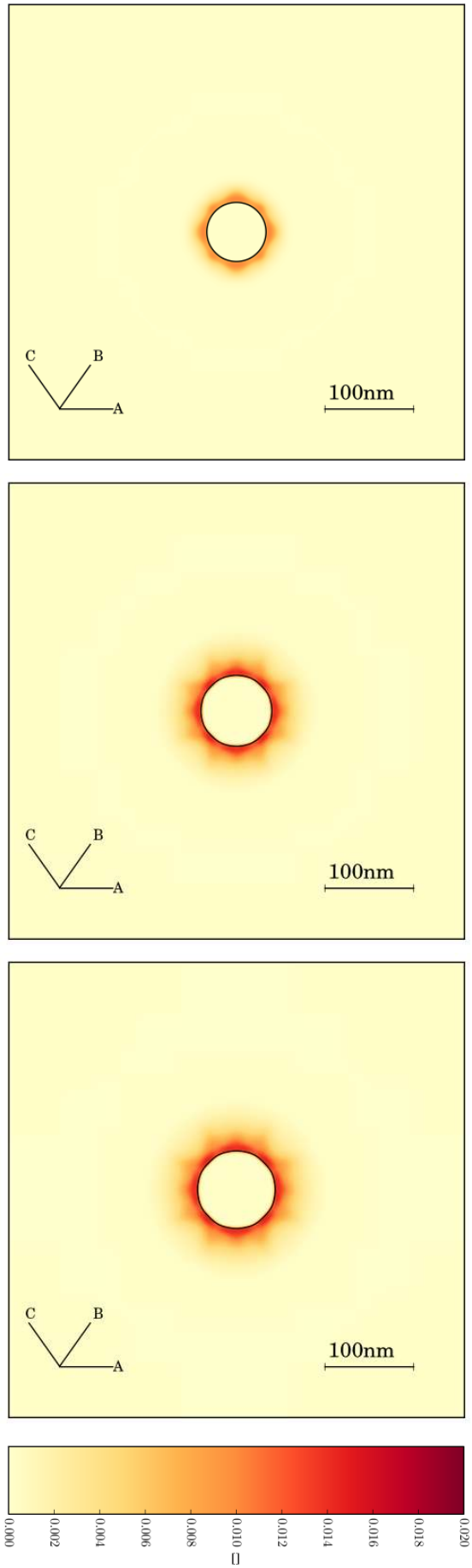

Figure 3.24: Growth of an elastic precipitate embedded in a supersaturated viscoplastic matrix, with a single crystalline behaviour. Maps of accumulated plastic slip in the matrix. The black line corresponds to the interface position $\phi = 0.5$.

Figure 3.25: Growth of an elastic precipitate embedded in a supersaturated viscoplastic matrix, with a single crystalline behaviour. Maps of the von Mises stresses. The black line corresponds to the interface position $\phi = 0.5$.

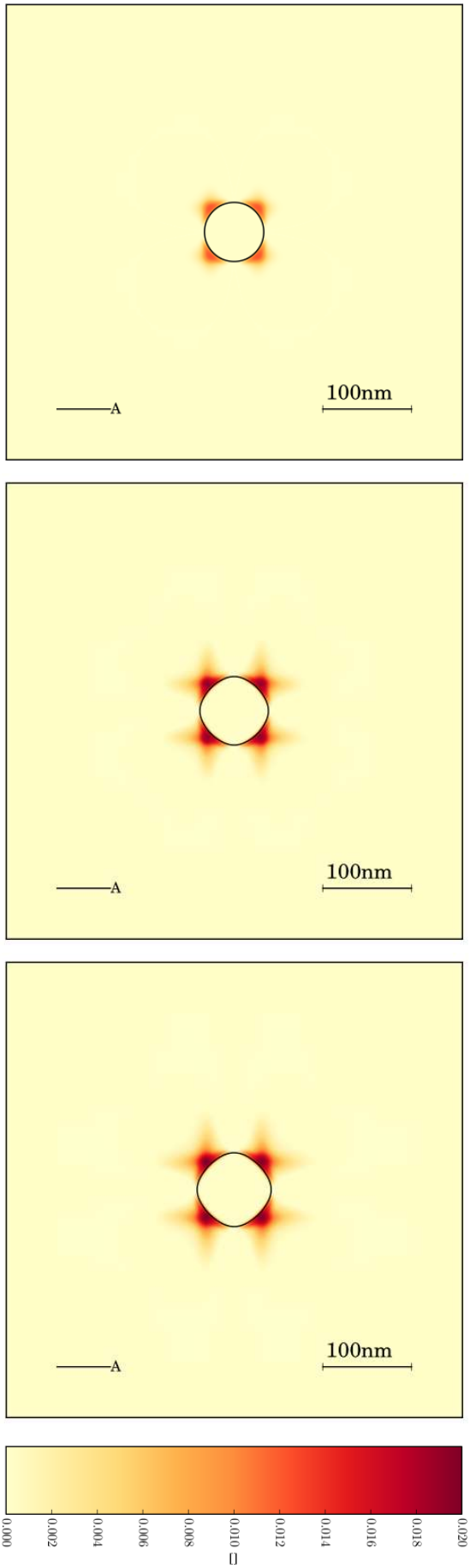

Figure 3.26: Growth of an elastic precipitate embedded in a supersaturated viscoplastic matrix, with a single crystalline behaviour. Maps of the accumulated plastic slip in the matrix. The black line corresponds to the interface position $\phi = 0.5$.

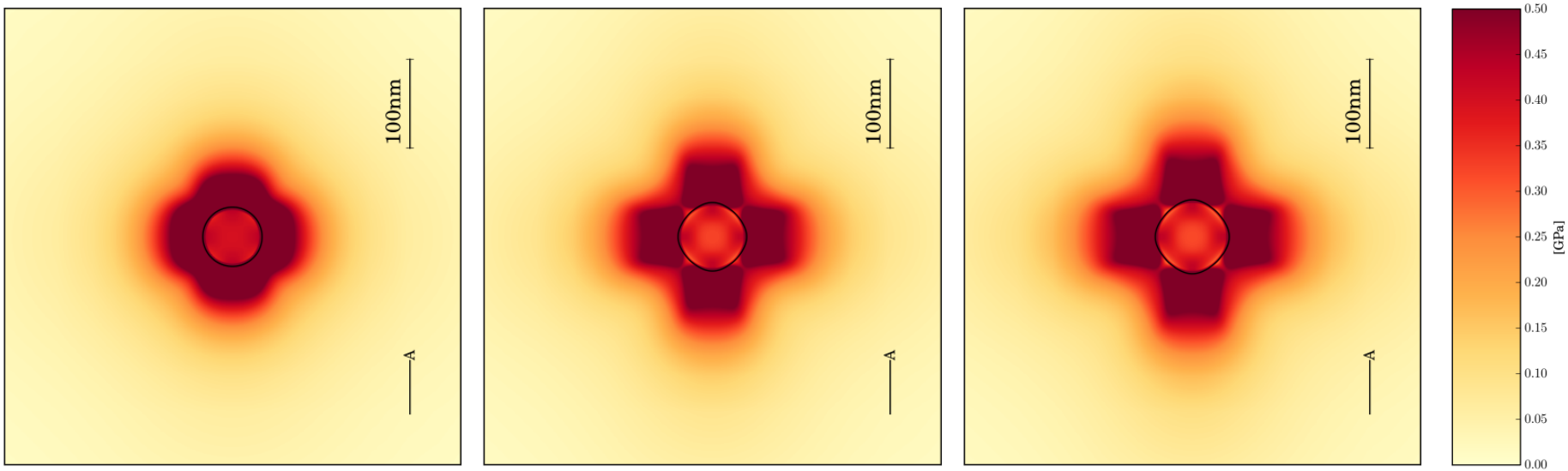

Figure 3.27: Growth of an elastic precipitate embedded in a supersaturated viscoplastic matrix, with a single crystalline behaviour. Maps of the von Mises stresses. The black line corresponds to the interface position $\phi = 0.5$.

3.10 Conclusions

The present chapter has been devoted to the formulation of a multicomponent-stress phase field framework, which accounts for the viscoplastic deformation of the phases on the basis of the homogenisation approach. Two phase field frameworks are built from the interpolation of different thermodynamic potentials, namely the Helmholz free energy and the Gibbs free energy. It is shown that The Clausius-Duhem relationship along with assumptions on non-dissipative phenomena provide the well-known homogenisation rules of Voigt/Taylor and Reuss/Sachs. The excess of elastic energy embedded in the Voigt/Taylor approach is identified and discussed. The evolutionary rules of the internal variables for viscoplasticity were obtained from the formulation of a dissipation potential, in the same spirit as what is done for the energy. It results that the internal variables of the individual phases are uncoupled from the phase field. The finite element implementation and the integration of the internal variables for both homogenisation approaches is discussed. It results that the Voigt/Taylor approach is more adapted to the Newton-Raphson algorithm. To compare both phase field models, finite element simulations restricted to the case of elasticity are performed. The results highlight a first order convergence to the sharp interface limit for the Voigt/Taylor and Reuss/Sachs approaches.

Preliminary finite element simulations, based on the Voigt/Taylor assumption, are performed in the case of viscoplasticity. The case of a growing precipitate embedded in a supersaturated matrix is thoroughly studied by separating the cases of a viscoplastic precipitate and a viscoplastic matrix. We show that the convergence towards the sharp interface limit is dependent viscoplasticity parameters. Therefore the simulations are then treated for a wide range of viscosity parameters. Quantitative two dimensional simulations of growing precipitates are then performed given reliable viscoplasticity parameters. The simulations show that the morphology of the growing precipitate depends on the viscoplasticity parameters. A morphological instability is also triggered when the precipitate becomes softer than the matrix phase. Faceting of the precipitate is also evidenced in the framework of crystal plasticity due to plastic anisotropy.

The present simulations are necessary for the forthcoming study of oxidation. As explained in Chapter 2, the growing oxide and the substrate can deform viscoplastically. The next simulations of oxide growth in the framework of homogenisation based on phase field approaches is *not* straightforward – which is also the case for interpolation based phase field approaches. One needs to clearly identify the influence of viscoplasticity. Parametric studies along with sensitivity analyses – mesh, time step, interface thickness – are thus needed. This chapter was devoted to such preliminary studies. The next chapter introduces the study of oxide growth in the built phase field approach. It is extended to multicomponent diffusion up to the simultaneous activation of plasticity in both phases along with mechanical loads. It is nevertheless restricted to the oxidation of single crystals, which is why only unidimensional simulations are performed.

References

[Abrivard et al., 2012a] Abrivard, G., Busso, E., Forest, S., and Appolaire, B. (2012a). Phase field modelling of grain boundary motion driven by curvature and stored energy gradients. Part I: Theory and numerical implementation. *Philosophical Magazine*, 92(28-30):3618–3642.

[Abrivard et al., 2012b] Abrivard, G., Busso, E., Forest, S., and Appolaire, B. (2012b). Phase field modelling of grain boundary motion driven by curvature and stored energy gradients. Part II: Application to recrystallisation. *Philosophical Magazine*, 92(28-30):3643–3664.

[Ammar et al., 2009a] Ammar, K., Appolaire, B., Cailletaud, G., Feyel, F., and Forest, S. (2009a). Finite element formulation of a phase field model based on the concept of generalized stresses. *Computational Materials Science*, 45(3):800 – 805.

[Ammar et al., 2009b] Ammar, K., Appolaire, B., Cailletaud, G., Feyel, F., and Forest, S. (2009b). Modélisation du couplage changement de phase-mécanique par la méthode des champs de phases et les techniques d'homogénéisation. In *Giens*.

[Ammar et al., 2009c] Ammar, K., Appolaire, B., Cailletaud, G., and Forest, S. (2009c). Combining phase field approach and homogenization methods for modelling phase transformation in elasto-plastic media. *European Journal of Computational Mechanics*, 18:485–523.

[Ammar et al., 2011] Ammar, K., Appolaire, B., Cailletaud, G., and Forest, S. (2011). Phase field modeling of elasto-plastic deformation induced by diffusion controlled growth of a misfitting spherical precipitate. *Philosophical Magazine Letters*, 91(3):164–172.

[Ammar et al., 2014] Ammar, K., Appolaire, B., Forest, S., Cottura, M., Le Bouar, Y., and Finel, A. (2014). Modelling inheritance of plastic deformation during migration of phase boundaries using a phase field method. *Meccanica*, 49(11):2699–2717.

[Asaro and Lubarda, 2006] Asaro, R. and Lubarda, V. (2006). *Mechanics of Solids and Materials*. University Press, Cambridge, UK.

[Aslan et al., 2011a] Aslan, O., Cordero, N. M., Gaubert, A., and Forest, S. (2011a). Micromorphic approach to single crystal plasticity and damage. *International Journal of Engineering Science*, 49:1311–1325.

[Aslan and Forest, 2009] Aslan, O. and Forest, S. (2009). Crack growth modelling in single crystals based on higher order continua. *Computational Materials Science*, 45:756–761.

[Aslan and Forest, 2011] Aslan, O. and Forest, S. (2011). The micromorphic versus phase field approach to gradient plasticity and damage with application to cracking in metal single crystals. In

de Borst, R. and Ramm, E., editors, *Multiscale Methods in Computational Mechanics*, pages 135–154. Lecture Notes in Applied and Computational Mechanics 55, Springer.

[Aslan et al., 2011b] Aslan, O., Quilici, S., and Forest, S. (2011b). Numerical modeling of fatigue crack growth in single crystals based on microdamage theory. *International Journal of Damage Mechanics*, 20(5):681–705.

[Besson, 2004] Besson, J. (2004). *Local approach to fracture*. Ecole des Mines de Paris–Les Presses.

[Besson et al., 2010] Besson, J., Cailletaud, G., Chaboche, J.-L., and Forest, S. (2010). *Nonlinear mechanics of materials*. Springer, 1 edition.

[Borden et al., 2012] Borden, M., Verhoosel, C., Scott, M., Hughes, T., and Landis, C. (2012). A phase-field description of dynamic brittle fracture. *Computer Methods in Applied Mechanics and Engineering*, 217–220:77–95.

[Borukhovich et al., 2014] Borukhovich, E., Engels, P., Boehlke, T., Shchyglo, O., and Steinbach, I. (2014). Large strain elasto-plasticity for diffuse interface models. *Modelling and Simulation in Materials Science and Engineering*, 22:034008.

[Busso and Cailletaud, 2005] Busso, E. and Cailletaud, G. (2005). On the selection of active slip systems in crystal plasticity. *International Journal of Plasticity*, 21(11):2212 – 2231.

[Busso and McClintock, 1996] Busso, E. and McClintock, F. (1996). A dislocation mechanics-based crystallographic model of a B2-type intermetallic alloy. *International Journal of Plasticity*, 12(1):1 – 28.

[Cahn and Hilliard, 1958] Cahn, J. and Hilliard, J. (1958). Free energy of nonuniform system. I. Interfacial free energy. *The Journal of Chemical Physics*, 28:258–267.

[Cahn and Larché, 1984] Cahn, J. and Larché, F. (1984). A simple model for coherent equilibrium. *Acta Metallurgica*, 32(11):1915 – 1923.

[Clarke, 2002] Clarke, D. (2002). Stress generation during high-temperature oxidation of metallic alloys. *Current Opinion in Solid State and Materials Science*, 6(3):237–244.

[Coleman and Noll, 1963] Coleman, B. and Noll, W. (1963). The thermodynamics of elastic materials with heat conduction and viscosity. *Arch. Rational Mech. and Anal.*, 13:167–178.

[Cottura et al., 2012] Cottura, M., Le Bouar, Y., Finel, A., Appolaire, B., Ammar, K., and Forest, S. (2012). A phase field model incorporating strain gradient viscoplasticity: Application to rafting in Ni-base superalloys. *Journal of the Mechanics and Physics of Solids*, 60(7):1243 – 1256.

[de Groot and Mazur, 1962] de Groot, S. and Mazur, P. (1962). *Non–equilibrium thermodynamics*. North Holland–Dover.

[Dreyer and Müller, 2000] Dreyer, W. and Müller, W. (2000). A study of the coarsening in tin/lead solders. *Int. J. Solids Structures*, 37:3841–3871.

[Durga et al., 2013] Durga, A., Wollants, P., and Moelans, N. (2013). Evaluation of interfacial excess contributions in different phase-field models for elastically inhomogeneous systems. *Modelling and Simulation in Materials Science and Engineering*, 21(5):055018.

[Finel et al., 2010] Finel, A., Le Bouar, Y., Gaubert, A., and Salman, U. (2010). Phase field methods: Microstructures, mechanical properties and complexity. *Comptes Rendus Physique*, 11:245–256.

[Flouriot et al., 2003] Flouriot, S., Forest, S., Cailletaud, G., Koster, A., Rémy, L., Burgardt, B., Gros, V., Mosset, S., and Delautre, J. (2003). Strain localization at the crack tip in single crystal CT specimens under monotonous loading: 3D finite element analyses and application to nickel-base superalloys. *International Journal of Fracture*, 124(1-2):43–77.

[Forest, 2009] Forest, S. (2009). The micromorphic approach for gradient elasticity, viscoplasticity and damage. *ASCE Journal of Engineering Mechanics*, 135:117–131.

[Forest et al., 2011] Forest, S., Ammar, K., and Appolaire, B. (2011). Micromorphic vs. phase-field approaches for gradient viscoplasticity and phase transformations. In Markert, B., editor, *Advances in Extended and Multifield Theories for Continua*, volume 59 of *Lecture Notes in Applied and Computational Mechanics*, pages 69–88. Springer Berlin Heidelberg.

[Forest et al., 2014] Forest, S., Ammar, K., Appolaire, B., Cordero, N., and Gaubert, A. (2014). Micromorphic approach to crystal plasticity and phase transformation. In Schroeder, J. and Hackl, K., editors, *Plasticity and beyond*, pages 131–198. CISM International Centre for Mechanical Sciences, Courses and Lectures No. 550, Springer.

[François et al., 2012] François, F., Pineau, A., and Zaoui, A. (2012). *Mechanical Behaviour of Materials. Volume 1: Micro and Macroscopic Constitutive Behaviour*. Solid Mechanics and its Applications, Vol. 180. Springer.

[Frolov and Mishin, 2012] Frolov, T. and Mishin, Y. (2012). Thermodynamics of coherent interfaces under mechanical stresses. I. Theory. *Phys. Rev. B*, 85:224106.

[Gaubert et al., 2008] Gaubert, A., Finel, A., Le Bouar, Y., and Boussinot, G. (2008). Viscoplastic phase field modelling of rafting in Ni-base superalloys. In Jeulin, D. and Forest, S., editors, *Continuum Models and Discrete Systems CMDS11*, pages 161–166. Mines Paris Les Presses.

[Gaubert et al., 2010] Gaubert, A., Le Bouar, Y., and Finel, A. (2010). Coupling phase field and viscoplasticity to study rafting in Ni-based superalloys. *Philosophical Magazine*, 90(1-4):375–404.

[Germain et al., 1983] Germain, P., Nguyen, Q., and Suquet, P. (1983). Continuum thermodynamics. *J. of Applied Mechanics*, 50:1010–1020.

[Guo et al., 2005] Guo, X., Shi, S., and Ma, X. (2005). Elastoplastic phase field model for microstructure evolution. *Applied Physics Letters*, 87(22):–.

[Guo et al., 2008] Guo, X., Shi, S., Zhang, Q., and Ma, X. (2008). An elastoplastic phase-field model for the evolution of hydride precipitation in zirconium, part i: smooth specimens. *Journal of Nuclear Materials*, 378:110–119.

[Gurtin, 1996] Gurtin, M. (1996). Generalized Ginzburg-Landau and Cahn-Hilliard equations based on a microforce balance. *Physica D: Nonlinear Phenomena*, 92(34):178 – 192.

[Halphen and Nguyen, 1975] Halphen, B. and Nguyen, Q. (1975). Sur les matériaux standard généralisés. *Journal de Mécanique*, 14:39–63.

[Hofacker and Miehe, 2012] Hofacker, M. and Miehe, C. (2012). Continuum phase field modeling of dynamic fracture: Variational principles and staggered FE implementation. *International Journal of Fracture*, 178:113–129.

[Hofacker and Miehe, 2013] Hofacker, M. and Miehe, C. (2013). A phase field model of dynamic fracture: Robust field updates for the analysis of complex crack patterns. *International Journal for Numerical Methods in Engineering*, 93:276–301.

[Hu and Chen, 2001] Hu, S. Y. and Chen, L. Q. (2001). A phase field model for evolving microstructures with strong elastic inhomogeneity. *Acta Metallurgica*, 49:1879–1890.

[Johnson, 1987] Johnson, W. (1987). Precipitate shape evolution under applied stress-thermodynamics and kinetics. *Metallurgical Transactions A*, 18(2):233–247.

[Kim et al., 1999] Kim, S., Kim, W., and Suzuki, T. (1999). Phase-field model for binary alloys. *Phys. Rev. E*, 60:7186–7197.

[Kundin et al., 2011] Kundin, J., Raabe, D., and Emmerich, H. (2011). A phase-field model for incoherent martensitic transformations including plastic accommodation processes in the austenite. *Journal of the Mechanics and Physics of Solids*, 59:2082–2102.

[Lemaitre and Chaboche, 1994] Lemaitre, J. and Chaboche, J.-L. (1994). *Mechanics of Solid Materials*. University Press, Cambridge, UK.

[Lemaitre and Desmorat, 2004] Lemaitre, J. and Desmorat, R. (2004). *Engineering damage mechanics: Ductile, Creep, Fatigue and Brittle Failures*. Springer Verlag, Berlin.

[Maugin, 1992] Maugin, G. A. (1992). *Thermomechanics of plasticity and fracture*. Cambridge University Press.

[Maugin, 1999] Maugin, G. A. (1999). *Thermomechanics of nonlinear irreversible behaviors*. World Scientific.

[Méric et al., 1991a] Méric, L., Poubanne, P., and Cailletaud, G. (1991a). Single crystal modeling for structural calculations: Part 1, model presentation. *Journal of engineering materials and technology*, 113:162–170.

[Méric et al., 1991b] Méric, L., Poubanne, P., and Cailletaud, G. (1991b). Single crystal modeling for structural calculations: Part 2, finite element implementation. *Journal of engineering materials and technology*, 113:162–170.

[Miehe et al., 2010a] Miehe, C., Hofacker, M., and Welschinger, F. (2010a). A phase field model for rate-independent crack propagation: Robust algorithmic implementation based on operator splits. *Computer Methods in Applied Mechanics and Engineering*, 199(45-48):2765–2778.

[Miehe et al., 2010b] Miehe, C., Welchinger, F., and Hofacker, M. (2010b). Thermodynamically–consistent phase field models of fracture: Variational principles and multifield FE implementations. *International Journal for Numerical Methods in Engineering*, 83:1273–1311.

[Mosler et al., 2014] Mosler, J., Shchyglo, O., and Montazer Hojjat, H. (2014). A novel homogenization method for phase field approaches based on partial rank-one relaxation. *Journal of the Mechanics and Physics of Solids*, 68(0):251–266.

[Müller, 2001] Müller, I. (2001). Thermodynamics of mixtures and phase field theory. *International Journal of Solids and Structures*, 38(67):1105 – 1113.

[Mullins and Sekerka, 1963] Mullins, W. and Sekerka, R. (1963). Morphological Stability of a Particle Growing by Diffusion or Heat Flow. *Journal of Applied Physics*, 34:323–329.

[Plapp, 2011] Plapp, M. (2011). Unified derivation of phase-field models for alloy solidification from a grand-potential functional. *PRE*, 84(3):031601.

[Pommier et al., 2015] Pommier, H., Busso, E., and Morgeneyer, T. (2015). A viscoplastic constitutive model based on evolving microstructural length scales: Application to AISI 316L austenitic stainless steel. *In Preparation*.

[Qu and Cherkaoui, 2006] Qu, J. and Cherkaoui, M. (2006). *Fundamentals of micromechanics of solids*. John Wiley & Sons Inc, Hoboken.

[Sanchez-Palencia and Zaoui, 1987] Sanchez-Palencia, E. and Zaoui, A. (1987). *Homogenization techniques for composite media*. Lecture Notes in Physics No. 272, Springer, Berlin.

[Shishvan et al., 2011] Shishvan, S., Mohammadi, S., Rahimian, M., and Van der Giessen, E. (2011). Plane-strain discrete dislocation plasticity incorporating anisotropic elasticity. *International Journal of Solids and Structures*, 48(2):374 – 387.

[Spatschek and Eidel, 2013] Spatschek, R. and Eidel, B. (2013). Driving forces for interface kinetics and phase field models. *International Journal of Solids and Structures*, 50(1415):2424 – 2436.

[Steinbach, 2009] Steinbach, I. (2009). Phase-field models in materials science. *Modelling and Simulation in Materials Science and Engineering*, 17(7):073001.

[Steinbach and Apel, 2006] Steinbach, I. and Apel, M. (2006). Multi phase field model for solid state transformation with elastic strain. *Physica D: Nonlinear Phenomena*, 217(2):153 – 160.

[Steinbach and Shchyglo, 2011] Steinbach, I. and Shchyglo, O. (2011). Phase-field modelling of microstructure evolution in solids: Perspectives and challenges. *Current Opinion in Solid State and Materials Science*, 15:87–92.

[Stiemer et al., 2010] Stiemer, M., Grosse-Woehrmann, A., Gladkov, S., Svendsen, B., Spatschek, R., and Steinbach, I. (2010). Efficient and reliable finite element techniques for phase field models. *International Journal of Materials Research*, 101:498–502.

[T. Uehara et al., 2007] T. Uehara, T., Tsujino, T., and Ohno, N. (2007). Elasto-plastic simulation of stress evolution during grain growth using a phase field model. *Journal of Crystal Growth*, 300:530–537.

[Tiaden et al., 1998] Tiaden, J., Nestler, B., Diepers, H., and Steinbach, I. (1998). The multiphase-field model with an integrated concept for modelling solute diffusion. *Physica D: Nonlinear Phenomena*, 115(12):73 – 86.

[Ubachs et al., 2004] Ubachs, R., Schreurs, P., and Geers, M. (2004). A nonlocal diffuse interface model for microstructure evolution of tin–lead solder. *Journal of the Mechanics and Physics of Solids*, 52:1763–1792.

[Ubachs et al., 2005] Ubachs, R., Schreurs, P., and Geers, M. (2005). Phase field dependent viscoplastic behaviour of solder alloys. *International Journal of Solids and Structures*, 42:2533–2558.

[Vignollet et al., 2014] Vignollet, J., May, S., Borst, R. d., and Verhoosel, C. (2014). Phase–field models for brittle and cohesive fracture. *Meccanica*.

[Villani et al., 2014] Villani, A., Busso, E., Ammar, K., Forest, S., and Geers, M. (2014). A fully coupled diffusional-mechanical formulation: numerical implementation, analytical validation, and effects of plasticity on equilibrium. *Archive of Applied Mechanics*, 84(9-11):1647–1664.

[Voyiadjis and Mozaffari, 2013] Voyiadjis, G. and Mozaffari, N. (2013). Nonlocal damage model using the phase field method: Theory and applications. *Int. J. Solids Structures*, 50:3136–3151.

[Wang and Khachaturyan, 1995] Wang, Y. and Khachaturyan, A. (1995). Shape instability during precipitate growth in coherent solids. *Acta Metall. mater.*, 43(5):1837–1857.

[Wang et al., 1993] Wang, Y., Khachaturyan, A., and Morris, J. J. (1993). Kinetics of strain-induced morphological transformation in cubic alloys with a miscibility gap. *Acta metall. mater.*, 41:279–296.

[Zaoui, 2002] Zaoui, A. (2002). Continuum micromechanics: Survey. *ASCE Journal of Engineering Mechanics*, 128:808–816.

[Zhou et al., 2008] Zhou, N., Shen, C., Mills, M., and Wang, Y. (2008). Contributions from elastic inhomogeneity and from plasticity to γ' rafting in single-crystal Ni–Al. *Acta Materialia*, 56(20):6156–6173.

CHAPTER

4 Application to oxidation of austenitic stainless steels single crystals under mechanical load

Contents

Ce chapitre est dédié à l'étude du mécanisme de la croissance interne d'une couche d'oxyde Cr_2O_3 dans un substrat composé d'un acier austénitique monocristallin. La théorie des champs de phases développée au cours du chapitre précédent est appliquée aux systèmes ternaire (Fe-Cr-O) et quaternaire (Fe-Cr-Ni-O) à haute température (900°C). Dans chacun des systèmes, deux phases sont considérées. Ces phases sont l'oxyde Cr_2O_3 en croissance dans un substrat austénitique γ-Fe. Dans un premier temps, il est fait abstraction des contraintes mécaniques pour simplifier la compréhension de la notion d'équilibre local. L'équilibre local est essentiel pour la caractérisation de la cinétique de croissance de transformations de phases pilotées par la diffusion. En effet, il décrit le déplacement des concentrations à l'interface lequelles sont désignées par la conode d'équilibre appelée conode opérative. L'espace des conodes opératives est de fait inclus dans l'espace des conodes qui est lui-même déterminé par la topologie du diagramme de phase (cf. chap. 2). La conode opérative se calcule avec la donnée des mobilités de diffusion – ou diffusivités – des constituants. Des explications plus détaillées sont données par [Perevoshchikova, 2012]. L'établissement de cet équilibre local est suivi par la modification des gradients des champs de concentration de part et d'autre de l'interface. Dans le cas chimique pur, il est montré que le système quaternaire présente un enrichissement en nickel proche de l'interface ainsi qu'une cinétique de croissance proche du cas ternaire. Ainsi, le nickel a peu d'effet, si bien qu'il sera négligé par la suite. Il est ensuite fait état de la dépletion en chrome – qui admet une solution analytique pour le présent cas unidimensionnel – qui est de l'ordre de quelques pourcents.

La superposition des contraintes mécaniques entraînant une modification du diagramme de phase, [Larché and Cahn, 1985], un nouvel équilibre local peut-être obtenu. Il est montré que la cinétique de croissance est peu impactée par les contraintes de croissance et aussi par les contraintes générées par un chargement mécanique ce qui peut être imputé à la stœchiométrie de l'oxyde. Finalement, l'évolution des contraintes au cours de l'oxydation est étudiée. Des simulations par éléments finis sont effectuées en prenant en compte les effets de la viscoplasticité et en étudiant diverses hypothèses sur les comportements mécaniques. Des chargements mécaniques variés sont étudiés et il résulte que la déformation viscoplastique du substrat peut entraîner de fortes contraintes de tension dans l'oxyde. Il est ainsi nécessaire de prendre en compte à l'avenir l'endommagement de la couche d'oxyde.

The present chapter is devoted to the growth of Cr_2O_3 inside an austenitic stainless steel. To this aim, the phase field framework, which has been developed in the previous chapter, is applied to the multicomponent systems (Fe-Cr-O) and (Fe-Cr-O-Ni). Each system embeds two phases, Cr_2O_3 and γ-Fe, for simplicity. The two aforementioned phases are hence accounted for by a single phase field variable ϕ. The phase field variable – or order parameter – is set to 0 within the substrate γ-Fe and 1 within the oxide Cr_2O_3. Oxide growth is simultaneously controlled by the supply of chromium and oxygen on each side of the metal-oxide interface. To this aim, the ternary system accounts for chromium and oxygen diffusion, whereas iron is discarded and can leave the substrate. For the case of the quaternary system, the additional nickel concentration is shown to reproduce the local nickel enrichment in the metallic substrate during the growth. Such a local enrichment is governed by the so-called local equilibrium, for which a comprehensive description is available in [Perevoshchikova, 2012]. The local equilibrium imposes the interface concentration. It is shown that chromium is depleted and a parabolic growth kinetics of spreading of the depletion is highlighted. This preliminary study is necessary to understand the role of the phase diagram on diffusion controlled phase transformations.

The second part of the chapter is devoted to the study of mechanical stresses, which is known to modify the local equilibrium, see [Larché and Cahn, 1985]. It is shown that stresses have here no clear impact on the growth kinetics, which is due to the stoichiometry of the oxide layer. Growth stresses are relaxed viscoplastically in both the oxide and the substrate. It is shown that viscoplastic relaxation can lead to almost negligible stress levels inside the oxide layer. Finally, various mechanical loads are applied during the growth of the oxide. The effect of the establishment of a stress of 300 MPa over 100 hours is studied in parallel with the effect of a series of loadings and unloadings ranging from 300

MPa to -300 MPa. Tensile stresses are thus generated in the oxide, which can be more likely followed by its brittle failure.

In the present chapter, the following assumptions are made,

- a stoichiometric oxide layer,
- the spontaneous oxide growth (or spontaneous interface chemical reactions),
- the chemical equilibrium of the two phases,
- heterogeneous elasticity of the two phases,
- a 1% in-plane growth strains within the oxide,
- viscoplaticity within the oxide only,
- viscoplasticity within both oxide and substrate and finally
- viscoplasticity of the substrate only.

Moreover, the following phenomena are neglected,

- the nucleation of the oxide layer,
- the influence of charges (electrochemistry),
- the Kirkendall-effect or vacancy fluxes (evolution of porosities),
- the brittle failure of the oxide layer,
- the oxide heterogeneous grain size distribution and
- the external oxide layer (Duplex oxide).

4.1 Ternary (Fe-Cr-O) and quaternary (Fe-Cr-O-Ni)

As mentioned above, the present study is devoted to the inner growth of Cr_2O_3 on an austenitic alloy γ-Fe. The growth is driven by the multicomponent diffusion of oxygen, chromium and nickel for the quaternary system. Later, stresses will be included and their negligible impact on the growth kinetics will be evidenced.

It is worth noting that the chapter deals with high temperature oxide growth (900°C). For low or elevated temperatures, the too small oxide layer thicknesses result in highly dispersed experimental measurements. Such a dispersion can have several causes, for instance the substrate roughness has to be considered. It is therefore preferred to rely on the high temperature experimental data. Moreover, at high temperature, diffusion is often said to dominate electrochemical effects so that the phase field framework seems to be well-suited. At such temperatures, creep cannot be neglected as evidenced by [Huntz et al., 1998], which is why the oxide viscoplastic relaxation will be accounted for. Oxide growth strains will be accounted for on the basis of the statements of [Clarke, 2002], that a 1% average in-plane strain is possible. Finally, the interface mobility, M_ϕ, is chosen to be high enough to disable the possibility of interface-controlled oxide growth and thus to restrict the study to diffusion-controlled phase transformations, see [Kim et al., 1999].

4.1.1 Ternary (Fe-Cr-O) and quaternary (Fe-Cr-Ni-O) phase diagram data

The phase diagram, that is defined by the topology of chemical free energies, is of fundamental importance in the chemical behaviour of multicomponent systems because mass transports are governed by the balancing of chemical forces, or the slopes of the free energies, that are also called the diffusion potentials. For simplicity, chemical free energies are chosen as quadratic potentials. Those quadratic potentials can be regarded, using the lexical field of topology, as elliptic paraboloids in the case of the ternary system. Each curvatures coefficient – or the second derivative of the quadratic potentials with respect to a given concentration field – is then calibrated independently from the others. The choice of a variety of curvatures governs the shape of the tie-lines beam, that is introduced in Chapter 2. To model oxide stoichiometry, the centre of rotation of such a tie-lines beam must be set as close as possible to a concentration set corresponding to the stoichiometric oxide. The oxide phase, here Cr_2O_3, and oxides in general are often reported to be stoichiometric, see [Hagel, 1965, Kofstad and Lillerud, 1982, Atkinson et al., 2003] amongst others. Such a stoichiometry takes the form of a triangular shaped two phase domain Cr_2O_3+γ-Feon a ternary phase diagram, see Fig. 2.13 in Chapter 2.

The curvature coefficients of the quadratic chemical free energy of Cr_2O_3 are approximated by equal curvatures k' for all components for simplicity. This curvatures is chosen to be sufficiently high to prevent the chemical composition of the oxide to deviate from stoichiometry. Conversely, the base metal (γ-Fe) is able to substantially deviate from stoichiometry. Chromium solubility within austenite is such that it can be significantly supersaturated within the iron-nickel austenitic phase. To model the chromium solubility in γ-Fe, the chemical free energy of γ-Fe along the chromium axis is endowed with a rather small curvature coefficient $k'' < k'$. Similarly, the nickel axis is endowed with an even smaller curvature coefficient $k''' < k''$. Finally, oxygen is assumed to have a very small solubility in austenite such that the oxygen curvature in γ-Fe is set equal to the highest curvature k'. In the following, the minimal values for the chemical free energies densities, or chemical free energies' wells, have been chosen to be (0, 0) and (2/5, 3/5), respectively for γ-Fe and Cr_2O_3, where the abscissa denotes the chromium concentration and the ordinate the oxygen concentration.

For the ternary system (Fe-Cr-O), the aforementioned dimensionless curvatures have been calibrated to mimic the ternary phase diagram of [Laheij et al., 1980]. The calibration has been performed on a set of two tie-lines. The chosen tie-lines are the ones delimiting the two phased domain of Cr_2O_3+γ-Fe as shown in Fig. 4.1. It must be noted that the obtained phase diagram is hence extremely simplified. Enhanced logarithmic free energy densities can nevertheless be used for a better description of the free energies but induce additional steps into the resolution algorithm. It is known that logarithmic free energies do not easily comply with the two phase model built by [Kim et al., 1999], which is used in this work. Nevertheless, some new phase field approaches can deal with logarithmic free energy densities more easily, *i.e.* [Steinbach et al., 2012], but were not implemented here. In fact, contrary to the aforementioned approach, the model of [Kim et al., 1999] allows to remove here a concentration field, decreasing thus the model dimensionality which is always accompanied by a decrease of computation time.

for the quaternary system, the aforementioned set of curvatures has been used along with energy minima located in (0, 0, 0.1) and (2/5, 3/5, 0). The additional axis corresponds to the concentration of nickel as shown in Fig. 4.2.

4.1.2 Diffusivity data

Diffusivities can be obtained experimentally, a brief literature overview is given in Table 4.1 and 4.2. They are expressed given the – jump – frequency factor A and the activation energy Q – the energetic barrier that the atom must overcome to move. Diffusion is thermally activated and the gas constant R and temperature T are used to evaluate the diffusivity at a given temperature [Gale and Totemeier, 2003]:

$$D(T) = A\exp\left(-\frac{Q}{RT}\right). \tag{4.1}$$

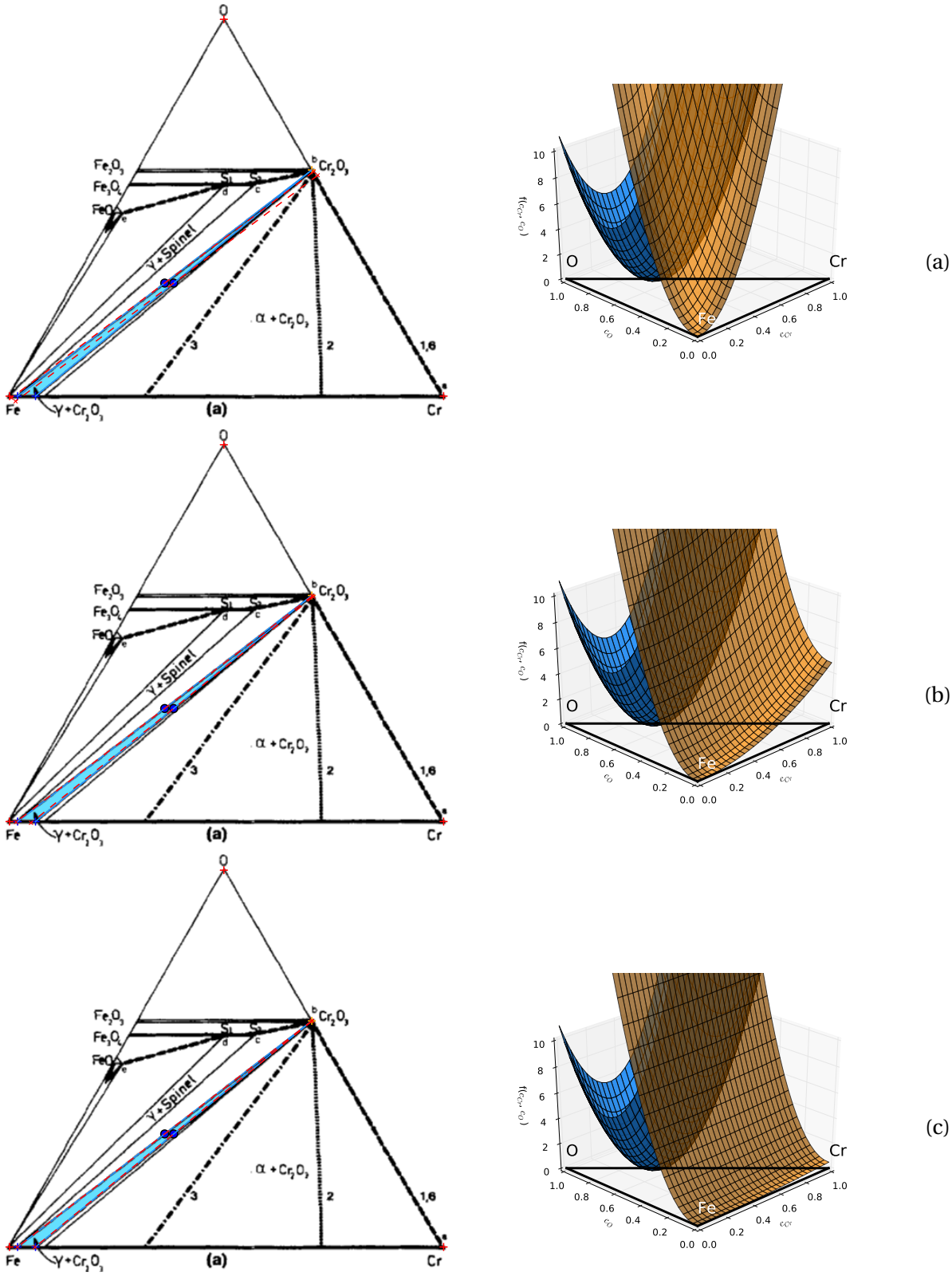

Figure 4.1: Calibration of the dimensionless curvatures for different ratios of chemical free energy curvatures $R = \frac{k'}{k''}$. (a) $R = 1$, (b) $R = 10$ and (c) $R = 100$, with their respective free energy density plots. The two red tie-lines between Cr_2O_3 and γ-Fe displayed on the phase diagram are better fitted with increasing R ratios.

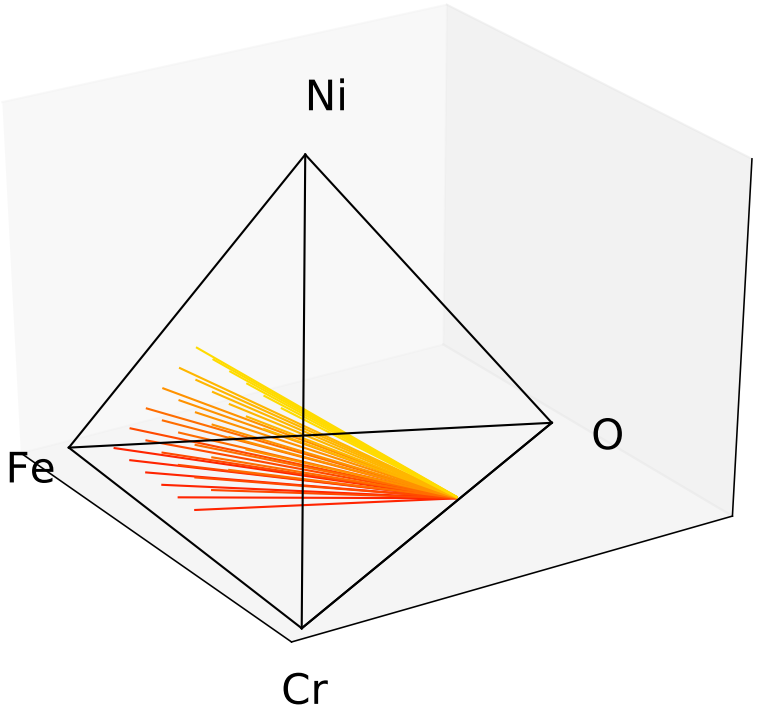

Figure 4.2: Calculated beam of tie-lines corresponding to the two-phased domain Cr_2O_3+γ-Fe for the quaternary system.

4.1.3 Study of the local equilibrium in multicomponent systems

Full field finite element simulations of oxide growth are here performed. Stresses are first neglected resulting in diffusion controlled oxide growth. The simulated domain consists in a slab of length L = 10.5 µm. The oxide phase is initialised at a depth of l = 60 nm to minimise the possible spurious effects between the diffuse interface and the free surface. The substrate contains initially chromium and nickel with respect to the classical compositions of AUSS. Despite the oxide film is stoichiometric, an additional linear gradient of oxygen is prescribed within it, which controls its growth. The oxide growth is therefore driven by oxygen overstoichiometry, that is prescribed at the free surface. In the literature, chromium and nickel are mentioned to diffuse in a substitutional manner within the iron based lattice of γ-Fe, *i.e.* [Cunat, 2002]. For the sake of simplicity, oxygen will be equally assumed to diffuse substitutionally within austenite. The diffusion mechanism of ions within the oxide is still discussed in the literature, [Atkinson et al., 2003]. Therefore, it will be assumed, as a first step, that ionic diffusion operates via both interstitial and substitutional sites of the oxide crystal lattice. It has been shown in Chapter 2, that the oxide crystal lattice embeds vacant octahedral sites. Therefore the concentrations in Cr_2O_3 will be slightly shifted due to the accounting of octahedral sites. It results that the aforementioned stoichiometric chemical free energy minimum located at (2/5, 3/5) shifts to (6/12, 4/12). It is worth noting this is a simplistic approach to obtain boundary conditions and that their validity must be questioned for further modelling.

The prescribed concentration of O^{2-} at the free surface governs the growth kinetics. The following boundary condition, accounting for the saturation of all octahedral sites in the oxide crystal lattice with oxygen, is then prescribed throughout the work,

$$\forall t,\ c_{\mathrm{O}}^{O_2} = \frac{8}{12} \simeq 0.67\,. \tag{4.2}$$

	A [$m^2.s^{-1}$]	Q[$kJ.mol^{-1}$]	Temp. range [°C]	$p_{O_2}[atm.]$	D [$m^2.s^{-1}$] at 900°C	Alloy comp.	Ref.
Cr	-	-	800		5.8×10^{-17}	16Cr-Fe	[Zhou, 2010]
Cr	-	-	800		5.8×10^{-20}	16Cr-Fe	[Zhou et al., 2010]
Cr	-	-	800	0.1	$D_{app} = 5.8\times10^{-20}$	30Cr-Ni	[Tsai et al., 1996]
					$D_B = 5.9\times10^{-22}$		
					$D_{GB} = 1.1\times10^{-16}$		
Cr	-	-	900	0.1	$D_{app} = 4.7\times10^{-19}$	30Cr-Ni	[Tsai et al., 1996]
					$D_B = 2.0\times10^{-21}$		
					$D_{GB} = 9.3\times10^{-16}$		
Cr	1.37×10^{-5}	255.6	1045-1550	-	6.1×10^{-19}	12Cr-Fe	[Auinger et al., 2011]
O	-	-	800		3.0×10^{-19}	16Cr-Fe	[Zhou, 2010]
O	-	-	800		3.0×10^{-20}	16Cr-Fe	[Zhou et al., 2010]
O	-	-	800	0.1	$D_{app} = 3.0\times10^{-20}$	30Cr-Ni	[Tsai et al., 1996]
					$D_B = 2.6\times10^{-22}$		
					$D_{GB} = 5.9\times10^{-17}$		
O	-	-	900	0.1	$D_{app} = 8.6\times10^{-20}$	30Cr-Ni	[Tsai et al., 1996]
					$D_b = 4.4\times10^{-21}$		
					$D_{gb} = 1.6\times10^{-16}$		
O	1.59×10^{-3}	422.6	1100-1450	-	1.3×10^{-25}	12Cr-Fe	[Auinger et al., 2011]

Table 4.1: Diffusivities in Cr_2O_3.

	A [$m^2.s^{-1}$]	Q[$kJ.mol^{-1}$]	Temp. range [°C]	D [$m^2.s^{-1}$] at 900°C	Alloy comp.	Ref.
Cr	0.58×10^{-4}	280.5	808-1200	1.0×10^{-17}	18Cr-8Ni	[Adda and Philibert, 1966]
Cr	0.13×10^{-4}	264.2	600-1300	1.25×10^{-17}	17Cr-12Ni	[Gale and Totemeier, 2003]
Cr	-	-	800	$D_B = 2.86\times10^{-19}$	16Cr	[Zhou, 2010]
				$D_{GB} = 1.57\times10^{-17}$		
Cr	-	-	800	6.0×10^{-20}	16Cr	[Zhou et al., 2010]
Cr	6.3×10^{-6}	243	750-1200	$D_B = 5.6\times10^{-17}$	Type 316	[Smith, 1975]
	1.5×10^{-3}	191	650-1000	$D_{GB} = 3.1\times10^{-12}$		
Cr	8.52×10^{-4}	250.8	800-900	6.75×10^{-17}		[Auinger et al., 2011]
O	$4.\times10^{-5}$	167.1	700-900	7.5×10^{-14}		[Auinger et al., 2011]
Fe	0.37×10^{-4}	279.7	600-1300	7.0×10^{-18}	17Cr - 12Ni	[Gale and Totemeier, 2003]
Fe	1.18×10^{-2}	281.5	700-900	2.33×10^{-17}		[Auinger et al., 2011]
Ni	0.58×10^{-4}	280.5	808-1200	1.0×10^{-17}	18Cr - 8Ni	[Adda and Philibert, 1966]
Ni	8.8×10^{-4}	251.2	600-1300	3.3×10^{-15}	17Cr - 12Ni	[Gale and Totemeier, 2003]

Table 4.2: Diffusivities in γ-Fe.

Moreover, the substrate initially contains 16% of chromium and 10% of nickel, which are equally imposed by Dirichlet boundary conditions far away from the interface in the substrate. Then the remaining boundary conditions are all defined by Neumann boundary conditions accounting for zero fluxes. Finally, all simulation parameters are summarised in Table 4.3. Boundary conditions are summarised in Fig. 4.3 and can be compared with partial pressures commonly used in classical Wagner theory.

Table 4.3: Parameters for the simulation of the oxide growth.

	Cr_2O_3	γ-Fe	interface
k_O [J.m^{-3}]	1.0×10^{11}	1.0×10^{11}	
k_{Cr} [J.m^{-3}]	1.0×10^{11}	1.0×10^{9}	
k_{Ni} [J.m^{-3}]	1.0×10^{11}	0.5×10^{9}	
$\hat{c}_O$ [-]	0.5	0.	
$\hat{c}_{Cr}$ [-]	0.33	0.	
$\hat{c}_{Ni}$ [-]	0.	0.5	
D_O [m^2.s^{-1}]	$8.\times10^{-18}$	5.6×10^{-17}	
D_{Cr} [m^2.s^{-1}]	4.7×10^{-19}	5.6×10^{-17}	
D_{Ni} [m^2.s^{-1}]	4.7×10^{-19}	5.6×10^{-18}	
δ [m]			$10.\times10^{-9}$
γ [J.m^{-2}]			1.

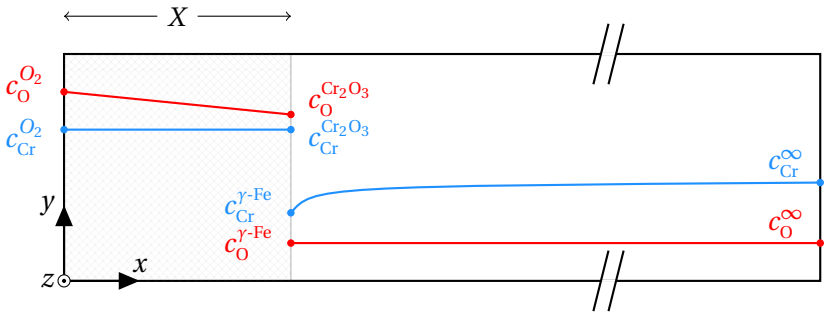

Figure 4.3: Representation of the growing oxide of thickness X (in grey) inside a semi-infinite substrate. Boundary conditions for concentrations, where $c_O^{O_2} = 0.67$, $c_{Cr}^{\infty} = 0.16$. All remaining external boundary conditions are zero mass fluxes. The interface concentration jump is prescribed by the chemical equilibrium.

The time evolution of the concentration fields during oxide growth can be calculated as illustrated in Fig. 4.6. The figures highlight the concentration jump at the metal oxide interface, which is prescribed by the chemical equilibrium discussed in Chapter 2. One can note that such a concentration jump at the metal oxide interface is established after a transient regime, which is clearly evidenced by looking at the concentration of the alloying elements – chromium and nickel – at the metal oxide interface in the substrate for the first and the second rows. The transient regime is due to the fact that chemical equilibrium is not fulfilled initially so that the interface is initially out of equilibrium. Nevertheless, the chemical equilibrium can be imposed at the beginning of the simulations by the prior calculation of the operative tie-line. This is possible in practice in 1D simulations, but such a calculation becomes much more complex in the two- and three dimensional cases when elasticity and

plasticity are accounted for. As already mentioned in Chapter 2, the ternary and quaternary systems respectively present one and two degrees of freedom. It then results that the chemical equilibrium ranges over an interval of tie-lines. The figure clearly emphasises that the selected tie-line is not the tie-line located at the minima of the chemical free energies, which are given in Table 4.3. Such a shift of the interface concentration – or tie-lines – can be represented on the ternary phase diagram, see Fig. 4.4.

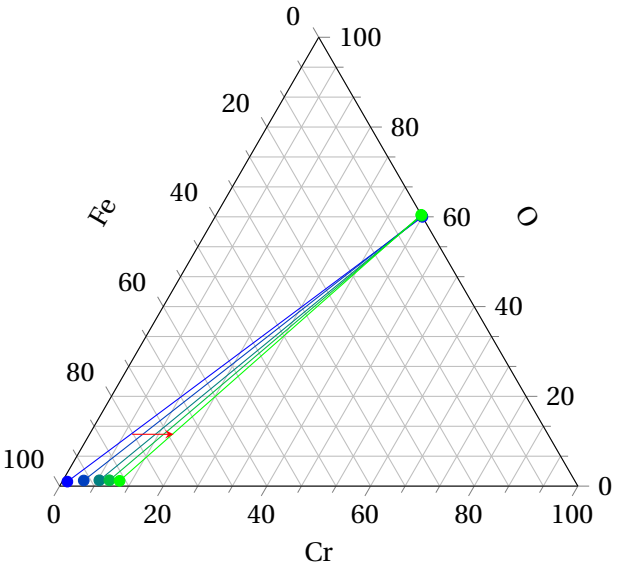

Figure 4.4: Ternary phase diagram on which the shift of interface concentration is represented. This shift illustrates the establishment of the local equilibrium. The red arrow represents the time axis and the concentration have been here normalised with respect to the concentrations defined in the simulations.

The above figure illustrates the establishment of the so-called operative tie-line, which occurs during the early stage of oxide growth. After such a rapid transitional regime, the "selected" operative tie-line can be shown to be time-independent – with respect to the present problem – and the growth becomes fully controlled only by the operative tie-line and the boundary conditions. Simulation results are presented in the form of concentration distance plots in Fig. 4.6 at different times. For such results, the establishment of the operative tie-line is clearly visible by the comparison of the interface concentrations of the second and third rows. Moreover, for both ternary and quaternary systems, the chromium depleted area close to the metal-oxide interface is shown to gradually increase in size. The oxygen gradient is shown to remain linear during the growth. The concentration of iron+nickel or iron, respectively for the ternary and for the quaternary systems, can be obtained using the mass balance. Is can be noted that, in the present model, the average value of iron+nickel or iron decreases during the oxide growth. Such a metal loss is possible if they are allowed to rapidly diffuse throughout the oxide layer and then react at the free surface to be either released or oxidised, which is mentioned to happen in the case of the duplex oxide layers in stainless steels – the outer oxide layers are enriched in iron. Finally, the present simulations are shown to reproduce the local nickel enrichment and the chromium depletion discussed in Chapter 2.

The growth kinetics is then studied for both cases – the ternary and the quaternary ones. The evolution of the oxide film thickness X is illustrated in Fig. 4.5. It follows that nickel slightly enhances the growth kinetics, which can be expected by carefully reviewing the operative tie-lines for each system. Then, the growth kinetics of the ternary and quaternary systems are fitted against a parabolic growth law. The present growth kinetics is then shown to fit almost perfectly the parabolic growth law, see Fig. 4.5 (b). Moreover, the calculated rate constants of the ternary and quaternary systems are quasi-equal. It has been mentioned previously that the growth kinetics is driven only by the operative tie-line along with the boundary conditions. One can then calculate the operative tie-line by solving

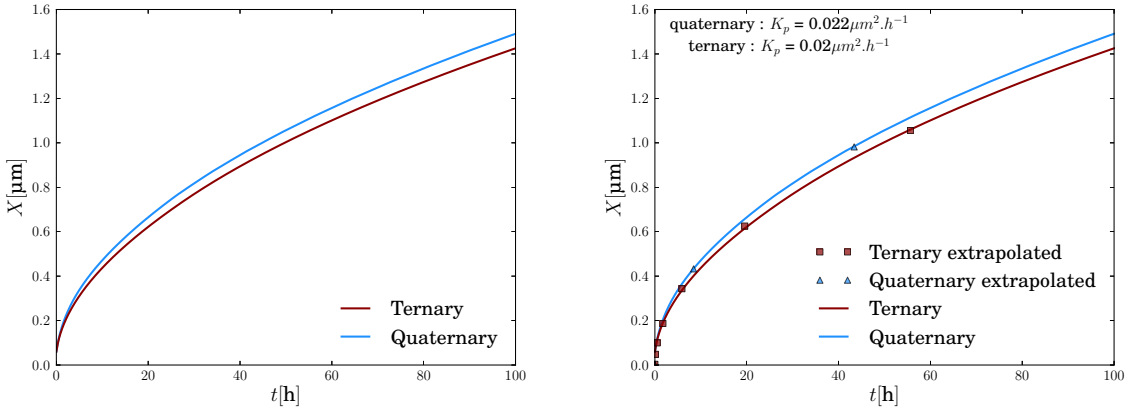

(a) (b)

Figure 4.5: Growth kinetics (a) and calibration of the rate constant for the quaternary and ternary systems (b).

the following system of equations:

$$\begin{aligned}
\mu_O^{Cr_2O_3} &= \mu_O^{\gamma\text{-Fe}}, \\
\mu_{Fe}^{Cr_2O_3} &= \mu_{Fe}^{\gamma\text{-Fe}}, \\
\mu_{Cr}^{Cr_2O_3} &= \mu_{Cr}^{\gamma\text{-Fe}}, \\
\mu_{Ni}^{Cr_2O_3} &= \mu_{Ni}^{\gamma\text{-Fe}}, \\
\dot{X}_O &= \dot{X}_{Cr} \quad \left(= \dot{X}_{Ni}\right), \\
\dot{X}_{Cr} &= \dot{X}_{Ni}
\end{aligned} \tag{4.3}$$

where the first four equations correspond to chemical equilibrium and the two remaining equations correspond to the solute balance, in the case of the quaternary system. The system of equations (4.3) – or the operative tie-line – can be solved for the ternary and quaternary systems. It results that the following operative tie-lines can be calculated – the procedure for the calculation is given in more details in the next section – and are given in Table 4.5 and 4.4, where the oxygen concentration at the interface and in the oxide is detailed:

Table 4.4: Constant tie-line for the quaternary system.

	Cr_2O_3	γ-Fe
c_O	0.5007	0
c_{Cr}	0.3	0.1
c_{Ni}	0	0.1

Table 4.5: Constant tie-line for the ternary system.

	Cr_2O_3	γ-Fe
c_O	0.5003	0
c_{Cr}	0.3	0.1

Such operative tie-lines can be both visualised, for instance, in the quaternary tetrahedron, as illustrated in Fig. 4.7 Finally, once the operative tie-lines are calculated, one can estimate the rate constants by using the formula (2.40) and (2.41) presented in Chapter 2. It is then noted that the operative tie-lines are quasi-identical for the case of the ternary and quaternary systems, and so are the growth kinetics. On the basis of such operative tie-lines, the aforementioned growth rate constants can be evaluated:

$$K \simeq 0.02\ \mu m^2.h^{-1}. \tag{4.4}$$

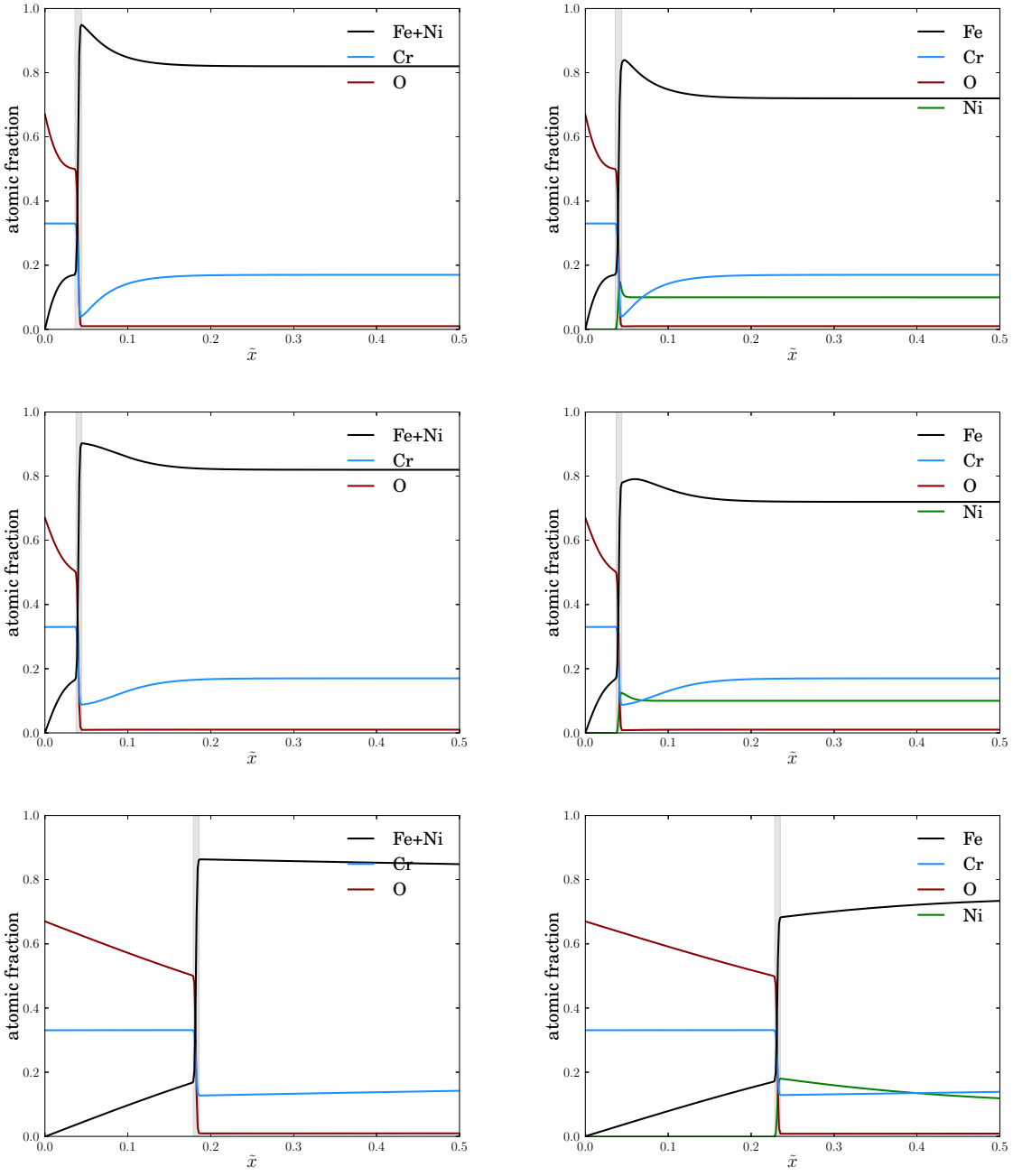

(a) (b)

Figure 4.6: Concentration distance profiles for (a) the ternary system and (b) the quaternary one. The grey domain represents the thickness of the diffuse interface.

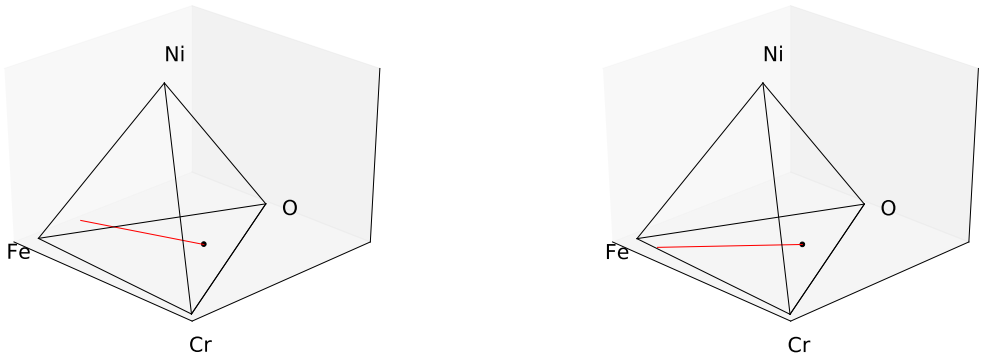

(a) (b)

Figure 4.7: Tie-lines corresponding to the local equilibrium condition (4.3) for (a) the quaternary and (b) the ternary systems, both visualised in the quaternary volume or tetrahedron.

This growth rate is close to the growth rates shown in Fig. 4.5.

4.1.4 Reassessment of the oxygen diffusivity

For the reasons mentioned above, an estimate for the range of oxygen diffusivities inside the oxide can be obtained on the basis of the rate constants obtained by [Sabioni et al., 2012a, Sabioni et al., 2012b]. Experimental rate constants are summarised in Table 4.6. The supersaturation of oxygen in the oxide

Table 4.6: Rate constants for the high temperature growth of Cr_2O_3 on a 304 stainless steel.

T [°C]	k_p [g^2.cm^{-4}.s^{-1}]	k_p [µm^2.h^{-1}]
750	3.1×10^{-14}	0.007
800	1.3×10^{-13}	0.028
850	2.1×10^{-13}	0.046
900	6.9×10^{-13}	0.151
950	1.4×10^{-12}	0.306

[Sabioni et al., 2012b]

is enforced by the boundary condition at the free surface and the stoichiometry at the oxide-metal interface as follows, see Eq. (A.9) in Appendix A:

$$\Omega_O = \frac{c_O^{\alpha} - c_O^{\alpha/\beta}}{c_O^{\alpha/\beta} - c_O^{\beta/\alpha}} = \frac{0.67 - 0.5}{0.5 - 0} = 0.34\,. \tag{4.5}$$

The range of the oxygen diffusivities inbetween 750°C and 950°C can be estimated to be:

$$\begin{array}{ccccc} (2\Omega_O)^{-1}\, k_p^{750^\circ C} & < & D_O^{Cr_2O_3} & < & (2\Omega_O)^{-1}\, k_p^{950^\circ C}\,, \\ 0.01 & < & D_O^{Cr_2O_3}\,[\mu m^2.h^{-1}] & < & 0.45\,, \\ 2.77 \times 10^{-18} & < & D_O^{Cr_2O_3}\,[m^2.s^{-1}] & < & 1.25 \times 10^{-16}\,. \end{array} \tag{4.6}$$

In the further studies devoted to oxidation, the diffusivity of oxygen will be set to $D_O^{Cr_2O_3} = 6 \times 10^{-18}$ m.s^{-2}.

4.2 A study of chromium depletion

4.2.1 A comprehensive description of local equilibrium

It has been shown previously that the chromium depletion is controlled by the operative tie-line. It follows that the phase diagram data must be considered in the study of the chromium depletion. It is worth noting that the chromium content of the alloy is gradually retrieved away from the interface. It has been shown that the chromium depleted area increases in size during the growth. Prior to the operative tie-line calculation, it is convenient to introduce the chromium supersaturation – which is also given in Eq. (A.32) in the Appendix A:

$$\Omega_{Cr}^{\beta} = \frac{c_{Cr}^{\infty} - c_{Cr}^{\beta/\alpha}}{c_{Cr}^{\alpha/\beta} - c_{Cr}^{\beta/\alpha}}. \tag{4.7}$$

The oxygen supersaturation has been defined in Eq. (4.5). The study of local equilibrium is here provided by solving the system of equations (4.3). For the ternary system, the additional kinetic condition is:

$$\dot{X}_O = \dot{X}_{Cr}, \tag{4.8}$$

where the interface velocities $\dot{X}$ are the interface velocities defined for the underlying binary cases, provided by Eq. (A.3) and (A.34) in Appendix A for instance. In the work, Eq. (4.8) can be rewritten – see Appendix A for more details:

$$\sqrt{\frac{1}{2} D_O^{\alpha} \Omega_O} = \sqrt{D_{Cr}^{\beta}} F^{-1}(\Omega_{Cr}), \tag{4.9}$$

where F is the transcendental function given by:

$$F : x \rightarrow \sqrt{\pi} x \exp\left(x^2\right) \mathrm{erfc}(x), \tag{4.10}$$

The ratio of diffusivities r is defined:

$$r = \frac{D_O^{Cr_2O_3}}{D_{Cr}^{\gamma\text{-Fe}}}. \tag{4.11}$$

Eq. (4.9) can also be rewritten:

$$F\left(\sqrt{\frac{1}{2} r \Omega_O}\right) = \Omega_{Cr}, \tag{4.12}$$

to be solved along with the chemical equilibrium condition. Therefore, the operative tie-line depends on the ratio r. Consequently, a set of supersaturations Ω_{Cr} and Ω_O will be selected during the growth.

In the present section, simulations of oxide growth will be performed with varying r ratios. The oxygen diffusivity will be fixed to the value defined in Table 4.3 and the chromium diffusivity will be varied with respect to the running value of r. The following values of r will be investigated, *e.g.* 0.3, 0.4, 0.5, 0.6, 0.7, 0.8, 2 and 4 as illustrated in Fig. 4.8. A Python script devoted to this study is available in H.5 in Appendix H. No clear influence of chromium diffusivity and initial content can be observed for the present range of ratios. Moreover, the model allows the chromium concentration to be negative, which is physically not acceptable. Such a behaviour can be graphically interpreted as a tie-line leaving the ternary triangle or the quaternary tetrahedron. The two aforementioned phenomena are embodied into the stoichiometry of the oxide and the use of quadratic chemical free energy densities. On the one hand, the shape of the stoichiometric oxide – as a highly curved elliptic paraboloid – will greatly reduce the shift of the oxygen concentration in the oxide at the metal-oxide interface. On the

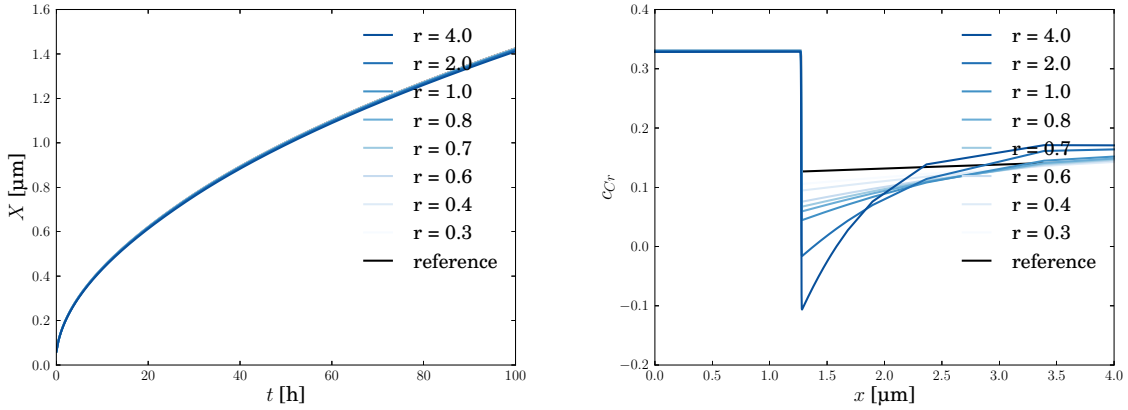

(a) (b)

Figure 4.8: Simulations of oxide growth for a variety of diffusivity ratios $r = D_O^{Cr_2O_3}/D_{Cr}^{\gamma\text{-Fe}}$. The simulated system is chosen as the ternary system (Fe-Cr-O). The resulting growth kinetics curves are reported in (a) along with a snapshot of the chromium profiles evidencing the deviation of the operative tie-line (b). Simulation parameters are given in Tab. 4.3.

other hand, the chromium concentration can be significantly shifted due to the small curvature of the chemical free energy density of γ-Fe, which is why the chromium depletion is greatly impacted.

Finally, the local equilibrium along with the corresponding rate constant can be obtained from a semi-analytic analysis as shown in Fig. 4.9 (a) and (b). The equilibrium interface concentration of oxygen is shown to be quasi-independent of the r ratio, whereas the chromium concentration rapidly decreases towards negative values, see Fig. 4.9 (a). It results that a half-line of ratios cannot be exploited in the simulations provided the current phase diagram topology. Fig. 4.9 (b) shows the growth rates calculated on the basis depending on the operative tie-line. The growth rates are equal for oxygen and chromium and are dependent on the diffusivity ratio r, which emphasises the role played by the operative tie-line during the growth. The previous growth rates were obtained by means

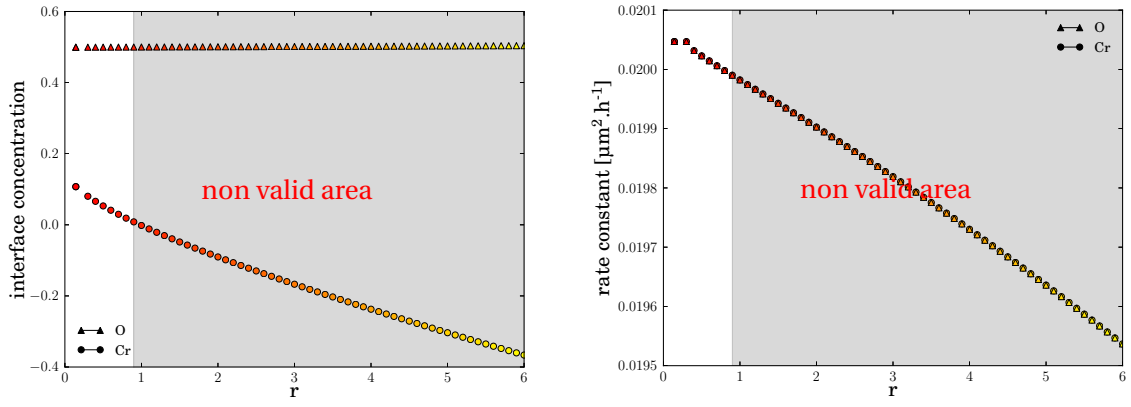

(a) (b)

Figure 4.9: The figure (a) illustrates the evolution of interface equilibrium concentrations as a function of the ratio of diffusivities r. The figure (b) shows the resulting rate constants calculated from the tie-lines obtained at different r. The grey shaded domains represent the non valid area, where the results are theoretically good but non physical due to the presence of negative chromium concentrations.

of a semi-analytic procedure. Simulations were performed in the same conditions for a validation purpose. Simulations results are illustrated in Fig. 4.10. The differences between the simulations and

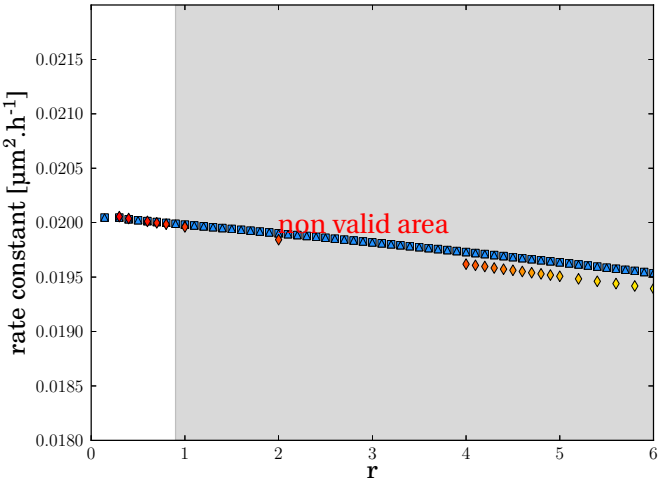

Figure 4.10: Evolution of the growth rate for different diffusivity ratios in the simulated ternary (Fe-Cr-O) system – curve with the diamond symbols. The blue curves represent the growth rates for the two underlying binary systems where triangles stand for the (Fe-Cr) system and the squares stand for the (Fe-O) system considering the operative tie-line of the ternary (Fe-Cr-O) system.

the semi-analytic results can be explained by the interpolation procedure of the growth rate. Such a post processing can be misled by the transient regime induced by the relaxation of the concentration at the interface. Nevertheless, the error is small as it is of the order of a few percent. From this prior study, one can notice the necessity to identify the operative tie-line to calculate the growth rate for instance.

4.2.2 Evolution of the chromium depleted area

The chromium depleted area can be defined in several ways. In the following, two definitions will be presented, which are as (**def. 1**) *the area for which the chromium content lies below a fixed value* or else as (**def. 2**) *the area between the interface and the intersection of the tangents at the interface and far away from the interface of the chromium concentration field.* The present study is restricted to (**def. 1**). Then, an appropriate ratio of diffusivities r will be chosen to avoid negative values of the chromium concentration field. To this aim, the reference case presented in Tab. 4.3 will here be studied.

The chromium depleted area is hence the distance between the metal-oxide interface and the median of the chromium concentration field in the substrate accordingly to (**def. 1**). It is illustrated in Fig. 4.11, which shows chromium profiles at different times. In the figure, the chromium depleted area is represented by a grey shaded area, which is delimited by two orange vertical lines. The orange lines are found at the interface and at the median point. The size evolution of the chromium depleted area is given by the red curve in Fig. 4.12 with the increase of the interface thickness (the blue curve). The growth kinetic curve of the chromium depleted area is provided from the raw data obtained for the calculation of the median concentration. This is why a small noise appears, which is presently harmless. It is shown in Fig. 4.12 (b) that the time evolution of the chromium depleted area is parabolic. Nevertheless, a very small discrepancy can be observed with increasing time which is probably caused by the finite size of the sample. Due to the similarities of the configurations, the problem of a semi-infinite medium defined in (Eq. 3.13) [Crank, 1975] will be considered:

$$\frac{c_{Cr}(x) - c_{Cr}^{\beta/\alpha}}{c_{Cr}^{\infty} - c_{Cr}^{\beta/\alpha}} = \mathrm{erf}\left(\frac{x}{2\sqrt{D_{Cr}^{\gamma\text{-Fe}}\, t}}\right). \tag{4.13}$$

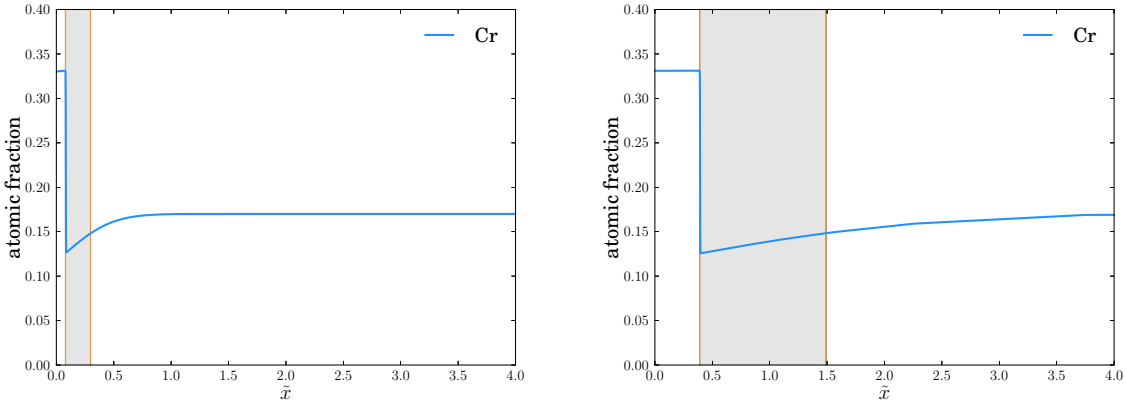

(a) (b)

Figure 4.11: Illustration of the chromium profile (in blue) against the dimensionless distance. Post-processing of the chromium depleted area (grey region) at different times (a-b).

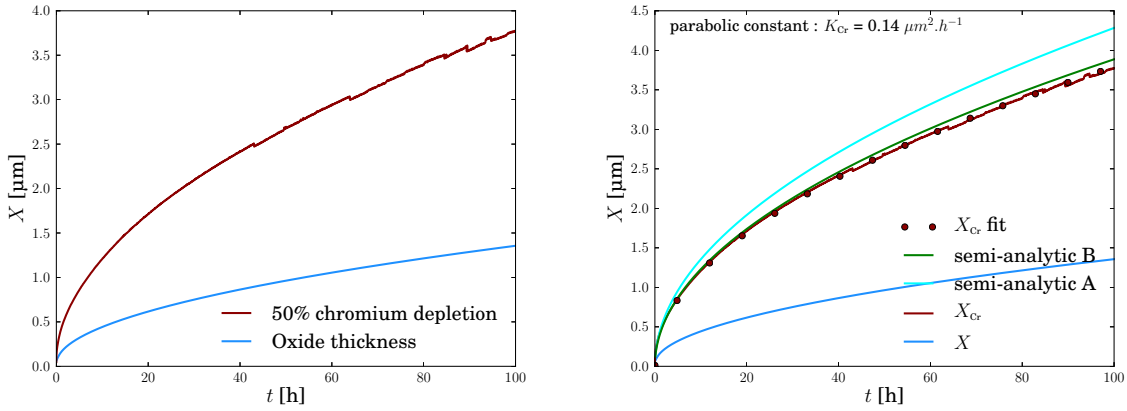

(a) (b)

Figure 4.12: The increase of the thickness of the chromium depleted area is parabolic: (a) simulation and (b) simulation + parabolic fit. In (a), the red curve is the post-processing of the size evolution of the grey domain shown in Fig. 4.11 and the blue curve is the oxide thickness.

where $c_{Cr}(x)$ can be set to the median concentration $c_{Cr}^{\text{med.}}$ and $c_{Cr}^{\infty} - c_{Cr}^{\beta/\alpha}$ the total variation of the concentration within the matrix. By definition of the median concentration, (4.13) rewrites:

$$\frac{1}{2} = \text{erf}\left(\frac{x^{\text{med.}}}{2\sqrt{D_{Cr}^{\gamma\text{-Fe}}\, t}}\right). \tag{4.14}$$

Again, using the solution provided in App. A (A.30), it comes that:

$$c_M^{\infty} - c(s) = -\sqrt{\pi}\, s^* (c_M^{\beta/\alpha} - c_M^{\alpha/\beta}) \exp\left(s^{*2}\right) \text{erfc}(s)\,. \tag{4.15}$$

The chromium depletion is then given by evaluating the variable of similitude s^* at the median point:

$$\frac{1}{2} = \sqrt{\pi}\, \frac{x^{\text{med.}}}{2\sqrt{D_{Cr}^{\gamma\text{-Fe}}\, t}} \exp\left(\left(\frac{x^{\text{med.}}}{2\sqrt{D_{Cr}^{\gamma\text{-Fe}}\, t}}\right)^2\right) \text{erfc}\left(\frac{x^{\text{med.}}}{2\sqrt{D_{Cr}^{\gamma\text{-Fe}}\, t}}\right). \tag{4.16}$$

By making use of the transcendental function F once more, one can establish the growth kinetics of the chromium depleted area:

$$x^{\text{med.}}(t) = \sqrt{4\left(F^{-1}\left(\frac{1}{2}\right)\right)^2 D_{Cr}^{\gamma\text{-Fe}}\, t} = \sqrt{0.15\,t}\,, \tag{4.17}$$

if the diffusivity has the unit $\mu m^2.h^{-1}$. In Fig. 4.12 (b), the cyan curve corresponds to the semi-analytic solution given by (4.14) while prescribing the time t, whereas the green curve corresponds to the semi-analytic solution given by (4.16) again while prescribing the time t. It is shown that the finite size of the simulation domain interferes slightly with the evolution of the chromium depletion at the end of the computations so that the obtained evolution of the chromium depleted area slightly diverges from the semi-analytic solution (green curve). Besides, it is shown that each analytic solution gives good estimates in the study of chromium depletion. Finally, the chromium concentration (initial chromium content and chromium depletion) has been shown here to have no role on the growth kinetics and that the study of the chromium depletion is embraced by the study of the local equilibrium, which can be obtained given a semi-analytic procedure for the unidimensional case – by the first evaluation of the chromium concentration drop at the interface and then the evolution of a depleted area with an arbitrary value that lies in between the interface and the bulk concentrations.

4.3 A study of oxide growth induced stresses

4.3.1 Definition of the mechanical problem

The problem of oxide growth stresses is addressed here under plane strain conditions. Generalised plane strain and tridimensional formulations of the problem have been performed as well but are not reported here. The oxide grows on a semi-infinite substrate, which is presently modelled by a large sample, with respect to the oxide thickness. The mechanical boundary conditions used throughout this chapter are the following:

- fixed bottom surface with respect to the ordinate axis
- fixed right surface with respect to the abscissa axis
- multi-point constraint on the top surface to ensure that it remains flat
- multi-point constraint on the left surface to ensure that it remains flat

The growth strains are modelled on the basis of an additional anisotropic eigenstrain. With respect to the mechanical conditions, only the in-plane strains are of importance here. The in plane strains, the ones in the directions y and z, are about 1% accordingly to [Clarke, 2002]. The mechanical problem combined with the chemical problem is then illustrated in Fig. 4.13. The elastic analysis of the current problem is found in Appendix D. The elastic analysis returns that the stress fields are homogeneous in each phase. Stresses are compressive in the oxide and tensile in the substrate when the in-plane strains are positive. Moreover, if the oxide thickness becomes negligible with respect to the sample size L, then zero stresses are found in the substrate.

The additional eigenstrain $\underset{\sim}{\boldsymbol{\varepsilon}}_{\star}^{Cr_2O_3}$ is injected in the oxide phase – Cr_2O_3 – to generate growth stresses, [Clarke, 2002]. Eigenstrain anisotropy is considered according to [Huntz et al., 1993] but it does not impact the simulation results given the simple problem geometry.

$$\underset{\sim}{\boldsymbol{\varepsilon}}_{\star}^{Cr_2O_3} = \begin{pmatrix} 0.02 & & \\ & 0.01 & \\ & & 0.01 \end{pmatrix}. \tag{4.18}$$

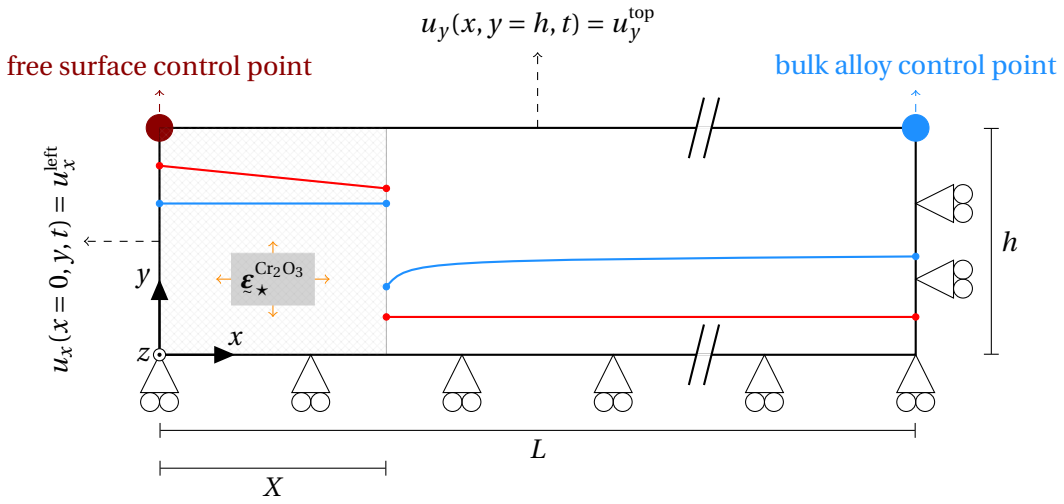

Figure 4.13: Representation of the growing oxide (in grey) inside a semi-infinite substrate. Mechanical boundary conditions where the left surface is a free surface and the height of the top surface is homogeneous – it remains flat anytime. The right surface is fixed along the depth axis x and the bottom surface is fixed along the height axis y. Chemical boundary conditions are given in Figure 4.3 and briefly recalled here by the concentration profiles of oxygen and chromium, respectively in red and blue. The control points will be used to acquire local the stress-strain curves during a mechanical loading.

In the following, the mean in-plane oxide stress, noted MOS below, will be treated, in a similar way as for [Huntz et al., 2002]:

$$\text{MOS} = \left\langle \sigma_{yy}^{Cr_2O_3} \right\rangle = \frac{1}{X(t)} \int_0^{X(t)} \sigma_{yy}(x)\text{dx}. \tag{4.19}$$

In the next section, mechanical loads will be prescribed at the top surface of the sample along its normal direction provided from the mean sample stress, noted MSS:

$$\text{MSS} = \left\langle \sigma_{yy} \right\rangle = \frac{1}{L} \int_0^{L} \sigma_{yy}(x)\text{dx}. \tag{4.20}$$

Moreover, as illustrated in Fig. 4.13, two control points are defined – the red and blue dots – to extract and analyse the local stress-strain curves. The control point in the substrate accounts for the stress-strain curve of the whole substrate as the stress appears to be homogeneous. However, the stresses in the oxide layer can be heterogeneous due to the interplay between stress relaxation effects and oxide growth. The control point in the oxide layer is set at the free surface, where such an interplay is minimised.

4.3.2 Impact of stresses on local equilibrium

Mechanical stresses are known to modify the chemical equilibrium, see [Cahn and Larché, 1984]. The equilibrium concentrations undergo an additional shift. Such a shift, depending on its magnitude, can have a significant impact on growth kinetics, see Eq. (E.9) in Appendix E for instance. The William point is the point of a phase diagram for which the phase coexistence vanishes due to the presence of elastic energy, [Cahn and Larché, 1984, Ammar et al., 2009]. Consequently, the growth kinetics can be modified by stresses depending on the magnitude of the induced shift of the operative tie-line. It is shown in Appendix D that the growth stresses are transmitted to the substrate due to the finite size of the sample. The amount of transmitted stresses depends on the sample thickness, and more precisely to the fraction of oxide, see Appendix D for more details.

Simulations restricted to the case of elasticity have been first performed. A prior study has been conducted to characterise the dependence on the sample length L of the growth stresses. Such a study can be also made analytically by combining the Appendices D and E. The simulations have been performed, using the elastic parameters defined in Table 4.7, accordingly to Chapter 2. The

Table 4.7: Elastic parameters.

	γ-Fe	Cr_2O_3
E [GPa]	185	210
ν [-]	0.3	0.3

simulations have shown large variation of stresses induced by the sample size L. The present large stress interval in the oxide is also shown to have a negligible impact on the growth kinetics, which can be attributed to the stoichiometry of the oxide. The shift of the operative tie-line in the oxide is hence not great enough to be able to modify the growth kinetics. Oxide stoichiometry, which is provided by the phase diagram data, then prescribes the interface concentration of oxygen to a quasi-constant value making the growth kinetics to be quasi-independent of stresses.

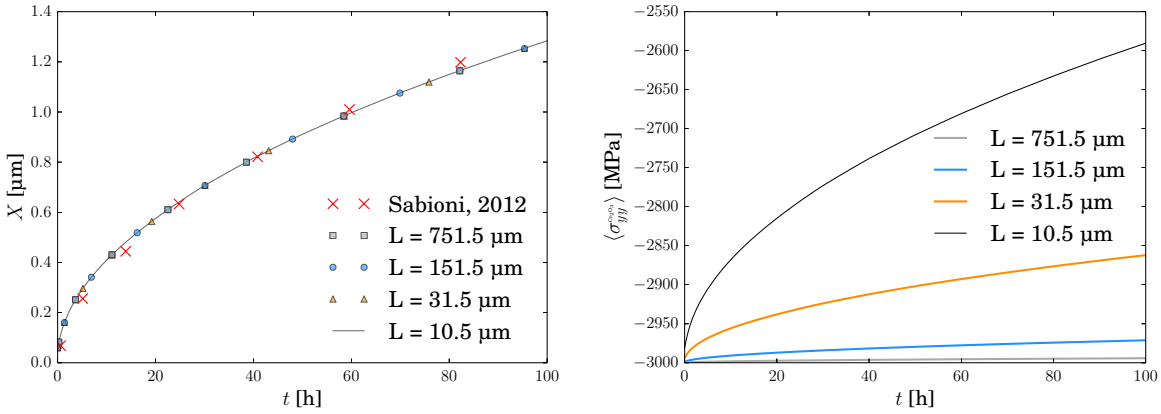

(a) (b)

Figure 4.14: Influence of the size of the sample on the oxide growth kinetics, in (a), and on the internal in plane stresses averaged within the oxide layer, in (b). The reference size is set to 10.5 µm and is compared to samples of size 31.5 µm, 151.5 µm and 751.5 µm.

In the following the substrate length will be chosen to be at least 500 times greater than the oxide penetration depth to reduce such edge effects.

4.3.3 Viscoplastic relaxation of the oxide

We now enhance the former elastic problem with the viscoplastic relaxation of the oxide. We first introduce a power-law creep, the parameters of which have been calibrated by [Mougin, 2001] and are given in Table 4.8. The creep power-law is recalled, see Eqs. (2.31) or (3.46):

Table 4.8: Parameters for the power-law creep of the oxide.

K [MPa.s$^{1/n}$]	n [-]	R_0 [MPa]
7738	5	1000, 500, 200, 100, 10

$$\dot{\underset{\sim}{\varepsilon}}_p = \left\langle \frac{\sigma_{\text{VM}} - R_0}{K} \right\rangle^n \sqrt{\frac{3}{2}} \frac{\underset{\sim}{\sigma}_{\text{dev}}}{\sqrt{\underset{\sim}{\sigma}_{\text{dev}} : \underset{\sim}{\sigma}_{\text{dev}}}}, \tag{4.21}$$

The results of the simulations are illustrated in Fig. 4.15. The sub-figure 4.15 (b) shows heteroge-

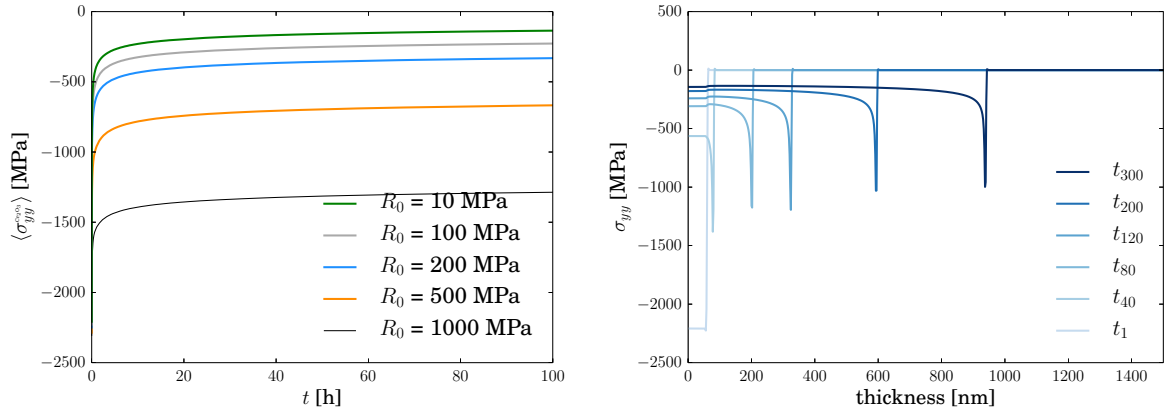

(a) (b)

Figure 4.15: (a) Influence of the yield stress R_0 on the evolution of the mean in plane growth stress in the oxide for a sample of thickness 751.5 µm. (b) Evolution of the stress-distance curves during the oxide growth when R_0 = 100 MPa.

neous in plane stresses in the oxide and homogeneous stresses in the substrate. The heterogeneous stresses in the oxide layer are generated by the combined formation of new oxide with high compressive stresses at the interface. Further, stresses are progressively relaxed resulting in the generation of a curved stress profile in the vicinity of the interface. The magnitude of the stress in the oxide is maximal at the metal-oxide interface and decreases rapidly away from the interface. Nevertheless, the distance for which the stresses are heterogeneous can become negligible for larger oxides which can justify the use of an averaged quantity for the description of stresses in the oxide layer done in [Huntz et al., 2002]. The MOS is written $\langle \sigma_{yy}^{Cr_2O_3} \rangle$ in the figures and is the variable used in the modelling approach developed in [Huntz et al., 1998]. Moreover, a stress artefact at the initial position of the interface is kept throughout the simulations, which can be attributed to a local small increase of the viscoplasticity inside the interface. No focus has been done on such a detail, which has been judged to be harmless for the further stress analysis. The sub-figure (a) shows that the mean stresses in the oxide are compressive and rapidly decrease towards an asymptotic value, which obviously depends linearly on the oxide yield stress R_0. In the following, the MOS will be analysed for a series of mechanical loads.

4.4 Effects of mechanical loads during oxide growth

The last part of the chapter is devoted to the study of oxide growth under different mechanical loads. It has been shown previously that oxide growth kinetics is not impacted by internal stresses, which will be the case for stresses induced by the loads as well. This is why the growth kinetics will not be discussed in the following. Mechanical loadings are here of three different kinds – with increasing complexity – that are the tensile, creep and fatigue tests. Mechanical loads are prescribed on the entire top surface of the sample so that they impact both the oxide and the substrate phases. The different loading sequences are illustrated in Fig. 4.16. Numerically, a mechanical load is applied by means of a prescribed force at an arbitrary point of the top surface of the specimen along with a MPC with respect to all nodes of the top surface. The prescribed force is therefore distributed over a set of points, which corresponds to a linear force and so to a stress for the two-dimensional case. The first mechanical load (Fig. 4.16 (a)) corresponds to a monotonic tensile test and is intended to reproduce the effects of the slow strain rate testing – also denoted SSRT or CERT in the literature. In

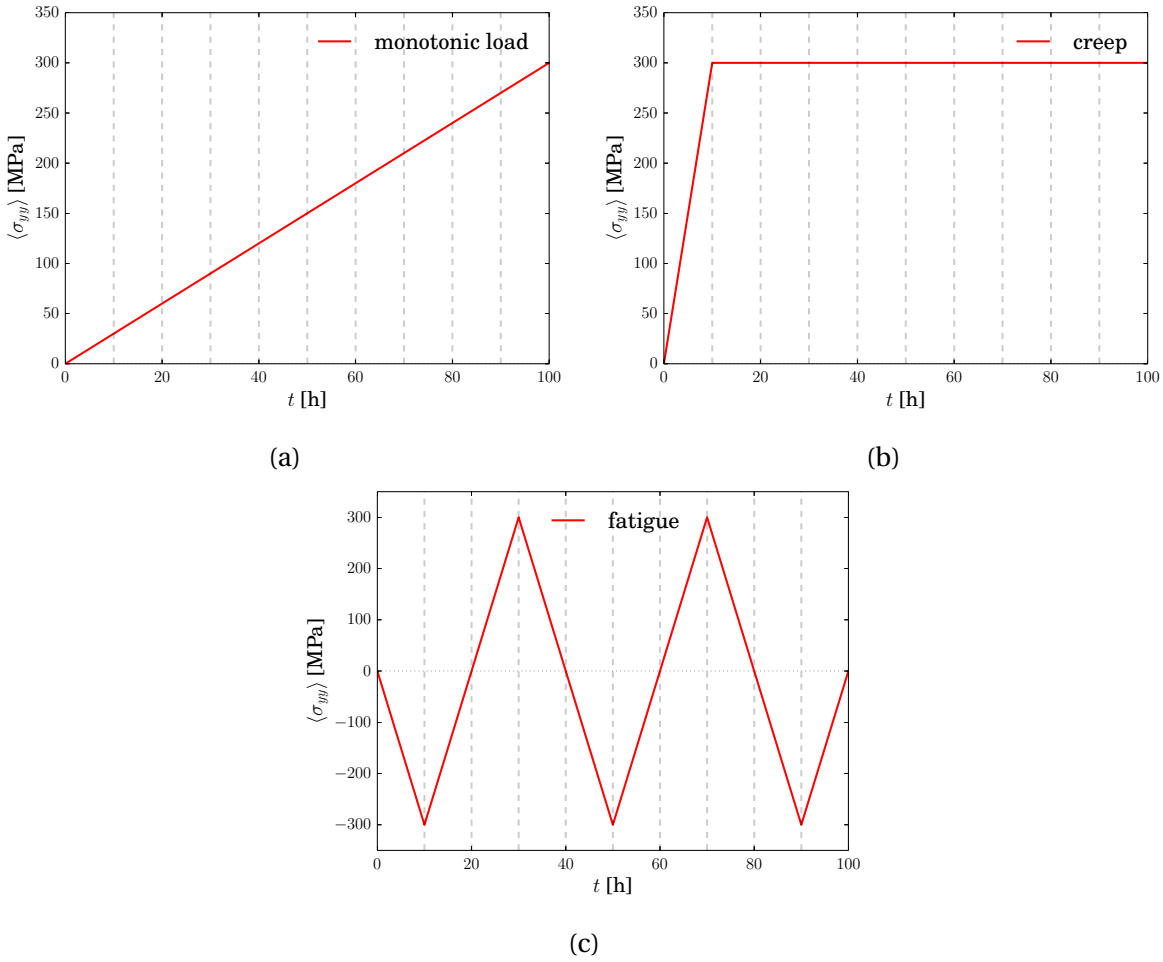

Figure 4.16: The figures show the evolution of the MSS defined in Eq. (4.20): (a) loading sequence for the slow strain rate test, (b) loading sequence for the creep test and (c) loading sequence for the fatigue test.

the case of the elastic substrate, the strain rate can be evaluated close to 10^{-6} s^{-1}, which is rapid in comparison to experimental work at low temperature. However, as the growth kinetics is higher at high temperatures, the current strain rate is comparable to the interface velocity, resulting in significant oxide growth during the loading, which is though to be necessary for the activation of initiation corrosion cracks. The prescribed stress at the top surface varies linearly from 0 MPa to 300 MPa, respectively at $t = 0$ h and $t = 100$ h. The 300 MPa stress is chosen according to the stress-strain curves of [Pommier et al., 2015] as shown in Chapter 2. Nevertheless, it represents a critical case and is close to the maximal stress that classical AUSS can sustain.

The second mechanical load (Fig. 4.16 (b)) is motivated by frequently U-bend tests used in the characterisation of the SCC behaviour of materials. U-bend tests are basically a sample in the form of a half-pipe that is bended along its longitudinal axis and kept so by a fixing bolt. The constant displacement of the sample can be modified into a constant loading by the additional action of a spring in-between the sample and the bolt, see [Baboian, 2004]. The creep test starts with a loading sequence from 0 MPa to 300 MPa over 10 hours. After that, the load is maintained up to 100 hours.

Finally, the last case consists in a fatigue loading (Fig. 4.16 (a)). It is intended to reproduce thermal fatigue, and therefore thermal stresses that components can endure during service for instance during shutdown and restart of PWRs for maintenance purposes. The fatigue test consists in cycles of loading-unloading sequences, here with a time period of 40 h, for which the sample is repeatedly put under tensile and compressive stresses. The stresses extrema are respectively 300 MPa and -300 MPa, which are critical loads.

In this section, three different cases will be investigated. The first case corresponds to a viscoplastic oxide growing on an elastic substrate, which appears to be the most unrealistic case. Nevertheless, it can be considered to be the extension of the work previously done in Chapter 3. The second case, corresponds to a viscoplastic oxide growing on a viscoplastic substrate. This case can be considered to be representative of high temperature oxidation, because evidences of the viscoplastic deformation of the oxide layer are reported in the literature. Finally, the third case corresponds to an elastic oxide that grows on a viscoplastic substrate. We think that this last case corresponds to the case of low temperature oxidation – below 500 °C – as the viscoplastic stain rates in the oxide layer are reported to be almost negligible in [Frost and Ashby, 1982]. It is worth noting that the failure of the oxide is never considered. The following calculated stress fields in the oxide layer suggest that such a failure can happen in almost all cases.

4.4.1 Effect of the mechanical load restricted to the viscoplastic relaxation of the oxide

The viscoplastic relaxation of the oxide is firstly considered here, whereas the substrate deforms elastically. The material parameters used for the viscoplastic deformation of the oxide are given in Table 4.8, for which an arbitrary yield stress $R_0 = 0$ MPa was chosen for simplicity. Heterogeneous elasticity is considered and elastic constants are provided in Table 4.7. The oxide is significantly growing during the mechanical loading, *i.e.* the characteristic times for the phase transformation and the mechanical loads are close to each other. It leads then to significant influence of oxide growth on the resulting stress fields. This behaviour is observed throughout the section.

Slow strain rate test

The application of a monotonic tensile load during oxidation, that is illustrated in Fig. 4.16 (a), results in the evolution of the MOS and MSS as shown in Fig. 4.17. The figure shows that stresses in

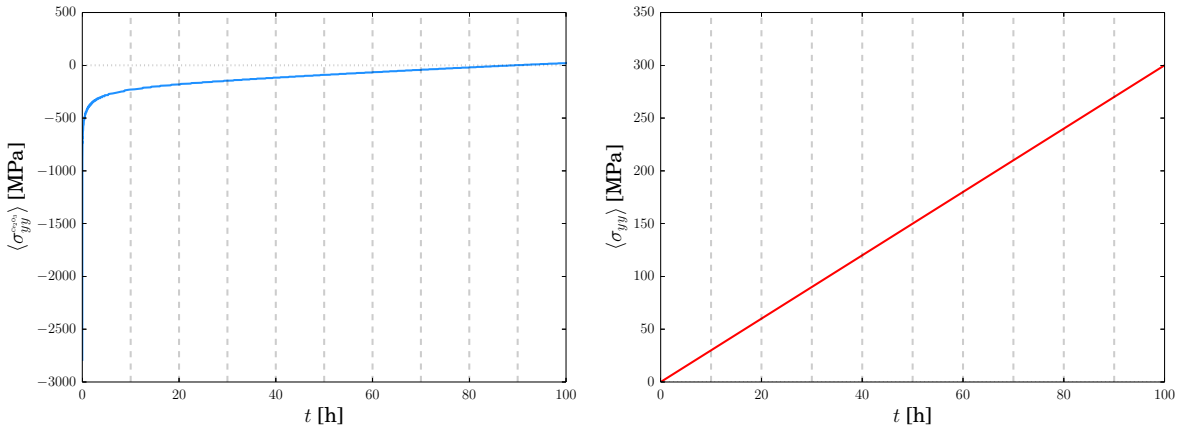

(a) (b)

Figure 4.17: (a) $\left\langle \sigma_{yy} \right\rangle^{Cr_2O_3}(t)$ is the mean σ_{yy} stress throughout the oxide layer only. (b) $\left\langle \sigma_{yy} \right\rangle(t)$ is the mean stress thoughout the specimen (oxide+substrate) for validation purpose.

the oxide are globally relaxed during the loading. The mean stresses are initially highly compressive, with compression levels about 2 GPa. Then they rapidly increase to reach 500 MPa always in a state of compression. After that, the stresses slowly increase at a constant rate, which may be related to the one of the mechanical load. Finally, positive mean stresses are generated within the oxide and are about a few tens of MPa. It is recalled that stresses within the oxide layer are heterogeneous, and that compressive stresses are generated during oxide growth in the vicinity of the metal-oxide interface. The stress away from the interface becomes dominant when the oxide thickness becomes

larger than several metal-oxide interface lengths. The increase of the mean stress can be first seen as the competition between the formation of new unrelaxed oxide – that comes with the introduction of highly compressive stresses – and the ongoing deformation of the oxide away from the metal-oxide interface. The mean stress becomes then obviously controlled by the mechanical load. After a given time, the mean stress becomes positive, which appears to happen first at the free surface of the oxide layer. It is worth noting also that the time dependence of oxide growth and the mechanical load are respectively parabolic and linear. This is why the mechanical load will necessarily become dominant in the resulting stress stain response.

The sub-figure (b) is used for validation purpose and will not be discussed hereafter. Nevertheless, it will be displayed for all cases, as it allows to remind graphically the loading conditions.

In the following, the two control points shown in Fig. 4.13 at the free surface and in the bulk alloy are used to display the stress-strain curves. It is worth noting that the total strain ε_{yy} is homogeneous for the present unidimensional case. Moreover, the total strain ε_{yy} is controlled by the substrate's mechanical behaviour as the simulation sample can be considered to be representative of a semi-infinite problem. Fig. 4.18 gives the stress-strain curves of the two aforementioned control points. The stress-strain curve at the free surface control point, in Fig. 4.18 (a) shows that the σ_{yy} stress on

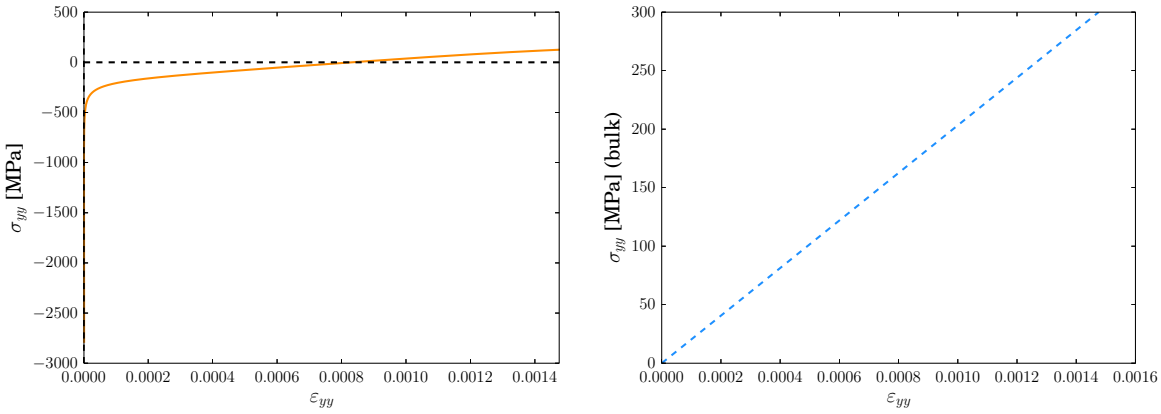

(a) (b)

Figure 4.18: (a) stress-strain curve of the free surface control point and (b) stress-strain curves of the bulk control point.

the free surface is greater than the mean oxide stress presented in Fig. 4.17. This result is expected as the viscoplastic relaxation can be shown to be more important away from the interface than in the vicinity of the interface, see Figure 4.15 (b). It results that tensile stresses can be found in the oxide at the end of the mechanical loading, with an extremum located at the free surface. The stress-strain curve for the bulk control point, see Fig. 4.18 (b) shows very little elastic deformation levels and a maximal stress of 300 MPa, as expected with respect to the prescribed load. The total strain ε_{yy} is small because the substrate is able to bear the load due to its pure elastic behaviour.

The first results can be summarised as follows, the oxide first relaxes viscoplastically to a stress value close to zero, with respect to the present zero yield stress. After that, the mechanical load takes over and generates tensile stresses inside the oxide layer at the free surface. Such tensile stresses are small because the elastic substrate keeps ε_{yy} down to low levels. Finally, such tensile stresses can possibly make the oxide to fail in a brittle manner. The failure of the oxide layer is then thought to be more likely initiated from the free surface.

Creep test

The effect of a creep load, which is illustrated in (Fig. 4.16 (b)), during oxide growth is here studied. The resulting curves are shown in Fig. 4.19 and 4.20. Here, the MOS is kept under a state of compression during the loading as shown in Fig. 4.19 (a). The MOS rapidly goes towards zero during

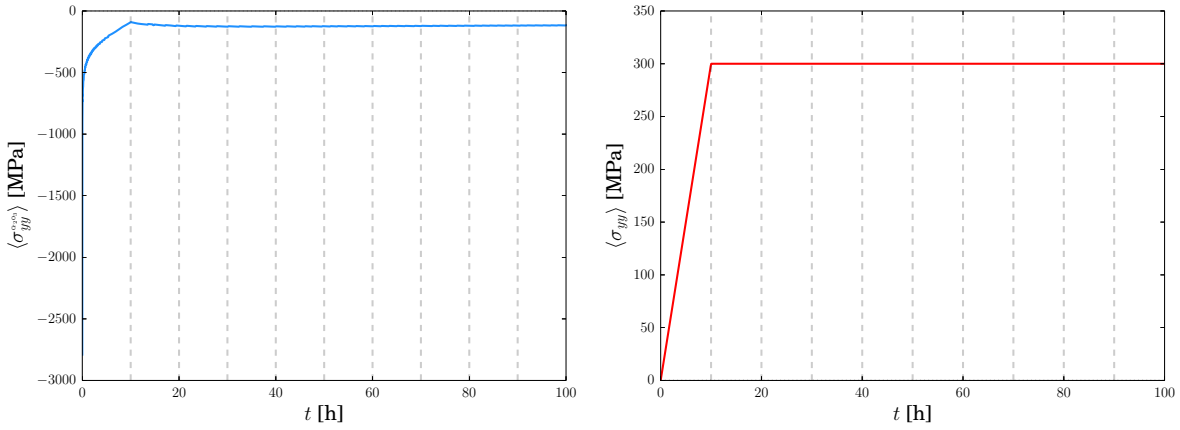

(a) (b)

Figure 4.19: (a) mean σ_{yy} stress in the oxide versus time and (b) mean stress in the substrate versus time.

the loading sequence and then veers off to a state of compression. Such a cusp occurring at the end of the loading sequence is generated by ongoing oxide growth. The growth of new unrelaxed oxide will then make the MOS to increase further. The depth at which the loading sequence ends is marked by highly heterogeneous growth stresses within the oxide. The stress heterogeneity is pictured in Fig. 4.21. The σ_{yy} stress in the oxide consists in two plateaus, one corresponding to the loading sequence and the other one to the creep load. Nevertheless, the oxide is kept in a state compression and its free surface barely experiments tensile stresses, see Fig. 4.20 (a). Once more, the elasticity of the substrate keeps the total strain down to low levels, which is beneficial for the oxide layer integrity, see Fig. 4.20 (b).

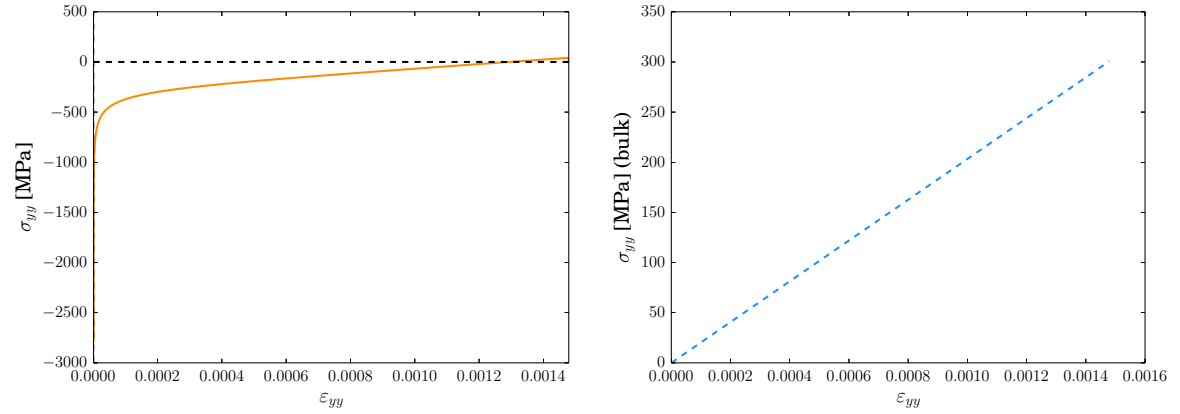

(a) (b)

Figure 4.20: (a) stress-strain curve of the free surface control point and (b) stress-strain curves of the bulk control point.

Fatigue test

The effect of the fatigue load presented in (Fig. 4.16 (c)) during the oxide growth is finally studied and the results are provided in Fig. 4.22 and 4.23. The MOS first relaxes during the initial compressive loading. After that, the MOS enters into an hysteresis loop as seen in Fig. 4.22 (a) and 4.23 (a). The results show that high levels of tensile σ_{yy} stresses can be generated by the combined action of stress relaxation and the injected tensile stresses during the cyclic load. The loading presently corresponds

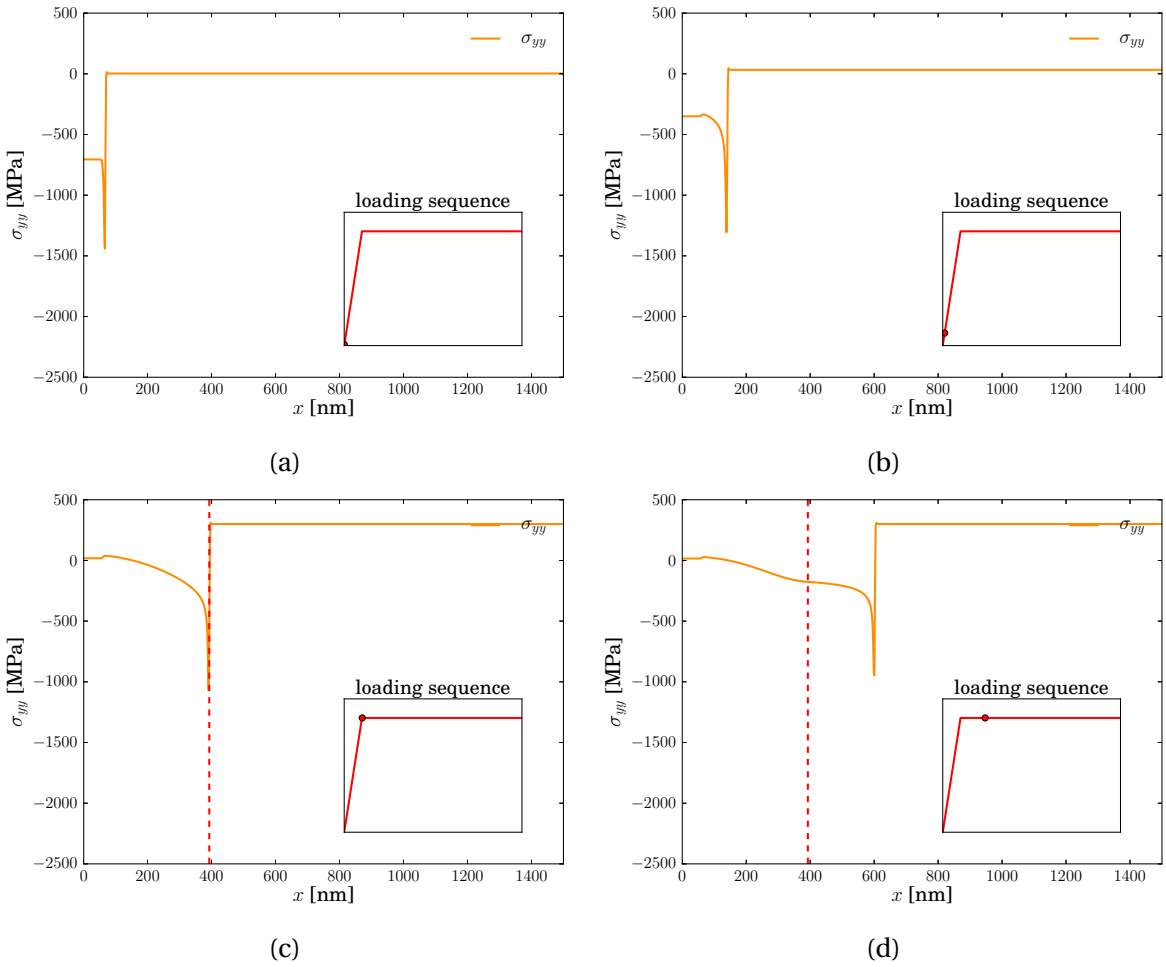

Figure 4.21: Evolution of the σ_{yy} stress throughout the sample at different times (a-b-c-d). The oxidation depth at which the loading sequence ends is denoted by a vertical red dashed line.

to the worst case with respect to the oxide integrity. The combination of compressive growth stresses along with the prescribed compressive stresses is followed by a rapid decrease of the growth stresses. Then the tensile load that follows is shown to be harmful as the oxide experiences about 300 MPa of tensile σ_{yy} stresses, which is almost equal to the prescribed load over the body. For this reasons, the brittle failure of the oxide is likely to occur, despite the total strains are kept at low levels, see Fig. 4.23 (b). Finally, as shown in Fig. 4.24, the mechanical cycling of the oxide tends to homogenise the σ_{yy} stress and even suppresses the artefact located at the initial interface position, which was discussed earlier in this chapter.

4.4.2 Viscoplastic relaxation of the oxide and the substrate

From now, the viscoplastic relaxation of the substrate will always be considered using the parameters in Tab. 4.8 and 4.9. The oxide grows on a (100) surface of an austenitic grain. It is also worth noting that the substrate prescribes the average strain rate of the oxide in the y direction, which becomes non negligible for when the viscoplasticity of the substrate is accounted for. It is followed with non negligible flow stresses in the oxide due to the use of high viscosity parameters in the oxide mechanical behaviour. This has been verified *a posteriori* but has not been reported in the manuscript to make the reading easier. The crystal plasticity laws are briefly recalled, first for the plastic slip rate, see Eq. (2.34) for details:

$$\dot{\gamma}_s = \left\langle \frac{|\tau_s - B_s| - S_s}{K} \right\rangle^n \text{sign}\left(\tau_s - B_s\right) . \tag{4.22}$$

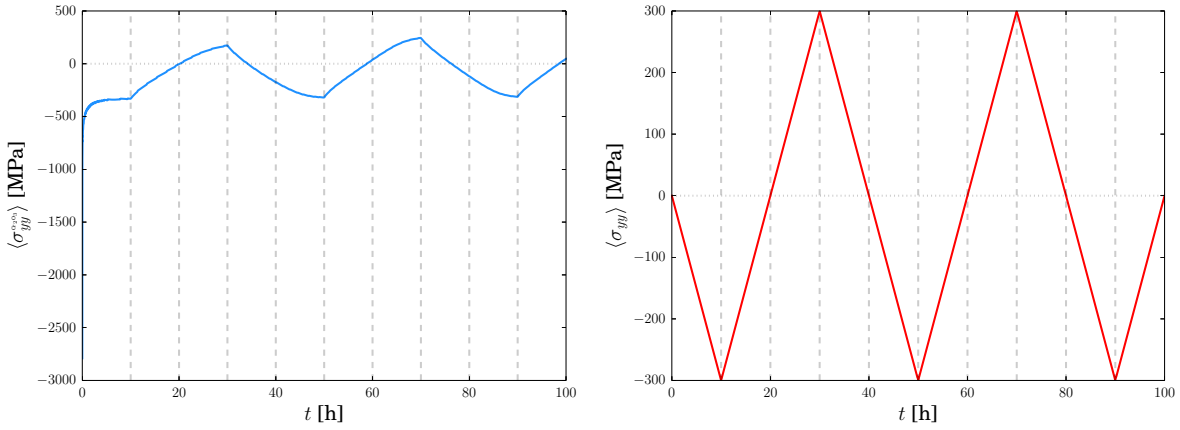

(a) (b)

Figure 4.22: (a) mean σ_{yy} stress in the oxide versus time and (b) mean stress in the substrate versus time.

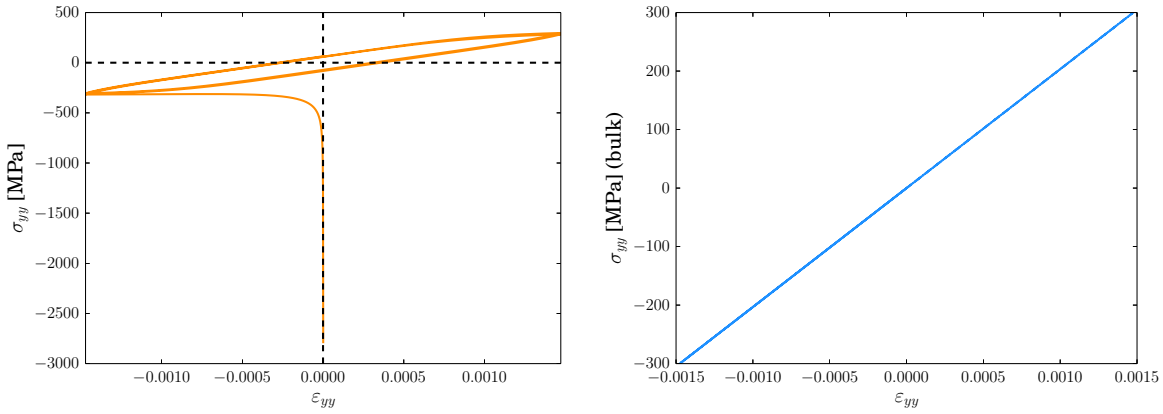

(a) (b)

Figure 4.23: (a) stress-strain curve of the free surface control point and (b) stress-strain curves of the bulk control point.

Table 4.9: Parameters for the crystal plasticity law for γ-Fe.

K [MPa.s$^{1/n}$]	n [-]	S_0 [MPa]	Q [MPa]	b [-]	c [MPa]	d [-]	h_{rs}
100	5	65	45	3	600	20	1

The isotropic hardening is defined as follows – see Eq. (2.37) for details,

$$S_s = S_0 + \Delta S \sum_r h_{rs} \left(1 - \exp\left(-b\gamma_s^{\text{acc}}\right)\right). \tag{4.23}$$

The nonlinear kinematic hardening evolution is governed by a ODE – see Eq. (2.36) for details:

$$B_s = C\alpha_s \quad \text{and} \quad \dot{\alpha}_s = \dot{\gamma}_s - d\alpha_s|\dot{\gamma}_s|. \tag{4.24}$$

Slow strain rate test

The application of a monotonic tensile load during oxidation (Fig. 4.16 (a)) results in the evolution of stress and stress-strain curves for the control points illustrated in Fig. 4.25 and 4.26. From now on,

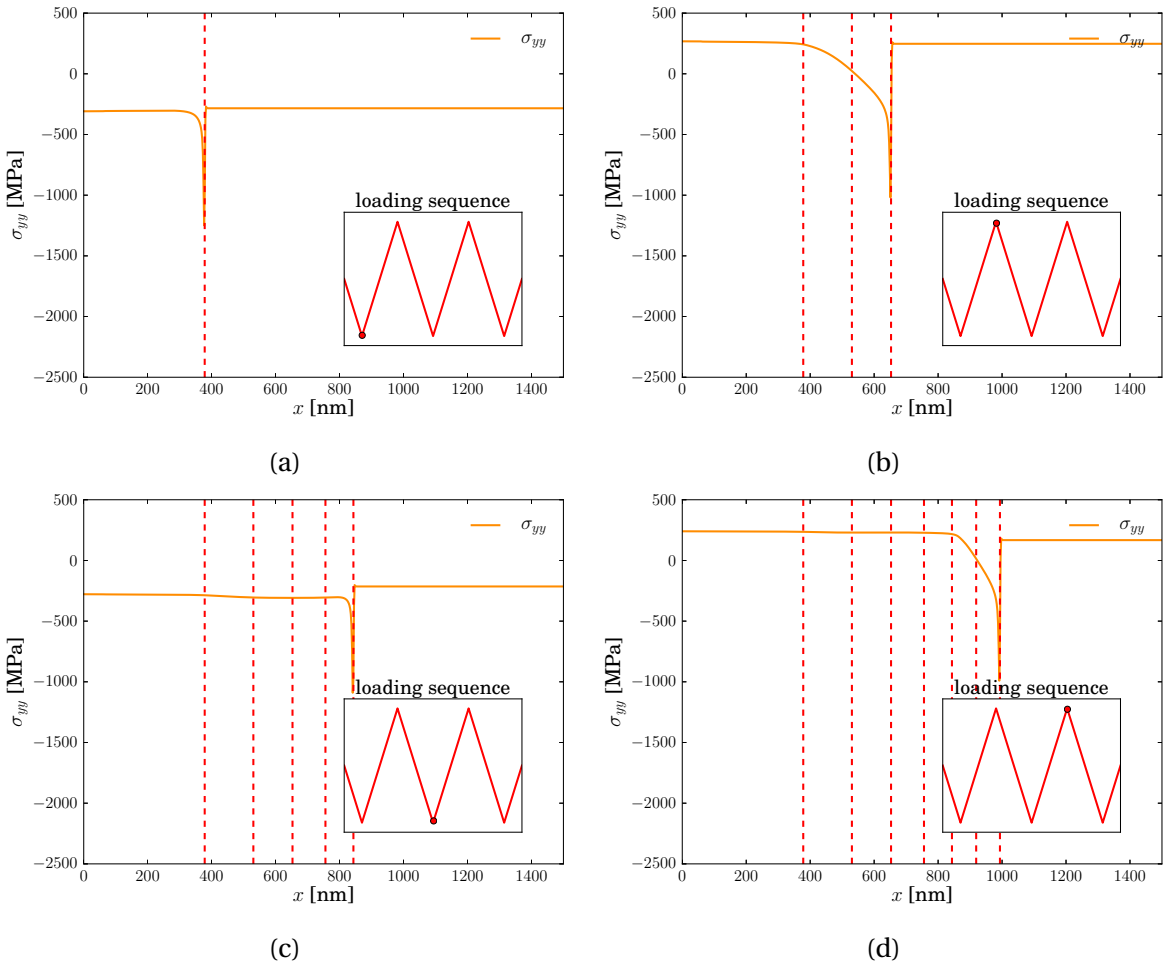

Figure 4.24: Evolution of the stress profile throughout the sample at different times (a-b-c-d). The oxidation depth at each steps of the loading sequence is denoted by a vertical red dashed line.

the accumulated plastic slip γ_{acc} is displayed in parallel with the MOS:

$$\gamma_{\text{acc}} = \int \sum_{s} |\dot{\gamma}_s| dt. \tag{4.25}$$

It results, by comparison with Fig. 4.22 (a), that the mean σ_{yy} stresses in the oxide increase rapidly while the substrate undergoes a plastic deformation. This is illustrated by the generation of accumulated slip in the substrate that is illustrated by the black dashed curve in Fig. 4.25 (a). Such a rapid increase is then followed by an increase of in plane oxide stresses proportional to the applied load once the substrate has been hardened. The Fig. 4.26 shows that the ε_{yy} strain goes up to 17% which is equally applied to the thin oxide film. Such large strains induce high levels of tensile stresses in the oxide layer. After that, the oxide is allowed to deform viscoplastically as shown in Fig. 4.25 (a) where the substrate's non linear response is also shown. It is then likely that the viscoplastic relaxation of the substrate will be followed by the failure of the oxide layer due to the high amounts of tensile stresses that are generated in the oxide – here above 500 MPa. This is how the in plane plastic – or viscoplastic – deformation of the substrate, that can happen locally, curses the oxide film integrity.

Creep test

The application of the creep load during oxidation (Fig. 4.16 (b)) results in the evolution of stress and stress-strain curves for the control points illustrated in Fig. 4.27 and 4.28. Again, the substrate's viscoplastic deformation, which occurs during the loading sequence, is accompanied by the genera-

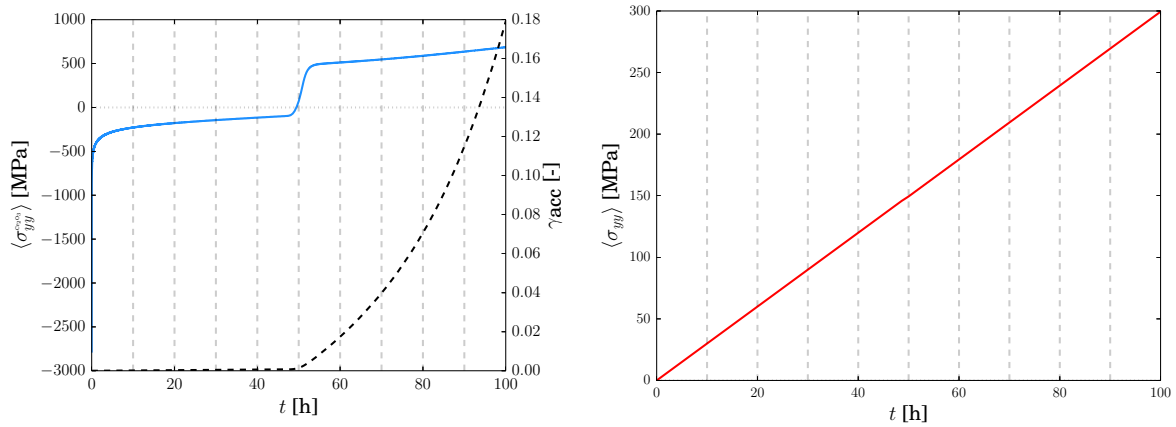

(a) (b)

Figure 4.25: (a) mean σ_{yy} stress in the oxide and accumulated plastic slip versus time and (b) mean stress in the substrate versus time.

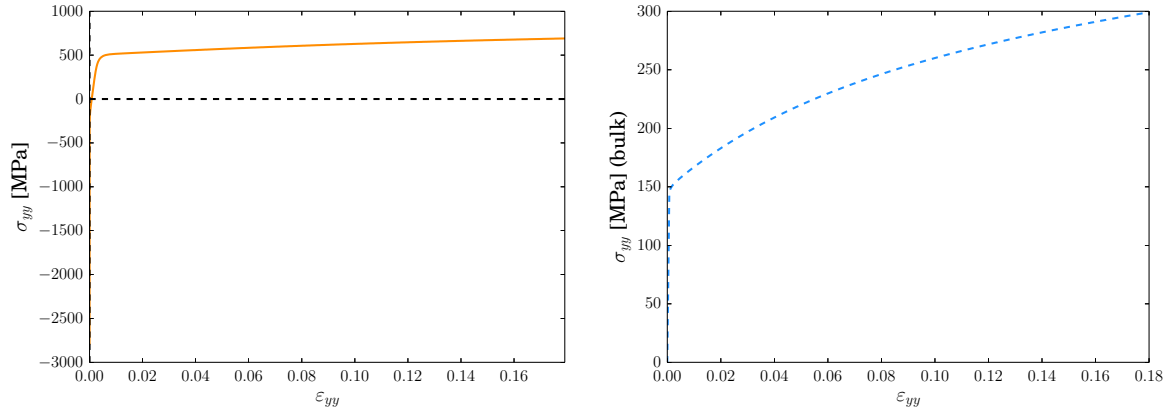

(a) (b)

Figure 4.26: (a) stress-strain curve of the free surface control point and (b) stress-strain curves of the bulk control point.

tion of high levels of σ_{yy} stresses in the oxide. After that, the aforementioned cusp is retrieved. However, the cups can is explained by the viscoplastic relaxation of the growth stresses, see Fig. 4.27 (a). In fact, stresses remain homogeneous away from the interface in the oxide layer during the mechanical loading and the growth. The oxide layer remains then in a state of tension during all the creep test. The first stage of creep is evidenced by the evolution of accumulated slip in the bulk shown in Fig. 4.27 (a). In the same time, the substrate is kept under a constant load, which is identical to the one that is prescribed at the interface, see Fig. 4.27 (b).

Fatigue test

The application of the fatigue load during oxidation (Fig. 4.16 (c)) results in the evolution of stress and stress-strain curves for the control points illustrated in Fig. 4.29 and 4.30. Here, the viscoplastic deformation of the substrate proceeds step by step due to the cycling. The phenomenon is known as ratcheting. However, the plastic strain tends towards a stabilised value, which has been verified on longer computations. Once more, the cyclic loading is shown to curse the oxide integrity. High tensile σ_{yy} stresses are found in the oxide when close to the maxima of the loading sequence, see Fig. 4.29 (a). The hysteresis curve during the cyclic plastic deformation in tension and compression is shown in Fig. 4.30. Such an hysteresis is equally found for the oxide and the mean ε_{yy} strains are always

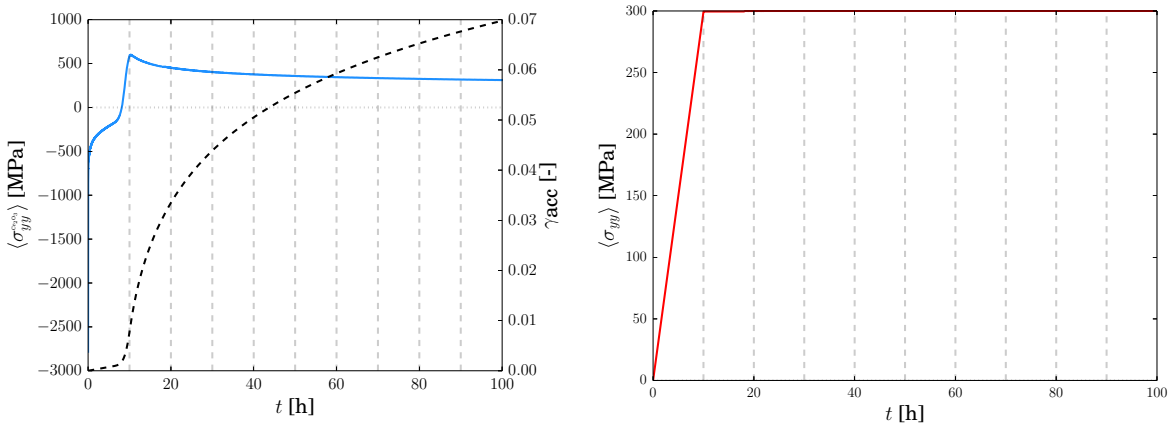

(a) (b)

Figure 4.27: (a) mean σ_{yy} stress in the oxide and accumulated plastic slip versus time and (b) mean stress in the substrate versus time.

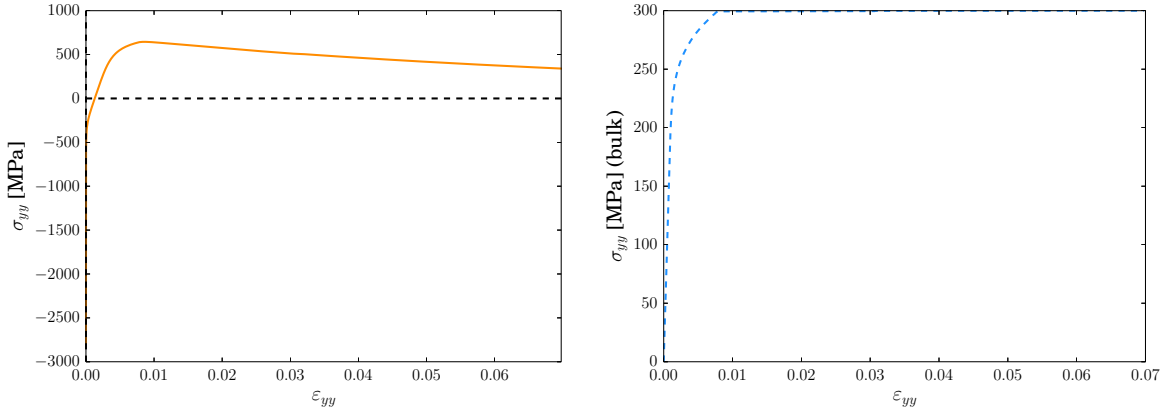

(a) (b)

Figure 4.28: (a) stress-strain curve of the free surface control point and (b) stress-strain curves of the bulk control point.

compressive.

4.4.3 Viscoplastic relaxation of the substrate only

In this last study, the viscoplastic deformation of the oxide is disabled. This is intended to be compared with the statements by [Huntz et al., 2002], that the oxide can uniquely accommodate the stress by its brittle failure. Moreover, the Young modulus of the oxide is higher than that of the substrate, which will obviously make the compressive stresses generated by the PBR to decrease rapidly when the substrate will undergo a viscoplastic or plastic deformation, thus rapidly bringing the oxide layer into a state of tension.

Slow strain rate test

The application of a monotonic tensile load during oxidation (Fig. 4.16 (a)) results in the evolution of stress and stress-strain curves for the control points illustrated in Fig. 4.31. Here, the σ_{yy} stresses in the oxide layer drastically increase up to 20 GPa while the viscoplastic deformation of the substrate increases. They are simultaneously plotted in Fig. 4.31 (a). The Fig. 4.32 shows the elastic response of the oxide and the typical plastic stress-strain of the substrate where about 12% of plastic stains are

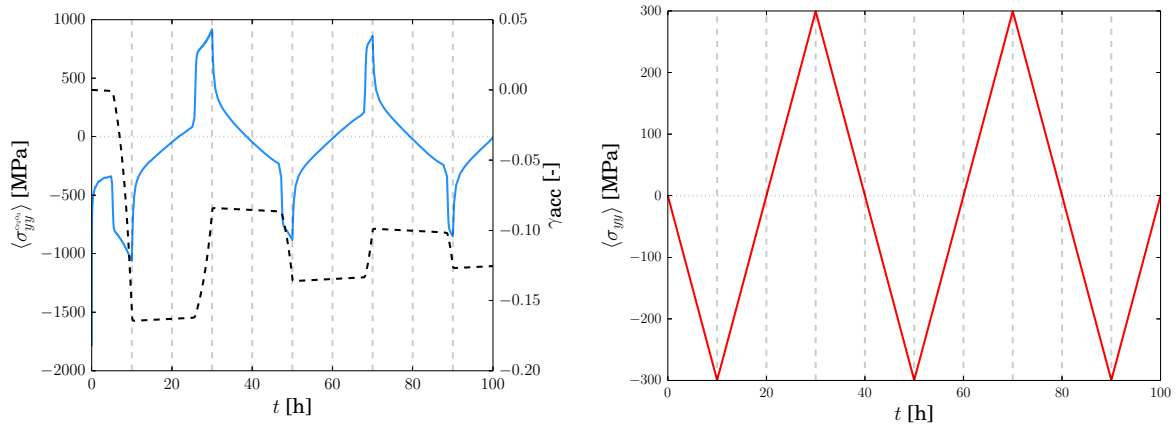

(a) (b)

Figure 4.29: (a) mean σ_{yy} stress in the oxide and accumulated plastic slip versus time and (b) mean stress in the substrate versus time.

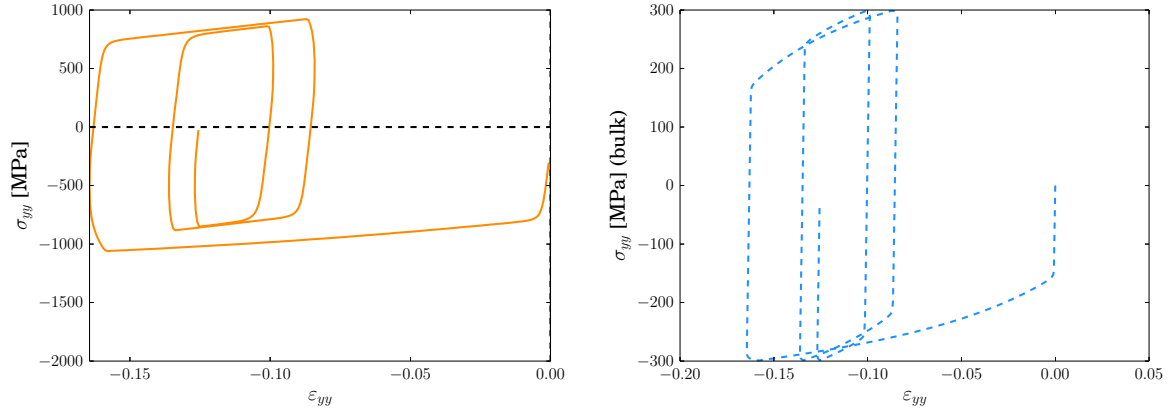

(a) (b)

Figure 4.30: (a) stress-strain curve of the free surface control point and (b) stress-strain curves of the bulk control point.

generated and transmitted to the oxide. It is here certain that the oxide film cannot sustain such a load and will fail.

Creep test

The application of the creep load during oxidation (Fig. 4.16 (b)) results in the evolution of stress and stress-strain curves for the control points illustrated in Fig. 4.33 and 4.34. Here, creep in the substrate induces large levels of viscoplastic deformations as shown in Fig. 4.33 (a). The stresses generated in the oxide layer follows a similar shape as in stage I creep. Moreover they are of tensile nature and rather large, up to tens of GPa. During the creep of the substrate the stress is not kept constant and the influence of the oxide becomes noticeable due to spurious edge effects, see Fig. 4.33 (b). Nevertheless, the oxide will not be able to sustain such stress levels so that the present configuration leads to the brittle failure of the oxide.

Fatigue test

The study ends with the effect of the plastic deformation in the substrate under cyclic loading. The application of the fatigue load during oxidation (Fig. 4.16 (c)) results in the evolution of stress and

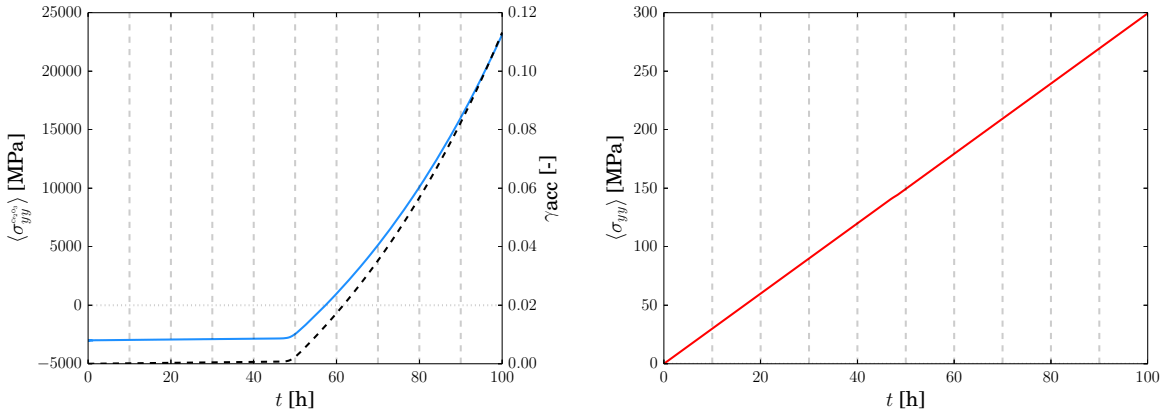

(a) (b)

Figure 4.31: (a) mean σ_{yy} stress in the oxide and accumulated plastic slip versus time and (b) mean stress in the substrate versus time.

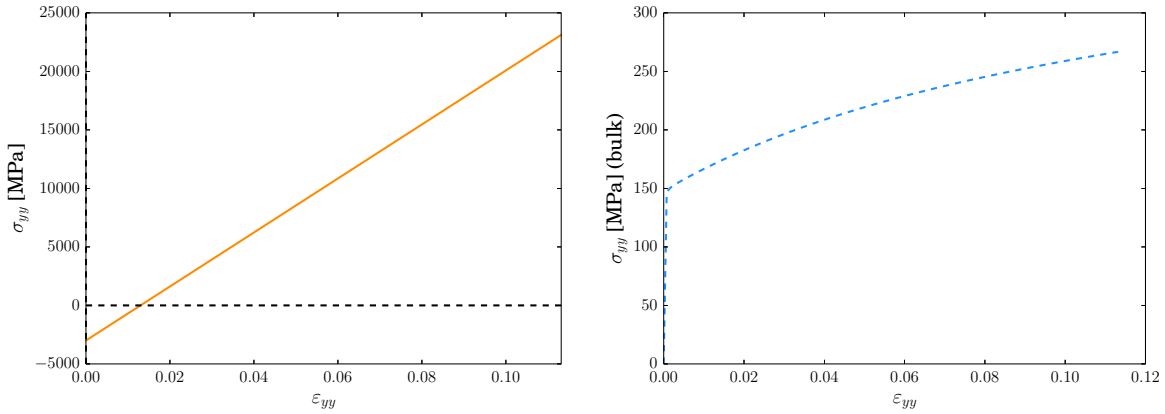

(a) (b)

Figure 4.32: (a) stress-strain curve of the free surface control point and (b) stress-strain curves of the bulk control point.

stress-strain curves for the control points illustrated in Fig. 4.35 and 4.36. It is shown in Fig. 4.35 (a) that the average stress in the oxide is always compressive. Again, steps of viscoplastic slip are reported at the end of each cycle. The plastic deformation of the substrate is kept under a compressive strain as shown in Fig. 4.35 (b), which explains the state of compression found in the oxide. Nevertheless, the compressive stresses are such that the failure can be anticipated for a further analysis. One can finally conclude that the growth of an oxide followed by the generation of compressive strains in the substrate can have a beneficial effect for the oxide film integrity.

4.5 Conclusions

The present chapter is devoted to the application of a multicomponent-stress coupled phase field model to the case of the growth of a planar oxide layer. The materials parameters of the phase field model are obtained from high temperature phase diagram and diffusion data of austenitic stainless steels available in the literature. Oxide growth is studied for the ternary (Fe-Cr-O) and quaternary (Fe-Cr-O-Ni) systems by first neglecting mechanical stresses. The well-known nickel enrichment at the metal-oxide interface is reproduced and its minor role on oxide growth kinetics is emphasised. The chromium depletion is then thoroughly studied by providing an analytic solution of the growth kinetics of the chromium depleted area. Oxide stoichiometry is shown to fix the oxide sided equilibrium

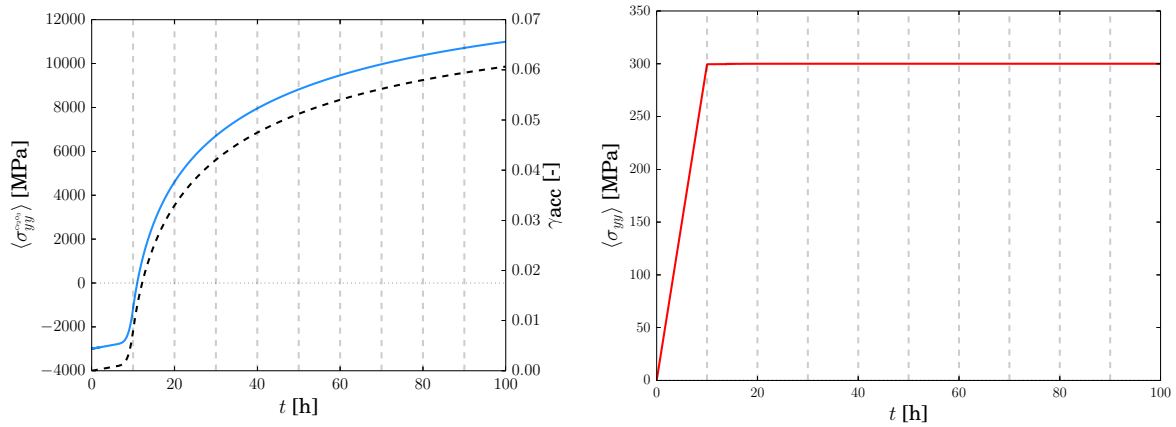

(a) (b)

Figure 4.33: (a) mean σ_{yy} stress in the oxide and accumulated plastic slip versus time and (b) mean stress in the substrate versus time.

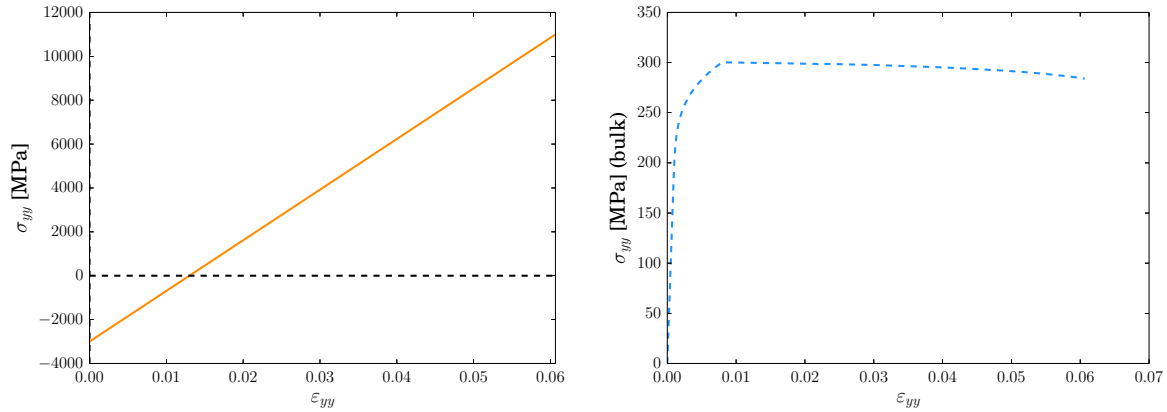

(a) (b)

Figure 4.34: (a) stress-strain curve of the free surface control point and (b) stress-strain curves of the bulk control point.

concentrations, resulting in almost no dependence of oxide growth kinetics on stresses. Oxide growth stresses are then studied for various mechanical loads and it is shown that the viscoplastic deformation of the substrate is of utmost importance. In fact, such a viscoplastic deformation will be followed by the brittle failure of the oxide layer, due to induced tensile stresses. The possible beneficial effect of compressive residual stresses in the substrate are also discussed. The present results can be seen as an extension of the work of [Huntz et al., 2002] for which the oxide growth was accounted solely on the basis of the rate constant. Mass transports were introduced according to the phase diagram data and the mechanical behaviour of the substrate has been enhanced with crystal plasticity. Such preliminary computations were intended to the exploration of the possible mechanical responses during coupled oxide growth under various mechanical loads. The chapter announces the forthcoming two dimensional simulations, for which grain boundary oxidation is addressed.

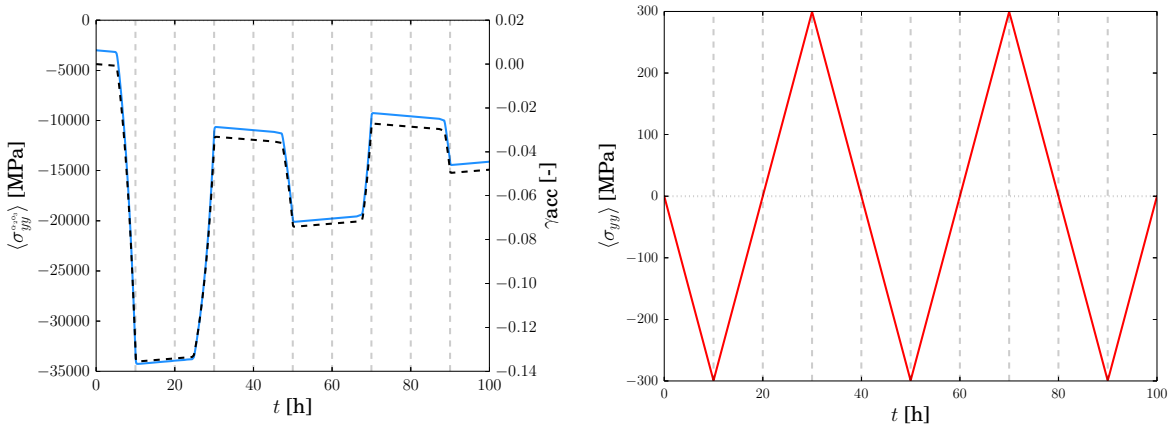

(a) (b)

Figure 4.35: (a) mean σ_{yy} stress in the oxide and accumulated plastic slip versus time and (b) mean stress in the substrate versus time.

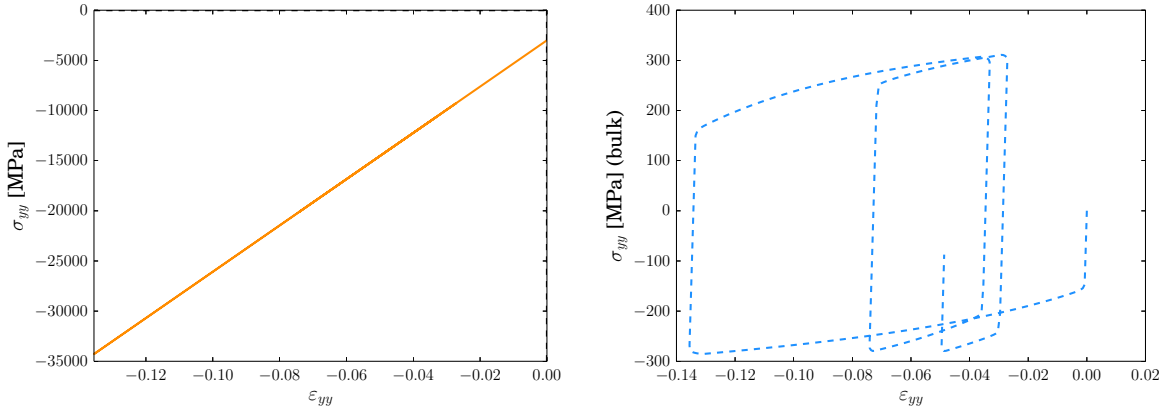

(a) (b)

Figure 4.36: (a) stress-strain curve of the free surface control point and (b) stress-strain curves of the bulk control point.

References

[Adda and Philibert, 1966] Adda, Y. and Philibert, J. (1966). *La diffusion dans les solides*. Number vol. 1 in Bibliothèque des sciences et techniques nucléaires. Institut National des Sciences et Techniques Nucléaires.

[Ammar et al., 2009] Ammar, K., Appolaire, B., Cailletaud, G., Feyel, F., and Forest, S. (2009). Modélisation du couplage changement de phase-mécanique par la méthode des champs de phases et les techniques d'homogénéisation. In *Giens*.

[Atkinson et al., 2003] Atkinson, K., Grimes, R., Levy, M., Coull, Z., and English, T. (2003). Accommodation of impurities in α-Al_2O_3, α-Cr_2O_3, α-Fe_2O_3. *Journal of the European Ceramic Society*, 23(16):3059–3070.

[Auinger et al., 2011] Auinger, M., Naraparaju, R., Christ, H.-J., and Rohwerder, M. (2011). Modelling high temperature oxidation in iron-chromium systems: combined kinetic and thermodynamic calculation of the long-term behaviour and experimental verification. *Oxidation of Metals*, 76(3-4):247–258.

[Baboian, 2004] Baboian, R. (2004). *Corrosion tests and standards : application and interpretation*. West Conshohocken, PA : ASTM International, 2nd ed edition. ASTM Stock Number: MNL20–2nd.

[Cahn and Larché, 1984] Cahn, J. and Larché, F. (1984). A simple model for coherent equilibrium. *Acta Metallurgica*, 32(11):1915 – 1923.

[Clarke, 2002] Clarke, D. (2002). Stress generation during high-temperature oxidation of metallic alloys. *Current Opinion in Solid State and Materials Science*, 6(3):237–244.

[Crank, 1975] Crank, J. (1975). *The mathematics of diffusion*. Clarendon press, Oxford, 2 edition.

[Cunat, 2002] Cunat, P. (2002). *The euro inox handbook of stainless steel*. Materials and applications series, Volume 1. Euro Inox.

[Frost and Ashby, 1982] Frost, H. and Ashby, F. (1982). *Deformation-mechanism maps: the plasticity and creep of metals and ceramics*. Pergamon Press.

[Gale and Totemeier, 2003] Gale, W. and Totemeier, T. (2003). *Smithells metals reference book*. Elsevier Science.

[Hagel, 1965] Hagel, W. C. (1965). Anion diffusion in α-Cr_2O_3. *Journal of the American Ceramic Society*, 48(2):70–75.

[Huntz et al., 2002] Huntz, A., Calvarin Amiri, G., Evans, H., and Cailletaud, G. (2002). Comparison of oxidation-growth stresses in NiO film measured by deflection and calculated using creep analysis or finite-element modeling. *Oxidation of Metals*, 57(5-6):499–521.

[Huntz et al., 1993] Huntz, A., Liu, C., Kornmeier, M., and Lebrun, J. (1993). The determination of stresses during oxidation of Ni: in situ measurements by XRD at high temperature. *Corrosion Science*, 35(58):989 – 997.

[Huntz et al., 1998] Huntz, A., Piant, A., Lebrun, J., and Daghigh, S. (1998). Evidence of stress relaxation in thermally grown oxide layers – experiments and modelling. *Materials Science and Engineering: A*, 248(12):44 – 55.

[Kim et al., 1999] Kim, S., Kim, W., and Suzuki, T. (1999). Phase-field model for binary alloys. *Phys. Rev. E*, 60:7186–7197.

[Kofstad and Lillerud, 1982] Kofstad, P. and Lillerud, K. (1982). Chromium transport through Cr_2O_3 scales I. On lattice diffusion of chromium. *Oxidation of Metals*, 17(3-4):177–194.

[Laheij et al., 1980] Laheij, M., Loo, F., and Metselaar, R. (1980). Phase relations in the Fe-Cr-O system at 1200°C investigated by means of a diffusion couple technique. *Oxidation of Metals*, 14(3):207–215.

[Larché and Cahn, 1985] Larché, F. and Cahn, J. (1985). Overview no. 41 the interactions of composition and stress in crystalline solids. *Acta Metallurgica*, 33(3):331 – 357.

[Mougin, 2001] Mougin, J. (2001). *Tenue mécanique de couches d'oxyde thermique générées sur le chrome et sur quelques aciers inoxydables ferritiques étude des contraintes et de l'adhérence*. PhD thesis, Institut National Polytechnique de Grenoble.

[Perevoshchikova, 2012] Perevoshchikova, N. (2012). *Modeling of austenite to ferrite transformation in steels*. PhD thesis, Université de Lorraine.

[Sabioni et al., 2012a] Sabioni, A., Ramos, R., Ji, V., and Jomard, F. (2012a). Oxygen diffusion study in oxidation films of the AISI 304 austenitic stainless steel. *Defect and Diffusion Forum*, 323-325:345–351.

[Sabioni et al., 2012b] Sabioni, A., Ramos, R., Ji, V., Jomard, F., Macedo, W., Gastelois, P., and Trindade, V. (2012b). About the role of chromium and oxygen ion diffusion on the growth mechanism of oxidation films of the AISI 304 austenitic stainless steel. *Oxidation of Metals*, 78(3-4):211–220.

[Smith, 1975] Smith, A. F. (1975). The diffusion of chromium in type 316 stainless steel. *Metal Science*, 9(1):375–378.

[Steinbach et al., 2012] Steinbach, I., Zhang, L., and Plapp, M. (2012). Phase-field model with finite interface dissipation. *Acta Materialia*, 60(67):2689 – 2701.

[Tsai et al., 1996] Tsai, S., Huntz, A., and Dolin, C. (1996). Growth mechanism of Cr_2O_3 scales: oxygen and chromium diffusion, oxidation kinetics and effect of yttrium. *Materials Science and Engineering: A*, 212(1):6 – 13.

[Zhou et al., 2010] Zhou, C., Ma, H., and Wang, L. (2010). Comparative study of oxidation kinetics for pure nickel oxidized under tensile and compressive stress. *Corrosion Science*, 52(1):210 – 215.

[Zhou, 2010] Zhou, H. (2010). *Stress-diffusion interaction during oxide-scale growth on metallic alloys*. PhD thesis, Georgia Institute of Technology.

CHAPTER

5 Grain boundary oxidation

Contents

Le présent chapitre traite de l'oxydation intergranulaire. La méthode des champs de phases développée dans le Chapitre 3 et directement mise en œuvre dans le Chapitre 4 est dorénavant étendue afin de prendre en compte les effets induits par un réseau de joints de grains sur la morphologie de la couche d'oxyde. Le substrat polycristallin est réduit à sa plus simple forme, qu'est le bicrystal. Chaque grain se voit attribuer une loi de comportement mécanique dont l'anisotropie dans le domaine plastique est liée aux différentes orientations cristallines. L'oxyde est quant-à-lui considéré comme étant une couche amorphe présentant une anisotropie de déformation libre, à l'instar du Chapitre 4. Pour modéliser la pénétration intergranulaire, la diffusivité est couplée avec le réseau de joints de grains du substrat et également avec le réseau de joints de grains oxydés. Dans ces deux réseaux, la diffusivité y est plus forte ce qui revient à générer des courts-circuits de diffusion. Les deux réseaux de joints de grains sont ici considérés comme des interfaces diffuses à l'image de l'interface métal oxyde. À ce titre, il est possible d'intégrer l'énergie de joints de grains du substrat dans le modèle de champs de phases. Cela permet de modéliser le phénomène de mouillage et de rendre compte de son importance sur la morphologie de l'interface métal oxyde par le biais d'études paramétriques.

L'objectif du chapitre est d'étudier les phénomènes possibles entrant en jeu de manière préalable à une amorce de fissure intergranulaire. Dans la littérature, les pénétrations inter- et intragranulaire d'oxyde sont suspectées être des sites privilégiés d'amorçage de fissures. Comme travail de référence, on retrouve dans les travaux d'Evans – [Evans, 1983] – que ces pénétrations induisent des contraintes de tensions dans le métal. Ces contraintes sont générées par une différence de volumes molaires entre la phase d'oxyde et celle du substrat et sont localisées en aval des pénétrations d'oxyde. De plus, la rupture par corrosion sous contrainte des aciers austénitiques est souvent marquée par un réseau de fissures intergranulaire, notamment sous irradiation.

L'étude de l'oxydation intergranulaire est donc essentielle pour mieux comprendre les micromécanismes de fissuration par corrosion sous contrainte. Le calcul numérique permet ainsi de mieux estimer les contraintes mécaniques locales. De plus, les effets viscoplastiques ainsi que ceux induits par un chargement extérieur peuvent être simulés grâce au modèle. Les probables scénarii de ruptures intergranulaires sont ici de deux natures. Le joint de grain oxydé peut rompre à la surface libre de l'oxyde du à un phénomène de concentration de contraintes en vis-à-vis de la pénétration intergranulaire. Le joint de grain présent dans le substrat peut également rompre de part l'ouverture provoquée par la pénétration d'oxyde. La rupture peut être d'autant plus rapide lorsque le joint de grain – oxydé ou non – voit sa résistance mécanique amoindrie par la ségrégation d'éléments d'alliages mais également d'éléments étrangers, dont l'hydrogène est un double exemple – il peut provenir aussi bien de l'environnement qu'être introduit dans le métal lors de sa fabrication.

This chapter is devoted to the study of grain boundary oxidation. The phase field method that is developed in Chapter 3 and used in Chapter 4 is extended to take into account the effects of the grain boundary network on the morphology of the growing oxide layer. First, the polycristalline substrate is here simplified to a bicrystal. The mechanical response of each grain is defined by crystal plasticity with respect to crystal orientations. The oxide layer is considered to be an homogeneous phase that is endowed with an anisotropic eigenstrain as done in Chapter 4. The grain boundary network is modelled as an additional field, which accounts for diffusion short circuits to model the growth of oxide intrusions along grain boundaries. Such a diffusion short circuit behaviour also occurs inside the oxidised grain boundary, which is localised within the oxide layer. The grain boundary energy can be easily accounted given an additional phase field parameter for the grain boundary. This locally modifies the chemical equilibrium and therefore the shape of the metal-oxide interface, which is known as wetting.

The aim of the present chapter is to study the stress fields generated during the growth of such oxide intrusions that lead to stress corrosion crack initiation. Evans, [Evans, 1983], emphasised that the stress fields around such oxide intrusion must be characterised by high tensile stresses in the base metal at the tip of the oxide intrusions. Such stresses are generated by the misfitting oxide with

respect to the substrate. Moreover, stress corrosion cracks in austenitic stainless steels are frequently found to grow along the grain boundary network, which is particularly true in the case of irradiation assisted stress corrosion cracking.

The study of grain boundary oxidation is required to understand the micromechanisms occurring during the environment assisted damage of materials. Numerical simulations allow to evaluate, with respect to the assumptions done in this work, the local stress fields in the vicinity of the oxide intrusion. The viscoplastic effects and those of external mechanical loads can be simulated as well. Two scenarios can be proposed with respect to the simulation results: the grain boundary can break due to (i) stress concentrations at the free surface or (ii) a opening stress generated by the oxide intrusion as reported in [Evans, 1983]. The failure of the grain boundary can be also promoted by the segregation of deleterious elements, that can be provided by the environment or by the alloy itself. For instance, hydrogen is known to diffuse throughout the oxide to be injected into the substrate and can also be found into the alloy composition.

5.1 Grain boundary diffusion

Grain boundary diffusion is recognised to be a leading transport mechanism at low and medium temperatures [Mishin and Herzig, 1999, Mishin, 2001]. For instance, the calculation of creep rates can be done in accordance with the mean grain diameter along with the grain boundary diffusivity, as for Coble-Nabarro creep. Fisher's grain boundary model, see [Fisher, 1951], represents a cornerstone of grain boundary engineering. Since then, the model has undergone several improvements, such as the coupling with segregation for instance. Fisher's grain boundary model basically considers the grain boundary as a high diffusivity path, which is endowed with a finite thickness of approximately 1 nm. This finite thickness represents approximately a few disordered atomic layers. In the work, such a high diffusivity path is replaced by a static phase field. The static phase field is diffuse and is also wider than the typical 1 nm width to allow the use of coarser meshes. Such a diffuse grain boundary is equally convenient for simulating mobile grain boundaries. The mobility of the grain boundaries can be described by an additional partial differential equations analogously to the evolution of the phase field that describes oxide growth. Examples of moving grain boundary problems are found in different topics such as recrystallisation, grain boundary migration or diffusion, *etc.*, for instance. The following work is based on the grain boundary model developed in [Abrivard et al., 2012a, Abrivard et al., 2012b], which was proposed to study recrystallisation. Here, a grain boundary is described using two additional phase fields θ and η, that account for the grain boundary orientation and its localisation – which is also called the crystallinity field. The notion of crystallinity can be misleading somehow as it is equal to zero within grains and equal to one in the diffuse disordered region. The crystallinity can be equally seen to be proportional to $\nabla\theta$. This becomes thus analogous to the treatment of the phase field variable ϕ, where $\nabla\phi$ locates the interface as a disordered region.

5.1.1 Fisher's grain boundary model

Fisher's grain boundary model is defined by a unit pulse diffusivity function that yields the grain boundary diffusivity within a 1 nm wide domain and the bulk diffusivity elsewhere for a single grain boundary. An illustration of Fisher's grain boundary model is provided in Fig. 5.1. Fick's second law admits an analytic solution for the constant source problem, defined by a semi-infinite domain on which a constant concentration of solute is prescribed at the free surface. Initially, the semi infinite domain does not contain any solute. The solute – or component – will then progressively diffuse within the solvant – or substrate. It has been shown that Fisher's grain boundary model results in an enhanced penetration along the grain boundary. Away from it, the model yields the analytic solution of the classical unidimensional constant source problem, see [Crank, 1975]. The analytic solution of Fisher's grain boundary model for the constant source problem is provided in [Le Claire, 1951, Whipple, 1954, Adda and Philibert, 1966, Kaur et al., 1989, Mehrer, 2007] amongst

others. This solution is recalled below,

$$\frac{c(x,y,t)}{c_0} = \operatorname{erfc}\left(\frac{x}{2\sqrt{D_{\text{bulk}}t}}\right) + \frac{x}{2\sqrt{2\pi D_{\text{bulk}}}}\int_1^{\infty}\frac{du}{u^{3/2}}\exp\left(-\frac{x^2}{4u}\right)\operatorname{erfc}\left(\frac{1}{2}\sqrt{\frac{\Delta-1}{\Delta-u}}\left(\frac{y-\frac{\delta}{2}}{\sqrt{D_{\text{bulk}}t}}+\frac{u-1}{\delta(\Delta-1)}\sqrt{D_{\text{bulk}}t}\right)\right), \tag{5.1}$$

where D is the bulk diffusivity, δ the grain boundary thickness, $\Delta = \dfrac{D_{\text{GB}}}{D_{\text{bulk}}}$ the ratio of grain boundary and bulk diffusivities and c_0 the constant concentration prescribed at the free surface. This analytic solution provides a validation step for the finite element implementation of Fisher's grain boundary model. It is recalled that such an analytic solution is often used in the experimental assessment of grain boundary diffusivity. In fact, tracer experiments are performed to reproduce the conditions defined in constant source problem. The experimental setup consists in the deposition of a thin layer of the diffusing specie, mostly isotopes, on a metal. With time, the thin layer will be partially absorbed by the substrate by diffusion. This is often accepted that the constant source solution are fulfilled if the diffusion path of isotopes stay enclosed within a single phase. It is worth noting that the constant source boundary conditions are not straightforward in practice, see [Le Claire, 1963].

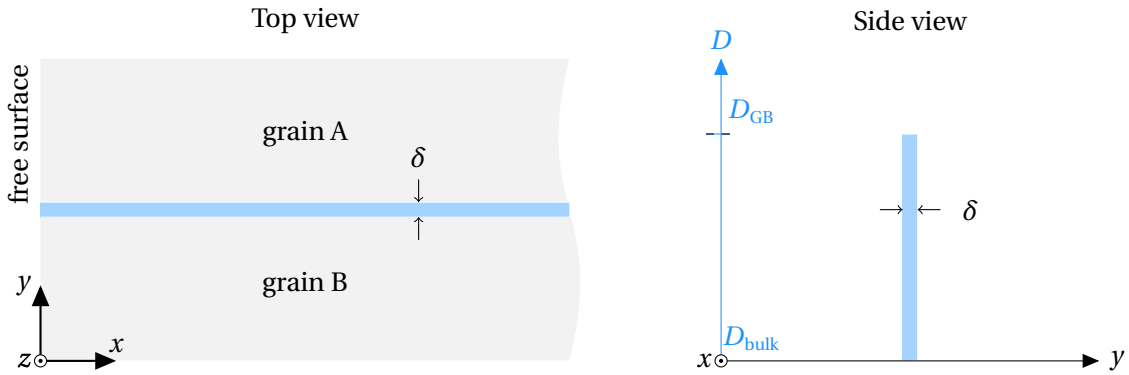

Figure 5.1: Illustration of Fisher's grain boundary model as classically done on the left where δ is the grain boundary thickness. The grain boundary is oriented along the x-axis. The right picture represents the unit step shaped diffusivity profile along a cross section of the grain boundary.

Some remarks on diffusion anisotropy

Diffusion anisotropy consists of the enhancement of the scalar grain boundary diffusivity D into a matrix form $[D]$ with respect to the material frame as follows,

$$[D] = \begin{pmatrix} D_x & 0 & 0 \\ 0 & D_y & 0 \\ 0 & 0 & D_z \end{pmatrix}, \tag{5.2}$$

where D_x, D_y and D_z are the diffusivities along the axis x, y and z respectively. Diffusion anisotropy can also be used for the grain diffusivity and more particularly when non cubic crystal lattices are involved, such as HCP. Nevertheless, in this work, we consider diffusion isotropy for the base metal and the oxide for simplicity. The grain boundary area is thought to be a highly anisotropic diffusion area where enhanced diffusion happens along the grain boundary surface, see [Mishin, 2001]. On the grain boundary surface, diffusion anisotropy can be related to the microstructure of the grain boundary. For instance, low angle grain boundaries can be modelled as dislocation's arrays for which the diffusivity along the direction of the parallel dislocation cores is higher than that in the perpendicular

direction due to pipe diffusion. In the present work, diffusion anisotropy is used to model the surface diffusion along the grain boundary. The elements of the diffusion matrix are chosen to be $D_y = D_{\text{bulk}}$ and $D_x, D_z = D_{\text{GB}}$ with respect to the grain boundary orientation shown in Fig. 5.1.

5.1.2 Diffuse grain boundary model

The diffuse grain boundary enters the finite element modelling in the form of two separate continuous fields analogously to [Abrivard, 2009]. Such fields are accounted for as static degrees of freedom in the finite element method. The field η is referred to as the crystallinity and locates the grain boundary. As previously said, the crystallinity can be misleading. Therefore it is worth recalling that is represents the region of crystalline disorder. The field η can be thus used to locate the grain boundary analogously to Fisher's grain boundary model. The second field θ, represents the crystal orientation and thus the tilt angle in the case of two dimensional problems. This field can be used to evaluate the grain boundary normal and then the anisotropic diffusivity matrix. The two fields are illustrated in Fig. 5.2.

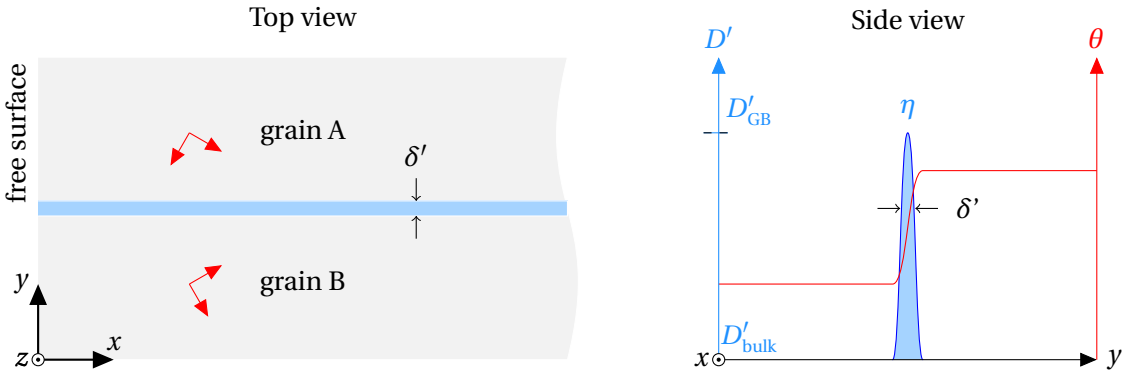

Figure 5.2: Illustration of the Diffuse grain boundary model of effective width δ'. The field η depicts the crystallinity or the region of disorder. The field θ represents the tilt angle between the two grains.

The diffused grain boundary of interest here can be compared to Fisher's grain boundary model. In the following, we choose a diffuse grain boundary profile so that the grain boundary phase fractions are equal in both simulations – $\int D(y)dy = \int D'(y)dy$. The profile of the diffuse grain boundary is defined by the field $\eta(y)$ as follows,

$$\eta(y) = 1 - \tanh^2\left(\frac{y - y_{\text{GB}}}{\lambda/2}\right), \tag{5.3}$$

where $\lambda = \delta' / \left(\log(0.95/0.05)\right)$ and δ' the grain boundary thickness, analogously to Eq. (C.25) while $z = 0.05$. The profile is thus the gradient of a hyperbolic tangent. Then, the grain boundary orientation $\theta(y)$ is defined as follows,

$$\theta(y) = \frac{1}{2}\left(1 - \tanh\left(\frac{y - y_{\text{GB}}}{\lambda/2}\right)\right). \tag{5.4}$$

It is worth noting that the grain boundary orientation is only used here to calculate the grain boundary normal so that the thickness over which the grain orientation changes does not impact the simulation results.

Henceforth, the sharp grain boundary model of Fisher and the current grain boundary model are compared, see Fig. 5.3.

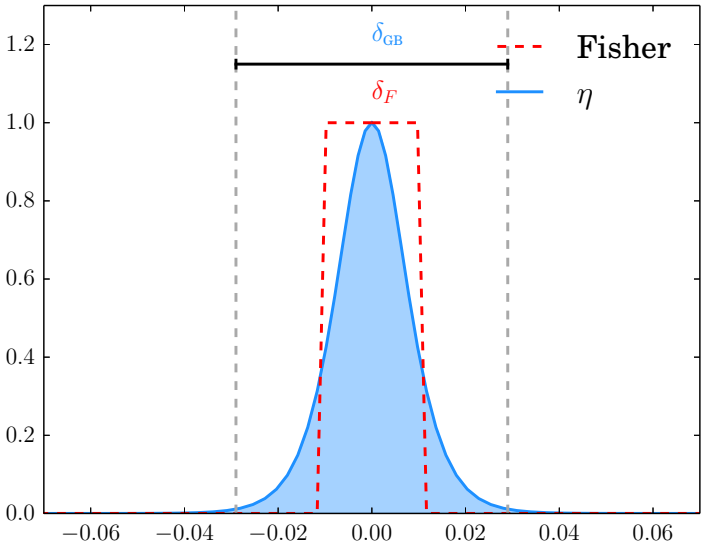

Figure 5.3: Grain boundary shapes for the Fisher model and the diffused model. Materials parameters are scaled, the figure denotes the intensity of the grain boundary field along the y axis shown in Figs. 5.1 and 5.2. Here, $\delta' = \delta_{GB}$ is the thickness of the diffused grain boundary which is wider than that of Fisher's grain boundary model. The area of both grain boundary models are equal resulting in a spread diffused grain boundary.

Fig. 5.3 shows Fisher's grain boundary profile in dashed red lines. The unit step function is equal to the grain boundary diffusivity between -0.01 and 0.01. In blue, the diffuse grain boundary is shown to be spread, resulting in the spreading of the concentration fields, which is observed in the simulation results hereafter. Here, the thickness of the diffuse grain boundary almost twice that of the sharp model of Fisher. This allow nevertheless to use coarser meshes, in the spirit of phase field modelling. In fact, the thickness of the unit step grain boundary model is often taken as 1 nm, which is presently too thin for our meshes and for the characteristic width of the diffuse metal oxide interface – about 10 nm. The grain boundary thickness is set to be close to the interface thickness for all the forthcoming simulations that are devoted to oxide growth.

5.1.3 Preliminary simulations on grain boundary diffusion

Simulations are here performed within the conditions of the constant source problem. Dirichlet boundary conditions are prescribed at the free surface. The prescribed concentration at the free surface is $c_0 = 0.16$, and isotropic or anisotropic diffusion are considered successively for each grain boundary model. Arbitrary physical parameters are here chosen for simplicity and are defined in Table 5.1.

Table 5.1: Dimensionless parameters for the classical constant source problem.

D_{GB}	D_{bulk}	c_0	t	δ
10^{-4}	10^{-7}	0.16	5×10^3	0.02

Simulation results are given in Fig. 5.4. The figure depicts the temporal evolution – with a time arrow from top to bottom – of the concentration field by displaying the concentration isovalues. The concentration isovalues are [0.04, 0.08, 0.12].

The subfigures on the left represent the concentration fields for Fisher's grain boundary model. The analytic solution in Eq. (5.1) is superimposed on the simulation results using, respectively, black

dashed and white dashed lines representing the concentration isovalues. The numerical solution for the case of diffusion anisotropy is equally displayed using red dashed concentration isovalues. It is seen that the three fields are perfectly superimposed so that the analytic solution is retrieved and the negligible impact of diffusion anisotropy on Fisher's grain boundary model is highlighted.

The Figs. 5.4 (b) show the concentration fields for the diffuse grain boundary model. The analytic solution of Fisher's grain boundary is plotted in black dashed lines for comparison purposes. It is first noticed that the concentration isovalues for the anisotropic case – the white dashed lines – are more spread than those of Fisher's grain boundary model. This spreading induces the loss of the dihedral angle between concentration isolines and the grain boundary. The extension of the isotropic diffuse grain boundary to the problem of a growing oxide phase can be shown to result in smoothed oxide intrusions, which is not what is observed in the literature. This is due to the fact that the effective width of the diffuse grain boundary is wider than Fisher's grain boundary. Moreover, the isotropic case is shown to be unable to deeply penetrate the base metal, contrary to the anisotropic case. The anisotropic case is shown here to be able to closely reproduce the grain boundary diffusion behaviour intrinsic to Fisher's grain boundary model. It is worth recalling that this anisotropic diffuse grain boundary can be used for coarser meshes. The present simulations suggest that the concentration fields for the anisotropic diffused grain boundary are more quantitative that those for the isotropic one.

The present results can be post-processed and averaged along the y-axis to be compared with experimental observations. In fact, most of the measurements are averaged concentrations with respect to the depth because of the very small resolution of this phenomenon, which is known as the sectioning method. Fig. 5.5 illustrates such an averaged concentration for the fields shown in Fig. 5.4. Now, experimenters face the inverse problem and are trying to retrieve the most accurate grain boundary diffusivity on the basis of analogous results to those of Fig. 5.5. It is recalled that they first need to ensure that the experimental setup fits the conditions defined in Fisher's grain boundary problem as close as possible.

Again, Figs. 5.5 (a) correspond to Fisher's grain boundary model, whereas Figs. 5.5 (b) correspond to the diffused grain boundary model. The logarithm of the concentration is displayed along the ordinate and the depth to the power 6/5 is displayed on the abscissa axis. It is mentioned that, for particular conditions that are not detailed in this work, a linear relationship between $\log c$ and $x^{6/5}$ can be found in certain configurations, see [Le Claire, 1963, Kučera, 1968] amongst others. The typical profiles for grain boundary diffusion shown in Chapter 2, Fig. 2.26 are hence retrieved. The simulation results reaffirm that diffusion anisotropy has no particular effect on the diffusion behaviour of Fisher's grain boundary model. The simulation results highlight the different behaviour between the isotropic and the anisotropic diffused grain boundaries. In fact, the anisotropic case is shown to penetrate the substrate deeper and shown more limited lateral extent of solute. This can be observed by looking at the average concentration of the isotropic grain boundary, which is firstly above the anisotropic one in the grain boundary diffusion domain and then goes below away from the free surface. This observation shows the need for diffusion anisotropy to model enhanced penetration of solute within the solvent – or in the base metal. It is also worth noting that the grain boundary diffusivity is obtained by measuring the slope of $\log c$ against $x^{6/5}$ in the grain boundary regime, see [Le Claire, 1963, Eq. (15)]. For particular values, this equation simplifies to,

$$D_{\mathrm{GB}}\delta' = 0.78\left(\frac{4D}{t}\right)\left(\frac{\partial \log c}{\partial x^{6/5}}\right)^{-5/3}, \tag{5.5}$$

In the present simulation and according to Eq. (5.5), the grain boundary diffusivity obtained in the case of isotropic diffusion will be approximately half the grain boundary diffusivity found in the anisotropic case. This reveals that there is a non negligible lateral extend of solute in the isotropic case. In the forthcoming simulations devoted to grain boundary oxidation, we choose to work with the anisotropic diffused grain boundaries.

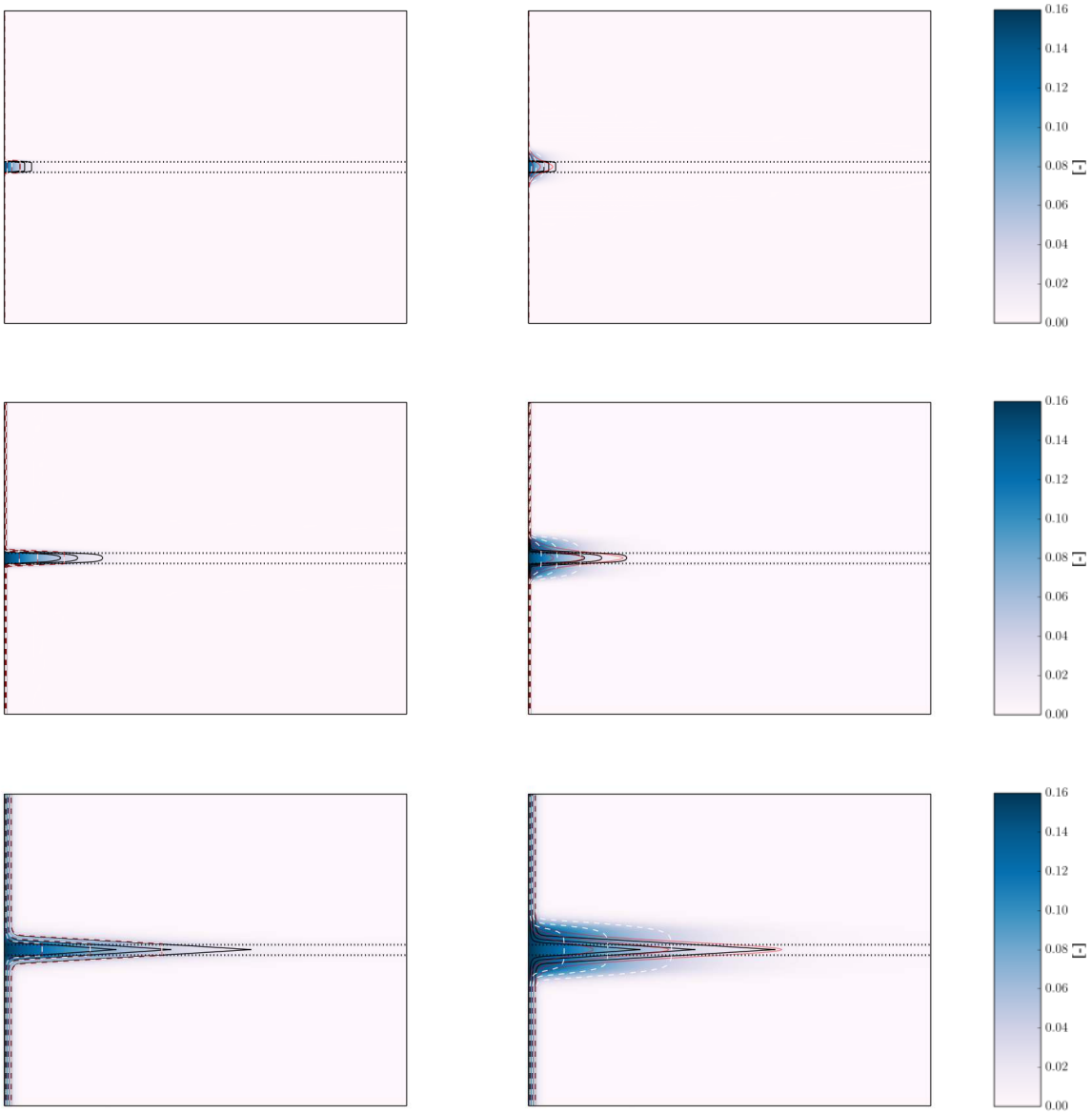

(a) (b)

Figure 5.4: Concentration maps for the constant source problem with isolines localised at $c = [0.04, 0.08, 0.12]$ and at different time $\tilde{t} = [10, 100, 1000]$: (a) results in the case of a step diffusivity with black isovalues corresponding to the analytic solution, white isovalues to simulation results with isotropic diffusion and finally red isovalues for anisotropic diffusion and (b) simulation results in the case of a diffused grain boundary, where the white isovalues denote isotropic diffusion and red isovalues denote the anisotropic one within the grain boundary.

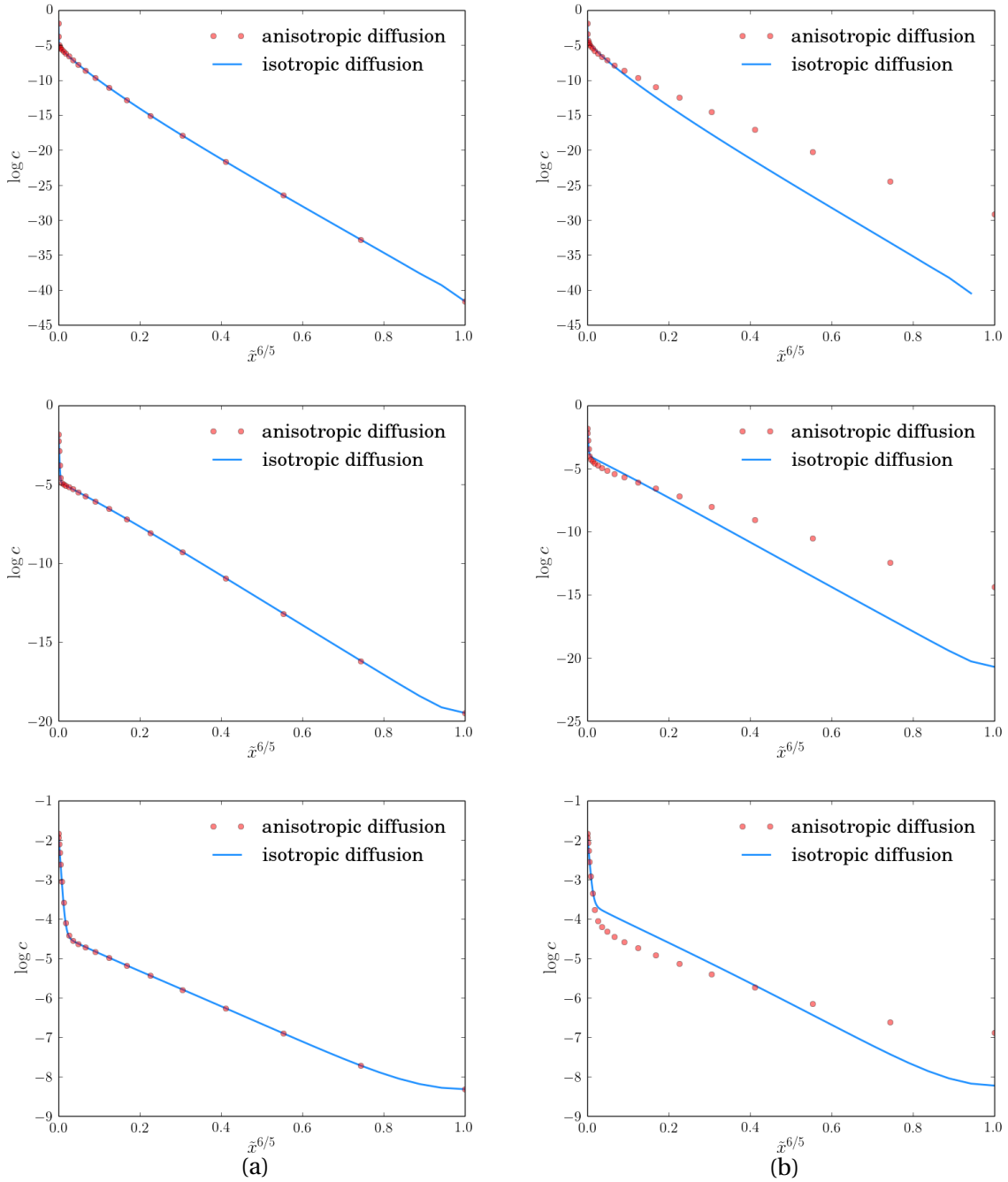

Figure 5.5: Unidimensional projection of the concentration on the depths axis showing the penetration of the mobile compound for (a) the Fisher model and (b) the diffuse grain boundary at increasing time $\tilde{t} = [10, 100, 1000]$. The curves reveal two diffusion regimes: bulk – in the vicinity of the free surface – and grain boundary. It is also noted that diffusion anisotropy has a strong impact on the response of the diffused grain boundary model.

5.2 Grain boundary wetting

The contact point between interfaces in solids is known to form triple junctions. The morphology of triple junctions is determined by the equilibrium conditions resulting in an equilibrium angle. Such an equilibrium angle is called the dihedral angle made by the metal-oxide interface and the grain boundary plane. The equilibrium relationships is known as the Taylor-Young formula and in Chapter 2 and involves interface excess energies. Wetting is the term often employed to describe such an equilibrium, see [Kaplan et al., 2013]. The modelling of wetting is done by the implementation of the grain boundary energy, which is straightforward within the phase field model.

5.2.1 Grain boundary excess energy

Grain boundaries are known to contain an excess of energy that can be either of chemical or mechanical in nature and can be anisotropic with respect to the microstructural patterns inside the grain boundary. In the following work, isotropic grain boundary excess energy is considered for simplicity. This excess energy can be easily accounted for within the phase field method as the grain boundary diffused field η can be used for this purpose. To this aim, an additional free energy density f_{GB} is included within the total free energy, see Eq. (3.14),

$$f_{\text{GB}} = \bar{h}(\phi)\chi\eta\,, \tag{5.6}$$

where χ is the averaged grain boundary free energy density, in the spirit of diffused interfaces. It comes that the integration of the grain boundary energy density over its thickness gives the well-known grain boundary energy γ_{GB}, which is expressed in J.m^{-2} [Balluffi, 1992],

$$\int_y f_{\text{GB}}\,dy = \gamma_{\text{GB}}\,. \tag{5.7}$$

The above equation allows then to calibrate χ from realistic values of γ_{GB}. This additional free energy as it is coupled with the phase field parameter ϕ enters the thermodynamic force associated with ϕ, which is here π and is defined in Chapter 3. In the case of a phase field model based on the Gibbs free energy, and assuming that the grain boundary excess Gibbs and Helmholtz free energy densities are equal, the driving force (3.80) can be rewritten as:

$$F_\phi^V = f^\alpha - f^\beta - \mu_{\text{i}}\left(c_{\text{i}}^\alpha - c_{\text{i}}^\beta\right) - \chi\eta\,. \tag{5.8}$$

This relationships expresses the coupling between the grain boundary and the evolutionary equation of the phase transformation. The equilibrium profile of the phase field is then modified by the grain boundary.

5.2.2 Simulation of grain boundary wetting

Problem description

The study of grain boundary wetting is conducted using the parameters defined in Table 4.3 for a bicrystal of surface area 400 × 300 nm^2, respectively, for the abscissa and ordinate axis. In such a bicrystal, either a cylindrical precipitate or a planar oxide layer is introduced in Figs. 5.6 and 5.7. At $t = 0$, the radius of the cylindrical precipitate, which is here a Cr_2O_3 nodule, is set to 100 nm and put in the centre of the simulation domain. Again, the planar interface is initially localised at the centre of the simulation domain. The boundary conditions are set to zero fluxes so that the average concentration is kept constant during the oxide nodule relaxation. The simulations are performed for the case of the ternary alloy using the parameters defined in Table 4.3 when mechanical stresses are neglected. The simulation parameters are recalled in Table 5.2. The system is allowed to relax over 1000 hours.

Table 5.2: Parameters for the simulation of the simulation of wetting.

	Cr_2O_3	γ-Fe	interface
k_O [J.m^{-3}]	1.0×10^{11}	1.0×10^{11}	
k_{Cr} [J.m^{-3}]	1.0×10^{11}	1.0×10^{9}	
$\hat{c}_O$ [-]	0.5	0.	
$\hat{c}_{Cr}$ [-]	0.33	0.	
D_O [m^2.s^{-1}]	$8.\times10^{-18}$	5.6×10^{-17}	
D_{Cr} [m^2.s^{-1}]	4.7×10^{-19}	5.6×10^{-17}	
δ [m]			$10.\times10^{-9}$
γ [J.m^{-2}]			0.1

Equilibrium shape

The Young Laplace equation is here recalled from Eq. (2.38):

$$\gamma_{\text{GB}} = 2\gamma_\phi \cos(\theta)\,, \tag{5.9}$$

where γ_{GB} is the grain boundary energy, γ_ϕ the metal-oxide interface energy and θ the dihedral angle formed by the interface and grain boundary at equilibrium, see Fig. 2.23. It is then noted that the Young-Laplace equation (2.38) is retrieved for all phase field simulations as seen in Figs. 5.6 and 5.7. The procedure for the calculation of the dihedral angle in Figs. 5.6 and 5.7 is the following :

- Interpolation of the arc made by one side of the metal oxide interface – the red dashed line –
- Calculation of the tangent of such an arc at the triple point – the gray dashed line –
- Calculation of the angle between the grain boundary and the tangent to the metal oxide interface

The material parameters used in the grain boundary simulations are its thickness δ' and its energy density χ, which enter the phase field framework developed in Chapter 3. From those two parameters, one can readily calculate the grain boundary energy γ_{GB} from the grain boundary profile η. Thus,

$$\begin{aligned}
\gamma_{\text{GB}} &= \int_{-\infty}^{+\infty} \chi\eta\, dy\,, \\
&= \chi \int_{-\infty}^{+\infty} \left(1-\tanh^2\left(\frac{y-y_0}{\lambda/2}\right)\right) dy\,, \\
&= \chi\frac{\lambda}{2}\left[\tanh\left(\frac{y-y_0}{\lambda/2}\right)\right]_{-\infty}^{+\infty}\,, \\
&= \chi\lambda\,.
\end{aligned} \tag{5.10}$$

The Young-Laplace formula (5.9) then gives the dihedral angle:

$$\theta = \arccos\left(\frac{\gamma_{\text{GB}}}{2\gamma_\phi}\right) = \arccos\left(\frac{\chi\lambda}{2\gamma_\phi}\right). \tag{5.11}$$

In the simulations, we choose arbitrary grain boundary energy densities χ for a given grain boundary thickness δ' :

$$\frac{\chi\lambda}{2\gamma_\phi} \in \{0.,0.2,0.4,0.6,0.8,1.\}\,. \tag{5.12}$$

The corresponding dihedral angle is displayed in Figs. 5.6 and 5.7.

Wetting driving force

Chemical equilibrium is prescribed in the present simulations so that the interface concentrations[1] are dependent on curvature – known as the Gibbs-Thomson effect – and on grain boundary energy but solely within the diffuse triple junction. The out-of-equilibrium triple junction – which is localised by the intersection of the grain boundary and the metal-oxide interface – drives the metal-oxide interface curvature evolution. This is why the evolution of the interface morphology is globally curvature driven. From here, it is interesting to recall the phase field driving force – see Eq. (3.119) for the planar interface:

$$F^V = \int_{-\infty}^{+\infty} h'(\phi) F_\phi^V \, dx. \tag{5.13}$$

This driving force contains the following additional term within the diffuse grain boundary,

$$F_{\text{wet.}} = \int_{-\infty}^{+\infty} -h'(\phi)\, \chi\eta \, dx = -\chi\eta. \tag{5.14}$$

This additional term is progressively compensated by the non zero curvature of the metal-oxide interface. Moreover, in the simulation, it is remarked that the tanh profile of the phase field is modified at it seems to contract in the vicinity of the grain boundary. This is why the analysis of the diffuse equilibrium is complex. Another way to compensate the grain boundary energy is to modify the interface concentrations that are known to govern the phase transformation kinetics. This is why it is necessary to evaluate the impact of wetting on the oxide growth kinetics, which will be done in the next section.

Heterogeneous driving force for the oxide nodule

For the reason mentioned above, it is necessary to characterise the evolution of the interface concentrations during the wetting process. The evolution of the chromium concentration during the wetting process is illustrated in Figs. 5.8 for the case of the oxide nodule. The case of the planar oxide layer will give analogous results and will therefore not be discussed. The chromium concentration field is shown to be heterogeneous in the substrate which indicates that the chemical equilibrium is not constant along the interface. The most depleted chromium areas are located in the vicinity of the grain boundary region, which can expected from preliminary 1D calculations of the tie-line accounting for Eq. (5.14). The heterogeneities of the chromium concentrations field then fade away during the wetting process. Moreover, the concentration heterogeneities are here rather small, *e.g.* of the order of 10^{-2}. This implies that the induced tie-line shift during wetting is almost negligible. The equilibrium angle is then slowly provided after more than 100 hours, which is much greater than the characteristic diffusion time for oxide growth in the framework of the constant source problem (about 5 hours). All simulations provided similar results, that are homogeneous concentration fields at equilibrium and almost negligible concentration heterogeneities during the wetting process.

Wetting kinetics for the planar oxide layer

Finally, the evolution of the triple point position is drawn considering the grain boundary energies, $\frac{\chi\lambda}{2\gamma_\phi} \in \{0, 0.2, 0.4, 0.6, 0.8, 1.\}$, for the case of the planar oxide layer, see Fig. 5.11. The post-processed simulation results are displayed in Fig. 5.9. This figure shows the evolution of the logarithm of the position of the triple junction for a given grain boundary energy less the position of the interface for the case of zero grain boundary energy to remove spurious effects encountered by the initial transient regime. It results that the time dependence of the wetting process is 0.44, which is close to

[1] The ones that drive the kinematics of the phase transformation

the parabolic growth rate. The case where, $\frac{\chi\lambda}{2\gamma_\phi} = \left\{0, \frac{1}{5}\right\}$, cannot be displayed as it is too close to the case $\frac{\chi\lambda}{2\gamma_\phi} = 0$, since the logarithm cannot be calculated as negative values are here involved.

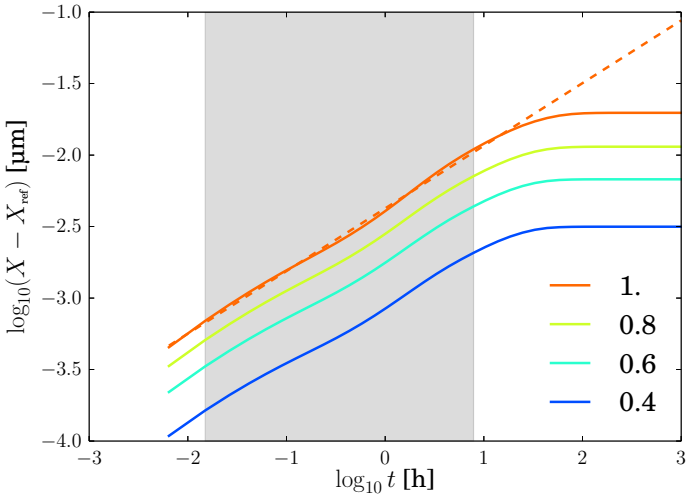

Figure 5.9: Evolution of the triple point position for different grain boundary energies when the grain boundary and bulk diffusivities are equal. The curve parameter is the ratio of grain boundary and interface energies, $\frac{\chi\lambda}{2\gamma_\phi}$. The increase of grain boundary energy is followed by a translation of the displacement curve of the triple point. The shaded grey area defines the domain for the linear regression, where the predicted slope is approximately 0.44.

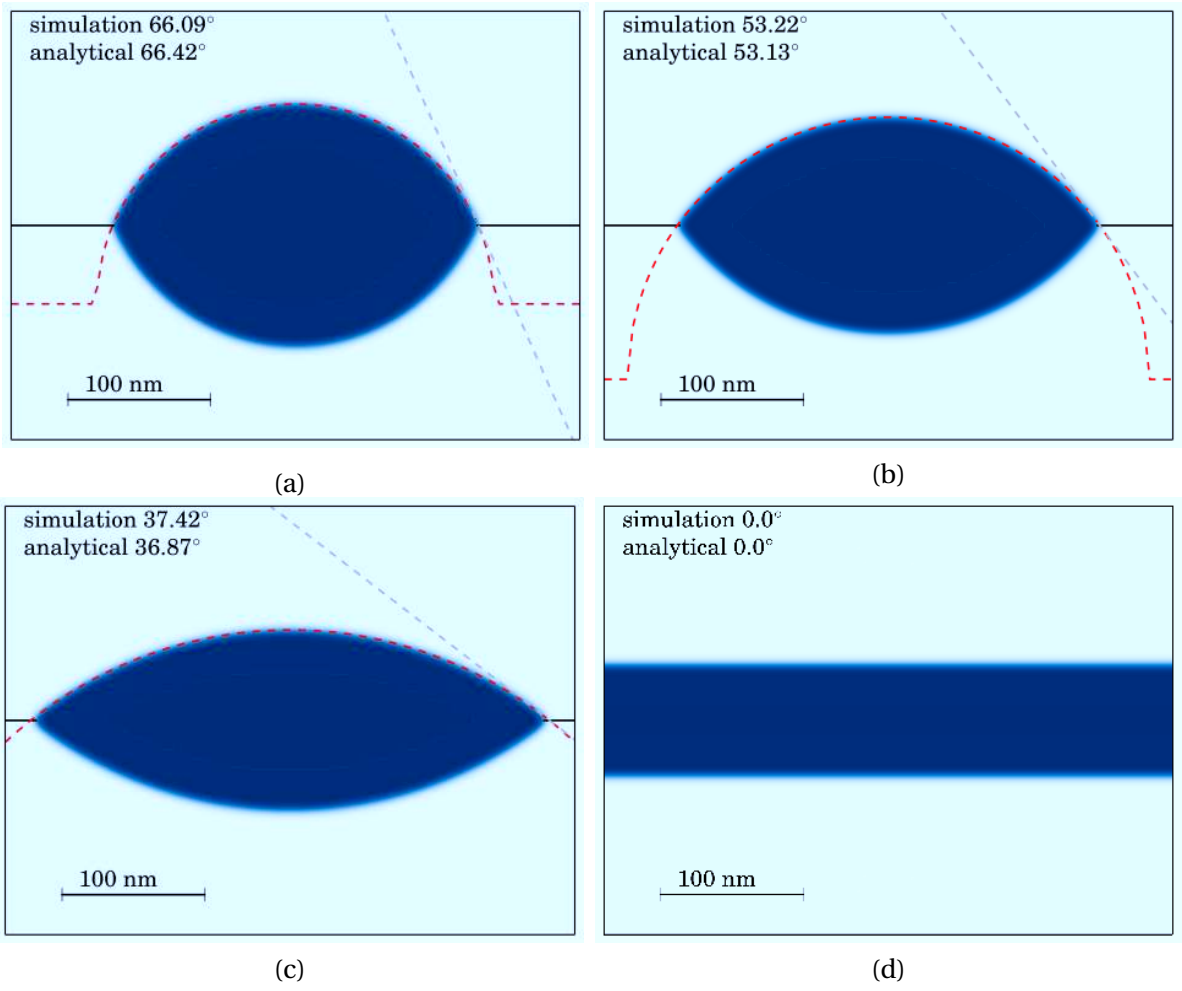

Figure 5.6: Wetting of an oxide precipitate along a grain boundary with δ = 10 nm and ϕ_{GB} = 1 J.m^{-2}. The solid white arc is used to post-process the wetting angle of the simulations, which is displayed in Fig. 2.23. Here, (a) χ such as cos(θ) = 0.4, (b) χ such as cos(θ) = 0.6, (c) χ such as cos(θ) = 0.8 and (d) χ such as cos(θ) = 1.0.

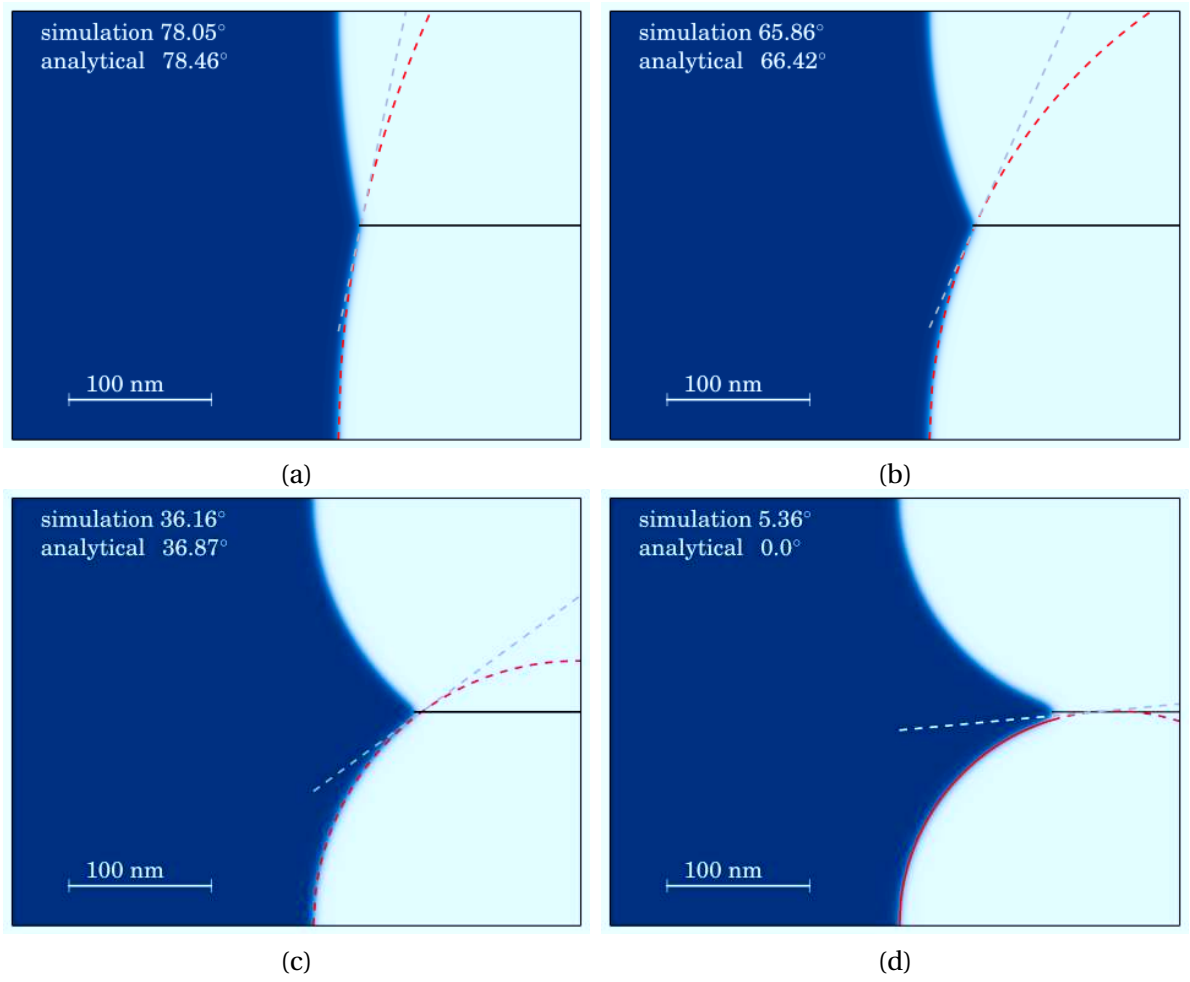

Figure 5.7: Wetting of the oxide layer along a grain boundary with $\delta = 10$ nm and $\phi_{GB} = 1$ J.m^{-2}. The dashed red arc is used to post-process the wetting angle of the simulations, which is displayed in Fig. 2.23. Here, (a) χ such as $\cos(\theta) = 0.2$, (b) χ such as $\cos(\theta) = 0.4$, (c) χ such as $\cos(\theta) = 0.8$ and (d) χ such as $\cos(\theta) = 1.0$.

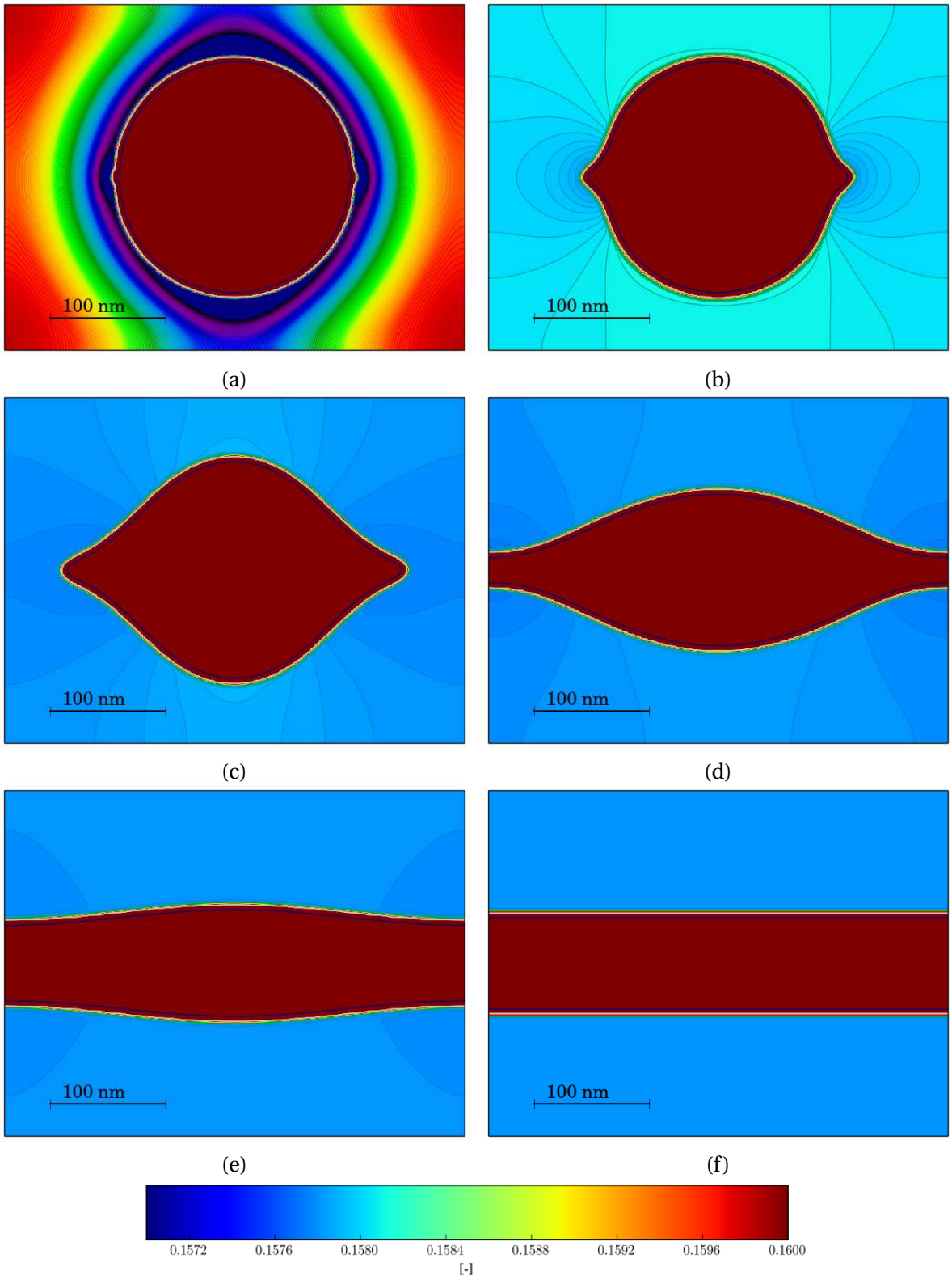

Figure 5.8: Evolution of the chromium concentration field during the wetting process, from (a) to (f) (respectively after 0.006, 0.3, 6, 34, 82, 933 hours of relaxation). The interface is localised by the solid line surrounding the precipitate.

Effect of heterogeneous diffusion on the wetting kinetics for the planar oxide layer

It is recalled that in the above wetting study, the grain boundary diffusivity was equal to the bulk diffusivity. In the following, the simulation of wetting behaviour is enhanced by considering isotropic heterogeneous diffusion in the matrix. Here, the chosen grain boundary diffusivity is two orders of magnitude greater than the bulk diffusivity. The resulting triple point motion for each case is illustrated in Fig. 5.10.

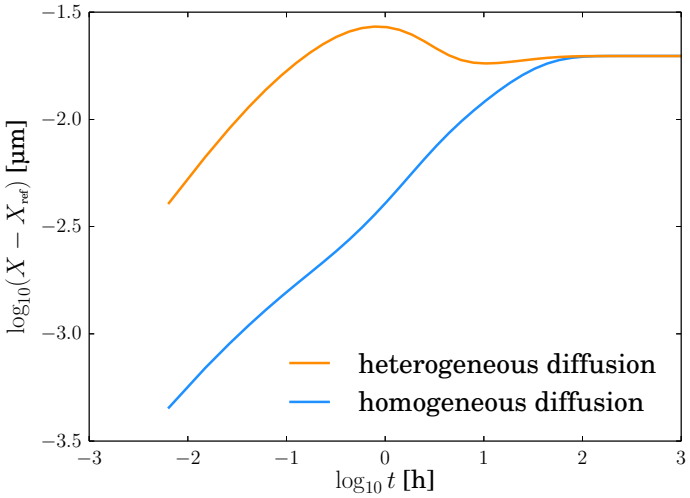

Figure 5.10: Evolution of the triple point position for heterogeneous and homogeneous diffusion and equal energies in all grain boundaries. The combined action of heterogeneous diffusion and wetting is shown to lead to an underdamped response. The equilibrium is reached approximately after same relaxation time for each simulation.

It becomes clear from Fig. 5.10 that grain boundary diffusivity plays a major role in the wetting process. The displacement of the triple point is much more rapid due to diffusion short circuit effects. An underdamped response is also found and the triple point overpasses its equilibrium position several times to finally reach its equilibrium position. Such equilibrium is finally found after quasi identical relaxation times for the two cases. The simulation emphasises the strong effect of heterogeneous diffusion on the dynamics of the dihedral angle, the one between the metal oxide interface and the grain boundary. Moreover, the time dependence of wetting is also shown to be close to a parabolic regime in the case of heterogeneous diffusion. Finally, the maps of the phase field that picture the metal oxide interface morphologies are displayed in Fig. 5.11 for the case of homogeneous diffusion on the left and heterogeneous diffusion on the right. The maps illustrate the large differences of the interface morphology induced by heterogeneous diffusion.

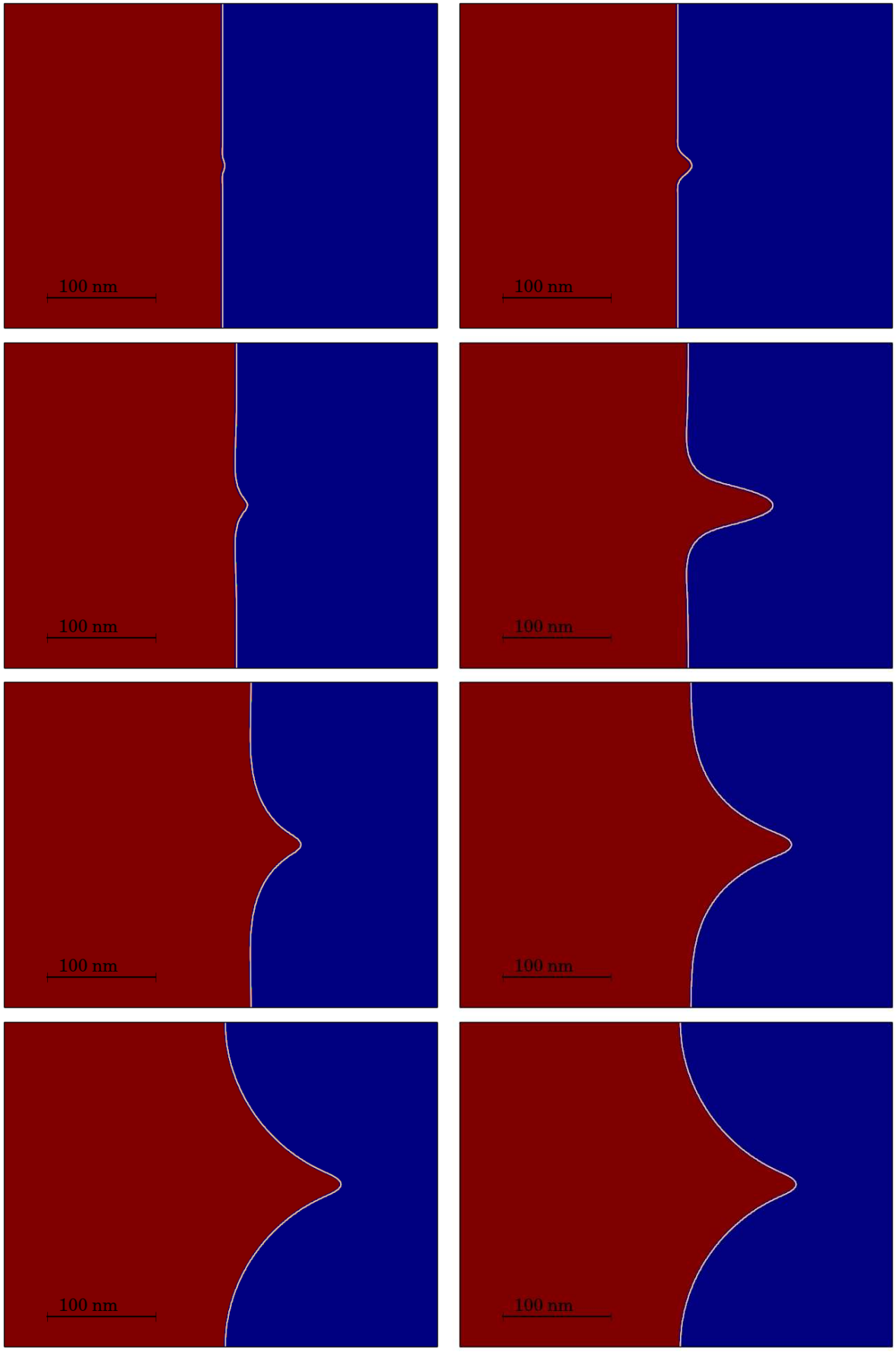

Figure 5.11: Wetting of the oxide layer with increasing time from top to bottom. The maps on the left hand side correspond to the homogeneous diffusion whereas the maps on the right hand side correspond to the heterogeneous diffusion.

5.3 Oxidation of a bicrystal

This section is devoted to the study of intergranular oxidation within the context of coupled heterogeneous diffusion and wetting. Here, stresses will henceforth assume to be induced by oxide misfit strains, as previously discussed in Chapters 2, 3 and 4. Heterogeneous diffusion is also considered as a constitutive element in grain boundary diffusion in both the substrate and oxide. For simplicity, enhanced grain boundary diffusion is here treated by modifying the ratio between bulk and grain boundary diffusion, denoted R_{GB}. Then, such a ratio is the same in the oxide and in the substrate for simplicity as follow,

$$R_{\text{GB}} = \frac{D_{\text{GB}}^{\text{Cr}_2\text{O}_3}}{D_{\text{bulk}}^{\text{Cr}_2\text{O}_3}} = \frac{D_{\text{GB}}^{\gamma\text{-Fe}}}{D_{\text{bulk}}^{\gamma\text{-Fe}}}, \tag{5.15}$$

During the following simulations, this ratio will be set to 10, 100, and 1000 as beyond such values, the oxide intrusion becomes needle shaped.

Simulation parameters

First, the misfit strain is modelled by using an additional eigenstrain $\varepsilon_{\star}^{\text{Cr}_2\text{O}_3}$ in the oxide phase. Expressing it in the coordinate frame used in Fig. 5.2 leaves,

$$\varepsilon_{\star}^{\text{Cr}_2\text{O}_3} = \begin{pmatrix} 0.02 & & \\ & 0.01 & \\ & & 0.01 \end{pmatrix}. \tag{5.16}$$

As stated in [Evans, 1983], the oxide intrusion will then generate tensile stresses in the substrate in the vicinity of the metal-oxide interface. In addition to that, stresses are here relaxed by means of isotropic and anisotropic viscoplasticity – respectively in the oxide and in the substrate – as discussed in Chapter 4. The remaining material parameters are defined in Table 4.9 for the mechanical behaviour of γ-Fe, Table 4.8 for the mechanical behaviour of Cr_2O_3 and in Table 4.3 for the chemical behaviour of each phase. In addition, the yield stress of the oxide phase is set to 200 MPa. Finally, the grain boundary energy is assumed to range between 0 and 240 mJ.m^{-2} assuming that realistic values can go up to 1000 mJ.m^{-2} and grain boundary diffusivity to be two orders of magnitude greater than bulk diffusivity for simplicity.

Geometry of the problem

An illustration of the finite element mesh is given in Fig. 5.12. Here, it is shown to be composed of a finely meshed area embedded within a coarse mesh. The fine mesh consists in a grid of 1 nm resolution. The resulting full mesh cannot be displayed here but an example is partially displayed in Appendix G. The simulation domain consists hence of a finely meshed area of $l \times h$ nm^2, which spreads into a coarser mesh of depth L and height H. Geometric progression in element sizes are used inside the coarse meshed areas for a smooth transition between the two regions.

The grain boundary is here perpendicular to the free surface, analogously to Fisher's grain boundary problem. The diffused grain boundary thickness is set to 10 nm, like for the metal-oxide interface. The oxide thin film has an initial depth of 60 nm to bypass the modelling of its nucleation and related numerical difficulties. Oxide growth is induced by the stoichiometry overshoot of oxygen at the free surface analogously to Chapter 4. Heterogeneous and anisotropic diffusion is used within both phases to ensure sufficient oxide penetration levels along the grain boundary. It is worth recalling that the short circuit diffusion behaviour of the oxidised grain boundary (inside the oxide layer) is to date not fully understood. Nevertheless, preliminary simulations showed that *it is needed for the formation of deep intergranular oxide intrusions*. Some aspects of experimental observations of a particular chemical behaviour of oxidised grain boundaries were discussed in Chapter 2.

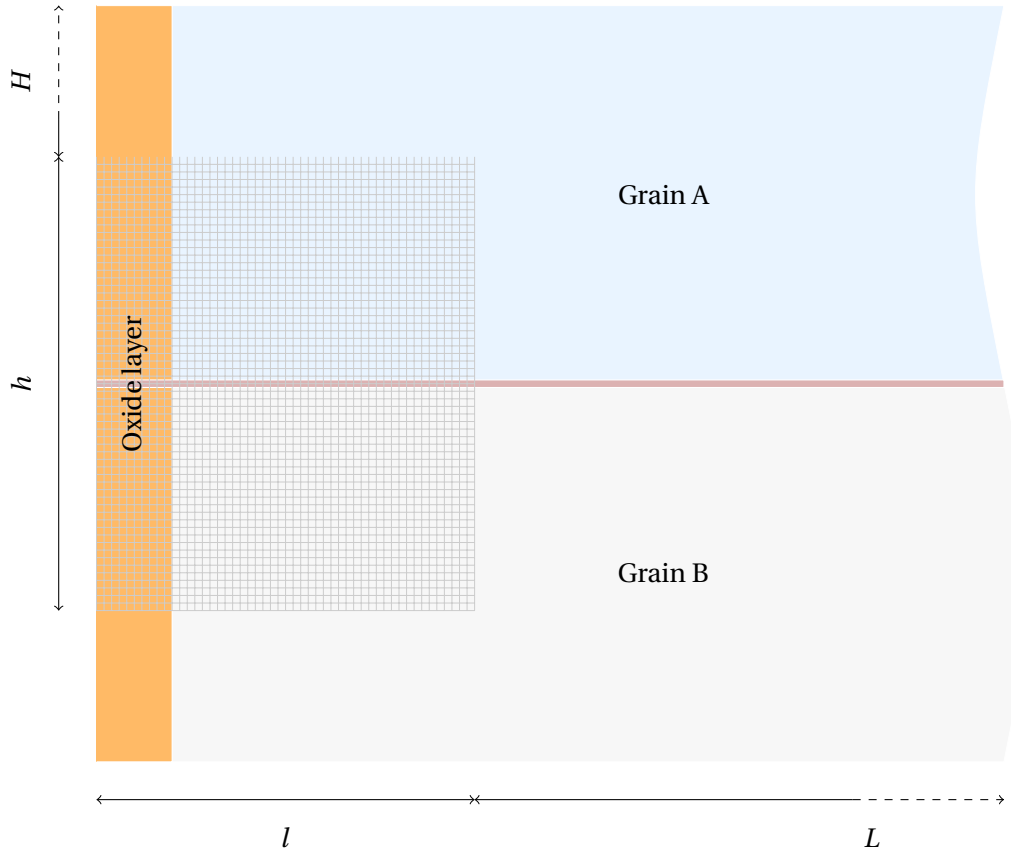

Figure 5.12: Schematic representation of the mesh used in the finite element simulations. The grain boundary is represented by the red line.

Preliminary simulations showed that the oxidised grain boundary must be considered as a diffusion short circuit to generate large enough oxide intrusion. In fact, the grain boundary energy solely cannot reasonably provide a sufficient change of the phase equilibrium to drag the oxide layer along the grain boundary. This is due to the fact that the oxide is stoichiometric and that the supply of oxygen is presently the rate limiting step. Moreover, curvature effects do not impact the oxide growth kinematics sufficiently as the curvature radii are about hundredth of nanometers. The equilibrium concentration of oxygen at the metal oxide interface is almost constant so that the diffusivity of oxygen within the oxide is the dominant parameter in the selection of the metal oxide interface morphology. It is worth recalling that experimental evidences of large penetration ratios has been observed in simulated primary water [Lozano-Perez et al., 2012]. Finally, if we reverse the oxide growth mechanism as being ensured by the supply of chromium, then the assumptions about the role of the grain boundary in the oxide will need to be reconsidered.

The mechanical boundary conditions are identical to the ones given in Fig. 4.13 in page 128 and the chemical boundary conditions are given in Fig. 4.3 in page 118 of this work.

5.3.1 Growth kinetics

Cubic oxide growth kinetics laws – in the form $t^{1/3}$ – have been suggested as being the result of the combined effects of bulk and intergranular oxidation, see [Irving, 1964]. In the literature, dominant grain boundary oxidation is mentioned to yield a power law in $t^{1/4}$, whereas the parabolic growth rate – in $t^{1/2}$ – is found in the bulk. The oxide intrusion growth kinetics is of fundamental importance as it can be related to crack growth laws in several coupled fatigue-oxidation problems, see [Reuchet and Remy, 1983a, Reuchet and Remy, 1983b, Reuchet and Remy, 1983c] amongst others. The phase field method can be used to improve such models to quantify the importance of the Pilling-Bedworth ratio and induced stresses as well as the growth rate of oxide intrusions, *etc.* Some authors

[Lozano-Perez et al., 2012] are trying to extract relevant quantities from the statistical distribution of oxide layers within polycrystalline materials by means of FIB sequential sectioning of the free surface of oxidised specimens. They revealed the promoted oxidation along grain boundaries and slip bands for AUSS in service conditions for PWRs. It resulted that the statistical distribution of oxide is characterised by a bimodal distribution as seen in Fig. 5.13. In this figure, the black curve corresponds to the full distribution of oxide within the base metal, which is separated into two parts. The blue curve corresponds to the bulk oxide and the red curve to the promoted oxide penetration along crystal defects such as grain boundaries and slip bands. Finally, the observations of [Lozano-Perez et al., 2012] allow to neglect the interplay between grain boundaries and also between slip bands as the interspacing is large with respect to the oxidation depth for AUSS in simulated primary water. The average oxidation behaviour can be obtained performing the summation of the oxidation behaviour of each oxide intrusion, for which a representative behaviour is possible from a single effective oxide intrusion. The case of the perpendicular grain boundary appears then as the worst possible case as the tensile stresses generated at the tip of the oxide intrusion are presently in the direction of the applied stress.

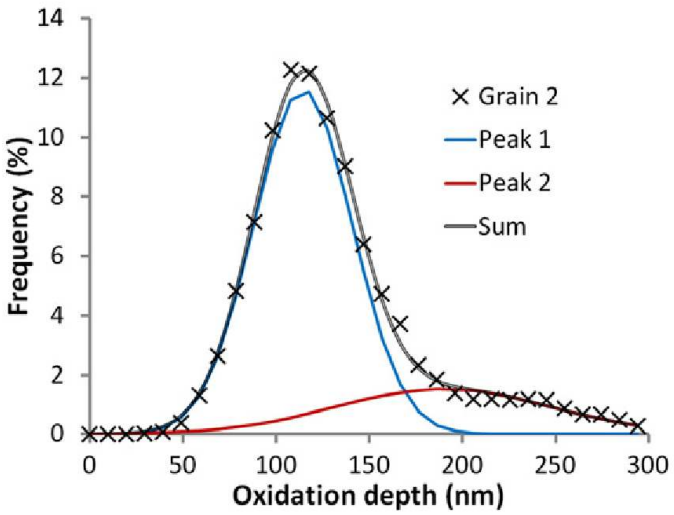

[Lozano-Perez et al., 2012]

Figure 5.13: Bimodal distribution of oxide in black. The red curve represents the bulk oxide and the blue oxide intrusions.

Note that the kinetics of the tail of such distribution in Fig. 5.13 – see the red curve (peak 2) – can play a role in stress corrosion cracking as the stress corrosion cracks are mainly found along oxide intrusions. For some coupled fatigue oxidation studies, a linear oxide growth rate has been found, see [Weiss and Pineau, 1993]. For such cases, the oxide failure – by dissolution, spallation, *etc.* – must be considered to induce breakaway oxidation and the corresponding quasi linear oxide growth rate. In the present study, oxide failure is not modelled and is left for a future study. Nevertheless, the growth kinetics of the oxide intrusion tip can be studied by means of simulations. Preliminary results were therefore obtained within a domain defined by $l = 500$ nm, $h = 400$ nm, $L = 2500$ nm and $H = 2500$ nm. The grain boundary is assumed to promote the diffusivity by two orders of magnitude in both the oxide and the base metal.

The resulting intergranular oxidation is illustrated in Fig. 5.15. The growth kinetics of the oxide tip – the tip is represented by the blue dot in Fig. 5.15 (b) – and the growth kinetics of the bulk – which follows the orange dot in Fig. 5.15 (b), respectively in the grain boundary and in the grain, are here discussed. The resulting growth kinetics curves are provided in Fig. 5.14 on the basis of the logarithm of penetration depth and time. The resulting time exponents, which are obtained by means of linear regressions, are 0.45 for the bulk and 0.31 for the tip of the oxide intrusion, which is close to what [Irving, 1964] proposed. The growth kinetics of the bulk is here not perfectly equal to $\frac{1}{2}$ which is

exactly the value found in the simulations performed in Chapter 4. This can be due to the influence of the coarse mesh used here or to the fact that the stationary regime has not been completely reached after 2 hours. Oxidation time is small due to the fact that the oxide intrusion rapidly leaves the finely meshed area so that the bulk oxidation is not significant. It is worth noting that remeshing techniques could be used here to circumvent such problems.

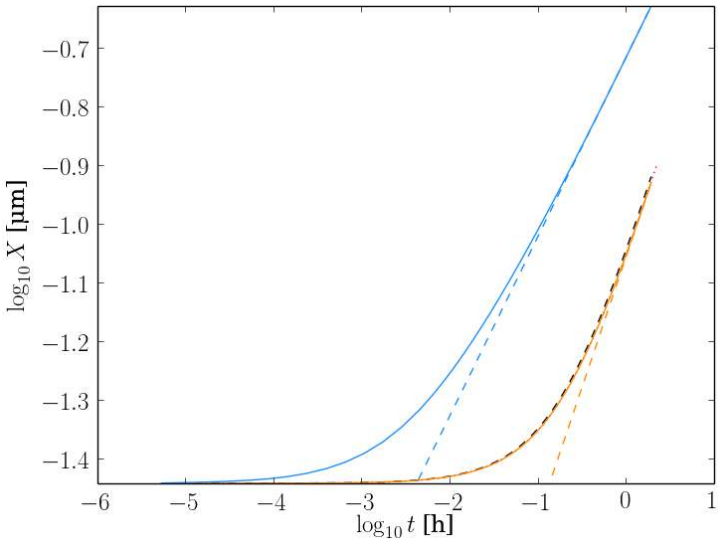

Figure 5.14: Oxide intrusion and bulk growth kinetics in the blue and orange curves respectively.

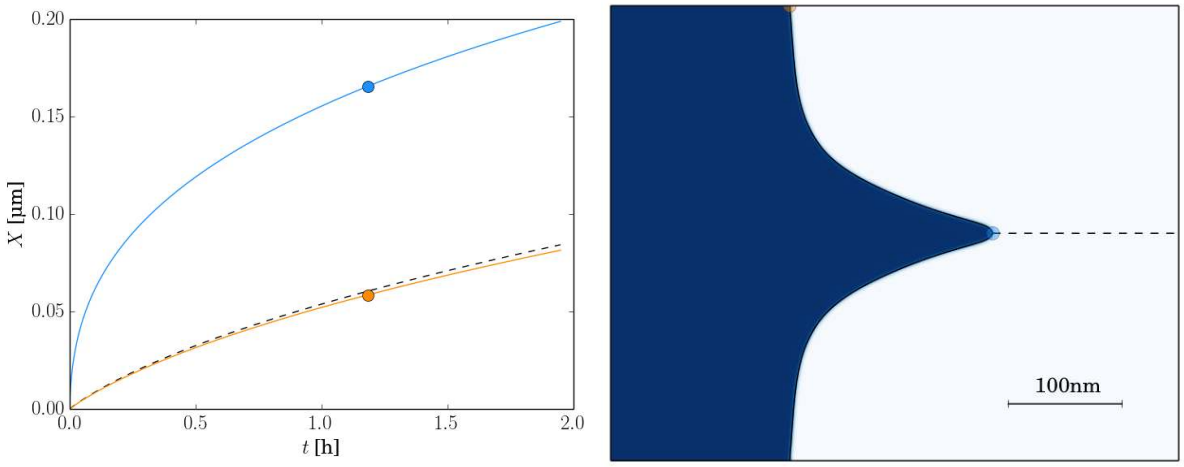

(a) (b)

Figure 5.15: Intergranular oxide growth: (a) shows the time evolution of the tip and bulk points of the metal-oxide interface along with the averaged oxide growth kinetics, respectively the solid blue, solid orange and black dashed curves and (b) snapshot of the metal-oxide interface at the time marked by the circles in (a).

5.3.2 Impact of the grain boundary energy on intergranular oxide growth

Intergranular oxide penetration is, in the present model, induced by the combined action of wetting and diffusion processes as emphasised in [Wolski and Laporte, 2008] for example. A parametric study has been performed to evaluate the importance of wetting with respect to the promoted diffusivity within the oxidised grain boundary. Elasticity is here neglected for simplicity, and diffusivities are taken from Table 5.2. Preliminary simulations are therefore performed within a domain defined by $l = 500$ nm, $h = 400$ nm, $L = 2500$ nm and $H = 2500$ nm that is illustrated in Fig. 5.12. In the following,

we choose to vary the grain boundary diffusivity along with the grain boundary energy to map the possible changes of the metal-oxide interface morphology. The lengths l and height h – see Fig. 5.12 – are varied with respect to the characteristic lengths of the grain boundary diffusion. The results of the parametric study are partially displayed in Fig. 5.16. It shows that wetting has a negligible impact on the metal-oxide interface morphology and that heterogeneous grain boundary diffusion controls the shape of the metal oxide interface and so the dihedral angle (the angle made by the metal-oxide interface and the grain boundary surface). Moreover, the evolution of the dynamic dihedral angle with respect to the grain boundary diffusion and grain boundary energy was determined. The results are not reported in this work because the influence of the grain boundary energy is not strong enough to be relevant. It is thought that the stoichiometic oxide inhibits the wetting effects as the oxygen interface concentration cannot be significantly shifted. Nevertheless, wetting has still a role to play in the selection of the operative tie-line at the tip of the oxide intrusion and can modify the equilibrium concentration of the alloying elements at the tip of the oxide intrusion, for instance for chromium.

5.3.3 Chromium depletion around the oxide tip

It is first recalled that bulk oxidation results in a generalised chromium depletion of a few percents due to the shift of the operative tie-line, see Chapter 4. This chromium depletion at the interface is often mentioned in the literature to be due to the selective oxidation of chromium and is determined by the interface composition, see [Killeen et al., 1976, Pragnell and Evans, 2006, Zhou et al., 2010] for instance. The heterogeneous distribution of the chromium concentration field can be observed around the oxide intrusion. Curvature effects are responsible for such a heterogeneous concentration distribution shown in Fig. 5.18 and more particularly at the triple point. A depleted chromium area is observed at the shoulders of the oxide intrusion, whereas a local enrichment of chromium is observed at the tip of the oxide intrusion. Away from the oxide intrusion and within the grain boundary, the chromium concentration field is depleted as observed in the literature, see [Couvant et al., 2009]. One can note that the depletion levels can be large and that a concentration-dependent diffusivity can significantly modify the current results.

Fig. 5.17 illustrates a snapshot of the chromium flux during intergranular oxidation, which is mainly found within the grain boundary region as expected. In addition, a non negligible chromium flux is also found directed towards the shoulders of the oxide intrusion, where the chromium depletion is observed.

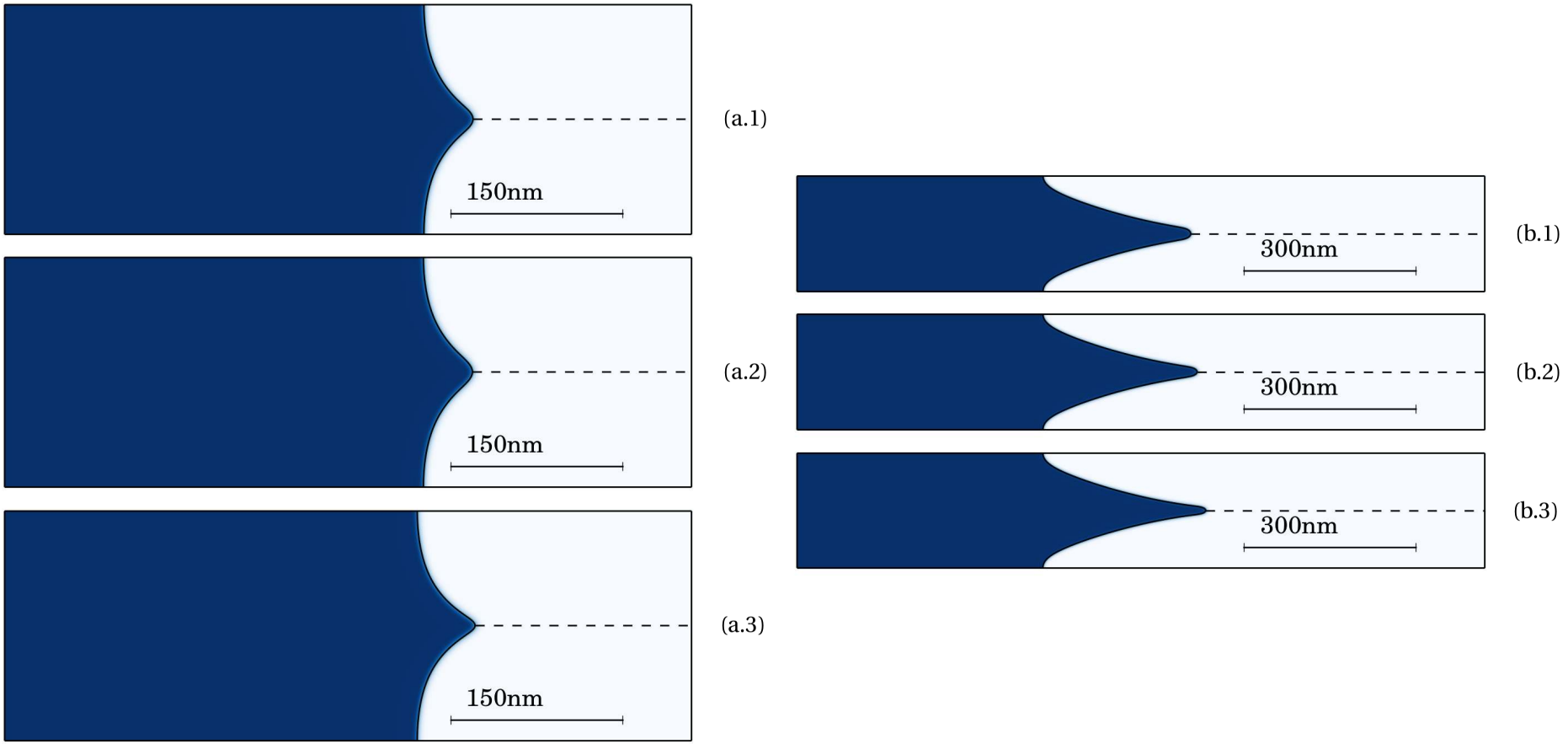

Figure 5.16: Parametric study for the combined effect of diffusivity and wetting on the interface morphology. Grain boundary diffusion is, respectively, one and two order of magnitude greater than bulk diffusion in the cases (a) and (b). The figures (a) and (b) illustrate the effect of wetting on the metal oxide interface morphology. The case (x.1) corresponds to a zero grain boundary excess energy, case (x.2) with an excess energy corresponding to 40% of complete wetting energy and case (x.3) to 120% of complete wetting energy.

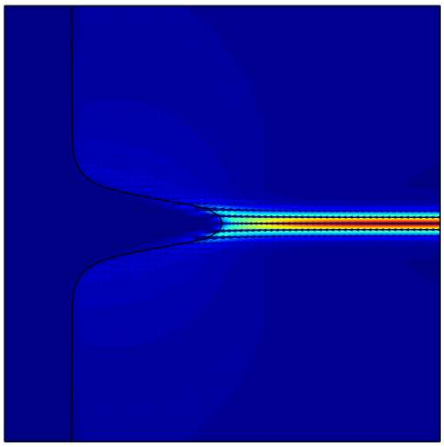

Figure 5.17: Illustration of the scaled chromium flux during intergranular oxide growth (the red colours indicate that is maximal within the grain boundary) predicted at the beginning of the formation of the oxide intrusion after 40 s of oxidation at 900°C. The solid black line represents the metal-oxide interface. The highest flux is found inside the grain boundary parallel to it. Another noticeable flux is found at the shoulders of the oxide intrusion, in a direction almost perpendicular to the curved interface.

A chromium depletion profile during intergranular growth is given in Fig. 5.18. It is noted that the grain boundary is slightly more depleted than the bulk away from the oxide intrusion. Nevertheless, the experimental observation of a depleted grain boundary seen in Chapter 2, Fig. 2.3 indicates much greater depletion levels inside the grain boundary. Here, the same grain boundary/bulk diffusivities ratio are used in the oxide and in the base metal. In the case where such a ratio is greater in the oxide, then the local equilibrium discussed in Chapter 4 will lower the chromium interface equilibrium concentration leading to an increased chromium depletion within the grain boundary.

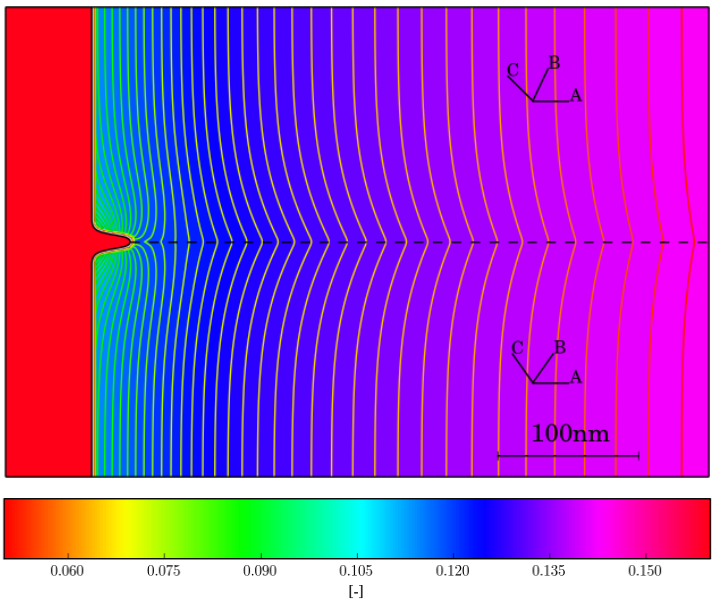

Figure 5.18: Predicted heterogeneous distribution of chromium due to the generalised selective oxidation of chromium and intergranular oxide growth.

5.3.4 Plastic relaxation inside and in the vicinity of oxide intrusions

It is first recalled that negligible stresses are found in the base metal for the case of the planar interface discussed in Chapter 4. It has been suggested by [Evans, 1983] that constant tensile stresses are generated in the base metal at the tip of the oxide intrusion. The tensile stress found at the tip of the oxide has been related to the oxide misfit strain.

In the present simulations, the heterogeneous stress fields are calculated. They are generated by the anisotropic eigenstrain embedded within the oxide phase, which accounts for the misfit between the two phases. The present stress fields are also relaxed by means of viscoplasticity in both the oxide and the substrate.

Hydrostatic stress field

The hydrostatic stress is first discussed, and is illustrated in Fig. 5.19 for two distinct times with time increasing from left to right.

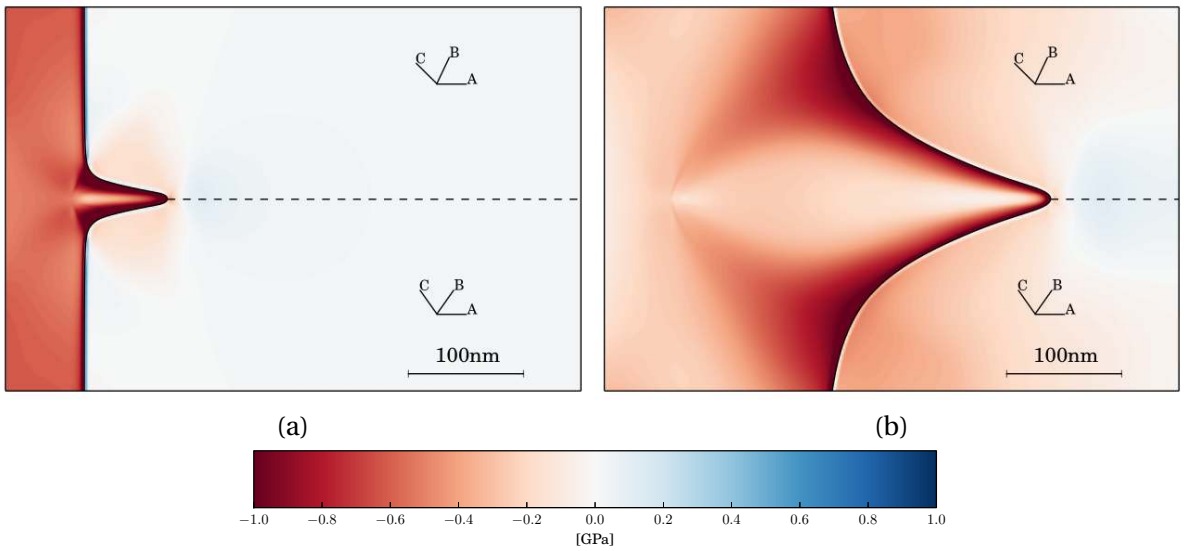

Figure 5.19: Predicted hydrostatic stress distribution during intergranular oxidation after (a) 3.5 minutes and (b) 2 hours.

The growth of the oxide intrusion generates heterogeneous hydrostatic stresses in both the oxide and the substrate. The hydrostatic stress σ_H is defined as follows,

$$\sigma_h = \frac{1}{3}\sigma_{ii}\,. \tag{5.17}$$

It is shown to be initially negative within the oxide and close to zero in the base metal, which indicates that the oxide is in a state of compression. During the growth of the oxide intrusion, the hydrostatic stress relaxes within the oxide phase due to viscoplasticity while some small perturbations are found in the vicinity of the growing oxide intrusion and new hydrostatic stresses are transmitted to the base metal in the surroundings of the oxide intrusion. The viscoplastic relaxation of the hydrostatic stress in the oxide is highly heterogeneous. The areas with lowest hydrostatic stresses are found within the oxidised grain boundary and in the vicinity of the oxide intrusion shoulders as seen in Fig. 5.19. In the base metal, the sides of the oxide intrusion are characterised by negative hydrostatic stresses, whereas the tip of the oxide intrusion with ˜400 MPa tensile stresses. Such results are expected, as the oxide intrusion pushes the two grains apart. The hydrostatic stress is maximal in the vicinity of the metal oxide interface because of the formation of new and undeformed oxide. This is why the interface itself shows the highest stress levels with respect to the phases. A clear stress gradient is thus observed within the oxide intrusion. The positive hydrostatic stress which is generated at the

tip of the oxide intrusion can be seen as a preferential segregation site for deleterious components such as hydrogen, oxygen, phosphorus, *etc.* For the case of hydrogen, a formula can be found in the literature, which relates the hydrostatic stress to the H_2 concentration, see [Guedes et al., 2014] for instance. In fact, hydrogen is a fast moving chemical component so that is can be directly related to the hydrostatic stress to guarantee the chemical equilibrium, see [Villani et al., 2014] – amongst others – for the thermodynamic formulation of the hydrostatic stress dependent chemical potential. Finally, it is worth noting that the hydrostatic stress field is shown to be less compressive inside the oxidised grain boundary, and on the free surface facing the oxide intrusion.

Von Mises stress field

The distribution of the predicted Mises stresses around the oxide intrusion and within it are shown in Fig. 5.20.

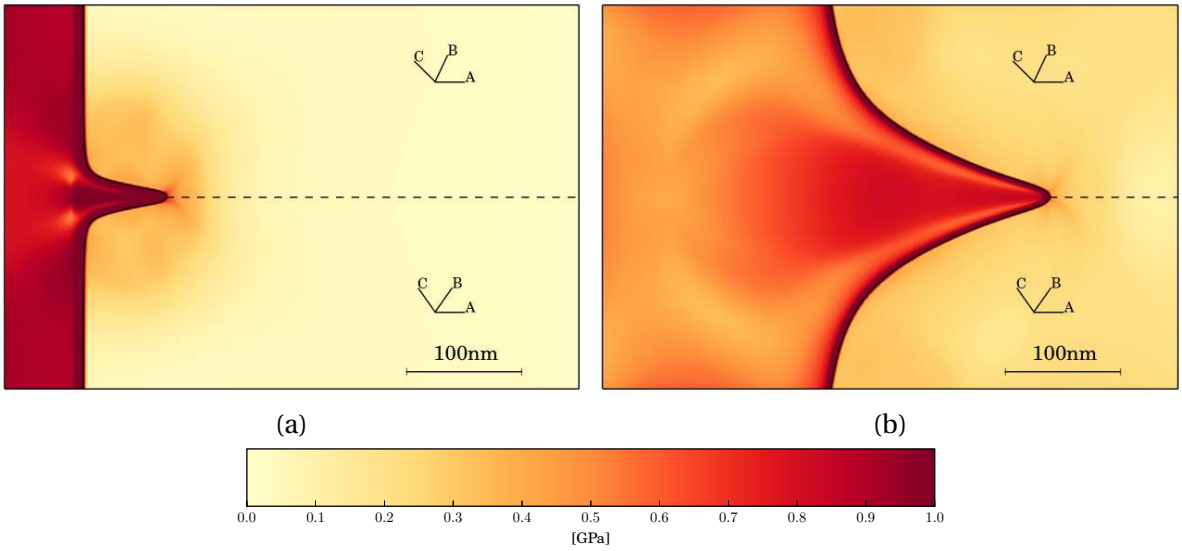

Figure 5.20: Predicted Mises stress distribution during intergranular oxidation after (a) 3.5 minutes and (b) 2 hours.

The resulting Mises stress is highly heterogeneous. In the substrate, the sides of the oxide intrusion are characterised with a diffuse Mises stress, which affects an area embedded within a circular domain of radius approximately the size of the oxide intrusion. At the tip of the oxide intrusion, the Mises stress shows a local extremum. Some small anisotropic effects are found in the vicinity of the oxide intrusion tip over a few tens of nanometers. The von Mises stress is so high that the viscoplastic deformation of the substrate is activated during the growth of such oxide intrusion. In the oxide phase, the Mises stress is also heterogeneous and is maximal in the vicinity of the metal-oxide interface for the reasons mentioned in the analysis of the hydrostatic stress. Finally one can note that the Mises stress is pear-shaped in the oxide layer, with respect to the curvature of the oxide intrusion's shoulders.

Viscoplastic deformation

The viscoplastic deformation, expressed as the accumulated viscoplasticity of the oxide layer, is illustrated in Fig. 5.21. The accumulated plastic strain p is obtained by integrating the viscoplastic strain rate as follows,

$$\dot{p} = \sqrt{\frac{2}{3}\dot{\underset{\sim}{\epsilon}}_p^{Cr_2O_3} : \dot{\underset{\sim}{\epsilon}}_p^{Cr_2O_3}}, \tag{5.18}$$

In the following, the quantity $h(\phi)p$ is displayed as the virtual viscoplastic deformation in the substrate has not physical signification. The accumulated deformation is shown to branch firstly into first three parts and then into five parts as shown in Fig. 5.21. The first three parts are located in the oxidised grain boundary and from the nucleus of the oxide intrusion to its shoulders. After that, the two secondary regions of high accumulated deformation are found from the nucleus position of the oxide intrusion to a position that is in between the primary branches. A closer look at the oxide intrusion nucleus shows that the plastic deformation is less activated in the continuation of the secondary branches. Finally, downstream the oxide intrusion nucleus position, it is noted that the accumulated viscoplastic deformation is rather low.

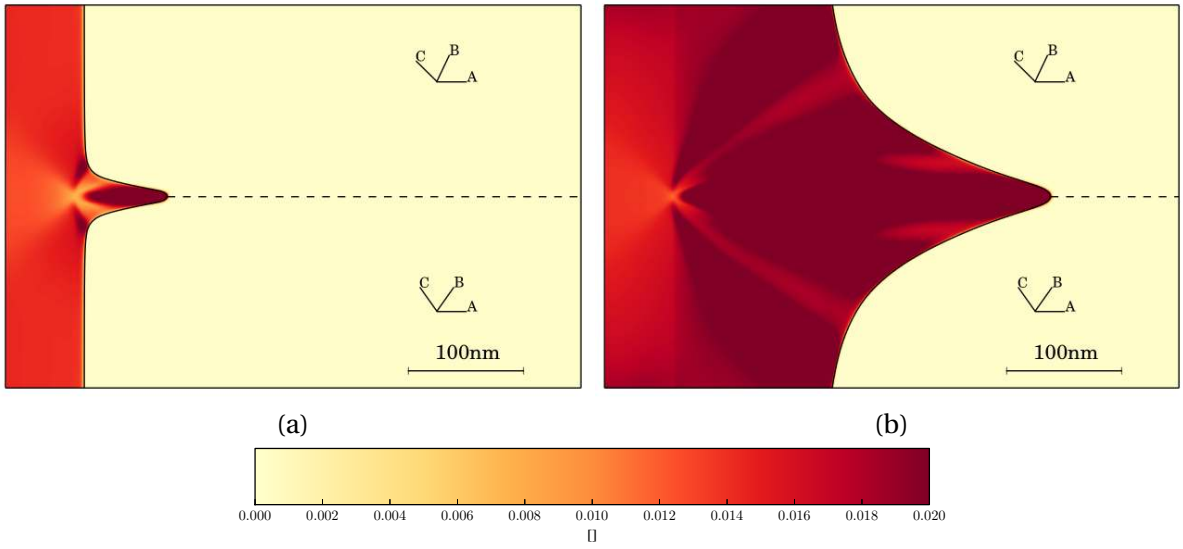

Figure 5.21: Predicted accumulated deformation during intergranular oxidation in the oxide after (a) 3.5 minutes and (b) 2 hours.

Then, the accumulated viscoplastic slip in the bicrystalline substrate is defined as follows,

$$\dot{\gamma}_{\text{acc}} = \sum_s |\dot{\gamma}_s| , \tag{5.19}$$

where s is the slip system. In the following, only $\bar{h}(\phi)\gamma_{\text{acc}}$ is displayed. This quantity is now discussed, and illustrated in Fig. 5.22.

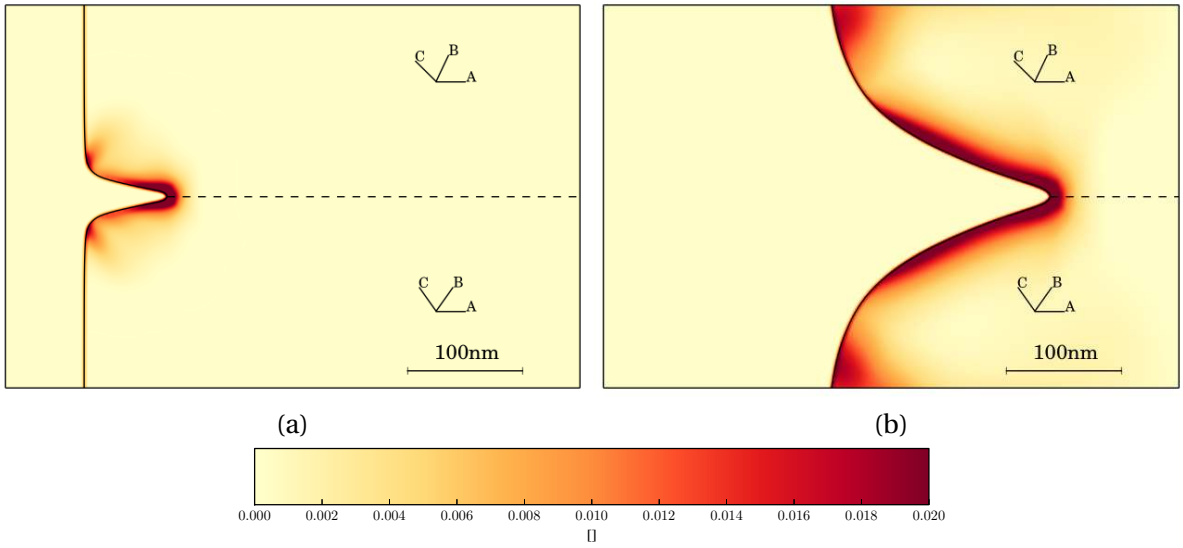

Figure 5.22: Predicted accumulated slip during intergranular oxidation in the oxide after (a) 3.5 minutes and (b) 2 hours.

The oxide intrusion tip is shown to induce high plastic activity, which is also the case for the shoulders of the oxide intrusion. The size of the plastic zone is rather small, about 40 nm thick. Such a plastic slip is accompanied by the production of hardening, which comes with increasing dislocation density. For such sizes, the dislocations may be observed by TEM for instance. The local increase in dislocation density can inhibit the chromium depletion at the metal-oxide interface. In fact, Hart's relationship, which was discussed in Chapter 2 can modify locally the operative tie-line – see Chapter 4 for details – and so the chromium depletion. If the chromium diffusivity increases, then the model will make the chromium equilibrium concentration within the metallic phase to increase as well.

5.3.5 Effects of an applied mechanical load on upper surface

The focus is now given to the grain boundary stress, and more particularly to the grain boundary opening stress, which is σ_{yy} given the grain boundary orientation. The grain boundary region is here separated in two parts, the one corresponding to the oxidised grain boundary and the other one to the grain boundary region within the base metal. Prior to the study of the effect of a mechanical load, the evolution of the grain boundary opening stress will be discussed for the reference case, which is stress-free intergranular oxidation. The stress field will be plotted along the grain boundary and away from the grain boundary perpendicular to the free surface, as illustrated in Fig. 5.23. This allows to simply compare bulk oxidation to the grain boundary oxidation.

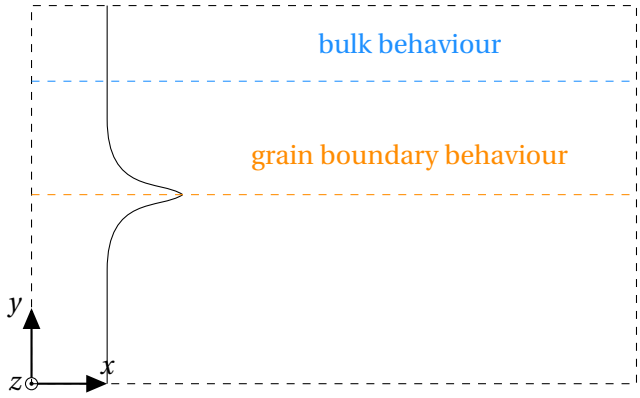

Figure 5.23: Illustration of the growth of a single oxide intrusion, where the black solid line represents the metal oxide interface. The stress fields are plotted along the blue dashed line to illustrate the bulk behaviour and along the orange dashed line to illustrate the grain boundary behaviour.

The resulting opening stress field is plotted along the grain boundary and for the bulk as well in Fig. 5.24 as depicted in Fig. 5.23.

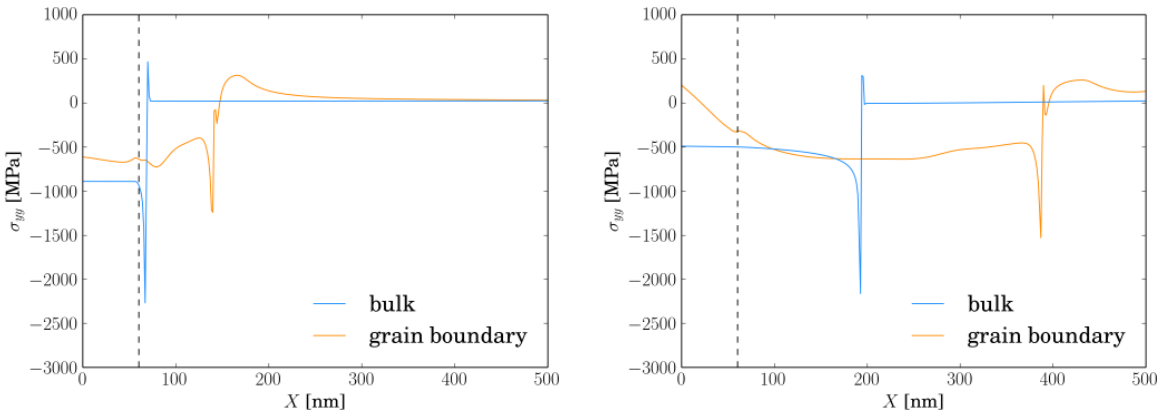

(a) (b)

Figure 5.24: Opening stress profiles at different oxidation times (3.5 minutes and 2 hours). The orange curves represent the opening stress within the grain boundary and the blue curve represents the field σ_{yy} for comparison purposes. The vertical dashed black line represents the initial position of the interface.

It is noted that the opening stress along the grain boundary is highly heterogeneous and one can also note the presence of a small artefact at the initial interface position. In the base metal, the opening stress shows a local maximum, as suggested by [Evans, 1983] at the tip of the oxide, which is also shown to slowly decrease. This is due to the fact that the oxide intrusion progressively slows down – because this phenomenon is in $t^{1/4}$ – and that the viscoplastic relaxation in the substrate increases in return. One can note that the σ_{yy} stress at the free surface, in the oxidised grain boundary is increasing with time and becomes positive with time, whereas compressive stresses are found away from the oxide intrusion. This can be a possible cause for the preferred failure of oxide along oxidised grain boundaries – and by extension oxidised slip bands. The cracks thus formed can then propagate along the oxidised grain boundary to the undamaged grain boundary in the substrate.

Another simulation was performed but enhanced with a 200 MPa creep stress applied along the y direction. Fig. 5.25 shows the evolution of the opening stress at the free surface along with the evolution of the maximum opening stress at the tip of the oxide intrusion against the running oxide intrusion tip depth. It is worth recalling that stresses do not impact the growth kinetics so that the oxide intrusions are found at the same depths at equal times.

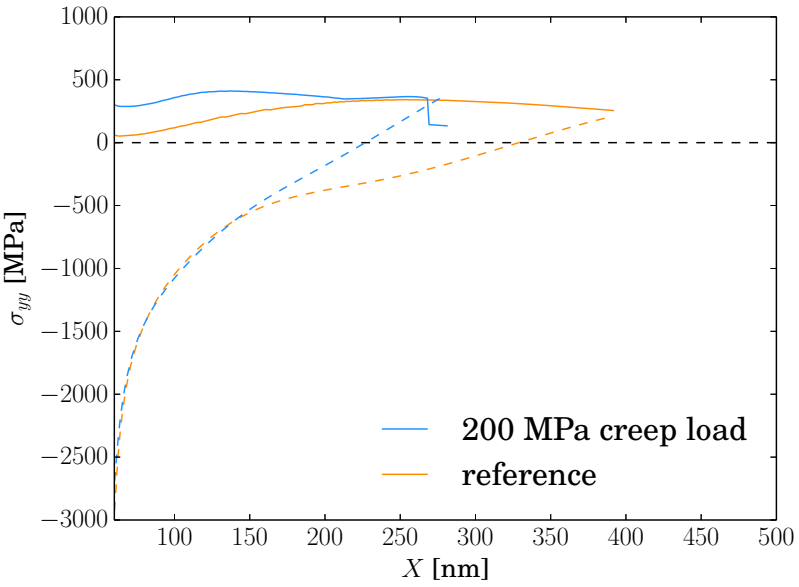

Figure 5.25: Comparison of the surface grain boundary opening stress (dashed lines) and the oxide tip opening stress (solid lines) with respect to the depth of the oxide intrusion.

This figure reveals that the depth is not – with respect to the assumptions made in this work – a relevant quantity to characterise the initiation of stress corrosion cracks, as a high dispersion can be generated by the history of loadings of the growing oxide. Moreover, the opening stress at the tip of the oxide intrusion is shown to be either almost constant or slowly decrease with time. The failure of the grain boundary inside the metal is possible either at the beginning of the oxide intrusion propagation where the maximum is reached and also due to embrittlement generated by segregated species, *e.g.* hydrogen, oxygen , phosphorus, *etc.* The figure also confirms the deleterious effect of the tensile applied stress as the oxide layer will fail more rapidly than for the stress-free case.

5.4 Modelling of oxidation-induced grain boundary damage

5.4.1 Preliminary thoughts on damage initiation

The grain boundary opening stress is shown to become tensile in nature at the free surface due to viscoplasticity. At the tip of the oxide intrusion, the opening stress is tensile as well but almost constant with peak value about 400 MPa. It has been shown that creep loading drastically impacts the opening stress and will consequently increase the failure rate of the oxide layer. From the present results, it is thought that crack can nucleate either at the free surface or at the tip of the oxide intrusion or both. The conditions required to initiate such cracks can be based on an opening stress that must be different in the oxide and in the base metal. Such a critical stress must be rather low in the oxide as oxides are known to be brittle. In the base metal, it must be high but it can be also decreased by considering possible segregated species. The segregation must be favoured by high hydrostatic stresses located at the oxide tip, which is also the place where an extremum of the opening stress can be found. If the crack operates in the base metal, it must be healed by the formation of new oxide inside, whereas cracks that are initiated at the free surface cannot heal. While damage can be modelled by an additional phase field, – see [Yang et al., 2011] for an example of coupled fracture diffusion problem based on the phase field approach – it seems that the homogenisation approach applied to local damage fields is here relevant. The two damage variables of each phase will be then uncoupled. Therefore, the vanishing of a damaged phase phase with respect to the formation of a new undamaged phase can be easily modelled. This process can be seen as a crack healing mechanism which is mentioned in [Weiss and Pineau, 1993]. Several damage laws can be found in the literature. In the following, the

damage model of [Aslan et al., 2011] is used. It is worth noting that a regularised expression of this damage internal variable can be found in [Sabnis, 2012]. Originally, the micro-damage model was intended to account for damage within the bulk of a crystalline solid. Here, it is specialised to account for the damage of the grain boundary with respect to a given fracture criterion.

5.4.2 Damage model

In the following, we choose an approach based on the evolution of a damage internal variable, presently d. This variable accounts for the opening of the grain boundary – or intergranular fracture – and is related to an additional damage strain, which enters the classical small strain partition as follows,

$$\underset{\sim}{\boldsymbol{\varepsilon}} = \underset{\sim}{\boldsymbol{\varepsilon}}_e + \underset{\sim}{\boldsymbol{\varepsilon}}_p + \underset{\sim}{\boldsymbol{\varepsilon}}_d \,, \tag{5.20}$$

where $\underset{\sim}{\boldsymbol{\varepsilon}}$ is the total strain, $\underset{\sim}{\boldsymbol{\varepsilon}}_e$ the elastic strain, $\underset{\sim}{\boldsymbol{\varepsilon}}_p$ the plastic strain and $\underset{\sim}{\boldsymbol{\varepsilon}}_d$ the damage strain. According to Voigt's approach, the damage strain can be calculated from the intrinsic damage strains of each phases, that are respectively $\underset{\sim}{\boldsymbol{\varepsilon}}_d^{\mathrm{Cr_2O_3}}$ and $\underset{\sim}{\boldsymbol{\varepsilon}}_d^{\gamma\text{-Fe}}$. We first need to introduce the damage variable into the set of state variables which become – in the spirit of the homogenisation approach in the phase field approach of Chapter 3,

$$\mathrm{STATE} = \{\phi, \nabla\phi, c_{\mathrm{i}}^{\alpha}, \underset{\sim}{\boldsymbol{\sigma}}^{\alpha}, \underset{\sim}{\boldsymbol{\varepsilon}}_p^{\alpha}, \underset{\sim}{\boldsymbol{\varepsilon}}_d^{\alpha}, d^{\alpha}, c_{\mathrm{i}}^{\beta}, \underset{\sim}{\boldsymbol{\sigma}}^{\beta}, \underset{\sim}{\boldsymbol{\varepsilon}}_p^{\beta}, \underset{\sim}{\boldsymbol{\varepsilon}}_d^{\beta}, d^{\beta}, \rho_s^{\beta}, x_s^{\beta}\} \,, \tag{5.21}$$

The evolution of the intrinsic damage strain fields is obtained on the basis of appropriate evolutionary laws. The dissipation potential is henceforth dependent of the following variables,

$$\Omega^* = \Omega^*(\pi^*, \nabla\mu_{\mathrm{i}}^{\alpha}, \nabla\mu_{\mathrm{i}}^{\beta}, \dot{\underset{\sim}{\boldsymbol{\varepsilon}}}_p^{\alpha}, \dot{\underset{\sim}{\boldsymbol{\varepsilon}}}_d^{\alpha}, Y^{\alpha}, \dot{\underset{\sim}{\boldsymbol{\varepsilon}}}_p^{\beta}, \dot{\underset{\sim}{\boldsymbol{\varepsilon}}}_d^{\beta}, Y^{\beta}, R_s^{\beta}, X_s^{\beta}; \phi) \,, \tag{5.22}$$

where $Y^{\alpha,\beta}$ are the thermodynamic forces associated to $d^{\alpha,\beta}$ and represent the critical stress for damage propagation in each phase. The damage strain rates read:

$$\dot{\underset{\sim}{\boldsymbol{\varepsilon}}}_d^{\alpha,\beta} = \dot{d}^{\alpha,\beta} \underline{\boldsymbol{n}} \otimes \underline{\boldsymbol{n}} \,, \tag{5.23}$$

where $\underline{\boldsymbol{n}}$ is the grain boundary normal and $d^{\alpha,\beta}$ an internal variable for damage. The scalar field $d^{\alpha,\beta}$ is calculated from a power law based dissipation potential coupled with the grain boundary field η and using $\underline{\boldsymbol{n}} \otimes \underline{\boldsymbol{n}} = \underset{\sim}{\boldsymbol{N}}$:

$$\dot{d}^{\alpha,\beta} = \eta \left\langle \frac{|\underset{\sim}{\boldsymbol{\sigma}}^{\alpha,\beta} : \underset{\sim}{\boldsymbol{N}}| - Y^{\alpha,\beta}}{K_d^{\alpha,\beta}} \right\rangle^{n_d^{\alpha,\beta}} \mathrm{sign}\left(\underset{\sim}{\boldsymbol{\sigma}}^{\alpha,\beta} : \underset{\sim}{\boldsymbol{N}}\right) \,, \tag{5.24}$$

where $K_d^{\alpha,\beta}$ and $n_d^{\alpha,\beta}$ are the viscosity parameters. Finally, the internal variable for damage ranges between zero and infinity. As a strain, it can either decrease or increase. The yield criterion for damage is defined as follows,

$$Y^{\alpha,\beta} = \left\langle Y_0^{\alpha,\beta} + H^{\alpha,\beta} d_{\mathrm{acc}}^{\alpha,\beta} \right\rangle \,, \tag{5.25}$$

where $Y_0^{\alpha,\beta}$ is the fracture stress of the undamaged phase, $H^{\alpha,\beta}$ the modulus for the decrease of the critical stress with respect to accumulated damage. The H modulus is therefore negative and the accumulated damage is calculated from $\dot{d}_{\mathrm{acc}}^{\alpha,\beta} = |\dot{d}^{\alpha,\beta}|$. Such a damage criterion can depend on hydrogen concentration, which can be calculated directly form the hydrostatic stress for instance. The variables d^{α} and d^{β} can thus be coupled with diffusion on the basis of bijective transformation to

the unit interval. The unit interval simplifies the physical interpretation of damage where zero corresponds to a non damaged material and one to a fully damaged material. In the present work, we use the following bijection,

$$D(d) = D_{\text{undamaged}} + \left(1 - \exp\left(-\tau_d d\right)\right)\left(D_{\text{damaged}} - D_{\text{undamaged}}\right), \tag{5.26}$$

where D is the effective diffusivity, $D_{\text{undamaged}}$ the diffusivity of the non damaged material, D_{damaged} the diffusivity of the fully damaged material and τ_d a fitting parameter used to describe the rate at which the damage variable d leads to the diffusivity of the fully damaged material.

5.5 Conclusions

The chapter has been devoted to the study of intergranular oxide penetrations in austenitic stainless steels. The diffusion short circuit behaviour of the grain boundary is first considered with respect to what is classically done in the literature although the present grain boundary field is assumed to be diffused. It is shown that the diffused grain boundary behaviour can be analogous to Fisher's grain boundary model when diffusion anisotropy is considered. Then, the grain boundary energy is known to modify the shape of the phases in contact with the grain boundary. It is shown that grain boundary energy can be easily implemented in the framework of the phase field method and that it impacts the chemical equilibrium. The present diffused grain boundary allows to retrieve the Young-Laplace formula. A parametric study was performed to quantify the effect of the grain boundary energy on the dynamics of the dihedral angle. It revealed that the grain boundary energy does not have a significant impact on the dynamics of the dihedral angle. This is due to the fact that the oxide is stoichiometric, which leads to small variations of equilibrium concentrations. The morphology of the growing oxide is then mainly controlled by the heterogeneous diffusivity in the oxide. Mechanical stresses have been analysed are resulted in the formation of stress concentrations at the tip of the oxide intrusion and at the free surface of the oxide layer along the grain boundary. Moreover, applied creep loads have been shown to make the free surface localised stress concentration to rapidly increase. This result emphasises the importance of the loading history of the growing oxide on crack initiation mechanisms in the field of stress corrosion cracking. The present model can be extended to the comprehensive study of damage by the selection of appropriate damage laws. To this aim, a damage model is finally proposed. The results on damage are unfortunately not presented in the work but are strongly desired to be published in a near future.

References

[Abrivard, 2009] Abrivard, G. (2009). *A coupled crystal plasticity - phase field formulation to describe microstructural evolution in polycrystalline aggregates during recrystallisation*. PhD thesis, Mines ParisTech.

[Abrivard et al., 2012a] Abrivard, G., Busso, E., Forest, S., and Appolaire, B. (2012a). Phase field modelling of grain boundary motion driven by curvature and stored energy gradients. Part I: Theory and numerical implementation. *Philosophical Magazine*, 92(28-30):3618–3642.

[Abrivard et al., 2012b] Abrivard, G., Busso, E., Forest, S., and Appolaire, B. (2012b). Phase field modelling of grain boundary motion driven by curvature and stored energy gradients. Part II: Application to recrystallisation. *Philosophical Magazine*, 92(28-30):3643–3664.

[Adda and Philibert, 1966] Adda, Y. and Philibert, J. (1966). *La diffusion dans les solides*. Number vol. 1 in Bibliothèque des sciences et techniques nucléaires. Institut National des Sciences et Techniques Nucléaires.

[Aslan et al., 2011] Aslan, O., Quilici, S., and Forest, S. (2011). Numerical modeling of fatigue crack growth in single crystals based on microdamage theory. *International Journal of Damage Mechanics*, 20(5):681–705.

[Balluffi, 1992] Balluffi, R. (1992). Grain boundary diffusion mechanisms in metals. *Journal of Electronic Materials*, 21(1):527–553.

[Couvant et al., 2009] Couvant, T., Legras, L., Herbelin, A., Musienko, A., Ilevbrev, G., Delafosse, D., Cailletaud, G., and Hickling, J. (2009). Development of understanding of the interaction between localized deformation and SCC of austenitic stainless steel exposed to primary PWR environment. In *Proceedings of the Fourteenth International Conference on Environmental Degradation of Materials in Nuclear Power Systems Water Reactors*, pages 182–194. American Nuclear Society (ANS).

[Crank, 1975] Crank, J. (1975). *The mathematics of diffusion*. Clarendon press, Oxford, 2 edition.

[Evans, 1983] Evans, H. (1983). The role of oxide grain boundaries in the development of growth stresses during oxidation. *Corrosion Science*, 23(5):495 – 506.

[Fisher, 1951] Fisher, J. C. (1951). Calculation of diffusion penetration curves for surface and grain boundary diffusion. *Journal of Applied Physics*, 22(1):74–77.

[Guedes et al., 2014] Guedes, D., Oudriss, A., Frappart, S., Courlit, G., Cohendoz, S., Girault, P., Creus, J., Bouhattate, J., Metsue, A., Thebault, F., Delattre, L., Koschel, D., and Feaugas, X. (2014). The influence of hydrostatic stress states on the hydrogen solubility in martensitic steels. *Scripta Materialia*, 8485(0):23 – 26.

[Irving, 1964] Irving, B. A. (1964). Effect of grain boundaries on the diffusional growth of oxides on metals. *Nature*, 204(4963):1083–1083.

[Kaplan et al., 2013] Kaplan, W., Chatain, D., Wynblatt, P., and Carter, W. (2013). A review of wetting versus adsorption, complexions, and related phenomena: the rosetta stone of wetting. *Journal of Materials Science*, 48(17):5681–5717.

[Kaur et al., 1989] Kaur, I., Gust, W., and für Metallforschung, M.-P.-I. (1989). *Fundamentals of Grain and Interphase Boundary Diffusion*. Ziegler Press.

[Killeen et al., 1976] Killeen, J., Smith, A., and Wild, R. (1976). Chromium depletion profiles after preferential removal of chromium from alloys. *Corrosion Science*, 16(8):551–559.

[Kučera, 1968] Kučera, J. (1968). A contribution to the analysis of grain boundary diffusion measurements. *Canadian Journal of Physics*, 46(13):1511–1521.

[Le Claire, 1951] Le Claire, A. (1951). Grain boundary diffusion in metals. *Philosophical Magazine Series 7*, 42(328):468–474.

[Le Claire, 1963] Le Claire, A. (1963). The analysis of grain boundary diffusion measurements. *British Journal of Applied Physics*, 14(6):351.

[Lozano-Perez et al., 2012] Lozano-Perez, S., Kruska, K., Iyengar, I., Terachi, T., and Yamada, T. (2012). The role of cold work and applied stress on surface oxidation of 304 stainless steel. *Corrosion Science*, 56(0):78 – 85.

[Mehrer, 2007] Mehrer, H. (2007). Grain-boundary diffusion. In *Diffusion in Solids*, volume 155 of *Springer Series in Solid-State Sciences*, pages 553–582. Springer Berlin Heidelberg.

[Mishin, 2001] Mishin, Y. (2001). 50 years of grain boundary diffusion: What do we know about it today? *Defect and Diffusion Forum*, 194-199:1113–1126.

[Mishin and Herzig, 1999] Mishin, Y. and Herzig, C. (1999). Grain boundary diffusion: recent progress and future research. *Materials Science and Engineering: A*, 260(12):55 – 71.

[Pragnell and Evans, 2006] Pragnell, W. and Evans, H. (2006). Chromium depletion at 2-dimensional features during the selective oxidation of a 20Cr25Ni austenitic steel. *Oxidation of Metals*, 66(3-4):209–230.

[Reuchet and Remy, 1983a] Reuchet, J. and Remy, L. (1983a). Fatigue oxidation interaction in a superalloy - application to life prediction in high temperature low cycle fatigue. *Metallurgical Transactions A*, 14A:141–149.

[Reuchet and Remy, 1983b] Reuchet, J. and Remy, L. (1983b). High temperature low cycle fatigue of MAR-M 509 superalloy I: The influence of temperature on the low cycle fatigue behavior from 20 to 1100°C. *Materials Science & Engineering*, 58:19–32.

[Reuchet and Remy, 1983c] Reuchet, J. and Remy, L. (1983c). High temperature low cycle fatigue of MAR-M 509 superalloy II: The influence of oxidation at high temperatures. *Materials science and Engineering*, 58:33–42.

[Sabnis, 2012] Sabnis, P. (2012). *Modelling the propagation and bifurcation of plasticity induced cracks in Nickel base single crystal superalloys*. PhD thesis, Mines ParisTech.

[Villani et al., 2014] Villani, A., Busso, E., Ammar, K., Forest, S., and Geers, M. (2014). A fully coupled diffusional-mechanical formulation: numerical implementation, analytical validation, and effects of plasticity on equilibrium. *Archive of Applied Mechanics*, 84(9-11):1647–1664.

[Weiss and Pineau, 1993] Weiss, J. and Pineau, A. (1993). Fatigue and creep-fatigue damage of austenitic stainless steels under multiaxial loading. *Metallurgical and Materials Transactions A*, 24:2247–2261.

[Whipple, 1954] Whipple, R. (1954). Concentration contours in grain boundary diffusion. *Philosophical Magazine Series 7*, 45(371):1225–1236.

[Wolski and Laporte, 2008] Wolski, K. and Laporte, V. (2008). Grain boundary diffusion and wetting in the analysis of intergranular penetration. *Materials Science and Engineering: A*, 495(12):138 – 146. Fifth International Conference on High Temperature Capillarity HTC-2007, Alicante, Spain.

[Yang et al., 2011] Yang, F., Liu, B., and Fang, D. (2011). Interplay between fracture and diffusion behaviors: Modeling and phase field computation. *Computational Materials Science*, 50(9):2554 – 2560.

[Zhou et al., 2010] Zhou, H., Qu, J., and Cherkaoui, M. (2010). Finite element analysis of oxidation induced metal depletion at oxide-metal interface. *Computational Materials Science*, 48(4):842 – 847.

CHAPTER

6 Conclusions

Contents

Le phénomène de corrosion sous contrainte est souvent décrit comme étant un phénomène de rupture différée. En effet, un essai type de CSC consiste en la mise en tension d'une éprouvette suivie de sa mise en contact avec un environnement hostile, et ce tout au long du chargement mécanique. Sans l'action de l'environnement, le chargement mécanique se verrait être bénin pour l'éprouvette. Or, on peut observer la rupture fragile de l'éprouvette, ce qui écarte l'hypothèse d'un endommagement de fluage. La rupture peut être localisée aux joints de grains oxydés mais également dans certaines bandes émergentes de localisation de la déformation plastique.

L'effet de l'environnement peut être observé principalement par la formation d'une couche d'oxyde. Cette même couche étant de nature fragile et admet en plus une faible résistance aux contraintes de traction. En accord avec les observations expérimentales, la rupture fragile observée à l'issu d'essais de CSC semble correspondre à la rupture de la couche d'oxyde. Mais il existe également une variété de phénomènes possibles à l'image de la fragilisation par l'hydrogène. Cette rupture de fragilisation par l'hydrogène peut être amorcée sous la surface du métal et ainsi être décorrélée de la rupture de la couche d'oxyde. La croissance de l'oxyde n'est en effet que la partie visible de l'iceberg que sont les nombreuses interations possibles entre l'environnement et le matériau.

La prévision de l'amorçage de fissures de CSC est extrêment complexe étant donné cette multitude de causes possibles de fragilisation du matériau. L'objectif du travail réside ainsi dans la formulation d'un modèle capable de rendre compte de ces différentes interactions afin d'explorer d'une manière plus "physique" et à travers la simulation numérique les interactions possibles conduisants à cette rupture fragile. Pour ce faire, il a été fait le choix de modéliser dans un premier temps la croissance de l'oxyde, afin de rendre compte de l'état mécanique mais aussi chimique de la surface du matériau. La méthode des champs de phases a été sélectionnée pour sa simplicité de mise en œuvre ainsi que pour sa flexibilité pour la modélisation de motifs d'interface complexes à l'image des intrusions d'oxydes.

Le modèle proposé dans ce travail est fondé sur les approches dites d'homogénéisation. Or, la formulation thermodynamique rigoureuse de ces méthodes est encore en cours de développement dans la communauté scientifique du champs de phases. C'est pourquoi une méthodologie rigoureuse a été mise en place pour la formulation de tels modèles et a été appliquée aux hypothèses de Voigt/Taylor ainsi que de Reuss/Sachs. Les approches d'homogénéisation offrent la possibilité de mélanger des comportements non-linéaires des phases de manière complétement découplée. Ainsi, des comportements non-linéaires comme la viscoplasticité de Norton et la plasticité cristalline sont étudiés au cours de la formulation du modèle. Se faisant, le modèle est capable de rendre compte du comportement non-linéaire et isotrope d'une phase d'oxyde et non-linéaire anisotrope du substrat métallique sur lequel cet oxyde croît. De ce travail de modélisation, il résulte également une meilleure compréhension de l'origine des hypothèses d'homogénéisation dans les modèles de champs de phases. Le modèle a permis également une meilleure compréhension des effets de la viscoplasticité au cours d'une transformation de phase. Il est notamment capable de décrire des effets de déstabilisation morphologiques d'une interface au cours d'une transformation de phase faisant intervenir des effets de la viscoplasticité. De plus, les limites des modèles de champs de phases en viscoplasticité ont été étudiées sur des calculs de référence pour les modèles de Voigt/Taylor et de Reuss/Sachs. Finalement, l'application du modèle a permis de mettre en évidence un phénomène de fragilisation par l'oxydation, qui peut être une conséquence de la croissance d'intrusions d'oxydes.

Des simulations par éléments finis de la croissance d'une couche oxyde de chromine sur un acier austénitique ont été ensuite effectuées. Les contraintes de croissances générées par l'oxyde ont été prises en compte au cours des calculs. Ces contraintes sont communément admises dans la littérature de l'oxydation à haute température et sont également jugées être nécessaires aux propriétés de passivation de la couche d'oxyde. L'oxyde formé étant ainsi dans un état de compression, sa rupture est donc peu probable sans l'action de sollicitations mécaniques additionnelles. Les simulations montrent que le chargement mécanique couplé aux effets de relaxation viscoplastique de l'oxyde et du substrat entraîne dans la quasi-totalité des cas la formation de contraintes de tensions à l'intérieur de la couche d'oxyde fragile. Un tel système résultera en l'accumulation d'un endommagement fragile à la surface de l'échantillon suite à un phénomène de dépassivation-repassivation. Sans l'action de l'environnement, l'échantillon devrait garder son intégrité, notamment dans le cas d'une simple sollicitation de fluage. L'application du modèle de croissance sur l'acier austénitique a permis également de mettre en évidence la non-influence des éléments d'alliages sur la cinétique d'oxydation de part la faible diffusivité de l'oxygène dans l'oxyde et de caractériser des profils de diffusion types qui peuvent être comparés avec des mesures expérimentales.

Il est aujourd'hui acquis que les joints de grains et également les bandes de localisation plastique agissent comme des court-circuits de diffusion. Du à cet effet de court-circuit, la morphologie de l'interface métal oxyde est fortement impactée et on observe des intrusions d'oxydes prenant la forme d'un dihèdre jusqu'à une forme de piquet. Ces intrusions d'oxyde agissent naturellement comme des concentrateurs de contraintes de part la différence des modules d'élasticité de l'oxyde et du substrat dans lequel l'oxyde croît. La dernière partie de la thèse est consacrée à l'étude de l'interaction du modèle de croissance d'oxyde avec un joint de grain. Il en ressort que la formation d'une intrusion d'oxyde accompagnée d'une relaxation viscoplastique résulte en l'injection de contraintes de tension dans le métal mais également de contraintes de tension à la surface libre et ceci de manière différée. Ces contraintes de tension peuvent déclencher l'amorçage de fissures dans la couche d'oxyde lorque des niveaux de pénétration intergranulaire suffisants sont atteints. De plus il est montré que l'application d'une contrainte de tension additionnelle réduit le temps d'amorçage et la profondeur de pénétration maximale d'oxyde dans un joint de grain non endommagé. Les résultats présentés au cours de cette thèse représentent un premier pas vers la compréhension du phénomène complexe de l'amorçage de fissures de CSC qui est souvent occulté dans la littérature. Dans ce travail, on retiendra que les grandeurs pertinentes pour décrire l'amorçage de fissures assistées par l'environnement sont :

- La déformation libre de l'oxyde
- Les paramètres de relaxation viscoplastique de l'oxyde et du substrat et l'histoire du chargement mécanique
- La contrainte imposée
- Le rapport des diffusivités de l'oxygène dans le joint de grain oxydé et dans l'oxyde

6.1 Towards the modelling of stress corrosion cracking

Stress corrosion cracking belongs to delayed cracking phenomena. In practice, a typical SCC test consists in the application of a tensile stress on a test sample within a corrosive (*e.g.* autoclave controlled) environment. If the sample were isolated from such an hostile environment, then, the load would be such that no damage could be observed. SCC tests are often followed by the brittle failure of the test sample hence excluding the possibility of creep damage as the leading failure mechanism. The failure is often localised along the grain boundaries and along emerging localised slip bands.

In this work, oxide growth was chosen to induce ductility losses within the metal. Oxides are often referred to as fragile in nature and are characterised by low critical yield stresses below which damage can be prevented. According to experimental observations, the brittle failure occurring in

SCC tests could correspond to the brittle failure of the oxide layer reported in this work. Nevertheless, a variety of other phenomena can be triggered as well, from which hydrogen embrittlement is often mentioned. The initiation of cracks caused by hydrogen embrittlement can occur below the free surface and hence without affecting the oxide integrity. In fact, oxide growth and failure is the tip of the iceberg of all possible environmentally-assisted cracking micromechanisms.

The prediction of SCC initiation time is then rather difficult given the variety of possible couplings causing the brittle failure of the material. This work aimed also at formulating a generic multiphysics model able to encompass several more additional coupling relationships leading to the embrittlement of the metal. The model developed in this work is intended to provide more physics in the analysis of SCC and relies on numerical simulation to better understand the possible interactions that can lead to the brittle failure of a ductile test sample under the action of a corrosive environment. The phase field method has been selected as a promising tool for its simplicity and flexibility to model complex interface patterns as for oxide intrusions for instance.

The proposed phase field model is based on homogenisation rules. To date, the rigorous thermodynamic formulation of such models is still under development in the phase field community. This is why a rigorous methodology has been proposed to formulate such models and has been applied to Voigt/Taylor and Reuss/Sachs schemes. Homogenisation based approaches allow to mix separate behaviour in a uncoupled manner. The non linear Norton flow and crystal plasticity have been incorporated into the model formulation given an adequate mixture of dissipation potentials. The model is thus able to deal with the non linear behaviour of a isotropic viscoplastic oxide phase growing on any anisotropic polycrystalline substrate. The work provides also a better understanding of the origin of homogenisation rules in phase field models. The model has also allowed the better understanding of the role of viscoplasticity during a phase transformation. Viscoplasticity has been shown to be able to trigger the destabilisation of a growing phase. Moreover, the limits of the Voigt/Taylor and Reuss/Sachs homogenisation models have been studied on a set of numerical experiments that can serve in the future to benchmark enhanced homogenisation and interpolation based phase field models.

6.2 Preliminary oxide growth simulations

Finite element simulation of oxide growth on a polycrystalline austenitic stainless steel based substrate have been performed and the growth stresses that can be provided by the growing oxide have been accounted for. Growth stresses are often mentioned in the literature of high temperature oxidation and are thought to be necessary to explain the passivation properties of the oxide, as such properties can be related to the PBR. It results that the growing oxide is in a state of compression and hence prevented from failure without the action of an additional external tensile stress. Simulations showed that mechanical loads coupled with viscoplastic relaxation effects involve the injection of tensile stresses within the fragile oxide layer for almost all cases. The system is thus thought to be followed by the accumulation of brittle damage at the free surface of the metal induced by a depassivation-repassivation phenomenon. It is worth noting that without the action of the environment, the test sample should be prevented from damage and more particularly for the case of a creep load that does not last long enough for creep damage to be initiated. The minimal impact of alloying elements on oxide growth kinetics has been also highlighted, which is due to the small oxygen diffusivity throughout the oxide layer. Finally, typical diffusion profiles have been calculated during oxide growth that could be compared with experimental measurements.

To date, it is well known that grain boundaries and localised slip bands act as diffusion short-circuits. It results that the morphology of the growing oxide in such crystal defects is highly impacted and oxide intrusions are observed as triangular shaped oxide patterns up to pegs (also called micro pegs) into the metal. Such oxide intrusions act as stress concentrators due to the difference of elastic moduli between the oxide and the metal. The last part of the thesis was devoted to the study of the growth of oxide intrusions and their impact on the local stress fields. The simulations show that the growth of a single oxide intrusion, where both the substrate and the oxide can relax viscoplastically,

is followed by the injection of delayed tensile stresses in the metal at the tip of the oxide intrusion and at the free surface in the fragile oxide layer given sufficient penetration levels of the intrusion. Moreover, it is shown that the application of an additional tensile stress over the whole simulation sample can decrease the SCC initiation time and the maximal penetration depth under which the grain boundary is prevented from damage. The results shown in the thesis are thought to be a first step in the understanding of the complex SCC crack initiation phenomenon, which is often discarded in the literature. It must be kept in mind that, in this work, the following components are needed for the simulation of crack initiation:

- the oxide eigenstrain,
- viscoplasticity parameters of the oxide and the substrate along with the loading history,
- the applied stress and
- the diffusivity ratio of oxygen within the oxide and along the oxidised grain boundary.

6.3 Long term perspectives

The model developed in this thesis is well-suited for the study of all kind of fatigue oxidation problems. In a near future, it can be used to better understand the engineering models developed in an industrial context for the prediction of SCC initiation times. The model highlights the physics of calibrated parameters of such empirical laws and can provide better estimates in the future. For instance, the SCC initiation time is though to have a highly non linear dependence on the applied stress in σ^{-7} in such models. The viscoplastic relaxation and a possible additional dependence of diffusion on stress can serve as explanation to such a non linear behaviour. Nevertheless, some aspects have been neglected and their influence must be considered in the future. First, the chemical free energies were simplified by quadratic potentials. The model needs first to be enhanced with logarithmic chemical free energies provided by accurate thermodynamic data from experimental databases such as CALPHAD. Finite strains can also be implemented to free the model from the small deformation hypothesis. The accurate characterisation of the mechanical behaviour and relaxation mechanisms of oxides would be a cornerstone for the determination of an accurate SCC initiation time. This is why experimental data must be fostered to be coupled with phase field models. A comprehensive description of the diffusion short circuit behaviour of oxidised grain boundaries has still to be done. Such a diffusion short-circuit is thought to act as a Trojan horse by allowing harmful oxide intrusions to grow into the metal. The diffusion short-circuit behaviour of localised slip bands has to be better understood by accounting for new couplings relationships between the dislocation density and oxide growth. Moreover, three dimensional effects as found in the oxidation of triple junctions remain to be studied. Three dimensional simulations are thought to be possible by using effective remeshing techniques and by the intensive use of highly parallel computations. The model can go further than the study of crack initiation by the addition of damage laws to study crack propagation. It can also be applied to a variety of metals used in the nuclear industry such as nickel based alloys. For instance, nickel based alloys can be maintained safe from SCC due to grain boundary carbide precipitation, whereas such a precipitation is known to be harmful for austenitic stainless steels. An enhanced version of the model should therefore be able to provide new insights on such phenomena by the addition of a carbide phase during grain boundary oxidation in nickel based alloys and steels.

Appendices

APPENDIX

A Calculation of growth rate constants

Contents

Analytic solutions for the problem of inner oxide growth are available if the substrate is assumed to be semi-infinite and reduced into a unidimensional problem, *i.e.* [Crank, 1975, Bhadeshia, 1985]. Two main cases are here distinguished: when diffusion of oxygen through the oxide layer is the rate limiting step and when the supply of reacting alloying element from the substrate is the rate limiting step.

A.1 Supply of oxygen

The problem could be reduced to a unidimensional diffusion problem as illustrated in Fig. A.1.

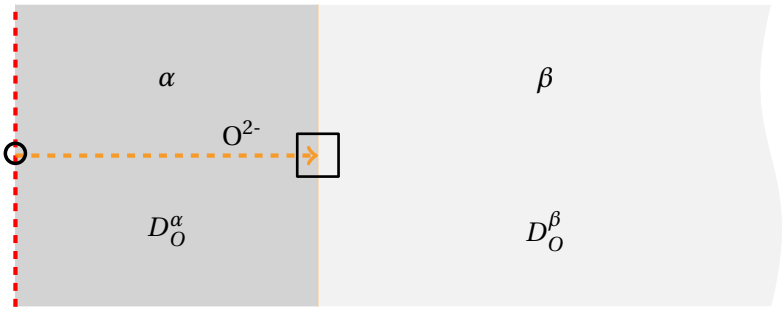

Figure A.1: Inner growth of α to β with diffusion of oxygen anions as the rate limiting step.

The typical concentration-distance curve is given in Fig. A.2

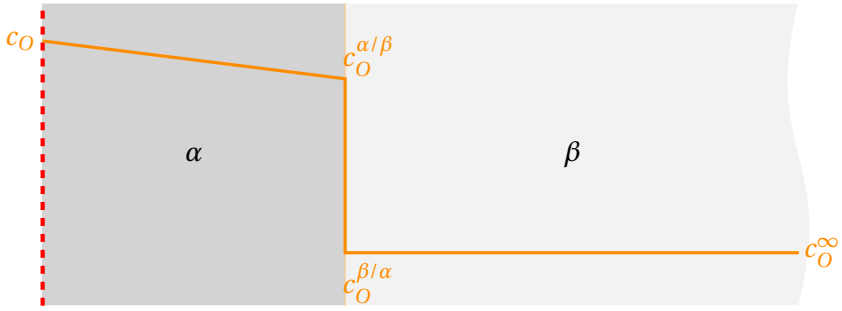

Figure A.2: Concentration-distance oxygen profile.

A.1.1 Mass transport

The boundary value problem is:

$$\frac{\partial c_O^{\alpha}}{\partial t} = D_O^{\alpha}\frac{\partial^2 c_O^{\alpha}}{\partial x^2} \quad \text{and} \quad \frac{\partial c_O^{\beta}}{\partial t} = D_O^{\beta}\frac{\partial^2 c_O^{\beta}}{\partial x^2}. \tag{A.1}$$

The following Dirichlet boundary conditions are used:

$$\forall t \in \Re^+, \begin{cases} c_O^{\alpha}(x=0) = c_O^0 & c_O^{\alpha}(x=X(t)) = c_O^{\alpha/\beta}(t) \\ c_O^{\beta}(x=X(t)) = c_O^{\beta/\alpha}(t) & c_O^{\beta}(x\to\infty) = c_O^{\infty} \end{cases}, \tag{A.2}$$

where $c_O^{\alpha/\beta}$ and $c_O^{\beta/\alpha}$ are the interface equilibrium concentrations – that ensure the chemical equilibrium, c_O^{∞}, the concentration in the substrate, far away from the interface and $X(t)$ the interface position. The motion of the interface is obtained by the difference of mass fluxes at the interface:

$$\forall t \in \Re^+, \dot{X}(c_O^{\alpha/\beta} - c_O^{\beta/\alpha}) = D_O^{\alpha}\frac{\partial c_O^{\alpha}}{\partial x} - D_O^{\beta}\frac{\partial c_O^{\beta}}{\partial x}. \tag{A.3}$$

It is worth noting that the concentrations $c_O^{\alpha/\beta}$ and $c_O^{\beta/\alpha}$ are time-independent.

A.1.2 Growth law

Given that the oxygen concentration gradient is zero in the substrate, the interface velocity equation (A.3) becomes:

$$\forall t \in \Re^+, \dot{X}(c_O^{\alpha/\beta} - c_O^{\beta/\alpha}) = D_O^{\alpha}\frac{\partial c_O^{\alpha}}{\partial x}. \tag{A.4}$$

The oxygen diffusion profile is a linear function of the distance enforced by A.1:

$$\forall t \in \Re^+, \dot{X}(c_O^{\alpha/\beta} - c_O^{\beta/\alpha}) = D_O^{\alpha}\frac{c_O^{\alpha} - c_O^{\alpha/\beta}}{X}, \tag{A.5}$$

for which the time dependent variables can be isolated:

$$\forall t \in \Re^+, \dot{X}X = D_O^{\alpha}\frac{c_O^{\alpha} - c_O^{\alpha/\beta}}{c_O^{\alpha/\beta} - c_O^{\beta/\alpha}}, \tag{A.6}$$

and time-integrated, recalling that the right-hand side is time independent:

$$\forall t \in \Re^+, \frac{1}{2} X(t)^2 = D_O^\alpha \frac{c_O^\alpha - c_O^{\alpha/\beta}}{c_O^{\alpha/\beta} - c_O^{\beta/\alpha}} t + A. \tag{A.7}$$

It results that the growth rate is parabolic, with the following growth rate constant, when $X(0) = 0$:

$$k_p = 2 D_O^\alpha \frac{c_O^\alpha - c_O^{\alpha/\beta}}{c_O^{\alpha/\beta} - c_O^{\beta/\alpha}}, \tag{A.8}$$

Using the supersaturation:

$$\Omega_O = \frac{c_O^\alpha - c_O^{\alpha/\beta}}{c_O^{\alpha/\beta} - c_O^{\beta/\alpha}}, \tag{A.9}$$

Eq. (A.8) results in:

$$k_p = 2 D_O^\alpha \Omega_O. \tag{A.10}$$

A.2 Supply of an alloying element

Modelling the oxidation behaviour of alloys requires to take diffusion of alloying elements into account.

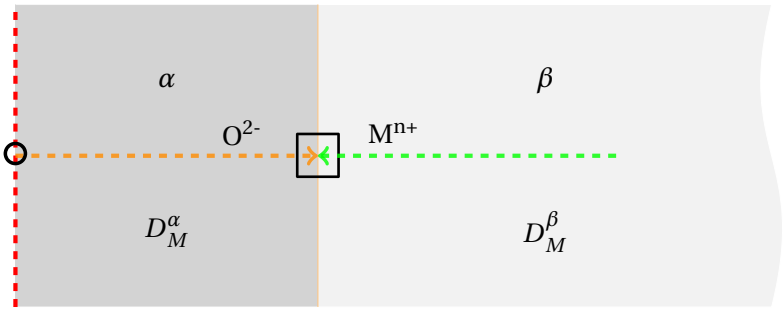

Figure A.3: Inner growth of α to β phases, with supply of metal cations as the rate-limiting step

The concentration-distance curve of the alloying element shows a typical depletion profile in the vicinity of the interface, as shown in Fig. A.4.

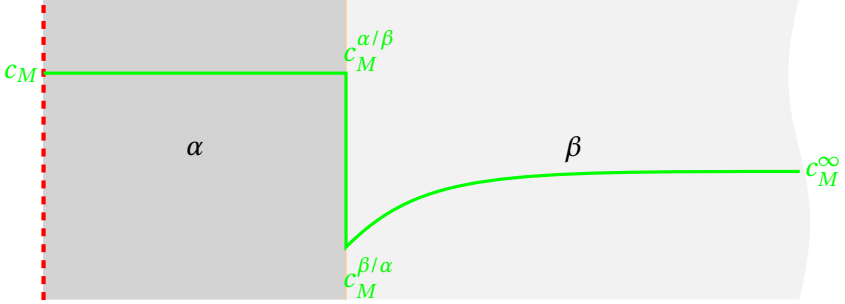

Figure A.4: Concentration-distance curve of an alloying component M.

A.2.1 Mass transport

The only concentration field of interest here is the one in the substrate. Therefore, the diffusion equation is solely solved for c_M^β:

$$\frac{\partial c_M^\beta}{\partial t} = D_M^\beta \frac{\partial^2 c_M^\beta}{\partial x^2}. \tag{A.11}$$

If the chemical equilibrium is assumed, the interface concentrations c_M^α and c_M^β become time-independent. The initial conditions are the following:

$$\text{at } t=0, \begin{cases} X(t=0)=0 \\ c_M^\beta(x=0) = c_M^{\beta/\alpha} \\ c_M^\beta(x>0) = c_M^\infty \end{cases}, \tag{A.12}$$

where Dirichlet boundary conditions are enforced:

$$\forall t>0, \begin{cases} c_M^\beta(x=X(t)) = c_M^{\beta/\alpha} \\ c_M^\beta(x\to\infty) = c_M^\infty \end{cases}. \tag{A.13}$$

Furthermore, mass balance dictates that,

$$\forall t>0,\ \dot{X}(c^{\beta/\alpha} - c^{\alpha/\beta}) = -D_M^\beta \frac{\partial c_M^\beta}{\partial x}\bigg|_{X(t)}. \tag{A.14}$$

A change of variable based on the variable of similitude s is made:

$$s = \frac{x}{2\sqrt{D_M^\beta t}}. \tag{A.15}$$

The diffusion equation could be rewritten as:

$$\frac{dc_M^\beta}{ds}\bigg|_x \frac{\partial s}{\partial t}\bigg|_x = D_M^\beta \frac{d}{ds}\left(\frac{dc_M^\beta}{ds}\bigg|_t \frac{\partial s}{\partial x}\bigg|_t\right)\bigg|_t \frac{\partial s}{\partial x}\bigg|_t, \tag{A.16}$$

with

$$\frac{\partial s}{\partial t} = -\frac{x}{4t\sqrt{D_M^\beta t}} = -\frac{s}{2t} \quad \text{and} \quad \frac{\partial s}{\partial x} = \frac{1}{2\sqrt{D_M^\beta t}}, \tag{A.17}$$

leads A.16 to the ordinary differential equation:

$$-s\frac{dc_M^\beta}{ds} = \frac{1}{2}\frac{d^2c}{ds^2}. \tag{A.18}$$

Interface concentrations are assumed time-independent, the value of the variable of similitude evaluated at the interface becomes constant as well:

$$s^* = \frac{X(t)}{2\sqrt{D_M^\beta t}}, \tag{A.19}$$

and:

$$\dot{X}(t) = \sqrt{\frac{D_M^\beta}{t}} s^* . \tag{A.20}$$

Rewriting (A.14) using (A.20) gives:

$$\sqrt{\frac{D_M^\beta}{t}} s^* (c_M^{\beta/\alpha} - c_M^{\alpha/\beta}) = -D_m^\beta \frac{dc_M^\beta}{ds}\Big|_{s^*} \frac{\partial s}{\partial x}\Big|_{X(t)}, \tag{A.21}$$

with

$$s^* (c_M^{\beta/\alpha} - c_M^{\alpha/\beta}) = -\frac{1}{2} \frac{dc_M^\beta}{ds}\Big|_{s^*} . \tag{A.22}$$

The ODE (A.18) can be rewritten using the initial condition $X(0) = 0$:

$$\frac{dA}{A} = -\frac{1}{2} s ds, \tag{A.23}$$

and integrated:

$$\log_e \left(\frac{A}{A_0} \right) = -s^2, \tag{A.24}$$

which can be reformulated into:

$$\frac{dc}{ds} = A_0 \exp\left(-s^2\right). \tag{A.25}$$

By integration:

$$[c]_s^\infty = A_0 \int_s^\infty \exp\left(-u^2\right) du, \tag{A.26}$$

which reads:

$$c_M^\infty - c_M^\beta(s) = A_0 \sqrt{\frac{\pi}{2}} \mathrm{erfc}(s). \tag{A.27}$$

A_0 can be retrieved by evaluating $A = \dfrac{dc_M^\beta}{ds}$ at the interface:

$$\frac{dc}{ds}\Big|_{s^*} = A_0 \exp\left(-s^{*2}\right). \tag{A.28}$$

Using the mass balance:

$$A_0 = -2 s^* (c_M^{\beta/\alpha} - c_M^{\alpha/\beta}) \exp\left(s^{*2}\right), \tag{A.29}$$

and:

$$c_M^\infty - c(s) = -\sqrt{\pi} s^* (c_M^{\beta/\alpha} - c_M^{\alpha/\beta}) \exp\left(s^{*2}\right) \mathrm{erfc}(s). \tag{A.30}$$

By evaluation at the interface:

$$-\frac{c_M^{\infty}-c_M^{\beta/\alpha}}{c_M^{\beta/\alpha}-c_M^{\alpha/\beta}}=\sqrt{\pi}s^*\exp\left(s^{*2}\right)\mathrm{erfc}(s^*)\,. \tag{A.31}$$

We note the supersaturation Ω_M^{β} to be:

$$\Omega_M^{\beta}=\frac{c_M^{\infty}-c_M^{\beta/\alpha}}{c_M^{\alpha/\beta}-c_M^{\beta/\alpha}}\,. \tag{A.32}$$

The supersaturation is connected with the variable of similitude with the function F, known as the transcendental function, where:

$$\Omega_M^{\beta}=F(s^*)\,. \tag{A.33}$$

The transcendental function has the form illustrated in Fig. A.5.

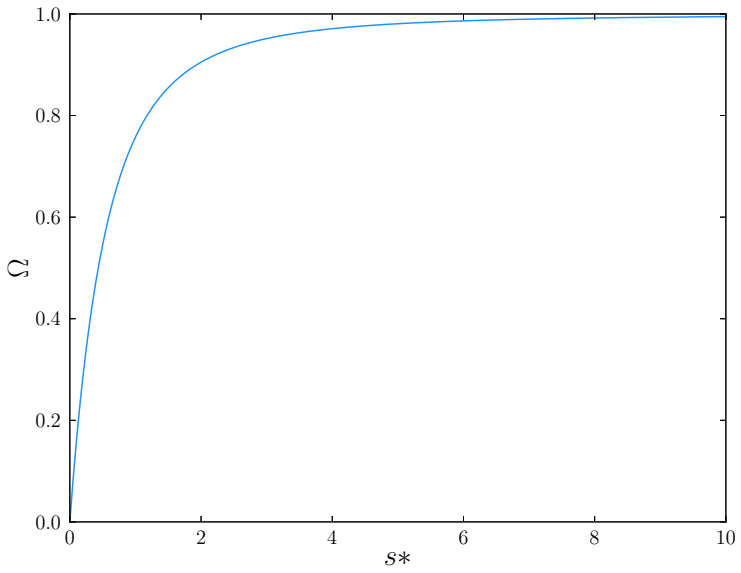

Figure A.5: Transcendental function

The inverse function F^{-1} of F can be injected in (A.20):

$$\dot{X}(t)=\sqrt{\frac{D_M^{\beta}}{t}}F^{-1}(\Omega_M^{\beta})\,. \tag{A.34}$$

The function F^{-1} is usually approximated by numerical methods.

A.2.2 Growth law

Given that the supersaturation is time independent, (A.34) can be integrated as follows:

$$X(t)=\sqrt{4D_M^{\beta}F^{-1}(\Omega_M^{\beta})^2 t}\,. \tag{A.35}$$

Resulting again in a parabolic rate constant:

$$k_p=4D_M^{\beta}F^{-1}(\Omega_M^{\beta})^2\,. \tag{A.36}$$

The parabolic growth implies then the continuous decrease of the gradient of alloying elements in the substrate. It results that the alloying depleted area increases with time.

A.3 Wagner growth theory

In this section, the oxide is considered as an ionic crystal, for which both electronic and ionic currents occur. The ionic transport is then likely to be controlled by the gradient of electric potential in the oxide layer [Fehlner and Mott, 1970]. The mass flux becomes then the addition of a diffusive and electric mass transport:

$$\underline{\boldsymbol{J}} = -L\nabla\mu - \frac{\sigma}{q}\nabla\Phi. \tag{A.37}$$

Moreover, we assume that the circuit is open so that local electroneutrality is enforced:

$$\nabla\cdot\left(\sum q_i \underline{\boldsymbol{J}}_i\right) = 0. \tag{A.38}$$

A.3.1 Mass transport

Wagner's theory is more general than the two previous cases as it contains a diffusion term and a convective term. The transport of charged species results then in both electronic and ionic transports. We note that the transport of electrons and electron holes is required for the ionisation process. For a charged specie i, and by neglecting the defects interactions, the current density is driven by a diffusive part proportional to the gradient of diffusion potential and a drift part proportional to the electric field:

$$\underline{\boldsymbol{I}}_i = -c_i\frac{D_i z_i q}{kT}\nabla\mu_i - c_i v_i z_i q\nabla\phi, \tag{A.39}$$

where q is the absolute value of the electronic charge, $-\nabla\phi = \underline{\boldsymbol{E}}$ the electric field deriving from the electrical potential ϕ, D_i the self-diffusivity or diffusion mobility of i, z_i the charge of i and v_i the electrical mobility of i. The Nernst-Einstein relation reads:

$$\frac{D_i}{kT} = \frac{v_i}{z_i q}. \tag{A.40}$$

It links the diffusivity to the conductivity.

It is possible to rewrite the mass transport equation (A.39):

$$\underline{\boldsymbol{I}}_i = -c_i v i\nabla\eta_i, \tag{A.41}$$

where:

$$\eta_i = \mu_i + z_i q\phi, \tag{A.42}$$

and introducing the conductivity σ_i:

$$v_i = \frac{\sigma_i}{z_i q}. \tag{A.43}$$

Now the total current can be separated into ionic and electronic currents depending on the nature of i, anion, cation, electron or hole:

$$\underline{\boldsymbol{I}} = \underline{\boldsymbol{I}}_{\text{ionic}} + \underline{\boldsymbol{I}}_{\text{electronic}}, \tag{A.44}$$

where the electronic current can be rewritten as follows:

$$\underline{\boldsymbol{I}}_{\text{electronic}} = \underline{\boldsymbol{I}}_e + \underline{\boldsymbol{I}}_h. \tag{A.45}$$

Using the mass transport equation (A.39):

$$\underline{\boldsymbol{I}}_{\text{electronic}} = \frac{1}{e}(\sigma_e \nabla\eta_e - \sigma_h \nabla\eta_h)\,. \tag{A.46}$$

Assuming the thermodynamic equilibrium of the intrinsic ionisation defect reaction results in:

$$\nabla\eta_e + \nabla\eta_h = 0\,. \tag{A.47}$$

The electronic current is finally written:

$$\underline{\boldsymbol{I}}_{\text{electronic}} = \frac{\sigma_{el}}{e}\nabla\eta_e\,, \tag{A.48}$$

with:

$$\sigma_{el} = \sigma_e + \sigma_h\,. \tag{A.49}$$

The same treatment is done for ionic transport:

$$\underline{\boldsymbol{I}}_{\text{ionic}} = \underline{\boldsymbol{I}}_{ca} + \underline{\boldsymbol{I}}_{an}\,, \tag{A.50}$$

and:

$$\underline{\boldsymbol{I}}_{\text{ionic}} = -\frac{1}{e}\left(\frac{\sigma_{ca}}{z_{ca}}\nabla\eta_{ca} + \frac{\sigma_{an}}{z_{an}}\nabla\eta_{an}\right). \tag{A.51}$$

Now the thermodynamic equilibrium is assumed to be unperturbed which could be directly written from the redox reaction:

$$|z_{an}|Me^{z_{ca}} + z_{ca}O^{z_{an}} \rightleftharpoons Me_{|z_{an}|}O_{z_{ca}}\,, \tag{A.52}$$

which gives:

$$|z_{an}|\mu_{ca} + z_{ca}\mu_{an} = \mu_{Ox}\,. \tag{A.53}$$

By taking the gradients of (A.53):

$$|z_{an}|\nabla\mu_{ca} + z_{ca}\nabla\mu_{an} = \nabla\mu_{Ox}\,. \tag{A.54}$$

Assuming that the oxide is stable and that oxide molecules are not mobile implies a zero gradient of chemical potential of the oxide:

$$|z_{an}|\nabla\mu_{ca} + z_{ca}\nabla\mu_{an} = \underline{\mathbf{0}}\,. \tag{A.55}$$

Such chemical potentials can be transformed into electrochemical potential due to the balance of electrical terms:

$$Me^{z_{ca}} + z_{ca}e^- \rightleftharpoons Me \quad \text{and} \quad O^{z_{an}} \rightleftharpoons O + |z_{an}|e^-\,, \tag{A.56}$$

which equilibrium is given by (A.42):

$$\mu_{ca} + z_{ca}e\phi = \eta_{ca} \quad \text{and} \quad \mu_{an} = \eta_{an} + |z_{an}|e\phi\,, \tag{A.57}$$

and therefore, after injection of (A.57) in (A.55):

$$|z_{an}|\nabla\eta_{ca} + z_{ca}\nabla\eta_{an} = \underline{\mathbf{0}}\,, \tag{A.58}$$

which finally gives:

$$\underline{\boldsymbol{I}}_{\text{ionic}} = -\frac{\sigma_i}{z_{ca}e}\nabla\eta_{ca} = -\frac{\sigma_i}{z_{an}e}\nabla\eta_{an}, \tag{A.59}$$

where:

$$\sigma_i = \sigma_{ca} + \sigma_{an}. \tag{A.60}$$

The total current can now be rewritten combining (A.48) and (A.59):

$$\underline{\boldsymbol{I}} = \frac{\sigma_{el}}{e}\nabla\eta_e - \frac{\sigma_i}{z_{ca}e}\nabla\eta_{ca}. \tag{A.61}$$

A.3.2 Growth law

The rate of built oxide is naturally proportional to the total ionic particle current:

$$\dot{X} = \frac{1}{z_{ca}|z_{an}|e}\underline{\boldsymbol{I}}_{ionic}\cdot\underline{\boldsymbol{n}}. \tag{A.62}$$

From (A.59), the above equation becomes:

$$\dot{X} = \frac{\sigma_i}{z_{ca}(z_{an}e)^2}\nabla\eta_{an}\cdot\underline{\boldsymbol{n}}. \tag{A.63}$$

To that point, it is convenient to assume that the thermodynamic equilibrium between ions and atoms is not perturbed by the currents such that:

$$\nabla\eta_{an} \sim \nabla\mu_{an}. \tag{A.64}$$

Now, (A.63) can be integrated in the limit of an infinitely small thickness increase δX, where $\underline{\boldsymbol{n}}$ is directed from the inner metal oxide interface (in) towards the outer free surface (out):

$$\dot{X}\delta X = \frac{\sigma_i}{z_{ca}(z_{an}e)^2}\int_{\mu_{an}^{out}}^{\mu_{an}^{in}}\nabla\mu_{an}, \tag{A.65}$$

which can be rewritten using the expression of the conductivity (A.43) with the Nernst-Einstein relation (A.40):

$$\dot{X}\delta X = \frac{1}{kT}\frac{1}{z_{ca}}\left(c_{an}D_{an} + c_{ca}D_{ca}\left(\frac{z_{ca}}{z_{an}}\right)^2\right)\int_{\mu_{an}^{out}}^{\mu_{an}^{in}}\delta\mu_{an}. \tag{A.66}$$

Further, the concentration of anions c_{an} and the concentration of cations c_{ca} is related by the stoichiometry of the oxide by $\frac{c_{ca}}{c_{an}} = \frac{|z_{an}|}{z_{ca}} = \frac{3}{2}$. For the growth of Cr_2O_3, the above equation reads:

$$\dot{X}\delta X = \frac{c_{an}}{kT}\frac{1}{2}\left(D_{an} + \frac{2}{3}D_{ca}\right)\int_{\mu_O^{out}}^{\mu_O^{in}}\delta\mu_O. \tag{A.67}$$

From:

$$\mu_O = \frac{1}{2}\mu_{O_2}, \tag{A.68}$$

it results that:

$$\dot{X}\delta X = \frac{c_{an}}{kT}\frac{1}{4}\left(D_{an} + \frac{2}{3}D_{ca}\right)\int_{\mu_{O_2}^{out}}^{\mu_{O_2}^{in}}\delta\mu_{O_2}. \tag{A.69}$$

Moreover, as the chemical potential can be expressed under a logarithmic form $\mu_i = \mu_i^0 + kT \log a_i$, it comes that:

$$\dot{X}\delta X = \frac{1}{4} c_{an} \left(D_{an} + \frac{2}{3} D_{ca} \right) \int_{\mathscr{P}_{O_2}^{out}}^{\mathscr{P}_{O_2}^{in}} \delta \log \mathscr{P}_{O_2}, \tag{A.70}$$

where the partial pressure has been chosen to describe the activity of oxygen, the integrand can be evaluated as follows:

$$\dot{X}\delta X = \frac{1}{4} c_{an} \left(D_{an} + \frac{2}{3} D_{ca} \right) \log \frac{\mathscr{P}_{O_2}^{in}}{\mathscr{P}_{O_2}^{out}}. \tag{A.71}$$

The above equation corresponds to the parabolic growth rate as in (A.6) leading to the following rate constant:

$$k_p = \frac{1}{2} c_{an} \left(D_{an} + \frac{2}{3} D_{ca} \right) \log \frac{\mathscr{P}_{O_2}^{in}}{\mathscr{P}_{O_2}^{out}}, \tag{A.72}$$

which is also found in [Kofstad, 1972, Huntz et al., 2007, Sabioni et al., 2005]. Wagner's theory is more complete in the sense that inner and outer growth are simultaneously accounted for. The above Wagner rate constant is frequently used to calibrate diffusivities along thin films. Nevertheless, as the rate constant is dependent on two diffusivities, the calibration of diffusivities from such methods becomes then strongly dependent on the underlying assumptions about the rate limiting step.

APPENDIX

B Calculation of the Jacobian matrix

Contents

The numerical approach for the three dimensional finite element modelling of the multi-physics problem is here developed by first choosing finite elements based on n nodes, each containing several degrees of freedom, that can be either scalar or vector valued. A Gauss integration procedure is performed where integration points' values are obtained from the product of shape functions matrices N, for scalar nodal values and $\mathbf{N}$ for vector nodal values, with the nodal values. Gradients can be computed from the product of the gradient operator $\mathbf{B}$, for scalar nodal values and the deformation matrix $\underline{\mathbf{B}}$, for vectorial nodal values, with the nodal values as well. The shape function matrix for scalar valued nodal values:

$$N = \begin{pmatrix} N_1 & \dots & N_k & \dots & N_n \end{pmatrix}. \tag{B.1}$$

Shape function matrix for vector valued nodal values:

$$\underline{\mathbf{N}} = \begin{pmatrix} N_1 & 0 & 0 & \dots & N_k & 0 & 0 & \dots & N_n & 0 & 0 \\ 0 & N_1 & 0 & \dots & 0 & N_k & 0 & \dots & 0 & N_n & 0 \\ 0 & 0 & N_1 & \dots & 0 & 0 & N_k & \dots & 0 & 0 & N_n \end{pmatrix}. \tag{B.2}$$

Gradient operator for the gradient of scalar valued nodal values:

$$B = \begin{pmatrix} N_{1,x} & \dots & N_{k,x} & \dots & N_{n,x} \\ N_{1,y} & \dots & N_{k,y} & \dots & N_{n,y} \\ N_{1,z} & \dots & N_{k,z} & \dots & N_{n,z} \end{pmatrix}, \tag{B.3}$$

Gradient operator for the gradient of vector valued nodal values:

$$\underline{\mathbf{B}} = \begin{pmatrix} N_{1,x} & 0 & 0 & \dots & N_{k,x} & 0 & 0 & \dots & N_{n,x} & 0 & 0 \\ 0 & N_{1,y} & 0 & \dots & 0 & N_{k,y} & 0 & \dots & 0 & N_{n,y} & 0 \\ 0 & 0 & N_{1,z} & \dots & 0 & 0 & N_{k,z} & \dots & 0 & 0 & N_{n,z} \\ N_{1,y} & N_{1,x} & 0 & \dots & N_{k,y} & N_{k,x} & 0 & \dots & N_{n,y} & N_{n,x} & 0 \\ N_{1,z} & 0 & N_{1,x} & \dots & N_{k,z} & 0 & N_{k,x} & \dots & N_{n,z} & 0 & N_{n,x} \\ 0 & N_{1,z} & N_{1,y} & \dots & 0 & N_{k,z} & N_{k,y} & \dots & 0 & N_{n,z} & N_{n,y} \end{pmatrix}. \tag{B.4}$$

The above gradient operator allows to calculate the symmetric gradient under the form of the Mandel tensor:

$$\underset{\sim}{\boldsymbol{\varepsilon}} = \begin{pmatrix} \varepsilon_{xx} \\ \varepsilon_{yy} \\ \varepsilon_{zz} \\ \sqrt{2}\varepsilon_{xy} \\ \sqrt{2}\varepsilon_{xz} \\ \sqrt{2}\varepsilon_{yz} \end{pmatrix}. \tag{B.5}$$

Stresses can then be computed after separating the elastic part of the total strain with the elasticity tensor $\underset{\approx}{\boldsymbol{\Lambda}}$, that can be here reduced into a 6×6 matrix:

$$\underset{\sim}{\boldsymbol{\sigma}} = \underset{\approx}{\boldsymbol{\Lambda}} : \underset{\sim}{\boldsymbol{\varepsilon}}_e . \tag{B.6}$$

Balance equations (3.9) are then evaluated at each elements from a Gauss integration procedure.

$$\begin{aligned} \sum_q \left(\pi(q) N(q) \{u^*\} - [\underline{\boldsymbol{\xi}}](q) \cdot \mathbf{B}(q) \{u^*\} \right) W(q) &= -\sum_r \zeta(r) N(r) \{u^*\} W(r), \\ \sum_q \left(\dot{c}_{\mathrm{i}}(q) N(q) \{v^*\} - [\underline{\boldsymbol{J}}_{\mathrm{i}}](q) \cdot \mathbf{B}(q) \{v^*\} \right) W(q) &= -\sum_r j_{\mathrm{i}}(r) N(r) \{v^*\} W(r), \\ \sum_q [\underset{\sim}{\boldsymbol{\sigma}}](q) \cdot \underline{\mathbf{B}}(q) \{\underline{\boldsymbol{w}}^*\} W(q) &= \sum_r [\underline{\boldsymbol{t}}](r) \cdot \mathbf{N}(r) \{\underline{\boldsymbol{w}}^*\} W(r). \end{aligned} \tag{B.7}$$

The residuals are then defined as follows,

$$\begin{aligned} \{R_\phi\} &= \sum_q \left(N(q)\pi(q) - \mathbf{B}^T(q)[\underline{\boldsymbol{\xi}}](q) \right) W(q) + \sum_r N(r)\zeta(r) W(r), \\ \{R_{c_i}\} &= \sum_q \left(N(q)\dot{c}_{\mathrm{i}}(q) - \mathbf{B}^T(q)[\underline{\boldsymbol{J}}_{\mathrm{i}}](q) \right) W(q) + \sum_r N(r) j_{\mathrm{i}}(r) W(r), \\ \{R_{\underline{\boldsymbol{u}}}\} &= \sum_q \underline{\mathbf{B}}^T(q)[\underset{\sim}{\boldsymbol{\sigma}}](q) W(q) - \sum_r \mathbf{N}^T(r)[\underline{\boldsymbol{t}}](r) W(r). \end{aligned} \tag{B.8}$$

The multiphysics element has now the following ordering,

$$\begin{pmatrix} \{\phi\} \\ \{c_i\} \\ \{\underline{\boldsymbol{u}}\} \end{pmatrix}, \tag{B.9}$$

which results in the following Jacobian,

$$J = \begin{pmatrix} \frac{\partial\{R_\phi\}}{\partial\{\phi\}} & \cdots & \frac{\partial\{R_\phi\}}{\partial\{c_i\}} & \cdots & \frac{\partial\{R_\phi\}}{\partial\{\underline{\boldsymbol{u}}\}} \\ \vdots & \ddots & \vdots & & \vdots \\ \frac{\partial\{R_{c_i}\}}{\partial\{\phi\}} & \cdots & \frac{\partial\{R_{c_i}\}}{\partial\{c_j\}} & \cdots & \frac{\partial\{R_{c_i}\}}{\partial\{\underline{\boldsymbol{u}}\}} \\ \vdots & & \vdots & \ddots & \vdots \\ \frac{\partial\{R_{\underline{\boldsymbol{u}}}\}}{\partial\{\phi\}} & \cdots & \frac{\partial\{R_{\underline{\boldsymbol{u}}}\}}{\partial\{c_i\}} & \cdots & \frac{\partial\{R_{\underline{\boldsymbol{u}}}\}}{\partial\{\underline{\boldsymbol{u}}\}} \end{pmatrix}, \tag{B.10}$$

used in the further calculation of the global stiffness matrix, which is not symmetric.

The sub-matrices of J read, regarding the phase field nodal value:

$$\begin{aligned} \frac{\partial\{R_\phi\}}{\partial\{\phi\}} &= \sum_q \left(N \otimes N(q) \frac{\partial \pi}{\partial \phi}(q) - \mathbf{B}^T(q) \frac{\partial[\underline{\boldsymbol{\xi}}]}{\partial\{\phi\}}(q) \right) W(q) \\ \frac{\partial\{R_\phi\}}{\partial\{c_i\}} &= \sum_q \left(N \otimes N(q) \frac{\partial \pi}{\partial c_i}(q) - \mathbf{B}^T(q) \frac{\partial[\underline{\boldsymbol{\xi}}]}{\partial\{c_i\}}(q) \right) W(q) \\ \frac{\partial\{R_\phi\}}{\partial\{\underline{\boldsymbol{u}}\}} &= \sum_q \left(N^T(q) \frac{\partial \pi}{\partial\{\underline{\boldsymbol{u}}\}}(q) - \mathbf{B}^T(q) \frac{\partial[\underline{\boldsymbol{\xi}}]}{\partial\{\underline{\boldsymbol{u}}\}}(q) \right) W(q) \end{aligned}, \tag{B.11}$$

and, for concentrations:

$$\begin{aligned} \frac{\partial\{R_{c_i}\}}{\partial\{\phi\}} &= \sum_q \left(N \otimes N(q) \frac{\partial \dot{c}_i}{\partial \phi}(q) - \mathbf{B}^T(q) \frac{\partial[\underline{\boldsymbol{J}}_i]}{\partial\{\phi\}}(q) \right) W(q) \\ \frac{\partial\{R_{c_i}\}}{\partial\{c_j\}} &= \sum_q \left(N \otimes N(q) \frac{\partial \dot{c}_i}{\partial c_j}(q) - \mathbf{B}^T(q) \frac{\partial[\underline{\boldsymbol{J}}_i]}{\partial\{c_j\}}(q) \right) W(q) \\ \frac{\partial\{R_{c_i}\}}{\partial\{\underline{\boldsymbol{u}}\}} &= \sum_q \left(N^T(q) \frac{\partial \dot{c}_i}{\partial\{\underline{\boldsymbol{u}}\}}(q) - \mathbf{B}^T(q) \frac{\partial[\underline{\boldsymbol{J}}_i]}{\partial\{\underline{\boldsymbol{u}}\}}(q) \right) W(q) \end{aligned}, \tag{B.12}$$

and lastly for displacements:

$$\begin{aligned} \frac{\partial\{R_{\underline{\boldsymbol{u}}}\}}{\partial\{\phi\}} &= \sum_q \underline{\mathbf{B}}^T(q) \frac{\partial[\underline{\boldsymbol{\sigma}}]}{\partial\{\phi\}}(q) W(q) \\ \frac{\partial\{R_{\underline{\boldsymbol{u}}}\}}{\partial\{c_i\}} &= \sum_q \underline{\mathbf{B}}^T(q) \frac{\partial[\underline{\boldsymbol{\sigma}}]}{\partial\{c_i\}}(q) W(q) \\ \frac{\partial\{R_{\underline{\boldsymbol{u}}}\}}{\partial\{\underline{\boldsymbol{u}}\}} &= \sum_q \underline{\mathbf{B}}^T(q) \frac{\partial[\underline{\boldsymbol{\sigma}}]}{\partial\{\underline{\boldsymbol{u}}\}}(q) W(q) \end{aligned}. \tag{B.13}$$

B.0.3 Derivatives for the Voigt/Taylor approach

In the Voigt/Taylor approach, π reads:

$$\pi = -\frac{1}{M_\pi}\dot{\phi} - W g'(\phi) - h'(\phi) F_\phi, \tag{B.14}$$

where

$$F_\phi = f^\alpha - f^\beta - \mu_\mathrm{i}\left(c_\mathrm{i}^\alpha - c_\mathrm{i}^\beta\right), \tag{B.15}$$

which leads to the following derivatives:

$$\begin{aligned} \frac{\partial \pi}{\partial \phi} &= -\frac{1}{M_\phi}\frac{\partial \dot{\phi}}{\partial \phi} - W g''(\phi) - h''(\phi) F_\phi \\ \frac{\partial \pi}{\partial c_i} &= -h' k_i^\alpha \left(c_i^\alpha - c_i^\beta\right) \end{aligned} \tag{B.16}$$

and

$$\begin{aligned}\frac{\partial \pi}{\partial\{u\}} &= \frac{\partial \pi}{\partial \underset{\sim}{\boldsymbol{\varepsilon}}}\frac{\partial \underset{\sim}{\boldsymbol{\varepsilon}}}{\partial\{\underline{\boldsymbol{u}}\}} &= -h'\left(\frac{\partial f^\alpha}{\partial \underset{\sim}{\boldsymbol{\varepsilon}}}-\frac{\partial f^\beta}{\partial \underset{\sim}{\boldsymbol{\varepsilon}}}\right)\underline{\mathbf{B}}\\ &= -h'\left(\frac{\partial f^\alpha}{\partial \underset{\sim}{\boldsymbol{\varepsilon}}^\alpha_e}\frac{\partial \underset{\sim}{\boldsymbol{\varepsilon}}^\alpha_e}{\partial \underset{\sim}{\boldsymbol{\varepsilon}}}-\frac{\partial f^\beta}{\partial \underset{\sim}{\boldsymbol{\varepsilon}}^\beta_e}\frac{\partial \underset{\sim}{\boldsymbol{\varepsilon}}^\beta_e}{\partial \underset{\sim}{\boldsymbol{\varepsilon}}}\right)\underline{\mathbf{B}}\\ &= -h'\left(\underset{\sim}{\boldsymbol{\sigma}}^\alpha-\underset{\sim}{\boldsymbol{\sigma}}^\beta\right)\underline{\mathbf{B}}\end{aligned} \tag{B.17}$$

Then using the state law (3.30) and (3.15), it comes:

$$\begin{aligned}\frac{\partial[\underline{\boldsymbol{\xi}}]}{\partial\{\phi\}} &= \frac{\partial[\underline{\boldsymbol{\xi}}]}{\partial\nabla\phi}\frac{\partial\nabla\phi}{\partial\{\phi\}} &= 6\gamma\frac{\delta}{z}\mathbf{B}\\ \frac{\partial[\underline{\boldsymbol{\xi}}]}{\partial\{c_i\}} &= 0\\ \frac{\partial[\underline{\boldsymbol{\xi}}]}{\partial\{\underline{\boldsymbol{u}}\}} &= 0\end{aligned} \tag{B.18}$$

The mass balance equation with (3.1):

$$\begin{aligned}\frac{\partial \dot{c}_i}{\partial\phi} &= h'\left(1-\frac{k_i^\alpha}{k_i^\beta}\right)\dot{c}_i^\alpha+\left(h''\dot{\phi}+h'\frac{\partial\dot{\phi}}{\partial\phi}\left(c_i^\alpha-c_i^\beta\right)\right)\\ \frac{\partial \dot{c}_i}{\partial c_i} &= h\frac{\partial \dot{c}_i^\alpha}{\partial c_i^\alpha}+\bar{h}\frac{\partial \dot{c}_i^\beta}{\partial c_i^\beta}\frac{k_i^\alpha}{k_i^\beta}+h'\dot{\phi}\left(1-\frac{k_i^\alpha}{k_i^\beta}\right)\\ \frac{\partial \dot{c}_i}{\partial\{\underline{\boldsymbol{u}}\}} &= 0\end{aligned} \tag{B.19}$$

and for the flux (3.44), (3.45), (3.29) and (3.25):

$$\begin{aligned}\frac{\partial[\underline{\boldsymbol{J}}_i]}{\partial\{\phi\}} &= \frac{\partial[\underline{\boldsymbol{J}}_i]}{\partial\phi}\frac{\partial\phi}{\partial\{\phi\}} = -L_i'(\phi)\nabla\mu_i^\alpha N\\ \frac{\partial[\underline{\boldsymbol{J}}_i]}{\partial\{c_i\}} &= \frac{\partial[\underline{\boldsymbol{J}}_i]}{\partial\nabla c_i}\frac{\partial\nabla c_i}{\partial\{c_i\}} = -L_i(\phi)k_i^\alpha\mathbf{B}\\ \frac{\partial[\underline{\boldsymbol{J}}_i]}{\partial\{\underline{\boldsymbol{u}}\}} &= 0\end{aligned} \tag{B.20}$$

Lastly, the Jacobian of the stress reads, recalling that $\underset{\sim}{\boldsymbol{\sigma}} = h\underset{\sim}{\boldsymbol{\sigma}}^\alpha + \bar{h}\underset{\sim}{\boldsymbol{\sigma}}^\beta$:

$$\begin{aligned}\frac{\partial \underset{\sim}{\boldsymbol{\sigma}}}{\partial\{\phi\}} &= \frac{\partial \underset{\sim}{\boldsymbol{\sigma}}}{\partial\phi}\frac{\partial\phi}{\partial\{\phi\}} = h'\left(\underset{\sim}{\boldsymbol{\sigma}}^\alpha-\underset{\sim}{\boldsymbol{\sigma}}^\beta\right)N\\ \frac{\partial \underset{\sim}{\boldsymbol{\sigma}}}{\partial\{c_i\}} &= 0\\ \frac{\partial \underset{\sim}{\boldsymbol{\sigma}}}{\partial\{\underline{\boldsymbol{u}}\}} &= \frac{\partial \underset{\sim}{\boldsymbol{\sigma}}}{\partial \underset{\sim}{\boldsymbol{\varepsilon}}}\frac{\partial \underset{\sim}{\boldsymbol{\varepsilon}}}{\partial\{\underline{\boldsymbol{u}}\}} = \left(h\underset{\approx}{\boldsymbol{\Lambda}}^\alpha+\bar{h}\underset{\approx}{\boldsymbol{\Lambda}}^\beta\right)\underline{\mathbf{B}} = \underset{\approx}{\boldsymbol{\Lambda}}^{\text{eff}}\underline{\mathbf{B}}\end{aligned} \tag{B.21}$$

B.0.4 Derivatives for the Reuss/Sachs approach

The Reuss/Sachs approach differs from the Voigt/Taylor approach for two thermodynamic forces π and $\underset{\sim}{\boldsymbol{\sigma}}$. First π reads:

$$\pi = -\frac{1}{M_\pi}\dot{\phi} - Wg'(\phi) - h'(\phi)F_\phi\,, \tag{B.22}$$

where

$$F_\phi = f^\alpha - f^\beta - \sum_i \mu_i\left(c_i^\alpha - c_i^\beta\right) - \underset{\sim}{\boldsymbol{\sigma}} : \left(\underset{\sim}{\boldsymbol{\varepsilon}}^\alpha - \underset{\sim}{\boldsymbol{\varepsilon}}^\beta\right). \tag{B.23}$$

Moreover, the stresses are homogenised, which reads:

$$\underset{\sim}{\boldsymbol{\sigma}} = \underset{\sim}{\boldsymbol{\sigma}}^{\alpha} = \underset{\sim}{\boldsymbol{\sigma}}^{\beta} \tag{B.24}$$

which leads to the following derivatives:

$$\begin{aligned} \frac{\partial \pi}{\partial \phi} &= -\frac{1}{M_\phi}\frac{\partial \dot{\phi}}{\partial \phi} - W g''(\phi) - h''(\phi) F_\phi \\ \frac{\partial \pi}{\partial c_i} &= -h' k_i^{\alpha}\left(c_i^{\alpha} - c_i^{\beta}\right) \end{aligned} \tag{B.25}$$

And

$$\begin{aligned} \frac{\partial \pi}{\partial \{\underline{\boldsymbol{u}}\}} = \frac{\partial \pi}{\partial \underset{\sim}{\boldsymbol{\sigma}}}\frac{\partial \underset{\sim}{\boldsymbol{\sigma}}}{\partial \{\underline{\boldsymbol{u}}\}} &= -h'\frac{\partial}{\partial \underset{\sim}{\boldsymbol{\sigma}}}\left(-\frac{1}{2}\underset{\sim}{\boldsymbol{\sigma}} : S^{\alpha} : \underset{\sim}{\boldsymbol{\sigma}} + \frac{1}{2}\underset{\sim}{\boldsymbol{\sigma}} : S^{\beta} : \underset{\sim}{\boldsymbol{\sigma}} - \underset{\sim}{\boldsymbol{\sigma}} : \left(\underset{\sim}{\boldsymbol{\varepsilon}}_{\star}^{\alpha} - \underset{\sim}{\boldsymbol{\varepsilon}}_{\star}^{\beta}\right)\right)\underline{\mathbf{B}} \\ &= h'\frac{\partial}{\partial \underset{\sim}{\boldsymbol{\sigma}}}\left(\underset{\sim}{\boldsymbol{\sigma}} : \left(\frac{1}{2}\left(S^{\alpha} - S^{\beta}\right) : \underset{\sim}{\boldsymbol{\sigma}} + \underset{\sim}{\boldsymbol{\varepsilon}}_{\star}^{\alpha} - \underset{\sim}{\boldsymbol{\varepsilon}}_{\star}^{\beta}\right)\right)\underline{\mathbf{B}} \\ &= h'\left(\frac{1}{2}\left(\left(S^{\alpha} - S^{\beta}\right) : \underset{\sim}{\boldsymbol{\sigma}} + \underset{\sim}{\boldsymbol{\sigma}} : \left(S^{\alpha} - S^{\beta}\right)\right) + \underset{\sim}{\boldsymbol{\varepsilon}}_{\star}^{\alpha} - \underset{\sim}{\boldsymbol{\varepsilon}}_{\star}^{\beta}\right)\underset{\approx}{\boldsymbol{S}}^{\mathrm{eff}-1}\underline{\mathbf{B}} \end{aligned} \tag{B.26}$$

And finally, the Jacobian of the stress reads:

$$\begin{aligned} \frac{\partial \underset{\sim}{\boldsymbol{\sigma}}}{\partial \{\phi\}} &= \frac{\partial \underset{\sim}{\boldsymbol{\sigma}}}{\partial \phi}\frac{\partial \phi}{\partial \{\phi\}} = 0 \\ \frac{\partial \underset{\sim}{\boldsymbol{\sigma}}}{\partial \{c_i\}} &= \frac{\partial \underset{\sim}{\boldsymbol{\sigma}}}{\partial c_i}\frac{\partial c_i}{\partial \{c_i\}} = 0 \\ \frac{\partial \underset{\sim}{\boldsymbol{\sigma}}}{\partial \{\underline{\boldsymbol{u}}\}} &= \frac{\partial \underset{\sim}{\boldsymbol{\sigma}}}{\partial \underset{\sim}{\boldsymbol{\varepsilon}}}\frac{\partial \underset{\sim}{\boldsymbol{\varepsilon}}}{\partial \{\underline{\boldsymbol{u}}\}} = \left(h\underset{\approx}{\boldsymbol{S}}^{\alpha} + \bar{h}\underset{\approx}{\boldsymbol{S}}^{\beta}\right)^{-1}\underline{\mathbf{B}} = \underset{\approx}{\boldsymbol{S}}^{\mathrm{eff}-1}\underline{\mathbf{B}} \end{aligned} \tag{B.27}$$

APPENDIX

C Calibration of the interface free energy parameters

Contents

C.1 Interface free energy density f_ϕ

The interface free energy for phase field models based on an additional order parameter ϕ is carried out by the additional interface free energy $f_\phi(\phi, \nabla\phi)$ if no excess free energy is injected from the interpolation of the bulk free energies. In the following, it will be assumed that this is the case and the interface free energy analysis is performed only from the following interface free energy, e.g. [Kim et al., 1998, Kim et al., 1999]:

$$F_\phi = \int_V f_\phi(\phi, \nabla\phi)\, dV = \int_V \left(W g(\phi) + \frac{1}{2}\alpha \nabla\phi^2 \right) dV\,, \tag{C.1}$$

where $g(\phi) = \phi^2(1-\phi)^2$ is the double well function, W the double well height, and α the gradient energy parameter. It is first noted that each part play against each other; respectively they penalise interfaces of infinite thickness and of zero thickness, such the width of the relaxed interface is finite with thickness δ inducing thus an averaged energy density of $\frac{\gamma}{\delta}$ into the material due to the interface.

The equilibrium or relaxed profile of the field ϕ is defined as ϕ_{eq} which satisfies the balance of micro-forces introduced earlier in the theory along with $\dot{\phi}_{\text{eq}} = 0$ anywhere:

$$\pi + \nabla \cdot \underline{\boldsymbol{\xi}} = 0\,, \tag{C.2}$$

that reads:

$$-\frac{\partial f_\phi}{\partial \phi}(\phi_{\text{eq}}) + \nabla \cdot \frac{\partial f_\phi}{\partial \nabla\phi}(\nabla\phi_{\text{eq}}) = 0\,. \tag{C.3}$$

It is noted that the above relationship can equally be obtained by nullifying the variational derivative of the free energy functional with respect to the field ϕ[1]. A more convenient way to solve equilibrium is based on the reformulation (C.3) after multiplication with $\nabla\phi_{\text{eq}}$, which is also known as the Beltrami relationships:

$$-\frac{\partial f_\phi}{\partial \phi}(\phi_{\text{eq}})\nabla\phi_{\text{eq}} + \nabla\cdot\frac{\partial f_\phi}{\partial \nabla\phi}(\nabla\phi_{\text{eq}})\nabla\phi_{\text{eq}} = 0\,. \tag{C.4}$$

The gradient of $f_\phi(\phi,\nabla\phi)$ writes:

$$\nabla f_\phi = \frac{\partial f_\phi}{\partial \phi}\nabla\phi + \frac{\partial f_\phi}{\partial \nabla\phi}\nabla\left(\nabla\phi\right), \tag{C.5}$$

which can be injected into (C.4):

$$-\nabla f_\phi(\phi_{\text{eq}},\nabla\phi_{\text{eq}}) + \frac{\partial f_\phi}{\partial \nabla\phi}\nabla\left(\nabla\phi_{\text{eq}}\right) + \nabla\cdot\frac{\partial f_\phi}{\partial \nabla\phi}(\nabla\phi_{\text{eq}})\nabla\phi_{\text{eq}} = 0\,, \tag{C.6}$$

Moreover, the second term of (C.4) can be equally rewritten:

$$\nabla\cdot\frac{\partial f_\phi}{\partial \nabla\phi}(\nabla\phi_{\text{eq}})\nabla\phi_{\text{eq}} = \nabla\left(\frac{\partial f_\phi}{\partial \nabla\phi}(\nabla\phi_{\text{eq}})\nabla\phi_{\text{eq}}\right) - \frac{\partial f_\phi}{\partial \nabla\phi}(\nabla\phi_{\text{eq}})\nabla\left(\nabla\phi_{\text{eq}}\right). \tag{C.7}$$

It results in (C.6) rewritten as follows:

$$\nabla\left(-f_\phi(\phi_{\text{eq}},\nabla\phi_{\text{eq}}) + \frac{\partial f_\phi}{\partial \nabla\phi}(\nabla\phi_{\text{eq}})\nabla\phi_{\text{eq}}\right) = 0\,, \tag{C.8}$$

resulting in

$$-f_\phi(\phi_{\text{eq}},\nabla\phi_{\text{eq}}) + \frac{\partial f_\phi}{\partial \nabla\phi}(\nabla\phi_{\text{eq}})\nabla\phi_{\text{eq}} = cst\,. \tag{C.9}$$

The constant term *cst* can be easily identified as zero, *e.g.* $\phi_{\text{eq}} = 1$ or $\phi_{\text{eq}} = 0$.

C.1.1 Evaluation of an interface thickness δ

In order to evaluate the interface thickness, the Beltrami relationship will be used in the unidimensional case and applied to the proposed free energy given in (C.1):

$$Wg(\phi_{\text{eq}}) = \frac{\alpha}{2}\left(\frac{d\phi_{\text{eq}}}{dx}\right)^2. \tag{C.10}$$

After taking the square root of (C.10):

$$\frac{d\phi_{\text{eq}}}{dx} = \sqrt{\frac{2W}{\alpha}g(\phi_{\text{eq}})}\,, \tag{C.11}$$

[1] In the literature, the use of the variational derivative (see Notations in page xii) of the free energy functional F_ϕ with respect to the field ϕ, resulting in the Euler-Lagrange equation, in order to obtain the evolutionary equation of the phase field parameter is widely spread. This is due to the fact that phase field modelling methods have been initiated in the framework of classical field theory. In the present work, the approach is different in the sense that it relies on the framework of non-equilibrium thermodynamics. Despite the two methods give identical results at the end, the framework of non-equilibrium thermodynamics offers a more detailed description of the physical phenomena as it introduces the separation between dissipative and conservative phenomena. It is recalled that dissipative phenomena are the ones which transform a potential energy into entropy or heat, *e.g.* the chemical energy dissipates into entropy whereas plasticity yields the elastic energy by production of heat. Nevertheless, in the present framework, strong assumptions are done regarding the nature of thermodynamic forces. They should be seen as extended concepts coming from the logic of non-equilibrium thermodynamics.

which also reads:

$$\frac{d\phi_{eq}}{dx} = \sqrt{\frac{2W}{\alpha}}\phi_{eq}\left(1-\phi_{eq}\right). \tag{C.12}$$

The evaluation of the interface thickness can now be done using (C.23) Indeed, we define the interface thickness as the distance from $\phi_{eq} = z$ to $\phi_{eq} = 1-z$ with $0 < z < 1$. A separation of variables is first needed:

$$dx = \sqrt{\frac{\alpha}{2W}}\frac{d\phi_{eq}}{\phi_{eq}(1-\phi_{eq})}, \tag{C.13}$$

which can be integrated from $\phi_{eq}\left(-\frac{\delta}{2}\right) = z$ to $\phi_{eq}\left(\frac{\delta}{2}\right) = 1-z$:

$$\begin{aligned}
\int_{-\frac{\delta}{2}}^{\frac{\delta}{2}} dx \quad = \quad \delta \quad &= \left|\sqrt{\frac{\alpha}{2W}}\int_z^{1-z}\frac{d\phi_{eq}}{\phi_{eq}(1-\phi_{eq})}\right| \\
&= \left|\sqrt{\frac{\alpha}{2W}}\int_z^{1-z}\left(\frac{1}{\phi_{eq}}+\frac{1}{1-\phi_{eq}}\right)d\phi_{eq}\right| \\
&= \left|\sqrt{\frac{\alpha}{2W}}\left[\log\left(\frac{\phi_{eq}}{1-\phi_{eq}}\right)\right]_z^{1-z}\right| \\
&= \left|\sqrt{\frac{2\alpha}{W}}\log\left(\frac{1-z}{z}\right)\right|
\end{aligned}, \tag{C.14}$$

where log is the natural logarithm also written $\log_e$ or ln.

C.1.2 Evaluation of the interface energy γ

The interface energy is defined as follows,

$$\gamma = \int_V f_\phi(\phi_{eq}, \nabla\phi_{eq})dV. \tag{C.15}$$

Again, the Beltrami identity (C.9) allows to reformulate (C.15) into:

$$\gamma = \alpha\int_V \left(\nabla\phi_{eq}\right)^2 dV. \tag{C.16}$$

Now the unidimensional case of an infinite plane is studied. The convergence of the following integral is assumed to be ensured by the construction of the phase field model. The interface energy can be then written:

$$\gamma = \alpha\int_{-\infty}^{+\infty}\left(\frac{d\phi_{eq}}{dx}\right)^2(x)dx. \tag{C.17}$$

From now on, a variable change can be supplied by the bijection:

$$\phi_{eq} : \left]-\infty,+\infty\right[\rightarrow \left]0,1\right[. \tag{C.18}$$

We use $\frac{\mathrm{d}\phi_{eq}}{\mathrm{dx}} = \phi'_{eq}$ to rewrite (C.17) into:

$$\gamma = \alpha\int_0^1 \frac{d\phi_{eq}}{dx}d\phi_{eq}. \tag{C.19}$$

And using (C.10) gives:

$$\gamma = \sqrt{2\alpha W}\int_0^1 \phi_{eq}\left(1-\phi_{eq}\right)d\phi_{eq}\,. \tag{C.20}$$

which gives:

$$\gamma = \sqrt{2\alpha W}\left[\frac{1}{2}\phi_{eq}^2 - \frac{1}{3}\phi_{eq}^3\right]_0^1. \tag{C.21}$$

And finally:

$$\gamma = \frac{\sqrt{\alpha W}}{3\sqrt{2}}. \tag{C.22}$$

C.1.3 Unidimensional relaxed phase field

Now the Beltrami condition allows equally to obtain the equilibrium field ϕ_{eq} explicitly, which can be useful for the initialisation of the phase field at the beginning of a simulation. The tanh method allows to solve (C.10):

$$\phi_{eq} = \frac{1}{2}\left(1-\tanh\left(\frac{x}{\Lambda}\right)\right), \tag{C.23}$$

where Λ is a parameter that can be identified as:

$$\Lambda = \sqrt{\frac{2\alpha}{W}}. \tag{C.24}$$

This can be reformulated in terms of interface thickness δ only.

$$\phi_{eq} = \frac{1}{2}\left(1-\tanh\left(\frac{x\log\left((1-z)/z\right)}{\delta}\right)\right). \tag{C.25}$$

C.1.4 Reformulation of the interface free energy

Using (C.22) and (C.14), the variables α and W can be rewritten as:

$$W = 6\frac{\gamma}{\delta}\log\left(\frac{1-z}{z}\right) \quad \text{and} \quad \alpha = \frac{3\gamma\delta}{\log\left(\frac{1-z}{z}\right)}, \tag{C.26}$$

which allows us to reformulate (C.1) into:

$$F_\phi = \int_V f_\phi(\phi,\nabla\phi)dV = \int_V 3\gamma\left(\frac{2\log\left(\frac{1-z}{z}\right)}{\delta}g(\phi) + \frac{\delta}{2\log\left(\frac{1-z}{z}\right)}\nabla\phi^2\right)dV, \tag{C.27}$$

By writing $\sigma = \dfrac{\delta}{2\log\left(\frac{1-z}{z}\right)}$ it comes that:

$$F_\phi = \int_V f_\phi(\phi,\nabla\phi)dV = \int_V 3\gamma\left(\frac{1}{\sigma}g(\phi) + \sigma\nabla\phi^2\right)dV, \tag{C.28}$$

where γ represents a surface energy and σ a quantity that is related to a length.

APPENDIX

D Unidimensionnal plane strain elastic analysis of misfitting precipitates embedded in a matrix

Contents

The present appendix is devoted to the calculation of elastic stress fields for a unidimensional case of a two-phase system with separate elastic properties under the state of plane strains. An additional transformation strain is embedded within the α phase, *e.g.* (D.3). The resulting stress and strain fields are then assumed homogeneous in each phase with a dependence on the phase fraction z only.

Two cases are studied, the first one corresponds to the case of zero average stress and the second one, the zero average strain case. For the sake of simplicity, Hooke's law will be expressed in terms of the Lamé coefficients λ and μ, instead of using the Young's modulus and Poisson's ratio, which are recalled here:

$$\lambda = \frac{E\nu}{(1+\nu)(1-2\nu)} \quad \text{and} \quad \mu = \frac{E}{2(1+\nu)}. \tag{D.1}$$

Hooke's law classically reads:

$$\underset{\sim}{\boldsymbol{\sigma}} = \lambda \mathrm{tr}\left(\underset{\sim}{\boldsymbol{\varepsilon}}_e\right) \underset{\sim}{\boldsymbol{I}} + 2\mu \underset{\sim}{\boldsymbol{\varepsilon}}_e. \tag{D.2}$$

The phase transformation strains is given by:

$$\underset{\sim}{\boldsymbol{\varepsilon}}_\star = \begin{pmatrix} \delta_x & 0 & 0 \\ & \delta_y & 0 \\ & & \delta_z \end{pmatrix}. \tag{D.3}$$

Further, for readability, we note $\bar{\delta} = \delta_x + \delta_y + \delta_z$.

D.1 Zero average stress or stress free strain

A possible configuration of the phases is illustrated in Fig. D.1:

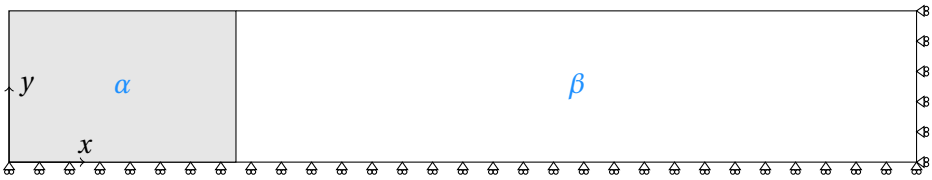

Figure D.1: Illustration of the two-phase system.

The boundary conditions write:

$$\begin{cases} \varepsilon_{zz}^{\alpha} = \varepsilon_{zz}^{\beta} = 0 & \text{(plane strain)} \\ \varepsilon_{yy}^{\alpha} = \varepsilon_{yy}^{\beta} = \varepsilon_{yy} & \text{(planar surfaces)} \\ \sigma_{xx}^{\alpha} = \sigma_{xx}^{\beta} = 0 & \\ z\sigma_{yy}^{\alpha} + \bar{z}\sigma_{yy}^{\beta} = 0 & \\ z\sigma_{zz}^{\alpha} + \bar{z}\sigma_{zz}^{\beta} = 0 & \end{cases} . \tag{D.4}$$

Using Hooke's law, the system of equations (D.4) becomes:

$$\begin{cases} \varepsilon_{xx}^{\alpha} = \dfrac{2\mu^{\alpha}\delta_x}{\Lambda^{\alpha}} + \dfrac{\lambda^{\alpha}}{\Lambda^{\alpha}}\left(\bar{\delta} - \varepsilon_{yy}\right) \\ \varepsilon_{xx}^{\beta} = -\dfrac{\lambda^{\beta}}{\Lambda^{\beta}}\varepsilon_{yy} \\ z\left(\lambda^{\alpha}\mathrm{tr}\left(\underset{\sim}{\boldsymbol{\varepsilon}}_e^{\alpha}\right) + 2\mu^{\alpha}\left(\varepsilon_{yy} - \delta_y\right)\right) + \bar{z}\left(\lambda^{\beta}\mathrm{tr}\left(\underset{\sim}{\boldsymbol{\varepsilon}}_e^{\beta}\right) + 2\mu^{\beta}\varepsilon_{yy}\right) = 0 \\ z\lambda^{\alpha}\mathrm{tr}\left(\underset{\sim}{\boldsymbol{\varepsilon}}_e^{\alpha}\right) + \bar{z}\lambda^{\beta}\mathrm{tr}\left(\underset{\sim}{\boldsymbol{\varepsilon}}_e^{\beta}\right) = z2\mu^{\alpha}\delta_z \end{cases} , \tag{D.5}$$

with which the following set of unknown is $\left\{\varepsilon_{xx}^{\alpha}, \varepsilon_{xx}^{\beta}, \varepsilon_{yy}\right\}$ will be resolved and where $\Lambda = \lambda + 2\mu$. Combining the last two equations of (D.5) gives ε_{yy}:

$$\varepsilon_{yy} = \frac{z\mu^{\alpha}\left(\delta_y + \delta_z\right)}{z\mu^{\alpha} + \bar{z}\mu^{\beta}} . \tag{D.6}$$

Now that strains are known, the stress fields are provided by Hooke's law (D.2). The elastic free energy density of each phase reads:

$$f_e^{\alpha} = \frac{1}{2}\left(\sigma_{yy}^{\alpha}\left(\varepsilon_{yy} - \delta_y\right) - \sigma_{zz}^{\alpha}\delta_z\right) \quad \text{and} \quad f_e^{\beta} = \frac{1}{2}\sigma_{yy}^{\beta}\varepsilon_{yy} . \tag{D.7}$$

Lastly, the elastic energy density reads:

$$f_e = zf_e^{\alpha} + \bar{z}f_e^{\beta} . \tag{D.8}$$

The elastic energy density is plotted in Fig. D.2 against the phase fraction z, while $\delta_x = \delta_y = 0.01$ and $\delta_z = 0$ for the case of homogeneous elasticity with $E^{\alpha} = E^{\beta} = 210$GPa and $\nu^{\alpha} = \nu^{\beta} = 0.3$ and the case of heterogeneous elasticity with $E^{\alpha} = 210$GPa, $E^{\beta} = 130$GPa and $\nu^{\alpha} = \nu^{\beta} = 0.3$:

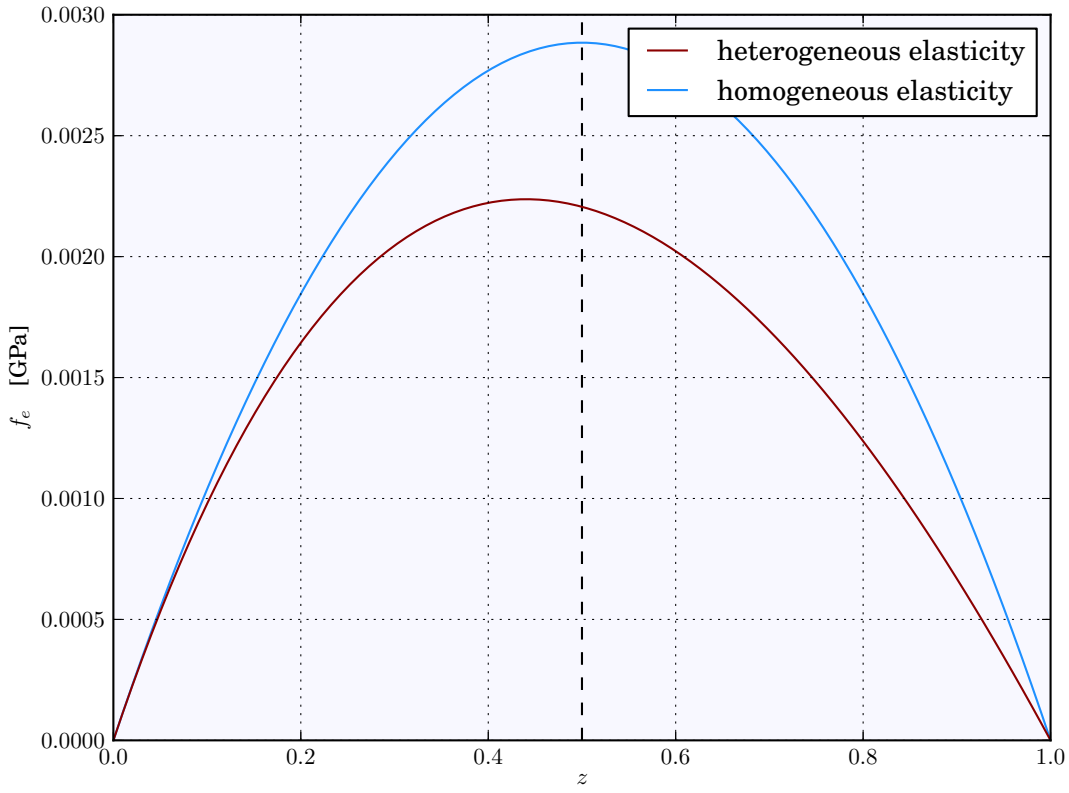

Figure D.2: Plot of the elastic energy against the phase fraction of a two-phase system assuming plane strain for the cases of homogeneous and heterogeneous elasticity, see appendix H.2 for the python script.

D.2 Zero average strain

A possible configuration of the phases is illustrated in Fig. D.3:

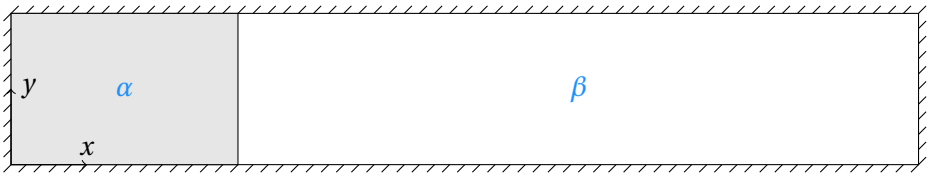

Figure D.3: Two-phase system in zero average strain conditions.

The boundary conditions write :

$$\begin{cases} z\varepsilon^{\alpha}_{xx} + \bar{z}\varepsilon^{\beta}_{xx} = 0 & \text{(strain free)} \\ \varepsilon^{\alpha}_{yy} = \varepsilon^{\beta}_{yy} = 0 & \text{(strain free)} \\ \varepsilon^{\alpha}_{zz} = \varepsilon^{\beta}_{zz} = 0 & \text{(plane strain)} \\ \sigma^{\alpha}_{xx} = \sigma^{\beta}_{xx} = \sigma_{xx} \end{cases}, \tag{D.9}$$

on which the set of unknown is $\left\{\varepsilon^{\alpha}_{xx}, \varepsilon^{\beta}_{xx}\right\}$ will be solved:

$$\begin{aligned} \varepsilon^{\beta}_{xx} &= -\frac{z}{\bar{z}}\varepsilon^{\alpha}_{xx} \\ \varepsilon^{\alpha}_{xx} &= \frac{\bar{z}\left(\lambda^{\alpha}\left(\delta_x+\delta_y+\delta_z\right)+2\mu^{\alpha}\delta_x\right)}{\bar{z}\Lambda^{\alpha}+z\Lambda^{\beta}} \end{aligned} \quad . \tag{D.10}$$

Now, stresses can be obtained *via* Hooke's law (D.2) and the elastic energies read:

$$f^{\alpha}_{e} = \frac{1}{2}\left(\sigma_{xx}\left(\varepsilon^{\alpha}_{xx}-\delta_x\right)-\sigma^{\alpha}_{yy}\delta_y-\sigma^{\alpha}_{zz}\delta_z\right) \qquad \text{and} \qquad f^{\beta}_{e} = \frac{1}{2}\sigma_{xx}\varepsilon^{\beta}_{xx}. \tag{D.11}$$

For the same conditions presented above, it results in Fig. D.4:

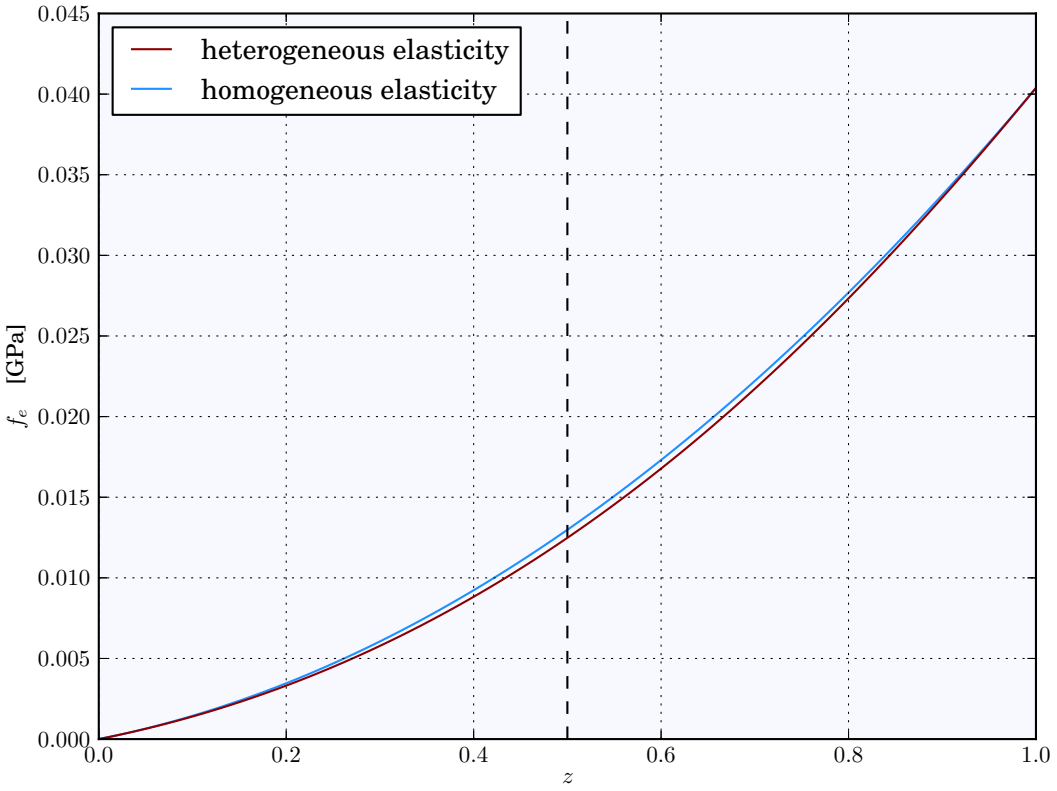

Figure D.4: Plot of the elastic energy against the phase fraction of a two-phase system assuming plane strain and for the cases of homogeneous and heterogeneous elasticity, see appendix H.1 for the python script.

APPENDIX

E Growth of a misfitting precipitate in a supersaturated matrix

Contents

The main purpose of this appendix is to understand the influence of the finite element and time discretisation on the convergence of the proposed phase field model. To that classical sensitivity analyses, an additional interface thickness sensitivity analysis must always be performed in the framework of phase field modelling. The interface thickness sensitivity analysis allows then to evaluate if computations can be referred as **quantitative** or else as **qualitative**. Indeed, simulations based on large interface thicknesses give a rough look at microstructural evolution phenomena, that can be improved by decreasing the interface thickness, bringing in turn accuracy at the expense of computational time.
It is important to say that the convergence is intrinsic to the phase field model. In the work, Reuss and Voigt's approaches have thus shown different rates of convergence. The resolution algorithm is based on Newton's algorithm combined with a Runge-Kutta method for the integration of internal variables. Reuss and Voigt's schemes share the same degrees of freedom but different constitutive laws and Jacobian matrices, which will obviously induce different rate of convergence regarding the resolution algorithm. It will be shown that the Reuss approach seems here to generate bigger iteration time in comparison with Voigt's scheme. Therefore, a glimpse on computation time will be catch to further select which one is the most efficient approach.
We propose then to benchmark Voigt- and Reuss's approaches on the simulation of the growth of a misfitting precipitate embedded in a supersaturated matrix using two distinct sets of boundary conditions, inspired from [Ammar, 2010]. The resulting fields will serve for the mesh sensitivity and interface thickness analyses. Whereas averaged values of the phase fraction and concentration will serve for the time sensitivity analysis.

E.1 Coherent phase equilibrium in binary alloys

Stresses can shift the chemical equilibrium between two solid phases, *i.e.* [Larché and Cahn, 1973, Larché and Cahn, 1978, Cahn and Larché, 1984, Larché and Cahn, 1985, Johnson and Voorhees, 1987, Lee and Tao, 1994, Johnson, 2000, Ammar et al., 2009]. Such a concentration shift may modify the growth kinetics. In some cases, it may even reverse the evolution of a microstructural evolution, *e.g.*

an Ostwald ripening phenomena, wherein small precipitates grow at the expense of the biggest ones when the elastic energy dominates capillarity effects [Johnson and Voorhees, 1987].

Following [Johnson and Voorhees, 1987, eq. 6 & 8] and [Larché and Cahn, 1978], the condition of coherent thermo-mechanic equilibrium between two phases enforces the pseudo-equilibrium condition along with a modified chemical equilibrium condition:

$$\mu^\alpha = \mu^\beta = \mu \qquad \text{and} \qquad \omega^\alpha - \omega^\beta - \underset{\sim}{\boldsymbol{\sigma}} : (\underset{\sim}{\boldsymbol{\varepsilon}}^\alpha - \underset{\sim}{\boldsymbol{\varepsilon}}^\beta) = 0\,. \tag{E.1}$$

In what follows, chemical free energy densities are chosen as simple elliptic paraboloids:

$$f_c^\alpha = \frac{1}{2}k^\alpha (c^\alpha - a)^2 \qquad \text{and} \qquad f_c^\beta = \frac{1}{2}k^\beta (c^\beta - b)^2\,. \tag{E.2}$$

The chemical equilibrium condition then rewrites:

$$\Delta f_c - \mu \Delta c + \Delta f_e - \underset{\sim}{\boldsymbol{\sigma}} : \Delta\underset{\sim}{\boldsymbol{\varepsilon}} = 0\,, \tag{E.3}$$

where

$$\Delta f_c = f_c^\alpha - f_c^\beta, \qquad \Delta c = c^\alpha - c^\beta, \qquad \Delta f_e = f_e^\alpha - f_e^\beta, \qquad \Delta\underset{\sim}{\boldsymbol{\varepsilon}} = \underset{\sim}{\boldsymbol{\varepsilon}}^\alpha - \underset{\sim}{\boldsymbol{\varepsilon}}^\beta. \tag{E.4}$$

Using the pseudo equilibrium condition, (E.3) rewrites into:

$$\mu(\frac{1}{2}\Delta c^\alpha - \frac{1}{2}\Delta c^\beta - \Delta c) + \Delta f_e - \underset{\sim}{\boldsymbol{\sigma}} : \Delta\underset{\sim}{\boldsymbol{\varepsilon}} = 0\,, \tag{E.5}$$

with

$$\Delta c^\alpha = c^\alpha - a, \qquad \Delta c^\beta = c^\beta - b. \tag{E.6}$$

If $k^\alpha = k^\beta = k$, (E.5) results in:

$$\mu(b-a) + \Delta f_e - \underset{\sim}{\boldsymbol{\sigma}} : \Delta\underset{\sim}{\boldsymbol{\varepsilon}} = 0\,. \tag{E.7}$$

Using again the pseudo equilibrium condition, it follows that:

$$c^\alpha = a - \frac{\Delta f_e - \underset{\sim}{\boldsymbol{\sigma}} : \Delta\underset{\sim}{\boldsymbol{\varepsilon}}}{k(b-a)} \qquad \text{and} \qquad c^\beta = b - \frac{\Delta f_e - \underset{\sim}{\boldsymbol{\sigma}} : \Delta\underset{\sim}{\boldsymbol{\varepsilon}}}{k(b-a)}\,, \tag{E.8}$$

which is similar to the condition obtained by Johnson1987b:

$$c^\alpha = a - \frac{\Delta f_e - \underset{\sim}{\boldsymbol{\sigma}} : \Delta\underset{\sim}{\boldsymbol{\varepsilon}}}{k^\alpha(b-a)} \qquad \text{and} \qquad c^\beta = b - \frac{\Delta f_e - \underset{\sim}{\boldsymbol{\sigma}} : \Delta\underset{\sim}{\boldsymbol{\varepsilon}}}{k^\beta(b-a)}\,, \tag{E.9}$$

which is more general approximation, assumed to remain valid in this work[1]. For clarity, we further write $\Gamma = \Delta f_e - \underset{\sim}{\boldsymbol{\sigma}} : \Delta\underset{\sim}{\boldsymbol{\varepsilon}}$.

To obtain the exact equilibrium, one must solve the following set of equations:

$$\begin{cases} \mu^\alpha \left(-\frac{1}{2}\left(1 - \frac{k^\alpha}{k^\beta}\right)\Delta c^\alpha - (a-b)\right) + \Gamma = 0 \\ \mu^\beta \left(-\frac{1}{2}\left(\frac{k^\beta}{k^\alpha} - 1\right)\Delta c^\beta - (a-b)\right) + \Gamma = 0 \end{cases} \tag{E.10}$$

[1] At equilibrium, one should verify that the terms $-\frac{1}{2}\left(\frac{k^\beta}{k^\alpha} - 1\right)\Delta c^\beta$ and $-\frac{1}{2}\left(1 - \frac{k^\alpha}{k^\beta}\right)\Delta c^\alpha$ remain negligible versus $a-b$ in order to use the formulation of Johnson in (E.9).

E.2 Analytic calculation of the equilibrium phase fraction

For a closed system, an equilibrium phase fraction z can be obtained by solving the mass conservation equation using (E.9):

$$c_0 = z c^\alpha(z) + \bar{z} c^\beta(z)\,, \tag{E.11}$$

where c_0 is the initial average concentration and where the evaluation of Γ has been done in Appendix D.

The case of zero average strain

For this case, it comes that:

$$\Gamma = -\frac{1}{2}\left(\sigma_{xx}\left(\varepsilon^\alpha_{xx} - \varepsilon^\beta_{xx} + \delta_x\right) + \sigma^\alpha_{yy}\delta_y + \sigma^\alpha_{zz}\delta_z\right). \tag{E.12}$$

If homogeneous elasticity is assumed, Γ can be shown to reduce into a linear function of z:

$$\Gamma = \frac{\delta^2}{2}\left(A' + B' z\right), \tag{E.13}$$

where A' and B' are constants, depending on materials parameters.

If equal chemical curvatures $k^\alpha = k^\beta = k$ are assumed, then the mass conservation equation (E.11) becomes a first order equation in z:

$$c_0 = za + \bar{z}b - \frac{\Gamma(z)}{k\,(b-a)}. \tag{E.14}$$

When chemical curvatures are not equal, the order of (E.11) goes up to the second order:

$$c_0 = za + \bar{z}b - \frac{\Gamma(z)}{b-a}\left(\frac{z}{k^\alpha} + \frac{\bar{z}}{k^\beta}\right). \tag{E.15}$$

In the general case of heterogeneous elasticity and chemistry, the order of (E.11) in z is such that the solution of the mass balance equation (E.11) will be better provided from a numerical approach as presented in the Python script H.3 in appendix H. For the same reasons, this approach will be repeated for the zero average stress case.

E.3 Zero average strain case

It this section phase fields computations are performed for validation purpose, using either the Voigt or the Reuss homogenisation schemes.

The simulation sample has the following properties:

A box of 200× 10 nm containing at $t = 0$, 10% of precipitate or α phase embedded in the middle of the matrix or β phase. Zero displacements and zero mass flux are imposed along the edges of the sample. The matrix is supersaturated of component 1 with value Ω (in green in Fig. E.1) leading to the growth of the precipitate. Due to the misfit strain of the precipitate, stresses will be generated, impacting thus the final phase fraction of precipitate. We assume that equilibrium is reached after 100 hours given our material data.

An illustration is given in Fig. E.1:

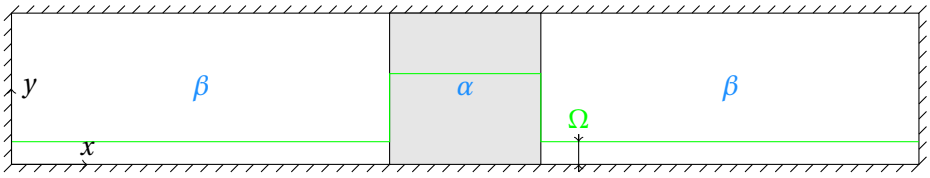

Figure E.1: Initial concentration profile

The following conditions and material properties are then used, from Tab. E.1:

Table E.1: Material properties.

	α	β
E	210 GPa	210 GPa
ν	0.3	0.3
k_1	100 GPa	1 GPa
a_1, b_1	0.33	0.
D_1	4.7e-19 $m^2.s^{-1}$	5.6e-17 $m^2.s^{-1}$

Finally, the interface properties must be defined, the energetic properties are given by the interface surface energy $\gamma = 1\,J.m^{-2}$ and the interface thickness δ given by the set $\{5\,nm, 2\,nm, 1\,nm, 0.5\,nm\}$. And regarding the kinetic properties of the interface, we choose the interface mobility high enough such that the growth kinetics remains always diffusion controlled.

Influence of the mesh resolution

In this section, we perform a mesh sensitivity analysis for the case $\delta = 5$ nm, with 5 meshes deduced from 10, 20, 30, 40, 50 elements to describe the interface of thickness δ, we choose also $\Gamma = 0.33/6$. First, we shut down stresses by setting the transformation strain to zero, so that the process is only diffusion-controlled. The responses are given in Fig. E.2 where the results for the Voigt approach are presented in the right hand side whereas results regarding the Reuss approach are given in the left hand side.

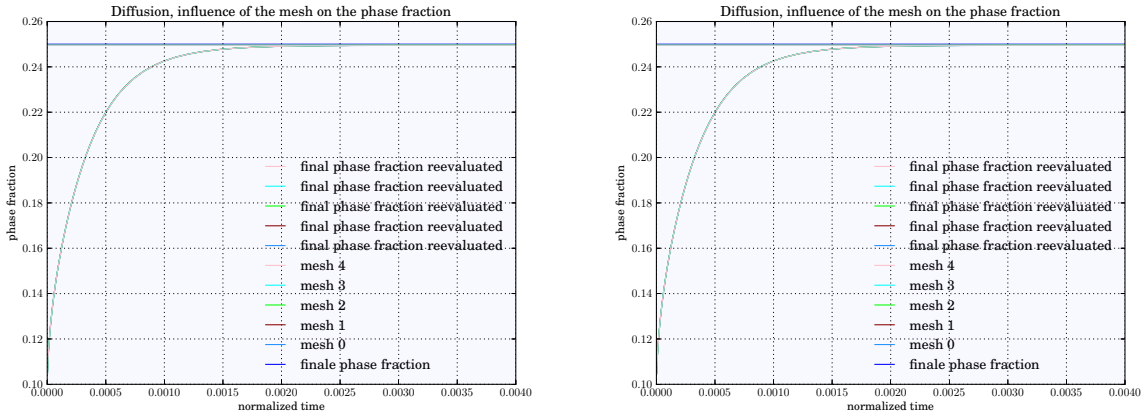

(a) (b)

Figure E.2: (a) Reuss, (b) Voigt

No clear influence of the meshing is noted. Now the mesh dependence of the average concentration during the calculation is given in Fig. E.3:

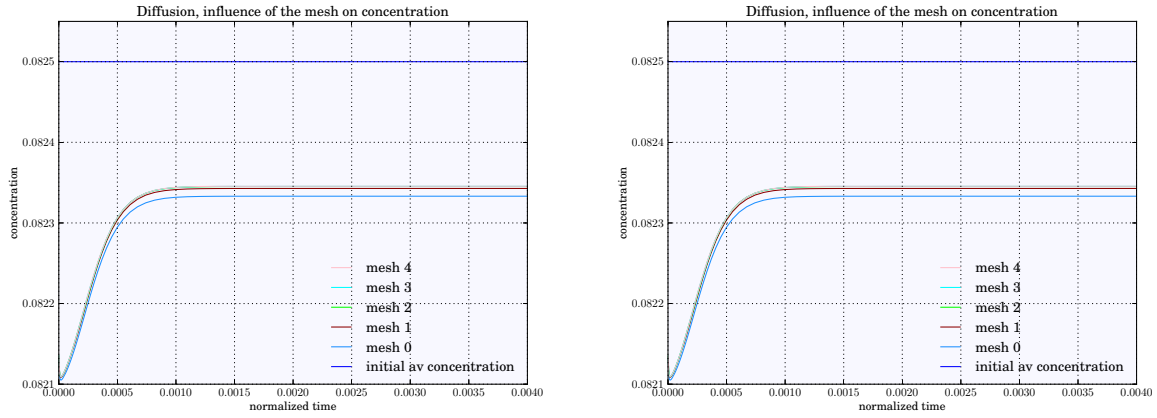

(a) (b)

Figure E.3: (a) Reuss, (b) Voigt

It can be noted that the average concentration goes up during the computation, the relative increase ranges from $\frac{|0.0821-0.0825|}{0.0825} = 0.0048$ to $\frac{|0.08235-0.0825|}{0.0825} = 0.0018$, which is small. In what follows, we decided that the coarser mesh, that still contains 10 linear elements within the interface of thickness δ, induces an acceptable spatial description of all fields.

Influence of the convergence criteria

Now the influence of the ratio of convergence is considered. Note that the time step follows as much as possible a geometric progression with scale factor or first time step dt_0 along with a common ratio q that is user defined, the first time step is provided by the relationships:

$$dt_0 = 0.8\frac{\delta^2}{\max(D)}. \tag{E.16}$$

Knowing that an absolute ratio is defined for each DOF, and that the parameters have been normalised, we choose the ratios given in Tab. E.2.

Table E.2: Convergence parameters.

	ϕ	c_1	q
R1	1.e-11	1.e-5	1.1
R2	1.e-13	1.e-7	1.1
R3	1.e-15	1.e-5	1.1
R4	1.e-15	1.e-5	1.01

The results are given in Fig.E.4 and Fig. E.5.

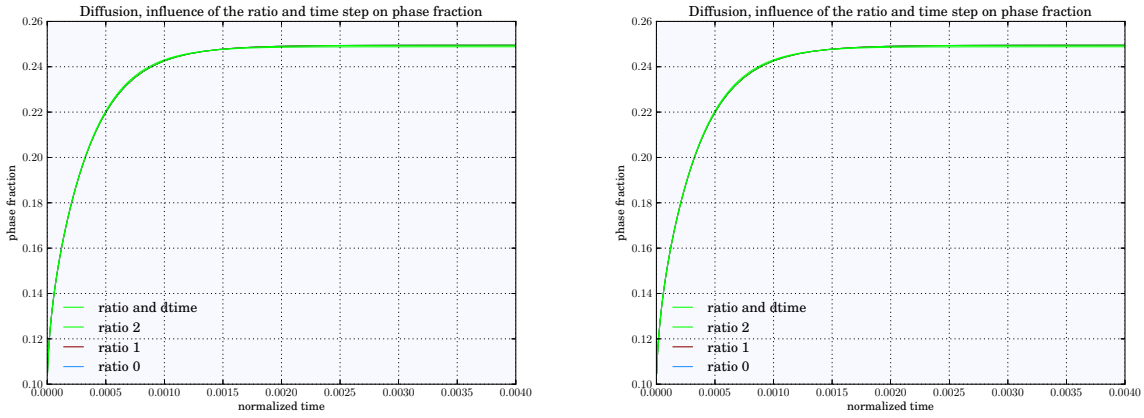

(a) (b)

Figure E.4: (a) Reuss, (b) Voigt

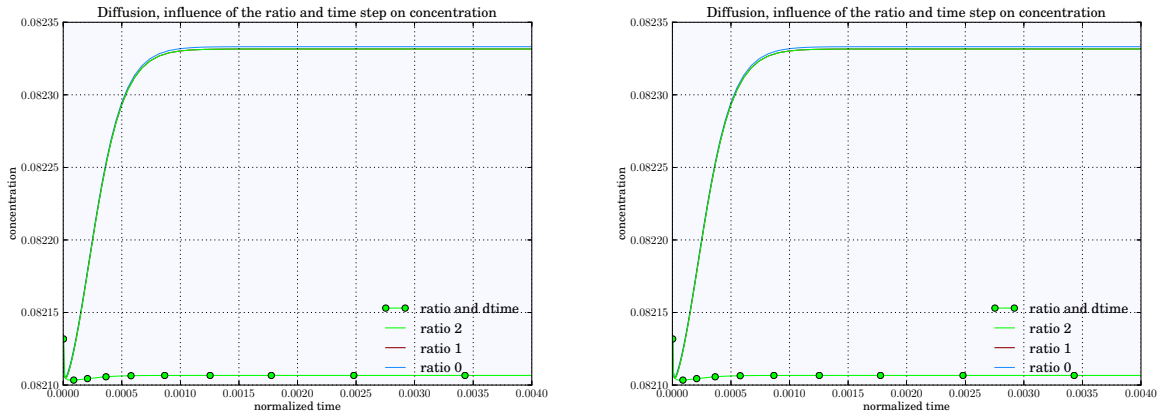

(a) (b)

Figure E.5: (a) Reuss, (b) Voigt

The ratio seems to be good enough but the time geometric progression seems too high and makes the system to loose the mass balance. We deduce that mass balance needs to be checked, *postmortem* to a computation or during it, to validate the reliability of the time stepping.

Influence of the interface thickness

The effect of reducing the interface thickness is given as follows. In the further computations, we use the two following ratios in Tab. E.3.

Table E.3: Convergence parameters.

	ϕ	c_1	q
$R_{5\text{ nm}}$	1.e-11	1.e-5	1.1
$R_{2\text{ and }1\text{ nm}}$	1.e-11	1.e-5	1.03
$R_{\text{small }dt}$	1.e-11	1.e-5	1.01

First, we note that the average concentration get closer from the analytic one with reducing interface thickness. In parallel to that, the first step is reduced because of (E.16), and the mesh density

naturally increases too, so that computations become less and less tractable. The results are given in Fig. E.6 and E.7. And we can note that the phase fraction may overshoot the analytic asymptotic one for smaller interface thickness for unsuitable time stepping.

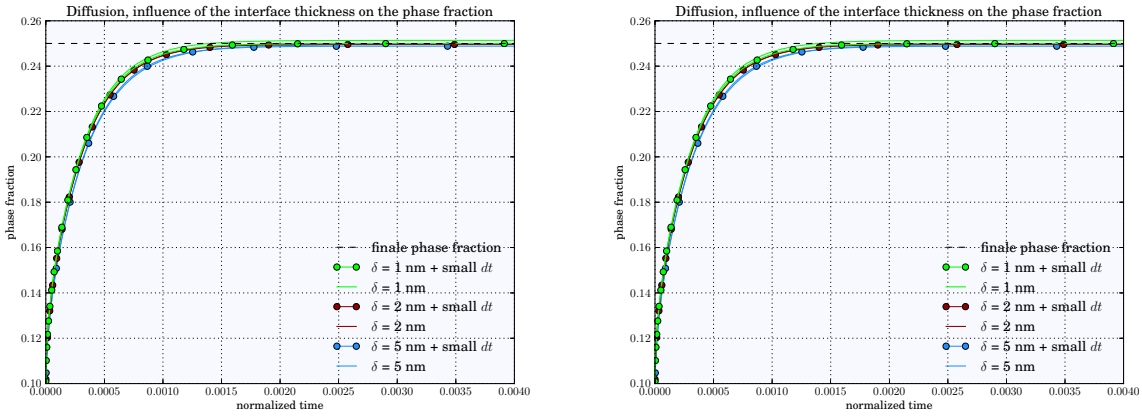

(a) (b)

Figure E.6: (a) Reuss, (b) Voigt

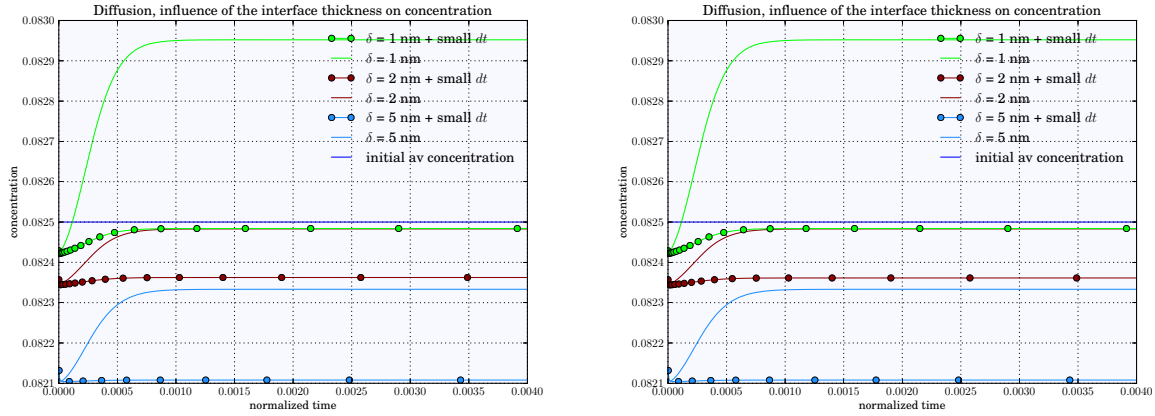

(a) (b)

Figure E.7: (a) Reuss, (b) Voigt

So far, Reuss and Voigt have been naturally perfectly identical, because no stresses were involved. The aim was to validate each numerical implementations.

Accounting of stresses

In the following, the same analysis will be performed but enhanced with the validation of the elastic stress fields, which are generated with the following misfit strain:

$$\underset{\sim}{\boldsymbol{\varepsilon}}^{\alpha}_{\star} = \begin{pmatrix} 0.01 & 0 & 0 \\ & 0.01 & 0 \\ & & 0 \end{pmatrix}. \tag{E.17}$$

Mesh sensitivity analysis

The concentration and stress fields are plotted against the distance within the sample in Fig. E.8, E.9, E.10 and Fig. E.11 for an interface thickness of 5 nm with varying mesh resolution 10, 20, 30, 40 elements within the interface. It can be noted that the rippling of the stress field σ_{xx} in the interface tends to vanish with increasing mesh resolution and that no differences can be done between each schemes at this level.

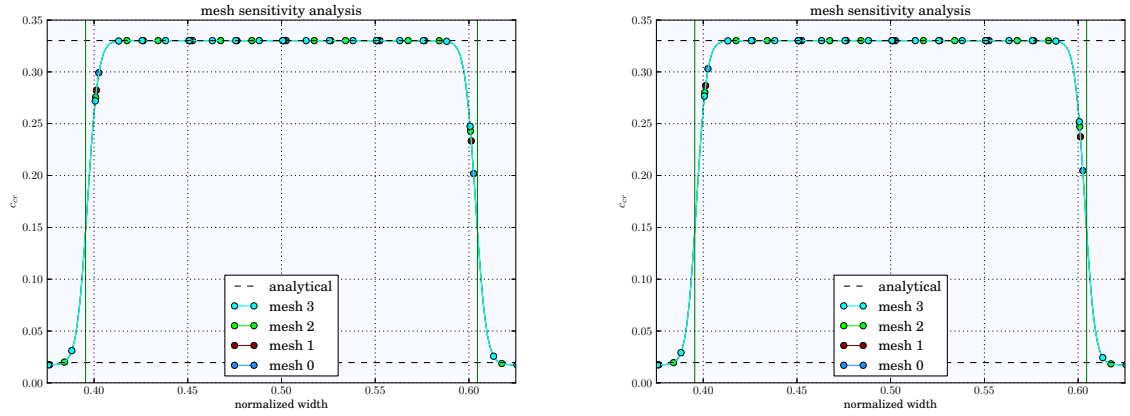

(a) (b)

Figure E.8: (a) Reuss, (b) Voigt

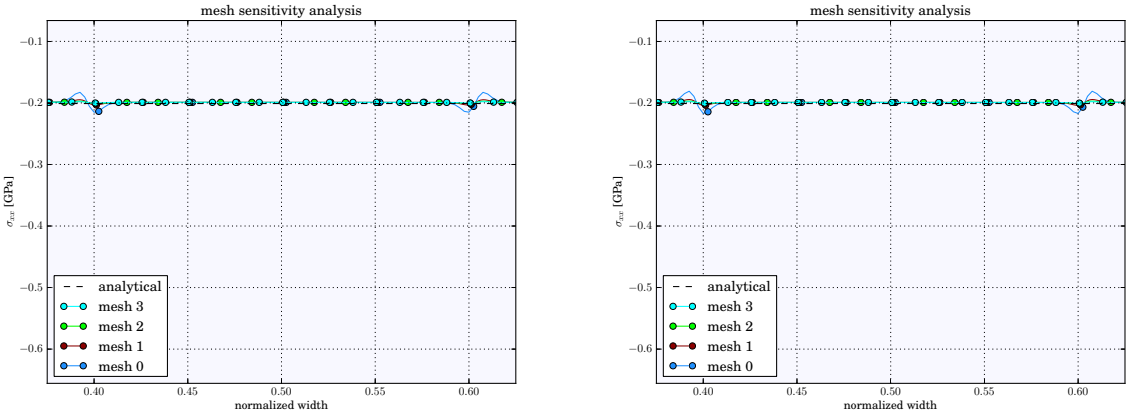

(a) (b)

Figure E.9: (a) Reuss, (b) Voigt

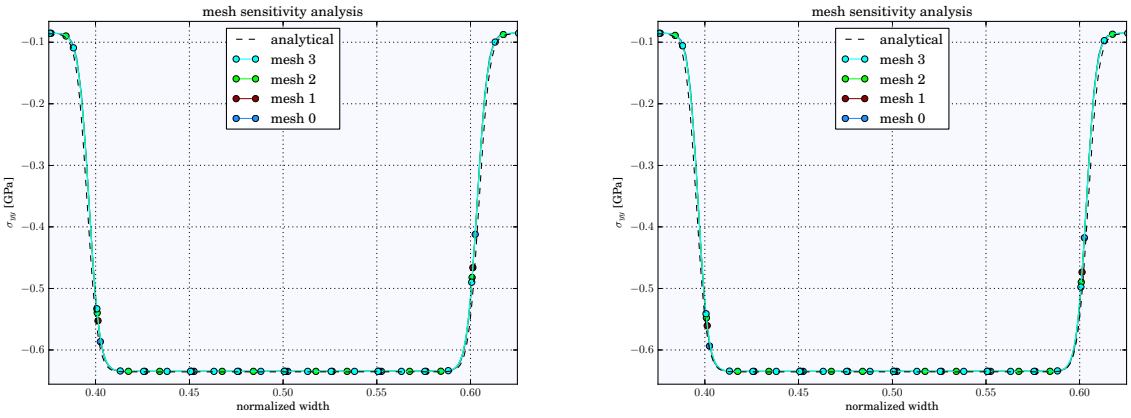

(a) (b)

Figure E.10: (a) Reuss, (b) Voigt

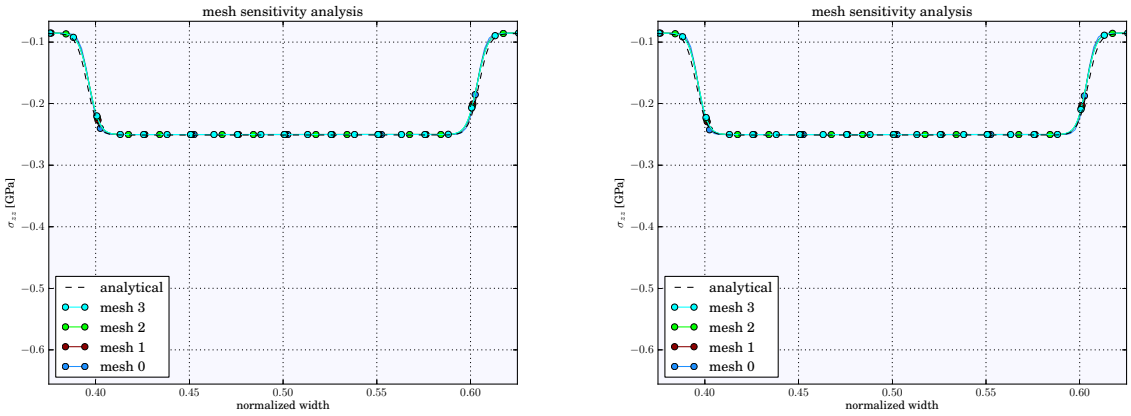

(a) (b)

Figure E.11: (a) Reuss, (b) Voigt

Influence of the interface thickness

Now the influence of the interface thickness on the growth kinetics when stresses are accounted for is studied in Fig. E.12.

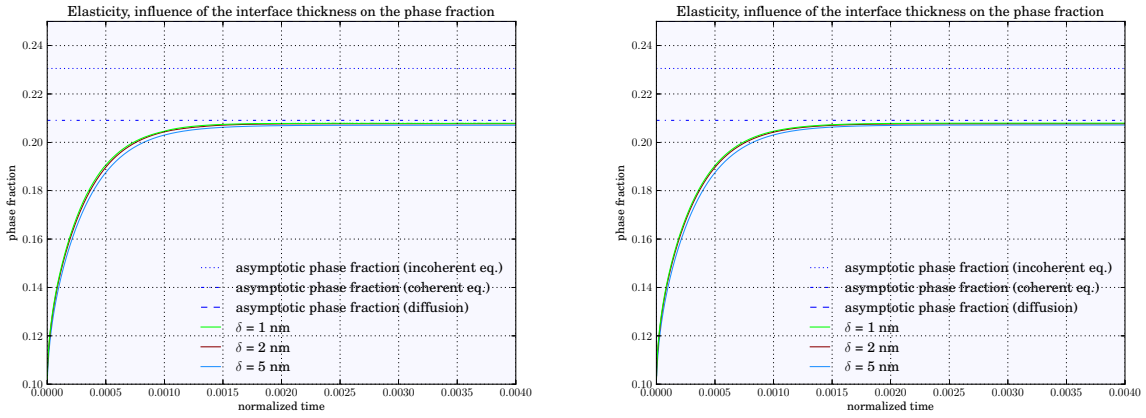

(a) (b)

Figure E.12: (a) Reuss, (b) Voigt

And both plots can be superimposed in Fig. E.13, showing almost no differences between each schemes.

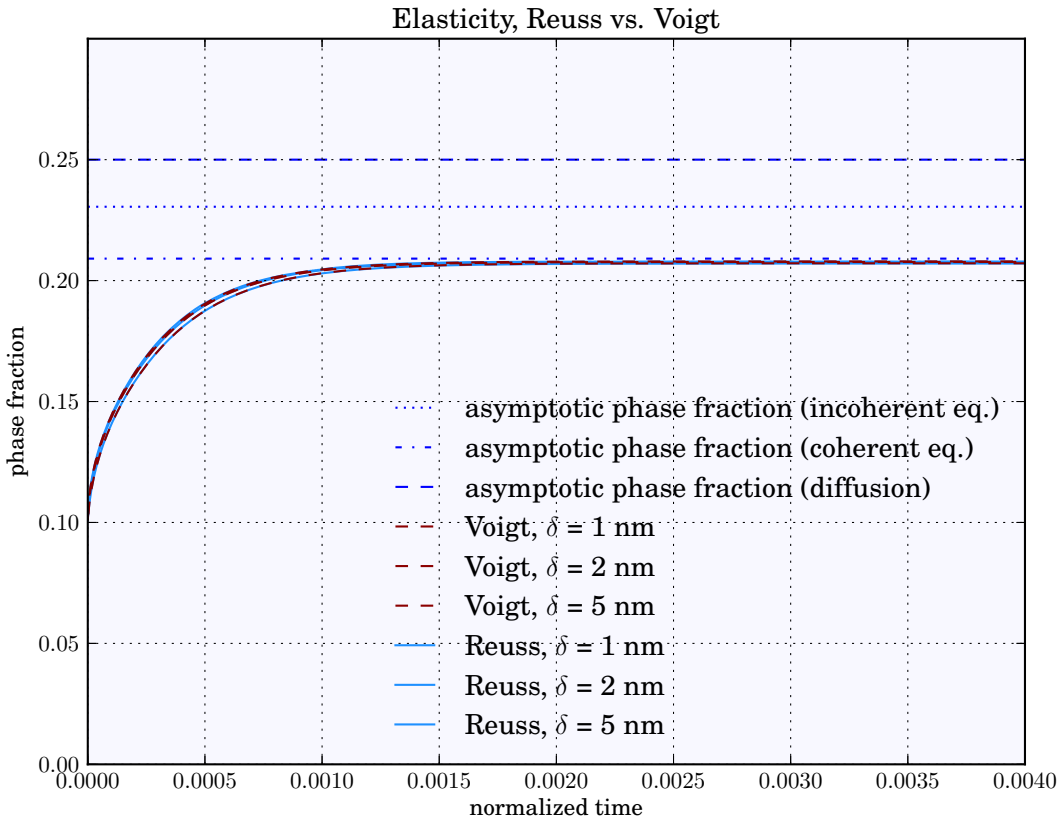

Figure E.13: Reuss vs. Voigt

And the influence on the fields is shown in Fig. E.14, E.15, E.16 and E.17.

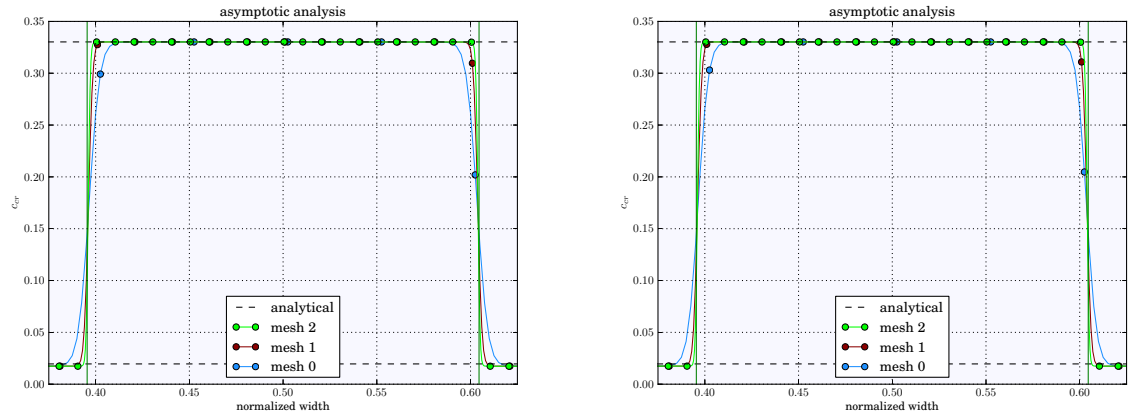

(a) (b)

Figure E.14: (a) Reuss, (b) Voigt

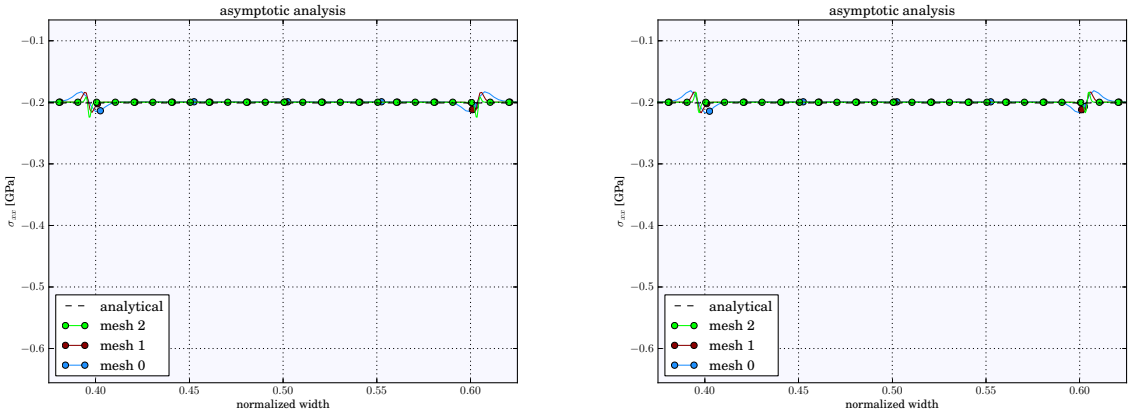

(a) (b)

Figure E.15: (a) Reuss, (b) Voigt

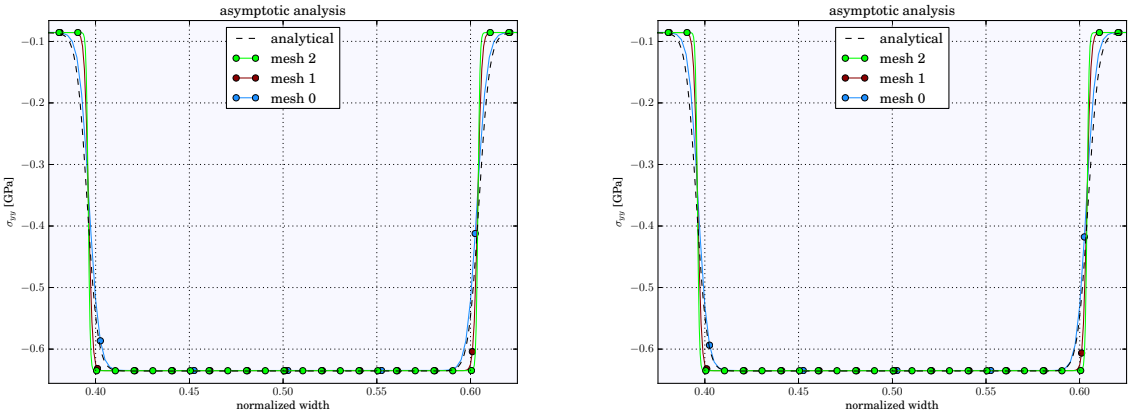

(a) (b)

Figure E.16: (a) Reuss, (b) Voigt

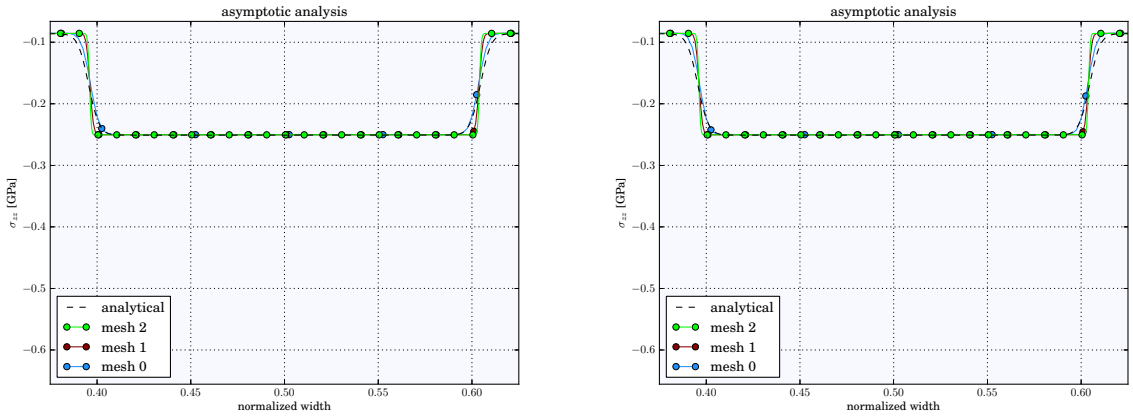

(a) (b)

Figure E.17: (a) Reuss, (b) Voigt

Mesh and time stepping sensitivity for viscoplasticity

Viscoplasticity implies the additional use of the Runge-Kutta algorithm, which is known to be strongly dependent on the time stepping as it belongs to implicit integration methods. Viscosity is accounted for from the classical Norton-Hoff law or power law creep, where $J(\underset{\sim}{\boldsymbol{\sigma}})$ is the von Mises stress, K is the viscosity, n the power-law exponent and R_0 a yield stress above which the material undergoes a plastic flow and the Macaulay brackets $\langle . \rangle$:

$$\underset{\sim}{\dot{\boldsymbol{\varepsilon}}}_p = \left\langle \frac{J(\underset{\sim}{\boldsymbol{\sigma}}) - R_0}{K} \right\rangle^n . \tag{E.18}$$

Three viscoplatic behaviours have been studied, from highly viscous to little viscous or from rate dependent to rate independent in terms of mechanics, based on the following material parameters:

Table E.4: Parameters for viscoplasticity, from highly viscous to little viscous.

	material 1	material 2	material 3
n	5	7	9
K [Mpa.s$^{1/n}$]	7783.7	601.7	145.1
R_0 [Mpa]	200	200	200

It is noted that the following computations will be performed based on Voigt's homogenisation scheme.

First, a mesh sensitivity analysis is performed in order to discard its influence on the temporal evolution of the phase field.

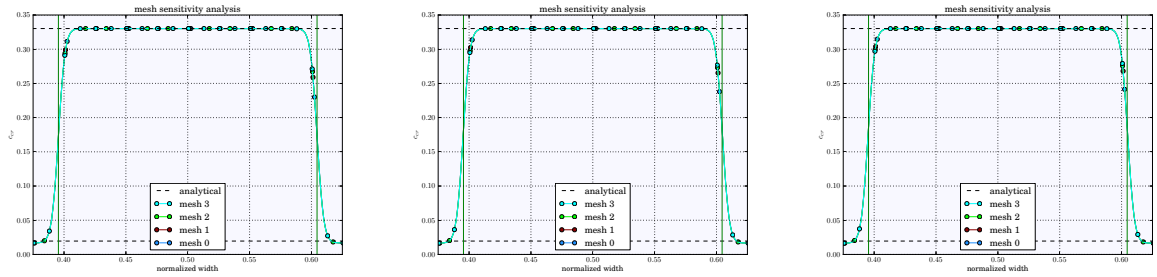

(a) (b) (c)

Figure E.18: (a) material 1, (b) material 2, (c) material 3

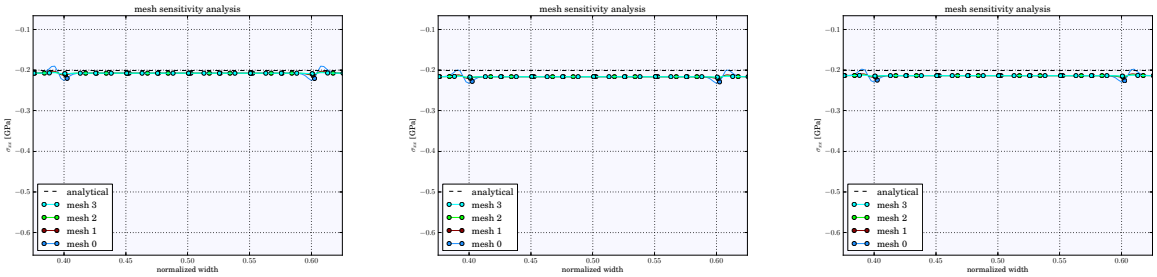

(a) (b) (c)

Figure E.19: (a) material 1, (b) material 2, (c) material 3

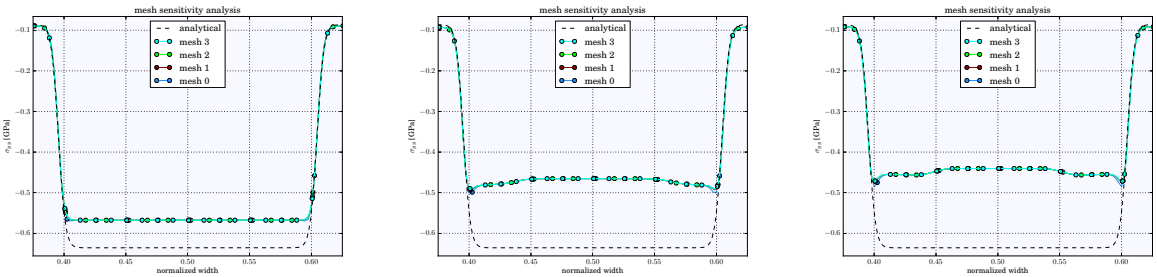

(a) (b) (c)

Figure E.20: (a) material 1, (b) material 2, (c) material 3

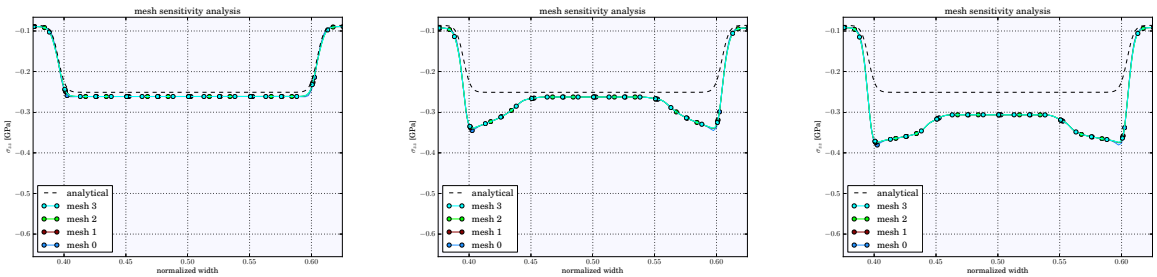

(a) (b) (c)

Figure E.21: (a) material 1, (b) material 2, (c) material 3

The time integration of viscoplastic materials are thereby shown to be independent of our selected mesh resolutions.

Now the influence of the time stepping is performed based on the coarser mesh for the less viscous material, which is the material 3.

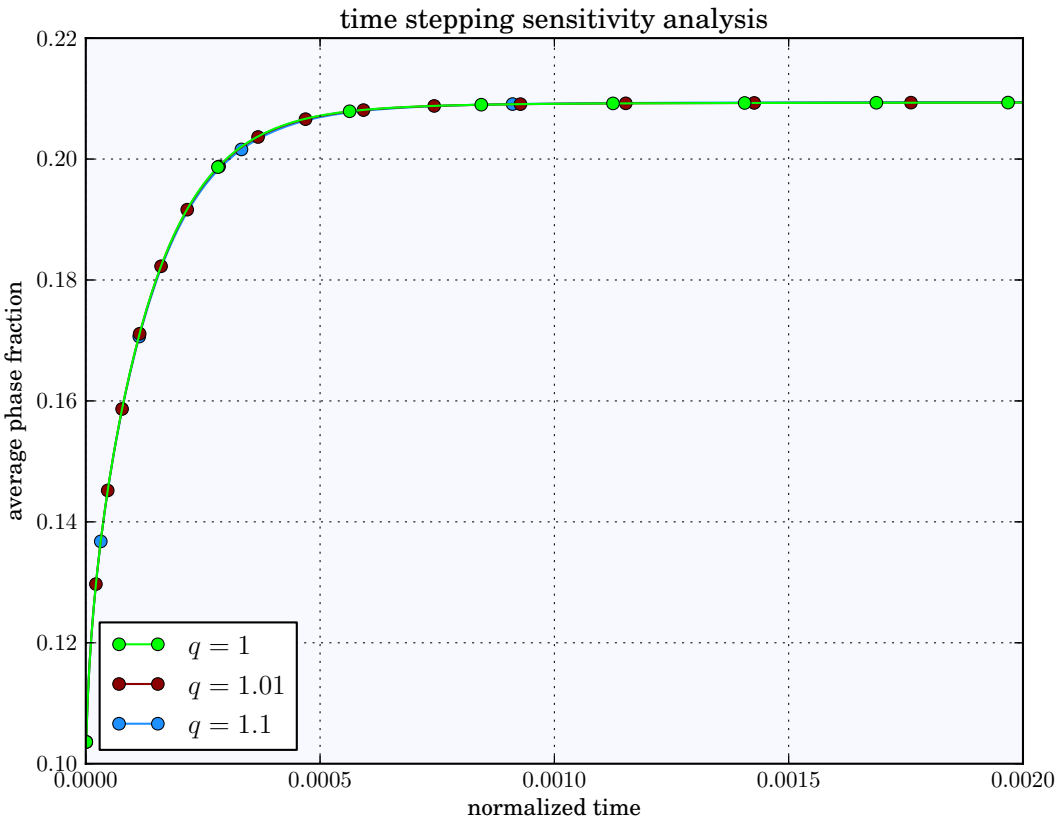

Figure E.22: Influence of the time stepping for the time evolution of material 3 after 100 hours of relaxation.

which shows that the computation has already reached a good convergence with the biggest time steps, because of a maximal relative error lying around 0.04%.

Then the effect of the interface thickness is quantified for the most viscous material,

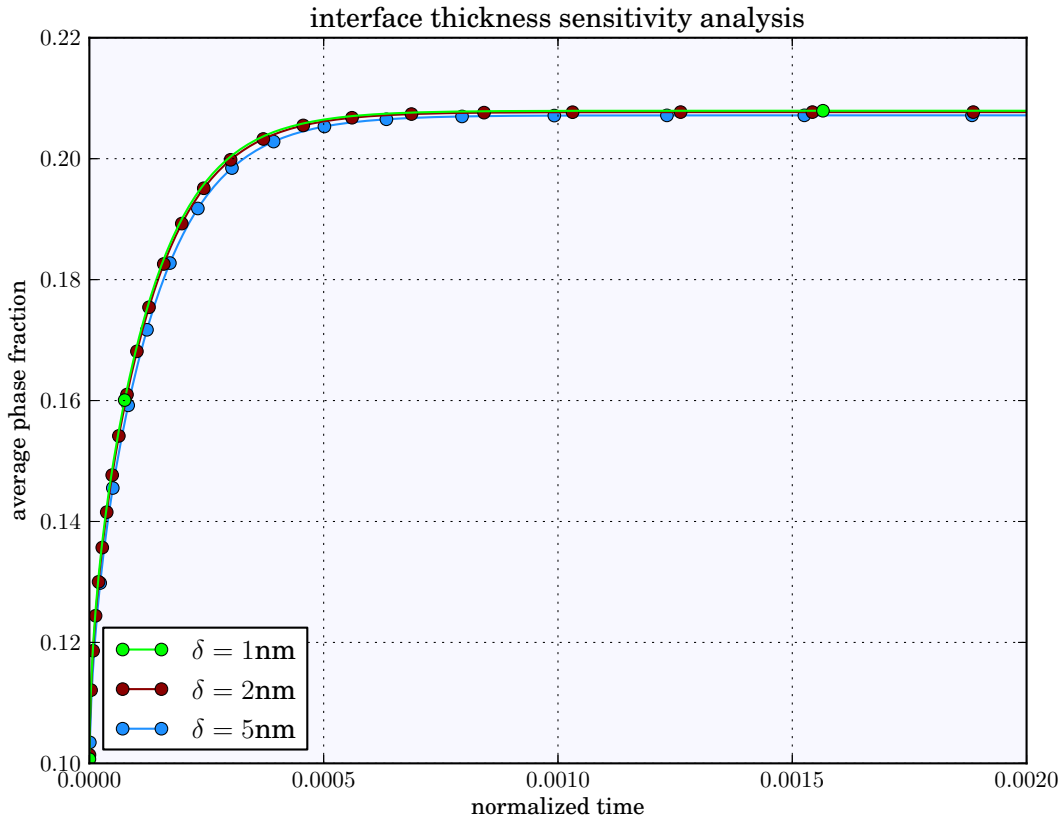

Figure E.23: Influence of the interface thickness for the time evolution of material 1.

For which the relative error does not exceed 1%, so that the model is converged in interface thickness.

E.4 Zero average stress

The case of zero average stress is interesting for the obtainment of binary phase diagram as the Bitter-Crum theorem can be exploited into the analytic solution (see [Ammar, 2010]). For this case, we will refer to Johnson's analytic solution for the dependence on stresses of the interface concentrations (E.8) along with and the elastic analysis done in appendix D in page 212. But, for the study of the influence of the computation parameters as the mesh and the time stepping, the study of this case is not relevant when the case of zero average strains has been already studied. But still, some results are shown here confirming the conclusions of the previous analysis.

The simulation sample is identical, see D.1.

Mesh sensitivity analysis

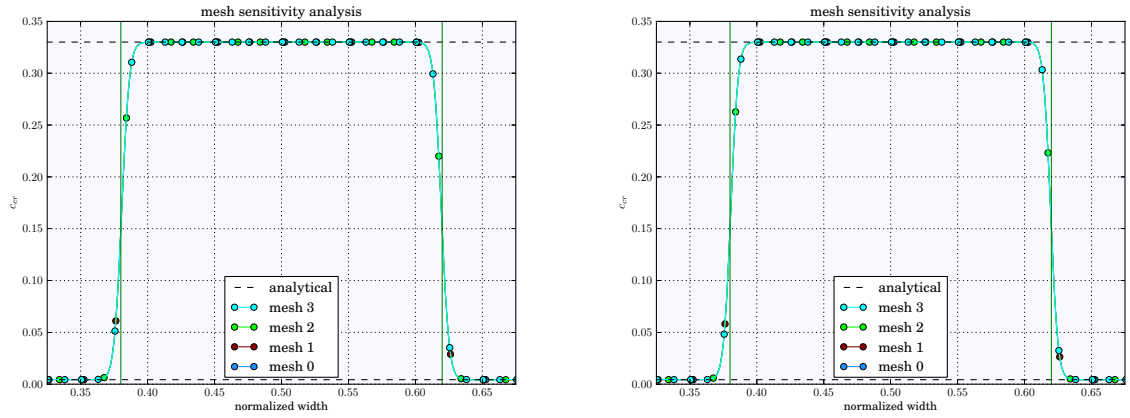

(a) (b)

Figure E.24: (a) Reuss, (b) Voigt

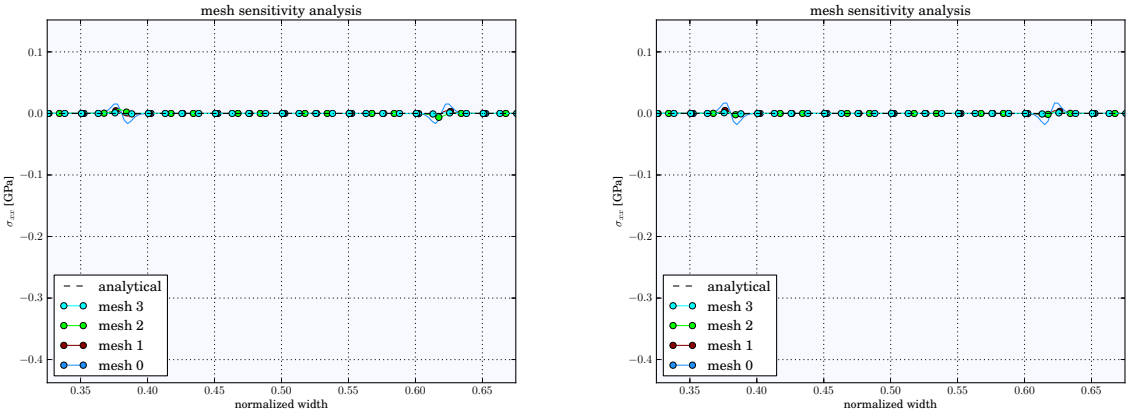

(a) (b)

Figure E.25: (a) Reuss, (b) Voigt

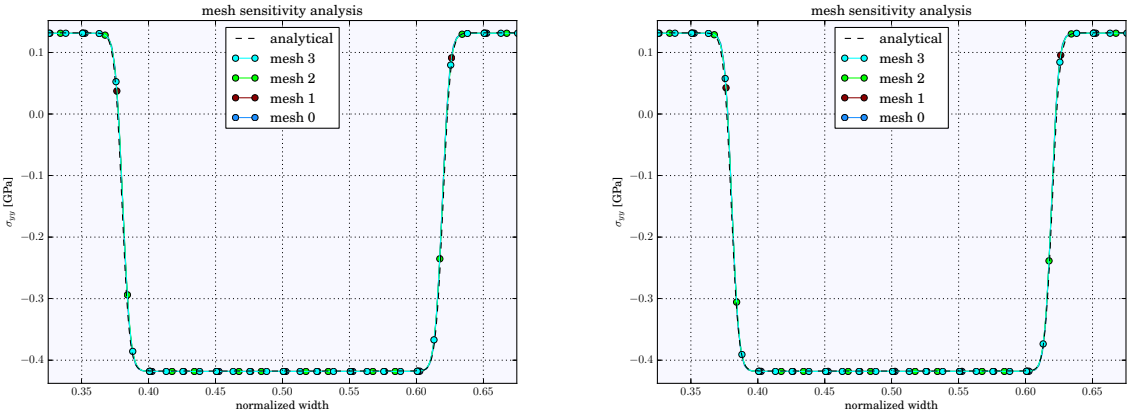

(a) (b)

Figure E.26: (a) Reuss, (b) Voigt

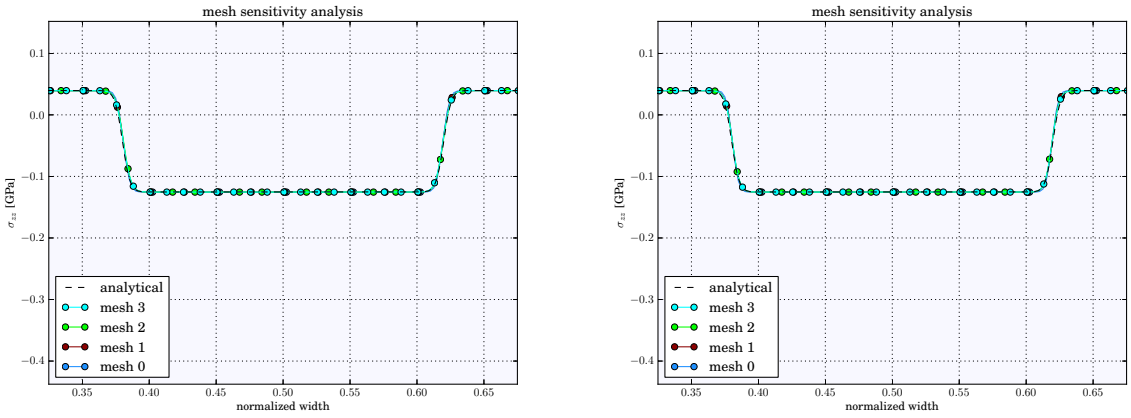

(a) (b)

Figure E.27: (a) Reuss, (b) Voigt

Influence of the interface thickness

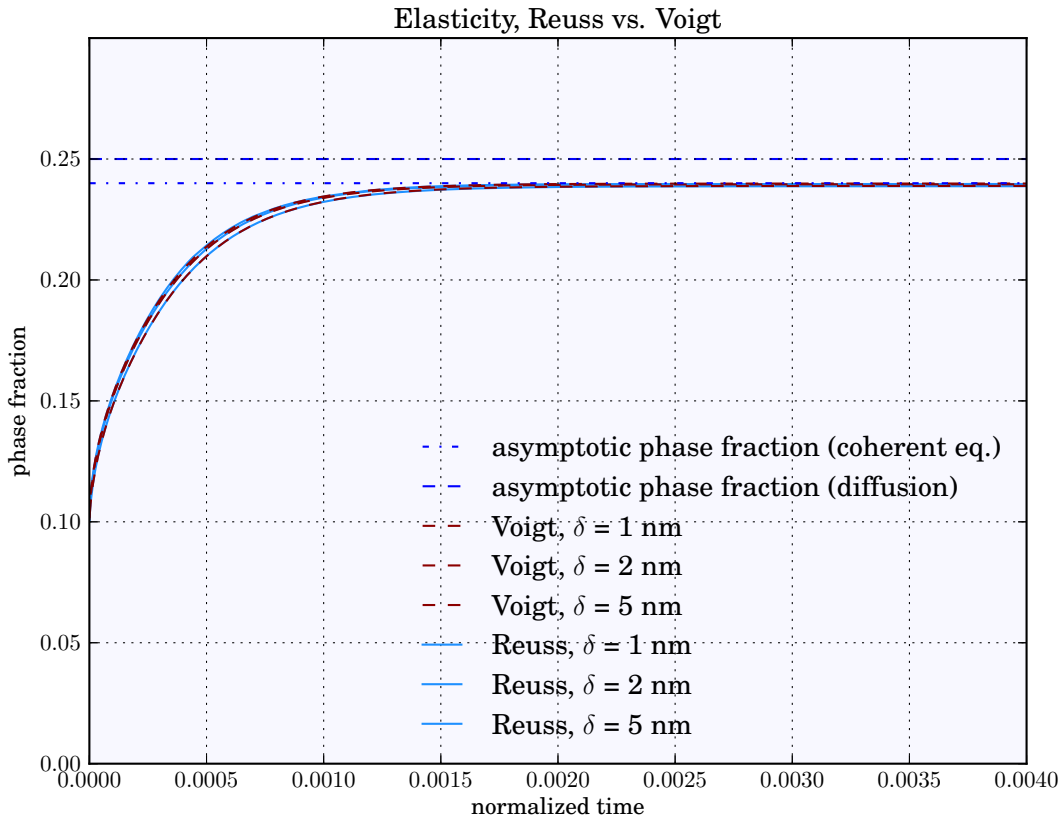

Figure E.28: Reuss vs. Voigt

APPENDIX

F Scaling of the boundary value problem

Contents

F.1 Typical mesh, simulation time and energy densities

The simulations performed in this work rely on a main domain, that is decomposed into several subdomains with different meshing resolutions. An example to that is illustrated in Fig. F.1.

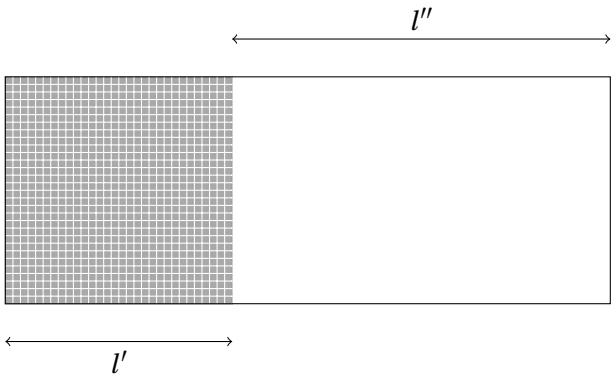

Figure F.1: Illustration of the typical mesh used for the simulation of oxide growth. The domain of size l' has the highest mesh resolution. Such a domain can be embedded in a bigger and coarser mesh.

F.2 Characteristic quantities

Prior to the nondimensionalisation, a set of characteristic physical quantities must be chosen. It consists of a characteristic length, time and energy density as shown in Table F.1. The characteristic length L in [m] of the sample is chosen to be the length of the finely meshed area, which is varied

in the work. The highest diffusivity is chosen to deduce a characteristic time τ in [s] provided the characteristic length. The characteristic time can also be set to the total time of the simulation so that the simulation starts at $t = 0$ and ends at $t = 1$. The characteristic energy density E_d in [J.m^{-3}] is chosen as being the smallest curvature coefficient $E_d = \min\{k\}$ of the multicomponent quadratic chemical free energies.

Table F.1: Characteristic physical parameters used for the nondimensionalisation.

L [nm]	τ [s]	E_d [GJ.m^{-3}]
l'	$\frac{l'^2}{\max\{D\}}$	$\min\{k\}$

F.3 Scaled quantities

Nondimensionalisation of all physical quantities is performed below, where the dimensionless quantities are denoted by a tilde symbol.

Simulation time, mesh size

The total simulation time, here t_s in [s], is scaled:

$$\tilde{t} = \frac{t_s}{\tau}. \tag{F.1}$$

The length of the mesh $l = l' + l''$ in [m] is scaled as follows,

$$\tilde{l} = \frac{l}{L}. \tag{F.2}$$

Interface mobility, energy and thickness

The interface mobility M_ϕ in [J^{-1}.m^3.s^{-1}] is scaled as follows,

$$\tilde{M}_\phi = M_\phi E_d \tau. \tag{F.3}$$

The interface thickness as follows,

$$\tilde{\delta} = \frac{\delta}{L}, \tag{F.4}$$

and the interface energy [J.m^{-2}] as follows,

$$\tilde{\gamma} = \frac{\gamma}{E_d L}. \tag{F.5}$$

Chemical free energy curvatures and diffusivities

The chemical free energy densities k [J.m^{-3}] are scaled as follows,

$$\tilde{k} = \frac{k}{E_d}. \tag{F.6}$$

The diffusivities D in [m^2.s^{-1}] are scaled as follows,

$$\tilde{D} = \frac{D\tau}{L^2}. \tag{F.7}$$

Mechanical parameters, elasticity and plasticity

The Young modulus E in [J.m^{-3}] are scaled as follows,

$$\tilde{E} = \frac{E}{E_d}. \tag{F.8}$$

Hardenings – Q and c – in [J.m^{-3}], here H are scaled as follows,

$$\tilde{H} = \frac{H}{E_d}. \tag{F.9}$$

Yield stresses in [J.m^{-3}] – R_0 and τ_0, here R are scaled:

$$\tilde{R} = \frac{R}{E_d}. \tag{F.10}$$

Viscosity parameters can be expressed in two ways – with the parameter A or the parameter K:

$$\dot{\varepsilon}_p = A\sigma^n = \left(\frac{\sigma}{K}\right)^n, \tag{F.11}$$

The parameter A [(J.m^{-3})$^{-n}$.s^{-1}] is scaled as follows,

$$\tilde{A} = AE_d^n T. \tag{F.12}$$

The parameter K [J.m^{-3}.s$^{1/n}$] is scaled as follows,

$$\tilde{K} = K\frac{1}{E_d}\frac{1}{T^{1/n}}. \tag{F.13}$$

F.4 Examples

F.4.1 Diffusion

The constant source problem is defined by a prescribed concentration c_0 – here $c_0 = 0.2$ – at the free surface of a semi-infinite substrate, initially empty of the considered chemical component. The component will then diffuse into the substrate following the analytic solution provided in [Crank, 1975, Eq 3.13]:

$$c(x,t) = c_0 \operatorname{erfc}\left(\frac{x}{2\sqrt{Dt}}\right), \tag{F.14}$$

where D is the diffusivity of the chemical component in the substrate. In the following, simulations are performed on the basis of realistic physical parameters, see Fig. F.1:

Table F.2: Physical parameters for the constant source problem.

l' [nm]	l'' [s]	k [GJ.m^{-3}]	D [m^2.s^{-1}]
1500	$500 \times l'$	1	5.6e-12

The nondimensionalisation is performed following the above section. The simulation results brought back to the physical quantities are then illustrated in Fig. F.3 and compared with the analytic solution.

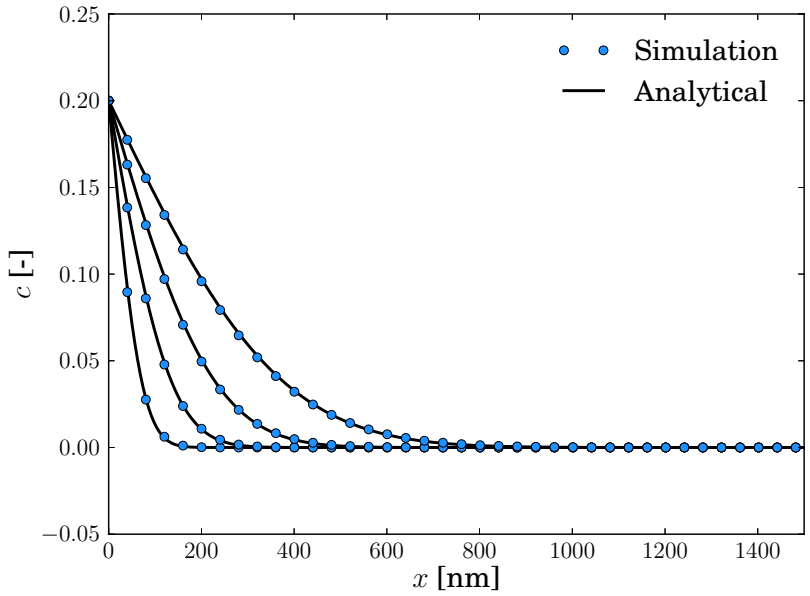

Figure F.2: Illustration of the nondimensionalised calculation versus the analytic solution of the constant source problem at different time steps.

Simulations with physical parameters did not passed the first increment hence emphasising the need for scaling.

F.4.2 Phase growth

The parabolic growth kinetics rules found in Appendix A, within which all details about the problem are given. Nondimensionalised simulations have been performed in Chapter 4 and the resulting growth rate were in accordance with the analytic ones. Therefore, it is not necessary to reproduce the results here.

F.4.3 Viscoplasticity

The present case is devoted to the case of viscoplastic stress relaxation. A phase is here put under compression by prescribing the top and bottom surfaces with zero displacements along with a non zero eigenstrain. The compressive stresses are then relaxed with a Norton law or power-law creep flow rule, see Eq. (4.21) for instance:

$$\dot{\underset{\sim}{\boldsymbol{\varepsilon}}}_p = \left\langle \frac{\sigma_{\mathrm{VM}} - R_0}{K} \right\rangle^n \sqrt{\frac{3}{2}} \frac{\underset{\sim}{\boldsymbol{\sigma}}_{\mathrm{dev}}}{\sqrt{\underset{\sim}{\boldsymbol{\sigma}}_{\mathrm{dev}} : \underset{\sim}{\boldsymbol{\sigma}}_{\mathrm{dev}}}}. \tag{F.15}$$

The chosen parameters are given in Table F.3.

Table F.3: Parameters for the power-law creep of the oxide.

K [MPa.s$^{1/n}$]	n [-]	R_0 [MPa]
7738	5	0

The eigenstrain in the phase is set to:

$$\underset{\sim}{\boldsymbol{\varepsilon}}_{\star}^{\mathrm{Cr_2O_3}} = \begin{pmatrix} 0. & & \\ & 0.01 & \\ & & 0. \end{pmatrix}. \tag{F.16}$$

Compressive stresses are then generated from the boundary conditions. Two cases are considered, one with nondimensionalisation an one without it for the reference case. The simulation results are illustrated in Fig. F.3.

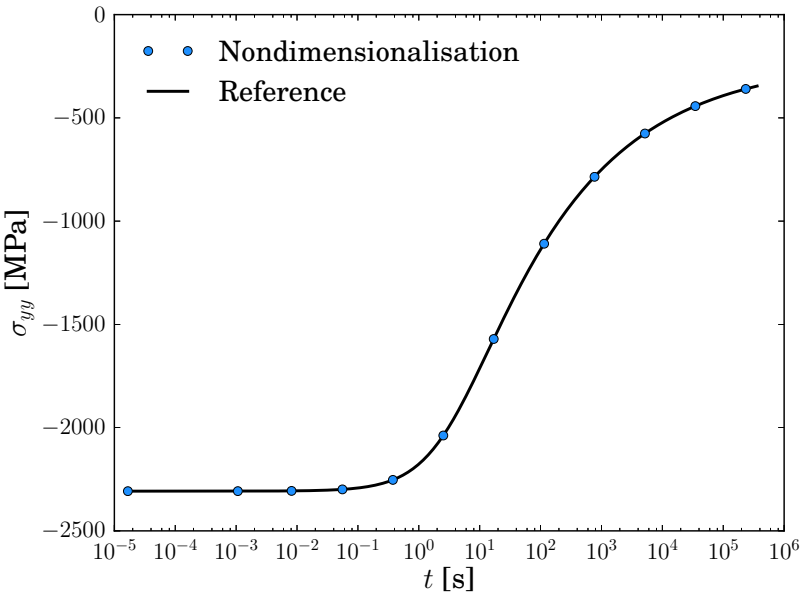

Figure F.3: Simulation results for both the nondimensionalised and reference cases.

The procedure for the nondimensionalisation is hence validated for viscoplasticity, diffusion and phase transformation.

APPENDIX

G Bicrystal finite element mesh

Contents

The finite element mesh for grain boundary oxidation is illustrated in Fig. G.1

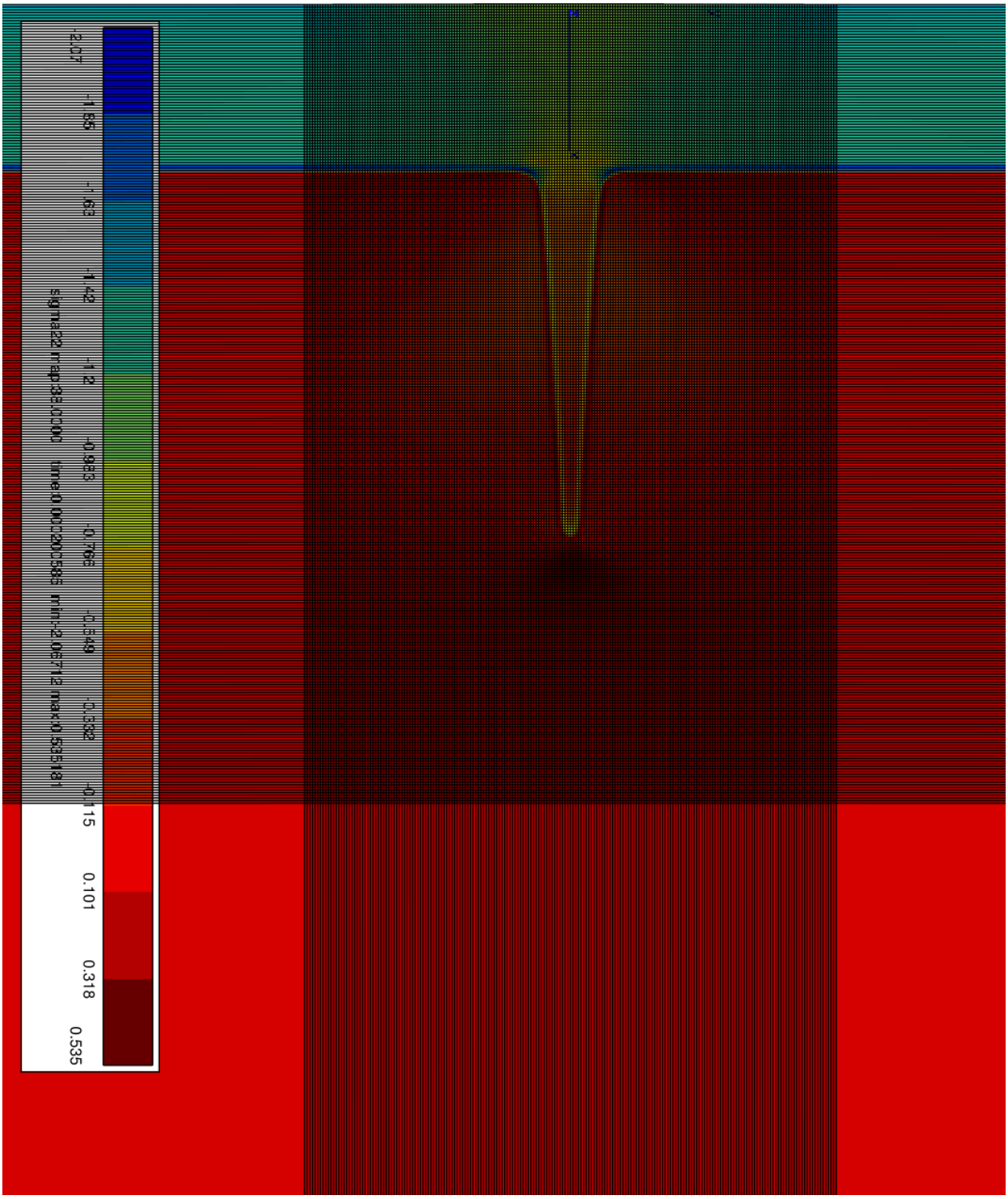

Figure G.1: Partial view of the finite element mesh used in the grain boundary oxidation.

APPENDIX

H Scripts

Contents

H.1 Elastic energy at zero strain

```
#!/usr/bin/env python

from scipy import *
import matplotlib.pyplot as plt

from matplotlib import rc
rc('font',**{'family':'times', 'weight':'normal', 'size':11})
rc('text', usetex=True)

### phase alpha
E_alpha = 210.
v_alpha = 0.3

lambda_alpha = E_alpha * v_alpha / ( (1. + v_alpha) * (1. - 2.* v_alpha) )
mu_alpha = E_alpha / ( 2. * (1. + v_alpha) )

Lambda_alpha = lambda_alpha + 2. * mu_alpha

### phase beta
E_beta = 210.
v_beta = 0.3

lambda_beta = E_beta * v_beta / ( (1. + v_beta) * (1. - 2.* v_beta) )
mu_beta = E_beta / ( 2. * (1. + v_beta) )

Lambda_beta = lambda_beta + 2. * mu_beta

### eigenstrain
delta_x = 0.01
delta_y = 0.01
delta_z = 0.

#####

def eps_xx_alpha(z):
    return (1.-z) * (lambda_alpha * (delta_x + delta_y + delta_z) + 2. * mu_alpha * delta_x ) / ( (1.-z) * Lambda_alpha + z * Lambda_beta)

def eps_xx_beta(z):
    return - z * (lambda_alpha * (delta_x + delta_y + delta_z) + 2. * mu_alpha * delta_x ) / ( (1.-z) * Lambda_alpha + z * Lambda_beta)

def sigma_xx_alpha(z):
    return lambda_alpha * (eps_xx_alpha(z) - delta_x - delta_y - delta_z) + 2. * mu_alpha * (eps_xx_alpha(z) - delta_x)

def sigma_yy_alpha(z):
    return lambda_alpha * ( eps_xx_alpha(z) - delta_x - delta_y - delta_z) - 2. * mu_alpha * delta_y

def sigma_zz_alpha(z):
    return lambda_alpha * ( eps_xx_alpha(z) - delta_x - delta_y - delta_z) - 2. * mu_alpha * delta_z
```

```
def sigma_xx_beta(z):
    return lambda_beta * eps_xx_beta(z) + 2. * mu_alpha * eps_xx_beta(z)

def sigma_yy_beta(z):
    return lambda_beta * eps_xx_beta(z)

def sigma_zz_beta(z):
    return lambda_beta * eps_xx_beta(z)

def f_e_alpha(z):
    return 0.5 * ( sigma_xx_alpha(z) * (eps_xx_alpha(z) - delta_x) - sigma_yy_alpha(z) * delta_y - sigma_zz_alpha(z) * delta_z )

def f_e_beta(z):
    return 0.5 * ( sigma_xx_beta(z) * eps_xx_beta(z) )

def F(z):
    return z * f_e_alpha(z) + (1.-z) * f_e_beta(z)

fig = plt.figure()
ax = fig.add_subplot(111, axisbg='GhostWhite')

X = linspace(0., 1., 100)

plt.xlabel(r'$z$')
plt.ylabel(r'$f_e$ \hspace{1ex} [\mbox{GPa}]')

plt.plot(X, F(X), color='DodgerBlue', label='homogeneous elasticity')
plt.axvline(x=0.5, linestyle='--', color='Black')

### phase alpha
E_alpha = 210.
v_alpha = 0.3

lambda_alpha = E_alpha * v_alpha / ( (1. + v_alpha) * (1. - 2.* v_alpha) )
mu_alpha = E_alpha / ( 2. * (1. + v_alpha) )

Lambda_alpha = lambda_alpha + 2. * mu_alpha

### phase beta
E_beta = 130.
v_beta = 0.3

lambda_beta = E_beta * v_beta / ( (1. + v_beta) * (1. - 2.* v_beta) )
mu_beta = E_beta / ( 2. * (1. + v_beta) )

Lambda_beta = lambda_beta + 2. * mu_beta

plt.plot(X, F(X), color='DarkRed', label='heterogeneous elasticity')

handles, labels = ax.get_legend_handles_labels()
ax.legend(handles[::-1], labels[::-1], frameon=True, loc='best')

plt.grid()

plt.savefig('elastic_energy_zero_av_strain.pdf', format='pdf')
```

H.2 Elastic energy at zero stress

```
#!/usr/bin/env python

from scipy import *
import matplotlib.pyplot as plt

from matplotlib import rc
rc('font',**{'family':'times', 'weight':'normal', 'size':11})
rc('text', usetex=True)

### phase alpha
E_alpha = 210.
v_alpha = 0.3

lambda_alpha = E_alpha * v_alpha / ( (1. + v_alpha) * (1. - 2.* v_alpha) )
mu_alpha = E_alpha / ( 2. * (1. + v_alpha) )

Lambda_alpha = lambda_alpha + 2. * mu_alpha

### phase beta
E_beta = 210.
v_beta = 0.3

lambda_beta = E_beta * v_beta / ( (1. + v_beta) * (1. - 2.* v_beta) )
mu_beta = E_beta / ( 2. * (1. + v_beta) )

Lambda_beta = lambda_beta + 2. * mu_beta

### eigenstrain
delta_x = 0.01
delta_y = 0.01
delta_z = 0.

#####

def eps_yy(z):
    return (z * mu_alpha * (delta_y + delta_z) ) / ( z*mu_alpha + (1.-z)*mu_beta )

def eps_xx_alpha(z):
    return lambda_alpha / Lambda_alpha * (delta_x + delta_y + delta_z - eps_yy(z)) + 2. * mu_alpha * delta_x / Lambda_alpha
```

```
def eps_xx_beta(z):
    return - lambda_beta / Lambda_beta * eps_yy(z)

def sigma_yy_alpha(z):
    return lambda_alpha * ( eps_xx_alpha(z) + eps_yy(z) - delta_x - delta_y - delta_z) + 2. * mu_alpha * (eps_yy(z) - delta_y)

def sigma_zz_alpha(z):
    return lambda_alpha * ( eps_yy(z) + eps_xx_alpha(z) - delta_x - delta_y - delta_z) - 2. * mu_alpha * delta_z

def sigma_zz_beta(z):
    return lambda_beta * ( eps_yy(z) + eps_xx_beta(z))

def sigma_yy_beta(z):
    return lambda_beta * ( eps_yy(z) + eps_xx_beta(z) ) + 2. * mu_beta * eps_yy(z)

def f_e_alpha(z):
    return 0.5 * ( sigma_yy_alpha(z) * (eps_yy(z) - delta_y) - sigma_zz_alpha(z) * delta_z )

def f_e_beta(z):
    return 0.5 * ( sigma_yy_beta(z) * eps_yy(z) )

def F(z):
    return z * f_e_alpha(z) + (1.-z) * f_e_beta(z)

fig = plt.figure()
ax = fig.add_subplot(111, axisbg='GhostWhite')

X = linspace(0., 1., 100)

plt.xlabel(r'$z$')
plt.ylabel(r'$f_e$ \hspace{1ex} [\mbox{GPa}]')

plt.plot(X, F(X), color='DodgerBlue', label='homogeneous elasticity')
plt.axvline(x=0.5, linestyle='--', color='Black')

### phase alpha
E_alpha = 210.
v_alpha = 0.3

lambda_alpha = E_alpha * v_alpha / ( (1. + v_alpha) * (1. - 2.* v_alpha) )
mu_alpha = E_alpha / ( 2. * (1. + v_alpha) )

Lambda_alpha = lambda_alpha + 2. * mu_alpha

### phase beta
E_beta = 130.
v_beta = 0.3

lambda_beta = E_beta * v_beta / ( (1. + v_beta) * (1. - 2.* v_beta) )
mu_beta = E_beta / ( 2. * (1. + v_beta) )

Lambda_beta = lambda_beta + 2. * mu_beta

plt.plot(X, F(X), color='DarkRed', label='heterogeneous elasticity')

handles, labels = ax.get_legend_handles_labels()
ax.legend(handles[::-1], labels[::-1], frameon=True, loc='best')

plt.grid()

plt.savefig('elastic_energy_zero_av_stress.pdf', format='pdf')
```

H.3 Computation of the final phase fraction for the zero average strain case

```
#!/usr/bin/env python

from sympy import *

a = 0.33
b = 0.

delta_x = 0.01
delta_y = 0.01
delta_z = 0.

bar_delta = delta_x + delta_y + delta_z

E_alpha = 60.
E_beta = 50.

v_alpha = 0.3
v_beta = 0.3

lambda_alpha = E_alpha * v_alpha / ( (1. + v_alpha) * (1. - 2.* v_alpha) )
mu_alpha = E_alpha / ( 2. * (1. + v_alpha) )

lambda_beta = E_beta * v_beta / ( (1. + v_beta) * (1. - 2.* v_beta) )
mu_beta = E_beta / ( 2. * (1. + v_beta) )

Lambda_alpha = lambda_alpha + 2.*mu_alpha
Lambda_beta = lambda_beta + 2.*mu_beta

k_alpha = 100.
k_beta = 1.

z = symbols('z', real=True)
```

```
bar_z = 1.-z

alpha = lambda_alpha * bar_delta + 2.*mu_alpha*delta_x

eps_xx_alpha = bar_z * alpha / ( bar_z * Lambda_alpha + z * Lambda_beta )
eps_xx_beta = - z * alpha / ( bar_z * Lambda_alpha + z * Lambda_beta )

sig_xx = lambda_alpha * ( eps_xx_alpha - bar_delta ) + 2.*mu_alpha*(eps_xx_alpha - delta_x)
sig_yy_alpha = lambda_alpha * ( eps_xx_alpha - bar_delta ) - 2.*mu_alpha*delta_y
sig_zz_alpha = lambda_alpha * ( eps_xx_alpha - bar_delta ) - 2.*mu_alpha*delta_z

sig_yy_beta = lambda_beta * eps_xx_beta
sig_zz_beta = lambda_beta * eps_xx_beta

delta_fe = 0.5 * ( sig_xx * ( eps_xx_alpha - eps_xx_beta - delta_x ) - sig_yy_alpha * delta_y - sig_zz_alpha * delta_z ) / ( b - a )
sigma_delta_eps = sig_xx  * (eps_xx_alpha - eps_xx_beta)

Gamma = - 0.5 * ( sig_xx * ( eps_xx_alpha - eps_xx_beta + delta_x ) + sig_yy_alpha * delta_y + sig_zz_alpha * delta_z ) / ( b - a )
# in the case of kais' thesis, ~p.84?
#Gamma = 0.5 * ( sig_xx * ( eps_xx_alpha - eps_xx_beta - delta_x ) - sig_yy_alpha * delta_y - sig_zz_alpha * delta_z ) / ( b - a )

#stress = False
stress = True

if stress:
    c_alpha = a - Gamma/k_alpha
    c_beta = b - Gamma/k_beta
else:
    c_alpha = a
    c_beta = b

f_ini = 0.1
c0 = 0.33 * f_ini + 0.33/6. * (1.-f_ini)

expr = z * c_alpha + bar_z * c_beta - c0

print '\n'
print '========== result =========='
expr = simplify(expr)
print "the expression to be solved : ", expr
print solve(expr)
```

H.4 Extrapolation within the diffuse interface

```
#!/usr/bin/env python

# this scripts allows to extrapolate the values of a field within the interface
# the plot must be examinated in order to evaluate the acceptability of the approximation and in order to further tune the programm

import numpy as np
import matplotlib.pyplot as plt

from scipy.optimize import curve_fit

from matplotlib import rc
rc('font',**{'family':'times', 'weight':'normal', 'size':11})
rc('text', usetex=True)

import sys

# first load the fields extracted on a line
x, phi, field = np.loadtxt(sys.argv[1], unpack=True, usecols=[1, 3, 4])

# extract the part of interest
x = x[int(len(x)/2)::]
phi = phi[int(len(phi)/2)::]
field = field[int(len(field)/2)::]

# functions used for the interpolation of the phase field field and the interpolation of the field of interest
def phi_func(x, x0, delta):
    return 0.5*(1.-np.tanh((x-x0)/delta))

def field_func(x, a, b, c):
    return a + b*x + c*x**2

# fit the phase field and find the position of the interface
popt, pcov = curve_fit(phi_func, x, phi)
Interface_pos = popt[0]

# separate the left hand side and right hand side values of the field of interest, 20 points is an arbitrary value that can be tuned
phi_max_index = (np.abs(phi-0.95)).argmin()
phi_min_index = (np.abs(phi-0.05)).argmin()

XL = max(0,phi_max_index-20)
XR = min(int(len(x)), phi_min_index+20)

x_left = x[XL:phi_max_index]
field_left = field[XL:phi_max_index]

x_right = x[phi_min_index:XR]
field_right = field[phi_min_index:XR]

# optimise the field of interest on the chosen function and find interface values
popt_left, pcov_left = curve_fit(field_func, x_left, field_left)
popt_right, pcov_right = curve_fit(field_func, x_right, field_right)

left_value = field_func(Interface_pos, popt_left[0], popt_left[1], popt_left[2])
right_value = field_func(Interface_pos, popt_right[0], popt_right[1], popt_right[2])
```

```
# plot to check
fig = plt.figure()
ax  = fig.add_subplot(111, axisbg='GhostWhite')

plt.plot(x, field, color='Black')
plt.axvline(x=Interface_pos, color='Black', linestyle='--')

plt.plot(x_left, field_left, marker='o', color='DodgerBlue')
plt.plot(x_right, field_right, marker='o', color='DarkRed')

plt.plot(x, field_func(x, popt_left[0], popt_left[1], popt_left[2]), linestyle='--', color='DodgerBlue')
plt.plot(Interface_pos, left_value, marker='s', color='DodgerBlue')

plt.plot(x, field_func(x, popt_right[0], popt_right[1], popt_right[2]), linestyle='--', color='DarkRed')
plt.plot(Interface_pos, right_value, marker='s', color='DarkRed')

delta = popt[1] * np.log(0.95/0.05)
plt.axvspan(Interface_pos - delta/2., Interface_pos + delta/2., color='red', alpha=0.5)

plt.grid()
plt.xlabel(r'normalized distance')
plt.ylabel(r'concentration')

# global check
#plt.show()

# zoom into the region of interest
values_jump = np.abs(left_value - right_value)
plt.xlim(min(x_left), max(x_right))
plt.ylim(min(left_value, right_value)-0.1*values_jump, max(left_value, right_value)+0.1*values_jump)

# local check
plt.show()

print left_value, right_value

exit()
```

H.5 Operative tie-line and growth rates

```
#!/usr/bin/env python

import numpy as np

from scipy import special, sqrt, exp
from scipy.optimize import fsolve

import matplotlib.pyplot as plt
from matplotlib import rc
rc('font',**{'family':'times', 'weight':'normal', 'size':11})
rc('text', usetex=True)
rc('axes', labelsize=20)
rc('xtick', labelsize=14)
rc('xtick.major', pad=6)
rc('ytick', labelsize=14)
rc('ytick.major', pad=6)

## quadratic free energy potential
def fm(x, y, k1, k2, c1, c2):
    return 0.5*(k1*(x-c1)**2 + k2*(y-c2)**2)

## chemical potentials
def mu_1(x, y, k1, k2, c1, c2):
    return fm(x, y, k1, k2, c1, c2) + ( k1*(x-c1)*(1-x) - k2*(y-c2)*y )

def mu_2(x, y, k1, k2, c1, c2):
    return fm(x, y, k1, k2, c1, c2) + ( -k1*(x-c1)*x + k2*(y-c2)*(1-y) )

def mu_3(x, y, k1, k2, c1, c2):
    return fm(x, y, k1, k2, c1, c2) + ( -k1*(x-c1)*x - k2*(y-c2)*y )

## transcendental function
def F(x):
    return sqrt(3.14)*x*special.erfc(x)*exp(x**2)

# supersaturations
def Omega_1(x, a, b):
    return (x - b)/(a-b)

def Omega_2(x, a, b):
    return (x - a)/(a-b)

## local equilibrium (kinetic condition (1 Eq.) + chemical equilibrium (3 Eqs.))
def equilibre_local(p, arg):
    c1_alpha, c2_alpha, c1_beta, c2_beta = p
    k1_alpha, k2_alpha, k1_beta, k2_beta, a1, a2, b1, b2, D1_beta, D2_alpha, c1_beta_s, c2_beta_s= arg
    return (F( sqrt( 0.5 * (D2_alpha / D1_beta) * Omega_2(c2_beta_s, c2_alpha, c2_beta))) - Omega_1(c1_beta_s, c1_alpha, c1_beta),
            mu_1(c1_alpha, c2_alpha, k1_alpha, k2_alpha, a1, a2) - mu_1(c1_beta, c2_beta, k1_beta, k2_beta, b1, b2),
            mu_2(c1_alpha, c2_alpha, k1_alpha, k2_alpha, a1, a2) - mu_2(c1_beta, c2_beta, k1_beta, k2_beta, b1, b2),
            mu_3(c1_alpha, c2_alpha, k1_alpha, k2_alpha, a1, a2) - mu_3(c1_beta, c2_beta, k1_beta, k2_beta, b1, b2))

## inverse of the transcendental function
def inverse_F(p, arg):
    return F(p) - arg

##### parameters
k1_alpha=100.
```

```
k1_beta=1.

k2_alpha=100.
k2_beta=100.

a1 = 0.33
a2 = 0.5

b1 = 0.01
b2 = 0.01

D2_alpha = 0.8
D1_beta =  5.6

c1_beta_s = 0.16
c2_beta_s = 0.67
###################

## initial diffusiviy ratio
R_ref = D2_alpha / D1_beta

## list of ratios
     listf = [R_ref, 0.3, 0.4, 0.5, 0.6, 0.7, 0.8, 0.9, 1., 1.1, 1.2, 1.3, 1.4, 1.5, 1.6, 1.7, 1.8, 1.9, 2., 2.1, 2.2, 2.3, 2.4, 2.5, 2.6, 2.7,
→    2.8, 2.9, 3., 3.1, 3.2, 3.3, 3.4, 3.5, 3.6, 3.7, 3.8, 3.9, 4., 4.1, 4.2, 4.3, 4.4, 4.5, 4.6, 4.7, 4.8, 4.9, 5, 5.1, 5.2, 5.3, 5.4, 5.5, 5.6,
→    5.7, 5.8, 5.9, 6]

L = len(listf)

## rate constants
K_O = []
K_CR = []

##### first plot
fig = plt.figure()
ax = fig.add_subplot(111)

cm = plt.get_cmap('autumn')

## find the operative tie-line
→     c1_alpha, c2_alpha, c1_beta, c2_beta  = fsolve(equilibre_local, (a1, a2, 0.11, 0.), args=([k1_alpha, k2_alpha, k1_beta, k2_beta, a1, a2, b1,
→    b2, D1_beta, D2_alpha, c1_beta_s, c2_beta_s]))

## plot some equilibrium concentrations (2 amongst 4)
plt.plot(R_ref, c1_beta, marker='o', color='black', label='Cr')
plt.plot(R_ref, c2_alpha, marker='^', color='black', label='O')

## calculate the supersaturation for the reference ratio
Omega_O = (0.67-c2_alpha)/(c2_alpha-c2_beta)
Omega_Cr = (0.16-c1_beta)/(c1_alpha-c1_beta)

## find the variable of similitude
S_simi = fsolve(inverse_F, (0.5), args=(Omega_Cr))

## append the growth rate
K_O.append(2.*D2_alpha*Omega_O)
K_CR.append(4.*D1_beta*S_simi**2)

# first guess for the chromium concentration
AA = 0.11

## plot a approximative ratio range of negative chromium equilibrium concentrations
plt.axvspan(0.9, 10., color='gray', alpha=0.3)

## find all tie-lines for all remaining ratios
for i in range(L):
    ## modify the chromium diffusivity with respect to the considered ratio
    D1_beta =  D2_alpha / listf[i]

    ## solve the tie-line
→         c1_alpha, c2_alpha, c1_beta, c2_beta  = fsolve(equilibre_local, (a1, a2, AA, 0.), args=([k1_alpha, k2_alpha, k1_beta, k2_beta, a1, a2,
→    b1, b2, D1_beta, D2_alpha, c1_beta_s, c2_beta_s]))

    ## modify the first guess for the next tie-line
    AA = c1_beta

    ## plot some equilibrium concentrations
    plt.plot(D2_alpha/D1_beta, c1_beta, marker='o', color=cm(i/(float(L))))
    plt.plot(D2_alpha/D1_beta, c2_alpha, marker='^', color=cm(i/(float(L))))

    ## calculate the supersaturations
    Omega_O = (0.67-c2_alpha)/(c2_alpha-c2_beta)
    Omega_Cr = (0.16-c1_beta)/(c1_alpha-c1_beta)

    ## deduce the variable of similitude
    S_simi = fsolve(inverse_F, (0.5), args=(Omega_Cr))

    ## and append the rate constant
    K_O.append(2.*D2_alpha*Omega_O)
    K_CR.append(4.*D1_beta*S_simi**2)

## legend stuff
handles, labels = ax.get_legend_handles_labels()
ax.legend(handles[::-1], labels[::-1], frameon=False, loc='best')

plt.xlabel(r'r')
plt.ylabel(r'interface concentration')

plt.xlim(0., 6.)

fig.savefig('local_equilibrium_chromium_depletion.pdf', format='pdf')

plt.close('all')
```

```
##########

## convert the list of growth rates to numpy arrays
K_O = np.array(K_O)
K_CR = np.array(K_CR)

## convert them to micrometers**2.s-1
K_O *= 0.00001 * 3600.
K_CR *= 0.00001 * 3600.

## save them in a file
file = open('rate_constant.txt', 'w')

## plot of the growth rates with respect to the ratios for the two components
fig = plt.figure()
ax = fig.add_subplot(111)

cm = plt.get_cmap('autumn')

## restore the first ratio
D1_beta = 5.6

## plot the first growth rates
plt.plot(D2_alpha/D1_beta, K_O[0], marker='o', color='black', label='Cr')
plt.plot(D2_alpha/D1_beta, K_CR[0], marker='^', color='black', label='O')

## plot the gray domain (approximately)
plt.axvspan(0.9, 10., color='gray', alpha=0.3)

## plot all growth rates
for i in range(L):
    ## calculate the diffusivity of chromium
    D1_beta =  D2_alpha / listf[i]

    ## plot the growth rates
    plt.plot(D2_alpha/D1_beta, K_O[i], marker='o', color=cm(i/(float(L))))
    plt.plot(D2_alpha/D1_beta, K_CR[i], marker='^', color=cm(i/(float(L))))

    ## store the growth rate in a file
    file.write(str(D2_alpha/D1_beta)+'\t'+str(K_O[i])+'\t'+str(K_CR[i])+'\n')

## no comment
file.close()

## plotting stuff
plt.axvline(x=4.6, linestyle='--', color='black')
plt.text(4.6, 0.007, r'$r_{\mbox{\tiny trans.}}$', size=16)

handles, labels = ax.get_legend_handles_labels()
ax.legend(handles[::-1], labels[::-1], frameon=False, loc='best')

plt.xlabel(r'r')
plt.ylabel(r'rate constant [\textmu m\textsuperscript{2}.h\textsuperscript{-1}]')

plt.xlim(0., 6.)
#plt.ylim(0.008, 0.026)

fig.savefig('local_equilibrium_chromium_depletion_rate_constants.pdf', format='pdf')

plt.close('all')
```

References

[Ammar, 2010] Ammar, K. (2010). *Modelling and simulation of phase transformation-mechanics coupling using a phase field method*. PhD thesis, Mines ParisTech.

[Ammar et al., 2009] Ammar, K., Appolaire, B., Cailletaud, G., Feyel, F., and Forest, S. (2009). Finite element formulation of a phase field model based on the concept of generalized stresses. *Computational Materials Science*, 45(3):800 – 805.

[Bhadeshia, 1985] Bhadeshia, H. (1985). *Diffusional formation of ferrite in iron and its alloys*. Progress in materials science. Pergamon Press.

[Cahn and Larché, 1984] Cahn, J. and Larché, F. (1984). A simple model for coherent equilibrium. *Acta Metallurgica*, 32(11):1915 – 1923.

[Crank, 1975] Crank, J. (1975). *The mathematics of diffusion*. Clarendon press, Oxford, 2 edition.

[Fehlner and Mott, 1970] Fehlner, N. and Mott, N. (1970). Oxidation in the thin film range. In *Oxidation of Metals and Alloys*.

[Huntz et al., 2007] Huntz, A., Reckmann, A., Haut, C., Sévérac, C., Herbst, M., Resende, F., and Sabioni, A. (2007). Oxidation of AISI 304 and AISI 439 stainless steels. *Materials Science and Engineering: A*, 447(1–2):266–276.

[Johnson, 2000] Johnson, W. (2000). Superficial stress and strain at coherent interfaces. *Acta Materialia*, 48(2):433 – 444.

[Johnson and Voorhees, 1987] Johnson, W. and Voorhees, P. (1987). Phase equilibrium in two-phase coherent solids. *Metallurgical Transactions A*, 18(7):1213–1228.

[Kim et al., 1998] Kim, S., Kim, W., and Suzuki, T. (1998). Interfacial compositions of solid and liquid in a phase-field model with finite interface thickness for isothermal solidification in binary alloys. *Phys. Rev. E*, 58:3316–3323.

[Kim et al., 1999] Kim, S., Kim, W., and Suzuki, T. (1999). Phase-field model for binary alloys. *Phys. Rev. E*, 60:7186–7197.

[Kofstad, 1972] Kofstad, P. (1972). *Nonstoichiometry, Diffusion, and Electrical Conductivity in Binary Metal Oxides*. Wiley - Interscience.

[Larché and Cahn, 1973] Larché, F. and Cahn, J. (1973). A linear theory of thermochemical equilibrium of solids under stress. *Acta Metallurgica*, 21:1051–1063.

[Larché and Cahn, 1978] Larché, F. and Cahn, J. (1978). Thermochemical equilibrium of multiphase solids under stress. *Acta Metallurgica*, 26:1579–1589.

[Larché and Cahn, 1985] Larché, F. and Cahn, J. (1985). Overview no. 41 the interactions of composition and stress in crystalline solids. *Acta Metallurgica*, 33(3):331 – 357.

[Lee and Tao, 1994] Lee, J. and Tao, W. (1994). Coherent phase equilibria: Effect of composition-dependent elastic strain. *Acta Metallurgica et Materialia*, 42(2):569 – 577.

[Sabioni et al., 2005] Sabioni, A., Huntz, A., Silva, F., and Jomard, F. (2005). Diffusion of iron in Cr_2O_3: polycrystals and thin films. *Materials Science and Engineering: A*, 392(12):254 – 261.

Modélisation de l'oxydation des aciers 316 polycristallins par une approche en champs de phases couplée avec la mécanique

Les aciers austénitiques et alliages à base de nickel sont des matériaux de choix pour leurs propriétés mécaniques à haute température. L'enrichissement en chrome améliore leur durabilité de par la formation d'une couche d'oxyde protectrice à l'exemple de la chromine (Cr_2O_3). Il est néanmoins établi, par des essais mécaniques sous vide, que l'oxydation réduit de manière notable leur durée de vie en fatigue. En effet, la croissance d'oxyde peut être accompagnée d'une introduction de défauts tels que l'injection de lacunes, d'éléments délétères comme l'hydrogène mais également de contraintes résiduelles, *etc.*, dans le métal. Les micromécanismes de fissuration sont ainsi régis par des interactions complexes entre l'environnement et la surface du métal, faisant intervenir composition chimique et microstructure.

Aujourd'hui, les enjeux de sécurité et de compétitivité font de la prévision de la durée de vie de ces alliages une nécessité pour l'industrie nucléaire. L'augmentation de la dimension des modèles permet de prendre en compte de manière explicite les interactions multiphysiques du couple oxyde/métal sous l'action d'un chargement mécanique. La thèse s'inscrit dans cette démarche et propose une formulation d'un modèle de champs de phases couplé avec la mécanique et fondé sur les principes de la thermodynamique des milieux continus. Le comportement effectif de l'interface est présentement obtenu *via* des méthodes d'homogénéisation permettant de combiner des comportements mécaniques dissemblables, à l'image d'un substrat ductile et de son oxyde fragile. Les contraintes induites par la formation d'oxyde et également par le chargement mécanique peuvent être relaxées viscoplastiquement, de manière isotrope et anisotrope, respectivement dans l'oxyde et dans le substrat. Des simulations par éléments finis de l'oxydation généralisée ainsi que de l'oxydation intergranulaire sous chargement mécanique sont effectuées. Ces dernières mettent en évidence la possibilité d'un phénomène d'oxydation catastrophique par la génération de contraintes de tensions dans l'oxyde fragile, lesquelles peuvent être localisées le long des intrusions d'oxyde dans les joints de grains.

Mots clés : oxydation, mécanique, polycristal, modélisation, champs de phases, éléments finis

Modelling the oxidation of polycrystalline austenitic stainless steels using a phase field approach coupled with mechanics

Austenitic stainless steels and nickel based alloys are widely used for their mechanical properties at high temperatures. Their durability can be increased by the addition of chromium resulting in the formation of a protective oxide layer such as chromia (Cr_2O_3). Nevertheless, it is established from vacuum mechanical tests that oxidation significantly decreases their fatigue life. In fact, oxide growth can be followed with the injection of defects such as vacancies, deleterious chemical elements and residual stresses, *etc.*, into the metal. The resulting cracking micromechanisms are therefore governed by complex interactions between the environment and the metal surface, implying the chemical composition and the microstructure of the metal.

To date, materials life prediction is a necessity for the nuclear industry due to safety and economic issues. The enhancement of the model dimensionality allows to explicitly account for multi-physics interactions between oxide and metallic phases under mechanical loads. The thesis is in line with it and relies on the development of a phase field model coupled with mechanics that heavily relies on the principles of continuum thermodynamics. The effective behaviour of the interface is obtained by homogenisation methods allowing the mixture of separate behaviours, as it is the case on a ductile metallic substrate and its fragile oxide. Oxide growth residual stresses and mechanical load induced stresses can be relaxed by viscoplasticity, which is isotropic and anisotropic respectively for the oxide and the substrate. Full field finite element simulations are performed to study both generalised and intergranular oxidation under mechanical loads. The simulations highlight the possibility of triggering breakaway oxidation by the generation of tensile stresses in the fragile oxide, which can be localised along oxide intrusions at grain boundaries.

Keywords: oxidation, mechanics, polycrystal, modeling, phase field, finite element

MINES ParisTech

ParisTech
INSTITUT DES SCIENCES ET TECHNOLOGIES
PARIS INSTITUTE OF TECHNOLOGY